THE UNIVERSITY OF TULSA
THE GRADUATE SCHOOL

ANALYSIS OF WELL TEST DATA FROM A RESTRICTED-ENTRY WELL UNDER MULTIPHASE FLOW CONDITIONS

by
Randahl Dean Roadifer

A dissertation submitted in partial fulfillment of
the requirements for the degree of Doctor of Philosophy
in the Discipline of Petroleum Engineering
The Graduate School
The University of Tulsa
1995

THE UNIVERSITY OF TULSA

THE GRADUATE SCHOOL

ANALYSIS OF WELL TEST DATA FROM A RESTRICTED-ENTRY WELL UNDER MULTIPHASE FLOW CONDITIONS

by

Randahl Dean Roadifer

A DISSERTATION

APPROVED FOR THE DISCIPLINE OF

PETROLEUM ENGINEERING

By Dissertation Committee

_____, Chairperson

_____

_____

_____

_____

ABSTRACT

Roadifer, Randahl Dean (Doctor of Philosophy in Petroleum Engineering)

Analysis of Well Test Data From a Restricted-Entry Well Under Multiphase Flow Conditions (585 pp. - Chapter IX)

Directed by Dr. Albert C. Reynolds, Jr.

(300 Words)

This work considers the analysis of pressure transient data obtained from a restricted-entry well under multiphase flow conditions. All results presented here were generated by a comprehensive, fully-implicit three-phase coning simulator developed as part of this work.

Semilog analysis of drawdown pressure data obtained from a restricted-entry well under multiphase flow conditions may be uninterpretable if there is movement of the fluid contacts towards the well. This result is true even if there is no production of the coning fluid.

For solution-gas systems overlain by a gas cap and/or underlain by an aquifer, drawdown pressure data often exhibit an apparent semilog straight line suggestive of pseudoradial flow. The total mobility computed from the slope of this semilog straight line, however, does not appear to have a physical interpretation.

For all cases considered in this study, including those cases in which the drawdown pressure data were uninterpretable, standard Horner analysis of the

pseudoradial flow pressure buildup data provides an excellent approximation to the thickness-averaged total mobility in the outer region of the reservoir. A new semi-theoretical procedure for analyzing solution-gas systems is presented.

Results indicate that approximating a gas cap or aquifer as a constant pressure boundary cannot be justified. It is shown that the pressure response obtained from a restricted-entry well in a multiphase reservoir with a constant pressure boundary is fundamentally different from that obtained from a restricted-entry well in a single-phase reservoir.

A pseudoskin correlation is presented for estimating the pseudoskin factor due to restricted-entry in reservoirs with multiple flowing phases. Extensive examples indicate this correlation yields reasonably accurate estimates of the pseudoskin factor for cases in which variations in saturation and fluid properties are small over the course of the well test.

ACKNOWLEDGEMENTS

My utmost appreciation and gratitude are expressed to Dr. Albert C. Reynolds, Jr. for his participation is this work as my advisor and for his guidance and advice during this study. Deep appreciation is also expressed to Dr. Leslie G. Thompson who participated in many helpful discussions during the course of this work. To Dr. Julio C. Diaz I wish to express my sincerest gratitude and appreciation for not only being on my committee, but also for enlightening me in the world of numerical linear algebra and iterative methods. Special thanks are also extended to Dr. Ram G. Agarwal and Dr. Jeff L. Hensley for their helpful suggestions regarding this work and this manuscript.

To Dr. Kaveh Dehghani, I wish to again express my sincere appreciation for all of those wonderful "unsolvable" problems which only required a person to think and to look for a solution from a different viewpoint.

Portions of this work were conducted under the auspices of The University of Tulsa Petroleum Reservoir Exploitation Projects (TUPREP). Financial support was provided in part by a Shell Foundation Fellowship, a Phillips Petroleum Fellowship and Amoco Production Company and are gratefully acknowledged.

Lastly, I dedicate this work to my wonderful wife Carol, whose sacrifices have been many, but without whose support and understanding this work could not have been accomplished. To my sons, Donald and Jeffery: "Daddy's Home!"

TABLE OF CONTENTS

LIST OF TABLES

LIST OF FIGURES

CHAPTER I

INTRODUCTION

In order to delay water and/or gas coning, wells are frequently completed over only a fraction of the productive zone. Wells completed in this manner are referred to as restricted-entry or partially penetrating wells. Important information sought on restricted-entry wells include procedures for the analysis of pressure transient data, the productivity loss caused by restricted entry and whether the well should be stimulated.

Considerable attention has been given to this type of well completion in the literature. Though the reason for completing wells in this manner is due to the existence of multiple phases (oil, gas and water) in the reservoir, the vast majority of studies on this subject consider only the single-phase flow of a slightly compressible fluid of constant compressibility and constant viscosity, e.g., see Refs. 1-21. In addition, the results of Refs. 1-14 are all restricted to homogeneous single-layer reservoirs.

Investigation of the restricted-entry well problem was first performed by Muskat[1] under an assumption of steady-state conditions. If wellbore storage effects and the influence of reservoir boundaries are negligible, pressure data obtained from a partially-penetrating well may exhibit two well defined semilog straight lines. In this case, Bilhartz and Ramey[2] have shown that a comprehensive analysis of the pressure data can be achieved using conventional semilog analysis techniques to obtain estimates of the total flow capacity, kh, the flow capacity

adjacent to the open interval, kh_w, the vertical permeability, k_z, the pseudoskin factor due to restricted-entry, s_b, and the mechanical skin factor, s, caused by damage or stimulation. While Ref. 2 only considered a single-layer reservoir, Yeh and Reynolds[16,18] and Yeh[19] extended their results to multilayer reservoirs. For cases where the first (early time) semilog straight line does not exist, Refs. 16 and 19 presented a type curve analysis procedure which can be combined with semilog analysis of pseudoradial flow pressure data to obtain a complete analysis. Unfortunately, if wellbore storage effects are significant, the first semilog straight line will not be exhibited by pressure data and the type curve analysis procedure of Refs. 16 and 19 will not be applicable.

When the first semilog straight line is not observed, either because it occurs too early in the analysis to be identified or is obscured by wellbore storage effects, analysis of the pressure data is usually based on semilog analysis of pseudoradial flow data or type curve matching. Analysis of the pressure data based on pseudoradial flow yields the total flow capacity and the total skin factor. Estimates of the mechanical skin factor, however, can only be obtained if the pseudoskin factor is known. Numerous correlations for estimating the pseudoskin factor have been presented in the literature for the case of single-layer[1–3,8–12] and multilayer[16–21] reservoirs. A common limitation to all of these correlations is that they require an independent estimate of the vertical permeability, or, of the ratio of the horizontal to vertical permeability. As mentioned previously, Refs. 18 and 19 presented type curves which could be used in conjunction with conventional semilog analysis of the pseudoradial flow data to obtain estimates of the effective vertical permeability, however, these type curves are not applicable when wellbore storage effects are significant.

Type curves for analyzing pressure data obtained from restricted-entry wells and distorted by wellbore storage and skin effects have been developed by several

investigators[7–8,12,14,21]. While the type curves of Refs. 7, 8 and 12 were developed from analytical solutions to the partially-penetrating well problem, the type curves of Ref. 21 were developed by applying a linear transformation to the type curves for fully-penetrating wells. Limitations in the application of these transformed type curves have been noted by several authors[12,14,21]. More specifically, they note that the skin and flow capacity values obtained will deviate more from the correct values as the penetration ratio decreases and the dimensionless wellbore length increases. The type curves of Refs. 7, 8 and 12 are difficult to apply in practice because a separate set of type curves are required for each specified value of penetration ratio[7,8,12], dimensionless wellbore length[12], or dimensionless wellbore storage coefficient[7]. Some of the difficulty in obtaining unique type curve match, however, has been alleviated by the inclusion of the pressure derivatives on the type curves of Refs. 7 and 14. Before leaving this discussion of wellbore storage, it should be noted that if the sandface flow rate is measured or can be computed from estimates of the wellbore storage coefficients, then deconvolution methods based on Duhamel's principle can be used to remove wellbore storage effects from the data[22].

For single-phase homogeneous flow, it is well known[2,3,9,16] that the skin factor computed from the pseudoradial flow semilog straight line represents a total skin factor, s_t given by

$$s_t = \frac{s}{b} + s_b \ , \tag{1.1}$$

where s denotes the mechanical skin factor, s_b the pseudoskin factor due to restricted-entry and $b = h_w/h$ is the penetration ratio.

References 23 and 24 noted that for water-oil systems, the Brons-Marting[3] correlation for s_b did not apply. Reference 35 also showed this correlation did not apply for solution-gas-drive systems. Reynolds et al.[20] developed a correlation

for s_b for two-layer systems and gave a preliminary indication that these results could be modified to compute s_b for oil-water systems. Using the multiphase analog to the penetration ratio suggested by Ref. 20, Refs. 25 and 26 gave preliminary indications that the correlation of Ref. 3 could then be used for oil-water systems and solution-gas-drive systems. References 20, 25 and 26 considered only multiphase reservoir systems with a zero mechanical skin factor.

When horizontal saturation gradients are negligible and there is negligible change in the vertical saturation profile during production, then the multiphase flow situation should be analogous to single-phase flow in a layered reservoir. References 16-21 discuss procedures or solutions that can be used to estimate the pseudoskin factor caused by restricted-entry in layered reservoirs; the results of Refs. 20 and 21 are restricted to two-layer reservoirs. Note that this would restrict the analogy of single-phase flow in a two-layer reservoir to a completely gravity segregated reservoir containing only two-phases. In reality, multiphase reservoirs generally have a transition zone separating segregated phases and in solution-gas systems, vertical and horizontal saturation gradients can develop rapidly within the reservoir. In trying to draw an analogy between multiphase and single phase reservoirs, it would then seem appropriate to draw that analogy with the single-phase multilayer reservoirs. This provided the motivation for Refs. 16-19 which have developed methods for computing the restricted-entry pseudoskin factor in multilayer reservoirs. For practical purposes, the method of Ref. 19 and the method of Ref. 17 yield similar results.

The physical similarities between the single-phase multilayered reservoirs and multiphase single-layer reservoirs also provides the motivation for extending the single-phase multilayer pseudoskin factor correlations of Refs. 16 (also in Ref. 18 and 19) and 17 to the multiphase systems considered in this work. In Chapter VIII we present a correlation[28] for the pseudoskin factor due to restricted-entry

in a multiphase reservoir. Numerical results for the extensive set of two-phase (oil-water, gas-water, oil-gas) and three-phase (oil-gas-water) examples considered in this study are presented and indicate this correlation yields reasonably accurate estimates of the pseudoskin factor for those cases in which variations in saturation and fluid properties are small over the course of the well test. When saturation variations are large and/or pressure dependent fluid properties vary significantly over the course of the well test, numerical results indicate this correlation may result in significant errors. Reference 150 has presented a method for correcting these errors in the damage skin and pseudoskin calculations resulting from the non-linearities due to multiphase flow effects and due to variations in the fluid properties.

References 23-38 have presented much material on the analysis of well test data obtained under multiphase flow conditions, though the results of Refs. 29-38 are restricted to one-dimensional radial flow and the results of Ref. 27 are for a horizontal well. Though Refs. 23-26 and 28 all consider vertical restricted-entry wells, Refs. 23 and 24 consider only oil-water reservoir systems and neglect gravity and capillary pressure effects. References 25 and 26 only consider multiphase reservoir systems in which a single phase is being produced. It should also be noted that while not directly addressing the analysis of well test data obtained under multiphase flow conditions, Refs. 21 and 5-8 assumed that a gas cap or aquifer could be modeled as a constant pressure boundary. The numerical results for all of the multiphase systems considered in this study, however, indicate the practice of approximating a gas cap or aquifer as a constant pressure boundary cannot be justified. In addition, we show through a series of numerical examples that the pressure response (pressure derivative) obtained for a well producing a multiphase reservoir containing a constant pressure boundary is fundamentally different from the pressure response obtained for a single-phase reservoir. We

discuss our numerical results as they relate to the constant pressure boundary assumption in more detail in Chapter V.

Because our new pseudoskin factor correlation is dependent upon the analysis of pressure transient data obtained under multiphase flow conditions, we must first consider procedures for that analysis. In Chapter VI we discuss the conditions under which semilog analysis of drawdown pressure transient data can be performed and procedures for that analysis are discussed. We show that semilog analysis of drawdown pressure data obtained from a restricted-entry well under multiphase flow conditions may be uninterpretable if there is movement of the fluid contacts towards the well, i.e., building of a water or gas cone. Note that this result is true even if there is no production of the coning fluid. For solution-gas systems overlain by a gas cap and/or underlain by an aquifer, we show that drawdown pressure data often exhibit an apparent semilog straight line suggestive of pseudoradial flow, however, we have been unable to provide a physical interpretation for the total mobility computed from the slope of this semilog straight line.

In Chapter VII we examine the analysis of pressure buildup data and present a new semi-theoretical procedure for analyzing solution-gas systems in which free gas is produced at the sandface. For all cases considered in this study, including those cases in which the drawdown pressure data were uninterpretable, we show that standard Horner analysis of the pseudoradial flow pressure buildup data provides an excellent approximation to the total-thickness-averaged mobility in the outer region of the reservoir.

Although the primary objectives of this study are to investigate the analysis of well test data obtained from a restricted-entry well under multiphase flow conditions, Chapter II and Appendices A-C contain a detailed discussion on the

development of the fully-implicit three-phase (oil-gas-water) coning model developed as part of this work. In depth validation studies for this model are presented in Chapter III, along with a comparison of various conjugate gradient type iterative solvers and preconditioning techniques investigated during the development stage of the model. One of the primary reasons for presenting this detailed discussion is that the mathematical model is developed as a simplified compositional model based on a two-pseudocomponent representation of the physical property data rather than the more conventional black-oil formulation. Advantages arising form this formulation include: (i) black oils, volatile oils, condensates and dry gases can all be simulated using the same mathematical framework; (ii) because of the compositional approach, either flash or differential physical property data can be used; and,(iii) this type of formulation maintains a degree of generalization in the model which allows for a simpler extension of the model to more complex problems (e.g., true compositional simulation and thermal recovery methods). Additionally, we feel that several considerations involved in the development of a three-phase coning model have never been adequately discussed in the literature. For this reason, we present detailed and rigorous discussions on the treatment of variable bubble-point and variable dew-point problems and the variable substitution logic required for their efficient treatment.

Due to recent advances in parallel computing architectures and the wide interest in local grid refinement, adaptive local grid refinement and adaptive-implicit time stepping techniques, domain decomposition was also investigated as an overall preconditioner for the conjugate gradient-type iterative solvers investigated during the course of this study. Background information on several common domain decomposition preconditioning techniques is presented in Chapter II. A comparison of the domain decomposition preconditioner and other more conventional preconditioners is presented in Chapter III along with a comparison of various Schur

complement preconditioners considered in association with the domain decomposition technique. Numerical results indicate that for various partitionings of the reservoir domain, the use of domain decomposition preconditioning for the iterative solvers can result in a reduction in the number of iterations required as compared to the more conventional block-incomplete-LU decomposition (BILU) and block-symmetric-Gauss-Siedel incomplete factorization (BSGS) preconditioned iterative methods. Simple computations show a potential for use in a parallel computing environment, however, the computational work (CPU time) required in a sequential computing environment is much greater than for the conventional preconditioners.

CHAPTER II

DEVELOPMENT OF A TWO-DIMENSIONAL $(r-z)$ THREE-PHASE BLACK OIL (SIMPLIFIED COMPOSITIONAL) RESERVOIR SIMULATOR

Here, a mathematical model is set forth which describes the physical process of producing fluids (oil-water-gas) at a restricted-entry well centrally located in a cylindrical reservoir which may be overlain by a gas cap and/or underlain by an aquifer. More specifically, the initial-boundary value problem and variations thereof are delineated. First, the initial-boundary value problem is presented in its most general form, without regard to the numerical method to be used to solve the system of nonlinear equations. Following this, the numerical method used to solve the problem is described. The initial-boundary value problem is arranged in a form appropriate to the solution technique and the numerical model used to obtain approximate solutions to the problem is presented. Various details concerning the numerical solution technique and the variable substitution logic employed to handle phase changes are also discussed.

It is noted here that while the initial-boundary value problem can be represented in a conventional black oil formulation, the mathematical model is developed as a simplified compositional model based on a two-pseudocomponent representation of the physical property data. In this regard, the mathematical formulation is similar to one presented by Ref. 39. As a result, conservation of mass in our system is expressed through molar balances, rather than the more common standard volume balances typically used in black-oil simulators. This

simplified compositional approach allows us to rigorously handle either variable bubble-point or variable dew-point problems while requiring the same physical property data as in conventional black oil simulators. Under this formulation, black oils, volatile oils, condensates and dry gases can all be simulated using the same mathematical framework. Because of the compositional approach, either flash or differential physical property data can be used. Additionally, this type of formulation maintains a degree of generalization in the model which allows for a simpler extension of the model to more complex problems (e.g., true compositional simulation and thermal recovery methods). Conversion from a conventional black-oil formulation to the simplified compositional formulation presented here is achieved through the use of the fluid property relationships presented in Appendix A.

2.1 Geometry and Physical Description

The geometry of the reservoir and physical depiction of the production process of a three phase (gas-oil-water) reservoir by a restricted-entry well are shown in Figure 2.1. As shown, the reservoir is represented in two-dimensional $(r-z)$ cylindrical coordinates with symmetry assumed in the angular coordinate direction. The primary reservoir (oil zone) may be overlain by a gas cap, underlain by an aquifer or both. Production of fluids into the wellbore can occur only where the wellbore is open to flow; however, this location can be arbitrarily specified. In the development of the mathematical model, the positive z-coordinate direction is considered to be vertically upwards. The reservoir may be either isotropic or anisotropic. The reservoir may be either homogeneous or heterogeneous, e.g. a skin zone may be present around the wellbore or the reservoir may be multilayered. Flow of fluids in the reservoir and at the wellbore may be single, two or three phase and is controlled only through the specification of the initial phase distributions in the reservoir, i.e., once the initial pressures and phase distributions in the reservoir are specified, the flow of fluids is controlled by the calculated fluid mobilities and flow potentials. Gravity and capillary pressure effects are included in the model.

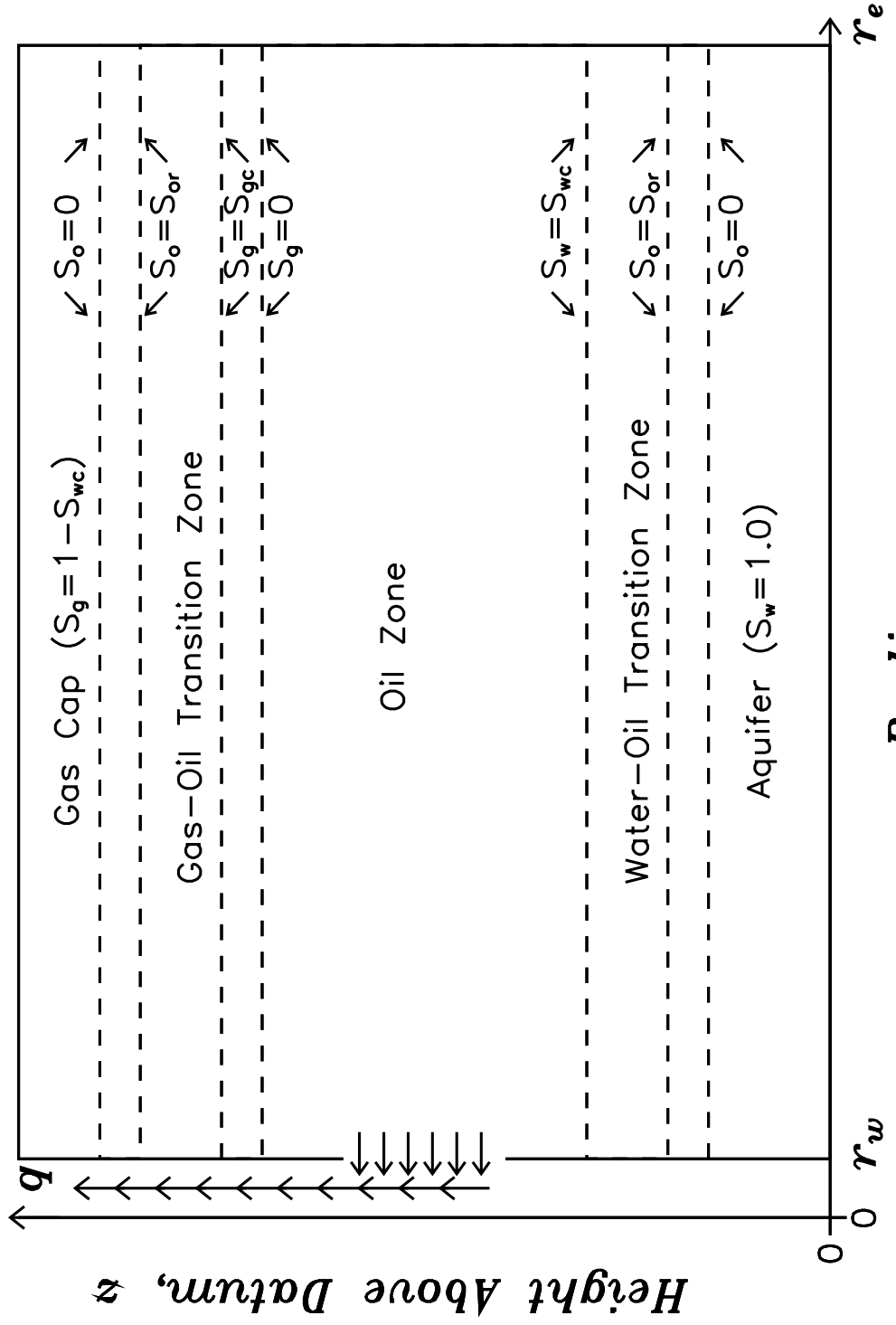

Fig. 2.1 – Schematic of a 3–phase reservoir produced from a restricted–entry well.

2.2 Model Assumptions

To simplify the model development while maintaining the integrity of the solutions consistent with the stated objectives of this study, the following assumptions and options concerning the reservoir description, phase behavior of fluids and flow of fluids through the reservoir are incorporated:

(i) Axisymmetrical flow about the wellbore.

(ii) Upper, lower and outer boundaries of the reservoir may be specified as either no-flow (Neumann) or constant potential and saturation (Dirichlet) boundaries. Specification of a constant potential and saturation boundary need not be the same as the initial potential and phase saturation distribution at the boundary. This options allows the modeling of fluid influx, fluid injection and fluid production at the boundaries of the reservoir. Each boundary can have a different boundary condition specified.

(iii) The reservoir rock may be either incompressible (constant porosity) or compressible (porosity a function of pressure).

(iv) The reservoir temperature is constant and equal throughout the reservoir.

(v) Initial reservoir phase pressures may be represented by the individual phase hydrostatic pressures in regions where only one phase is mobile, and related through capillary pressures when multiple phases are mobile.

(vi) The PVT behavior of the hydrocarbon mixture can be represented by two pseudocomponents 1 and 2, where we consider component 1 to represent the lighter hydrocarbon fractions and component 2 the heavier fractions.

(vii) Both pseudocomponents can be present in both the oil and gas phases, but are assumed to be insoluble in the aqueous phase.

(viii) Water exists only in the aqueous phase.

(ix) When two hydrocarbon phases are present, all fluid and physical properties are unique functions of either the appropriate phase pressure or saturation. If only one hydrocarbon phase is present, that phase's fluid properties are a function of both pressure and saturation pressure; i.e., an undersaturated oil's fluid properties would be a function of both the pressure and the bubble-point pressure and an undersaturated gas's properties would be a function of both the pressure and the dew-point pressure.

(x) The three-phase gas relative permeability can be represented by the two-phase (gas-oil) gas relative permeability curve, the three-phase water permeability can be represented by the two-phase (water-oil) water relative permeability and the three-phase oil relative permeability can be represented by any of the following three-phase oil relative permeability correlations: Stone's[40] method 1, Stone's[41] method 2, the method of MacDonald and Coats[42] or a modified[43] Stone's method 2.

(xi) The velocities of all three phases can be expressed by Darcy's law.

(xii) The production of fluids may be specified as a constant surface oil rate, a constant surface gas rate, a constant surface water rate, a constant surface total fluid rate, a constant total reservoir volumetric rate, a constant mass rate, a constant molar rate or at a specified bottomhole wellbore pressure.

2.3 Mathematical Model

In this section we develop the general form of the initial-boundary value problem subject to the assumptions listed above. A complete description of the problem requires a set of differential or algebraic equations describing the conservation of mass and momentum, phase composition and saturation constraints,

appropriate boundary and initial conditions, and methods of calculating fluid and physical properties. Fluid and physical property relations are presented in Appendix A.

The conservation of mass within our system can be expressed by writing the continuity equation for each component, resulting in the following equation for the "light" hydrocarbon component (component #1)

$$-c\nabla \cdot (x_1 \overline{\rho}_o \vec{v}_o + y_1 \overline{\rho}_g \vec{v}_g) = \frac{\partial}{\partial t}[\phi(x_1 \overline{\rho}_o S_o + y_1 \overline{\rho}_g S_g)] \ , \tag{2.3.1}$$

for the "heavy" hydrocarbon component (component #2)

$$-c\nabla \cdot (x_2 \overline{\rho}_o \vec{v}_o + y_2 \overline{\rho}_g \vec{v}_g) = \frac{\partial}{\partial t}[\phi(x_2 \overline{\rho}_o S_o + y_2 \overline{\rho}_g S_g)] \tag{2.3.2}$$

and for the water component

$$-c\nabla \cdot (\overline{\rho}_w \vec{v}_w) = \frac{\partial}{\partial t}[\phi(\overline{\rho}_w S_w)] \ . \tag{2.3.3}$$

Here, c is merely a units conversion factor equal to 5.61458 ft^3/RB. Note that we have chosen to express the conservation of mass in terms of the moles of each component; i.e., $\overline{\rho}$ represents the molar density, and x_i and y_i, $i = 1, 2$ represent the mole fractions of components 1 and 2 in the liquid and vapor hydrocarbon phases, respectively. Expressions for determining these properties from the standard black-oil properties are included in Appendix A.

Modified for our specification of the positive z-direction, Darcy's Law is used to express the phase velocities:

$$\vec{v}_m = -1.127 \times 10^{-3}[k]\lambda_{rm}(\nabla p_m + \rho_m g \nabla z) \quad , m = o, w, g \ , \tag{2.3.4}$$

where λ_{rm} is the phase relative mobility defined by

$$\lambda_{rm} = \frac{k_{rm}}{\mu_m} \quad , m = o, w, g \tag{2.3.5}$$

and $[k]$ is the absolute permeability tensor. Substituting our expression for Darcy's Law into equations (2.3.1) through (2.3.3), we obtain our flow equations for the light hydrocarbon component

$$c_1 \nabla \cdot [x_1 \overline{\rho}_o [k] \lambda_{ro} (\nabla p_o + \rho_o g \nabla z) + y_1 \overline{\rho}_g [k] \lambda_{rg} (\nabla p_g + \rho_g g \nabla z)]$$

$$= \frac{\partial}{\partial t} [\phi (x_1 \overline{\rho}_o S_o + y_1 \overline{\rho}_g S_g)] \ , \tag{2.3.6}$$

the heavy hydrocarbon component

$$c_1 \nabla \cdot [x_2 \overline{\rho}_o [k] \lambda_{ro} (\nabla p_o + \rho_o g \nabla z) + y_2 \overline{\rho}_g [k] \lambda_{rg} (\nabla p_g + \rho_g g \nabla z)]$$

$$= \frac{\partial}{\partial t} [\phi (x_2 \overline{\rho}_o S_o + y_2 \overline{\rho}_g S_g)] \tag{2.3.7}$$

and water

$$c_1 \nabla \cdot [\overline{\rho}_w [k] \lambda_{rw} (\nabla p_w + \rho_w g \nabla z)] = \frac{\partial}{\partial t} [\phi (\overline{\rho}_w S_w)] \ , \tag{2.3.8}$$

where c_1 is a units conversion factor. If oil-field units are used and time is specified in days, then $c_1 = 0.006328 \ ft^2 \cdot cp/[md \cdot psi \cdot day]$.

In addition to our flow equations, we also require the following capillary and saturation relations to hold:

$$p_{cog} = p_g - p_o \ , \tag{2.3.9}$$

$$p_{cow} = p_o - p_w \ , \tag{2.3.10}$$

$$S_o + S_w + S_g = 1.0 \ . \tag{2.3.11}$$

Equations (2.3.6) through (2.3.11) represent a set of six equations in the six unknowns: $p_o,\ p_g,\ p_w,\ S_o,\ S_g$ and S_w for the case of a saturated oil (or gas). For the case of an undersaturated oil, S_g is known and our unknown becomes the bubble-point pressure, p_b. For the case of an undersaturated gas, S_o is known and our unknown becomes the dew-point pressure, p_d; i.e., S_g and p_b are mutually exclusive variables, as are S_o and p_d. It is easily shown that only three of these relations (unknowns) are independent. We will come back to this point once we have completely specified our initial-boundary value problem.

To complete the description of our problem, we require that appropriate initial and boundary conditions be specified. For the initial condition we require that the reservoir fluids be in a state of gravity and capillary equilibrium; i.e., the reservoir be in a state of static equilibrium at which velocities of all phases are zero. Aziz and Settari[43] have shown that under these conditions, the initial pressure and saturation distribution in the reservoir is uniquely determined by specifying one pressure and two reference saturations. More specifically, we are free to specify any one of the phase pressures, however, we note that the location for this pressure must be specified in the region where that phase is mobile. If this pressure were to be specified in a region in which that phase is nonexistent or not mobile, then our initialization procedure would become a trial-and-error process until we reached a point in the reservoir where that phase is mobile. This restriction also applies to our two reference saturations; e.g., it is required that we specify $S_w \geq S_{wc}$ at some location in the oil-water transition zone and $S_g \geq S_{gc}$ at some location in the oil-gas transition zone. Note that if we specify $S_w = S_{wc}$ or $S_g = S_{gc}$, then the location that these saturations are specified at must correspond exactly to the first location within the transition zone in which they occur.

Under the condition of static equilibrium and within the region of the reservoir where the phase is mobile, the phase pressures are functions of z only:

$$\left.\frac{dp_m}{dz}\right|_{\Omega_m} = -\gamma_m\Big|_{\Omega_m} \quad , m = o, w, g \tag{2.3.12a}$$

where Ω_m represents the region of the reservoir where that phase is mobile and we define the phase gravity, γ_m as

$$\gamma_m = \frac{\rho_m g}{g_c} \quad , m = o, w, g \ . \tag{2.3.12b}$$

We can integrate equation (2.3.12) over any interval of the mobile phase region to obtain

$$p_m(z_2) - p_m(z_1) = -\int_{z_1}^{z_2} \gamma_m \, dz \quad , m = o, w, g \ ; \ \{z_1, z_2\} \in \Omega_m \ . \tag{2.3.13}$$

Here we have assumed $z_2 > z_1$. Equation (2.3.13) is useful for defining the initial pressure distribution within the mobile region, provided one of the pressures, $p_m(z_2)$ or $p_m(z_1)$, is known.

In those regions of the reservoir where a phase is immobile, its phase pressure will follow the mobile-phase density gradient as related through the endpoint capillary pressure relation between the two phases; e.g., for elevations above the oil-water contact, $z > z_{owc}$, the water saturation is equal to the connate water saturation, S_{wc}, and the water-phase pressure is related to the oil-phase pressure through

$$p_w(z) = p_o(z) - p_{cow}(S_{wc}) \quad , z > z_{owc} \ , \ z \in \Omega_o \tag{2.3.14}$$

where throughout we assume the reservoir is water wet. There are a variety of these relations that will hold under different circumstances. We therefore postpone

giving the exact relations which completely specify the initial conditions in the reservoir until specific problems to be considered are discussed.

The no-flow or Neumann boundary conditions are represented mathematically by specifying that the gradient of the phase potentials normal to the boundary be zero at the boundary. In terms of pressures and fluid densities, our boundary conditions become for the outer boundary

$$\left.\frac{\partial p_m}{\partial r}\right|_{r=r_e} = 0 \quad , m = o, w, g \ , \tag{2.3.15}$$

the lower boundary

$$\left.\left(\frac{\partial p_m}{\partial z} + \gamma_m\right)\right|_{z=0} = 0 \quad , m = o, w, g \tag{2.3.16}$$

and the upper boundary

$$\left.\left(\frac{\partial p_m}{\partial z} + \gamma_m\right)\right|_{z=h} = 0 \quad , m = o, w, g \ . \tag{2.3.17}$$

For that part of the inner boundary not open to flow, we have

$$\left.\frac{\partial p_m}{\partial r}\right|_{r=r_w} = 0 \quad , m = o, w, g \quad ; \ 0 \le z \le h_{w_1} \quad ; \ h_{w_2} \le z \le h \ . \tag{2.3.18}$$

The inner boundary condition for the open interval depends upon our specification of the method of production. For production at a constant bottomhole pressure we have

$$p_{wb} = p_o\Big|_{z=h_{w_1}} = p_g\Big|_{z=h_{w_1}} = p_w\Big|_{z=h_{w_1}} = p_{wbc} \tag{2.3.19a}$$

and

$$p_{wf}(z) = p_{wb} - \overline{\gamma}(z)(z - h_{w_1}) \quad , h_{w_1} \le z \le h_{w_2} \ , \tag{2.3.19b}$$

where $\overline{\gamma}$ is given by

$$\overline{\gamma}(z) = \left[\frac{\int_{h_{w_1}}^{z} (q_o\gamma_o + q_g\gamma_g + q_w\gamma_w)\, dz}{\int_{h_{w_1}}^{z} (q_o + q_g + q_w)\, dz}\right] \ , \ h_{w_1} \le z \le h_{w_2} \qquad (2.3.19c)$$

and p_{wbc} is the constant pressure specified by the user. Production at a constant surface rate is represented by writing Darcy's Law at the wellbore for the required phase. For specification of a constant surface oil rate, we have

$$q_{osc} = \frac{2\pi(1.127 \times 10^{-3})r_w}{\overline{\rho}_{osc}} \int_{h_{w_1}}^{h_{w_2}} k_h \left(x_2 \overline{\rho}_o \lambda_{ro} \frac{\partial p_o}{\partial r} + y_2 \overline{\rho}_g \lambda_{rg} \frac{\partial p_g}{\partial r}\right)_{r_w} dz \ , \quad (2.3.20)$$

for a constant surface gas rate,

$$q_{gsc} = \frac{2\pi(1.127 \times 10^{-3})r_w}{\overline{\rho}_{gsc}} \int_{h_{w_1}}^{h_{w_2}} k_h \left(x_1 \overline{\rho}_o \lambda_{ro} \frac{\partial p_o}{\partial r} + y_1 \overline{\rho}_g \lambda_{rg} \frac{\partial p_g}{\partial r}\right)_{r_w} dz \ , \quad (2.3.21)$$

and for a constant surface water rate we have

$$q_{wsc} = \frac{2\pi(1.127 \times 10^{-3})r_w}{\overline{\rho}_{wsc}} \int_{h_{w_1}}^{h_{w_2}} k_h \left(\overline{\rho}_w \lambda_{rw} \frac{\partial p_w}{\partial r}\right)_{r_w} dz \ . \qquad (2.3.22)$$

Specification of a constant total surface rate simply results in

$$q_{tsc} = q_{osc} + q_{gsc} + q_{wsc} \ , \qquad (2.3.23)$$

where q_{osc}, q_{gsc} and q_{wsc} are given by Eqs. 2.3.21, 2.3.22 and 2.3.23, respectively. Production at a constant total reservoir volumetric rate is given by

$$q_t = 2\pi(1.127 \times 10^{-3})r_w \int_{h_{w_1}}^{h_{w_2}} k_h \left(\lambda_{ro} \frac{\partial p_o}{\partial r} + \lambda_{rg} \frac{\partial p_g}{\partial r} + \lambda_{rw} \frac{\partial p_w}{\partial r}\right)_{r_w} dz \ . \quad (2.3.24)$$

Production at a constant total molar rate can be specified as

$$\overline{m}_t = q_{osc}\overline{\rho}_{osc} + q_{gsc}\overline{\rho}_{gsc} + q_{wsc}\overline{\rho}_{wsc} \ , \tag{2.3.25}$$

and specification of production at a constant total mass rate results in

$$m_t = q_{osc}\rho_{osc} + q_{gsc}\rho_{gsc} + q_{wsc}\rho_{wsc} \ , \tag{2.3.26}$$

where ρ_{osc}, ρ_{gsc} and ρ_{wsc} are the densities of the oil component, gas component and water, respectively, evaluated at standard conditions of pressure and temperature ($p_{sc} = 14.7\ psi$: $T_{sc} = 60\ ^oF$).

For the case of constant potential (pressure) outer, lower or upper boundaries, we replace Eqs. 2.3.15-2.3.17, respectively, by

$$p_m\Big|_{r=r_e} = p_{mc}\Big|_{r=r_e} \ , m = o, w, g \ , \tag{2.3.27}$$

$$p_m\Big|_{z=0} = p_{mc}\Big|_{z=0} \ \ m = o, w, g \tag{2.3.28}$$

and

$$p_m\Big|_{z=h} = p_{mc}\Big|_{z=h} \ , m = o, w, g \ . \tag{2.3.29}$$

Here, p_{mc} represents specified constant phase pressures. We note that our numerical simulator includes an option to specify these as either being equal to the initial values of those pressures in the reservoir or to read in user specified values. Because the phase saturations are directly related through the capillary pressures, we note that Eqs. 2.3.27-2.3.29 are sufficient to completely specify our outer, lower and upper boundary conditions for this case. We also note that one could alternatively specify one phase pressure and two saturations at each of these boundaries.

As mentioned previously, Eqs. 2.3.6 through 2.3.11 represent a set of six equations in the six unknowns: p_o, p_g, p_w, S_o (or p_d), S_g (or p_b), and S_w. If production is specified at a constant surface, reservoir, mass or molar rate, we include one of Eqs. 2.3.20-2.3.26 and have an additional unknown, p_{wb}. Of our seven unknowns, only four are independent. Through the use of the capillary pressure relations, Eqs. 2.3.9 and 2.3.10, and the saturation constraint, Eq. 2.3.11, we can eliminate three of the unknowns from our equations. While in a strictly mathematical sense it makes no difference which of the unknowns we eliminate, a judicious selection may simplify our resulting equations and, therefore, the solution of those equations. In selecting the primary (independent) variables, one should also consider the solution method to be employed. Based on these considerations, we have chosen as our primary variables the oil phase pressure, p_o, gas phase saturation, S_g, water phase saturation, S_w, and the bottomhole wellbore pressure, p_{wb}. Because the particular variables which are known or unknown may change, for instance when a phase boundary is crossed, we will discuss the selection of primary variables further when we discuss the numerical solution technique.

Using the capillary pressure relations and saturation constraint, we eliminate the variables p_g, p_w and S_o from our flow equations to obtain for the light hydrocarbon component

$$c_1 \nabla \cdot [x_1 \overline{\rho}_o[k] \lambda_{ro} (\nabla p_o + \rho_o g \nabla z) + y_1 \overline{\rho}_g[k] \lambda_{rg} (\nabla (p_o + p_{cog}) + \rho_g g \nabla z)]$$

$$= \frac{\partial}{\partial t} \{\phi [x_1 \overline{\rho}_o (1 - S_w - S_g) + y_1 \overline{\rho}_g S_g]\} \tag{2.3.30}$$

for the heavy hydrocarbon component

$$c_1 \nabla \cdot [x_2 \overline{\rho}_o[k] \lambda_{ro} (\nabla p_o + \rho_o g \nabla z) + y_2 \overline{\rho}_g[k] \lambda_{rg} (\nabla (p_o + p_{cog}) + \rho_g g \nabla z)]$$

$$= \frac{\partial}{\partial t}\{\phi[x_2\overline{\rho}_o(1 - S_w - S_g) + y_2\overline{\rho}_g S_g]\} \tag{2.3.31}$$

and for water

$$c_1 \nabla \cdot [\overline{\rho}_w[k]\lambda_{rw}(\nabla(p_o - p_{cow}) + \rho_w g \nabla z)] = \frac{\partial}{\partial t}[\phi(\overline{\rho}_w S_w)] \tag{2.3.32}$$

It is useful if we now express our flow equations in cylindrical coordinates with the assumed symmetry in the angular direction. Eqs. 2.3.30-2.3.32 therefore become for the light component

$$\frac{c_1}{r}\frac{\partial}{\partial r}\left[r x_1 \overline{\rho}_o k_h \lambda_{ro}\frac{\partial p_o}{\partial r} + r y_1 \overline{\rho}_g k_h \lambda_{rg}\frac{\partial(p_o + p_{cog})}{\partial r}\right] +$$

$$c_1\frac{\partial}{\partial z}\left\{x_1\overline{\rho}_o k_z \lambda_{ro}\left(\frac{\partial p_o}{\partial z} + \gamma_o\right) + y_1\overline{\rho}_g k_z \lambda_{rg}\left[\frac{\partial(p_o + p_{cog})}{\partial z} + \gamma_g\right]\right\}$$

$$= \frac{\partial}{\partial t}\{\phi[x_1\overline{\rho}_o(1 - S_w - S_g) + y_1\overline{\rho}_g S_g]\}\ , \tag{2.3.33}$$

for the heavy component

$$\frac{c_1}{r}\frac{\partial}{\partial r}\left[r x_2 \overline{\rho}_o k_h \lambda_{ro}\frac{\partial p_o}{\partial r} + r y_2 \overline{\rho}_g k_h \lambda_{rg}\frac{\partial(p_o + p_{cog})}{\partial r}\right] +$$

$$c_1\frac{\partial}{\partial z}\left\{x_2\overline{\rho}_o k_z \lambda_{ro}\left(\frac{\partial p_o}{\partial z} + \gamma_o\right) + y_2\overline{\rho}_g k_z \lambda_{rg}\left[\frac{\partial(p_o + p_{cog})}{\partial z} + \gamma_g\right]\right\}$$

$$= \frac{\partial}{\partial t}\{\phi[x_2\overline{\rho}_o(1 - S_w - S_g) + y_2\overline{\rho}_g S_g]\} \tag{2.3.34}$$

and for water

$$\frac{c_1}{r}\frac{\partial}{\partial r}\left[r\overline{\rho}_w k_h \lambda_{rw}\frac{\partial(p_o - p_{cow})}{\partial r}\right] + c_1\frac{\partial}{\partial z}\left\{\overline{\rho}_w k_z \lambda_{rw}\left[\frac{\partial(p_o - p_{cow})}{\partial z} + \gamma_w\right]\right\}$$

$$= \frac{\partial}{\partial t}[\phi(\overline{\rho}_w S_w)] \tag{2.3.35}$$

For our initial conditions, we need to specify the oil phase pressure, p_o, the gas saturation, S_g, and the water saturation, S_w, throughout the reservoir. As discussed earlier, this is accomplished by specifying one pressure and two saturations at appropriate reference locations within the reservoir:

$$p_o(z) = p_o(z^r) \quad , z = z^r \tag{2.3.36}$$

$$S_g(z) = S_{gc} \quad , z = z_{goc} \tag{2.3.37}$$

$$S_w(z) = S_{wc} \quad , z = z_{owc} \tag{2.3.38}$$

Note here that we are defining the gas-oil contact as the vertical location where the gas phase first becomes mobile the oil-water contact similarly as the vertical location (as we move downwards) where the water phase first becomes mobile. The initial pressures and saturations throughout the rest of the reservoir are automatically fixed according to the appropriate hydrostatic pressure relation and capillary pressure - saturation relations.

The no-flow outer boundary condition now becomes:

$$\left.\frac{\partial p_o}{\partial r}\right|_{r=r_e} = 0 \ , \tag{2.3.39a}$$

$$\left.\frac{\partial (p_o + p_{cog})}{\partial r}\right|_{r=r_e} = 0 \tag{2.3.39b}$$

and

$$\left.\frac{\partial (p_o - p_{cow})}{\partial r}\right|_{r=r_e} = 0 \ . \tag{2.3.39c}$$

The no-flow lower boundary condition is represented by

$$\left.\left(\frac{\partial p_o}{\partial z} + \gamma_o\right)\right|_{z=0} = 0 \ , \tag{2.3.40a}$$

$$\left[\frac{\partial(p_o + p_{cog})}{\partial z} + \gamma_g\right]\Big|_{z=0} = 0 \qquad (2.3.40b)$$

and

$$\left[\frac{\partial(p_o - p_{cow})}{\partial z} + \gamma_w\right]\Big|_{z=0} = 0 \ . \qquad (2.3.40c)$$

The no-flow upper boundary condition is similarly represented by

$$\left(\frac{\partial p_o}{\partial z} + \gamma_o\right)\Big|_{z=h} = 0 \ , \qquad (2.3.41a)$$

$$\left[\frac{\partial(p_o + p_{cog})}{\partial z} + \gamma_g\right]\Big|_{z=h} = 0 \qquad (2.3.41b)$$

and

$$\left[\frac{\partial(p_o - p_{cow})}{\partial z} + \gamma_w\right]\Big|_{z=h} = 0 \ . \qquad (2.3.41c)$$

The boundary condition along the unperforated section of the wellbore is represented by

$$\frac{\partial p_o}{\partial r}\Big|_{r=r_w} = 0 \quad , 0 \le z < h_{w_1} \ , h_{w_2} < z \le h \qquad (2.3.42a)$$

$$\frac{\partial(p_o + p_{cog})}{\partial r}\Big|_{r=r_w} = 0 \quad , 0 \le z < h_{w_1} \ , h_{w_2} < z \le h \qquad (2.3.42b)$$

$$\frac{\partial(p_o - p_{cow})}{\partial r}\Big|_{r=r_w} = 0 \quad , 0 \le z < h_{w_1} \ , h_{w_2} < z \le h \qquad (2.3.42c)$$

The inner boundary condition along the perforated section of the wellbore remains unchanged for the case of a specified bottomhole pressure,

$$p_{wb} = p_o\Big|_{z=h_{w_1}} \qquad (2.3.43a)$$

$$p_{wf}(z) = p_{wb} - \overline{\gamma}(z)(z - h_{w_1}) \quad , h_{w_1} \le z \le h_{w_2} \qquad (2.3.43b)$$

$$\overline{\gamma}(z) = \left[\frac{\int_{h_{w_1}}^{z} (q_o\gamma_o + q_g\gamma_g + q_w\gamma_w)\,dz}{\int_{h_{w_1}}^{z} (q_o + q_g + q_w)\,dz}\right] \quad , \; h_{w_1} \le z \le h_{w_2} \tag{2.3.43c}$$

and is modified as follows for the case of a specified constant surface oil production rate,

$$q_{osc} = \frac{2\pi(1.127\times10^{-3})r_w}{\overline{\rho}_{osc}} \int_{h_{w_1}}^{h_{w_2}} k_h \left[x_2\overline{\rho}_o\lambda_{ro}\frac{\partial p_o}{\partial r} + y_2\overline{\rho}_g\lambda_{rg}\frac{\partial(p_o + p_{cog})}{\partial r}\right]_{r=r_w} dz \;, \tag{2.3.44}$$

for the case of a specified constant surface gas production rate

$$q_{gsc} = \frac{2\pi(1.127\times10^{-3})r_w}{\overline{\rho}_{gsc}} \int_{h_{w_1}}^{h_{w_2}} k_h \left(x_1\overline{\rho}_o\lambda_{ro}\frac{\partial p_o}{\partial r} + y_1\overline{\rho}_g\lambda_{rg}\frac{\partial(p_o + p_{cog})}{\partial r}\right)_{r_w} dz \tag{2.3.45}$$

and for a specified constant surface water rate we have

$$q_{wsc} = \frac{2\pi(1.127\times10^{-3})r_w}{\overline{\rho}_{wsc}} \int_{h_{w_1}}^{h_{w_2}} k_h \left(\overline{\rho}_w\lambda_{rw}\frac{\partial(p_o - p_{cow})}{\partial r}\right)_{r_w} dz \;. \tag{2.3.46}$$

Production at a constant reservoir volumetric rate now becomes

$$q_t = c_2 r_w \int_{h_{w_1}}^{h_{w_2}} k_h \left[\lambda_{ro}\frac{\partial p_o}{\partial r} + \lambda_{rg}\frac{\partial(p_o + p_{cog})}{\partial r} + \lambda_{rw}\frac{\partial(p_o - p_{cow})}{\partial r}\right]_{r=r_w} dz \;, \tag{2.3.47}$$

where $c_2 = 2\pi(1.127\times10^{-3})$. The specifications of a constant total surface rate, total mass rate or total molar rate retain the same form as before, but with the phase flow rates now defined by Eqs. 2.3.44-2.3.46, i.e., for a constant total surface volumetric rate we have

$$q_{tsc} = q_{osc} + q_{gsc} + q_{wsc} \;, \tag{2.3.48}$$

for a constant molar production rate we have

$$\overline{m}_t = q_{osc}\overline{\rho}_{osc} + q_{gsc}\overline{\rho}_{gsc} + q_{wsc}\overline{\rho}_{wsc} \tag{2.3.49}$$

and for a constant mass production rate we have

$$m_t = q_{osc}\rho_{osc} + q_{gsc}\rho_{gsc} + q_{wsc}\rho_{wsc} \ . \tag{2.3.50}$$

For the case of constant potential (pressure) outer, lower or upper boundaries, Eqs. 2.3.27-2.3.29 become, respectively, for the outer boundary

$$p_o\Big|_{r=r_e} = p_{oc}\Big|_{r=r_e} \ , \ 0 \le z \le h \ , \tag{2.3.51a}$$

$$(p_o + p_{cog})\Big|_{r=r_e} = (p_o + p_{cog})_c\Big|_{r=r_e} \ 0 \le z \le h \ , \tag{2.3.51b}$$

$$(p_o - p_{cow})\Big|_{r=r_e} = (p_o - p_{cow})_c\Big|_{r=r_e} \ , \ 0 \le z \le h \ , \tag{2.3.51c}$$

for the lower boundary

$$p_o\Big|_{z=0} = p_{oc}\Big|_{z=0} \ , \ r_w < r \le r_e \ , \tag{2.3.52a}$$

$$(p_o + p_{cog})\Big|_{z=0} = (p_o + p_{cog})_c\Big|_{z=0} \ , \ r_w < r \le r_e \ , \tag{2.3.52b}$$

$$(p_o - p_{cow})\Big|_{z=0} = (p_o - p_{cow})_c\Big|_{z=0} \ , \ r_w < r \le r_e \ , \tag{2.3.52c}$$

and for the upper boundary

$$p_o\Big|_{z=h} = p_{oc}\Big|_{z=h} \ , \ r_w < r \le r_e \ , \tag{2.3.53a}$$

$$(p_o + p_{cog})\Big|_{z=h} = (p_o + p_{cog})_c\Big|_{z=h} \ , \ r_w < r \le r_e \tag{2.3.53b}$$

$$(p_o - p_{cow})\Big|_{z=h} = (p_o - p_{cow})_c\Big|_{z=h} \ , \ r_w < r \leq r_e \ , \qquad (2.3.53c)$$

where, here again, the c subscript in Eqs. 2.3.51-2.3.53 just indicates that the specified potentials may be either initial values in the reservoir or some other desired value.

Equations 2.3.33 through 2.3.42 and the appropriate form of Eqs. 2.3.43-2.3.50 completely specify our initial-boundary value problem. For the case of a constant pressure outer boundary, Eqs. 2.3.39 are replaced with Eqs. 2.3.51; for a constant pressure lower boundary, we replace Eqs. 2.3.40 with Eqs. 2.3.52; and, for a constant pressure upper boundary, we replace Eqs. 2.3.41 with Eqs. 2.3.53.

2.4 Solution Method and Numerical Model

2.4.1 Newton's Method

An analysis of the differential equations comprising our initial-boundary value problem indicates that the equations are highly nonlinear. These nonlinearities arise because the fluid and physical properties are themselves functions of the primary variables for which we wish to solve. These nonlinearities are compounded because, in general, the functional relationships between the fluid and physical properties and the primary variables are also nonlinear. Due to the complexity of our initial-boundary value problem and the highly nonlinear nature of the equations, suitable linearization of the equations is required in order to obtain a solution.

Linearization methods available include variations of Newton's method[43] which are widely accepted for their generally fast convergence. There are three variations of Newton's method, and each will be briefly explained with an example of one equation in one unknown and then generalized to the case of multiple equations in multiple unknowns.

Suppose we wish to solve the equation

$$f(x) = 0 \tag{2.4.1}$$

where the variable x is a real number. The classical Newton-Raphson technique (sometimes referred to as the variable tangent method) may be expressed as follows:

(1) Make an initial guess of $x^k = x_{\text{guess}}$

(2) Calculate the function, $f(x^k)$

(3) Calculate the first derivative of the function, $f'(x^k)$

(4) Calculate the next guess for x as

$$x^{k+1} = x^k - \frac{f(x^k)}{f'(x^k)} \tag{2.4.2}$$

(5) Check the convergence of the solution as

$$|x^{k+1} - x^k| \leq \varepsilon \tag{2.4.3}$$

If the difference between the calculated value and the guessed value of x is less than the convergence criterion, then the solution has been obtained. If the difference is greater than the specified tolerance, then steps (2)-(5) are repeated using the value of x calculated in step (4) as the new guess.

The second variation of Newton's method, sometimes referred to as the variable secant or chord method, is identical to the classical method except for

how the derivative of the function is calculated. In this variation, the derivative is calculated from successive iterations as follows:

$$f'(x^k) = \frac{f(x^k) - f(x^{k-1})}{x^k - x^{k-1}} \tag{2.4.4}$$

The third variation of Newton's method is referred to as the fixed tangent, fixed secant or stationary method. In this method, the derivative of the function is calculated only once using the initial guess for the variable x.

Both variations of the classical Newton's method have the advantage of reducing the amount of work required per iteration to calculate the new value of x; however, both variations have the disadvantage of a slower rate of convergence. While the classical method requires the most computational work, it converges the fastest. The stationary method requires the least amount of work, but has the slowest rate of convergence. The optimum weighting of these two factors is difficult to ascertain, and can only be determined through a trial-and-error process for complex problems.

Newton's method is readily extended to obtain solutions to a system of equations in multiple unknowns. Suppose we have n equations

$$\vec{F} = F_1,\ F_2,\ \ldots,\ F_n \tag{2.4.5}$$

in the n unknowns

$$\vec{x} = x_1,\ x_2,\ \ldots,\ x_n \tag{2.4.6}$$

Then we seek the solution to the system of equations

$$\vec{F}(\vec{x}) = 0 \tag{2.4.7}$$

Let us also define $\vec{\delta x}$ as

$$\vec{\delta x} = (x_1^{k+1} - x_1^k),\ (x_2^{k+1} - x_2^k),\ \ldots,\ (x_n^{k+1} - x_n^k) \tag{2.4.8}$$

With some rearranging of the basic iteration equation, Newton's method can be stated for the multiple equations in multiple unknowns case as

$$J^k \vec{\delta x} = -\vec{F}(\vec{x}^k) \tag{2.4.9}$$

where J^k is the Jacobian matrix of the partial derivatives of the functions

$$F_1,\ F_2,\ \ldots,\ F_n \tag{2.4.10}$$

with respect to the variables

$$x_1,\ x_2,\ \ldots,\ x_n \tag{2.4.11}$$

at the k^{th} iteration level, or

$$J^k = \frac{\partial F_i}{\partial x_j^k}\ ,\ 1 \le i \le n\ ,\ 1 \le j \le n \tag{2.4.12}$$

We can also express the Jacobian in matrix form as

$$J^k = \begin{pmatrix} \frac{\partial F_1}{\partial x_1} & \frac{\partial F_1}{\partial x_2} & \cdots & \frac{\partial F_1}{\partial x_n} \\ \frac{\partial F_2}{\partial x_1} & \frac{\partial F_2}{\partial x_2} & \cdots & \frac{\partial F_2}{\partial x_n} \\ \vdots & \vdots & \ddots & \vdots \\ \frac{\partial F_n}{\partial x_1} & \frac{\partial F_n}{\partial x_2} & \cdots & \frac{\partial F_n}{\partial x_n} \end{pmatrix}^k \tag{2.4.13}$$

To implement the Newton's method iteration scheme, we note that instead of solving for the unknown variables directly, we solve for the difference in successive iteration values, i.e.,

$$\delta x_i = (x_i^{k+1} - x_i^k)\ \ ,\ 1 \le i \le n \tag{2.4.14}$$

Subsequent guesses for the variables are then determined as

$$x_i^{k+1} = x_i^k + \delta x_i \quad , \; 1 \leq i \leq n \tag{2.4.15}$$

Convergence of the Newton iteration scheme can be determined either through a test on the residuals of the functions

$$\max_{1 \leq i \leq n} |F_i(x_j^{k+1})_{1 \leq j \leq n}| \leq \varepsilon_F \tag{2.4.16}$$

or through a test on the residuals of the successive iteration values of the variables themselves

$$\max_{1 \leq j \leq n} |x_j^{k+1} - x_j^k| \leq \varepsilon_x \tag{2.4.17}$$

2.4.2 Finite-Difference Approximation

2.4.2.a Definition and Construction of Finite-Difference Grids

The first step to any finite-difference discretization scheme is the construction and definition of the finite-difference grids. Let N_r be the number of grids in the radial direction and N_z be the number of grids in the vertical direction. Also, let N_T denote the total number of grids, where $N_T = N_r \times N_z$. The index notation to be used is as follows:

r_i radial position of grid point i

$r_{i+\frac{1}{2}}$ radial position of the grid block boundary between grid point i and grid point $i+1$

z_k vertical position of grid point k

$z_{k+\frac{1}{2}}$ vertical position of the grid block boundary between grid point k and grid point $k+1$

Grid points are located vertically using a block-centered scheme (i.e., grid block boundaries are established first, with the grid points then centered between the boundaries). The grid block boundaries are specified as follows:

$$z_{k+\frac{1}{2}}|_{k=0} = 0 \tag{2.4.18}$$

$$z_{k+\frac{1}{2}} = \text{specified} \quad , \ 1 \leq k < N_z \tag{2.4.19}$$

$$z_{k+\frac{1}{2}}|_{k=N_z} = h \tag{2.4.20}$$

As a matter of index notation, let us also denote N_{zw_1} to be the vertical direction discrete index of the grid block whose lower block boundary is located at h_{w_1}; i.e.,

$$z_{k-\frac{1}{2}}|_{k=N_{zw_1}} = h_{w_1} \tag{2.4.21}$$

Additionally, let N_{zw_2} denote the vertical direction discrete index of the grid block which has its upper block boundary located at h_{w_2}; i.e.,

$$z_{k+\frac{1}{2}}|_{k=N_{zw_2}} = h_{w_2} \tag{2.4.22}$$

Given the grid block boundary locations, determination of the vertical grid point locations is straight forward:

$$z_k = \frac{1}{2}(z_{k+\frac{1}{2}} + z_{k-\frac{1}{2}}) \quad , 1 \leq k \leq N_z \tag{2.4.23}$$

If the lower and upper reservoir boundaries are constant pressure boundaries, then we define two additional vertical grid points:

$$z_k|_{k=0} = 0 \tag{2.4.24}$$

and

$$z_k|_{k=N_z+1} = h \tag{2.4.25}$$

In addition to the locations of the grid points and the grid block boundaries, the definitions of two control element faces are required and help to simplify our expressions later on:

$$\Delta z_k = (z_{k+\frac{1}{2}} - z_{k-\frac{1}{2}}) \quad , 1 \leq k \leq N_z \tag{2.4.26}$$

$$\Delta z_{k+\frac{1}{2}} = (z_{k+1} - z_k) \quad , 0 \leq k \leq N_z \tag{3.4.27}$$

Geometric progression is used to generate the radial position of the grid points. This results in closely spaced grid points near the wellbore where conditions change rapidly with time. First, a grid expansion factor, α, is determined as:

$$\alpha = \left(\frac{r_e}{r_w}\right)^{1/N_r} \tag{2.4.28}$$

A ficticious grid point at the inner boundary is then calculated as

$$r_0 = \frac{r_w \ln \alpha}{\alpha - 1} \tag{2.4.29}$$

All of the radial grid points and grid block boundaries can now be determined from, respectively

$$r_i = \alpha r_{i-1} \quad , \ 1 \leq i \leq N_r + 1 \tag{2.4.30}$$

and

$$r_{i+\frac{1}{2}} = \frac{r_{i+1} - r_i}{\ln \alpha} \quad , \ 1 \leq i \leq N_r \ . \tag{2.4.31}$$

The volume of each individual grid cell (i,k) can now be defined as

$$V_{i,k} = \pi(r^2_{i+\frac{1}{2}} - r^2_{i-\frac{1}{2}})\Delta z_k \ , \ \begin{cases} 1 \le i \le N_r \\ 1 \le k \le N_z \end{cases} \tag{2.4.32}$$

Formulation of a finite difference procedure also requires us to define discrete time steps. To do so, we let $t^0 = 0$ and specify our time steps Δt^n such that

$$t^{n+1} = t^n + \Delta t^n \tag{2.4.33}$$

where t^{n+1} denotes the value of time at the $n+1$ time step.

2.4.2.b Discretization of Space and Time Variables

Each of the differential equations to be solved can be shown to be a linear combination of terms that have the general form $\Delta[\mathcal{T}\Delta X]$. For cylindrical coordinates with angular symmetry, the following finite-difference formulation is used:

$$\Delta[\mathcal{T}\Delta X] = \Delta_r[\mathcal{T}_r\Delta_r X] + \Delta_z[\mathcal{T}_z\Delta_z X] \tag{2.4.34}$$

where

$$\Delta_r[\mathcal{T}_r\Delta_r X] = \mathcal{T}_{r,i+\frac{1}{2},k}(X_{i+1,k} - X_{i,k}) - \mathcal{T}_{r,i-\frac{1}{2},k}(X_{i,k} - X_{i-1,k}) \tag{2.4.35}$$

and

$$\Delta_z[\mathcal{T}_z\Delta_z X] = \mathcal{T}_{z,i,k+\frac{1}{2}}(X_{i,k+1} - X_{i,k}) - \mathcal{T}_{z,i,k-\frac{1}{2}}(X_{i,k} - X_{i,k-1}) \tag{2.4.36}$$

Prior to continuing, several definitions will be made which help to simplify the expressions for the discretized form of our differential equations. Let

$$a_{i+\frac{1}{2},k} = \frac{2\pi r_{i+\frac{1}{2}}\Delta z_k}{(r_{i+1} - r_i)} \ , \ \begin{cases} 1 \le i \le N_r \\ 1 \le k \le N_z \end{cases} \ , \tag{2.4.37}$$

$$a_{1/2} = \frac{2\pi r_w \Delta z_k}{(r_1 - r_w)} \quad , \; 1 \le k \le N_z \tag{2.4.38}$$

and

$$a_{i,k+\frac{1}{2}} = \frac{\pi(r^2_{i+\frac{1}{2}} - r^2_{i-\frac{1}{2}})}{\Delta z_{k+\frac{1}{2}}} \; , \; \begin{cases} 1 \le i \le N_r \\ 0 \le k \le N_z \end{cases} \quad . \tag{2.4.39}$$

The following definitions for the phase transmissibilities will also help to simplify our expressions for the discretized equations. The radial direction transmissibilities are defined as

$$\mathcal{T}_{rm\,,i+\frac{1}{2},k} = c_1 a_{i+\frac{1}{2},k} (k_h \overline{\rho}_m \lambda_{rm})_{i+\frac{1}{2},k} \; , \; \begin{cases} m = o, w, g \\ 0 \le i \le N_r \\ 1 \le k \le N_z \end{cases} \tag{2.4.40}$$

and the vertical direction transmissibilities are defined as

$$\mathcal{T}_{zm\,,i,k+\frac{1}{2}} = c_1 a_{i,k+\frac{1}{2}} (k_z \overline{\rho}_m \lambda_{rm})_{i,k+\frac{1}{2}} \; , \; \begin{cases} m = o, w, g \\ 1 \le i \le N_r \\ 0 \le k \le N_z \end{cases} \tag{2.4.41}$$

where c_1 is a units conversion factor which depends upon the units used for all other variables. If oil-field (English) units are used and time is specified in days, then $c_1 = 0.006328 \; ft^2 \cdot cp/[md \cdot psi \cdot day]$. In Eqs. 2.4.40 and 2.4.41, the absolute permeabilities at the grid block boundaries are taken to be a weighted harmonic average of the grid block permeabilities, i.e.,

$$k_{i+\frac{1}{2}} = \frac{\ln(r_{i+1}/r_i) k_i k_{i+1}}{\ln(r_{i+1}/r_{i+\frac{1}{2}}) k_i + \ln(r_{i+\frac{1}{2}}/r_i) k_{i+1}} \tag{2.4.42a}$$

and

$$k_{z\,k+\frac{1}{2}} = \frac{\Delta z_k \Delta z_{k+1} k_{zk} k_{zk+1}}{\Delta z_{k+1} k_{zk} + \Delta z_k k_{zk+1}} \quad . \tag{2.4.42b}$$

Also note that Hawkins'[44] formula is used to incorporate a skin zone into the simulator, i.e.,

$$s = \left(\frac{k}{k_s} - 1\right) \ln\left(\frac{r_s}{r_w}\right) , \qquad (2.4.42c)$$

and the vertical permeability in the skin zone is approximated from

$$\left(\frac{k_{zs}}{k_z}\right) = \left(\frac{k_s}{k}\right) . \qquad (2.4.42d)$$

The finite difference formulation used to approximate the differentials with respect to time can be expressed as

$$\Delta_t[X] = \frac{(X^{n+1} - X^n)}{\Delta t^n} \qquad (2.4.43a)$$

We note here that the variable X can actually represent several variables; e.g.,let $X = YZ$, then

$$\Delta_t[X] = \frac{(Y^{n+1}Z^{n+1} - Y^n Z^n)}{\Delta t^n} \qquad (2.4.43b)$$

2.4.2.c Treatment of Nonlinearities

When solving a system of nonlinear partial differential equations, treatment of the nonlinearities is critical. Abou-Kassem and Farouq Ali[45] state that a proper method of handling the nonlinearities involved is necessary for a meaningful and stable solution to be obtained. Handling of the nonlinear terms involves their approximation in both time and space.

Approximation of the nonlinear terms in space is accomplished by using single-point upstream weighting of the property, which is the method used predominately in the literature. Single-point upstream weighting in the radial direction can be expressed as

$$X^m_{i+\frac{1}{2},k} = \begin{cases} X^m_{i,k} & \text{for flow from } i \text{ to } i+1 \\ X^m_{i+1,k} & \text{for flow from } i+1 \text{ to } i \end{cases} , \; m = o, w, g , \qquad (2.4.44)$$

where X^m stands for gravity, density, viscosity, mole fraction, or relative permeability of phase m. A similar expression can be written for the one-point upstream weighting of the nonlinear terms in the vertical direction:

$$X^m_{i,k+\frac{1}{2}} = \begin{cases} X^m_{i,k} & \text{for flow from } k \text{ to } k+1 \\ X^m_{i,k+1} & \text{for flow from } k+1 \text{ to } k \end{cases} \quad , \; m = o, w, g \; . \tag{2.4.45}$$

The direction of the fluid flow is determined from the sign of the differential of the phase potential

$$\nabla(p_m + \gamma_m z) \quad , \; m = o, w, g \; . \tag{2.4.46}$$

In practice, we check the sign of the finite-difference approximation to the phase potential differential across the grid block boundaries; i.e., at the block boundary $(, i+\frac{1}{2}, k)$ between grid point $(, i, k)$ and grid point $(, i+1, k)$, we determine the phase flow directions as

$$\Delta_r(\Phi_{m\,,i+\frac{1}{2},k}) \begin{cases} < 0 & \text{flow from } (i,k) \text{ to } (i+1,k) \\ > 0 & \text{flow from } (i+1,k) \text{ to } (i,k) \end{cases} \quad , \; m = o, w, g \tag{2.4.47}$$

where

$$\Delta_r(\Phi_{m\,,i+\frac{1}{2},k}) = (p_{m\,,i+1,k} - p_{m\,,i,k}) \; , \; m = o, w, g \; . \tag{2.4.48}$$

Clearly, if the differential is zero, then there is no flow across that boundary. In terms of the oil phase pressures, Eq. 2.4.48 becomes for the oil phase

$$\Delta_r(\Phi_{o\,,i+\frac{1}{2},k}) = (p_{o\,,i+1,k} - p_{o\,,i,k}) \tag{2.4.49a}$$

for the gas phase

$$\Delta_r(\Phi_{g\,,i+\frac{1}{2},k}) = (p_{o\,,i+1,k} - p_{o\,,i,k} + p_{cog\,,i+1,k} - p_{cog\,,i,k}) \tag{2.4.49b}$$

and for the water phase

$$\Delta_r(\Phi_{w\,,i+\frac{1}{2},k}) = (p_{o\,,i+1,k} - p_{o\,,i,k} + p_{cow\,,i,k} - p_{cow\,,i+1,k}) \tag{2.4.49c}$$

Similar expressions result for evaluating the phase flow directions at the vertical grid block boundaries (i.e., at $(i, k+\frac{1}{2})$):

$$\Delta_z(\Phi_{m\,,i,k+\frac{1}{2}}) \begin{cases} < 0 & \text{flow from } (i,k) \text{ to } (i,k+1) \\ > 0 & \text{flow from } (i,k+1) \text{ to } (i,k) \end{cases} , \; m = o,w,g \; , \tag{2.4.50}$$

where

$$\Delta_z(\Phi_{m\,,i,k+\frac{1}{2}}) = (p_{m,i,k+1} - p_{m,i,k} + \overline{\gamma}_{m\,,i,k+\frac{1}{2}} \Delta z_{k+\frac{1}{2}}) \; , \; m = o,w,g \tag{2.4.51}$$

and $\overline{\gamma}_{m\,,i,k+\frac{1}{2}}$ is a volumetric averaged phase gravity determined as

$$\overline{\gamma}_{m\,,i,k+\frac{1}{2}} = \frac{\gamma_{m\,,i,k+1} \Delta z_{k+1} + \gamma_{m\,,i,k} \Delta z_k}{\Delta z_{k+1} + \Delta z_k} \; , \; m = o,w,g \tag{2.4.52}$$

In terms of the oil phase pressure only, Eq. (2.4.51) becomes for the oil phase

$$\Delta_z(\Phi_{o\,,i,k+\frac{1}{2}}) = (p_{o\,,i,k+1} - p_{o\,,i,k} + \overline{\gamma}_{o\,,i,k+\frac{1}{2}} \Delta z_{k+\frac{1}{2}}) \tag{2.4.53a}$$

for the gas phase

$$\Delta_z(\Phi_{g\,,i,k+\frac{1}{2}}) = (p_{o\,,i,k+1} - p_{o\,,i,k} + p_{cog\,,i,k+1} - p_{cog\,,i,k} + \overline{\gamma}_{g\,,i,k+\frac{1}{2}} \Delta z_{k+\frac{1}{2}}) \tag{2.4.53b}$$

and for the water phase

$$\Delta_z(\Phi_{w\,,i,k+\frac{1}{2}}) = (p_{o\,,i,k+1} - p_{o\,,i,k} + p_{cow\,,i,k} - p_{cow\,,i,k+1} + \overline{\gamma}_{w\,,i,k+\frac{1}{2}} \Delta z_{k+\frac{1}{2}}) \tag{2.4.53c}$$

Note that because the flow direction for each phase is determined by the difference in the potential for that phase, it is possible for the individual phases to flow in opposite directions.

The approximation of the nonlinear terms in time is crucial for the stability of the finite-difference equations. Aziz and Settari[43] state that stability problems become severe especially in the simulation of multidimensional flow around a single well, where high flow velocities are attained due to the convergent nature of the flow towards the well. Problems involving solution gas and a vertical or inclined coordinate are also known to give rise to serious stability problems as soon as the gas phase becomes mobile. This "gas percolation" problem arises when free gas is released from solution as the pressure decreases below the bubble-point. The low gas viscosity results in a high mobility and the gas flows upwards (percolates) with relatively high velocities.

Blair and Weinaug[46] have shown that much of the stability problem results from the explicit treatment of transmissibilities. Additional factors affecting the stability include the large difference in the densities of the liquid and gas phases, the stronger nonlinearity of the pressure-dependent functions of the gas, and the highly nonlinear nature of the capillary pressures. Aziz and Settari[43] also note that the production terms must be approximated in the same fashion as the interblock transmissibilities in order to maintain stability when saturations change near production wells.

Based on these observations and the complexity of the problem under consideration, a fully-implicit treatment (evaluation at the $n+1$ time level) of all variables was deemed necessary to insure the stability of the computations.

This improvement in the stability of the computations is not without cost. The fully implicit treatment of the equations and their simultaneous solution inherently require increased computational labor. Overall, however, MacDonald

and Coats[42] found that a fully-implicit model is substantially more efficient for problems involving high capillary forces and small computing grid blocks at the wellbore. A thorough treatment of the stability analysis, truncation errors and computational labor involved with various solution methods is given by Aziz and Settari[43] and Peaceman[47].

2.4.2.d Fully Implicit Discretization of Equations

Prior to presenting the finite-difference form of the equations representing our initial-boundary value problem, we note that whenever a term or group of terms is not specified as being evaluated at a particular time level (e.g., $n+1$), it is understood that they are evaluated implicitly (at the $n+1$ time level). Because variations of Newton's method will be used to solve the system of nonlinear equations, we also require that our primary equations be in the appropriate residual form, e.g., $F(\vec{x}) = 0$.

The fully implicit finite-difference form of our flow equation, Eq. 2.3.33, for component #1, therefore, becomes

$$
\begin{aligned}
F_{1,i,k} = \\
&[x_1 \mathcal{T}_{ro}]_{i+\frac{1}{2},k}(p_{o,i+1,k} - p_{o,i,k}) + \\
&[y_1 \mathcal{T}_{rg}]_{i+\frac{1}{2},k}(p_{o,i+1,k} - p_{o,i,k} + p_{cog,i+1,k} - p_{cog,i,k}) - \\
&[x_1 \mathcal{T}_{ro}]_{i-\frac{1}{2},k}(p_{o,i,k} - p_{o,i-1,k}) - \\
&[y_1 \mathcal{T}_{rg}]_{i-\frac{1}{2},k}(p_{o,i,k} - p_{o,i-1,k} + p_{cog,i,k} - p_{cog,i-1,k}) + \\
&[x_1 \mathcal{T}_{zo}]_{i,k+\frac{1}{2}}(p_{o,i,k+1} - p_{o,i,k} + \overline{\gamma}_{o,i,k+\frac{1}{2}} \Delta z_{k+\frac{1}{2}}) + \\
&[y_1 \mathcal{T}_{zg}]_{i,k+\frac{1}{2}}(p_{o,i,k+1} - p_{o,i,k} + p_{cog,i,k+1} - p_{cog,i,k} + \overline{\gamma}_{g,i,k+\frac{1}{2}} \Delta z_{k+\frac{1}{2}}) - \\
&[x_1 \mathcal{T}_{zo}]_{i,k-\frac{1}{2}}(p_{o,i,k} - p_{o,i,k-1} + \overline{\gamma}_{o,i,k-\frac{1}{2}} \Delta z_{k-\frac{1}{2}}) - \\
&[y_1 \mathcal{T}_{zg}]_{i,k-\frac{1}{2}}(p_{o,i,k} - p_{o,i,k-1} + p_{cog,i,k} - p_{cog,i,k-1} + \overline{\gamma}_{g,i,k-\frac{1}{2}} \Delta z_{k-\frac{1}{2}}) - \\
&\frac{V_{i,k}}{\Delta t}\{[\phi(x_1 \overline{\rho}_o S_o + y_1 \overline{\rho}_g S_g)]_{i,k}^{n+1} - [\phi(x_1 \overline{\rho}_o S_o + y_1 \overline{\rho}_g S_g)]_{i,k}^{n}\} \\
&= 0
\end{aligned}
\tag{2.4.54}
$$

Note that in the discretized form of our flow equation we have included the oil saturation, S_o, instead of eliminating it as we did in Eq. 2.3.33. This is simply a matter of convenience as we still require that the oil saturation be determined from the appropriate time level values of the gas and water saturations; e.g.,

$$S_{o}{}_{,i,k}^{n+1} = 1 - S_{w}{}_{,i,k}^{n+1} - S_{g}{}_{,i,k}^{n+1} \tag{2.4.55}$$

Our finite-difference equation for component #2 is

$$\begin{aligned}
F_{2\,,i,k} = & \\
& [x_2 \mathcal{T}_{ro}]_{i+\frac{1}{2},k}(p_{o\,,i+1,k} - p_{o\,,i,k}) + \\
& [y_2 \mathcal{T}_{rg}]_{i+\frac{1}{2},k}(p_{o\,,i+1,k} - p_{o\,,i,k} + p_{cog\,,i+1,k} - p_{cog\,,i,k}) - \\
& [x_2 \mathcal{T}_{ro}]_{i-\frac{1}{2},k}(p_{o\,,i,k} - p_{o\,,i-1,k}) - \\
& [y_2 \mathcal{T}_{rg}]_{i-\frac{1}{2},k}(p_{o\,,i,k} - p_{o\,,i-1,k} + p_{cog\,,i,k} - p_{cog\,,i-1,k}) + \\
& [x_2 \mathcal{T}_{zo}]_{i,k+\frac{1}{2}}(p_{o\,,i,k+1} - p_{o\,,i,k} + \overline{\gamma}_{o\,,i,k+\frac{1}{2}} \Delta z_{k+\frac{1}{2}}) + \\
& [y_2 \mathcal{T}_{zg}]_{i,k+\frac{1}{2}}(p_{o\,,i,k+1} - p_{o\,,i,k} + p_{cog\,,i,k+1} - p_{cog\,,i,k} + \overline{\gamma}_{g\,,i,k+\frac{1}{2}} \Delta z_{k+\frac{1}{2}}) - \\
& [x_2 \mathcal{T}_{zo}]_{i,k-\frac{1}{2}}(p_{o\,,i,k} - p_{o\,,i,k-1} + \overline{\gamma}_{o\,,i,k-\frac{1}{2}} \Delta z_{k-\frac{1}{2}}) - \\
& [y_2 \mathcal{T}_{zg}]_{i,k-\frac{1}{2}}(p_{o\,,i,k} - p_{o\,,i,k-1} + p_{cog\,,i,k} - p_{cog\,,i,k-1} + \overline{\gamma}_{g\,,i,k-\frac{1}{2}} \Delta z_{k-\frac{1}{2}}) - \\
& \frac{V_{i,k}}{\Delta t}\{[\phi(x_2 \overline{\rho}_o S_o + y_2 \overline{\rho}_g S_g)]_{i,k}^{n+1} - [\phi(x_2 \overline{\rho}_o S_o + y_2 \overline{\rho}_g S_g)]_{i,k}^{n}\} \\
= & \; 0
\end{aligned} \tag{2.4.56}$$

and for water

$$\begin{aligned}
F_{3\,,i,k} = & \\
& [\mathcal{T}_{rw}]_{i+\frac{1}{2},k}(p_{o\,,i+1,k} - p_{o\,,i,k} + p_{cow\,,i,k} - p_{cow\,,i+1,k}) - \\
& [\mathcal{T}_{rw}]_{i-\frac{1}{2},k}(p_{o\,,i,k} - p_{o\,,i-1,k} + p_{cow\,,i-1,k} - p_{cow\,,i,k}) + \\
& [\mathcal{T}_{zw}]_{i,k+\frac{1}{2}}(p_{o\,,i,k+1} - p_{o\,,i,k} + p_{cow\,,i,k} - p_{cow\,,i,k+1} + \overline{\gamma}_{w\,,i,k+\frac{1}{2}} \Delta z_{k+\frac{1}{2}}) -
\end{aligned}$$

$$[\mathcal{T}_{zw}]_{i,k-\frac{1}{2}}(p_{o,i,k}-p_{o,i,k-1}+p_{cow,i,k-1}-p_{cow,i,k}+\overline{\gamma}_{w,i,k-\frac{1}{2}}\Delta z_{k-\frac{1}{2}})-$$
$$\frac{V_{i,k}}{\Delta t}\{[\phi\overline{\rho}_w S_w]^{n+1}_{i,k}-[\phi\overline{\rho}_w S_w]^{n}_{i,k}\}$$
$$=0 \qquad (2.4.57)$$

As mentioned previously, when we specify a constant production rate we require an additional primary equation to account for the additional unknown, p_{wb}. For production at a constant surface oil rate, q_{osc}, we have as our additional primary equation

$$F_4=\frac{1}{5.615\overline{\rho}_{osc}}\Bigg\{\sum_{k=N_{zw_1}}^{N_{zw_2}}[x_{2,1/2,k}\mathcal{T}_{ro,1/2,k}(p_{o,1,k}-p_{wf,k})+$$
$$y_{2,1/2,k}\mathcal{T}_{rg,1/2,k}(p_{o,1,k}+p_{cog,1,k}-p_{wf,k})]^{n+1}\Bigg\}-q_{osc}$$
$$=0\ . \qquad (2.4.58)$$

For production at a constant surface gas rate, q_{gsc}, we obtain

$$F_4=\frac{1}{5.615\overline{\rho}_{gsc}}\Bigg\{\sum_{k=N_{zw_1}}^{N_{zw_2}}[x_{1,1/2,k}\mathcal{T}_{ro,1/2,k}(p_{o,1,k}-p_{wf,k})+$$
$$y_{1,1/2,k}\mathcal{T}_{rg,1/2,k}(p_{o,1,k}+p_{cog,1,k}-p_{wf,k})]^{n+1}\Bigg\}-q_{gsc}$$
$$=0\ . \qquad (2.4.59)$$

Production at a constant surface water rate, q_{wsc}, results in the following equation:

$$F_4=\frac{1}{5.615\overline{\rho}_{wsc}}\Bigg\{\sum_{k=N_{zw_1}}^{N_{zw_2}}[\mathcal{T}_{rw,1/2,k}(p_{o,1,k}-p_{cow,1,k}-p_{wf,k})]^{n+1}\Bigg\}-q_{wsc}$$
$$=0\ . \qquad (2.4.60)$$

A constant total surface production rate, q_{tsc}, is represented by the equation

$$F_4 = \frac{1}{5.615\overline{\rho}_{osc}}\left\{\sum_{k=N_{zw_1}}^{N_{zw_2}} [x_{2,1/2,k}\mathcal{T}_{ro,1/2,k}(p_{o,1,k} - p_{wf,k})+ \right.$$
$$\left. [y_{2,1/2,k}\mathcal{T}_{rg,1/2,k}(p_{o,1,k} + p_{cog,1,k} - p_{wf,k})]^{n+1}\right\}+$$
$$\frac{1}{5.615\overline{\rho}_{gsc}}\left\{\sum_{k=N_{zw_1}}^{N_{zw_2}} [x_{1,1/2,k}\mathcal{T}_{ro,1/2,k}(p_{o,1,k} - p_{wf,k})+ \right.$$
$$\left. y_{1,1/2,k}\mathcal{T}_{rg,1/2,k}(p_{o,1,k} + p_{cog,1,k} - p_{wf,k})]^{n+1}\right\}+$$
$$\frac{1}{5.615\overline{\rho}_{wsc}}\left\{\sum_{k=N_{zw_1}}^{N_{zw_2}} [\mathcal{T}_{rw,1/2,k}(p_{o,1,k} - p_{cow,1,k} - p_{wf,k})]^{n+1}\right\} - q_{tsc}$$
$$= 0\ . \qquad (2.4.61)$$

Production at a constant reservoir volumetric rate becomes

$$F_4 = \frac{1}{5.615}\left\{\sum_{k=N_{zw_1}}^{N_{zw_2}} [\frac{1}{\overline{\rho}_{o,1/2,k}}\mathcal{T}_{ro,1/2,k}(p_{o,1,k} - p_{wf,k})+ \right.$$
$$\frac{1}{\overline{\rho}_{g,1/2,k}}\mathcal{T}_{rg,1/2,k}(p_{o,1,k} + p_{cog,1,k} - p_{wf,k})+$$
$$\left. \frac{1}{\overline{\rho}_{w,1/2,k}}\mathcal{T}_{rw,1/2,k}(p_{o,1,k} - p_{cow,1,k} - p_{wf,k})]^{n+1}\right\} - q_t$$
$$= 0\ . \qquad (2.4.62)$$

The primary equation for a constant total molar rate, $\overline{m}_t$, is

$$F_4 = \left\{\sum_{k=N_{zw_1}}^{N_{zw_2}} [x_{2,1/2,k}\mathcal{T}_{ro,1/2,k}(p_{o,1,k} - p_{wf,k})+ \right.$$
$$\left. [y_{2,1/2,k}\mathcal{T}_{rg,1/2,k}(p_{o,1,k} + p_{cog,1,k} - p_{wf,k})]^{n+1}\right\}+$$
$$\left\{\sum_{k=N_{zw_1}}^{N_{zw_2}} [x_{1,1/2,k}\mathcal{T}_{ro,1/2,k}(p_{o,1,k} - p_{wf,k})+ \right.$$

$$y_{1,1/2,k}\mathcal{T}_{rg,1/2,k}(p_{o,1,k}+p_{cog,1,k}-p_{wf,k})]^{n+1}\Big\}+$$
$$\Big\{\sum_{k=N_{zw_1}}^{N_{zw_2}}[\mathcal{T}_{rw,1/2,k}(p_{o,1,k}-p_{cow,1,k}-p_{wf,k})]^{n+1}\Big\}-\overline{m}_t$$
$$=\ 0\ , \tag{2.4.63}$$

and for a constant total mass rate, m_t, we have

$$F_4 = M_2\Big\{\sum_{k=N_{zw_1}}^{N_{zw_2}}[x_{2,1/2,k}\mathcal{T}_{ro,1/2,k}(p_{o,1,k}-p_{wf,k})+$$
$$[y_{2,1/2,k}\mathcal{T}_{rg,1/2,k}(p_{o,1,k}+p_{cog,1,k}-p_{wf,k})]^{n+1}\Big\}+$$
$$M_1\Big\{\sum_{k=N_{zw_1}}^{N_{zw_2}}[x_{1,1/2,k}\mathcal{T}_{ro,1/2,k}(p_{o,1,k}-p_{wf,k})+$$
$$y_{1,1/2,k}\mathcal{T}_{rg,1/2,k}(p_{o,1,k}+p_{cog,1,k}-p_{wf,k})]^{n+1}\Big\}+$$
$$M_w\Big\{\sum_{k=N_{zw_1}}^{N_{zw_2}}[\mathcal{T}_{rw,1/2,k}(p_{o,1,k}-p_{cow,1,k}-p_{wf,k})]^{n+1}\Big\}-m_t$$
$$=\ 0\ , \tag{2.4.64}$$

where, M_1, M_2 and M_w are the molecular weights of the light hydrocarbon component, the heavy hydrocarbon component and water, respectively.

In each of Eqs. 2.4.58-2.4.64, the flowing wellbore pressure, p_{wf}, adjacent to grid block k is evaluated as

$$p_{wf,k}^{\nu+1\ n+1}|_{k=N_{zw_1}} = p_{wb}^{\nu+1\ n+1} \tag{2.4.65}$$

$$p_{wf,k}^{\nu+1\ n+1} = p_{wb}^{\nu+1\ n+1} - \sum_{l=N_{zw_1}+1}^{N_{zw_2}}\overline{\gamma}_l^{\nu\ n+1}\Delta z_{l-1/2} \tag{2.4.66}$$

where ν is the Newton's method iteration level and

$$\overline{\gamma}_l^{\,n+1\,\nu} = \frac{(q_{ol}\gamma_{ol} + q_{gl}\gamma_{gl} + q_{wl}\gamma_{wl})^{n+1\,\nu}}{(q_{ol} + q_{gl} + q_{wl})^{n+1\,\nu}} \tag{2.4.67}$$

and

$$q_{ol}^{n+1\,\nu} = \frac{1}{\rho_{ol}^{n+1\,\nu}} \sum_{m=N_{zw_1}}^{l} \mathcal{T}_{ro}{}_{,1/2,m}^{n+1\,\nu}(p_{o}{}_{,1,m}^{n+1\,\nu} - p_{wf}{}_{,m}^{n+1\,\nu}) \tag{2.4.68}$$

$$q_{gl}^{n+1\,\nu} = \frac{1}{\rho_{gl}^{n+1\,\nu}} \sum_{m=N_{zw_1}}^{l} \mathcal{T}_{rg}{}_{,1/2,m}^{n+1\,\nu}(p_{o}{}_{,1,m}^{n+1\,\nu} + p_{cog}{}_{,1,m}^{n+1\,\nu} - p_{wf}{}_{,m}^{n+1\,\nu}) \tag{2.4.69}$$

$$q_{wl}^{n+1\,\nu} = \frac{1}{\rho_{wl}^{n+1\,\nu}} \sum_{m=N_{zw_1}}^{l} \mathcal{T}_{rw}{}_{,1/2,m}^{n+1\,\nu}(p_{o}{}_{,1,m}^{n+1\,\nu} - p_{cow}{}_{,1,m}^{n+1\,\nu} - p_{wf}{}_{,m}^{n+1\,\nu}) \tag{2.4.70}$$

Here, $\rho_{m}{}_{,l}^{n+1\,\nu} = \rho_m(p_{wf}{}_{,l}^{n+1\,\nu}), m = o, w, g$. For the purposes of Newton's method, we always make the assumption

$$p_{wf}{}_{,k} = f(p_{wb}) \neq f(S_{w,k}, S_{g}{}_{,k}, p_{o}{}_{,1,k}) \tag{2.4.71}$$

For the case of a specified bottomhole pressure, we invoke Eqs. 2.4.65-2.4.71 only to obtain the required values of $p_{wf}{}_{,k}$. Once the complete solution to the initial-boundary value problem is obtained, we can determine the individual phase flow rates at any level ($N_{zw_1} \leq k \leq N_{zw_2}$) in the wellbore from Eqs. 2.4.68-2.4.70, with all variables evaluated at the $n+1$ time step, i.e.:

$$q_{o}{}_{,k}^{n+1} = \frac{1}{\rho_o(p_{wf}{}_{,k}^{n+1})} \sum_{l=N_{zw_1}}^{k} \mathcal{T}_{ro}{}_{,1/2,l}^{n+1}(p_{o}{}_{,1,l}^{n+1} - p_{wf}{}_{,l}^{n+1}) \quad , \tag{2.4.72}$$

$$q_{g}{}_{,k}^{n+1} = \frac{1}{\rho_g(p_{wf}{}_{,k}^{n+1})} \sum_{l=N_{zw_1}}^{k} \mathcal{T}_{rg}{}_{,1/2,l}^{n+1}(p_{o}{}_{,1,l}^{n+1} + p_{cog}{}_{,1,l}^{n+1} - p_{wf}{}_{,l}^{n+1}) \tag{2.4.73}$$

and

$$q_{w,k}^{n+1} = \frac{1}{\rho_w(p_{wf,k}^{n+1})} \sum_{l=N_z w_1}^{k} \mathcal{T}_{rw,1/2,l}^{n+1}(p_{o,1,l}^{n+1} - p_{cow,1,l}^{n+1} - p_{wf,l}^{n+1}) \ . \quad (2.4.74)$$

Surface flow rates for each phase can be determined by solving Eqs. 2.4.58-2.4.60 for ${q_{osc}}^{n+1}$, ${q_{gsc}}^{n+1}$ and ${q_{wsc}}^{n+1}$, respectively.

In practice, two methods are available for incorporating the no-flow boundary conditions (outer, lower, upper and inner). The first method simply requires that we specify the phase transmissibilities at the no-flow boundaries to be equal to zero. Using this method, we can express the no-flow outer boundary condition as

$$\mathcal{T}_{ro,N_r+1/2,k} = 0 \quad , \ 1 \le k \le N_z \ , \quad (2.4.75a)$$

$$\mathcal{T}_{rg,N_r+1/2,k} = 0 \quad , \ 1 \le k \le N_z \quad (2.4.75b)$$

and

$$\mathcal{T}_{rw,N_r+1/2,k} = 0 \quad , \ 1 \le k \le N_z \ ; \quad (2.4.75c)$$

the no-flow lower boundary condition as

$$\mathcal{T}_{zo,i,1/2} = 0 \quad , \ 1 \le i \le N_r \ , \quad (2.4.76a)$$

$$\mathcal{T}_{zg,i,1/2} = 0 \quad , \ 1 \le i \le N_r \quad (2.4.76b)$$

and

$$\mathcal{T}_{zw,i,1/2} = 0 \quad , \ 1 \le i \le N_r \ ; \quad (2.4.76c)$$

the no-flow upper boundary condition as

$$\mathcal{T}_{zo,i,N_z+1/2} = 0 \quad , \ 1 \le i \le N_r \ , \quad (2.4.77a)$$

$$\mathcal{T}_{zg\,,i,N_z+1/2} = 0 \quad , \; 1 \leq i \leq N_r \tag{2.4.77b}$$

and

$$\mathcal{T}_{zw\,,i,N_z+1/2} = 0 \quad , \; 1 \leq i \leq N_r \; ; \tag{2.4.77c}$$

and the no-flow part of the inner boundary condition as

$$\mathcal{T}_{ro\,,1/2,k} = 0 \begin{cases} 1 \leq k < N_{zw_1} \\ N_{zw_2} < k \leq N_z \end{cases} \quad , \tag{2.4.78a}$$

$$\mathcal{T}_{rg\,,1/2,k} = 0 \begin{cases} 1 \leq k < N_{zw_1} \\ N_{zw_2} < k \leq N_z \end{cases} \tag{2.4.78b}$$

and

$$\mathcal{T}_{rw\,,1/2,k} = 0 \begin{cases} 1 \leq k < N_{zw_1} \\ N_{zw_2} < k \leq N_z \end{cases} \quad . \tag{2.4.78c}$$

The second method for treating the no-flow boundary conditions, often referred to as the reflection or mirror technique, requires that we introduce "mirror image" ficticious grid points across the boundaries. These image grid points are then specified as having the same phase potentials as their image grid points within our system domain. Use of this method results in the following for our outer boundary conditions

$$(p_{o\,,i+1,k} - p_{o\,,i,k}) = 0 \begin{cases} i = N_r \\ 1 \leq k \leq N_z \end{cases} \quad , \tag{2.4.79a}$$

$$(p_{o\,,i+1,k} - p_{o\,,i,k} + p_{cog\,,i+1,k} - p_{cog\,,i,k}) = 0 \begin{cases} i = N_r \\ 1 \leq k \leq N_z \end{cases} \tag{2.4.79b}$$

and

$$(p_{o\,,i+1,k} - p_{o\,,i,k} + p_{cow\,,i,k} - p_{cog\,,i+1,k}) = 0 \begin{cases} i = N_r \\ 1 \leq k \leq N_z \end{cases} \quad ; \tag{2.4.79c}$$

for our lower boundary conditions

$$(p_{o,i,k} - p_{o,i,k-1} + \overline{\gamma}_{o,i,k-\frac{1}{2}} \Delta z_{k-\frac{1}{2}}) = 0 \begin{cases} 1 \leq i \leq N_r \\ k = 1 \end{cases} , \tag{2.4.80a}$$

$$(p_{o,i,k} - p_{o,i,k-1} + p_{cog,i,k} - p_{cog,i,k-1} + \overline{\gamma}_{g,i,k-\frac{1}{2}} \Delta z_{k-\frac{1}{2}}) = 0 \begin{cases} 1 \leq i \leq N_r \\ k = 1 \end{cases} \tag{2.4.80b}$$

and

$$(p_{o,i,k} - p_{o,i,k-1} + p_{cow,i,k-1} - p_{cog,i,k} + \overline{\gamma}_{w,i,k-\frac{1}{2}} \Delta z_{k-\frac{1}{2}}) = 0 \begin{cases} 1 \leq i \leq N_r \\ k = 1 \end{cases} ; \tag{2.4.80c}$$

for our upper boundary conditions

$$(p_{o,i,k+1} - p_{o,i,k} + \overline{\gamma}_{o,i,k+\frac{1}{2}} \Delta z_{k+\frac{1}{2}}) = 0 \begin{cases} 1 \leq i \leq N_r \\ k = N_z \end{cases} , \tag{2.4.81a}$$

$$(p_{o,i,k+1} - p_{o,i,k} + p_{cog,i,k+1} - p_{cog,i,k} + \overline{\gamma}_{g,i,k+\frac{1}{2}} \Delta z_{k+\frac{1}{2}}) = 0 \begin{cases} 1 \leq i \leq N_r \\ k = N_z \end{cases} \tag{2.4.81b}$$

and

$$(p_{o,i,k+1} - p_{o,i,k} + p_{cow,i,k} - p_{cow,i,k+1} + \overline{\gamma}_{w,i,k+\frac{1}{2}} \Delta z_{k+\frac{1}{2}}) = 0 \begin{cases} 1 \leq i \leq N_r \\ k = N_z \end{cases} ; \tag{2.4.81c}$$

and for the no-flow part of our inner boundary conditions

$$(p_{o,1,k} - p_{wf,k}) = 0 \begin{cases} 1 \leq k < N_{zw_1} \\ N_{zw_2} < k \leq N_z \end{cases} , \tag{2.4.82a}$$

$$(p_{o,1,k} + p_{cog,1,k} - p_{wf,k}) = 0 \begin{cases} 1 \leq k < N_{zw_1} \\ N_{zw_2} < k \leq N_z \end{cases} \tag{2.4.82b}$$

and

$$(p_{o,1,k} - p_{cow,1,k} - p_{wf,k}) = 0 \begin{cases} 1 \leq k < N_{zw_1} \\ N_{zw_2} < k \leq N_z \end{cases} \quad . \tag{2.4.82c}$$

Lastly, the discretized form of our initial conditions is required. As mentioned previously, we begin by specifying one reference pressure and two reference saturations at appropriate reference locations within the reservoir:

$$p_o(z) = p_o(z^r) \quad , z = z^r \ , \tag{2.4.83a}$$

$$S_g(z) = S_{gc} \quad , z = z_{goc} \tag{2.4.83b}$$

and

$$S_w(z) = S_{wc} \quad , z = z_{owc} \ . \tag{2.4.83c}$$

The initial pressures and saturations throughout the rest of the reservoir are automatically fixed according to the appropriate hydrostatic pressure relation and capillary pressure - saturation relations, assuming the capillary pressure - saturation relations are uniquely defined over the entire range of possible saturations. This requirement will be discussed further as we proceed.

Some notes on the notation to be used for the initial condition specification are required for clearity: let N_{zref} represent the maximum discrete vertical index for which $z_k \leq z^r$; let N_{zowc} represent the maximum discrete vertical index for which $z_k \leq z_{owc}$; and let us define N_{zgoc} as the minimum discrete vertical index for which $z_k \geq z_{goc}$. These definitions are represented graphically on Fig. 2.2. For the development to be presented here, we have also assumed that z^r is within a region of the reservoir for which the oil phase is mobile. Additionally, throughout the development it will be assumed that the vertical specification of the initial

conditions uniquely determines the radial specification; e.g., $p_{o,i+1,k} = p_{o,i,k}$, $0 \leq i \leq N_r - 1$.

The next step requires that we determine the phase pressures throughout the reservoir. Because these pressures are determined differently depending upon which phases are present and which phases are mobile, we proceed in a piecewise manner through the reservoir.

$$p_{o,i,k} = {p_o}^r + \gamma_o({p_o}^r)(z^r - z_k) \quad , \; k = N_{zref} \tag{2.4.84a}$$

$$p_{o,i,k} = p_{o,i,k+1} + \gamma_{o,i,k+1}\Delta z_{k+\frac{1}{2}} \quad , \; N_{zowc} + 1 \leq k \leq N_{zref} - 1 \tag{2.4.84b}$$

$$p_o(z_{owc}) = p_{o,i,k} + \gamma_{o,i,k}(z_k - z_{owc}) \quad , \; k = N_{zowc} + 1 \tag{2.4.84c}$$

$$p_w(z_{owc}) = p_o(z_{owc}) - p_{cow}(S_{wc}) \tag{2.4.84d}$$

$$p_{w,i,k} = p_w(z_{owc}) + \gamma_w(p_w(z_{owc}))(z_{owc} - z_k) \quad , \; k = N_{zowc} \tag{2.4.84e}$$

$$p_{w,i,k} = p_{w,i,k+1} + \gamma_{w,i,k+1}\Delta z_{k+\frac{1}{2}} \quad , \; 1 \leq k \leq N_{zowc} - 1 \tag{2.4.84f}$$

$$p_{o,i,k} = p_o(z_{owc}) + \gamma_o(p_o(z_{owc}))(z_{owc} - z_k) \begin{cases} k = N_{zowc} \\ p_{o,i,k} > p_{w,i,k} + p_{cow}(S_{wmax}) \end{cases} \tag{2.4.84g}$$

$$p_{o,i,k} = p_{o,i,k+1} + \gamma_{o,i,k+1}\Delta z_{k+\frac{1}{2}} \begin{cases} 1 \leq k \leq N_{zowc} \\ p_{o,i,k} > p_{w,i,k} + p_{cow}(S_{wmax}) \end{cases} \tag{2.4.84h}$$

$$p_{o,i,k} = p_{w,i,k} + p_{cow}(S_{wmax}) \begin{cases} 1 \leq k \leq N_{zowc} \\ p_{o,i,k} \leq p_{w,i,k} + p_{cow}(S_{wmax}) \end{cases} \tag{2.4.84i}$$

$$p_{cow,i,k} = p_{o,i,k} - p_{w,i,k} \quad , \; 1 \leq k \leq N_{zowc} \tag{2.4.84j}$$

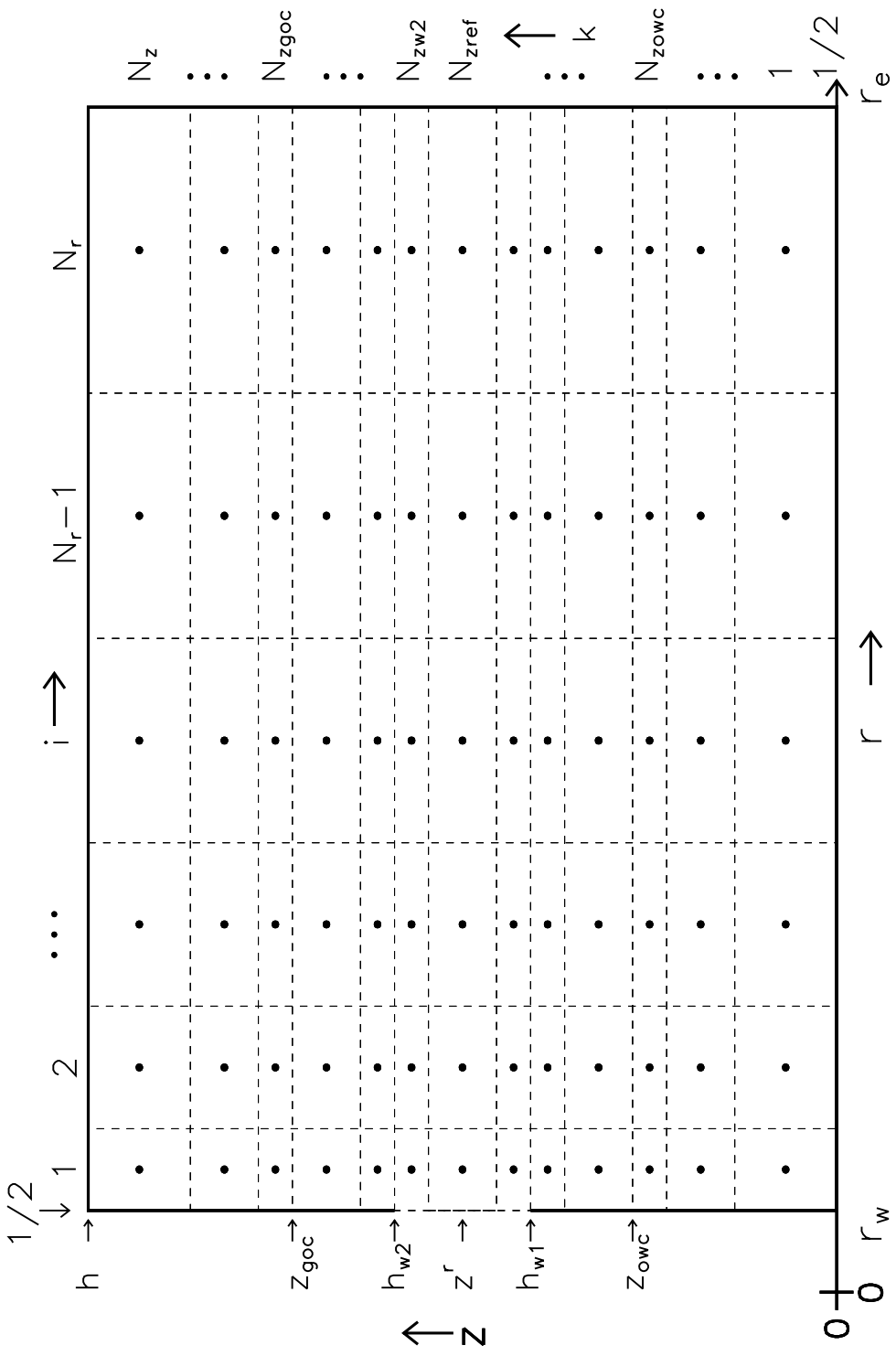

Fig. 2.2 — Definitions used with finite–difference grid.

$$p_{o,i,k} = p_{o,i,k-1} - \gamma_{o,i,k-1}\Delta z_{k-\frac{1}{2}} \quad , \; N_{zref} + 1 \leq k \leq N_{zgoc} - 1 \tag{2.4.84k}$$

$$p_o(z_{goc}) = p_{o,i,k} - \gamma_{o,i,k}(z_{goc} - z_k) \quad , \; k = N_{zgoc} - 1 \tag{2.4.84l}$$

$$p_g(z_{goc}) = p_o(z_{goc}) + p_{cog}(S_{gc}) \tag{2.4.84m}$$

$$p_{g,i,k} = p_g(z_{goc}) - \gamma_g(p_g(z_{goc}))(z_k - z_{goc}) \quad , \; k = N_{zgoc} \tag{2.4.84n}$$

$$p_{g,i,k} = p_{g,i,k-1} - \gamma_{g,i,k-1}\Delta z_{k-\frac{1}{2}} \quad , \; N_{zgoc} + 1 \leq k \leq N_z \tag{2.4.84o}$$

$$p_{o,i,k} = p_o(z_{goc}) - \gamma_o(p_o(z_{goc}))(z_k - z_{goc}) \begin{cases} k = N_{zgoc} \\ p_{o,i,k} > p_{g,i,k} - p_{cog}(S_{or}) \end{cases} \tag{2.4.84p}$$

$$p_{o,i,k} = p_{o,i,k-1} - \gamma_{o,i,k-1}\Delta z_{k-\frac{1}{2}} \begin{cases} N_{zgoc} + 1 \leq k \leq N_z \\ p_{o,i,k} > p_{g,i,k} - p_{cog}(S_{or}) \end{cases} \tag{2.4.84q}$$

$$p_{o,i,k} = p_{g,i,k} - p_{cog}(S_{or}) \begin{cases} N_{zgoc} \leq k \leq N_z \\ p_{o,i,k} \leq p_{g,i,k} - p_{cog}(S_{or}) \end{cases} \tag{2.4.84r}$$

$$p_{g,i,k} = p_{g,i,k+1} + \gamma_{g,i,k+1}\Delta z_{k+\frac{1}{2}} \begin{cases} k \leq N_{zgoc} - 1 \\ p_{g,i,k} > p_{o,i,k} + p_{cog}(S_{omax}) \end{cases} \tag{2.4.84s}$$

$$p_{g,i,k} = p_{o,i,k} + p_{cog}(S_{omax}) \begin{cases} k \leq N_{zgoc} - 1 \\ p_{g,i,k} \leq p_{o,i,k} + p_{cog}(S_{omax}) \end{cases} \tag{2.4.84t}$$

$$p_{cog,i,k} = p_{g,i,k} - p_{o,i,k} \quad , \; 1 \leq k \leq N_z \tag{2.4.84u}$$

Having defined the initial pressure distribution throughout the reservoir, we can now proceed to the specification of the initial saturation distributions. For the water saturations we have

$$S_{w,i,k} = S_{wc} \quad , \; k > N_{zowc} \tag{2.4.85a}$$

and

$$S_{w,i,k} = S_w(p_{cow,i,k}) \quad , \; k \leq N_{zowc} \tag{2.4.85b}$$

and for the gas saturations we have

$$S_{g,i,k} = S_g(p_{cog,i,k}) \quad , \; 1 \leq k \leq N_z \; . \tag{2.4.86}$$

Equations 2.4.83-2.4.86 completely specify our initial conditions. There are several extremely important assumptions implied in the above specification of the initial conditions, however. First, we note that Eq. 2.4.84r combined with Eq. 2.4.86 limits the minimum oil saturation possible in the gas zone to the residual oil saturation, S_{or}. This is because the gas-oil capillary pressure curve is undefined for oil saturations less than residual oil saturation. In a physical sense, we would expect the oil saturation to decrease as we move up through the gas zone. There are a variety of methods available that will allow us to maintain this sence of physical reality. The first method would be to define a "pseudo-capillary pressure" relationship over the range ($0 \leq S_o \leq S_{or}$). We note that this method appears to be simply trading one non-physical characteristic for another non-physical characteristic, however, we feel that the modeling of the overall physics of the reservoir production process will be greatly enhanced. If this method is to be employed, several modifications to our equations are required. First, Eqs. 2.4.84p-2.4.84r are modified to

$$p_{o,i,k} = p_o(z_{goc}) - \gamma_o(p_o(z_{goc}))(z_k - z_{goc}) \begin{cases} k = N_{zgoc} \\ p_{o,i,k} > p_{g,i,k} - p_{cog}(S_{omin}) \end{cases} \tag{2.4.87a}$$

$$p_{o,i,k} = p_{o,i,k-1} - \gamma_{o,i,k-1}\Delta z_{k-\frac{1}{2}} \begin{cases} N_{zgoc} + 1 \leq k \leq N_z \\ p_{o,i,k} > p_{g,i,k} - p_{cog}(S_{omin}) \end{cases} \tag{2.4.87b}$$

$$p_{o,i,k} = p_{g,i,k} - p_{cog}(S_{or}) \begin{cases} N_{zgoc} \leq k \leq N_z \\ p_{o,i,k} \leq p_{g,i,k} - p_{cog}(S_{omin}) \end{cases} \tag{2.4.87c}$$

where $S_{omin} = 0$. Equation (2.4.86) then requires no modification. One of the advantages of this method over others rests in the fact that additional equations are not required to properly pose our initial-value boundary problem.

Another extremely important assumption in the specification of the initial conditions is the implied assumption that the drainage capillary pressure curves are being used; i.e., we require that the capillary pressure curves be uniquely defined in the intervals $(1 - S_{or} \leq S_w \leq 1)$ and $(0 \leq S_g \leq S_{gc})$ for the oil-water and gas-oil capillary pressure curves, respectively. The advantage to using the drainage capillary pressure curves lies in the fact that they allow the oil saturation to go to zero (e.g., in an aquifer) and they allow the gas saturation to go to zero (e.g., in the case of an oil reservoir of large vertical extent where the oil near the top of the pay is below the bubble-point pressure and where the oil near the bottom of the pay is above the bubble-point pressure).

If imbibition capillary pressure curves are to be used and we wish to be able to represent such physical cases as mentioned above, then we again must employ some other initialization method. Once again, the simplest approach may be to simply extend the the capillary pressure curves via a simple chord from the last non-zero capillary pressure to zero capillary pressure at $S_o = 1 - S_{wc}$ and $S_w = 1$ for the gas-oil and oil-water capillary pressure curves, respectively. The advantage to this approach is that we do not have to modify our equations and our initial-value boundary problem remains well posed.

Generally speaking, drainage capillary pressure curves are used in the initialization of reservoir fluid distributions as it is commonly assumed that the hydrocarbons accumulated via a displacement of the water originally existing in the reservoir rock; i.e., drainage is a process by which the water (wetting phase) saturation decreases and imbibition is a process by which the wetting phase saturation increases.

As mentioned, there are other methods which could be used to completely specify our initial conditions and here we mention one additional method. Instead of modifying the capillary pressure curves, one could also choose to use a method other than the capillary pressure curves to determine the saturations where the capillary pressure curves are not defined. For example, one might use linear extrapolation of the saturation profiles within the respective phases' mobile regions of the reservoir. As previously mentioned, this requires us to modify some of our equations. First, Eq. 2.4.84i is modified to

$$p_{o\,,i,k} = p_{w\,,i,k} \begin{cases} 1 \le k \le N_{zowc} \\ p_{o\,,i,k} \le p_{w\,,i,k} \end{cases} \tag{2.4.88}$$

and Eq. 2.4.84r is modified as

$$p_{g\,,i,k} = p_{o\,,i,k} \begin{cases} k \le N_{zgoc} - 1 \\ p_{g\,,i,k} \le p_{o\,,i,k} \end{cases} . \tag{2.4.89}$$

Equations for determining the saturations are now modified. Equation 2.4.86 becomes in the region above the gas-oil contact

$$S_{g\,,i,k} = S_g(p_{cog\,,i,k}) \begin{cases} N_{zgoc} \le k \le N_z \\ p_{cog\,,i,k} < p_{cog}(S_{or}) \end{cases} , \tag{2.4.90a}$$

$$S_{g\,\mathrm{ex}} = S_{g\,,i,k-1} + \Big(\frac{S_{g\,,i,k-1} - S_{g\,,i,k-2}}{z_{k-1} - z_{k-2}}\Big)\Delta z_{k-\frac{1}{2}} \begin{cases} N_{zgoc} \le k \le N_z \\ p_{cog\,,i,k} \ge p_{cog}(S_{or}) \end{cases} , \tag{2.4.90b}$$

$$S_{g\,,i,k}|_{k \ge N_{zgoc}} = \begin{cases} S_{g\,\mathrm{ex}} & \text{for } S_{g\,\mathrm{ex}} < 1 - S_{wc} \\ 1 - S_{wc} & \text{for } S_{g\,\mathrm{ex}} \ge 1 - S_{wc} \end{cases} , \tag{2.4.90c}$$

and in the region below the gas-oil contact

$$S_{g\,,i,k} = S_g(p_{cog\,,i,k}) \begin{cases} k < N_{zgoc} \\ p_{cog\,,i,k} > 0 \end{cases} , \tag{2.4.90d}$$

$$S_{g\,\mathrm{ex}} = S_{g\,,i,k+1} + \Big(\frac{S_{g\,i,k+2} - S_{g\,,i,k+1}}{z_{k+2} - z_{k+1}}\Big)\Delta z_{k+\frac{1}{2}} \begin{cases} k < N_{zgoc} \\ \\ p_{cog\,,i,k} = 0 \end{cases} \qquad (2.4.90e)$$

and

$$S_{g\,,i,k} = \begin{cases} S_{g\,\mathrm{ex}} & \text{for } S_{g\,\mathrm{ex}} > 0 \\ \\ 0 & \text{for } S_{g\,\mathrm{ex}} \leq 0 \end{cases} . \qquad (2.4.90f)$$

Equation 2.4.85b for determining the water saturation below the water-oil contact must also be modified to

$$S_{w\,,i,k} = S_w(p_{cow\,,i,k}) \begin{cases} k \leq N_{zowc} \\ \\ p_{cow\,,i,k} > 0 \end{cases} , \qquad (2.4.91a)$$

$$S_{w\,\mathrm{ex}} = S_{w\,,i,k+1} + \Big(\frac{S_{w\,i,k+2} - S_{w\,,i,k+1}}{z_{k+2} - z_{k+1}}\Big)\Delta z_{k+\frac{1}{2}} \begin{cases} k \leq N_{zowc} \\ \\ p_{cow\,,i,k} = 0 \end{cases} \qquad (2.4.91b)$$

and

$$S_{w\,,i,k} = \begin{cases} S_{w\,\mathrm{ex}} & \text{for } S_{w\,\mathrm{ex}} < 1 \\ \\ 1 & \text{for } S_{w\,\mathrm{ex}} \geq 1 \end{cases} . \qquad (2.4.91c)$$

Because variations of Newton's method are to be used to solve our nonlinear system of equations, we also require expressions for the Jacobian matrix coefficients to complete the specification of our numerical system. In keeping with our desire to make our simulator as robust and numerically accurate as possible, we have chosen to calculate the Jacobian coefficients analytically, rather than approximating them numerically; i.e., the chain rule is used to fully expand the partial derivatives of the primary equations (2.4.54-2.4.64) with-respect-to the primary variables and then the primary variables and their derivatives are inserted. This is in contrast to the common practice of evaluating the primary equations at two different values of the primary variables and then dividing the difference of those results by the difference in the values of the primary variable used. Additional computational cost involved in calculating the Jacobian coefficients analytically was considered

to be negligible. A complete listing of the analytic expressions for the Jacobian coefficients is presented in Appendix B.

2.4.3 Conjugate Gradient-Type Iterative Methods for Solving Nonsymmetric Systems of Linear Equations

The numerical implementation of Newton's method is quite straight forward, requiring only that we set up our matrices in an appropriate manner. Prior to continuing, let us recall that we can represent Newton's method in matrix form as

$$J^{\nu}\vec{\delta x} = \vec{F}(\vec{x}^{\nu}) \tag{2.4.92}$$

(or equivalently as $Ax = b$) where $\vec{F}(\vec{x}^{\nu})$ is the vector array containing our primary equations (Eqs. 2.4.55-2.4.57) evaluated at every grid point in our system using the ν^{th} Newton's method iteration level values of our independent unknowns, $\vec{x}^{\nu}$. If production is specified at a constant rate, then $\vec{F}(\vec{x}^{\nu})$ also contains our wellbore constraint equation (one of Eqs. 2.4.58-2.4.64). The vector array $\vec{x}^{\nu}$ denotes our independent unknowns (p_o, $\{S_g$, p_b or p_d and $S_w)$ at every grid point, calculated at the ν^{th} iteration level of Newton's method at the $n+1$ time level. For the case of a specified constant production rate, $\vec{x}^{\nu}$ also contains the flowing (shut-in) bottomhole pressure, ${p_{wb}}^{\nu}$ (p^{ν}_{ws}). The vector array $\vec{\delta x}$ denotes the difference in the successive Newton's method iteration values of all unknowns, and J^{ν} represents the Jacobian matrix of the partial derivatives of all our primary equations with respect to all of our unknowns, computed using the ν^{th} iteration level values of the unknowns.

For large systems of linear equations, it is well known that direct solution methods can be expensive, both in terms of work and storage requirements. In recent years, several conjugate gradient-type iterative methods for the solution of nonsymmetric systems of linear equations have been presented in the

literature[48–60]. Methods such as the truncated version of Vinsome's[48] method, Orthomin(k), have been used very successfully with various preconditioners to solve the nonsymmetric linear systems which arise in reservoir simulation (e.g., see Refs. 61-63).

Saad and Schultz[49–51] presented a generalized minimum residual method, GMRES(k), as an alternative to the Orthomin(k)[48] and GCR(k)[55] methods. Rather than using $A^T A$ orthogonal basis vectors for the subspace of dimension k from which the approximate solution x_k is constructed, Saad and Schultz show how simple orthogonality of the basis vectors suffices to construct a solution which minimizes the residual norm over the subspace. Saad and Schultz[51], thereby, show that, for k large, GMRES($k+1$) can obtain the same approximate solution as GCR(k) or Orthomin(k) using about half the storage and a third less work.

Recently, Van der Vorst[52] presented a variation (Bi-CGSTAB) of the conjugate gradient-squared (CG-S)[53] iterative method for the solution of nonsymmetric linear systems. Ref. 51 indicated that the method is often competitive with other methods such as GMRES[49], and for this reason, the Bi-CGSTAB method and a variant Bi-CGSTAB-P were implemented in our simulator.

Numerical results reported by Refs. 51 and 64 and our own investigation[65] tend to confirm the superiority of GMRES over GCR and Orthomin. GMRES has also been found in this study to be less costly than the Bi-CGSTAB iterative methods. These results are discussed further in Chapter III.

The theoretical developments of these methods are well covered in the literature and are not repeated here. Rather, we simply present the algorithms for the practical application of GMRES(k), Orthomin(k) and Bi-CGSTAB, as implemented in our simulator, in Appendix C.

2.4.4 Preconditioning

It is well known that the convergence rate of the conjugate gradient method can be related to the condition number, or more specifically, to the eigenvalue distribution of the matrix A. The convergence properties for the GMRES(k) method are presented in Ref. 51 where the convergence rate is shown to be bounded by the eigenvalue distribution of the system.

The idea of preconditioning consists of modifying the original system in such a way as to improve the convergence rate of the iterative process. In general, we seek to replace the system

$$Ax = b \tag{2.4.93}$$

by an equivalent system

$$Cy = d \tag{2.4.94}$$

which has a spectral condition number closer to unity, i.e., letting $\{\lambda_j\}_{j=1}^{n}$ denote the eigenvalues of C, we wish to have $\max|\lambda_j|/\min|\lambda_j|$ as close to unity as possible. If we let Q be a square invertible matrix, then the preconditioned system (2.4.94) can take on one of the following forms:

$$\begin{aligned} Q^{-1}Ax &= Q^{-1}b \quad \text{(left preconditioning)}, \\ Q_L^{-1}AQ_R^{-1}Q_Rx &= Q_L^{-1}b \quad \text{(split preconditioning)} \\ &\text{or} \\ AQ^{-1}Qx &= b \qquad \text{(right preconditioning)}. \end{aligned} \tag{2.4.95}$$

Advantages arising from using one particular form of preconditioning vary with the system to be solved and particular choice for Q and are not discussed here. Rather, we simply state that both left and right preconditioning have been incorporated into our simulator.

The choice of the preconditioner, Q, can be crucial to the success of the preconditioned iterative method. Desirable properties for the preconditioner include that it be sparse, easy to factor and a good approximation of A. This last property means that we wish the spectral condition number of $Q^{-1}A$ to be substantially smaller than that of A. All of these properties underscore the fact that to be useful, the gains in the convergence rate of the underlying iterative method for the preconditioned problem must more than offset the cost of preconditioning.

In recent years, a variety of preconditioners have been proposed for solving the sparse linear systems arising in reservoir simulation (e.g., see Refs. 54,62,63,66-72). Two incomplete factorization methods, namely, block-incomplete-LU decomposition (BILU) and block-symmetric-Gauss-Seidel (BSGS) have been investigated and incorporated into our simulator. Domain decomposition as the overall preconditioner, along with a variety of preconditioners for the subdomain systems and Schur complement/capacitance matrix, were also investigated[65] and are discussed in the next section.

Suppose we let

$$A = L + D + U \tag{2.4.96}$$

where D is the block-diagonal of the matrix A, L is strictly lower block-triangular and U is strictly upper block-triangular. An incomplete block-decomposition of the matrix A has the form

$$Q = (L+F)F^{-1}(U+F) \tag{2.4.97}$$

where F is a block-diagonal matrix. For block-incomplete-LU decomposition we impose the restriction

$$\text{block diagonal } (A-Q) \equiv 0 \tag{2.4.98}$$

thereby requiring F to satisfy

$$F = D - \text{block diagonal } [LF^{-1}U] \tag{2.4.99}$$

This incomplete decomposition is a block version of the Dupont-Kendall-Rachford decomposition[72].

For the block-symmetric-Gauss-Seidel factorization we simply require that

$$F = D \tag{2.4.100}$$

Many variations on these factorizations are possible; for instance, the number of extra bands included in the incomplete factorization can be increased to give a more accurate factorization at the price of increased work per iteration. Incomplete factorizations which incorporate a diagonal modification to give a zero row sum error matrix can also be used[73]. No variations in these factorizations have been incorporated into our simulator at this time.

In a sense, preprocessing of the system (e.g., different orderings of the grid cells) can also be used in combination with incomplete factorization. Betté et al.[54] and Díaz et al.[74] considered block-diagonal scaling of the system prior to iteration. Ref. 74 reported that for difficult problems in thermal simulation, block-diagonal scaling can significantly enhance the rate of convergence of norm-reducing iterative methods. Reordering schemes, including natural ordering, D2 ordering,[67] D4 ordering,[68,69,71,75] minimum degree ordering,[71] quotient minimum degree ordering,[76] and automated nested disection[76] have been used.

In the context of Gaussian elimination, the goal of reordering is to obtain a permuted system

$$\tilde{A}\tilde{x} = \tilde{b} \tag{2.4.101}$$

which can be solved more easily than the system represented by Eq. 2.4.92. Here, $\tilde{A} = PAR$, $\tilde{x} = R^T x$ and $\tilde{b} = Pb$, where P and R are permutation matrices chosen, for example, such that the factorization of $\tilde{A}$ incurs less fill-in than the factorization of A.

To justify why reordering should add to the benefits of incomplete factorizations, consider the following heuristic argument presented by Simon[76]:

> The goal of any reordering is to produce a permutation so that the permuted system (2.4.101) has less fill-in than the original system (2.4.93). The number of nonzeros in the factors of $\tilde{A}$ is less than the number of nonzeros in the factors of A. Suppose now an incomplete factorization of both A and $\tilde{A}$ is performed and (say) all fill-in is discarded, i.e., only an incomplete factorization based on the structure of A and $\tilde{A}$ is computed. Then, since in the system (2.4.101) a full factorization would have incurred less overall fill-in than in (2.4.93), the incomplete factor captures a larger share of the complete factor in (2.4.101) than in (2.4.93)....Thus, for a comparatively small effort, a reordering may improve the quality of an incomplete factorization.

Though reordering schemes are not explicitly used in this study, it will be shown later in this work that the use of domain decomposition as a preconditioner results in a natural reordering that may or may not be of benefit. We note that no matter how we order our unknowns and equations, our Jacobian matrix will be extremely sparse in nature, i.e., most of the entries will be zero. As an example, consider the case of a 50×50 grid structure with all three phases present in every grid. Our Jacobian matrix will then be of order 7500, but there will be at most 15 non-zero entries in any one row (neglecting the wellbore constraint equation).

With the exception of the domain decomposition preconditioned systems, we simply employ a natural row-wise ordering of the grid cells. Within each grid cell, the active equations are arranged in the order F_1, F_2, F_3 and the primary variables are arranged in the order p_o, $\{S_g$, p_b, or $p_d\}$ and S_w. For those cases in which a constant production rate is specified, the wellbore constraint equation

is ordered last, as is the wellbore pressure. As an example, consider the two-dimensional finite-difference grid with natural ordering shown in Fig. 2.3.

The structure of the Jacobian matrix for a standard five-point finite-difference operator is shown in Fig. 2.4, where each entry in the matrix corresponds to the active equations and primary unknowns in the corresponding grid block. The off-diagonal elements result from the coupling of the wellbore constraint equation. For example, for any given row, $l = i + N_r(k-1)$, of the matrix in Fig. 2.4, the X actually represents the submatrix

$$X_l = \begin{pmatrix} \frac{\partial F_{1,i,k}}{\partial p_{o,i,k}} & \frac{\partial F_{1,i,k}}{\partial S_{g,i,k}} & \frac{\partial F_{1,i,k}}{\partial S_{w,i,k}} \\ \frac{\partial F_{2,i,k}}{\partial p_{o,i,k}} & \frac{\partial F_{2,i,k}}{\partial S_{g,i,k}} & \frac{\partial F_{2,i,k}}{\partial S_{w,i,k}} \\ \frac{\partial F_{3,i,k}}{\partial p_{o,i,k}} & \frac{\partial F_{3,i,k}}{\partial S_{g,i,k}} & \frac{\partial F_{3,i,k}}{\partial S_{w,i,k}} \end{pmatrix}, \qquad (2.4.102a)$$

where the subscript i,k denotes the radial and vertical discrete grid block corresponding to that row of the matrix. Each T represents the submatrix

$$T_l = \begin{pmatrix} \frac{\partial F_{1,,i,k}}{\partial p_{o,i-1,k}} & \frac{\partial F_{1,i,k}}{\partial S_{g,i-1,k}} & \frac{\partial F_{1,i,k}}{\partial S_{w,i-1,k}} \\ \frac{\partial F_{2,i,k}}{\partial p_{o,i-1,k}} & \frac{\partial F_{2,i,k}}{\partial S_{g,i-1,k}} & \frac{\partial F_{2,i,k}}{\partial S_{w,i-1,k}} \\ \frac{\partial F_{3,i,k}}{\partial p_{o,i-1,k}} & \frac{\partial F_{3,i,k}}{\partial S_{g,i-1,k}} & \frac{\partial F_{3,i,k}}{\partial S_{w,i-1,k}} \end{pmatrix}, \qquad (2.4.102b)$$

each S represents the submatrix

$$S_l = \begin{pmatrix} \frac{\partial F_{1,i,k}}{\partial p_{o,i,k-1}} & \frac{\partial F_{1,i,k}}{\partial S_{g,i,k-1}} & \frac{\partial F_{1,i,k}}{\partial S_{w,i,k-1}} \\ \frac{\partial F_{2,i,k}}{\partial p_{o,i,k-1}} & \frac{\partial F_{2,i,k}}{\partial S_{g,i,k-1}} & \frac{\partial F_{2,i,k}}{\partial S_{w,i,k-1}} \\ \frac{\partial F_{3,i,k}}{\partial p_{o,i,k-1}} & \frac{\partial F_{3,i,k}}{\partial S_{g,i,k-1}} & \frac{\partial F_{3,i,k}}{\partial S_{w,i,k-1}} \end{pmatrix}, \qquad (2.4.102c)$$

each U represents the submatrix

$$U_l = \begin{pmatrix} \frac{\partial F_{1,i,k}}{\partial p_{o,i+1,k}} & \frac{\partial F_{1,i,k}}{\partial S_{g,i+1,k}} & \frac{\partial F_{1,i,k}}{\partial S_{w,i+1,k}} \\ \frac{\partial F_{2,i,k}}{\partial p_{o,i+1,k}} & \frac{\partial F_{2,i,k}}{\partial S_{g,i+1,k}} & \frac{\partial F_{2,i,k}}{\partial S_{w,i+1,k}} \\ \frac{\partial F_{3,i,k}}{\partial p_{o,i+1,k}} & \frac{\partial F_{3,i,k}}{\partial S_{g,i+1,k}} & \frac{\partial F_{3,i,k}}{\partial S_{w,i+1,k}} \end{pmatrix}, \qquad (2.4.102d)$$

11	12	13	14	15
6	7	8	9	10
1	2	3	4	5

* Wellbore ordered as grid #16.

Fig. 2.3 - Example two-dimensional finite-difference grid with standard ordering.

$$
\begin{pmatrix}
X & U & & & & V & & & & & & & & & Y \\
T & X & U & & & & V & & & & & & & & \\
 & T & X & U & & & & V & & & & & & & \\
 & & T & X & U & & & & V & & & & & & \\
 & & & T & X & & & & & V & & & & & \\
S & & & & & X & U & & & & V & & & & Y \\
 & S & & & & T & X & U & & & & V & & & \\
 & & S & & & & T & X & U & & & & V & & \\
 & & & S & & & & T & X & U & & & & V & \\
 & & & & S & & & & T & X & & & & & V \\
 & & & & & S & & & & & X & U & & & Y \\
 & & & & & & S & & & & T & X & U & & \\
 & & & & & & & S & & & & T & X & U & \\
 & & & & & & & & S & & & & T & X & U \\
 & & & & & & & & & S & & & & T & X \\
* & Z & & & & Z & & & & & Z & & & & W
\end{pmatrix}
$$

* - Wellbore constraint equation.

Fig. 2.4 - Matrix structure for five-point finite-difference scheme with normal ordering and fully coupled wellbore constraint equation.

and each V represents the submatrix

$$V_l = \begin{pmatrix} \frac{\partial F_{1,i,k}}{\partial p_{o,i,k+1}} & \frac{\partial F_{1,i,k}}{\partial S_{g,i,k+1}} & \frac{\partial F_{1,i,k}}{\partial S_{w,i,k+1}} \\ \frac{\partial F_{2,i,k}}{\partial p_{o,i,k+1}} & \frac{\partial F_{2,i,k}}{\partial S_{g,i,k+1}} & \frac{\partial F_{2,i,k}}{\partial S_{w,i,k+1}} \\ \frac{\partial F_{3,i,k}}{\partial p_{o,i,k+1}} & \frac{\partial F_{3,i,k}}{\partial S_{g,i,k+1}} & \frac{\partial F_{3,i,k}}{\partial S_{w,i,k+1}} \end{pmatrix} . \qquad (2.4.102e)$$

Each Y in Fig. 2.4 represents

$$Y_l = \begin{pmatrix} \frac{\partial F_{1,i,k}}{\partial p_{wb}} \\ \frac{\partial F_{2,i,k}}{\partial p_{wb}} \\ \frac{\partial F_{3,i,k}}{\partial p_{wb}} \end{pmatrix}_{1,k} , \qquad (2.4.103)$$

each Z represents

$$Z_m = \left(\frac{\partial F_4}{\partial p_{o,1,k}} \quad \frac{\partial F_4}{\partial S_{g,1,k}} \quad \frac{\partial F_4}{\partial S_{w,1,k}} \right) \qquad (2.4.104)$$

where m repesents the column of the matrix in Fig. 2.4 and $1,k$ denotes the discrete grid block it corresponds to. Finally, W is simply

$$W = \left(\frac{\partial F_4}{\partial p_{wb}} \right) . \qquad (2.4.105)$$

Note that if a grid block is undersaturated, $S_g = 0$ ($S_o = 0$), then the partial derivatives with-respect-to gas saturation in Eqs. 2.4.102 and 2.4.104 are replaced by the partial derivatives with-respect-to the saturation pressure, p_b (p_d).

Based on the results of Refs. 54 and 74, options for both right and left block-diagonal scaling of the linear system prior to iteration have been incorporated into our simulator. For the linear systems considered in this study, however, block-diagonal scaling of the system prior to iteration has failed to improve the convergence rate of the iterative method.

2.4.5 Domain Decomposition Techniques

Domain decomposition can generally be referred to as a class of techniques for solving partial differential equations on a given domain by first decomposing the domain into smaller domains and then obtaining the overall solution by solving smaller problems on these subdomains. The theoretical origins to domain decomposition can be traced back to Schwarz's[77] alternating procedure.

Domain decomposition methods can be attractive in many situations. No doubt, one of the primary reasons for the intensive research ongoing in this area is due to the recent advances in parallel computing architecture and the natural route to parallelism provided by various domain decomposition techniques. Domain decomposition methods can even prove beneficial in a sequential computing environment when the advantages obtained in isolating the subproblems outweigh the extra work required.

Apart from the parallel computing advantages of domain decomposition methods, other reasons exist for considering their use. Irregular shaped domains can be decomposed into subdomains of regular shape for which discrete operators of a regular structure can be obtained. Regions of discontinuous coefficients or substantially different physics can be isolated into different subdomains.

Many of the domain decomposition methods proposed so far in the literature employ some form of preconditioned conjugate gradient method for its solution. In this study, we consider a method wherein domain decomposition is used as an overall preconditioner for the conjugate gradient-type iterative methods incorporated into our simulator and discussed in *Section 2.4.3* of Chapter II, i.e., GMRES(k), Orthomin(k) and Bi-CGSTAB. Various preconditioners are considered for both the subdomain systems of linear equations and for the Schur

complement/capacitance matrix system. Here, we present a description and discussion of the Schur complement and partitioned matrix domain decomposition techniques and their implementation in the iterative methods. Preconditioners for the subdomain systems of linear equations and the Schur complement system of equations are also discussed along with the parallelizable aspects of these two domain decomposition procedures.

Apparently originating with Ref. 78, a number of domain decomposition methods which make use of preconditioned conjugate gradient-type iteration in the outer loop have recently been proposed. In this section we discuss two such methods known as Schur complement methods (e.g., Refs. 79-81) and full partitioned matrix methods which are based on block Gaussian elimination and do not make explicit use of the reduced Schur complement system (e.g., Ref. 82).

The simplest decomposition on which these two methods can be compared (and the only one considered in this study) is that involving two simply connected subdomains. Consider, for example, the finite difference grid in Fig.2.3 and suppose we decompose this discrete system into two subdomains, Ω_1 and Ω_2, simply connected through the boundary, Γ_3, as shown in Fig. 2.5. Further, if we order the finite difference grids as shown in Fig. 2.5, i.e., the grids in subdomain Ω_1 are ordered first, followed by Ω_2 and finally the boundary Γ_3 between the two subdomains, we obtain the matrix structure depicted in Fig. 2.6. Note that for the system considered in this study, i.e., one which directly couples a wellbore constraint equation, the wellbore constraint equation appears in the first subdomain.

Clearly, for this system we can write Eq. 2.4.93 in the expanded form

$$\begin{pmatrix} A_{11} & 0 & A_{13} \\ 0 & A_{22} & A_{23} \\ A_{31} & A_{32} & A_{33} \end{pmatrix} \begin{pmatrix} x_1 \\ x_2 \\ x_3 \end{pmatrix} = \begin{pmatrix} b_1 \\ b_2 \\ b_3 \end{pmatrix} \tag{2.4.106}$$

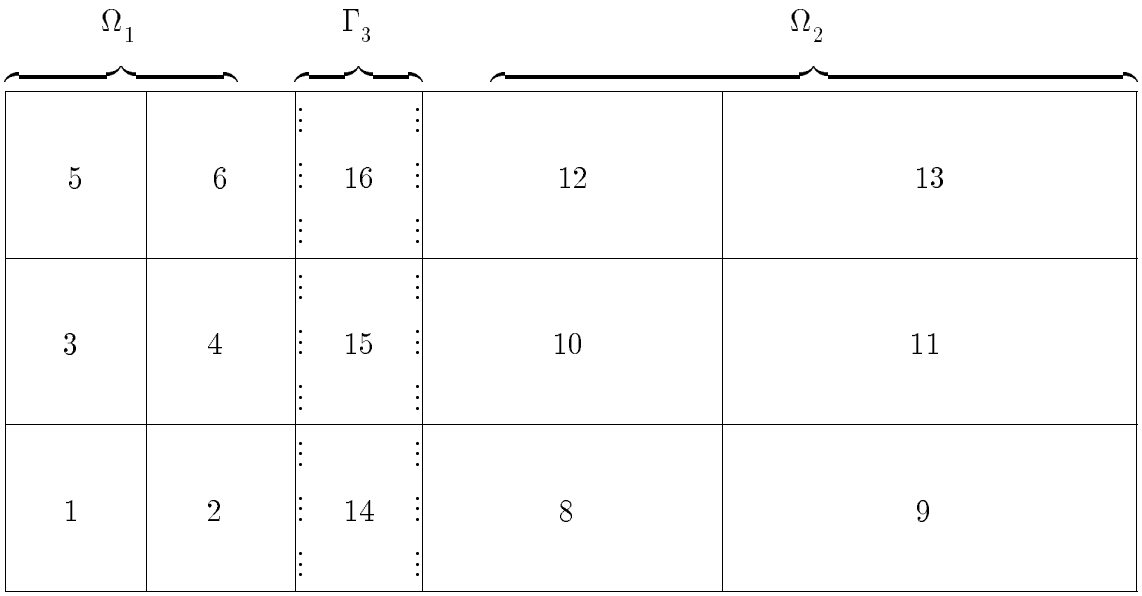

* Wellbore ordered as grid #7.

Fig. 2.5 - Example two-dimensional finite-difference grid with domain decomposition ordering ($N_{R_1} = 2$).

$$
\begin{array}{c}
 \\
 \\
 \\
 \\
\Omega_1 \\
 \\
 \\
 \\
* \\
 \\
 \\
\Omega_2 \\
 \\
 \\
 \\
 \\
\Gamma_3 \\
 \\
\end{array}
\begin{array}{c}
\begin{array}{cccccccccccccccc}
 & & & \Omega_1 & & & & & & \Omega_2 & & & & & \Gamma_3 & \\
\end{array} \\
\left(\begin{array}{cccccccccccccccc}
X & U & V & & & & Y & & & & & & & & & \\
T & X & & V & & & & & & & & & & U & & \\
S & & X & U & V & & Y & & & & & & & & & \\
 & S & T & X & & V & & & & & & & & & U & \\
 & & S & & X & U & Y & & & & & & & & & \\
 & & & S & T & X & & & & & & & & & & U \\
Z & & Z & & Z & & W & & & & & & & & & \\
 & & & & & & & X & U & V & & & & T & & \\
 & & & & & & & T & X & & V & & & & & \\
 & & & & & & & S & & X & U & V & & & T & \\
 & & & & & & & & S & T & X & & V & & & \\
 & & & & & & & & & S & & X & U & & & T \\
 & & & & & & & & & & S & T & X & & & \\
 & T & & & & & & U & & & & & & X & V & \\
 & & & T & & & & & & U & & & & S & X & V \\
 & & & & & T & & & & & & U & & & S & X
\end{array}\right)
\end{array}
$$

* - Wellbore constraint equation.

Fig. 2.6 - Matrix structure for five-point finite-difference scheme with domain decomposition ordering and fully coupled wellbore constraint equation.

where x_1 and x_2 are the unknowns in subdomains Ω_1 and Ω_2, respectively, and x_3 represents the unknowns on the boundary, Γ_3. The matrices A_{11}, A_{22} and A_{33} correspond to the discrete difference operator on Ω_1, Ω_2 and Γ_3. The matrices A_{13}, A_{23}, A_{31} and A_{32} correspond to the coupling of the unknowns in Ω_1 and Ω_2 with those in Γ_3. Let us also denote the dimensions of A_{11}, A_{22} and A_{33} as n_1, n_2 and n_3, respectively, with $n = n_1 + n_2 + n_3$.

Schur Complement Methods

The Schur complement or capacitance matrix system can formally be obtained by performing a block Gaussian elimination on Eq. 2.4.106, resulting in

$$\begin{pmatrix} A_{11} & 0 & A_{13} \\ 0 & A_{22} & A_{23} \\ 0 & 0 & C \end{pmatrix} \begin{pmatrix} x_1 \\ x_2 \\ x_3 \end{pmatrix} = \begin{pmatrix} b_1 \\ b_2 \\ \tilde{b}_3 \end{pmatrix} . \tag{2.4.107}$$

The Schur complement system is given by

$$C x_3 = \tilde{b}_3 \tag{2.4.108}$$

where C is the Schur complement,

$$C = A_{33} - A_{31} A_{11}^{-1} A_{13} - A_{32} A_{22}^{-1} A_{23} \tag{2.4.109}$$

and

$$\tilde{b}_3 = b_3 - A_{31} A_{11}^{-1} b_1 - A_{32} A_{22}^{-1} b_2 . \tag{2.4.110}$$

The right-hand side of the capacitance system, i.e., Eq. 2.4.110, can be evaluated by solving two subdomain problems, one each on Ω_1 and Ω_2. The Schur complement, Eq. 2.4.109, however, can be expensive to construct because it generally requires n_3 solves on each subdomain. Once the solution to the capacitance system, Eq. 2.4.108, is known, the entire system, Eq. 2.4.107, can easily be solved

by back substitution. Early domain decomposition methods (e.g., Ref. 83) solved the capacitance system, Eq. 2.4.108 using direct methods. Because C is generally dense, a direct method for solving Eq. 2.4.108 could be prohibitively expensive if n_3 is large.

Recently, more efficient techniques have been developed in which a variant of the capacitance matrix method becomes an iterative solution for the capacitance system using conjugate gradient-type methods[80,84–86]. Schur complement methods of this type can be realized by taking A in algorithms GMRES(k), Orthomin(k) and Bi-CGSTAB (Appendix C) to be C and selecting an appropriate preconditioner, Q. Note that the iterations now occur on vectors of length n_3. Each iteration in these methods then requires one solution on each of the subdomains Ω_1 and Ω_2 to form the matrix-vector products involving C; e.g., to obtain the vector u in algorithm Orthomin(k) we need to evaluate the matrix-vector product Cz. This product can be evaluated by first solving

$$\begin{pmatrix} A_{11} & 0 \\ 0 & A_{22} \end{pmatrix} \begin{pmatrix} y_1 \\ y_2 \end{pmatrix} = \begin{pmatrix} -A_{13} \cdot z_1 \\ -A_{23} \cdot z_2 \end{pmatrix} \tag{2.4.111}$$

and then computing the product Cz as

$$Cz = A_{33} z_3 + A_{31} y_1 + A_{32} y_2 \ . \tag{2.4.112}$$

Note that the Schur complement, C, is never explicitly computed.

The main differences among the methods reported in the literature lie in the treatment of the preconditioner, Q. A detailed discussion of each of these preconditioners is beyond the scope of this work, but we do comment on a few. The Bjørstad and Widlund[85] and Chan[87] preconditioners have been shown (e.g., Ref. 88) theoretically to result in the smallest condition number for $Q^{-1}C$ when

Ω is a rectangle and Ω_1 and Ω_2 are symmetrically disposed about the interface. Indeed, both methods are exact in this case; i.e., $Q = C$ and their methods converge in one step. The Golub and Mayers[81] preconditioner has been shown to be nearly as good as these methods (e.g., see Refs. 85,87-89) and the Dryja[80] preconditioner slightly worse. Glowinski et al.[84] simply chose the original matrix A_{33} as the preconditioning matrix Q.

Partitioned Matrix Methods

One of the main disadvantages of working with the Schur complement system is that the subdomain solves are presumed to be carried out exactly and are therefore expensive to compute; i.e., in the general case, direct solvers or nested iterations are required in computations such as Cz. Alternative methods which do not require the subdomain solves be carried out exactly have been developed (e.g., Ref. 82) in which preconditioned conjugate gradient-type iterations are used to solve the full system in the form of Eq. 2.4.106. These methods are referred to as partitioned matrix methods and can be realized by taking A in algorithms GMRES(k), Orthomin(k) or Bi-CGSTAB to be the whole matrix A and selecting an appropriate preconditioner, Q.

A theorem by Eisenstat presented in Ref. 88 shows that preconditioned conjugate gradient (PCG) iteration applied to the Schur complement system, $Cx_3 = \tilde{b}_3$, with initial iterate x_3^0 and preconditioner M is equivalent to PCG iteration applied to the entire domain system, $Ax = b$, with initial iterate

$$x^0 = \begin{pmatrix} A_{11}^{-1}(b_1 - A_{13}x_3^0) \\ A_{22}^{-1}(b_2 - A_{23}x_3^0) \\ x_3^0 \end{pmatrix} \tag{2.4.113}$$

and preconditioner

$$Q = \begin{pmatrix} A_{11} & 0 & A_{13} \\ 0 & A_{22} & A_{23} \\ A_{31} & A_{32} & (M + A_{31}A_{11}^{-1}A_{13} + A_{32}A_{22}^{-1}A_{23}) \end{pmatrix} \tag{2.4.114}$$

That this is true can easily be shown by considering the case where the Bjørstad and Widlund[85] or Chan[87] preconditioners are exact, i.e., $M = C$. Clearly, for this case $Q = A$ and the PCG iteration will converge in one step.

Bramble, Pasciak and Schatz[82,90] developed an efficient implementation of partitioned matrix preconditioners of the form (2.4.114) which does not require the subdomain solves be exact. Based on the decomposition of the matrix A (Eq. 2.4.106) as

$$A = \begin{pmatrix} A_{11} & 0 & 0 \\ 0 & A_{22} & 0 \\ A_{31} & A_{32} & C \end{pmatrix} \begin{pmatrix} I & 0 & A_{11}^{-1}A_{13} \\ 0 & I & A_{22}^{-1}A_{23} \\ 0 & 0 & I \end{pmatrix} \tag{2.4.115}$$

a preconditioner for A can be derived as

$$Q = \begin{pmatrix} B_{11} & 0 & 0 \\ 0 & B_{22} & 0 \\ A_{31} & A_{32} & M \end{pmatrix} \begin{pmatrix} I & 0 & B_{11}^{-1}A_{13} \\ 0 & I & B_{22}^{-1}A_{23} \\ 0 & 0 & I \end{pmatrix} \tag{2.4.116}$$

where the B_{ii}'s are some approximation to the A_{ii}'s and M is any of the Schur complement preconditioners previously discussed. A simplified version of the Bramble et al.[90] percondition is presented in Chapter III.

Bramble et al.[90] used both the Bjørstad and Widlund[85] and Dryja[80] preconditioners as the preconditioner M for C, and for the case of Laplace's equation on a rectangle, fast Fourier transforms for the approximations B_{11} and B_{22}.

Based on a block-incomplete decomposition of the entire matrix, A, Meurant[91,92] shows how a preconditioner, M, for the Schur complement can be derived as

$$M = B_{33} - A_{31}B_{11}^{-1}A_{13} - A_{32}B_{22}^{-1}A_{23} \tag{2.4.117}$$

where the B_{ii}'s are some approximation to the matrices, A_{ii}. In his work, Meurant used a block-incomplete-LU decomposition approximation, B_{11}, for A_{11}, a block-incomplete-UL decomposition approximation, B_{22}, for A_{22} and simply used A_{33} as its own approximation, B_{33}. Rather than using the approximation (Eq. 2.4.117) directly for M, Meurant took the approximation one step further, only using the diagonals of the B_{ii}'s; i.e.,

$$M = A_{33} - A_{31}D_{11}^{-1}A_{13} - A_{32}D_{22}^{-1}A_{23} \tag{2.4.118}$$

where the D_{ii}'s are the derived diagonals of the matrices B_{ii}, e.g., the F in Eqs. 2.4.97 and 2.4.99.

Application of the Bramble et al.[90] preconditioner is then straight forward. Consider, for example, that we wish to precondition the residual vector, i.e., we wish to solve the system

$$Qz = r \tag{2.4.119}$$

for the preconditioned residual vector z. We first use forward substitution to solve

$$\begin{pmatrix} B_{11} & 0 & 0 \\ 0 & B_{22} & 0 \\ A_{31} & A_{32} & M \end{pmatrix} \begin{pmatrix} w_1 \\ w_2 \\ w_3 \end{pmatrix} = \begin{pmatrix} r_1 \\ r_2 \\ r_3 \end{pmatrix} \tag{2.4.120}$$

for w, then use back substitution to solve

$$\begin{pmatrix} I & 0 & B_{11}^{-1}A_{13} \\ 0 & I & B_{22}^{-1}A_{23} \\ 0 & 0 & I \end{pmatrix} \begin{pmatrix} z_1 \\ z_2 \\ z_3 \end{pmatrix} = \begin{pmatrix} w_1 \\ w_2 \\ w_3 \end{pmatrix} \tag{2.4.121}$$

for z.

Several aspects of this application of the preconditioner which can be performed in parallel are readily identifiable. For instance, in solving Eq. 2.4.120, the systems

$$B_{11} w_1 = r_1 \tag{2.4.122}$$

and

$$B_{22} w_2 = r_2 \tag{2.4.123}$$

can be solved in parallel for w_1 and w_2, respectively. The matrix-vector products $A_{31} w_1$ and $A_{32} w_2$ can also be calculated in parallel. Following the solution of the system

$$M w_3 = r_3 - A_{31} w_1 - A_{32} w_2 \tag{2.4.124}$$

for z_3 (note that $z_3 = w_3$) then the rest of the preconditioned residual vector can be calculated in parallel as

$$z_2 = w_2 - B_{22}^{-1} A_{23} w_3 \tag{2.4.125}$$

and

$$z_1 = w_1 - B_{11}^{-1} A_{13} w_3 \tag{2.4.126}$$

2.4.6 Direct Solver

To provide a means for testing our iterative solver and to insure the accuracy of the results obtained, a sparse direct Gaussian elimination routine[93] has also been implemented in our simulator. Many of the features of the Harwell sparse matrix package MA28 are discussed in the paper by Duff and Reid[93], and here we note

only a few of them of practical concern. First, we note that the data interface with the Harwell routines is very convenient from a user standpoint, requiring no ordering of the nonzeros, but only that each nonzero be labeled with its row and column number.

Second, we note that the Harwell code uses Gaussian elimination for the direct solution of sparse unsymmetric sets of linear equations. It is well known that the ordering of the unknowns of a sparse system of linear equations can drastically affect the amount of computation and storage required for a direct solution using Gaussian elimination, and, also, can have a drastic affect on the stability of the numerical solution. Several non-standard ordering schemes which reduce the computing time and storage requirements from those for the standard ordering schemes for Gaussian elimination are discussed by Price and Coats[94], however, they do not discuss potential stability problems which could arise from those orderings. Unlike other sparse direct solution routines[95,96] which do not employ pivoting, the Harwell package impliments a scheme for pivot selection, attributed to Markowitz[97], which maintains stability requirements, while at the same time places an upper bound on the amount of fill-in that could be produced from the selection of that pivot. This facet of the Harwell package implies that the user does not necessarily have to place the unknowns and equations in any particular order since the Harwell routines will check them anyway and reorder them appropriately. From a practical standpoint, however, and especially when large numbers of equations and unknowns are involved, ordering of the equations and unknowns in such a manner as to minimize the potential fill-in prior to the calling of the Harwell routines should result in a significant savings in computing costs (overhead) since much fewer rearrangements of the equations and unknowns should be required. In this work, the Harwell routines have been used solely to validate the numerical results obtained from the iterative solvers incorporated in

our simulator and discussed previously in this chapter. As such, no investigation into the effects of various reordering schemes was performed and we simply state that when the Harwell routines are used, a normal ordering of the unknowns and equations is used.

2.4.7 Notes on Variable Substituion and Treatment of Variable Bubble-Point or Variable Dew-Point Problems

Many reservoir simulation problems involve situations in which the bubble-point or dew-point pressure can vary throughout the reservoir. Many examples exist, including gas injection into an undersaturated reservoir, waterflooding of saturated reservoirs and even primary production of a solution-gas-drive reservoir, retrograde condensate reservoir or an oil reservoir overlain by a gas cap. A variety of publications (e.g., Refs. 98-105) have discussed the physical and numerical aspects involved in modeling variable bubble-point or variable dew-point problems.

Steffenson and Sheffield[98] modeled a collapsing gas saturation during a waterflood. When a negative gas saturation is detected at the end of a time step in their model, Ref. 98 sets the bubble-point pressure equal to the estimated pressure where S_g became zero. This pressure was estimated by assuming gas saturation varies linearly with pressure near the bubble-point pressure, and, therefore, could be determined simply by linear interpolation over the time step; i.e., the bubble-point pressure could be determined from

$$p_b{}^{n+1} = p_o{}^n + \frac{S_g{}^n}{(S_g{}^n - S_g{}^{n+1})}(p_o{}^{n+1} - p_o{}^n) \ . \qquad (2.4.127)$$

The gas saturation in these grid blocks was set equal to zero, the oil saturation set equal to $1 - S_w$ and the oil saturation in adjacent saturated grid blocks was adjusted to account for material balance errors associated with the calculated

negative gas saturation. Variations in the bubble-point pressure due to mixing of undersaturated oils flowing into a common grid block were neglected.

Spillette et al.[99] assumed that a cell remains saturated or undersaturated throughout the time step. After a pressure solution was obtained, they solved saturation equations for water and gas saturations. If a grid block was determined to be undersaturated ($S_g < 0$), the bubble-point pressure was adjusted to account for the negative gas saturation and the water saturation in the cell was modified to conserve oil.

Cook et al.[100] mearly monitor the free gas saturation and set the bubble-point pressure equal to the grid block pressure when the gas saturation dissappears. They do, however, account for changes in the bubble-point pressure due to the mixing of undersaturated oils and/or movement of free gas into a grid block containing undersaturated oil.

Similar to Ref. 98, Thomas et al.[102] modeled a collapsing gas saturation using a reservoir simulator based on an IMPES-type formulation. Once the pressure had been solved for implicitly and saturations solved for explicitly, the bubble-point pressure could be determined from one of two equations in which the accumulation terms had been modified to account for the variation in bubble-point pressure.

For applications such as the modeling of CO_2 injection in which changes in saturation pressure are very large, Stright et al.[103] found that explicit treatment of saturation pressure, as was employed by Kazemi[101], severely limits the stability of a coning simulator. They found a fully-implicit treatment of the saturation pressure necessary to obtain stability comparable with conventional coning models. For saturated grid blocks, the formulation employed by Ref. 103 is similar to that of Ref. 106. For undersaturated grid blocks, modifications to the mass

accumulation terms were presented and it was stated that for stability reasons, implicit terms with-respect-to the saturation pressure would need to be included in the flow terms involving R_s.

Ammer et al.[105] simply check the status of each grid block prior to each iteration, and it the gas saturation has become negative, set the gas saturation to zero and the bubble-point pressure is set slightly ($0.01\ psi$) below the grid block pressure.

In the context of using Newton's method to solve our nonlinear system of equations, implementation of the variable substitution logic required for variable bubble-point or variable dew-point problems simply requires that we substitute the appropriate partial derivative ($\partial/\partial S_g$, $\partial/\partial p_b$ or $\partial/\partial p_d$) in the Jacobian matrix during each iteration, and appropriately calculate the physical properties and their derivatives (see Appendix A).

For the first Newton iteration of each time step, our primary variables are known. Following each successive Newton iteration, however, we need to check whether a saturation pressure has been crossed. There are three possibilities we need to consider: at the previous iteration level, (i) the grid block contained saturated oil and gas, $0 < {S_g}^{n+1}_{\nu} < 1$, (ii) the grid block contained undersaturated oil, ${p_o}^{n+1}_{\nu} > {p_b}^{n+1}_{\nu}$ (${S_g}^{n+1}_{\nu} = 0$) or, (iii) the grid block contained undersaturated gas, in which case we may have either ${p_o}^{n+1}_{\nu} > {p_{du}}^{n+1}_{\nu}$ or ${p_o}^{n+1}_{\nu} < {p_{dl}}^{n+1}_{\nu}$, where p_{du} is the upper dew-point pressure and p_{dl} is the lower dew-point pressure and which implies in both cases that ${S_g}^{n+1}_{\nu} = (1 - {S_w}^{n+1}_{\nu})$.

For the case in which the grid block contained saturated oil and gas at the previous Newton iteration level, there are three possible results (determined by a check on the gas saturation) at the end of the current iteration level: two

hydrocarbon phases coexist in the grid block

$$0 < S_g{}^{\nu+1}_{n+1} < 1 \ , \tag{2.4.128a}$$

the hydrocarbons exist only in a liquid oil phase (i.e., crossed a bubble-point)

$$S_g{}^{\nu+1}_{n+1} \leq 0 \tag{2.4.128b}$$

or the hydrocarbons exist only in the gas phase (i.e., crossed a dew-point)

$$S_g{}^{\nu+1}_{n+1} \geq (1 - S_w{}^{\nu+1}_{n+1}) \ . \tag{2.4.128c}$$

Note that for all of these case, we consider the grid block pressure to be correctly determined. No modification is required for the first case, and the gas saturation will remain one of the primary variables we solve for during the next Newton iteration.

The second case requires saturations and fluid properties be modified to account for the calculated negative gas saturation. An estimate of the pressure at which the gas saturation became zero (the bubble-point pressure) is required and is obtained by assuming a linear relationship between the gas saturation and pressure near the bubble-point[98]; i.e.,

$$p_b{}^{\nu+1}_{n+1} = p_o{}^{\nu}_{n+1} + \frac{S_g{}^{\nu}_{n+1}}{(S_g{}^{\nu}_{n+1} - S_g{}^{\nu+1}_{n+1})}(p_o{}^{\nu+1}_{n+1} - p_o{}^{\nu}_{n+1}) \ . \tag{2.4.129a}$$

Following calculation of the bubble-point pressure, the gas and oil saturations are modified according to

$$S_g{}^{\nu+1}_{n+1} = 0 \tag{2.4.129b}$$

and

$$S_o{}^{\nu+1}_{n+1} = (1 - S_w{}^{\nu+1}_{n+1}) \ . \qquad (2.4.129c)$$

Unlike Ref. 98, no attempts to correct material balance errors which may occur due to the negative gas saturation are made. Rather, we assume that material balance has been maintained while the physical solution is not correct; i.e., the gas saturation and bubble-point pressure are incorrect. It is interesting to note that for cases in which negative gas saturations were never corrected, Ref. 98 reported that: " even though physically unrealistic saturations were computed ... material balance was preserved for each of the phases." Rather than correcting the material balance, we seek to correct the gas saturation and bubble-point pressure to obtain a physically meaningful solution ($S_g \geq 0$). In this regard, we seek that bubble-point pressure, $p_b{}^{\nu+1}_{n+1}$, which causes the following two relationships to hold:

$$[x_1(p_o{}^{\nu+1}_{n+1})\overline{\rho}_o(p_o{}^{\nu+1}_{n+1})S_o{}^{\nu+1}_{n+1} + y_1(p_o{}^{\nu+1}_{n+1})\overline{\rho}_g(p_o{}^{\nu+1}_{n+1})S_g{}^{\nu+1}_{n+1}]_{uncorrected}$$
$$= [x_1(p_o{}^{\nu+1}_{n+1}, p_b{}^{\nu+1}_{n+1})\overline{\rho}_o(p_o{}^{\nu+1}_{n+1}, p_b{}^{\nu+1}_{n+1})S_o{}^{\nu+1}_{n+1}]_{corrected} \qquad (2.4.130a)$$

and

$$[x_2(p_o{}^{\nu+1}_{n+1})\overline{\rho}_o(p_o{}^{\nu+1}_{n+1})S_o{}^{\nu+1}_{n+1} + y_2(p_o{}^{\nu+1}_{n+1})\overline{\rho}_g(p_o{}^{\nu+1}_{n+1})S_g{}^{\nu+1}_{n+1}]_{uncorrected}$$
$$= [x_2(p_o{}^{\nu+1}_{n+1}, p_b{}^{\nu+1}_{n+1})\overline{\rho}_o(p_o{}^{\nu+1}_{n+1}, p_b{}^{\nu+1}_{n+1})S_o{}^{\nu+1}_{n+1}]_{corrected} \ . \qquad (2.4.130b)$$

Numerical experiments indicate near exact satisfication (i.e., typically within 10^{-4} percent) of Eqs. 2.4.130 when Eq. 2.4.129a is used to estimate the bubble-point pressure. For the next Newtonian iteration, the bubble-point pressure in the grid block is substituted for the gas saturation as the primary variable we solve for.

Modification of the fluid saturations and fluid properties for the third case, in which we have crossed a dew-point pressure and our gas saturation has been overestimated, follows directly from the case above. By direct analogy to the bubble-point problems discussed above, the dew-point pressure is estimated by again assuming a linear relationship between saturation and pressure near the dew-point, i.e.,

$$p_d{}^{\nu+1}_{n+1} = p_o{}^{\nu}_{n+1} + \frac{S_o{}^{\nu}_{n+1}}{(S_o{}^{\nu}_{n+1} - S_o{}^{\nu+1}_{n+1})}(p_o{}^{\nu+1}_{n+1} - p_o{}^{\nu}_{n+1}) \ . \qquad (2.4.131a)$$

Note that Eq. 2.4.131a automatically accounts for the possiblity of there being two dew-point pressures; i.e., if the pressure is increasing and we cross the dew-point, then $(p_o{}^{\nu+1}_{n+1} - p_o{}^{\nu}_{n+1}) > 0$ and, therefore, $p_d{}^{\nu+1}_{n+1} > p_o{}^{\nu}_{n+1}$ and we have crossed an upper dew-point; if the pressure is decreasing and we cross the dew-point, then $(p_o{}^{\nu+1}_{n+1} - p_o{}^{\nu}_{n+1}) < 0$ and, therefore, $p_d{}^{\nu+1}_{n+1} < p_o{}^{\nu}_{n+1}$ and we have crossed a lower dew-point. For the next Newtonian iteration, the dew-point pressure is substituted for the gas saturation as the primary variable we solve for in this grid block. Note, it is important that we keep track of or be able to determine which dew-point pressure we are crossing. This will become more clear when we discuss the case of an undersaturated gas existing in the grid block at the previous iteration level.

Second, the gas and oil saturations are modified according to

$$S_g{}^{\nu+1}_{n+1} = (1 - S_w{}^{\nu+1}_{n+1}) \qquad (2.4.131b)$$

and

$$S_o{}^{\nu+1}_{n+1} = 0 \ . \qquad (2.4.131c)$$

We have now accounted for the three possibilities which could occur at the end of an iteration when the grid block contained saturated oil and gas at the previous Newton iteration.

The next case we consider is a grid block containing undersaturated oil at the old iteration level. Again, we consider the grid block pressure to be correctly determined at the end of each Newton iteration. During the Newton iterations, two possible cases exist for the new iteration level. First, the grid block may still contain undersaturated oil, as determined by the calculated grid block pressure being greater than the calculated bubble-point pressure within the grid block, i.e., ${p_o}^{\nu+1}_{n+1} > {p_b}^{\nu+1}_{n+1}$. No change in the methodology from the previous iteration level is required for this case, and the bubble-point pressure, p_b remains the primary variable we solve for during the next iteration.

The second possibility here is that the calculated grid block pressure is less than the calculated bubble-point pressure, i.e., ${p_o}^{\nu+1}_{n+1} < {p_b}^{\nu+1}_{n+1}$. Because we have dropped below the bubble-point pressure, free gas must exist in the grid block and a methodology is required to modify the gas and oil phase saturations to account for this. Additionally, our calculated bubble-point pressure will be slightly in error due to the errors in the fluid saturations. Though the variable bubble-point problem has received a fair amount of discussion in the literature (see above), there has been much less treatment of the case where the calculated grid block pressure falls below the calculated bubble-point pressure. This is surprising considering this author's experience has shown that the proper treatment of this problem has much more to do with the stability of the solution method than does the treatment when passing upwards through the bubble-point.

Ref. 102 states that the modified oil and gas equations (recall they are using an IMPES type of formulation) contain known δp_b terms, where $\delta p_b = {p_b}^{n+1} - {p_b}^{n}$, but they then state that a simple linear extrapolation of pressure and bubble-point versus time is used to estimate δp_b. If the bubble-point pressure is not changing with time prior to the crossing of the bubble-point, then it is not clear how linear extrapolation can be used to obtain the new bubble-point pressure. The authors

also fail to mention their methodolgy for correcting the oil and gas saturations to account for the grid block now containing saturated oil and gas, and how these new saturations affect the new bubble-point pressure.

While developing the simulator presented in this study, several methods were tried to properly account for this case. A methodology was tried in which the gas saturation was simply set to some small value (say, ${S_g}^{\nu+1}_{n+1} = 1 \times 10^{-6}$) and the oil saturation corrected as ${S_o}^{\nu+1}_{n+1} = (1 - {S_w}^{\nu+1}_{n+1} - {S_g}^{\nu+1}_{n+1})$. A corrected bubble-point pressure was then calculated according to

$$ {p_b}^{\nu+1}_{n+1} = p_b({R_{sb}}^{\nu+1}_{n+1}) \ , \qquad (2.4.132a) $$

where

$$ {R_{sb}}^{\nu+1}_{n+1} = R_s + \frac{5.615 {S_g}^{\nu+1}_{n+1} B_o}{{S_o}^{\nu+1}_{n+1} B_g} \ , \qquad (2.4.132b) $$

and the PVT properties R_s, B_o and B_g were evaluated at ${p_o}^{\nu+1}_{n+1}$. Also note that oil field units are being used in Eq. 2.4.132b, i.e., R_s and R_{sb} have units of $scf/STBO$, B_o has units of $RB/STBO$ and B_g has units of $ft^3/scfg$. Unfortunately, this methodology caused our Newton iterations to become oscillatory in many grid blocks (residual oscillated between increasing and decreasing). Additionally, the grid block would oscillate back and forth between an undersaturated liquid state and a saturated multiphase state.

Another method was tried in which both the grid block pressure and the calculated bubble-point pressure were assumed to be correct (as well as the water saturation). The gas and oil saturations were then estimated directly from the obvious rearrangement of Eq. 2.4.132b. Like the previous method, this method also resulted in many grid blocks oscillating back and forth between an undersaturated liquid state and a saturated multiphase state.

Finally, a simple iterative method was developed that (i) corrects both the bubble-point pressure and the hydrocarbon saturations, (ii) is convergent and (iii) results in no oscillations between Newton iterations. Again, we assume that the grid block pressure has been calculated correctly. After setting ${S_g}_{n+1}^{\nu+1} = 0$, the iterative procedure can then be stated as follows:

(Step 1) Assume all variables are correct, i.e.,

$$S_g = {S_g}_{n+1}^{\nu+1} = 0 \ , \tag{2.4.133a}$$

$$S_o = (1 - {S_w}_{n+1}^{\nu+1}) \tag{2.4.133b}$$

and

$$p_b = {p_b}_{n+1}^{\nu+1} \ . \tag{2.4.133c}$$

(Step 2) Estimate a corrected gas saturation, ${S_g}^*$ as

$${S_g}^* = \frac{(R_{sb} - R_s) S_o B_g}{5.615 B_o} \ . \tag{2.4.133d}$$

(Step 3) Correct the oil saturation,

$$S_o = 1 - S_w - {S_g}^* \ . \tag{2.4.133e}$$

(Step 4) Calculated relative error between iterations:

$$E = \frac{|{S_g}^* - S_g|}{{S_g}^*} \ . \tag{2.4.133f}$$

(Step 5) Assign estimated gas saturation:

$$S_g = S_g{}^* \ . \tag{2.4.133g}$$

(Step 6) Update bubble-point point pressure from

$$R_{sb} = R_s + \frac{5.615 S_g B_o}{S_o B_g} \tag{2.4.133h}$$

and

$$p_b = p_b(R_{sb}) \ . \tag{2.4.133i}$$

(Step 7) Test convergence:

IF $E > \varepsilon_{S_g}$ **THEN**

Repeat Steps 2-8

ELSE

QUIT

ENDIF

We have found a convergence tolerance of $\varepsilon_{S_g} = 10^{-6}$ sufficient and note that at most two passes through the iterative scheme are required to achieve convergence, and often only one pass is necessary. For the next Newtonian iteration, the gas saturation is substituted for the bubble-point pressure as the primary variable we solve for in this grid block.

The final case we consider is a grid block containing undersaturated gas at the old iteration level. Again, we consider the grid block pressure to be correctly determined at the end of each Newton iteration. During the Newton iterations, two possible cases exist for the new iteration level. First, the grid block may still contain undersaturated gas, as determined by either (i) the calculated grid block pressure being greater than the calculated dew-point pressure when the dew-point

pressure is an upper dew-point, i.e., ${p_o}^{\nu+1}_{n+1} > {p_d}^{\nu+1}_{u\,n+1}$ and (ii) the calculated grid block pressure being less than the calculated dew-point pressure when the dew-point pressure is a lower dew-point, i.e., ${p_o}^{\nu+1}_{n+1} < {p_d}^{\nu+1}_{l\,n+1}$. To determine whether the dew-point is an upper dew-point or a lower dew-point, we simply examine the oil volatility, r_v, versus pressure curve. If two dew-point pressures are possible for the same fluid composition (i.e., oil volatility), then the oil volatility curve will exhibit a minimum at a particular pressure, say p_{inf} (e.g., see Fig. 2.7). If ${p_d}^{\nu+1}_{n+1} < p_{inf}$ then it is a lower dew-point and if ${p_d}^{\nu+1}_{n+1} > p_{inf}$ then it is an upper dew-point. Also note that calculation of fluid properties and their derivatives will require us to know whether our pressure is below the lower dew-point pressure or above the upper dew-point pressure. No change in the Newtonian iteration logic from the previous iteration level is required for this case, and the dew-point pressure, p_d remains the primary variable we solve for during the next iteration.

The second possibility, as determined from the conditions specified above, is that we we have crossed a dew-point from the undersaturated gas region to the saturated gas-oil region of the phase envelope. Analogous to the crossing of the bubble-point pressure discussed above, a liquid hydrocarbon phase must exist in the grid block and a methodology is required to modify the gas and oil phase saturations to account for this. Our calculated dew-point pressure will also be slightly in error due to the errors in the fluid saturations and must be corrected. To this end, an iterative procedure completely analogous to the one described above is used to correct the saturations and dew-point pressure. First, the oil saturation is reset to ${S_o}^{\nu+1}_{n+1} = 0$ and then the procedure follows directly as:

(Step 1) Assume all variables are correct, i.e.,

$$S_o = {S_o}^{\nu+1}_{n+1} = 0 \ , \qquad (2.4.134a)$$

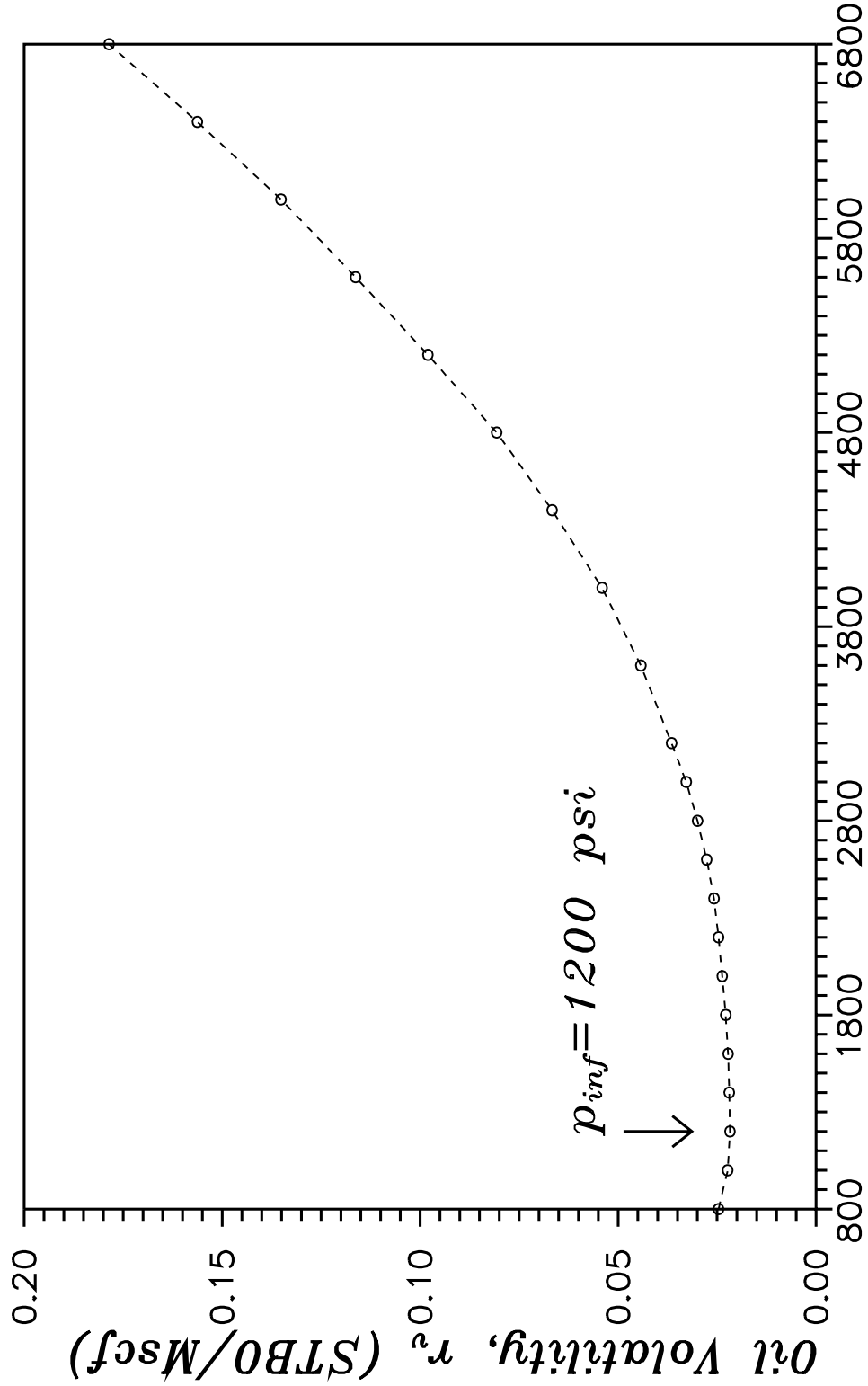

Fig. 2.7 – Oil volatility plot (data from Ref. 38).

$$S_g = (1 - S_w{}^{\nu+1}_{n+1}) \tag{2.4.134b}$$

and

$$p_d = p_d{}^{\nu+1}_{n+1} \ . \tag{2.4.134c}$$

(Step 2) Estimate a corrected oil saturation, $S_o{}^*$ as

$$S_o{}^* = \frac{5.615(r_{vd} - r_v)S_g B_o}{B_g} \ . \tag{2.4.134d}$$

(Step 3) Correct the gas saturation,

$$S_g = 1 - S_w - S_o{}^* \ . \tag{2.4.134e}$$

(Step 4) Calculated relative error between iterations:

$$E = \frac{|S_o{}^* - S_o|}{S_o{}^*} \ . \tag{2.4.134f}$$

(Step 5) Assign estimated oil saturation:

$$S_o = S_o{}^* \ . \tag{2.4.134g}$$

(Step 6) Update dew-point pressure from

$$r_{vd} = r_v + \frac{S_o B_g}{5.615 S_g B_o} \tag{2.4.134h}$$

and

$$p_d = p_d(r_{vd}) \ . \tag{2.4.134i}$$

(Step 7) Test convergence:

IF $E > \varepsilon_{S_o}$ **THEN**

Repeat Steps 2-8

ELSE

QUIT

ENDIF

Here again, we have found a convergence tolerance of $\varepsilon_{S_o} = 10^{-6}$ sufficient. For the next Newtonian iteration, we switch the primary variables we solve for to include the gas saturation and to eliminate the dew-point pressure within this grid block.

Lastly, we note that because we employ a variable substitution logic which allows us to implicitly calculate the saturation pressure (bubble-point or dew-point) when a single hydrocarbon phase exists within a grid block, variations in the saturation pressure due to mixing are automatically accounted for.

2.5 Summary

Details of the mathematical and numerical formulation describing the physical process of producing fluids (oil-water-gas) at a restricted-entry well centrally located in a cylindrical reservoir which may be overlain by a gas cap and/or underlain by an aquifer have been presented.

Background information on a variety of preconditioners, including several domain decomposition techniques, for conjugate gradient-type iterative methods has been presented.

Lastly, a detailed and rigorous discussion on the treatment of variable bubble-point and variable dew-point problems and the variable substitution logic required for their efficient treatment has been presented and a simple iterative

method developed which (i) corrects both the bubble-point (dew-point) pressure and the hydrocarbon saturations, (ii) is convergent and (iii) results in no oscillations between Newton iterations.

CHAPTER III
MODEL VALIDATION

In this chapter, we present numerical results intended to verify the accuracy of the numerical reservoir simulator developed as part of this study. Obviously, the best validation of a numerical model is a comparison of numerical results to available analytical solutions. In this regard, numerical results are compared to the well known 1-D radial and 2-D restricted-entry analytical solutions for the constant rate production of a single phase slightly compressible fluid of constant compressibility and constant viscosity from a homogeneous and isotropic reservoir.

Unfortunately, the non-linearity of the multiphase problems considered in this study generally preclude development of analytic solutions. We note that Ref. 141 did develop an analytical solution in terms of a multiphase pseudopressure for the reservoir and wellbore response due to production at a constant surface oil rate from a fully-penetrating well in a homogeneous and isotropic reservoir initially at the bubble-point pressure. Unfortunately, this solution contains a term which is not known *a priori* and depends precisely on the solution to which it is a part. No analytical solutions, therefore, exists with which a comparison can be made with the numerical results obtained from our simulator. The next most dependable and convincing method for validating the results obtained from the numerical simulation of a physical process is when the numerical results can be compared directly with experimental or field data. Lacking either of these sources of data, the remaining method for validation is the comparison of model results to the results published in the literature for similar numerical models, or if available,

to the results obtained directly from similar numerical models with an established acceptance for accuracy. For multiphase systems, we compare results obtained from our simulator to results presented in the literature and obtained from other simulators for (i) the production of oil and gas from a radial reservoir containing only oil and gas, (ii) the production of oil and water from a well partially penetrating a reservoir containing only oil and water, and (iii) the production of oil, gas and water from a restricted-entry well in a multilayered reservoir containing all three phases.

Additionally, we mention that material balance calculations over each time step are performed by our simulator for all simulation runs. While material balance calculations are not by themselves an absolute indication of accuracy, when combined with physically reasonable pressure and saturation distributions in the reservoir, they do ensure that no serious errors have occurred. In all of the simulation runs performed in this study, the maximum material balance error recorded was less than 0.01%, and material balance errors were consistently less than $10^{-4}\%$.

In the last part of this chapter, we compare solution methods for the linear systems of equations generated through the use of Newton's method. Comparisons are made between a direct solution method and several conjugate gradient-type iterative solvers. In addition, comparisons are made between several preconditioning techniques, including a domain decomposition based preconditioning technique. In the context of domain decomposition, comparisons are alos made between several preconditioning techniques for the Schur complement of the system.

3.1 Comparison With Analytic Solutions

3.1.1 Single-Phase One-Dimensional Flow

In this section, we consider an infinite cylindrical reservoir of uniform thickness produced by a well located at the center of the reservoir and fully penetrating

the formation thickness. The porosity and absolute permeability are assumed to be constant and independent of position, save for a thin altered permeability region (skin zone) around the well. The reservoir is assumed to contain a single fluid of slight and constant compressibility and constant viscosity. The initial pressure is assumed to be uniform throughout the reservoir and we consider production at a constant surface oil rate.

Using the standard definitions of dimensionless pressure

$$p_D(r_D, t_D) = \frac{kh[p_i - p(r,t)]}{141.2 q_o B_o \mu_o} \ , \tag{3.1.1}$$

dimensionless time

$$t_D = \frac{0.006328kt}{\phi c_t \mu_o r_w^2} \tag{3.1.2}$$

and dimensionless radius

$$r_D = \frac{r}{r_w} \ , \tag{3.1.3}$$

the solution to the above described problem is the well known exponential-integral or Theis[107] solution given by

$$p_D(r_D, t_D) = -\frac{1}{2}\mathrm{Ei}\left(\frac{-{r_D}^2}{4t_D}\right) + s \ . \tag{3.1.4}$$

It is also well known that when the log-approximation to the exponential integral is valid, Eq. 3.1.4 can be expressed as

$$p_D(r_D, t_D) = \frac{1}{2}[\ln({t_D}/{r_D}^2) + 0.80907 + 2s] \ . \tag{3.1.5}$$

At the wellbore, Eq. 3.1.5 becomes

$$p_{wD}(t_D) = \frac{1}{2}[\ln(t_D) + 0.80907 + 2s] \ , \tag{3.1.6}$$

where the dimensionless wellbore pressure is given by

$$p_{wD}(t_D) = \frac{kh[p_i - p_{wf}(t)]}{141.2 q_o B_o \mu_o} \ . \tag{3.1.7}$$

Using the data in Table 3.1, two simulation runs were made, one for a zero skin factor and one for a skin factor of $s = 5$. Dimensionless wellbore pressures were calculated using Eq. 3.1.7 and the wellbore pressures predicted by the simulator. Dimensionless wellbore pressures were also calculated using Eq. 3.1.6. Figure 3.1 shows a comparison between the dimensionless wellbore pressures predicted by Eq. 3.1.6 and those computed from the results of the simulator. Clearly there is an excellent match between the simulator and the analytical solution for these cases.

3.1.2 Single-Phase Two-Dimensional Flow

In this section, we consider an infinite cylindrical reservoir of uniform thickness produced by a well located at the center of the reservoir and only partially penetrating the formation thickness. The porosity and absolute permeability are assumed to be constant and independent of position, save for a thin altered permeability region (skin zone) around the well. The reservoir is assumed to contain a single fluid of slight and constant compressibility and constant viscosity. The initial pressure is assumed to be uniform throughout the reservoir and we consider production at a constant surface oil rate.

Under these assumptions, Gringarten[108] presented an analytical solution to the restricted-entry well problem as

$$p_D(r_D, z_D, t_D) = -\frac{1}{2}\mathrm{Ei}\left(\frac{-{r_D}^2}{4t_D}\right) + \frac{4}{\pi b}\sum_{n=1}^{\infty}\left\{\frac{1}{n}\sin\left(\frac{n\pi b}{2}\right)\cos\left[n\pi\left(z_D m + \frac{b}{2}\right)\right]\right.$$
$$\left.\cos(n\pi z_D)\int_{\frac{r_D^2}{4t_D}}^{\infty}\exp\left\{-\left[u + \frac{1}{4u}\left(\frac{n\pi r_D}{h_D}\right)^2\right]\right\}\frac{du}{u}\right\} , \tag{3.1.8}$$

Table 3.1

Case OIL-1 Reservoir, Fluid and Production Parameters

$\phi = 0.2$	
$k = 50$	(md)
$k_z/k = 0.1$	
$r_e = 10000$	(ft)
$r_w = 0.25$	(ft)
$h_w = 20$	(ft)
$h = 20$	(ft)
$q_o = 200$	(STB/D)
$t_p = 10$	$(days)$
$\mu_o = 1.0$	(cp)
$c_o = 1 \times 10^{-5}$	(psi^{-1})
$r_s = 0.55347$	(ft)

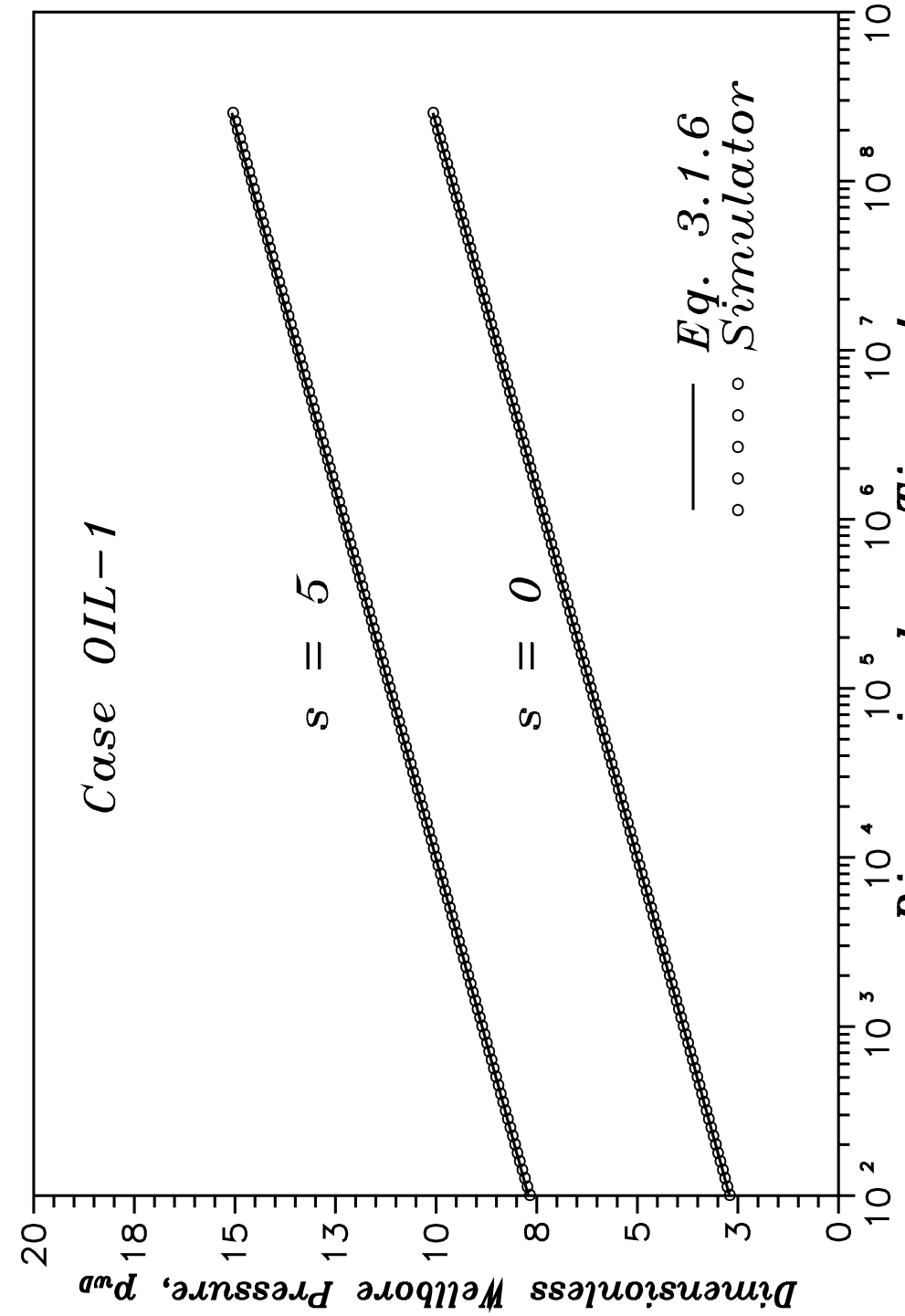

Fig. 3.1 – Comparison of simulator results to analytical solution.

where b is the penetration ratio given by

$$b = \frac{h_w}{h} \ , \tag{3.1.9}$$

z_D is the dimensionless height given by

$$z_D = \frac{z}{h} \ , \tag{3.1.10}$$

h_D is the dimensionless thickness given by

$$h_D = \frac{h}{r_w}\sqrt{\frac{k}{k_z}} \tag{3.1.11}$$

and z_{Dm} is the dimensionless location of the open interval given by

$$z_{Dm} = \min\{z_{D1}, z_{D2}\} \ . \tag{3.1.12}$$

Here, z_{D1} and z_{D2} represent the dimensionless distances from the top of the open interval to the top of the reservoir and from the bottom of the open interval to the bottom of the reservoir, respectively. Referring to Fig. 2.2, we then have $z_{D1} = (h - h_{w_2})/h$ and $z_{D2} = h_{w_1}/h$

In deriving Eq. 3.1.8, Ref. 108 assumed a uniform-flux wellbore condition. Under conditions where gravitational and frictional effects are negligible, then as discussed by many authors (e.g., see Refs. 1,11 and 12), a more realistic inner boundary condition would appear to be that of an infinite-conductivity wellbore in which the pressure in the wellbore is independent of location in the wellbore and the integral of the flux over the perforated interval is equal to the specified production rate. Refs. 1, 11 and 12 compared the pressure responses obtained using both inner boundary conditions and found that the infinite-conductivity

solution for a restricted-entry well could be obtained by computing the uniform-flux solution at the corresponding equivalent average pressure point, $z^*_D = z^*/h$, which is that point in the wellbore at which the pressure obtained from both the uniform-flux wellbore and the infinite-conductivity wellbore are identical. Refs. 11 and 12 present correlations for z^*_D as a function of the dimensionless well length, h_{wD}, given by

$$h_{wD} == \frac{h_w}{r_w}\sqrt{\frac{k}{k_z}} \ . \tag{3.1.13}$$

The dimensionless pressure drop at the wellbore ($r_D = 1$) can therefore be obtained from

$$p_{wD}(t_D) = -\frac{1}{2}\mathrm{Ei}\left(-\frac{1}{4t_D}\right) + \frac{4}{\pi b}\sum_{n=1}^{\infty}\left\{\frac{1}{n}\sin\left(\frac{n\pi b}{2}\right)\cos\left[n\pi\left(z_D m + \frac{b}{2}\right)\right]\right.$$
$$\left.\cos(n\pi b z^*_D)\int_{\frac{1}{4t_D}}^{\infty}\exp\left\{-\left[u + \frac{1}{4u}\left(\frac{n\pi}{h_D}\right)^2\right]\right\}\frac{du}{u}\right\} + \frac{s}{b} \ , \tag{3.1.14}$$

The equivalent average pressure point, z^*_D, can be obtained from either Fig. 4 of Ref. 11 or Fig. 2 of Ref. 12. Note that we have included the mechanical skin factor in Eq. 3.1.14 also.

Using the data in Table 3.2, two simulation runs were made, one for a zero skin factor, $s = 0$, and one for a skin factor of $s = 5$. Dimensionless wellbore pressures were calculated using Eq. 3.1.7 and the wellbore pressures predicted by the simulator. Dimensionless wellbore pressures were also calculated using Eq. 3.1.14. Figure 3.2 shows a comparison between the dimensionless wellbore pressures predicted by Eq. 3.1.14 and those computed from the results of the simulator. Again, there is an excellent match between the simulator and the analytical solution for these cases.

Table 3.2

Case OIL-2 Reservoir, Fluid and Production Parameters

$\phi = 0.2$	
$k = 50$	(md)
$k_z/k = 0.1$	
$r_e = 10000$	(ft)
$r_w = 0.25$	(ft)
$h_w = 10$	(ft)
$h = 50$	(ft)
$h_{w_1} = 40$	(ft)
$q_o = 200$	(STB/D)
$t_p = 10$	$(days)$
$\mu_o = 1.0$	(cp)
$c_o = 1 \times 10^{-5}$	(psi^{-1})
$r_s = 0.55347$	(ft)
$b = 0.2$	
$h_D = 632.456$	
$h_{w_D} = 126.491$	
$z_D m = 0$	
$z_D^* \approx 0.73$	(Fig. 2, Ref. 12)

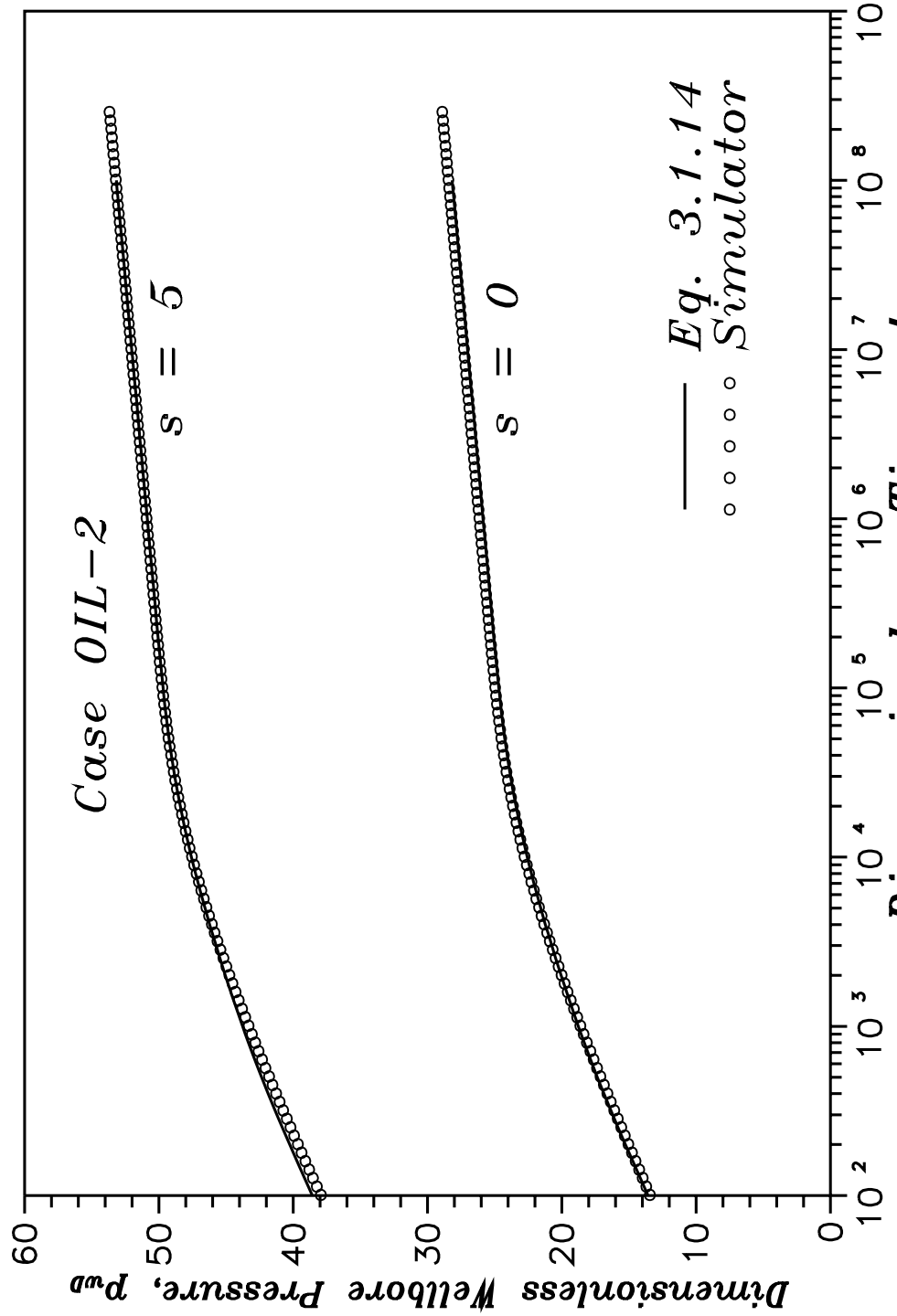

Fig. 3.2 – Comparison of simulator results to analytical solution.

3.2 Comparison With Other Numerical Results

In this section, we compare results obtained from our simulator to results either published in the literature or obtained directly from other available reservoir simulators. In addition to validating the results obtained from our simulator, the wide range of examples chosen here were intended to test every aspect of our simulator and provide a test of the robustness of the numerical formulation. To this end, we have chosen to examine a single-phase four-layer commingled reservoir produced by a fully penetrating well, a single-layer two-phase (oil-gas) reservoir produced from a fully-penetrating well, a two-phase (oil-water) reservoir produced from a restricted-entry well, and a three-phase (oil-gas-water) reservoir produced from a restricted-entry well. Details of each example are included in the sections that follow.

3.2.1 Single-Phase Four-Layer Commingled Reservoir

For the commingled reservoir case, we consider a four-layer commingled reservoir. Each layer is 4 $feet$ thick with absolute radial permeabilities of 50, 40, 30 and 20 (md) in layers 1 through 4, respectively. The porosity is 0.2 in each layer and each layer is considered to contain a single-phase slightly compressible fluid of constant compressibility ($1 \times 10^{-6}\ psi^{-1}$) and constant viscosity (1.0 cp). The wellbore radius is 0.25 $feet$ and the radial extent of the reservoir is 1600 $feet$. The reservoir is produced at a constant rate of 100 STB/day for a period of 100 $days$ and then shut in for a period of 100 $days$.

Figures 3.3 and 3.4 show a comparison of the drawdown and buildup wellbore pressure response, respectively, obtained from our simulator with the pressure response obtained from a simulator previously developed by A.C. Reynolds at the

University of Tulsa and discussed in detail in Refs. 16 and 18-20. Clearly there is an excellent match between the two simulators.

During the build-up phase of the simulation, wellbore crossflow (backflow) is evident, and as a further check on the simulator, the individual layer flow rates were compared between the two simulators, with the results plotted in Fig. 3.5. Again, there is an excellent match between the two simulators.

3.2.2 Two-Phase (Oil-Gas) One-Dimensional Flow

The first multiphase example considered is a one-dimensional cylindrical reservoir containing both oil and gas, but initially just above the bubble-point pressure. Table 3.3 contains the pertinent reservoir, fluid and production parameters for this example. The Set 1 relative permeability curves and Set 1 PVT properties included in Chapter IV are also used. The reservoir is produced at a constant surface oil rate for 10 *days*, then shut in for a 10 *day* buildup test.

For this case, two additional simulators were used to generate results to which we could compare the results obtained from our simulator. The first simulator was developed by and is discussed in detail in Ref. 109. The second simulator is a commercially available and widely used simulator, ECLIPSE[110]. In Fig. 3.6, the wellbore pressures obtained from each of the simulators are compared and show nearly identical results.

Fig. 3.7 shows a comparison of the calculated oil saturation in the first grid block during both the drawdown and buildup periods. Here, we see an excellent match between our simulator and the commercial simulator ECLIPSE, however, there is a slight difference between our results and the simulator of Ref. 109. This difference is most probably due to the fact that both our simulator and the ECLIPSE simulator employ a fully-implicit solution scheme in which all variables

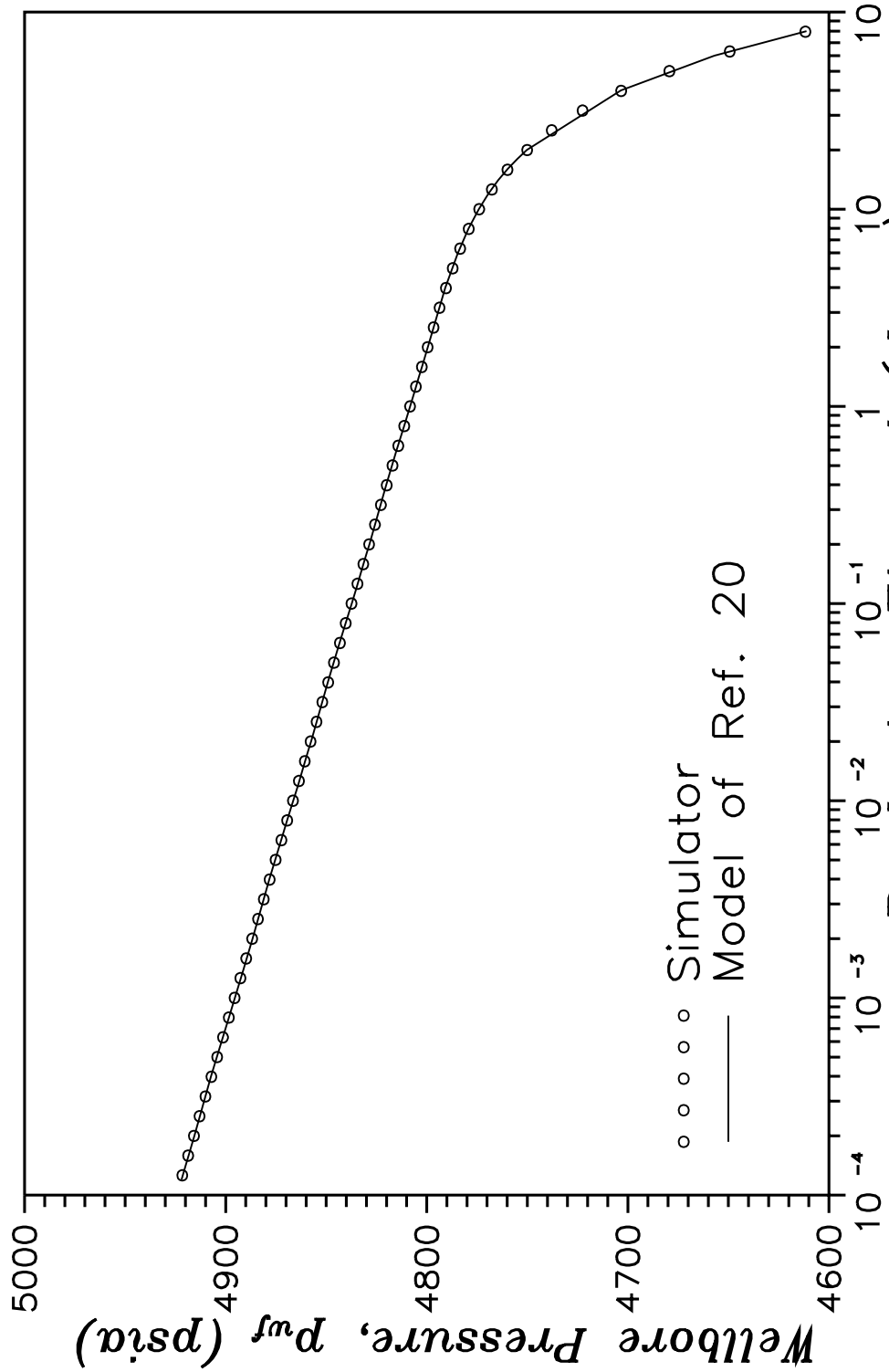

Fig. 3.3 — Comparison of drawdown results — commingled reservoir.

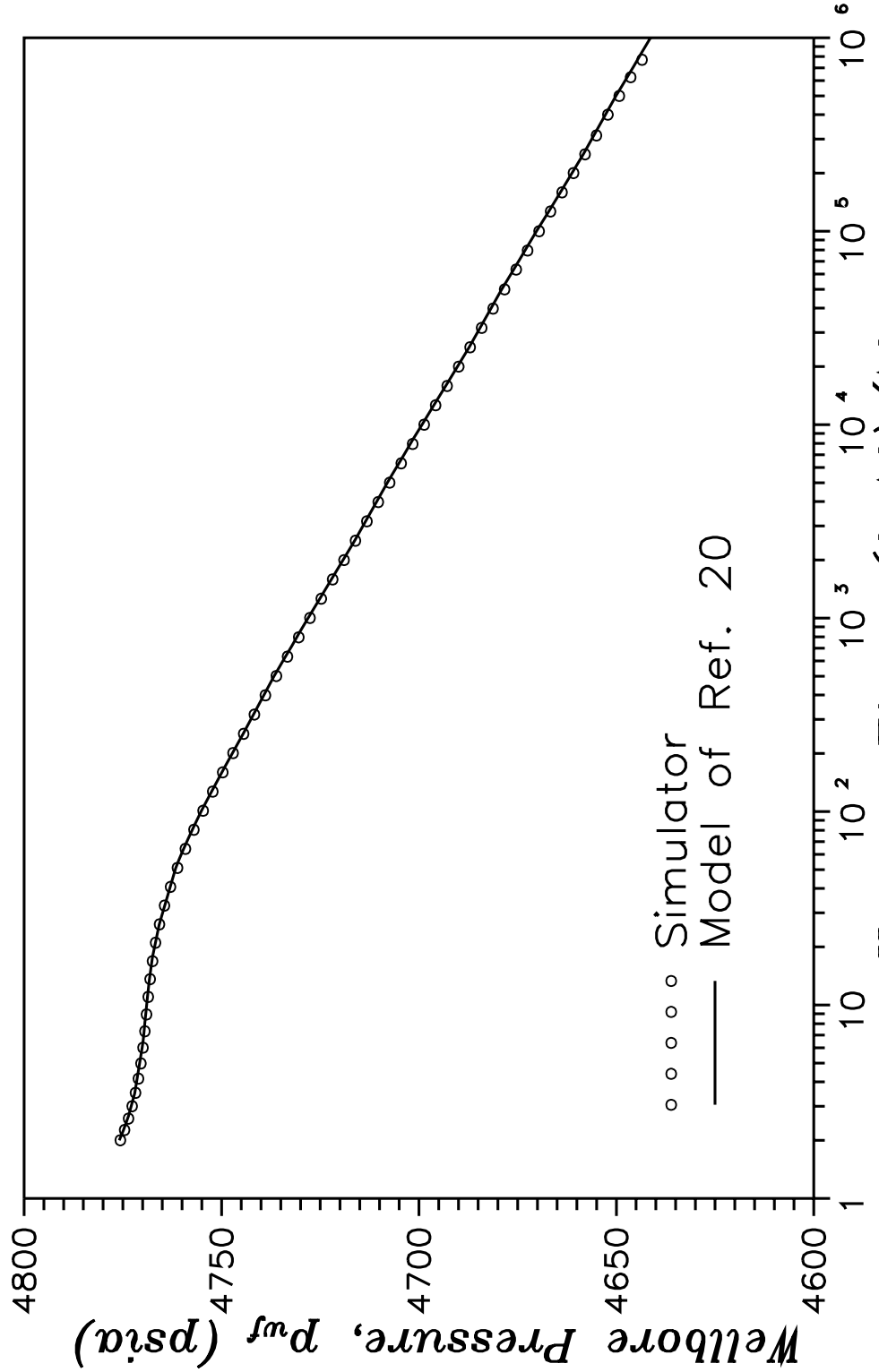

Fig. 3.4 — Comparison of buildup results — commingled reservoir.

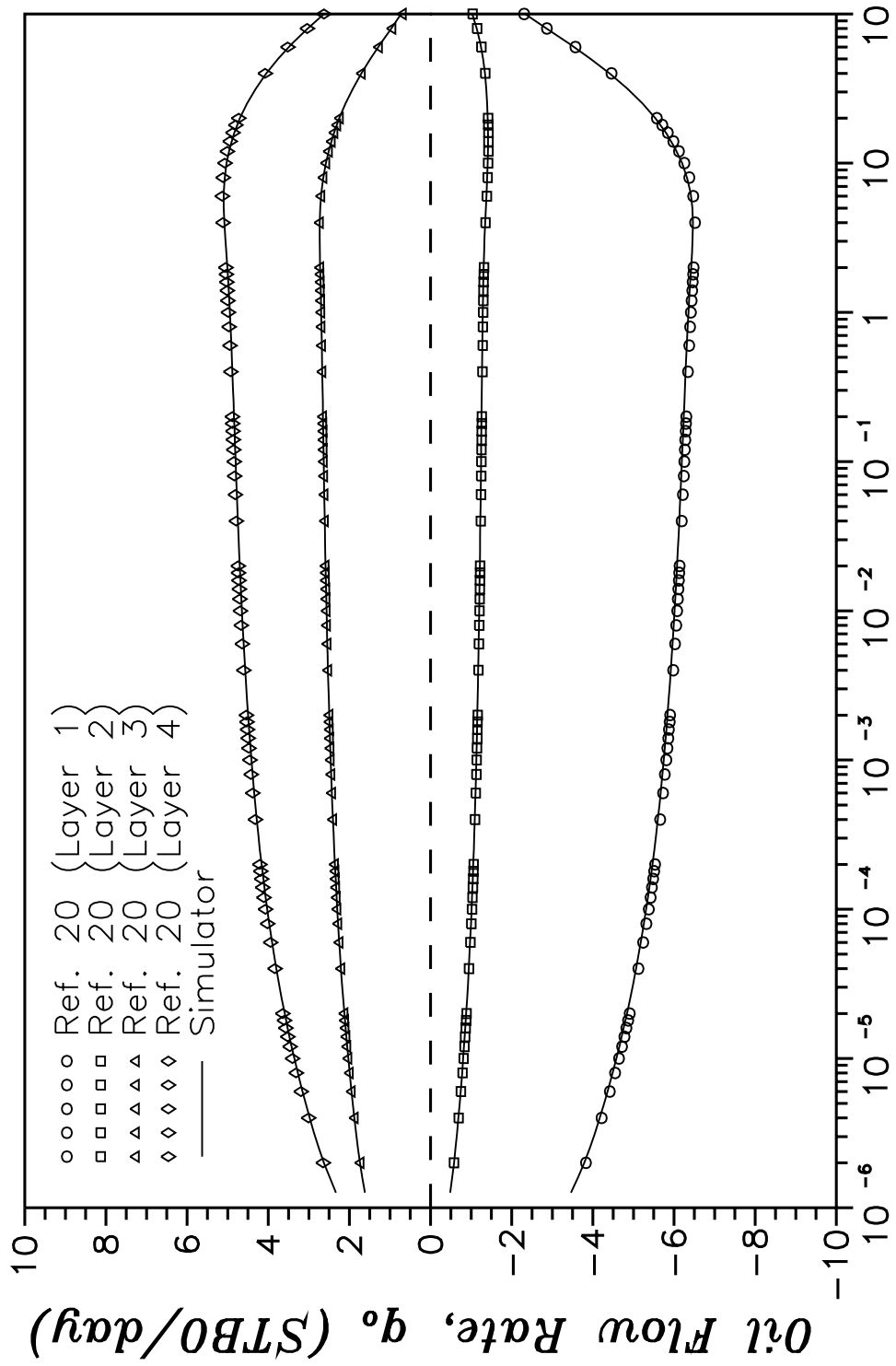

Fig. 3.5 – Comparison of layer flowrates during wellbore crossflow.

Table 3.3

Case SG1 - Reservoir, Fluid and Production Parameters

$\phi = 0.2$	
$k = 30$	(md)
$r_e = 6600$	(ft)
$r_w = 0.328$	(ft)
$h_w = 15.547$	(ft)
$h = 15.547$	(ft)
$q_o = 200$	(STB/D)
$t_p = 10$	$(days)$
$p_i = 3600.001$	$(psia)$
$p_{bi} = 3600.0$	$(psia)$
$S_{oi} = 1.0$	

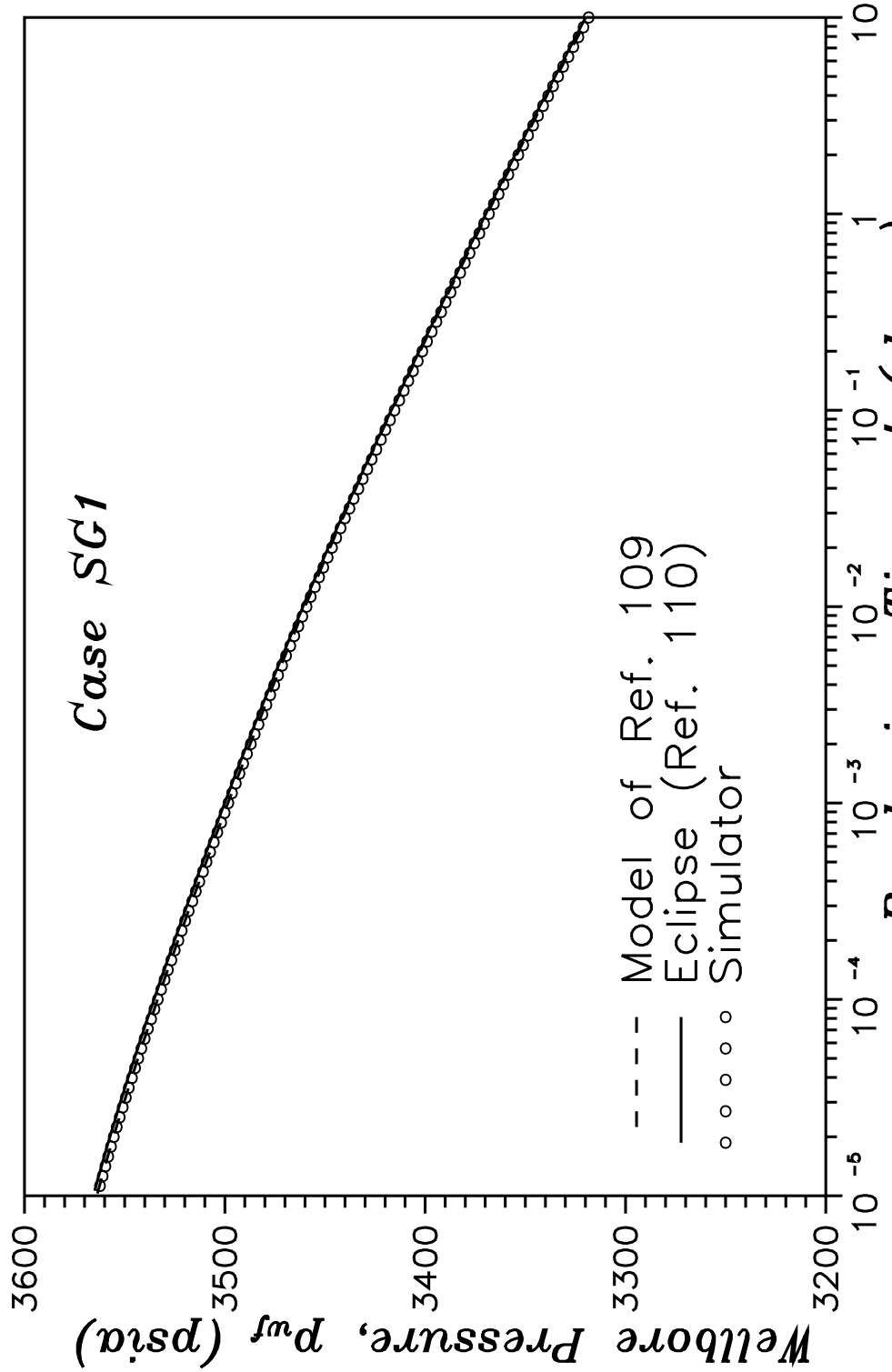

Fig. 3.6 — Comparison of drawdown wellbore pressures.

are solved for simultaneously, whereas the simulator of Ref. 109 uses a sequential solution method in which first the pressure solution is obtained holding the saturations fixed, then the saturation solution is obtained holding the pressures fixed. In any event, we note that the difference is small, occurring only in the third decimal place in the saturations.

3.2.3 Two-Phase (Oil-Water) Two-Dimensional Flow

The next case we considered during the validation stage of our model development is a problem presented by Chu et al.[23] involving two-phase (oil-water) flow to a restricted-entry well in a cylindrical reservoir with closed top, bottom and outer boundaries. The cases considered here are for a homogeneous reservoir 32 feet thick with an initial saturation profile as shown in Fig. 3.8. Note that S_w varies from 0.8 at the bottom of the reservoir to $S_w = 0.15$ at the top of the reservoir. For this problem, the critical water saturation is $S_{wc} = 0.20$ and residual oil saturation is $S_{or} = 0.2$. Gravity and capillary pressure effects are not considered, i.e., are considered negligible. Three permeability ratios are considered: $k_z/k = 0.01$ (Case A), $k_z/k = 0.1$ (Case B) and $k_z/k = 1.0$ (Case C). The well is perforated only over the top half of the reservoir, i.e., the well penetration ratio, b, is 0.5. The reservoir was produced for 100 days at a constant total surface rate of 100 STB/day and then shut in for a period of 100 days. Eight four-foot thick vertical grids and 40 radial grids were used. All other pertinent information may be obtained from Ref. 23.

Figure 3.9 compares the drawdown period wellbore pressure response obtained from our simulator with the results presented by Ref. 23 for all three cases considered. The pressure match is excellent for all three cases.

Figures 3.10-3.12 compare the buildup wellbore pressure response obtained from our simulator with the results presented by Chu et al.[23] for Cases A-C,

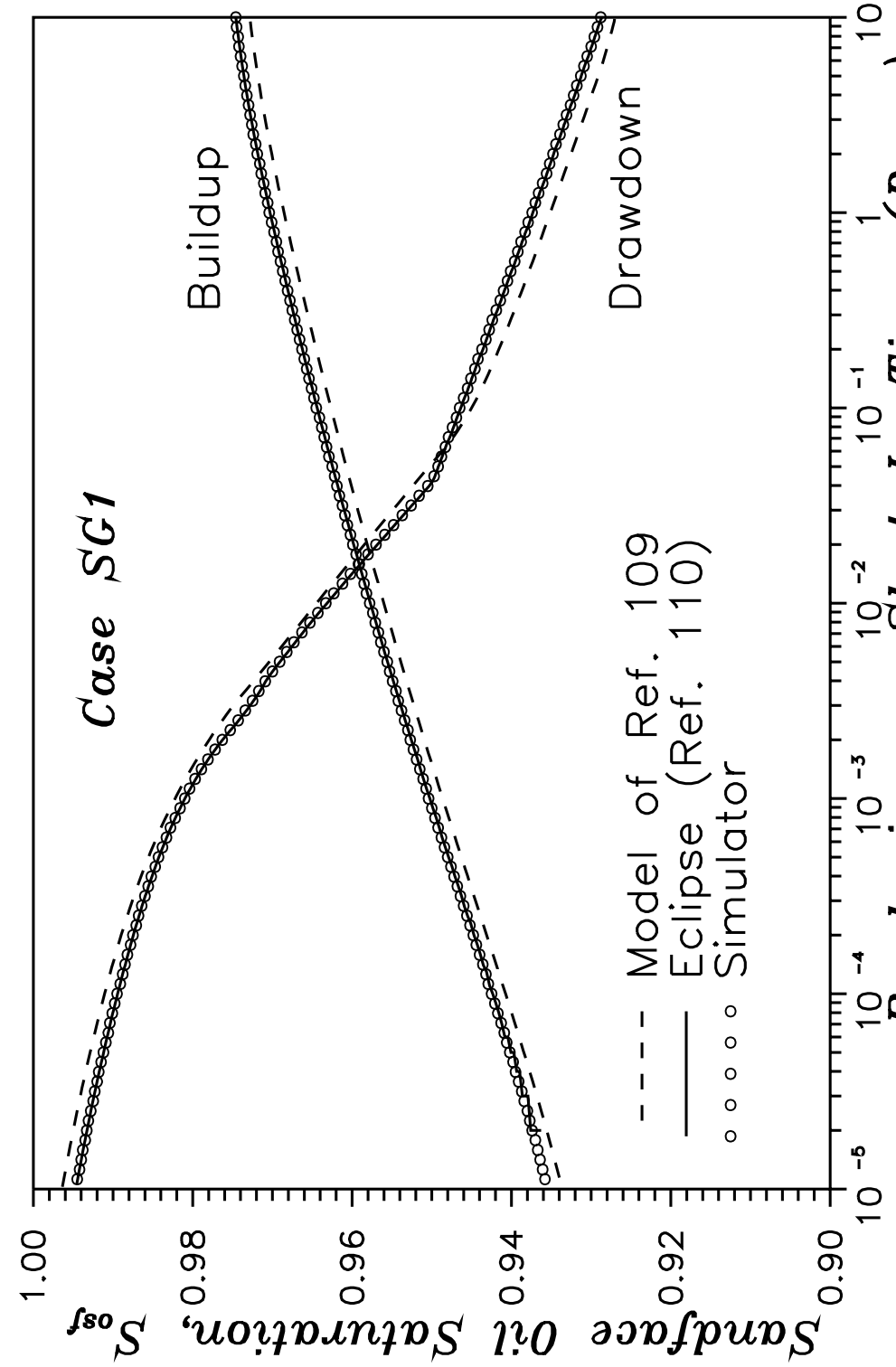

Fig. 3.7 — Comparison of sandface oil saturations.

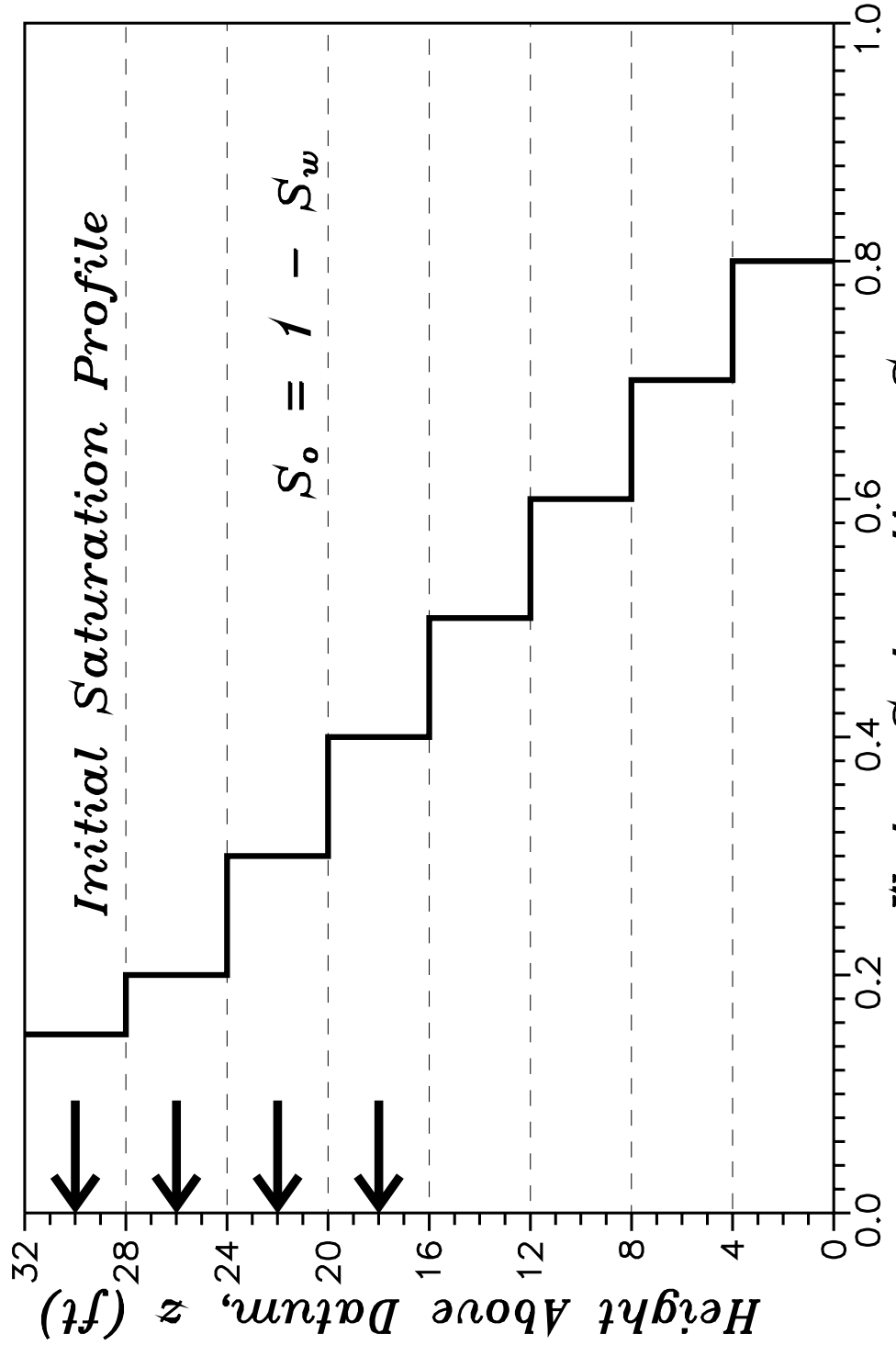

Fig. 3.8 – Initial saturation profile (oil–water coning example).

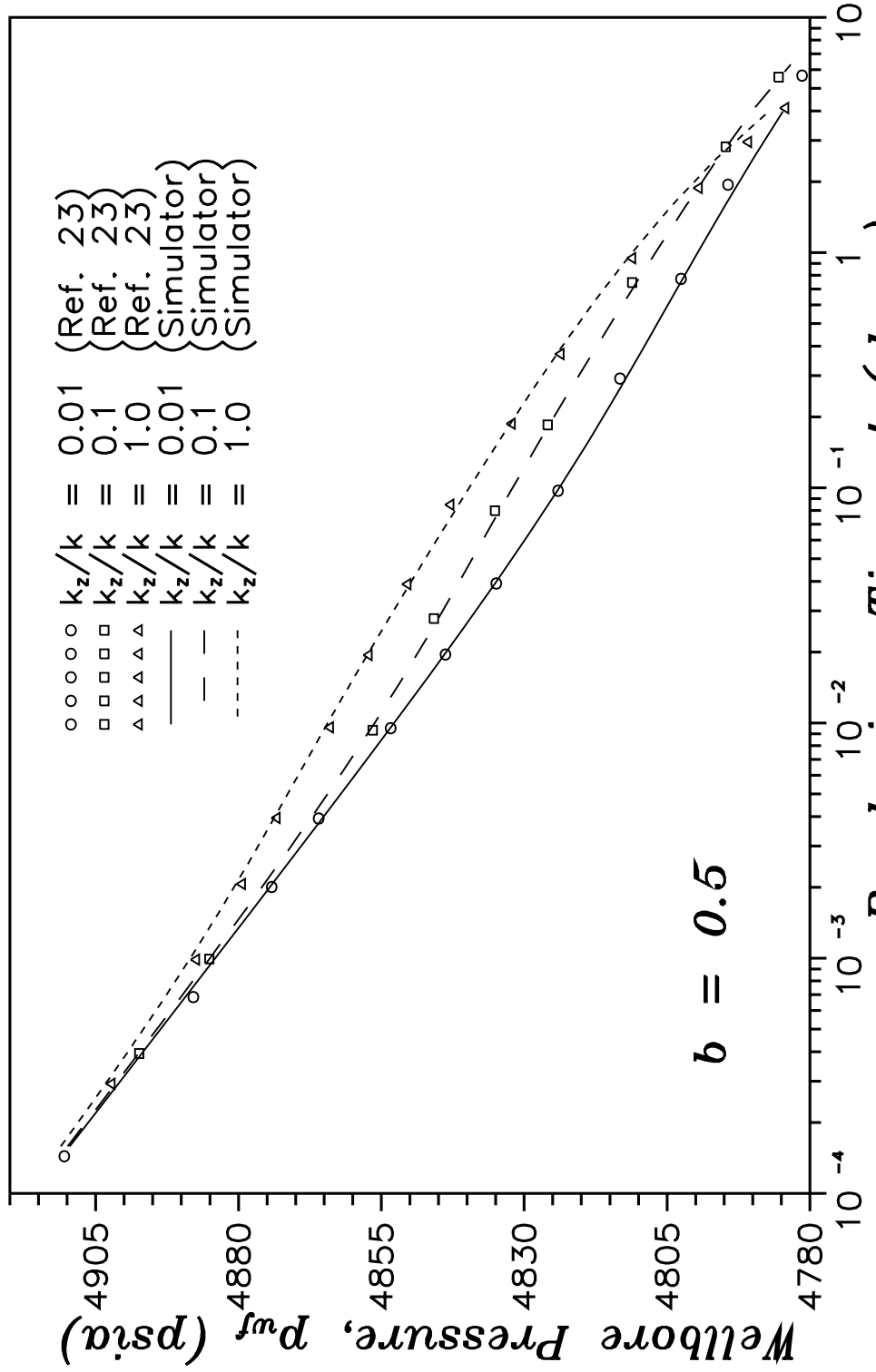

Fig. 3.9 — Comparison of drawdown pressure responses for oil—water coning example.

respectively. Here, we clearly see a difference of approximately 5 *psi* between our results and the results of Chu et al. for all three cases. The Chu et al. data used were obtained by digitizing results from a figure presented in Ref. 24.

Upon examination of other output data, it was noted that the sandface oil saturation increased dramatically during the buildup period. Figure 3.13 shows the sandface oil saturation predicted by our simulator for the fourth vertical grid from the top of the reservoir. Because gravity and capillary pressure effects were not included, we were at first unable to explain this phenomena. Upon further investigation, however, we discovered that our simulator was predicting that wellbore crossflow was occurring during the buildup period. For this case, it is difficult to predict the nature and magnitude of crossflow from purely physical arguments. We note that mathematically, our wellbore constraint equation does not prevent crossflow from occurring.

Although the difference between our simulation results and the Chu et al. results is not great, we also compared our results with those obtained from a commercially available simulator[110] for the Case A example. Figure 3.14 shows a comparison between the buildup pressure responses for the two simulators. We see an excellent match between the two.

Figures 3.15 and 3.16, respectively, compare the sandface oil saturation and individual "layer" oil flow rates obtained from ECLIPSE[110] and from our simulator. In Fig. 3.15, the sandface oil saturation was measured at the fourth vertical grid from the top of the reservoir. The reference grids identified in Fig. 3.16 are as measured from the top of the reservoir. The agreement between the two sets of results is excellent.

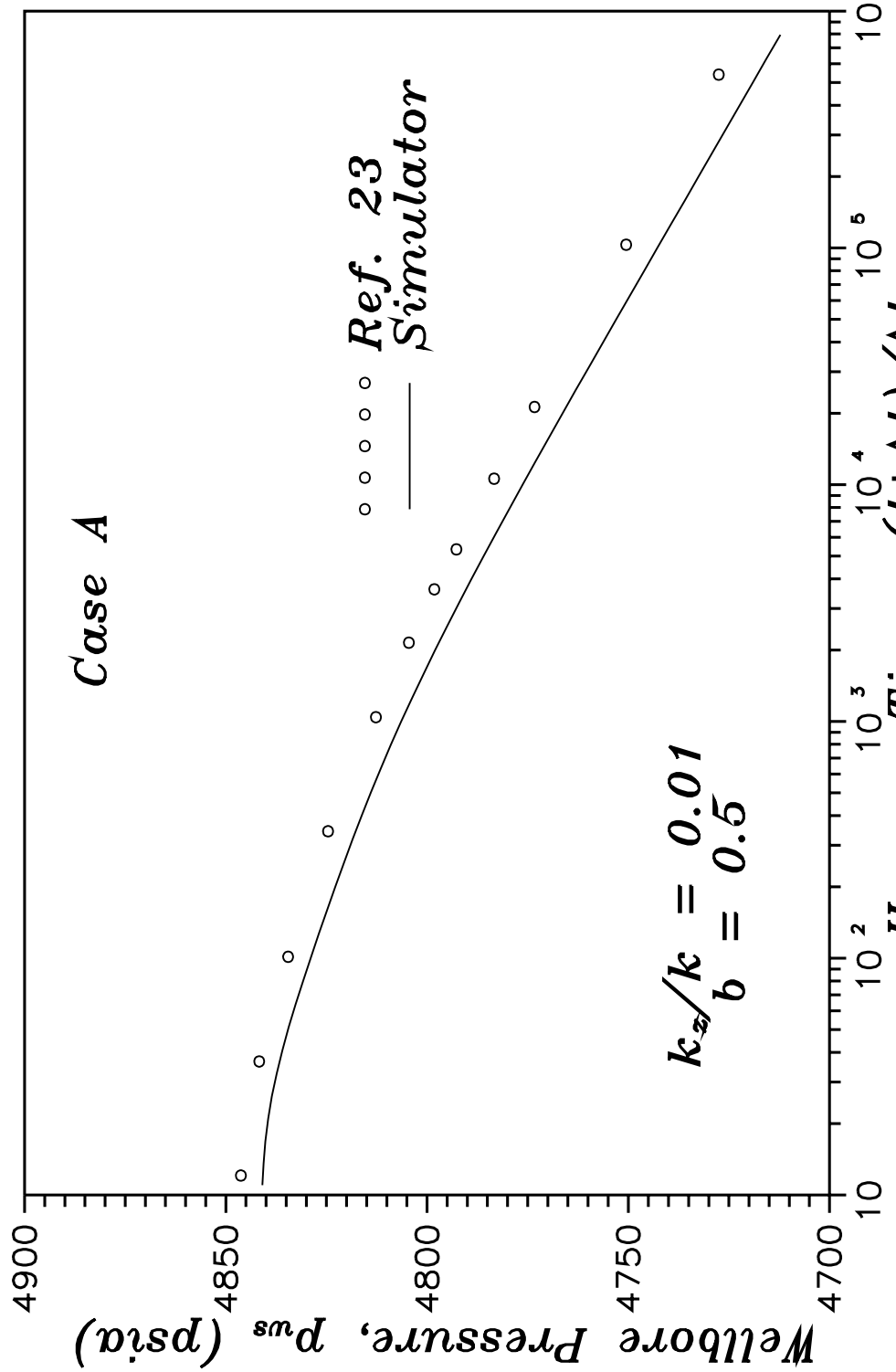

Fig. 3.10 – Comparison of wellbore shut–in pressures (Case A).

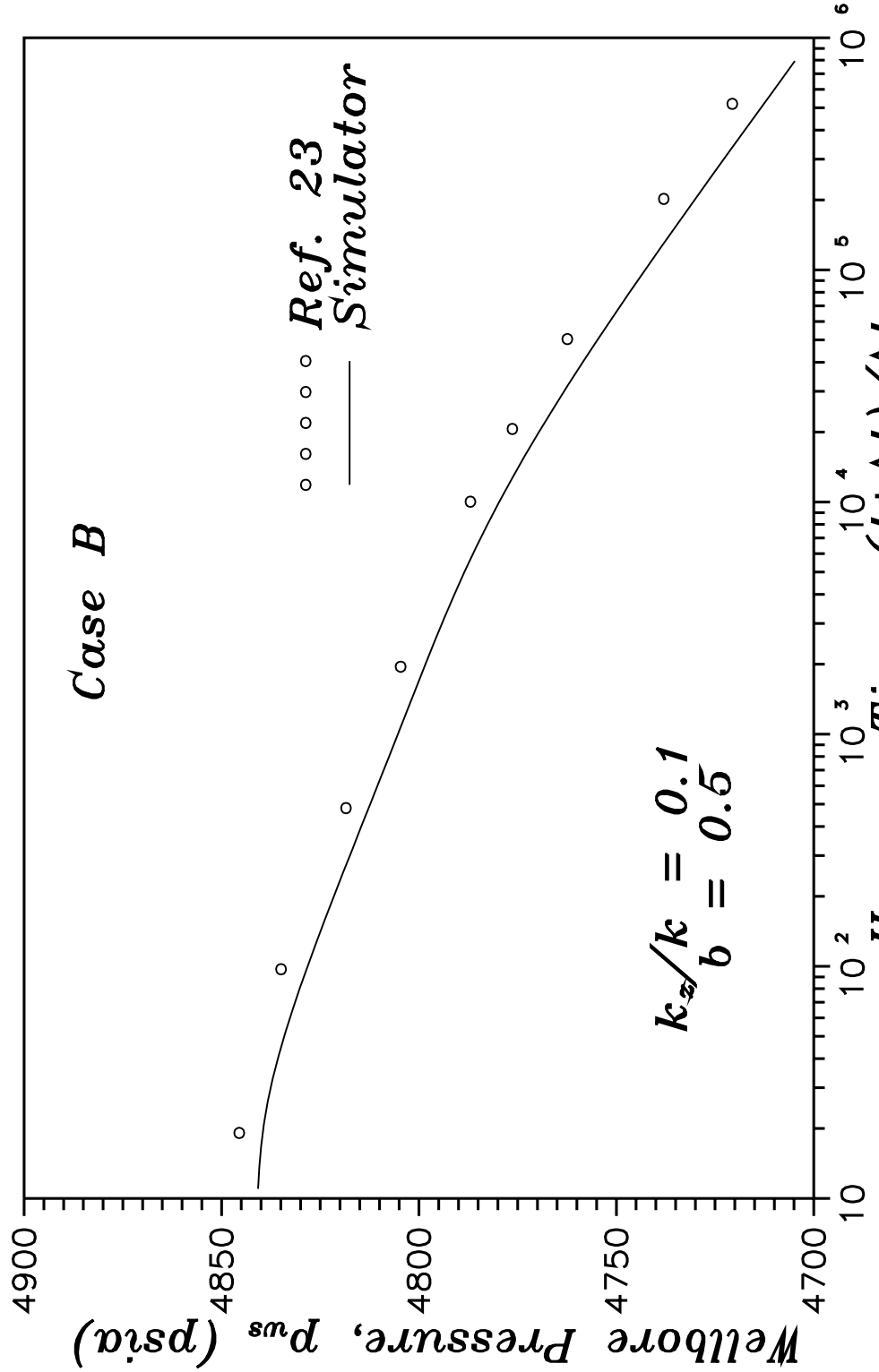

Fig. 3.11 – Comparison of wellbore shut–in pressures (Case B).

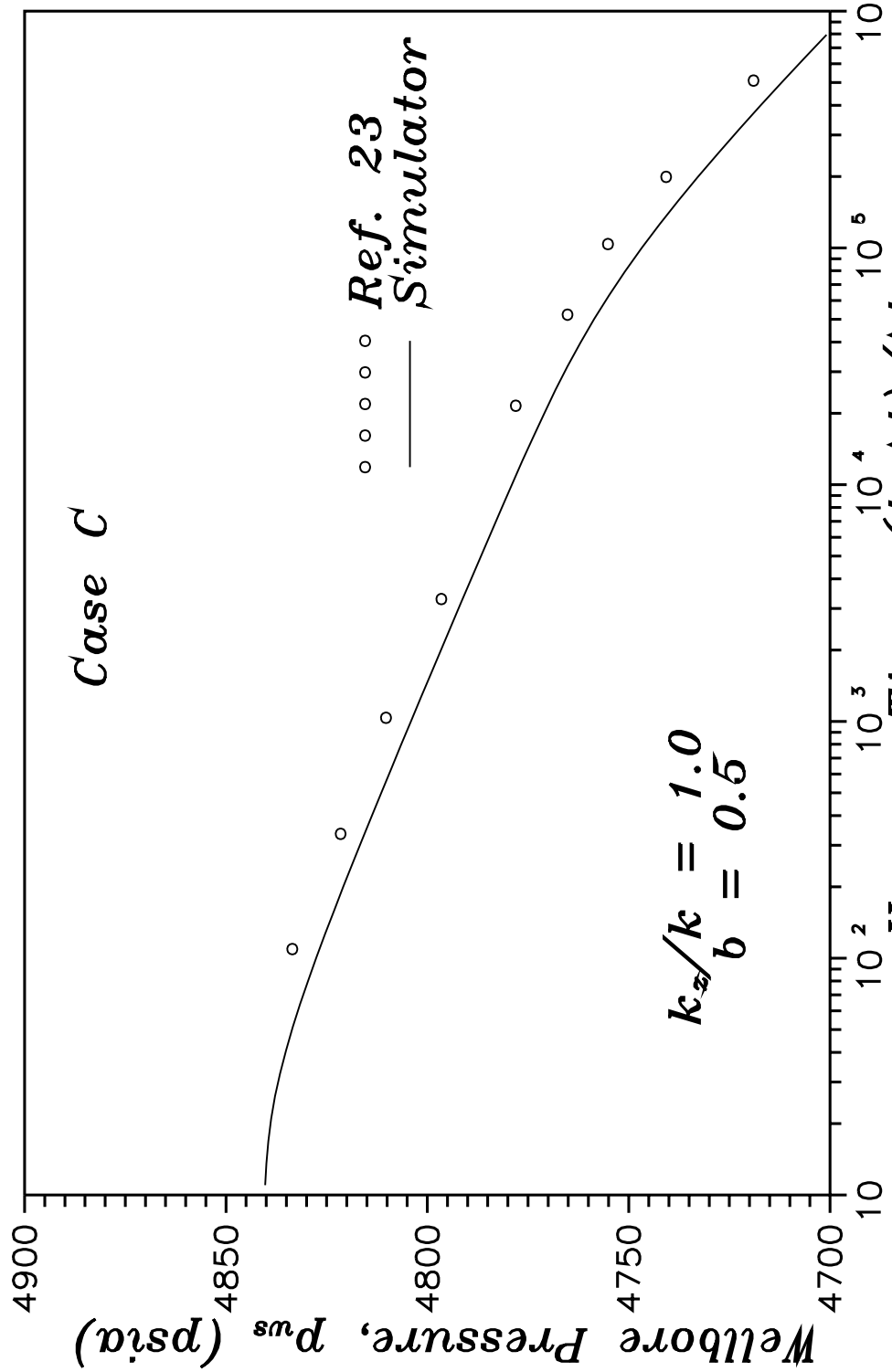

Fig. 3.12 – Comparison of wellbore shut–in pressures (Case C).

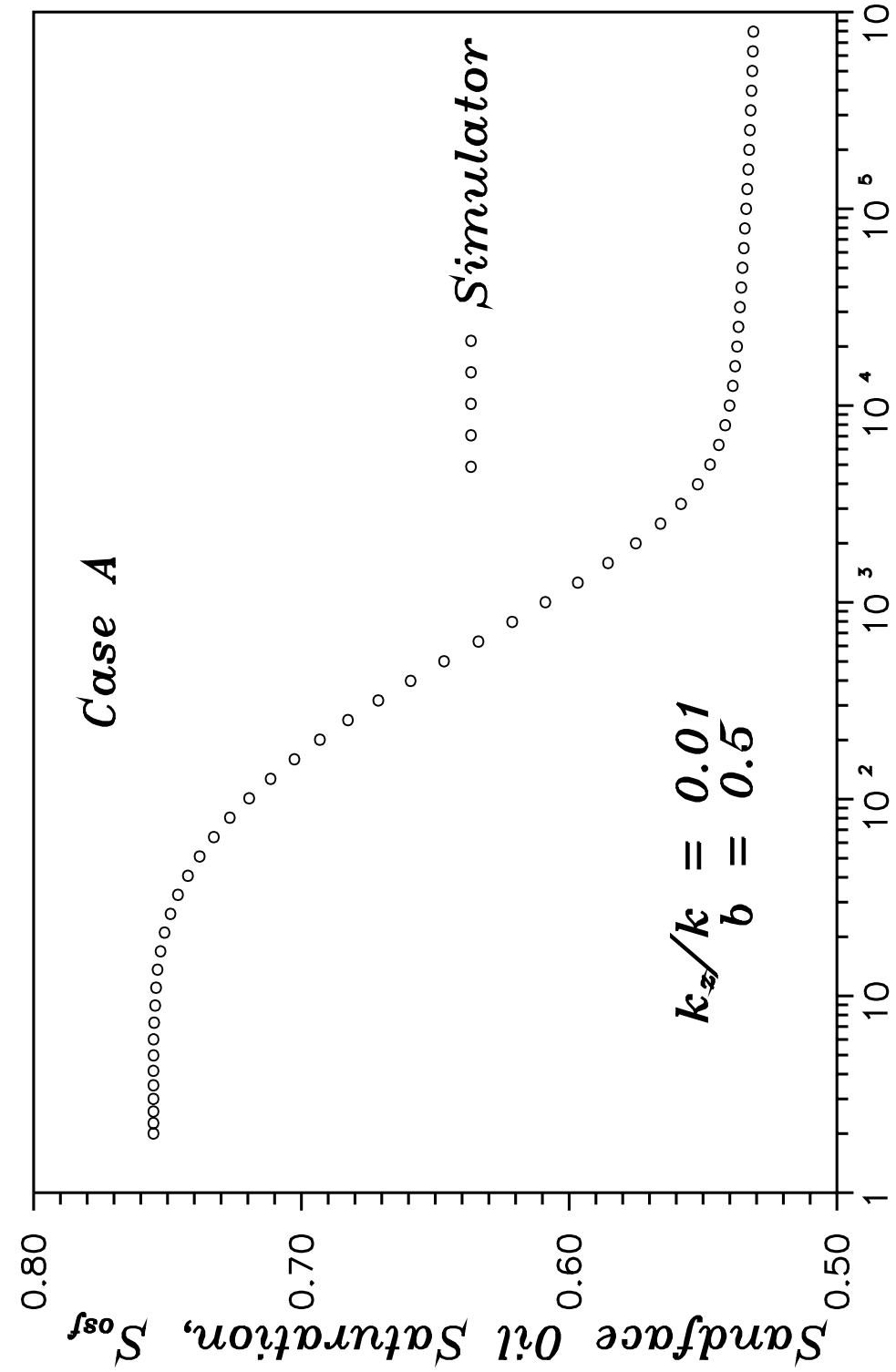

Fig. 3.13 – Buildup sandface oil saturation (Case A).

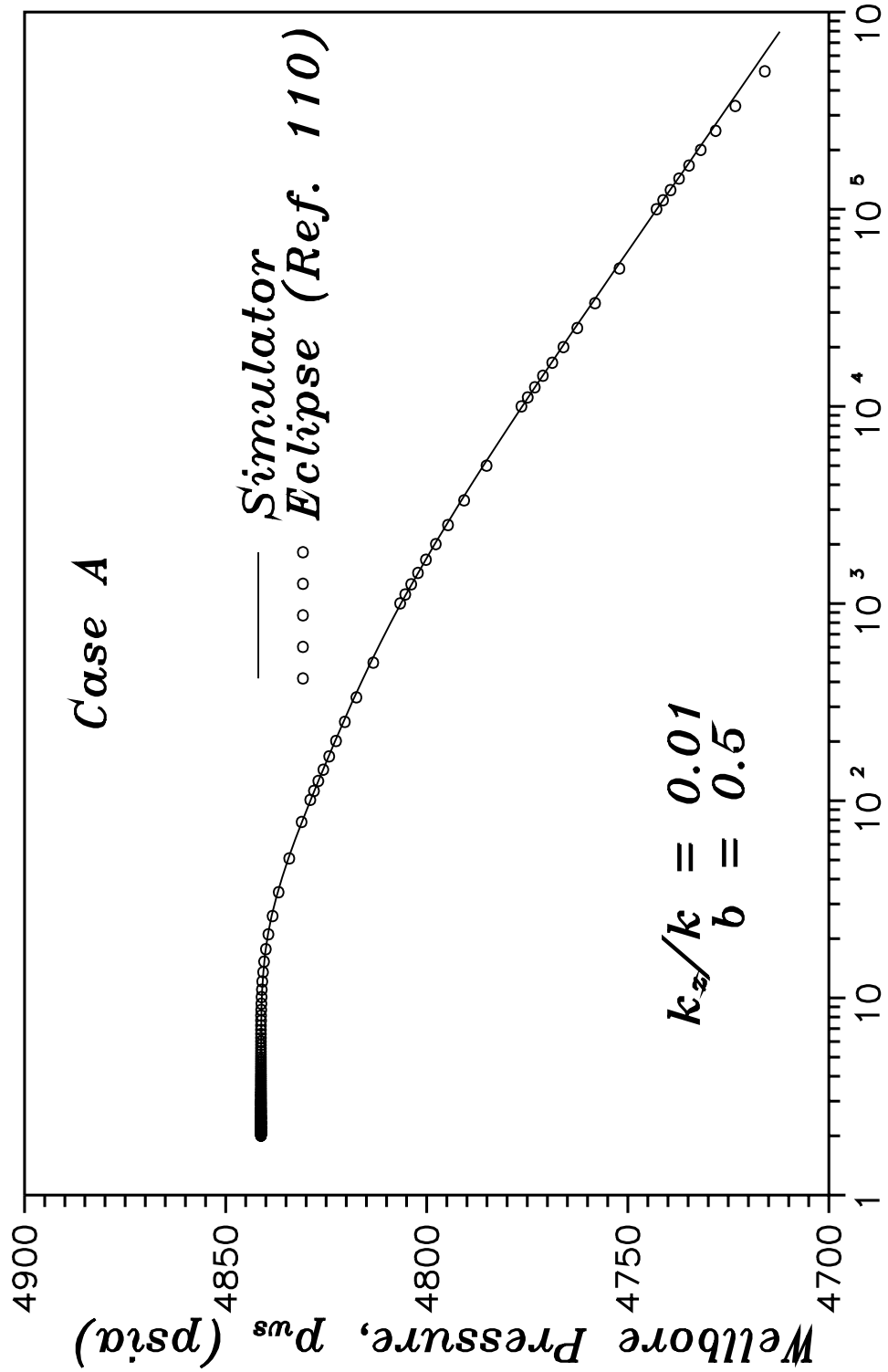

Fig. 3.14 – Comparison of shut–in wellbore pressures (Case A).

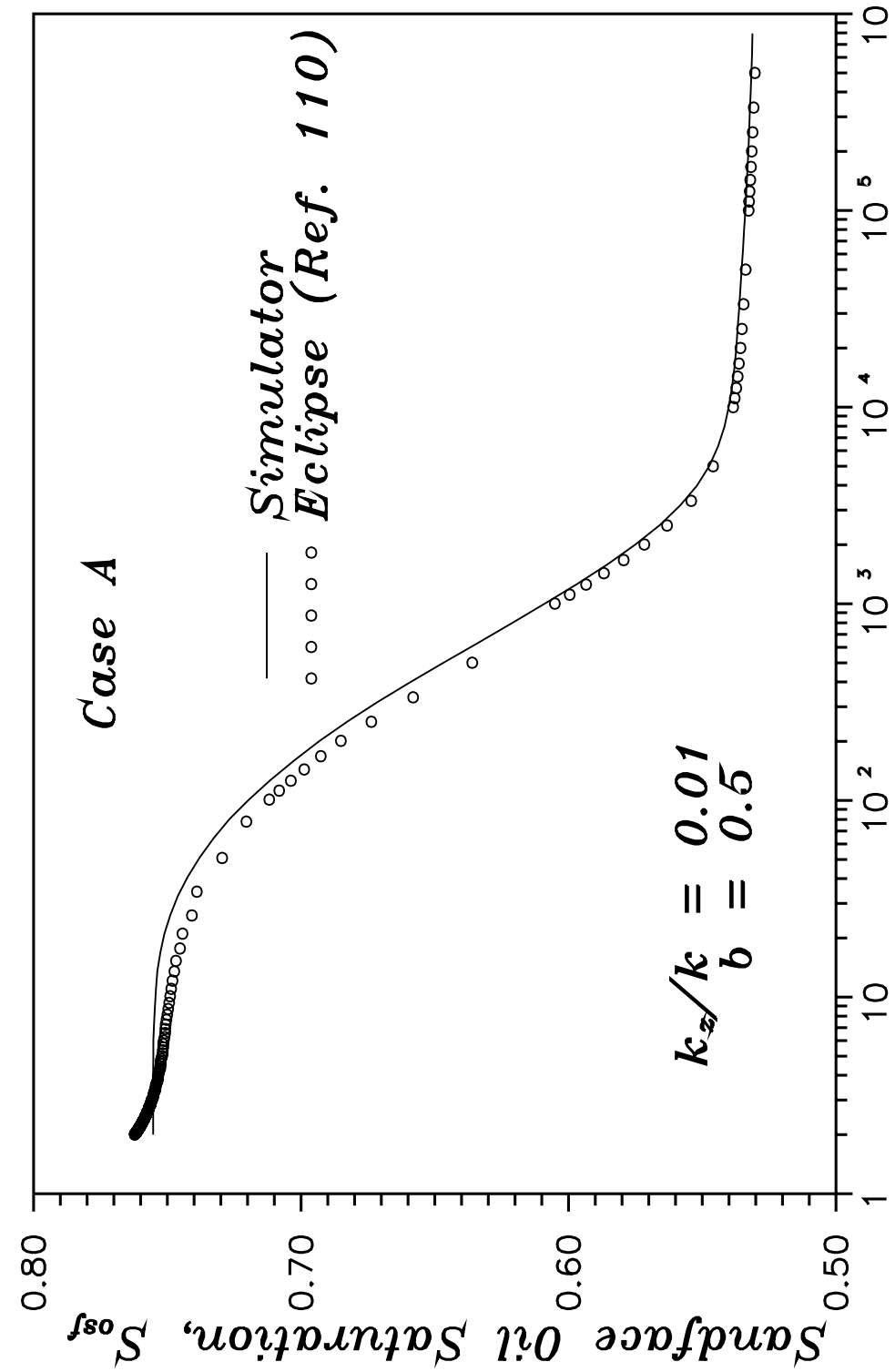

Fig. 3.15 – Comparison of buildup sandface oil saturations (Case A).

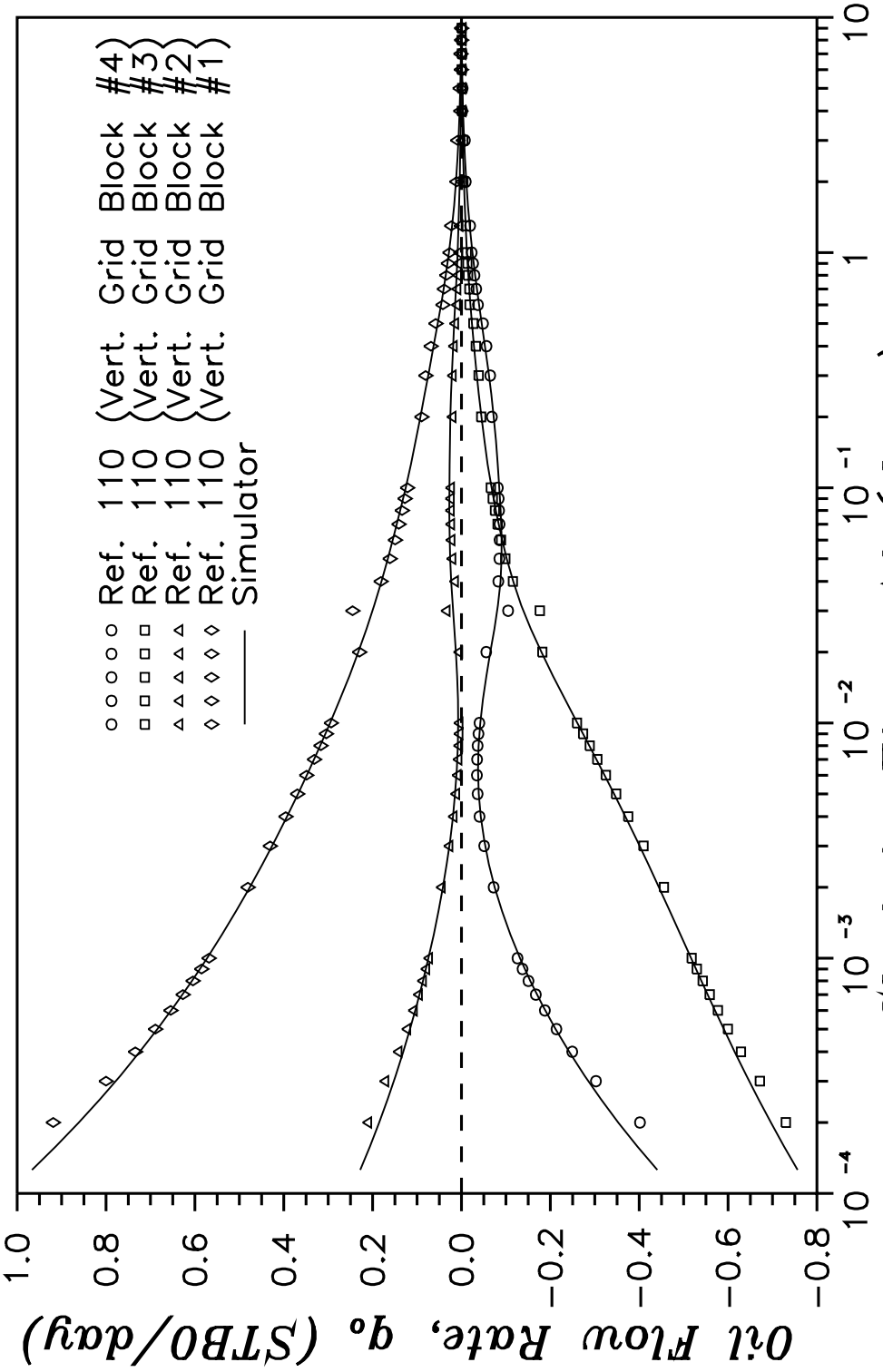

Fig. 3.16 – Comparison of individual "layer" oil flow rates (Case A).

3.2.4 Three-Phase (Oil-Gas-Water) Two-Dimensional Flow

The three-phase coning example considered here is the SPE Second Comparative Solution Project[111] and all pertinent data may be found in Ref. 111. This problem is a single-well radial cross section ($r - z$ model) that involves gas and water coning as well as gas repressuring. Weinstein et al.[111] state "this is a difficult problem that provides a good test of the stability and convergence behavior of any simulator." Weinstein et al. also note that the problem is rather artificial in that it involves rate variations that would be unlikely to occur in practice and, the solution GOR is unusually high for oil with such a high density. They note that both of these characteristics make the problem more difficult to solve, increasing its value as a test of simulation techniques.

As a brief description of the problem, the reservoir is both heterogeneous and anisotropic, consisting of 15 layers of different porosity and permeability. The reservoir contains a bottom aquifer and a gas cap. Only the seventh and eighth layers are perforated. The reservoir is to be produced according to the following rate schedule (subject to a minimum bottomhole flowing pressure of 3000 $psia$):

Time Period ($days$)	Oil Production Rate ($STBO/day$)
1 to 10	1000
10 to 50	100
50 to 720	1000
720 to 900	100

For this problem, results obtained from eleven different simulators developed at eleven different companies are presented in Ref. 111. These results, presented in graphical form, were digitized and plotted along with the results from

our simulator for comparison in Figs. 3.17 through 3.20. On these four figures, the open circles represent the results from the eleven other simulators, and the dark circles represent the results from our simulator. Figure 3.17 is a plot of the bottomhole flowing pressure versus time, Fig. 3.18 is a plot of the oil production rate versus time, Fig. 3.19 is a plot of the producing gas-oil ratio, and Fig. 3.20 is a plot of the fractional water cut versus time.

Though we do not know the "correct" solution to this problem, we can say that the results from our simulator fall well within the range of the results from the other simulators. Initial fluids in place were also calculated for this problem and values obtained include: initial oil in place = 28.86 MMSTBO; initial water in place = 73.99 MMSTBW; and, initial gas in place = 47.04 MMMscf. These values for the initial fluids in place also compare extremely well with those values reported in Ref. 111, as does the time at which the reservoir goes on decline, determined to be 220 days form our simulation results. Due to the complexity of this problem, these results add greatly to the confidence level in our simulator, and, at this point, we feel satisfied that our simulator is operating correctly.

As a side note unrelated to the actual model validation studies, but requested in Ref. 111 for completeness, we also report on the numerical and computational aspects of the solution for the SPE Second Comparative Study. Eighty-six fixed timesteps were used to solve the problem, no timestep cuts were performed and 303 nonlinear updates (updates of the Jacobian matrix) were performed. The entire solution required 11.7 CPU seconds on an IBM RS6000 model 590. We also note that the computer code has not been optimized in the sense that no vectorization of the code has been performed.

3.3 Analysis of Linear System Solution Methods

To investigate the capabilities of the iterative solution methods, preconditioners and domain decomposition techniques discussed in this study, a variety of

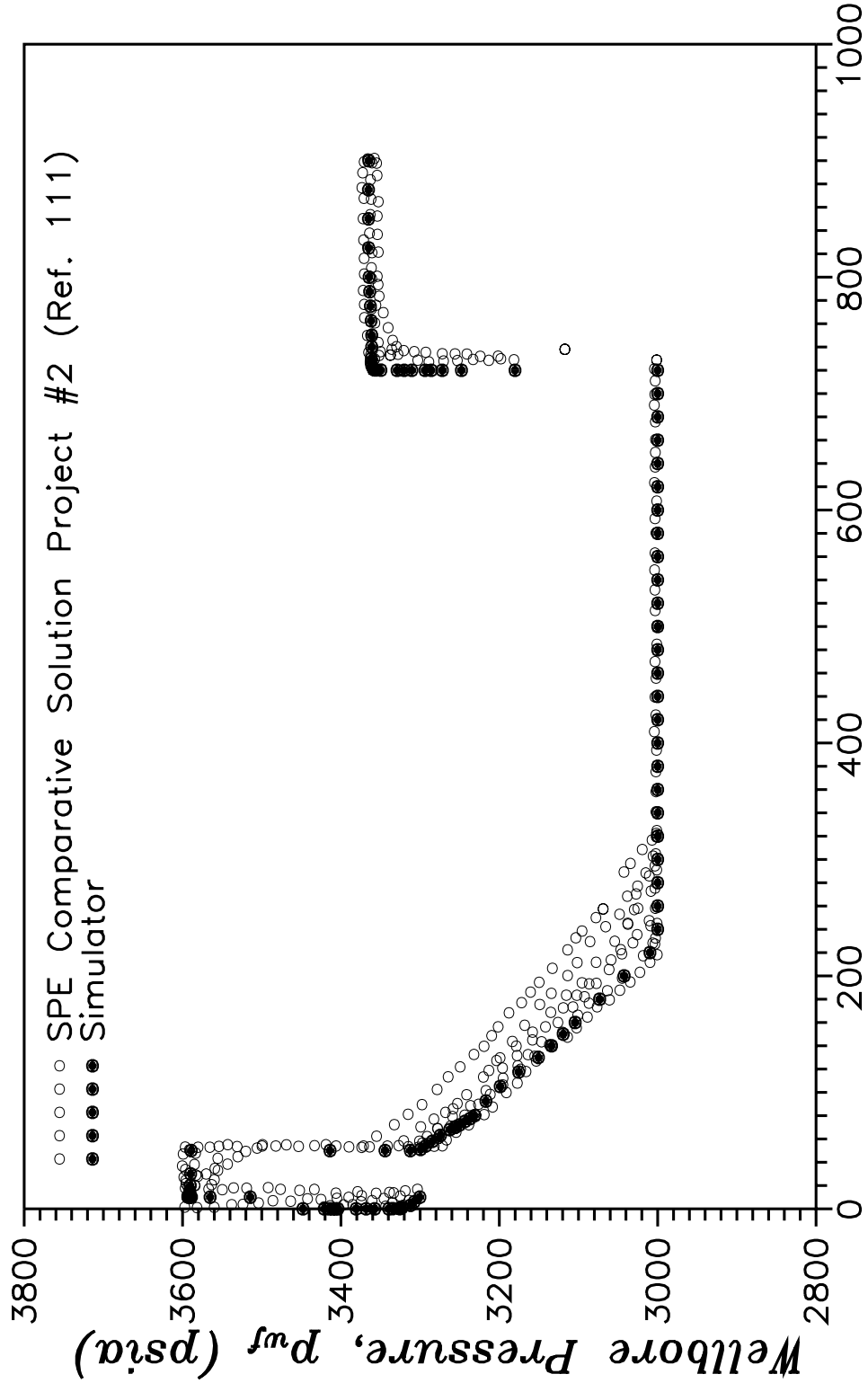

Fig. 3.17 – Comparison of flowing wellbore pressures.

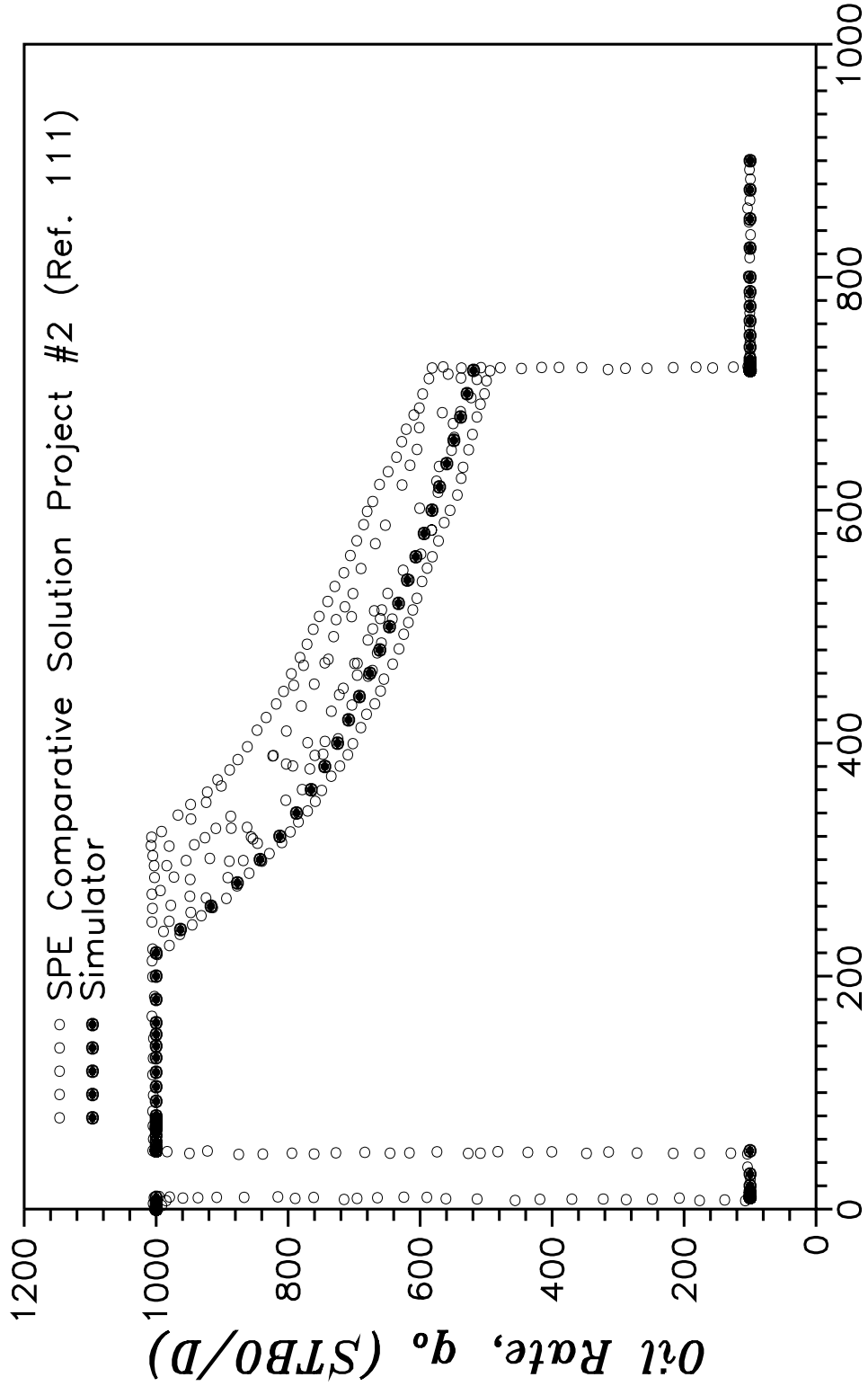

Fig. 3.18 – Comparison of oil flow rates.

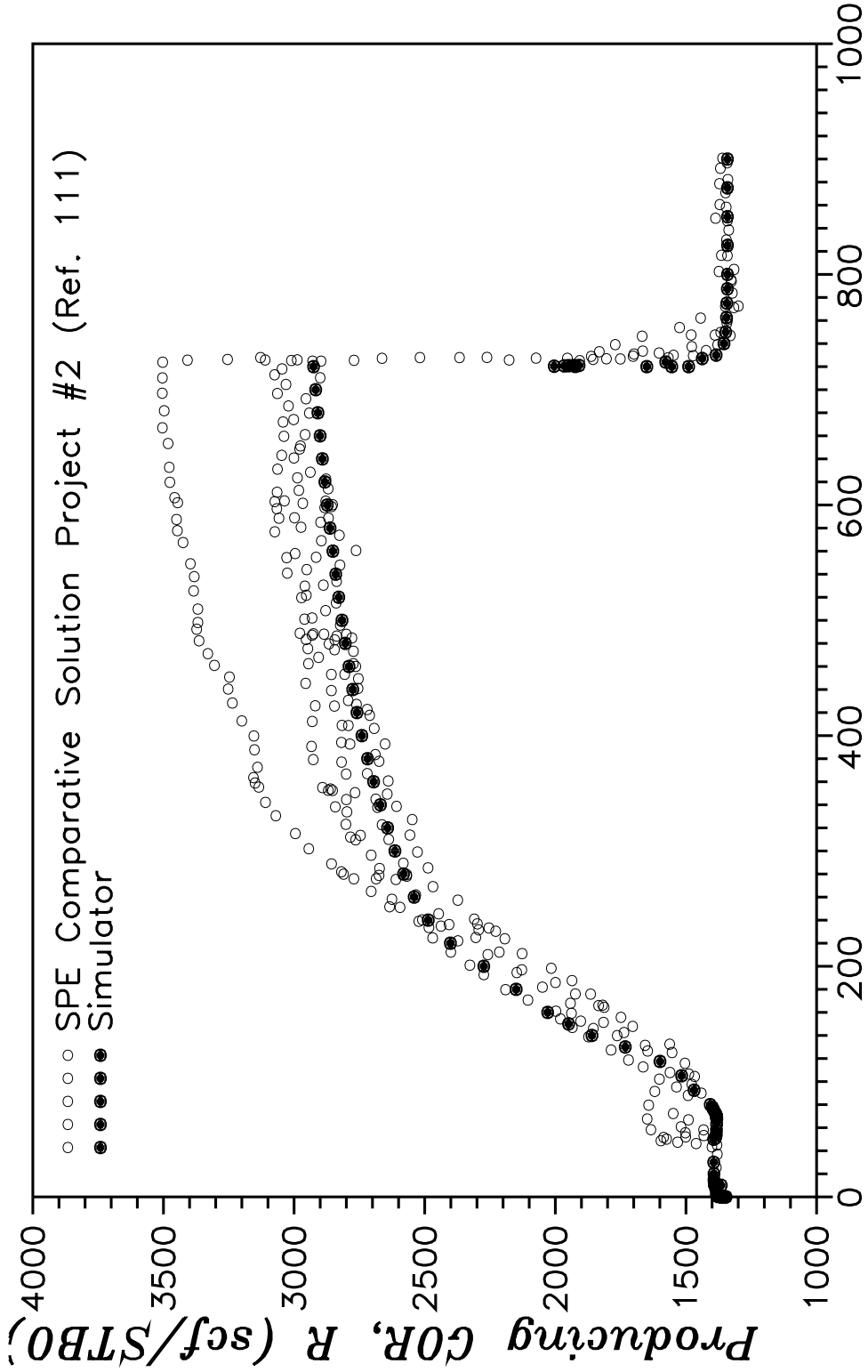

Fig. 3.19 – Comparison of producing gas–oil ratios.

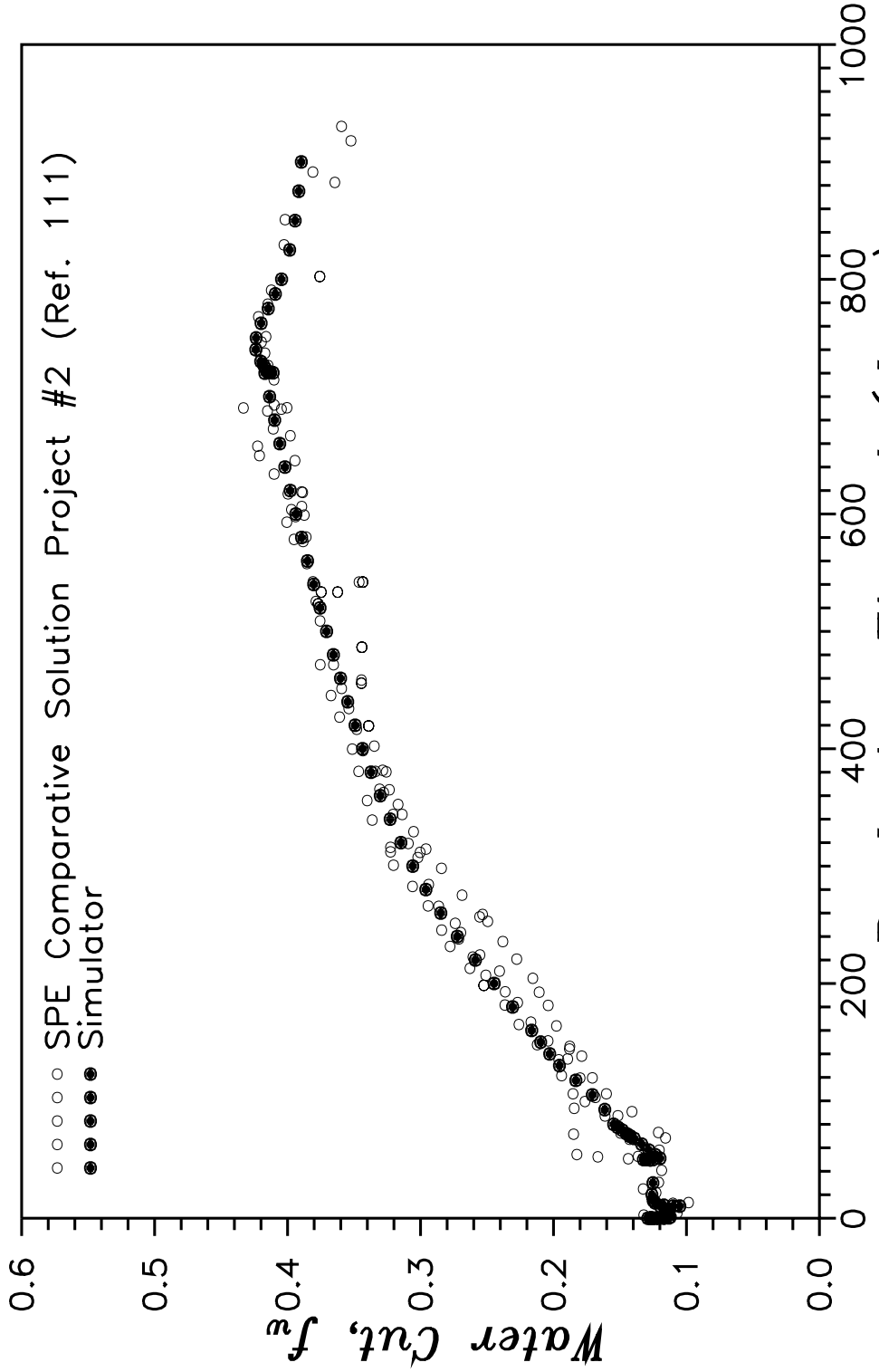

Fig. 3.20 – Comparison of calculated water cut.

test problems have been used. These include the one-dimensional single-phase example discussed in Section 3.1.1, the two-dimensional single-phase restricted-entry problem discussed in Section 3.1.2, the two-phase oil-water coning example discussed in Section 3.2.3, the SPE Second Comparative Solution Project[111] (three-phase oil-gas-water) example discussed in Section 3.2.4, and a two-dimensional two-phase (oil-gas) restricted-entry problem to be discussed shortly. These problems were selected in part because they cover a range of the typical type of problem encountered in industry. Additionally, the SPE Second Comparative Solution Project[111] (three-phase oil-gas-water) example was chosen because of the already mentioned (Section 3.2.4) difficulty of the problem. Unless otherwise noted, all CPU timings reported in this section are for the code running on an Apollo DN10000 computer running Domain OS v.SR10.4. zzzz

Test Problem #1

The three-phase coning example considered here is the SPE Second Comparative Solution Project[111] discussed in *Section 3.2.4*. Three representative matrices were generated for this problem and are henceforth referred to as test problems T1A, T1B and T1C. By test matrices we mean that three Jacobian matrices and corresponding right-hand-side vectors generated during the course of simulating this problem were output to be used in our investigation of the linear solvers incorporated in our simulator. Recall that 15 vertical and 10 radial grids are used for the SPE Second Comparative Solution Project. Test problem T1A was generated at a producing time of 1 day with a time step size of 1 day. Test problem T1B was generated at a producing time of 200 days with a time step size of 20 days. For test problem T1C, the reservoir is on decline (i.e., the reservoir is being produced at a constant bottomhole pressure of 3000 psia) and the example matrix was generated at a producing time of 620 days with a time step size of 100 days.

Test Problem #2

The second test problem comes from the two-phase oil-water coning example discussed in Section 3.2.3. Forty radial and eight vertical grids are used. This problem was chosen to aid in isolating the effect of the location ($N_{R1}+1$) of the boundary Γ_3 on the convergence of the domain decomposition preconditioned iterative methods and to provide a less complex system for the analysis of the BILU and BSGS preconditioners. One example matrix was generated at a producing time of 0.1 day with a time step size of 0.01 day, and is henceforth referred to as test problem T2A.

Test Problem #3

This problem considers a homogeneous and isotropic reservoir 100 feet thick and having a radial extent of 6000 feet. Twenty vertical and 25 radial grids are used. Water is considered to be both incompressible and at irreducible saturation for this problem. The entire reservoir is initially above the bubble point pressure ($p_{bi} = 3600$ psia), with an initial pressure of 3610 psia at the top of the reservoir. The well is perforated only over the bottom quarter of the reservoir; i.e., the bottom five grids. The Set 1 PVT and Set 1 relative permeability data (Chapter IV) are used. The reservoir is produced at a constant surface oil rate of 200 STBO/day.

The partial derivatives with respect to gas saturation found in the Jacobian matrix for fully implicit simulators are typically the largest magnitude components and have much to do with the conditioning of the entire matrix system. Test problem #3 was chosen in an attempt to see if isolating that region of the reservoir where free gas exists affects the convergence rate of the domain decomposition preconditioned iterative methods.

Six representative matrices were generated for this problem and are henceforth referred to as test problems T3A–T3F. The producing times and time step sizes at the time of their generation are listed in the following table:

Test Problem	Producing Time ($days$)	Time Step Size ($days$)
T3A	0.1	0.1
T3B	10	1
T3C	100	10
T3D	1000	50
T3E	2000	100
T3F	4000	100

To emphasize the difference between direct and iterative solution methods, the first part of our analysis compares execution times between the sparse direct solver[93] included in our simulator and one of the iterative solution methods[49–51] (GMRES(K)).

In the second part of the analysis, we examine and compare the three iterative methods, GMRES(k)[49–51], Orthomin(k)[48] and Bi-CGSTAB[52] (and it's variant Bi-CGSTAB-P[52]) included in our simulator. The preconditioners BILU and BSGS are compared for each method. For the restarted methods GMRES(k) and Orthomin(k), we also examine the effect of the number of orthogonalizations on the convergence properties of the methods. As a prelude to the domain decomposition techniques, the effects of reordering are also examined.

In the last part of our analysis, we examine domain decomposition as an overall preconditioner to the iterative methods. Note here that domain decomposition is investigated only with the method GMRES(k), though the general conclusions should hold for any of the iterative methods investigated in this study. The domain decomposition preconditioner considered here is the one developed

by Bramble et al.[90]. Additionally, a variety of preconditioners for the Schur complement are tested and the effect of how the domain is partitioned, i.e., where the boundary Γ_3 is located, is analyzed.

For all of the test problems and for the analysis of the iterative methods, the convergence criteria used for the iterative solvers was that the two norm of the preconditioned residual be reduced to 10^{-10} times the two norm of the non-preconditioned initial residual, i.e.,

$$\|Q^{-1}r\|_2 \leq 10^{-10}\|r^0\|_2 \tag{3.3.1}$$

Note that from a practical standpoint, experience has shown that a tolerance of 10^{-6} is sufficient for single phase or two-phase oil-water systems and the tolerance of 10^{-10} is required only for those systems containing gas. Also note that the Bi-CGSTAB method does not as part of the iterative process supply us with the preconditioned residual, and we, therefore, had to include an additional step within the method to calculate the preconditioned residual. The additional CPU time required for this calculation was, however, accounted for and is not included in the CPU times reported for this method. This puts our comparison of the iterative methods all on the same basis.

3.3.1 Comparison of Direct and Iterative Solution Methods

For each of the test problems just described in the previous section, and for many additional test problems involving both single-phase and multiphase systems, the number of radial and vertical grid blocks used were varied to generate systems of linear equations of various orders. Our simulator was then run twice for each size of linear system, once using the sparse direct Gaussian elimination routine[93] to solve the generated linear system of equations and once using the iterative solution method GMRES(k) with BILU preconditioning. The CPU time

required by each solution method to solve the linear system of equations was recorded for each nonlinear iteration and an average value was calculated. These results are shown if Fig. 3.21 for the various sized systems and test problems considered.

Figure 3.21 clearly shows the superiority of the iterative solution method GMRES(k) over the direct solution method for all of the cases considered. At the least, we see that the iterative solution method is an order of magnitude (10 times) faster than the direct solution method for the single- and two-phase cases for systems of order $n \leq 1000$. For the three-phase example considered or for the cases for which $n > 1000$ we see that the iterative method varies between 1.5 and 2.4 orders of magnitude (50-400) times faster than the direct solution method.

3.3.2 Comparison of Iterative Methods and Effect of the Number of Orthogonalizations

Our analysis begins by considering each of the four iterative methods GMRES(k), Orthomin(k), Bi-CGSTAB and Bi-CGSTAB-P without preconditioning and with full orthogonalization, i.e., $k = n$. For symmetric positive definite systems of linear equations, each of these methods have been shown to be finite methods, i.e., in exact arithmetic, each will terminate in at most n iteration steps. Each of these iterative methods, however, were developed as methods for the solution of nonsymmetric systems of linear equations. While from a practical point of view, full orthogonalization would never be used in these iterative methods and some form of preconditioning would also be used, it is instructive to investigate the convergence behavior of the methods themselves for some of the typical linear systems of equations generated by our simulator. As discussed in Chapter II, the Jacobian matrices generated are sparse and generally nonsymmetric and nondiagonally dominate.

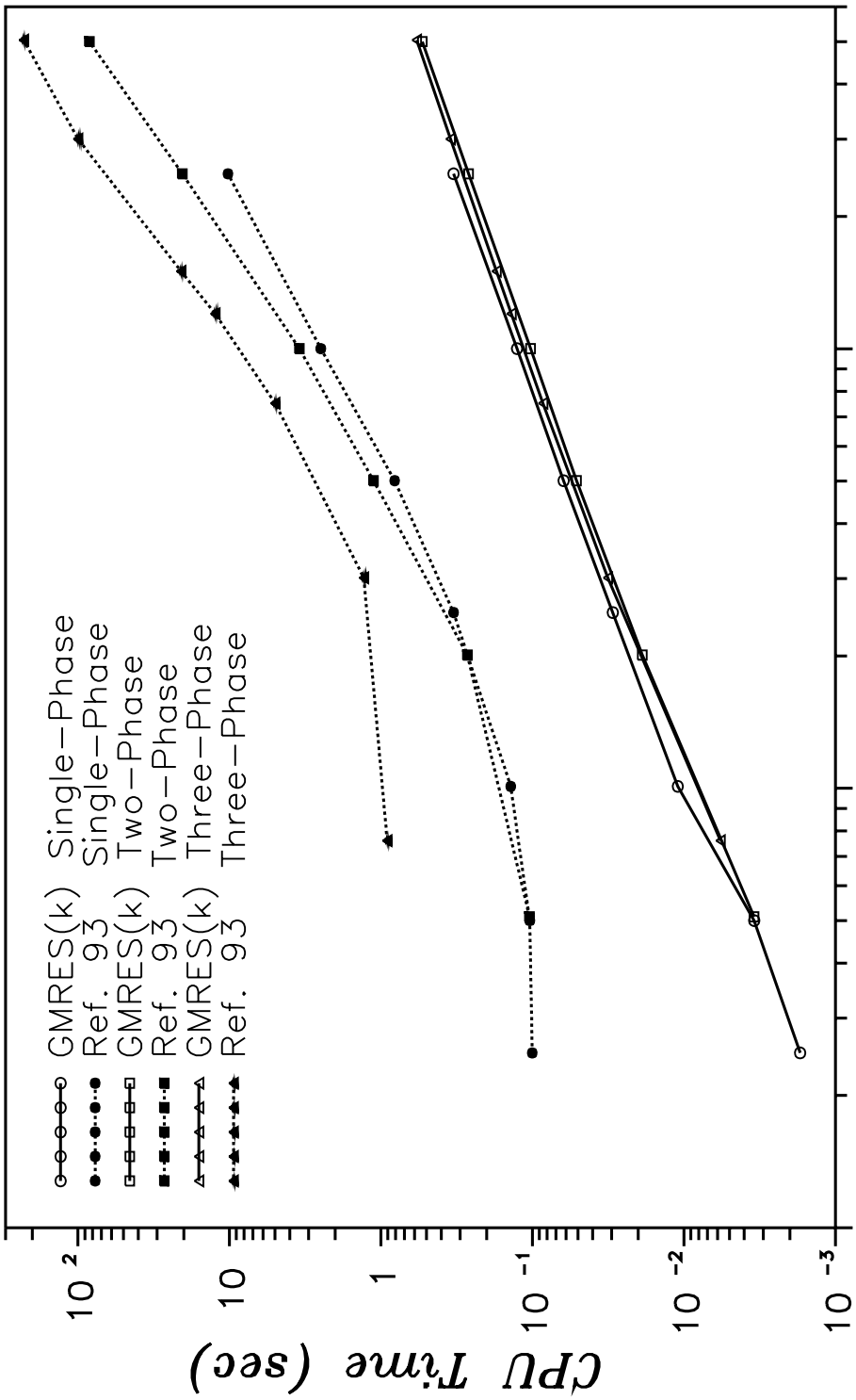

Fig. 3.21 – Comparison of direct and iterative solution methods.

Figure 3.22 shows the convergence behavior of the iterative methods for test problem T1A ($n = 401$). Method GMRES(k) required 400 iterations to converge to the specified tolerance. Method Orthomin(k) failed to converge, becoming stationary after 100 iterations. Both Bi-CGSTAB and the variant Bi-CGSTAB-P displayed extreme oscillatory behavior and failed to converge. Similar results were observed for the test problem T2A matrix ($n = 641$) and the test problem T3 matrices ($n = 1001$), with GMRES(k) converging in close to n iterations, Orthomin(k) failing to converge at all, becoming stationary part way through the process, and both variants of Bi-CGSTAB failing to converge and displaying the same oscillatory behavior.

The effect of the number of orthogonalizations, k, on the convergence rate of both GMRES(k) and Orthomin(k) was investigated using test problems T1A and T2A. BILU preconditioning was used for all runs and the results are shown in Figs. 3.23–3.26. In all figures, the $l_2\text{–}norm$ shown is actually the $l_2\text{–}norm$ of the preconditioned residual.

Figure 3.23 shows the effect of the number of orthogonalizations on the method GMRES(k). In general, the greater the number of orthogonalizations, fewer iterations are required.

Figure 3.24 shows the effect of the number of orthogonalizations on the method Orthomin(k) for test problem T1A. Here again, we see that Orthomin(k) had some problems converging, i.e., for $k \leq 5$, Orthomin(k) failed to converge. For $k = 10$ and $k = 15$ the method converged nicely. Only a slight improvement is seen in the convergence rate for $k = 15$ over that for $k = 10$.

The effect of k on the convergence rate of GMRES(k) for test problem T2A is shown in Fig. 3.25. Here we see a significant improvement in the convergence rate of GMRES(k) with an increase in the number of orthogonalizations.

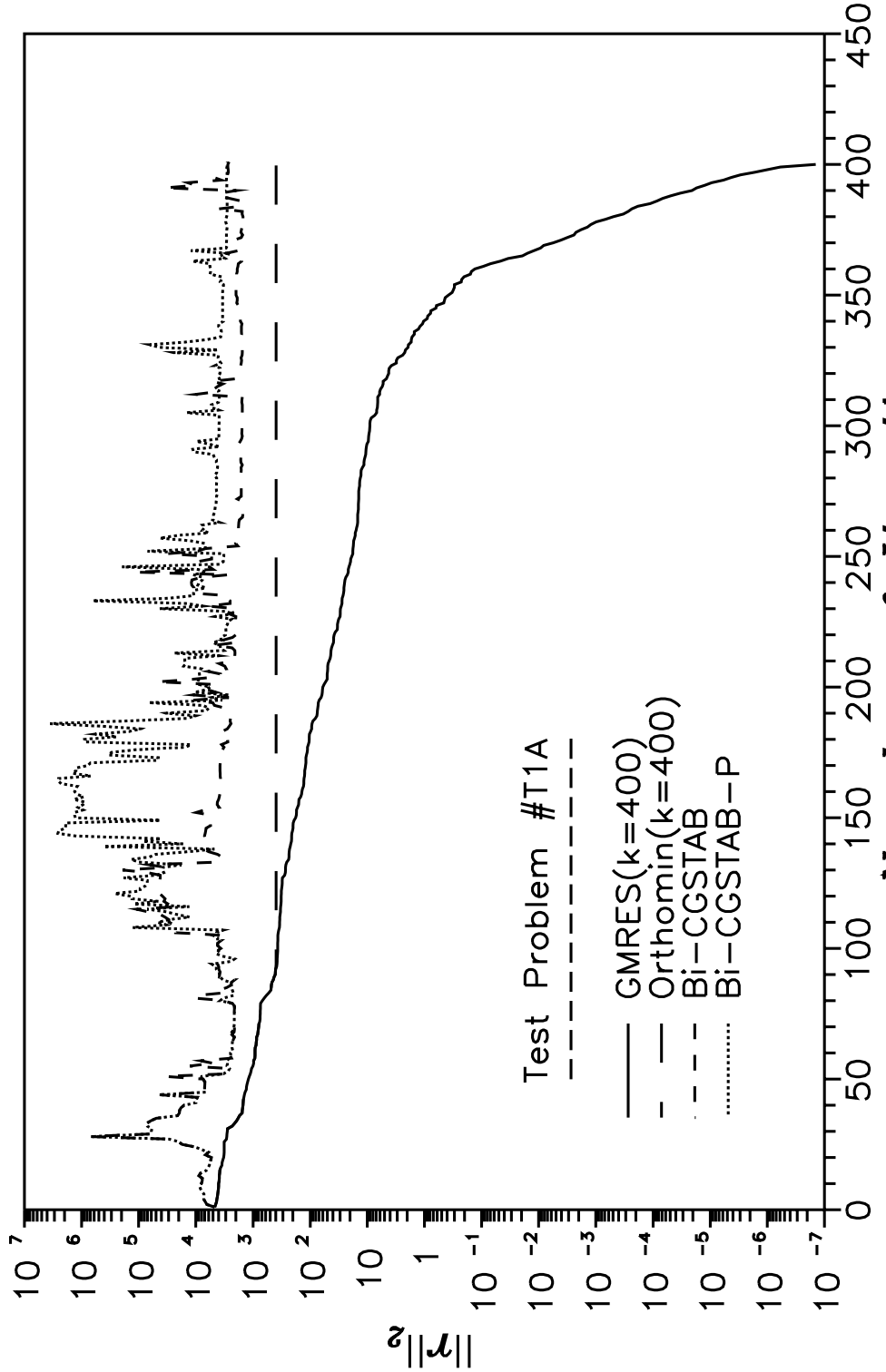

Fig. 3.22 – Full orthogonalization for Test Problem T1A (no preconditioning).

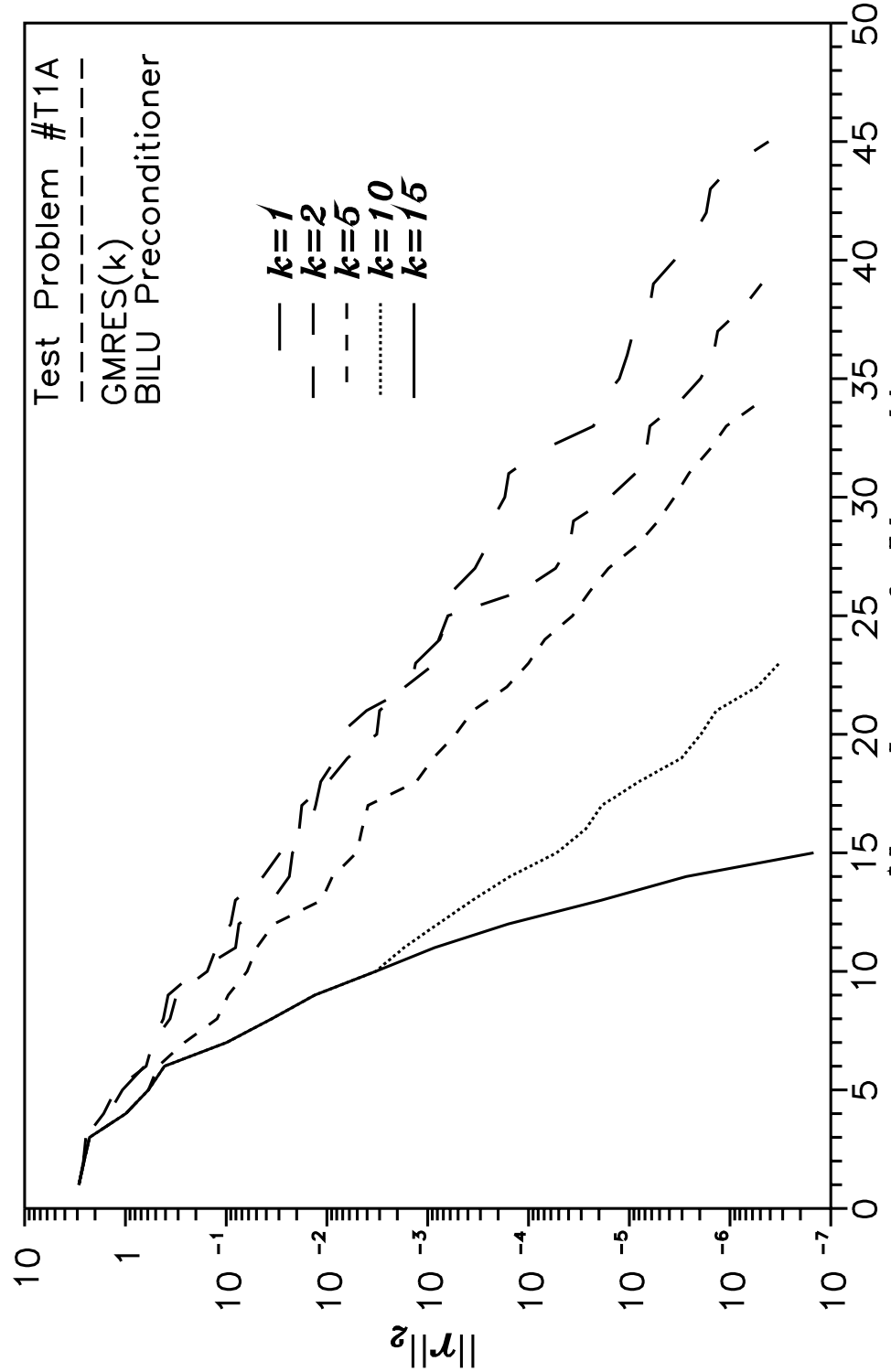

Fig. 3.23 – Effect of number of orthogonalizations on GMRES(k).

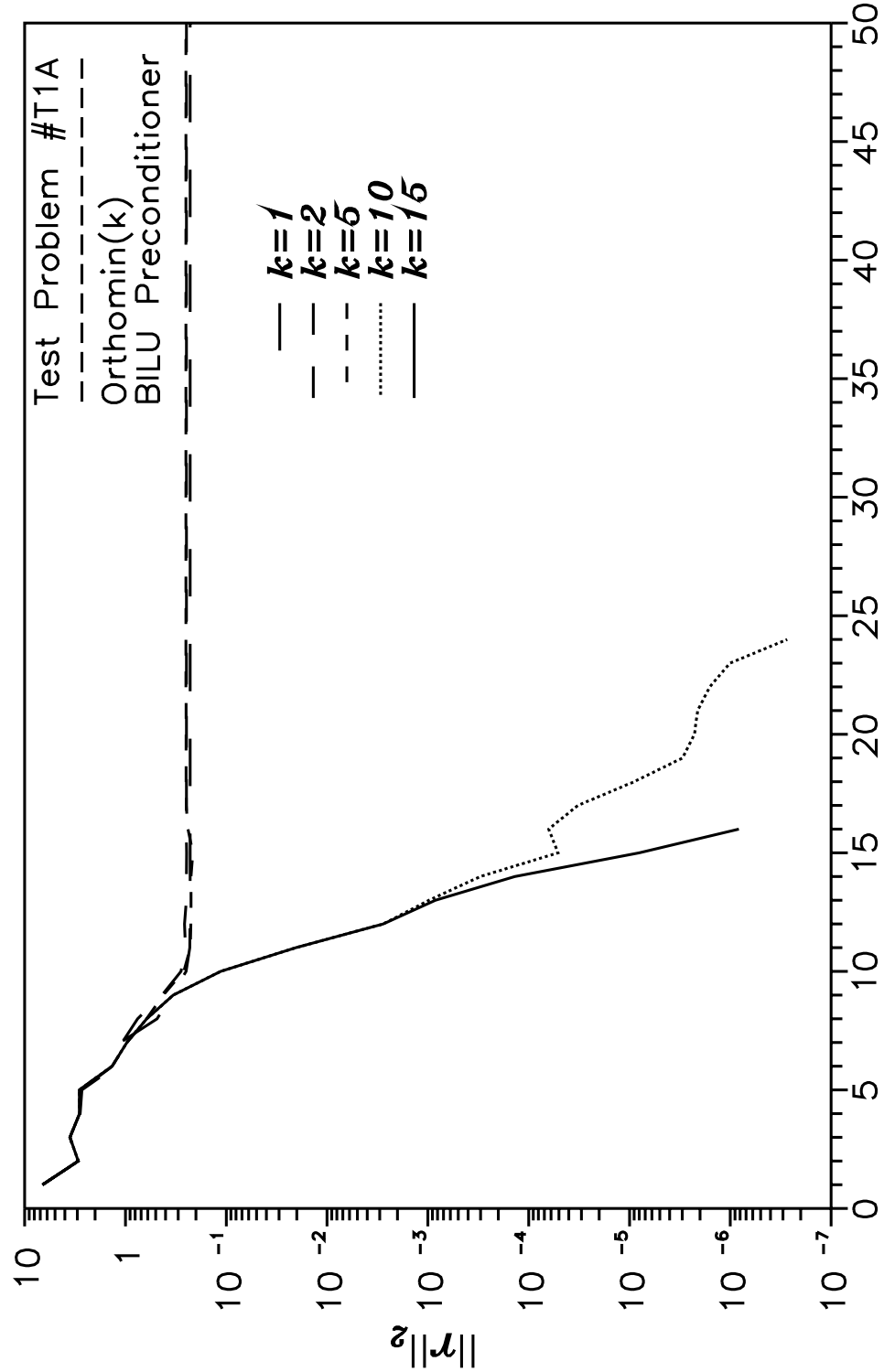

Fig. 3.24 – Effect of number of orthogonalizations on Orthomin(k).

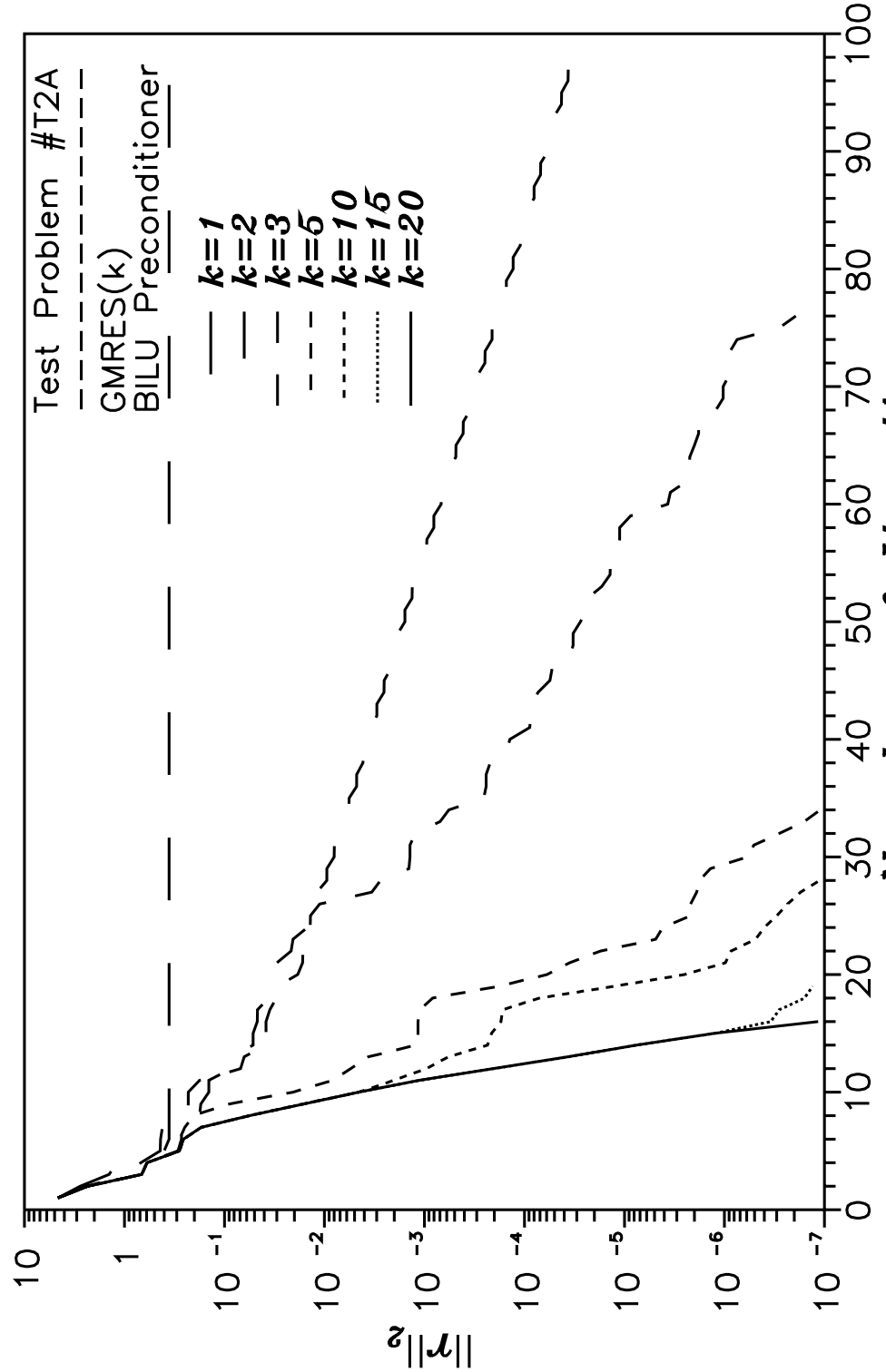

Fig. 3.25 – Effect of number of orthogonalizations on GMRES(k).

Problem T2A results for Orthomin(k) are shown in Fig. 3.26. Again, for $k \leq 5$, Orthomin(k) failed to converge. For $k \geq 10$, Orthomin(k) appears to have no problem converging and, again, we see that the effect of increasing the number of orthogonalizations, k, is much less significant than for GMRES(k).

Fig. 3.27 for problem T1A and Fig. 3.28 for problem T2A show a comparison between GMRES(k) and Orthomin(k) for various values of k, and also include results for BILU preconditioned Bi-CGSTAB and Bi-CGSTAB-P. As far as the convergence rate (number of iterations) is concerned, these figures show Bi-CGSTAB and the variant Bi-CGSTAB-P outperforming both GMRES(k) and Orthomin(k) for both test problems. For test problem T1A (Fig. 3.27), method GMRES(k) outperformed Orthomin(k) for each value of the restart parameter k. For test problem T2A, the test results are more varied, with Orthomin(k) performing better than GMRES(k) for values of $k = 10$ and $k = 15$, and GMRES(k) requiring less iterations than Orthomin(k) for $k = 20$.

Based purely on the convergence rate (number of iterations) and the discussion above, Bi-CGSTAB and Bi-CGSTAB-P would appear to be better methods than either GMRES(k) or Orthomin(k). Additional factors, however, need to be considered in the practical application of these methods. Table 3.4 shows the CPU time in seconds on an Apollo DN10000 computer required by each of these methods to solve both test problems T1A and T2A. For test problem T1A, GMRES(15) required 14.3 percent less CPU time than Orthomin(15), 43 percent less CPU time than Bi-CGSTAB-P and 71.9 percent less CPU time than Bi-CGSTAB. For test problem T2A, GMRES(20) required 21.6 percent less CPU time than Orthomin(15), 19.8 percent less CPU time than Bi-CGSTAB-P and 89.3 percent less CPU time than Bi-CGSTAB. These results and many additional results not shown clearly indicate the computational superiority of GMRES(k) over the other

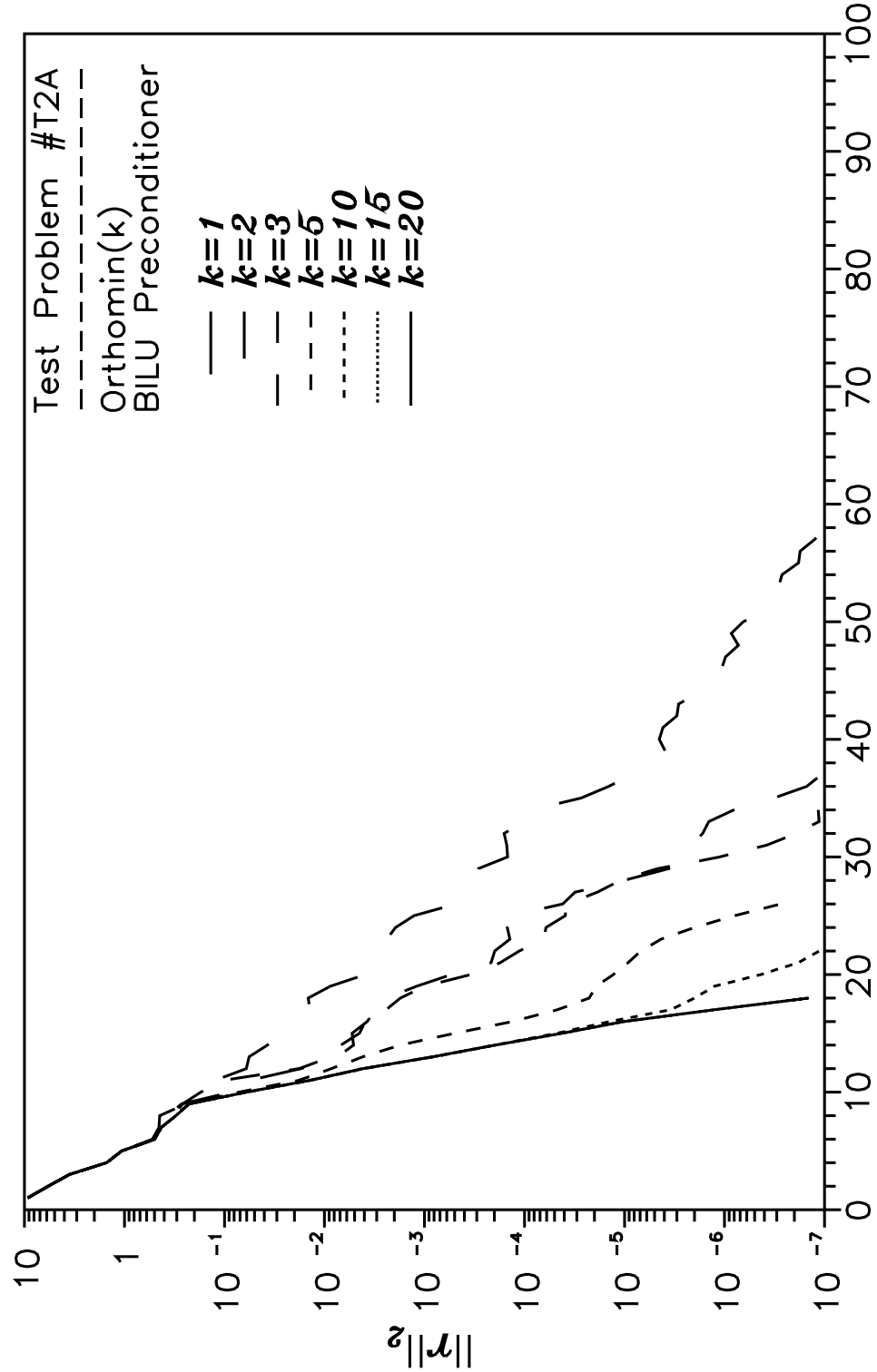

Fig. 3.26 – Effect of number of orthogonalizations on Orthomin(k).

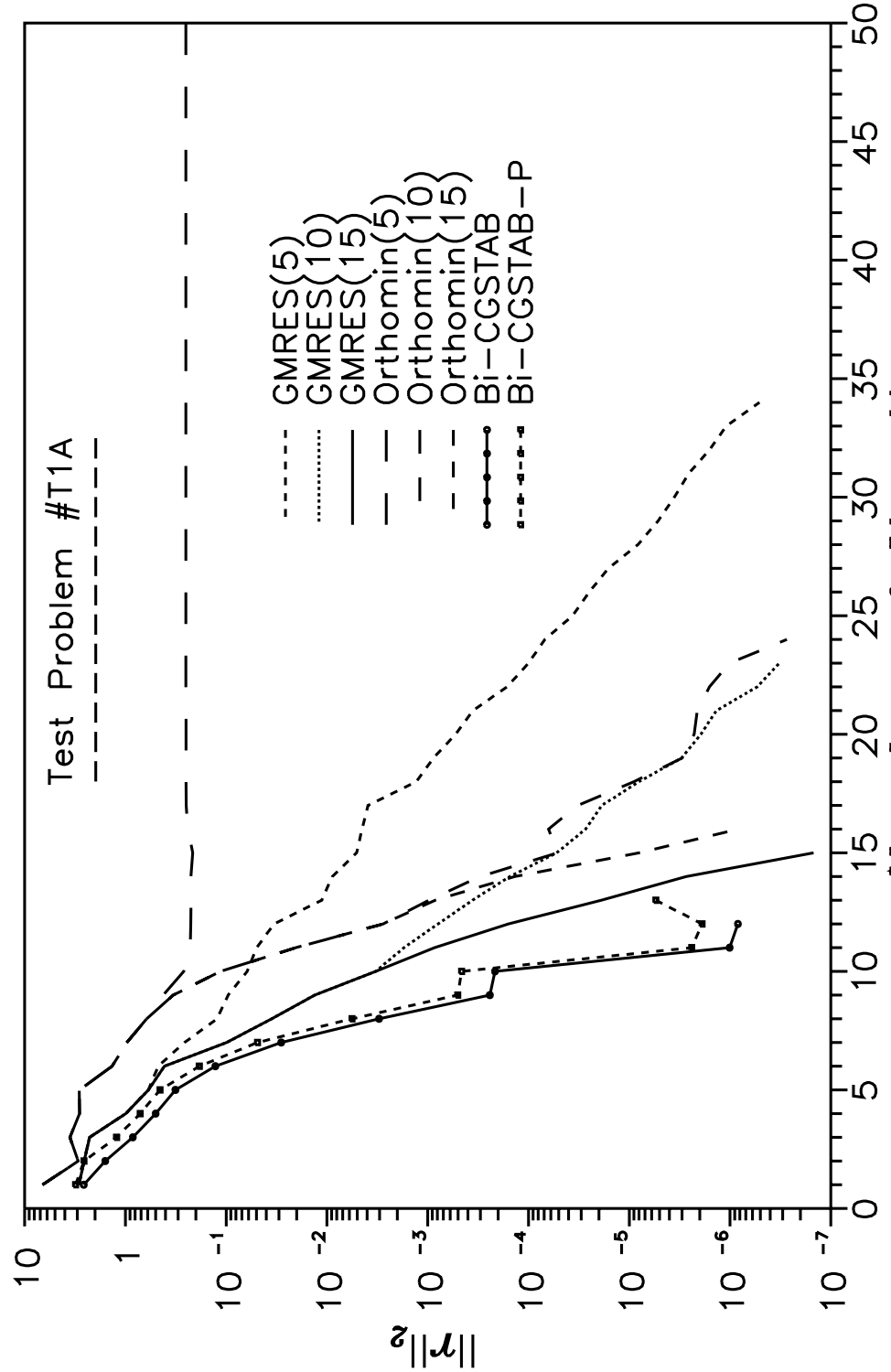

Fig. 3.27 – Comparison of iterative methods for test problem T1A.

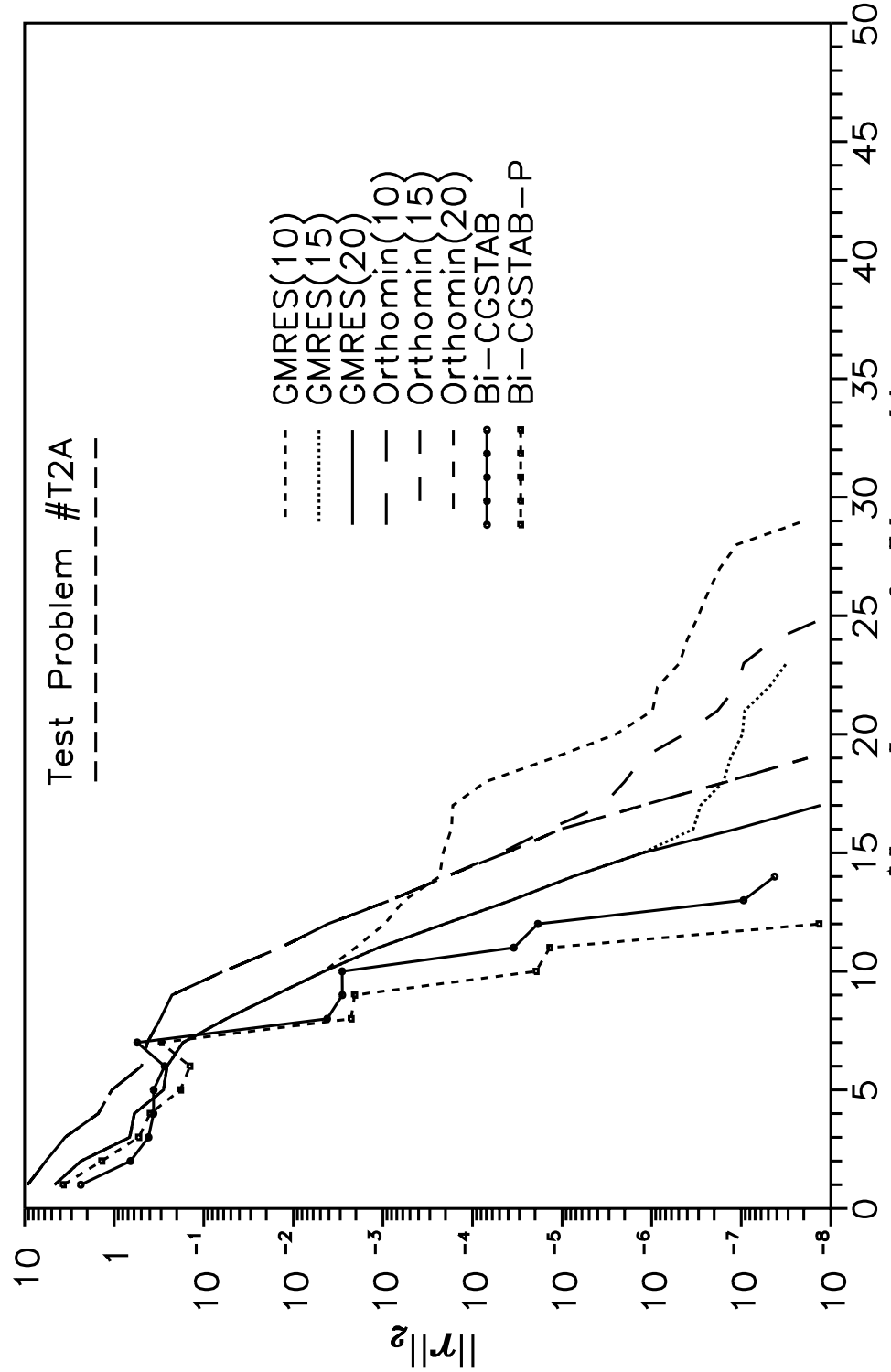

Fig. 3.28 – Comparison of iterative methods for test problem T2A.

methods considered. Additionally, these results clearly indicate the computational preference of the variant Bi-CGSTAB-P over the Bi-CGSTAB method.

Lastly, we note that there is one additional factor which should be considered when comparing these methods, i.e., the memory requirements. Ref. 52 clearly shows that in addition to the memory required for A, x, b, r and the preconditioner Q (or part thereof), the methods Bi-CGSTAB and Bi-CGSTAB-P require four additional n-length vectors. As shown by Ref. 51, GMRES(k) has memory requirements of $(k+1)\times n$ in addition to A, x, b, r and the preconditioner Q, and Orthomin(k) requires $(2k+1)\times n$ additional storage.

Based on the discussion above and the numerical results, GMRES(k) would appear to be the method of choice when memory requirements are not a concern, i.e., the problem is small or small k required to obtain a solution in a reasonable number of iterations. Should memory requirements become a constraint, then the variant Bi-CGSTAB-P would appear to be an attractive alternative to GMRES(k), though computational cost would increase slightly (≈ 20 percent).

Throughout the rest of this chapter, and indeed the rest of this study, all numerical results pertain to those obtained using GMRES(k) as the method of choice for solving the linear system of equations.

3.3.3 Comparison of Preconditioners BILU and BSGS

Method GMRES(k) was used to examine the effect of the preconditioners BSGS and BILU for test problems T1A, T1C and T3A with the results shown in Figs. 3.29–3.31, respectively. In every case, preconditioner BILU greatly outperformed the BSGS preconditioner. It is interesting to note that this occurs even though the l_2–$norm$ of the preconditioned residual is always less for the first few iterations for the BSGS preconditioned system. It is not clear as to why this happens. While it is known[112] that BILU preconditioning tends to generate a linear

Table 3.4

CPU Timings - Test Problems T1A and T2A

Case	Method	Precond.	k	Iterations	CPU (sec)
T1A	GMRES	BILU	1	45	2.001
T1A	GMRES	BILU	2	39	1.345
T1A	GMRES	BILU	5	34	0.979
T1A	GMRES	BILU	10	23	0.671
T1A	GMRES	BILU	15	15	0.456
T1A	Orthomin	BILU	1	401	9.093
T1A	Orthomin	BILU	2	401	9.269
T1A	Orthomin	BILU	5	401	9.753
T1A	Orthomin	BILU	10	24	0.693
T1A	Orthomin	BILU	15	17	0.521
T1A	Bi-CGSTAB	BILU	N/A	13	0.784
T1A	Bi-CGSTAB-P	BILU	N/A	14	0.652
T2A	GMRES	BILU	1	641	44.381
T2A	GMRES	BILU	2	138	7.191
T2A	GMRES	BILU	3	83	3.905
T2A	GMRES	BILU	5	42	1.881
T2A	GMRES	BILU	10	29	1.256
T2A	GMRES	BILU	15	24	1.048
T2A	GMRES	BILU	20	17	0.783
T2A	Orthomin	BILU	1	63	2.479
T2A	Orthomin	BILU	2	42	1.715
T2A	Orthomin	BILU	3	38	1.592
T2A	Orthomin	BILU	5	29	1.278
T2A	Orthomin	BILU	10	25	1.188
T2A	Orthomin	BILU	15	19	0.952
T2A	Orthomin	BILU	20	19	0.961
T2A	Bi-CGSTAB	BILU	N/A	15	1.482
T2A	Bi-CGSTAB-P	BILU	N/A	12	0.938

system whose eigenvalues are clustered near one, it is not exactly known how the BSGS preconditioner affects the eigenvalue distribution. Because of the symmetry assumed in the BSGS preconditioner and the fact that our Jacobian matrix is not symmetric, one may postulate that the effect of the symmetric preconditioner is to create several clusters of eigenvalues and it is the elimination of the cluster of larger eigenvalues that occurs early on in the iteration process, resulting in the better early preconditioning of the residual. Further work in this area is required to fully understand this behavior.

3.3.4 Effect of Domain Decomposition Reordering on Standard BILU Preconditioned Iterative Methods

As a prelude to investigating domain decomposition techniques, the three test problems T1B, T1C and T2A were used to examine the effect of the domain decomposition reordering on standard BILU preconditioned iterative methods. For each problem, method GMRES(k) with $k = 10$ was used. Results for test problem T2A are shown in Fig. 3.32. Note that for this problem, $N_{R1} = 40$ corresponds to the natural row ordering.

As shown in Fig. 3.32 for test problem T2A and similarly for the other test problems, the use of the domain decomposition ordering resulted in poorer convergence than for the natural row ordering. Additionally, as the fictitious domain boundary location ($N_{R1} + 1$) was moved closer to the wellbore, more iterations were required to achieve convergence. This occurs in spite of the fact that some of the reorderings resulted in a better spectral condition number for the preconditioned matrix (see Table 3.5).

3.3.5 Comparison of Schur Complement Preconditioners

Four preconditioners for the Schur complement have been examined and include the BSGS approximation to A_{33}, the BILU approximation to A_{33}, the matrix

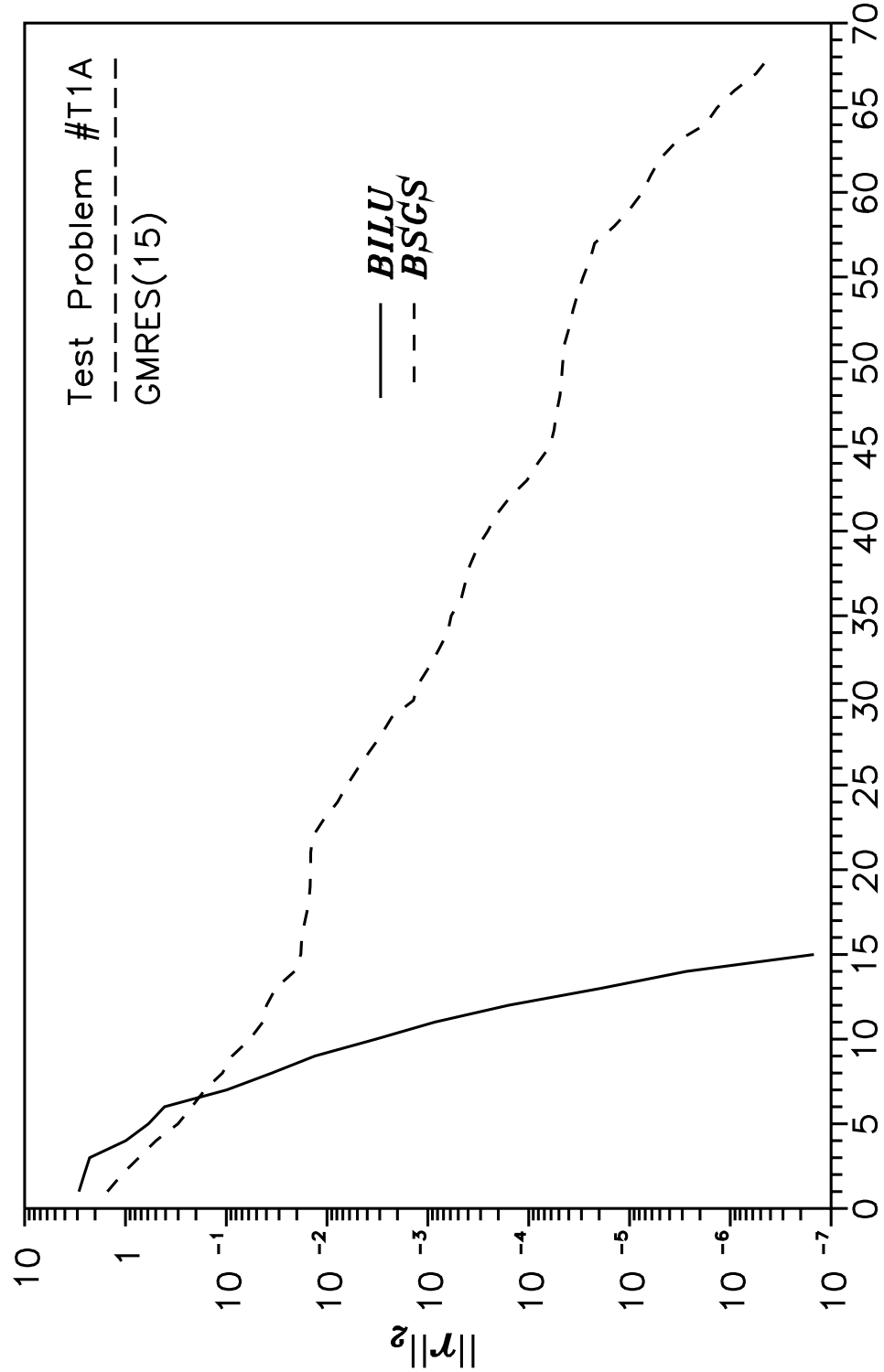

Fig. 3.29 – Comparison of BILU and BSGS preconditioners.

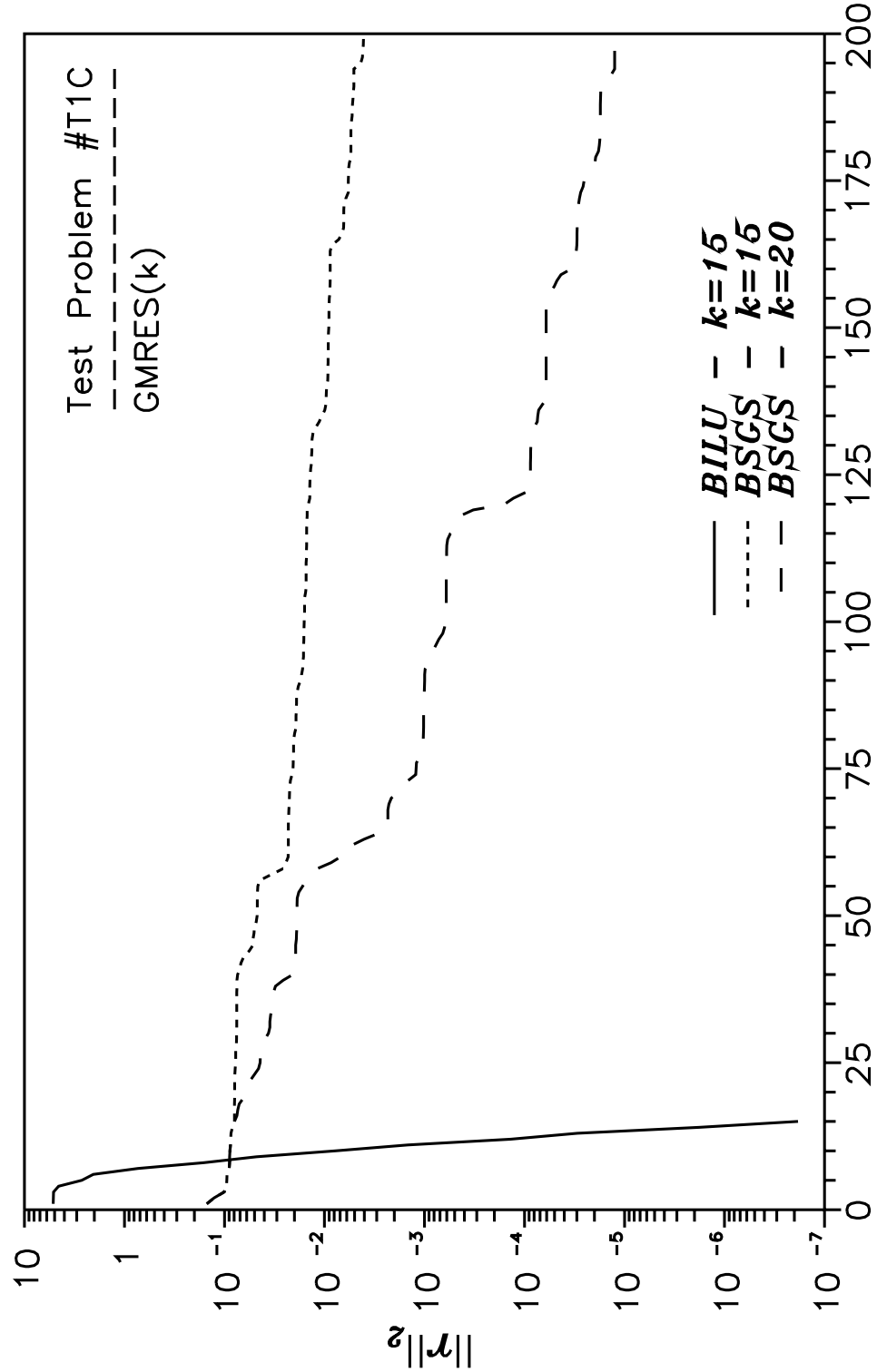

Fig. 3.30 – Comparison of BILU and BSGS preconditioners.

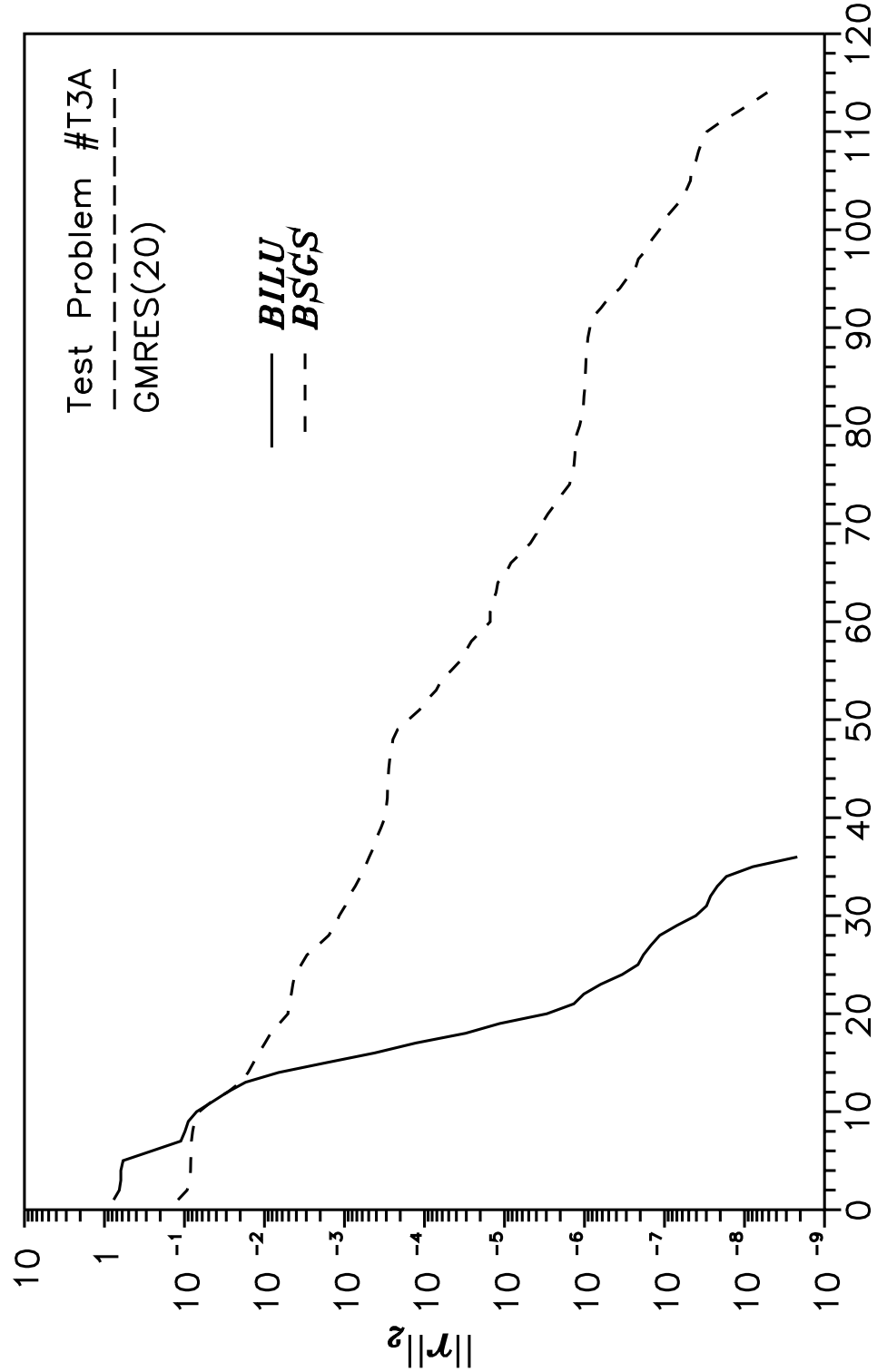

Fig. 3.31 – Comparison of BILU and BSGS preconditioners.

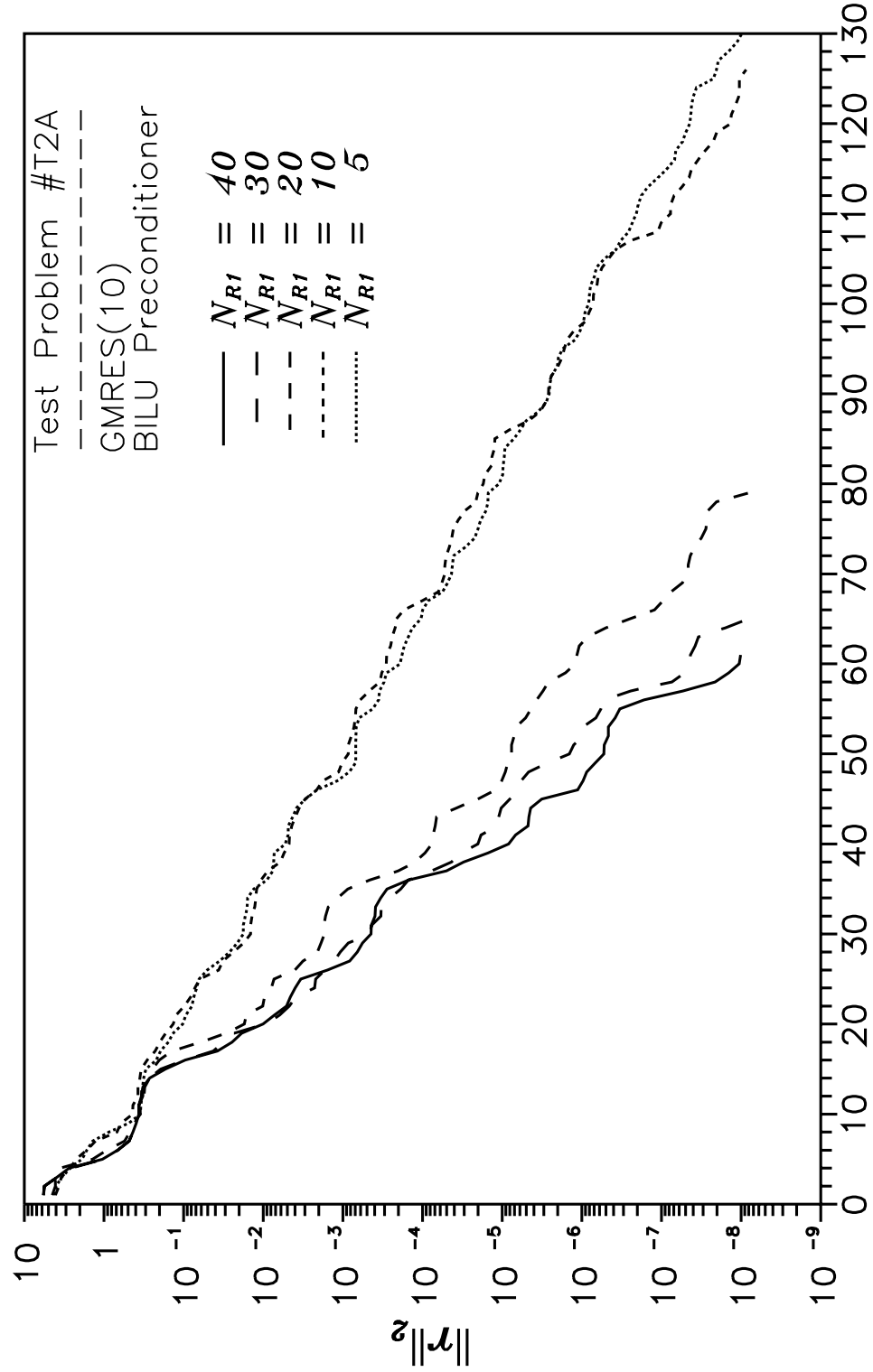

Fig. 3.32 — Effect of domain decomposition reordering.

Table 3.5

Spectral Condition Numbers of Standard BILU

Preconditioned Domain Decomposition Reordered Matrices

Test Problem	N_{R1}	$\kappa(Q^{-1}A)$
T1B	10*	1.05×10^{13}
	10**	2.45×10^{9}
	7	2.48×10^{9}
	5	2.11×10^{9}
	2	2.62×10^{9}
T1C	10*	3.34×10^{9}
	10**	3.20×10^{5}
	7	2.96×10^{5}
	5	3.66×10^{5}
	2	2.08×10^{5}
T2A	40*	1.44×10^{10}
	40**	5.13×10^{5}
	30	5.20×10^{5}
	20	1.84×10^{6}
	10	2.23×10^{6}
	5	2.23×10^{6}

* $Q = I$; ** Natural Ordering

A_{33} itself and Meurant's[91,92] simplified preconditioner (Eq. 2.4.118), hereto referred to as M_{M2}. Results are shown in Figs. 3.33–3.35 for test problems T1A, T1C and T2A, respectively. Method GMRES(k) with $k = 15$ and BILU preconditioning for the subdomains were used in each case.

The results clearly show Meurant's preconditioner performs the best for each of the test problems, with little difference between the other three Schur complement preconditioners. Indeed, the BILU approximation to A_{33} and the matrix A_{33} itself produce identical results. This should have been expected since the matrix A_{33} is block tridiagonal and the block-incomplete-LU decomposition BILU produces an exact decomposition of A_{33}.

Only for test problem T2A (Fig. 3.35) did the use of Meurant's preconditioner improve the convergence rate enough to offset the cost of using domain decomposition as the overall preconditioner. Note, this is true only for the case of where we compare to the solution obtained using standard BILU preconditioned GMRES(15). If we go back to Table 3.4, we see that BILU preconditioned GMRES(20) is still substantially faster as far as the total CPU time required. Table 3.6 lists the total iterations and CPU time required for each of these test problems and for each of the Schur complement preconditioners, along with the total iterations and CPU time required by the standard BILU preconditioned system solved using GMRES(15).

3.3.6 Effect of Boundary Γ_3 Location

The effect of the domain boundary Γ_3 location was investigated using test problems T3A–T3F. GMRES(k) with $k = 50$ was used for all problems. Additionally, BILU preconditioning for the subdomain solves and M_{M2} preconditioning for the Schur complement were used for all problems.

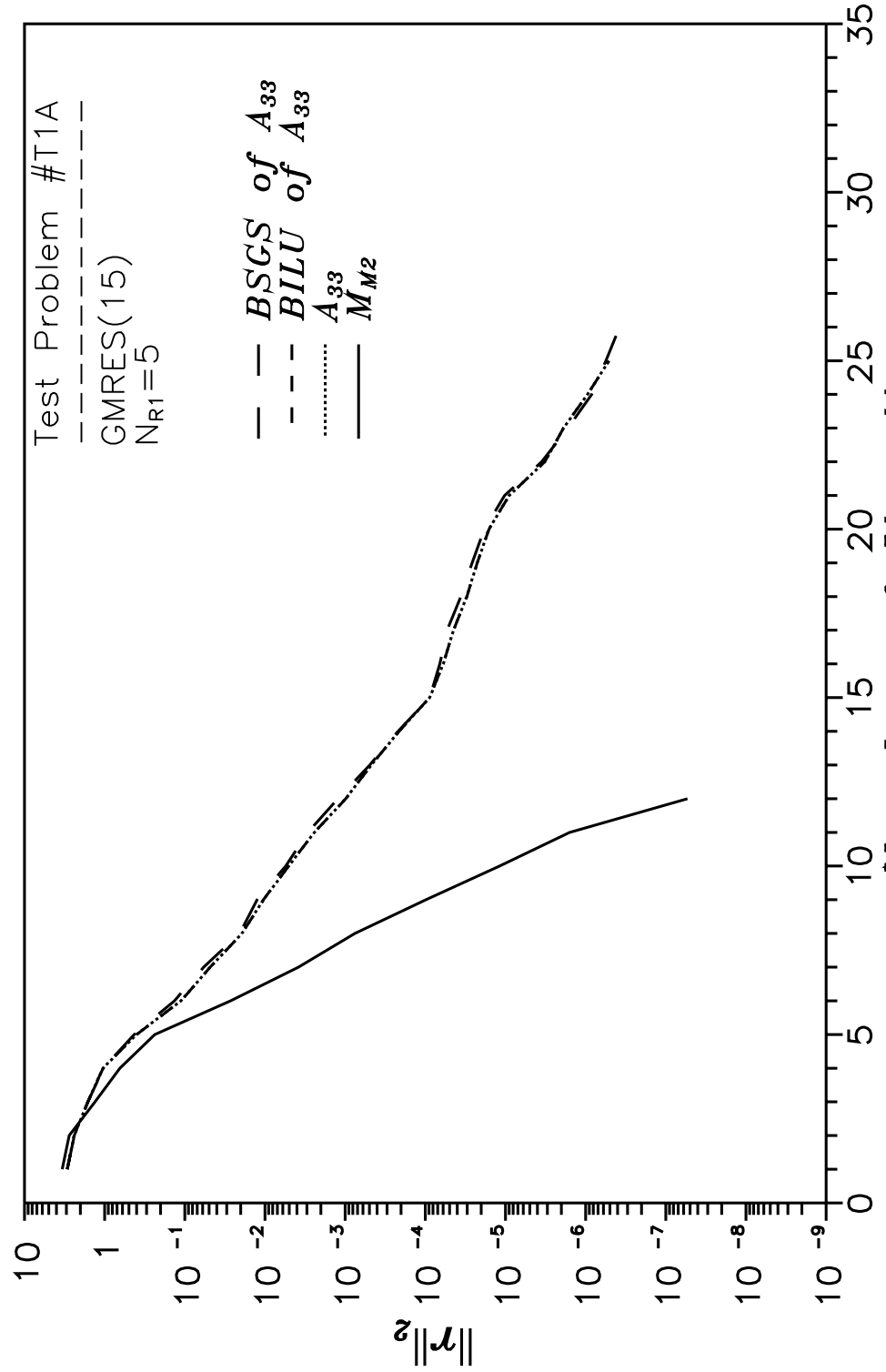

Fig. 3.33 – Comparison of Schur complement preconditioners.

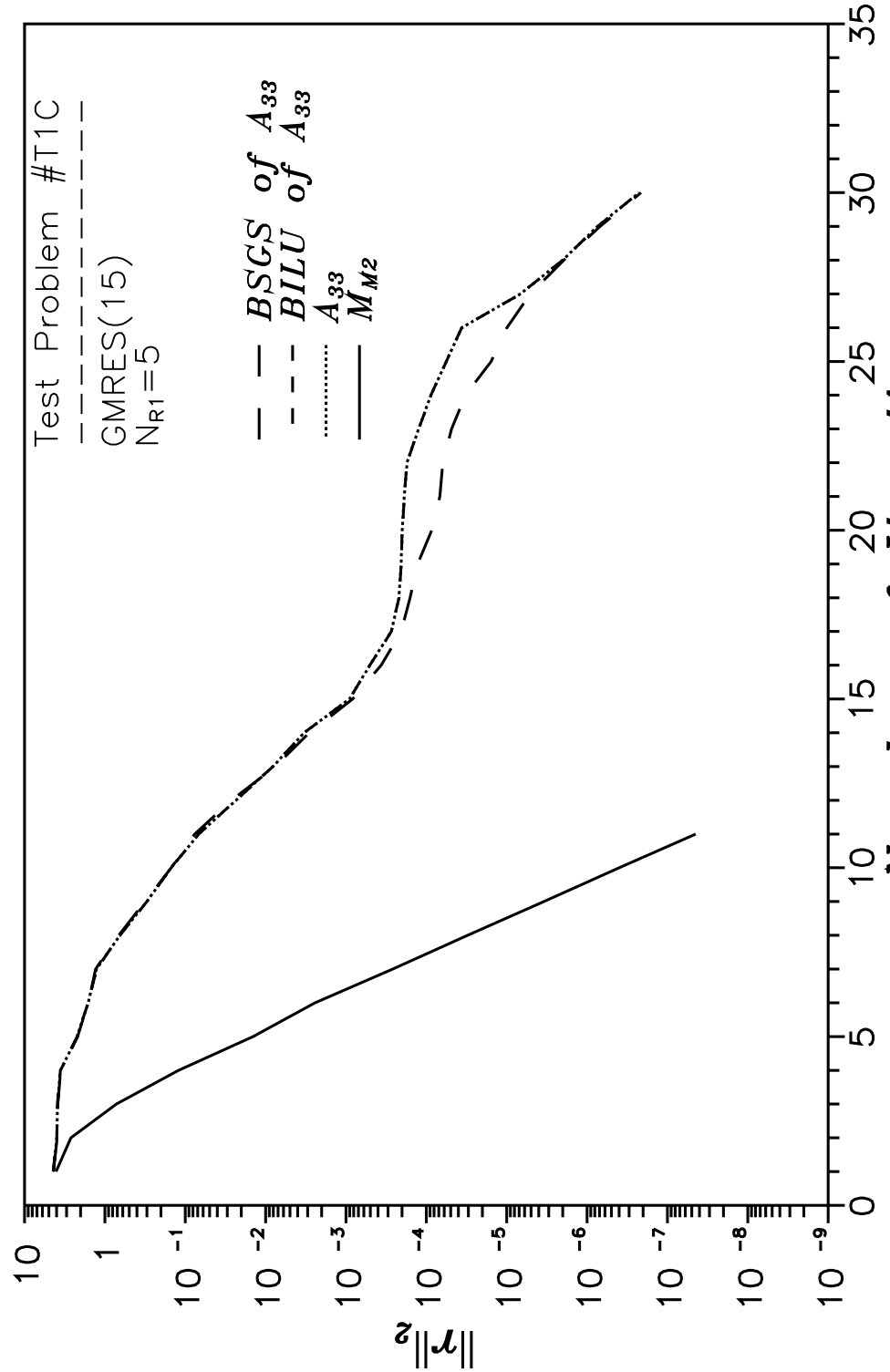

Fig. 3.34 – Comparison of Schur complement preconditioners.

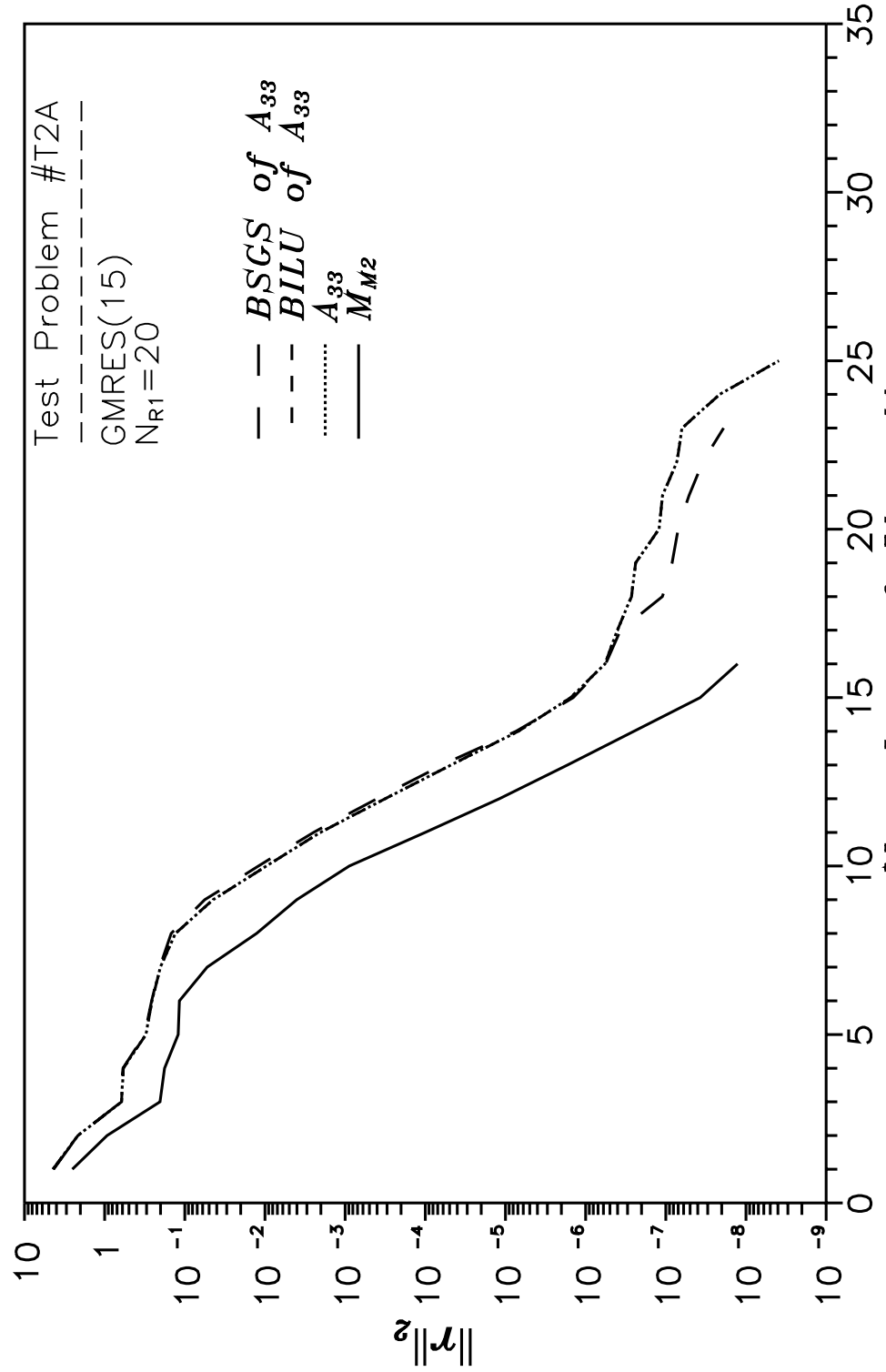

Fig. 3.35 – Comparison of Schur complement preconditioners.

Table 3.6

CPU Timings for Domain Decomposition

Preconditioned Systems T1A, T1C and T2A

Test Problem	Domain Decomp. Used ?	Schur Complement Preconditioner	Iterations	CPU Time (seconds)
T1A	no	BILU	15	0.463
T1A	yes	BSGS	26	1.053
T1A	yes	BILU	25	1.021
T1A	yes	A_{33}	25	1.073
T1A	yes	M_{M2}	12	0.542
T1C	no	BILU	15	0.420
T1C	yes	BSGS	30	1.114
T1C	yes	BILU	30	1.119
T1C	yes	A_{33}	30	1.168
T1C	yes	M_{M2}	11	0.473
T2A	no	BILU	24	1.042
T2A	yes	BSGS	23	1.357
T2A	yes	BILU	25	1.459
T2A	yes	A_{33}	25	1.459
T2A	yes	M_{M2}	16	1.013

Test problems T3A–T3F represent matrices generated at increasing times in the producing life of the reservoir. As the reservoir is produced, more and more of the reservoir falls below the bubble point pressure, giving rise to more and more free gas. Figure 3.36 shows the discrete free gas distribution for each of the test problems T3A–T3F. Each of the marks in the figure represents a discrete grid block, with the O's representing a grid block containing only undersaturated oil and the lower case g's representing grid blocks containing both saturated oil and free gas.

Figures 3.37–3.39 are plots of the l_2-norm of the preconditioned residual versus the number of iterations for a variety of boundary Γ_3 locations ($N_{R1}+1$) for each the test problems T3A, T3C and T3E, respectively. Note that the curves for $N_{R1}=25$ represent the solution to the problem using the iterative method with standard BILU preconditioning and not domain decomposition. Though a little difficult to analyze, Figs. 3.38–3.40 indicate there are several partitionings of the reservoir domain in each case for which the convergence rate of the domain decomposition preconditioned system was better than that for the BILU preconditioned system. Results for the test problems T3B, T3D and T3F were similar in nature. These figures show a boundary location of $N_{R1}+1=15$ resulted in the fewest iterations for each of the test problems (also for problems T3B, T3D and T3F). On average, the domain decomposition preconditioned systems required 8 percent fewer iterations than the BILU preconditioned method for this boundary location. Even with this improvement in the convergence rate, however, the CPU time required to solve the system increases an average of 35.9 percent over that required by the BILU preconditioned methods.

In an attempt to better isolate the effect of the boundary Γ_3 location, the number of iterations required for convergences versus the number of radial grids, N_{R1}, in domain Ω_1 were plotted for each of the test problems. Figures

Fig. 3.36 - Discrete phase distribution for test problems T3A–T3f.

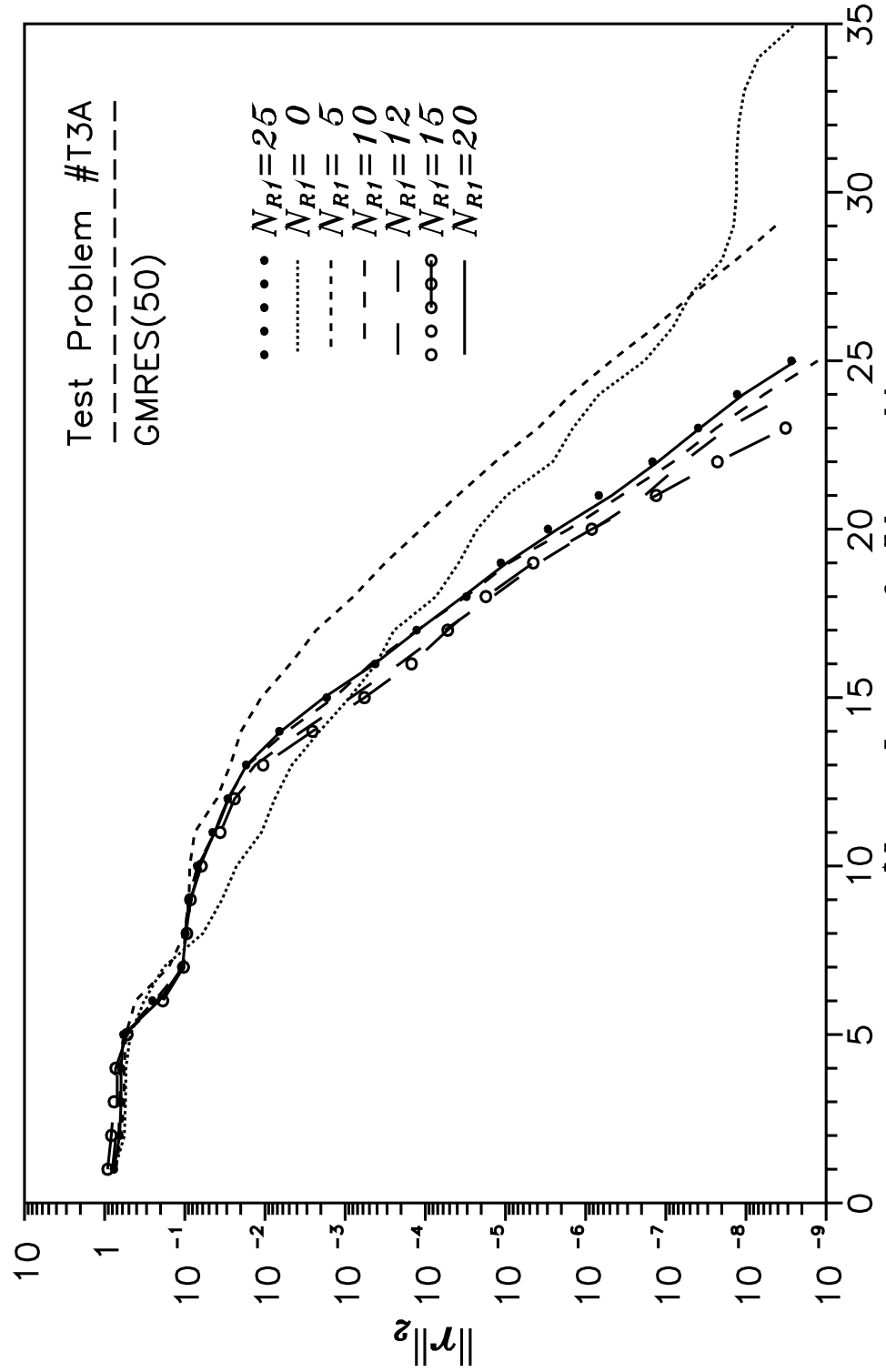

Fig. 3.37 – Effect of boundary location, $N_{R1}+1$, (Problem T3A).

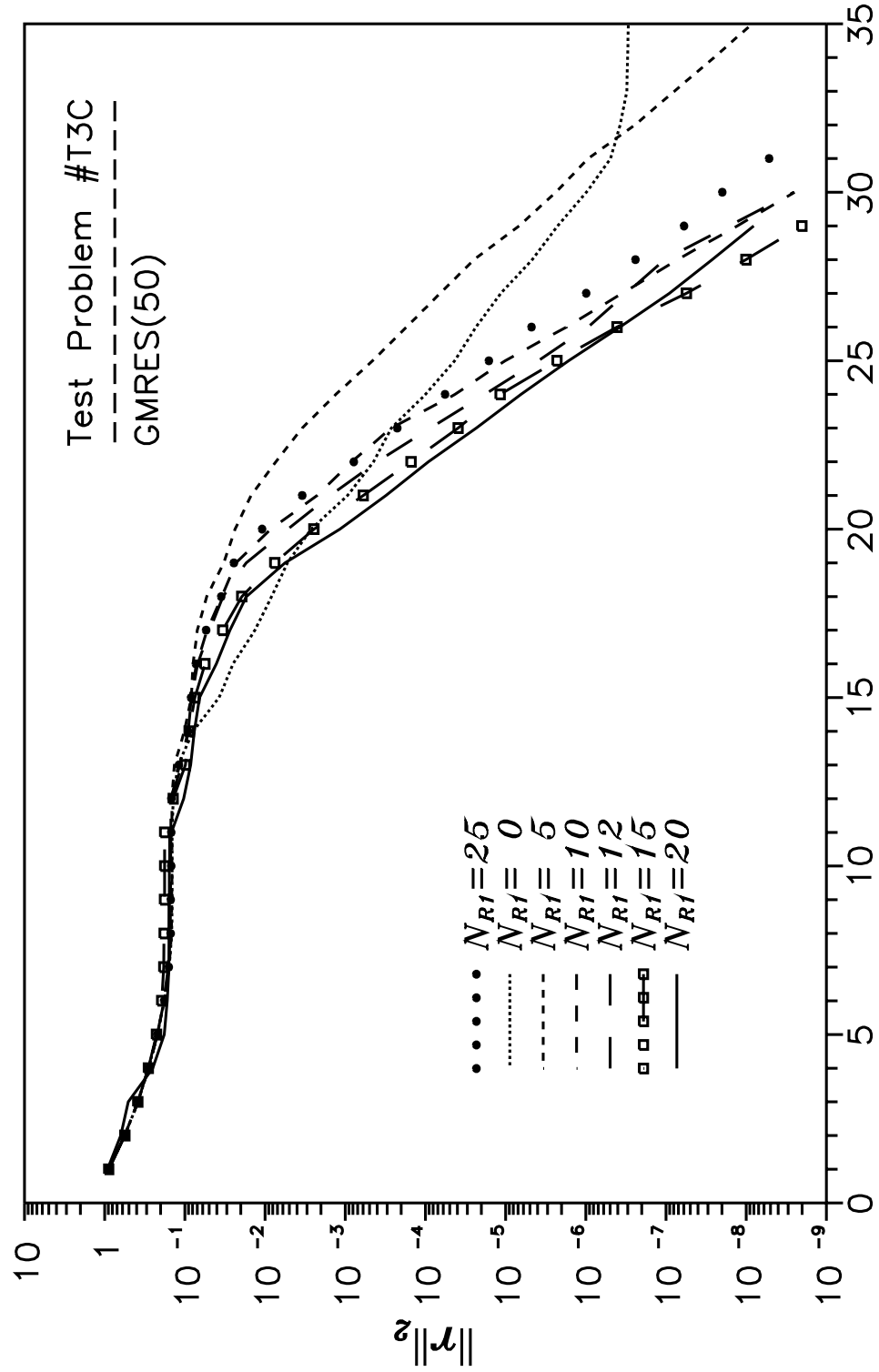

Fig. 3.38 – Effect of boundary location, $N_{R1}+1$, (Problem T3C).

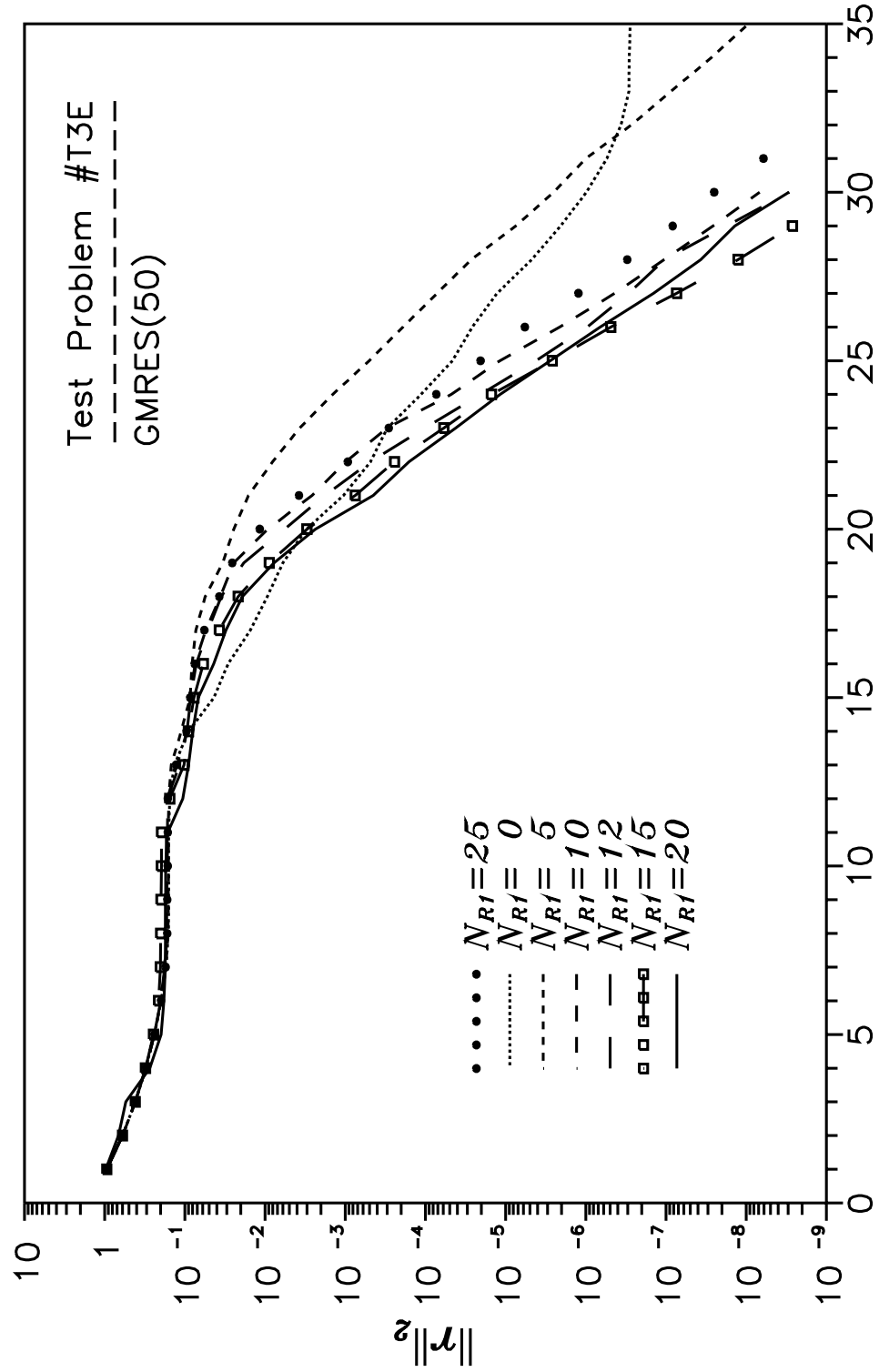

Fig. 3.39 – Effect of boundary location, $N_{R1}+1$, (Problem T3E).

3.40–3.42 are such plots for test problems T3B, T3D and T3F, respectively. All of these plots show a minimum in the required number of iterations when the domain boundary is located near the 15^{th} grid block. Referring to Fig. 3.36, no trend or correlation between this location of the domain boundary and the regions of single and multiple phases is apparent. Whether the failure to see a trend in the results or obtain a correlation was due to the physical nature of the test problem, not fully isolating the multiphase regions in one subdomain, or some other reason is still unclear. We do note, however, that due to the radial nature of the test problems considered in this study, by dividing the reservoir equally by the number of grid blocks, the aspect ratio of the largest to smallest gridblock in each subdomain will be approximately equal, at least within an order of magnitude. Note for test problem T1A with 10 radial grids, the minimum number of iterations occurred when the domain boundary was located at the sixth radial grid and for test problem T2A, the minimum number of iterations occurred when the domain boundary was located at the 17^{th} radial grid block.

From a parallel programming point of view, we note that a symmetric decomposition of the domain is preferred from the standpoint of equalizing the work load of each processor, and it is all the better if that decomposition results in the most efficient solution as related to the global convergence rate of the iterative method. Based on the numerical results reported above, suppose that 60 percent of the CPU time is spent on the subdomain 1 solves and 40 percent on the subdomain 2 solves (the actual ratio of the two is approximately this) and let the CPU time required for the sequential solution using BILU preconditioning be 1.0 seconds. The CPU time required by the domain decomposition preconditioned method on two parallel processors would then be 60 percent of 1.359 seconds, or 0.8 seconds. The theoretical speedup, S_P on two processors would then be 1.25; i.e.,

$$S_P = \frac{T_1}{T_P} = \frac{1.0}{0.8} = 1.25 \ , \tag{3.3.2}$$

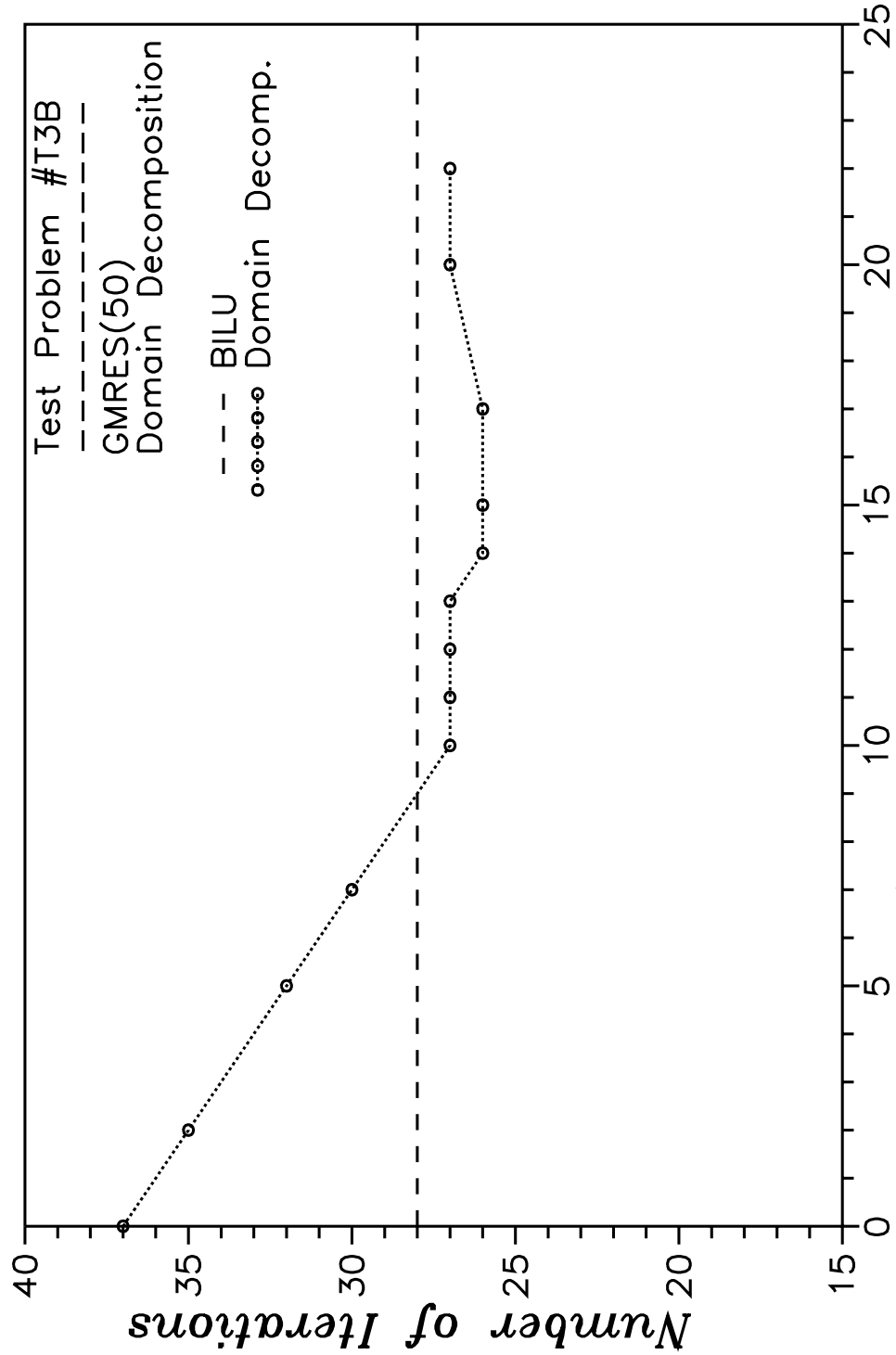

Fig. 3.40 — Effect of boundary location, $N_{R1}+1$, (Problem T3B).

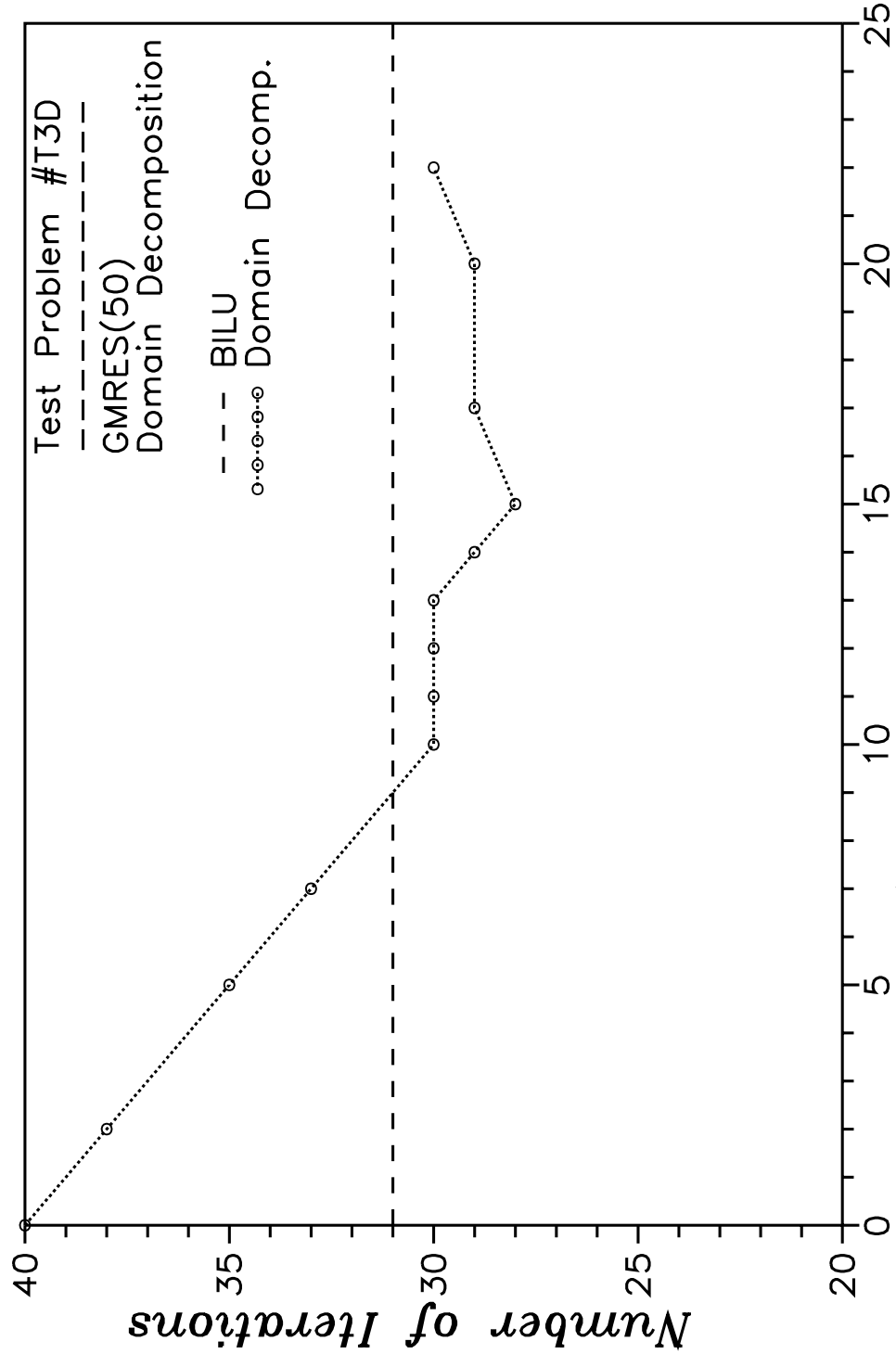

Fig. 3.41 — Effect of boundary location, $N_{R1}+1$, (Problem T3D).

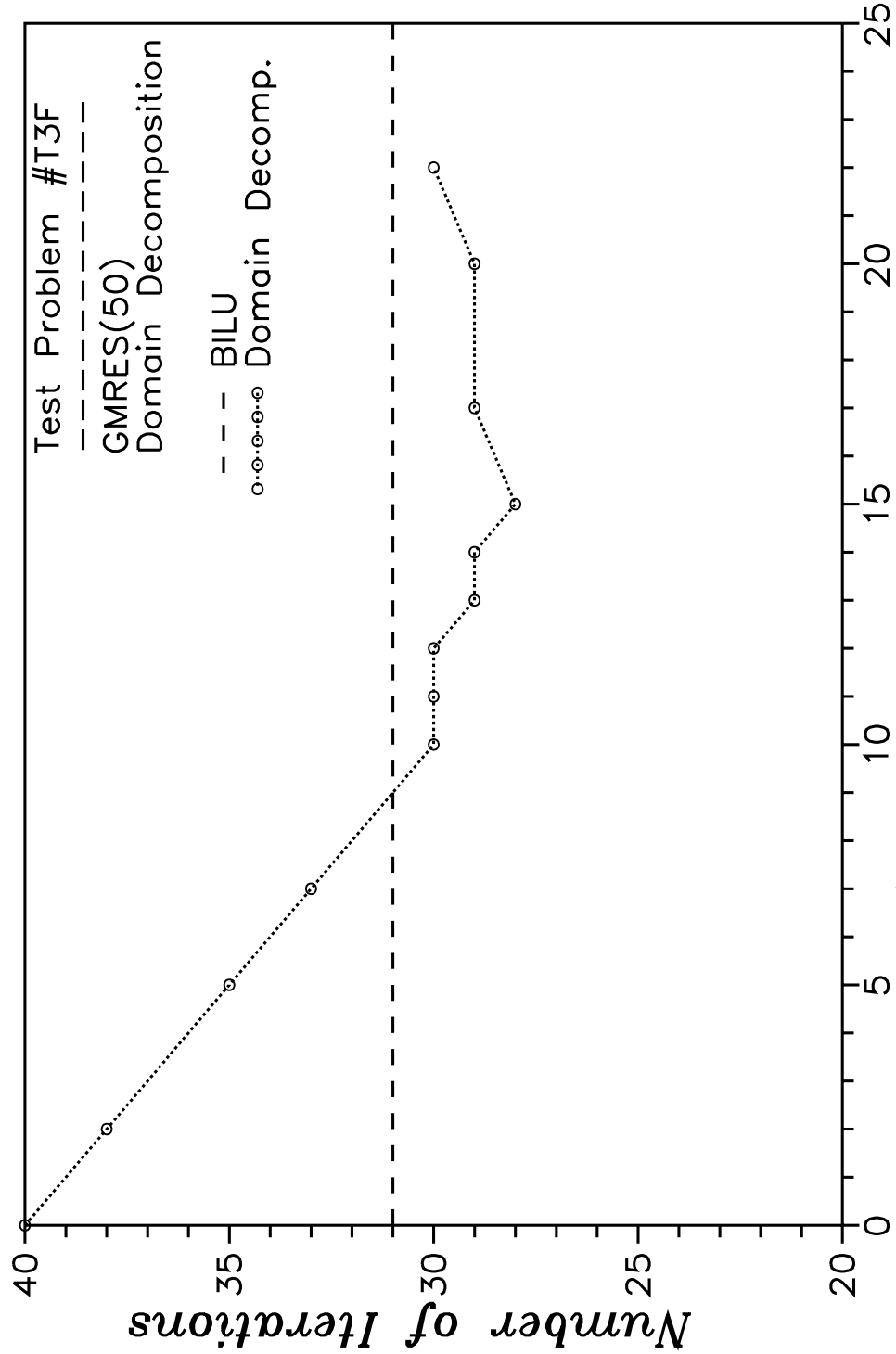

Fig. 3.42 – Effect of boundary location, $N_{R1}+1$, (Problem T3F).

where T_1 is the time required for the best sequential algorithm on a single processor and T_P the time required for the parallel algorithm on P processors. Furthermore, the efficiency can be calculated to be $E_P = 0.625$, where the efficiency is defined as

$$E_P = \frac{S_P}{P} \ . \tag{3.3.3}$$

The theoretical cost of the parallel computations is

$$C_P = T_P \cdot P \ , \tag{3.3.4}$$

or, $C_P = 1.6$, and the effectiveness, defined as

$$F_P = \frac{S_P}{C_P} \ , \tag{3.3.5}$$

is $F_P = 0.78$.

3.4 Summary

Results obtained from the three-phase fully-implicit coning simulator developed as part of this work have been compared to results obtained from various analytical solutions[108], published data[23,24,111] and and other numerical simulators, both research[16,18–20,109] and commercial[110], for a variety of one-dimensional and two-dimensional single-phase, two-phase (oil-gas and oil-water) and three-phase reservoir systems. In all cases, there was an excellent match (comparison) between the results obtained from these other sources and the simulator developed in this work.

In addition to a sparse direct solver[93], three conjugate gradient-type iterative methods, GMRES(k)[49–51], Orthomin(k)[48] and Bi-CGSTAB[52] (and it's variant Bi-CGSTAB-P[52]), for the solution of nonsymmetric systems of linear

equations have been fully implemented in our simulator. Preconditioning options for the iterative methods include block-symmetric-Gauss-Seidel incomplete factorization (BSGS), block-incomplete-LU decomposition (BILU), and a domain decomposition preconditioner (partition matrix method) based on the Bramble et al.[90] preconditioner. Additionally, for the domain decomposition overall preconditioner, options are included for using either BSGS or BILU preconditioning for the subdomains and one of four (BSGS of A_{33}, BILU of A_{33}, A_{33} and M_{M2}[45,46]) preconditioners for the Schur complement.

Ten representative matrices were generated for three test problems which were used to investigate various aspects of the iterative methods and preconditioners. The primary results of this investigation are as follows:

(i) For type of problem and typical size of problem considered in this work, the preconditioned conjugate gradient-type iterative methods incorporated in our simulator are between 1.5 and 2.4 orders of magnitude faster than the direct solution method incorporated in our simulator.

(ii) Without preconditioning and with full orthogonalization, method GMRES appears to be a more robust iterative method than Orthomin, Bi-CGSTAB or Bi-CGSTAB-P for the nonsymmetric linear systems investigated; i.e., GMRES converges, whereas Orthomin, Bi-CGSTAB and Bi-CGSTAB-P do not.

(iii) The effect of the number of orthogonalizations used is much greater for GMRES(k) than for Orthomin(k); i.e., as k is increased, the convergence rate for GMRES(k) improves more significantly than for Orthomin(k). This may be due in part to the restarting of the iterative process for GMRES(k).

(iv) For the test problems considered, Orthomin(k) required preconditioning and greater than five orthogonalizations to converge.

(v) Based purely on the convergence rate (number of iterations), preconditioned methods Bi-CGSTAB and Bi-CGSTAB-P slightly outperformed methods GMRES(k) and Orthomin(k).

(vi) Based on computational efficiency (CPU time), method GMRES(k) significantly outperforms methods Orthomin(k) and Bi-CGSTAB-P, and almost doubles the performance of method Bi-CGSTAB.

(vii) For the problems considered in this work, the BILU preconditioner greatly outperformed the BSGS preconditioner; i.e., resulted in a much improved convergence rate (reduced number of iterations) for the iterative method. It is interesting to note that this occurs even though the $l_2\text{–}norm$ of the preconditioned residual is always less for the first few iterations for the BSGS preconditioned system.

(viii) The effect of domain decomposition grid ordering on standard BILU preconditioned iterative methods is to decrease the convergence rate (increase the number of iterations).

(ix) Four preconditioners for the Schur complement have been examined in conjunction with the use of a domain decomposition technique as the overall preconditioner and include the BSGS approximation to A_{33}, the BILU approximation to A_{33}, the matrix A_{33} itself and Meurant's[91,92] simplified preconditioner, M_{M2}. Results clearly show Meurant's preconditioner performs the best for each of the test problems considered, with little difference between the other three Schur complement preconditioners.

(x) Though certain partitionings of the reservoir domain resulted in the domain decomposition preconditioned iterative method requiring less iterations that the BILU preconditioned iterative method, this partitioning

could not be determined *a priori*. Even with the improved convergence rate, the domain decomposition method considered was computationally more expensive (required more CPU time) than the BILU preconditioned method.

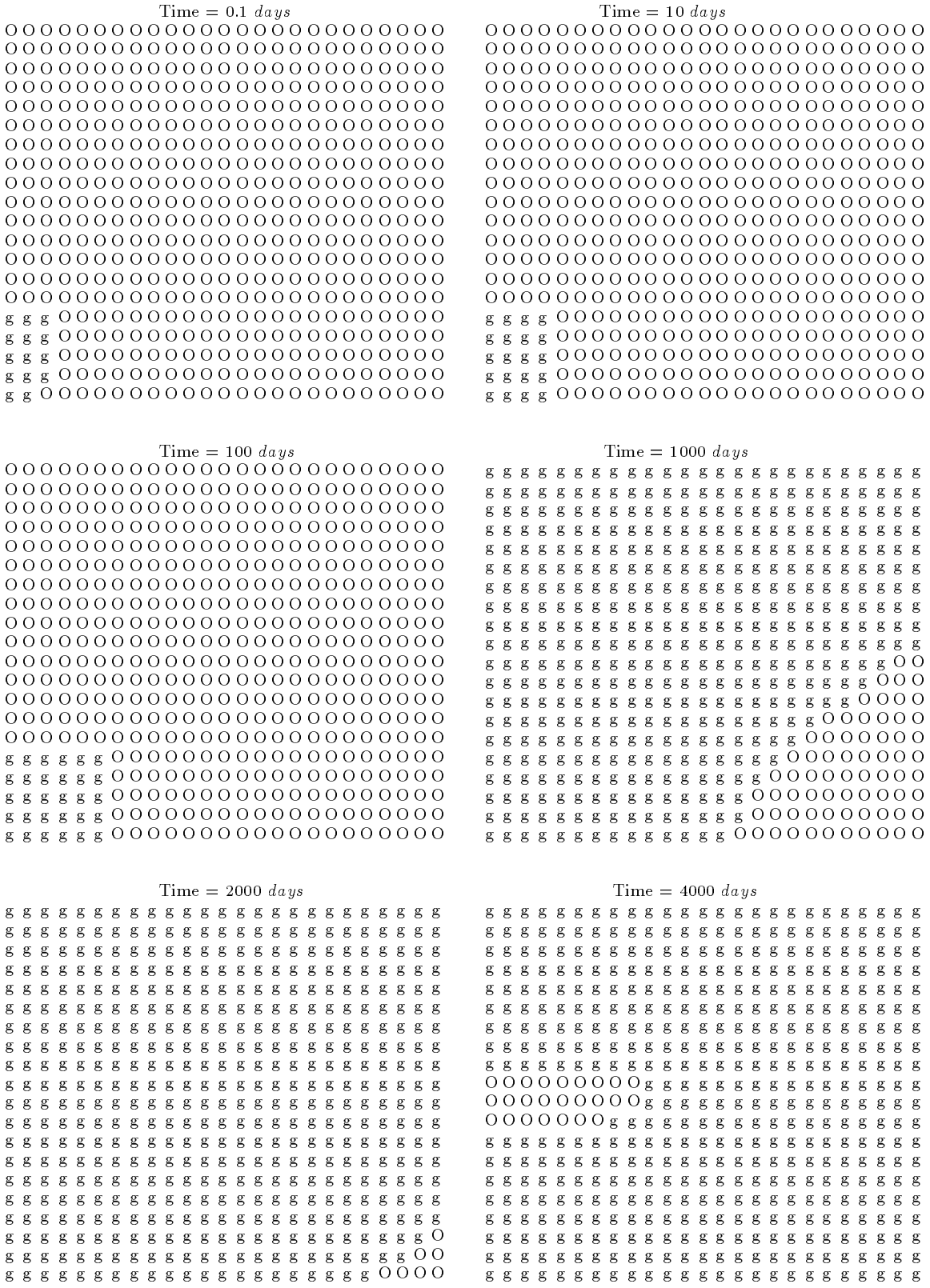

Fig. 3.36 - Discrete phase distribution for test problems T3A–T3F.

CHAPTER IV
RESERVOIR SYSTEMS INVESTIGATED AND THEORETICAL BACKGROUND INFORMATION

In this chapter, we present the reservoir and fluid descriptions for all of the cases investigated in this study. In addition, the physical and theoretical background information used to form the basis of our interpretation and analysis of the pressure data obtained for each of the simulated well tests for these cases is presented and discussed.

4.1 Multiphase Reservoir Systems Investigated

Figures 4.1-4.5 show vertical cross-sections of the reservoir with the lower and upper boundaries and fluid saturations indicated for each of the two-dimensional (r–z) oil reservoir - aquifer systems (cases OW-**), gas reservoir - aquifer systems (cases GW-**), oil reservoir - gas cap systems (cases OG-**), water reservoir - gas cap systems (cases WG-**), and oil reservoir - gas cap - aquifer systems (cases OGW**), respectively, considered in this study. The "**" in the case designations above refer to a number-letter (e.g., 3B) or letter-letter (e.g., AB) combination indicating the location of the lower boundary for reservoir systems containing an aquifer or the location of the upper boundary for reservoir systems containing a gas cap. Fig. 4.1, for example, shows that the lower boundary for case OW-3B is 40 ft below the top of the reservoir and that 40 ft has an initial water saturation of $S_w = 0.2$. Case OW-7B, on the other hand, has the lower boundary located 300 ft below the top of the reservoir, with the top 40 ft of the

reservoir having an initial water saturation of $S_w = 0.2$ and the lower 260 ft having an initial water saturation of $S_w = 1.0$. For cases "OGW-**" (Fig. 4.5), the first "*" is a letter indicating the location of the lower boundary and the second "*" the location of the upper boundary; e.g., case OGW-BC represents a 70 ft oil zone underlain by a 20 ft aquifer and overlain by a 30 ft gas cap.

Throughout this work, a case designation ending with "S3" (e.g., OG-3BS3) indicates a mechanical skin factor of $s = 5$ was incorporated into the simulation for that reservoir system and a case designation ending with "S4" (e.g., OGWABS4) indicates a mechanical skin factor of $s = 10$ was modeled in the simulation for that reservoir. These cases are discussed in Chapter VII where methods for estimating the pseudoskin factor due to restricted-entry and the mechanical skin factor in multiphase reservoirs are presented and discussed.

Unless otherwise stated, all reservoir systems have no-flow lower, upper and outer boundaries. Reservoir systems being modeled with a constant pressure lower, upper or outer boundary generally will have a case designation ending in an "X", "Y" or "Z". These cases are discussed in detail in Chapter VI.

Base case parameters (e.g., absolute permeability, porosity, etc.) for each of these reservoir systems and the deviations from the base case parameters for each reservoir system are listed in Tables 4.1-4.5. The two-phase relative permeability curves used for are shown in Figs. 4.6 and 4.7. For cases OGW**, the three-phase oil relative permeability is approximated using Stone's[41] second method. The correlations of Ref. 113 were used to generate solution gas-oil ratios and oil formation volume factors (Fig. 4.8), the correlations of Refs. 114 and 115 were used to generate oil viscosities (Fig. 4.9), the correlation of Ref. 116 was used to generate gas compressibility factors which were converted to gas formation volume factors (Fig. 4.10) and the correlation of Ref. 117 was used to generate gas

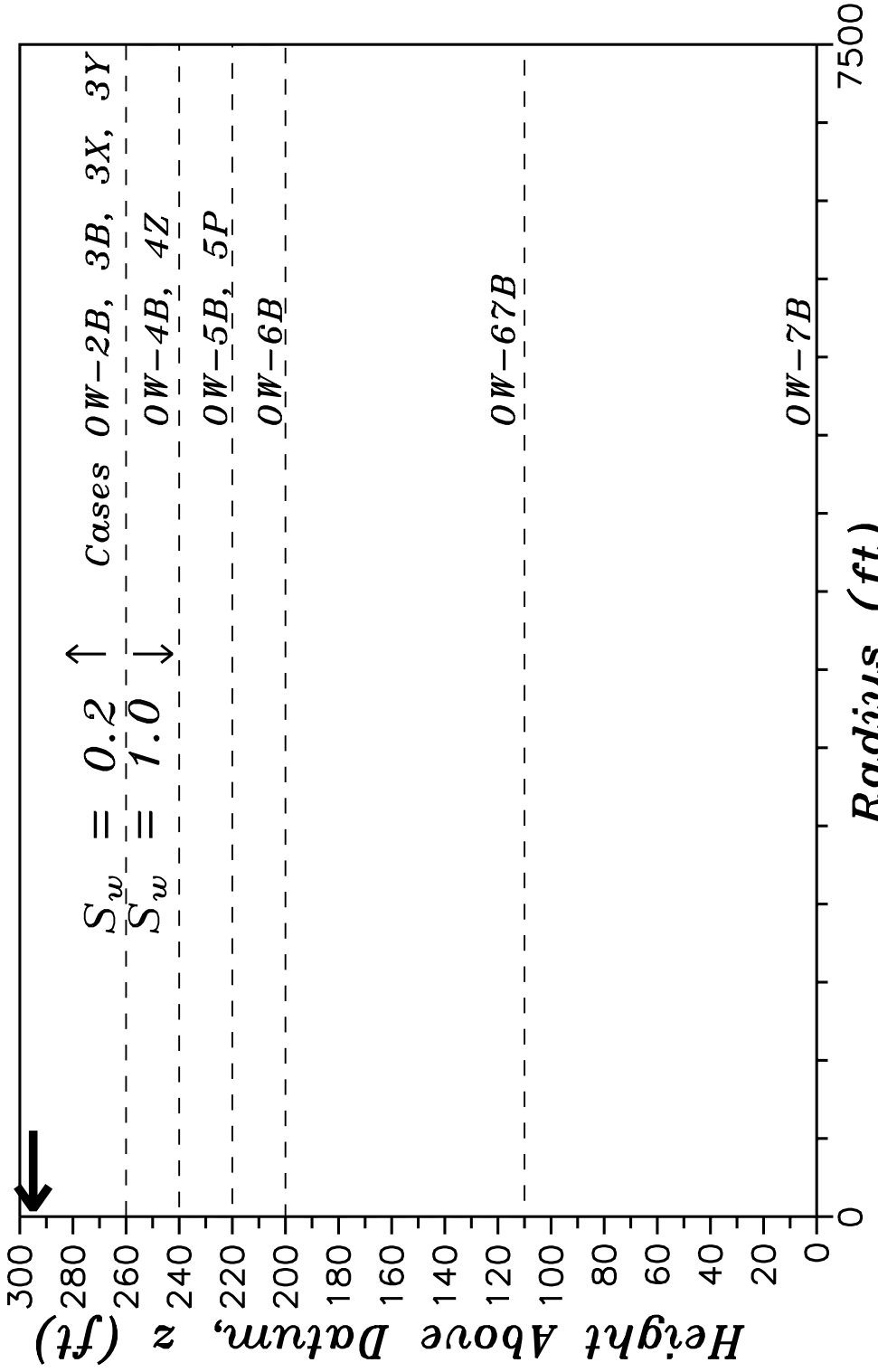

Fig. 4.1 – Boundary location and saturation profile for oil–water systems.

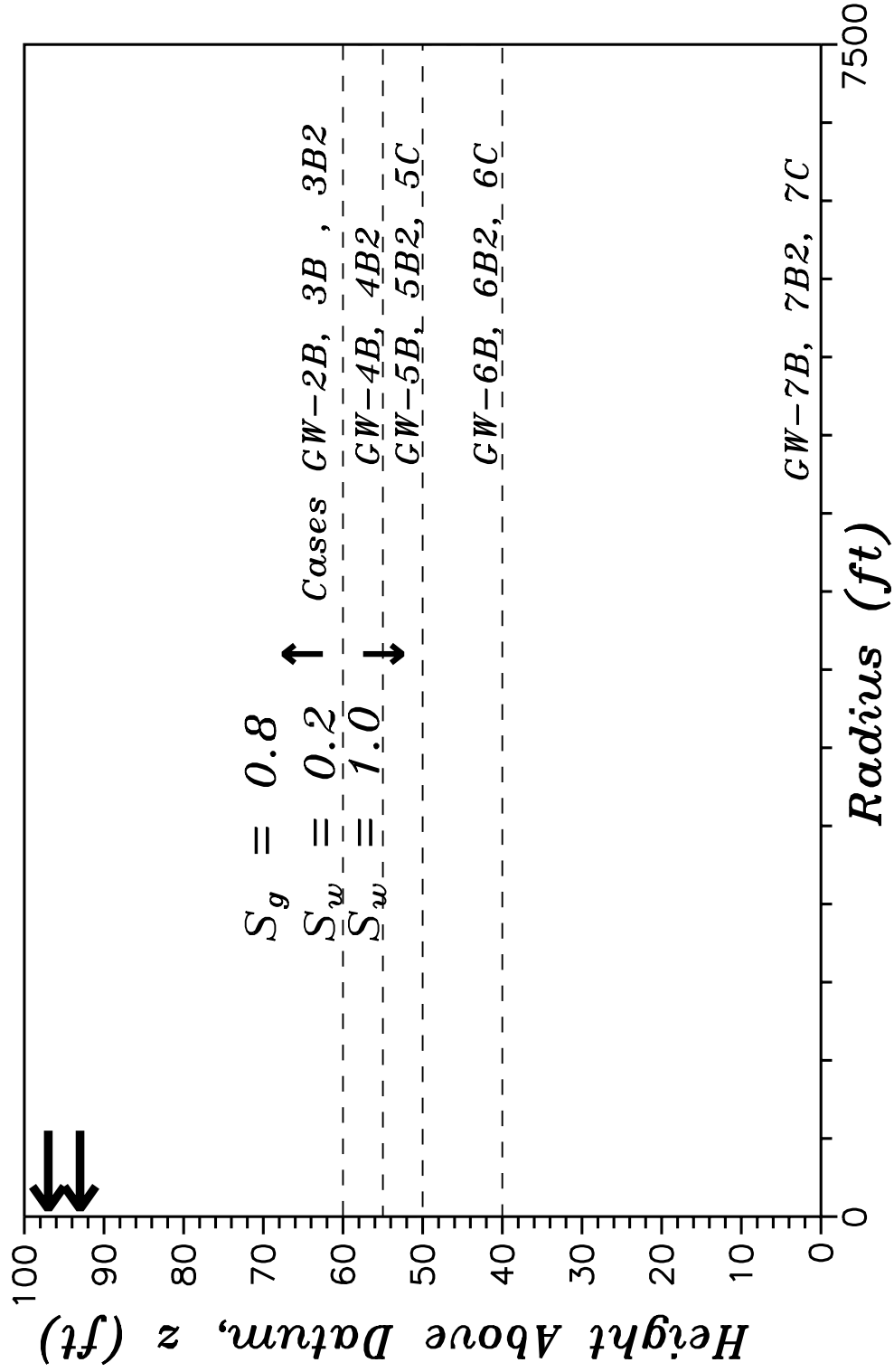

Fig. 4.2 – Boundary location and saturation profile for gas–water systems.

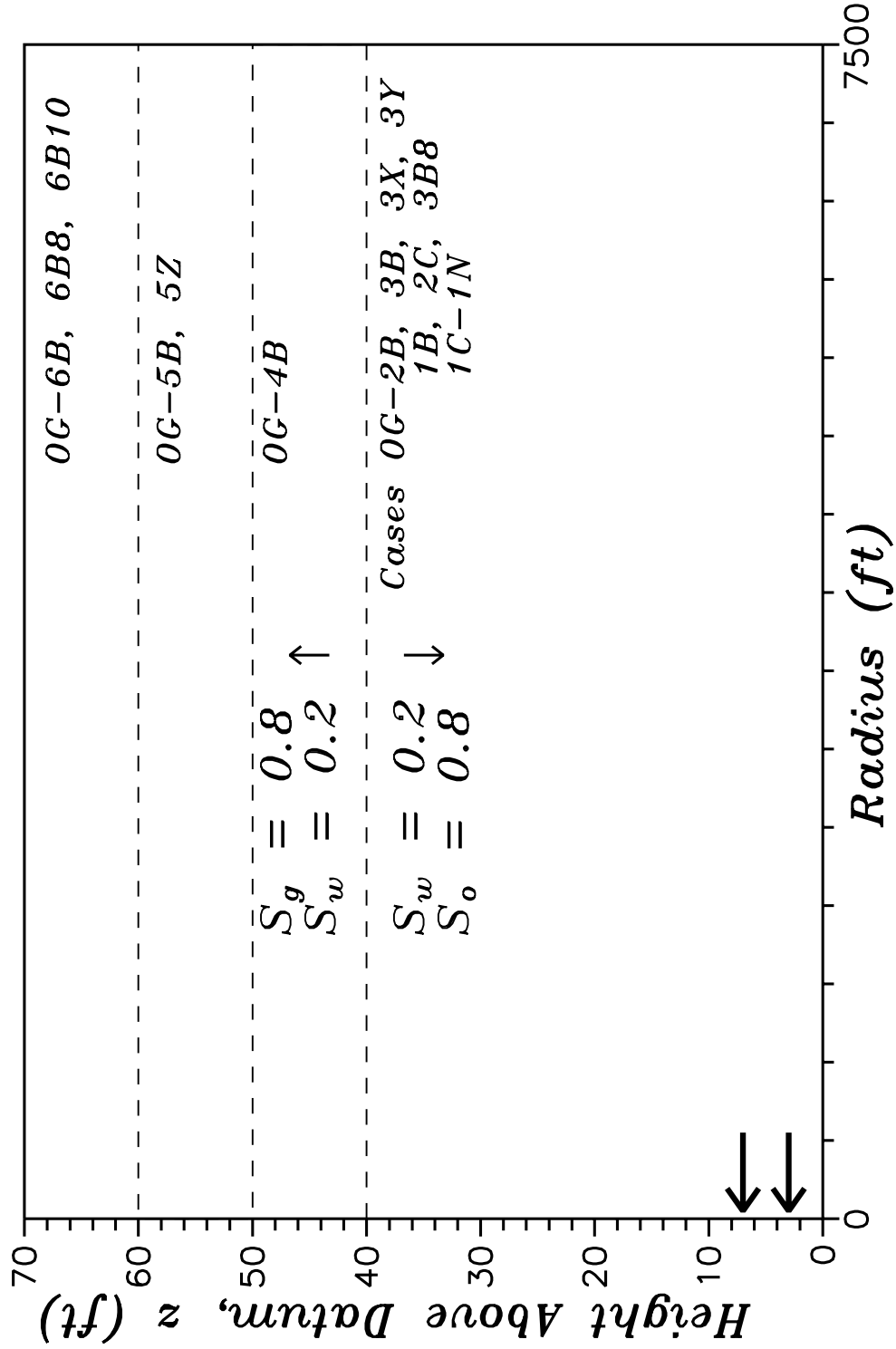

Fig. 4.3 – Boundary location and saturation profile for oil–gas systems.

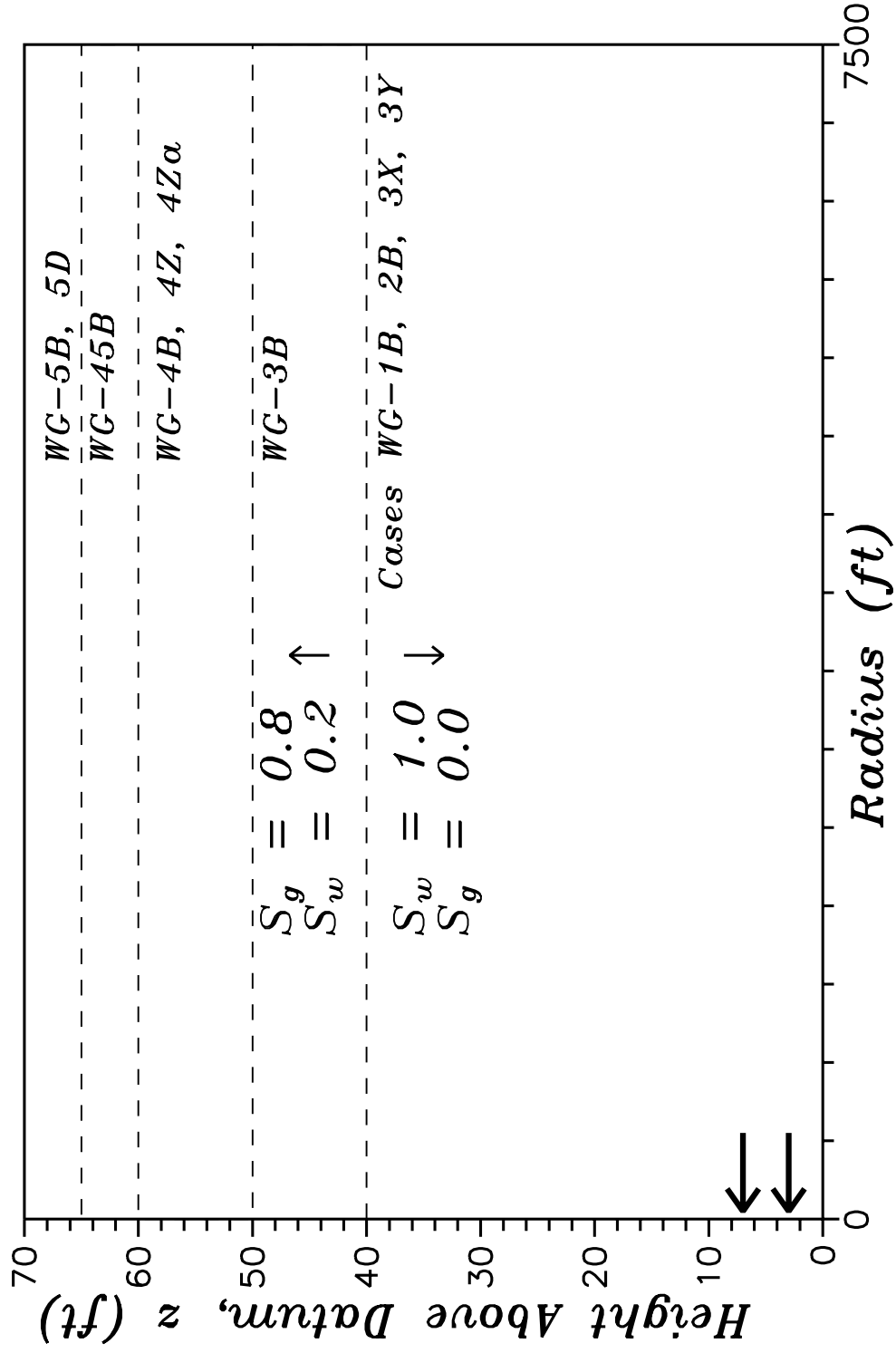

Fig. 4.4 – Boundary location and saturation profile for water–gas systems.

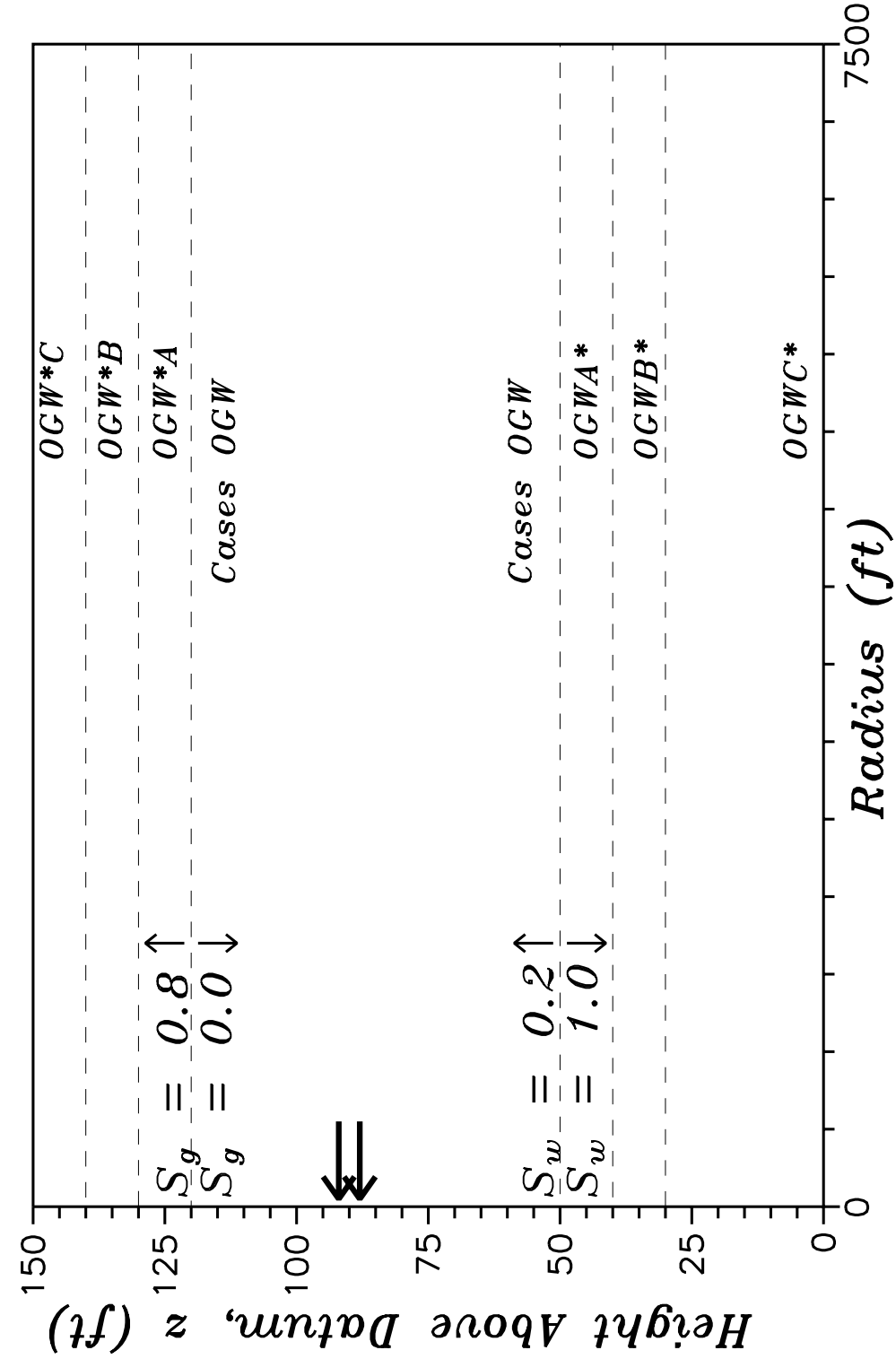

Fig. 4.5 – Boundary locations and saturation profile for oil–gas–water systems.

viscosities (Fig. 4.11). For the oil-water cases OW-**, and only those cases, the oil phase is considered to be a slightly compressible fluid of constant compressibility and constant viscosity. For all of the cases in which the water saturation is greater than residual, the water phase is considered to be a slightly compressible fluid of constant compressibility and constant viscosity.

For each of the reservoir systems described above, the three-phase fully-implicit coning simulator developed as part of this work was used to simulate a 10 (day) drawdown test, followed by a 10 (day) buildup test. A buildup test of this duration is of course not practical, but the length of the test allows us to investigate fully the buildup response. Methods for the analysis of pressure buildup data are presented and discussed in Chapter VII. The radial extent of each reservoir system modeled was made large enough to insure that all results pertain to the infinite-acting period; i.e., wellbore pressures were not affected by the no-flow outer boundary. Whenever we refer to the "true" or "actual" values of a parameter, we are refering to values of that parameter obtained directly from the simulator. Though over two hundred single and multiphase examples are considered in this study, only a few representative cases are discussed in detail.

4.2 Background Information

Many of the methods for analyzing pressure transient data obtained under multiphase flow conditions are based on the modifications to the single phase flow problem suggested by Perrine[29] and later justified by Martin[30]. The primary contribution of their work was the suggestion that total and individual phase mobilities could be determined if the appropriate flow rates were known, e.g., they suggested that the total mobility could be estimated as

$$\lambda_t = \frac{162.6 q_t}{mh} \ , \tag{4.2.1}$$

Table 4.1A

Base Case Parameters

Oil Reservoir - Aquifer Systems (Cases OW-)**

$\phi = 0.2$	$k = 50\ (md)$	$k_z/k = 0.1$
$r_e = 7500\ (ft)$	$r_w = 0.25\ (ft)$	$h_w = 40\ (ft)$
$h = 40\ (ft)$	$q_t = 200\ (STB/D)$	$t_p = 10\ (days)$
$\mu_w = 0.8\ (cp)$	$c_w = 3 \times 10^{-6}\ (psi^{-1})$	
$\mu_o = 1.0\ (cp)$	$c_o = 10^{-5}\ (psi^{-1})$	
$p_i = 3600\ (psia)$ at $z = z_{owc}$		
k_{row} = SET 1	k_{rw} = SET 1	

$S_w = 0.2$ (top 40 ft);

1.0 (elsewhere).

No-flow lower boundary condition (NF-L.B.C.).

Gravity effects included.

Table 4.1B

Deviations from the Base Case Parameters

Oil Reservoir - Aquifer Systems (Cases OW-)**

Case	Variation
OW-2B	- Base Case;
OW-2BS3	- $s = 5$;
OW-2BS4	- $s = 10$;
OW-3A	- $h_w = 10\ (ft)$; $k_z = 50\ (md)$;
OW-3B	- $h_w = 10\ (ft)$;
OW-3BS3	- $h_w = 10\ (ft)$; $s = 5$;
OW-3BS4	- $h_w = 10\ (ft)$; $s = 10$;
OW-3X	- $h_w = 10\ (ft)$; CP-LBC w/$S_o = 0.8$
OW-3Y	- $h_w = 10\ (ft)$; CP-LBC w/$S_w = 1.0$
OW-4B	- $h = 60\ (ft)$; $h_w = 10\ (ft)$;
OW-4BS3	- $h = 60\ (ft)$; $h_w = 10\ (ft)$; $s = 5$;
OW-4BS4	- $h = 60\ (ft)$; $h_w = 10\ (ft)$; $s = 10$;
OW-4Z	- $h = 60\ (ft)$; $h_w = 10\ (ft)$; CP-LBC w/$S_w = 1.0$
OW-5B	- $h = 80\ (ft)$; $h_w = 10\ (ft)$;
OW-5BS3	- $h = 80\ (ft)$; $h_w = 10\ (ft)$; $s = 5$;
OW-5BS4	- $h = 80\ (ft)$; $h_w = 10\ (ft)$; $s = 10$;
OW-5P	- $h = 80\ (ft)$; $h_w = 10\ (ft)$; $k_z = 50\ (md)$;
OW-5S	- $h = 80\ (ft)$; $h_w = 10\ (ft)$; $q_o = 400(STB/day)$;

Table 4.1B (Continued)

Deviations from the Base Case Parameters

Oil Reservoir - Aquifer Systems (Cases OW-)**

Case	Variation
OW-6B	- $h = 100\ (ft)$; $h_w = 10\ (ft)$;
OW-6BS3	- $h = 100\ (ft)$; $h_w = 10\ (ft)$; $s = 5$;
OW-6BS4	- $h = 100\ (ft)$; $h_w = 10\ (ft)$; $s = 10$;
OW-7B	- $h = 300\ (ft)$; $h_w = 10\ (ft)$;
OW-7BS3	- $h = 300\ (ft)$; $h_w = 10\ (ft)$; $s = 5$;
OW-7BS4	- $h = 300\ (ft)$; $h_w = 10\ (ft)$; $s = 10$;
OW-7O	- $h = 300\ (ft)$; $h_w = 10\ (ft)$; no gravity;
OW-7P	- $h = 300\ (ft)$; $h_w = 10\ (ft)$; $k_z = 50\ (md)$;
OW-7Q	- $h = 300\ (ft)$; $h_w = 10\ (ft)$; $h_w = 20\ (ft)$;
OW-7S	- $h = 300\ (ft)$; $h_w = 10\ (ft)$; $q_o = 400\ (STB/day)$;

Table 4.2A

Base Case Parameters

Gas Reservoir - Aquifer Systems (Cases GW-)**

$\phi = 0.2$ $k = 20\ (md)$ $k_z = 5\ (md)$

$r_e = 7500\ (ft)$ $r_w = 0.25\ (ft)$ $h_w = 40\ (ft)$

$h = 40\ (ft)$ $t_p = 10\ (days)$ $q_g = 10\ (MMscf/D)$

$\mu_w = 0.8\ (cp)$ $s = 0$ $c_w = 1 \times 10^{-6}\ (psi^{-1})$

$p_i = 2500\ (psia)$ at $z = z_{gwc}$

k_{rg} = SET 2 k_{rw} = SET 2

$S_w = 0.2$ (top 40 ft);

1.0 (elsewhere).

No-flow lower boundary condition (NF-L.B.C.).

No-flow upper boundary condition (NF-U.B.C.).

Gravity effects included.

Table 4.2B

Deviations from the Base Case Parameters

Gas Reservoir - Aquifer Systems (Cases GW-)**

Case	Variation			
GW-2B	- Base Case;			
GW-2BS3	- $s = 5$;			
GW-2BS4	- $s = 10$;			
GW-3B	-	$h_w = 10\ (ft)$;		
GW-3B2	-	$h_w = 10\ (ft)$;	$q_g = 1\ (MMscf/D)$;	
GW-3BS3	-	$h_w = 10\ (ft)$;	$q_g = 1\ (MMscf/D)$;	$s = 5$;
GW-3BS4	-	$h_w = 10\ (ft)$;	$q_g = 1\ (MMscf/D)$;	$s = 10$;
GW-4B	- $h = 45\ (ft)$;	$h_w = 10\ (ft)$;		
GW-4B2	- $h = 45\ (ft)$;	$h_w = 10\ (ft)$;	$q_g = 1\ (MMscf/D)$;	
GW-4BS3	- $h = 45\ (ft)$;	$h_w = 10\ (ft)$;	$q_g = 1\ (MMscf/D)$;	$s = 5$;
GW-4BS4	- $h = 45\ (ft)$;	$h_w = 10\ (ft)$;	$q_g = 1\ (MMscf/D)$;	$s = 10$;
GW-4C	- $h = 45\ (ft)$;	$h_w = 45\ (ft)$;	$k_z = 0\ (md)$;	
GW-5B	- $h = 50\ (ft)$;	$h_w = 10\ (ft)$;		
GW-5B2	- $h = 50\ (ft)$;	$h_w = 10\ (ft)$;	$q_g = 1\ (MMscf/D)$;	
GW-5BS3	- $h = 50\ (ft)$;	$h_w = 10\ (ft)$;	$q_g = 1\ (MMscf/D)$;	$s = 5$;
GW-5BS4	- $h = 50\ (ft)$;	$h_w = 10\ (ft)$;	$q_g = 1\ (MMscf/D)$;	$s = 10$;
GW-5C	- $h = 50\ (ft)$;	$h_w = 50\ (ft)$;	$k_z = 0\ (md)$;	
GW-6B	- $h = 60\ (ft)$;	$h_w = 10\ (ft)$;		
GW-6B2	- $h = 60\ (ft)$;	$h_w = 10\ (ft)$;	$q_g = 1\ (MMscf/D)$;	
GW-6BS3	- $h = 60\ (ft)$;	$h_w = 10\ (ft)$;	$q_g = 1\ (MMscf/D)$;	$s = 5$;
GW-6BS4	- $h = 60\ (ft)$;	$h_w = 10\ (ft)$;	$q_g = 1\ (MMscf/D)$;	$s = 10$;
GW-6C	- $h = 60\ (ft)$;	$h_w = 60\ (ft)$;	$k_z = 0\ (md)$;	

Table 4.2B (Continued)

Deviations from the Base Case Parameters

Gas Reservoir - Aquifer Systems (Cases GW-)**

Case	Variation
GW-7B	- $h = 100\ (ft)$; $h_w = 10\ (ft)$;
GW-7B2	- $h = 100\ (ft)$; $h_w = 10\ (ft)$; $q_g = 1\ (MMscf/D)$;
GW-7BS3	- $h = 100\ (ft)$; $h_w = 10\ (ft)$; $q_g = 1\ (MMscf/D)$; $s = 5$;
GW-7BS4	- $h = 100\ (ft)$; $h_w = 10\ (ft)$; $q_g = 1\ (MMscf/D)$; $s = 10$;
GW-7C	- $h = 100\ (ft)$; $h_w = 100\ (ft)$; $k_z = 0\ (md)$;

Table 4.3A

Base Case Parameters

Oil Reservoir - Gas Cap Systems (Cases OG-)**

$\phi = 0.2$ $k = 50\ (md)$ $k_z = 5\ (md)$

$r_e = 7500\ (ft)$ $r_w = 0.25\ (ft)$ $h_w = 40\ (ft)$

$h = 40\ (ft)$ $t_p = 10\ (days)$ $q_o = 200\ (STBO/D)$

$\mu_w = 0.8\ (cp)$ $s = 0$ $c_w = 0\ (psi^{-1})$

$p_i = 3600\ (psia)$ at $z = z_{goc}$

k_{rg} = SET 1 k_{rog} = SET 1

$S_o = 0.8$ (bottom 40 ft);

0.0 (elsewhere).

$S_w = 0.2$ (everywhere);

No-flow lower boundary condition (NF-L.B.C.).

No-flow upper boundary condition (NF-U.B.C.).

Gravity effects included.

Table 4.3B

Deviations from the Base Case Parameters

Oil Reservoir - Gas Cap Systems (Cases OG-)**

Case	Variation			
OG-1B	- no gravity - single vertical grid block			
OG-1BS3	- no gravity;	$s = 5$;		
OG-1BS4	- no gravity;	$s = 10$;		
OG-2B	- Base Case;			
OG-2C	- no gravity;			
OG-3B	-	$h_w = 10\ (ft)$;		
OG-3BS3	-	$h_w = 10\ (ft)$;	$s = 5$;	
OG-3BS4	-	$h_w = 10\ (ft)$;	$s = 10$;	
OG-3X	-	$h_w = 10\ (ft)$;	CP-UBC w/$S_o = 0.8$	
OG-3Y	-	$h_w = 10\ (ft)$;	CP-UBC w/$S_g = 0.8$	
OG-4B	- $h = 50\ (ft)$;	$h_w = 10\ (ft)$;		
OG-4BS3	- $h = 50\ (ft)$;	$h_w = 10\ (ft)$;	$s = 5$;	
OG-4BS4	- $h = 50\ (ft)$;	$h_w = 10\ (ft)$;	$s = 10$;	
OG-4B2	- $h = 50\ (ft)$;	$h_w = 10\ (ft)$;		$q_o = 100\ (STBO/D)$;
OG-4B2S3	- $h = 50\ (ft)$;	$h_w = 10\ (ft)$;	$s = 5$;	$q_o = 100\ (STBO/D)$;
OG-4B2S4	- $h = 50\ (ft)$;	$h_w = 10\ (ft)$;	$s = 10$;	$q_o = 100\ (STBO/D)$;
OG-5B	- $h = 60\ (ft)$;	$h_w = 10\ (ft)$;		
OG-5BS3	- $h = 60\ (ft)$;	$h_w = 10\ (ft)$;	$s = 5$;	
OG-5BS4	- $h = 60\ (ft)$;	$h_w = 10\ (ft)$;	$s = 10$;	
OG-5Z	- $h = 60\ (ft)$;	$h_w = 10\ (ft)$;	CP-UBC w/$S_g = 0.8$	
OG-6B	- $h = 70\ (ft)$;	$h_w = 10\ (ft)$;		
OG-6BS3	- $h = 70\ (ft)$;	$h_w = 10\ (ft)$;	$s = 5$;	
OG-6BS4	- $h = 70\ (ft)$;	$h_w = 10\ (ft)$;	$s = 10$;	

Table 4.4A

Base Case Parameters

Water Reservoir - Gas Cap Systems (Cases WG-)**

$\phi = 0.2$	$k = 50\ (md)$	$k_z = 5\ (md)$
$r_e = 7500\ (ft)$	$r_w = 0.25\ (ft)$	$h_w = 40\ (ft)$
$h = 40\ (ft)$	$t_p = 10\ (days)$	$q_w = 200\ (STBW/D)$
$\mu_w = 0.8\ (cp)$	$s = 0$	$c_w = 3 \times 10^{-6}\ (psi^{-1})$
k_{rg} = SET 2	k_{rw} = SET 2	$\rho_{wsc} = 51.485\ (lb/ft^3)$

$S_w = 1.0$ (bottom 40 ft);

0.2 (elsewhere).

No-flow lower boundary condition (NF-L.B.C.).

No-flow upper boundary condition (NF-U.B.C.).

Gravity effects included.

Table 4.4B

Deviations from the Base Case Parameters

Water Reservoir - Gas Cap Systems (Cases WG-)**

Case	Variation			
WG-1B	- Base Case;			
WG-2B	-	$h_w = 10\ (ft)$;		
WG-2BS3	-	$h_w = 10\ (ft)$;	$s = 5$;	
WG-2BS4	-	$h_w = 10\ (ft)$;	$s = 10$;	
WG-3B	- $h = 50\ (ft)$;	$h_w = 10\ (ft)$;		
WG-3BS3	- $h = 50\ (ft)$;	$h_w = 10\ (ft)$;	$s = 5$;	
WG-3BS4	- $h = 50\ (ft)$;	$h_w = 10\ (ft)$;	$s = 10$;	
WG-3X	-	$h_w = 10\ (ft)$;	CP-UBC w/$S_w = 1.0$	
WG-3Y	-	$h_w = 10\ (ft)$;	CP-UBC w/$S_w = 0.2$	
WG-4B	- $h = 60\ (ft)$;	$h_w = 10\ (ft)$;		
WG-4BS3	- $h = 60\ (ft)$;	$h_w = 10\ (ft)$;	$s = 5$;	
WG-4BS4	- $h = 60\ (ft)$;	$h_w = 10\ (ft)$;	$s = 10$;	
WG-4Z	- $h = 60\ (ft)$;	$h_w = 10\ (ft)$;	CP-UBC w/$S_w = 0.2$	
WG-4Za	- $h = 60\ (ft)$;	$h_w = 10\ (ft)$;	CP-UBC w/$S_w = 0.2$	no gravity
WG-45B	- $h = 65\ (ft)$;	$h_w = 10\ (ft)$;		
WG-5B	- $h = 70\ (ft)$;	$h_w = 10\ (ft)$;		
WG-5D	- $h = 70\ (ft)$;	$h_w = 10\ (ft)$;	$\phi = 0.01\ , 40\ (ft) \leq z \leq 70\ (ft)$;	
WG-5BS3	- $h = 70\ (ft)$;	$h_w = 10\ (ft)$;	$s = 5$;	
WG-5BS4	- $h = 70\ (ft)$;	$h_w = 10\ (ft)$;	$s = 10$;	

Table 4.5A

Base Case Parameters

Oil Reservoir - Gas Cap - Aquifer Systems (Cases OGW)**

$\phi = 0.2$	$k = 50\ (md)$	$k_z = 5\ (md)$
$r_e = 7500\ (ft)$	$r_w = 0.25\ (ft)$	$h_w = 70\ (ft)$
$h_o = 70\ (ft)$	$t_p = 10\ (days)$	$q_o = 200\ (STBO/D)$
$\mu_w = 0.8\ (cp)$	$s = 0$	$c_w = 1 \times 10^{-5}\ (psi^{-1})$
k_{rg} = SET 2	k_{rog} = SET 2	$r_s = 0.54166(ft)$
k_{rw} = SET 1	k_{row} = SET 1	

$S_w = 1.0$ (in aquifer);

0.2 (elsewhere).

$S_g = 0.8$ (in gas cap);

0.0 (elsewhere).

$S_o = 0.8$ (in oil zone);

0.0 (elsewhere).

No-flow lower boundary condition (NF-L.B.C.).

No-flow upper boundary condition (NF-U.B.C.).

Gravity effects included.

Table 4.5B

Deviations from the Base Case Parameters

Oil Reservoir - Gas Cap - Aquifer Systems (Cases OGW)**

Case	Variation			
OGW	- Base Case;			
OGWAA	- $h_a = 10\ (ft)$;	$h_g = 10\ (ft)$;	$h_w = 10\ (ft)$;	
OGWAAS3	- $h_a = 10\ (ft)$;	$h_g = 10\ (ft)$;	$h_w = 10\ (ft)$;	$s = 5$;
OGWAAS4	- $h_a = 10\ (ft)$;	$h_g = 10\ (ft)$;	$h_w = 10\ (ft)$;	$s = 10$;
OGWAB	- $h_a = 10\ (ft)$;	$h_g = 20\ (ft)$;	$h_w = 10\ (ft)$;	
OGWABS3	- $h_a = 10\ (ft)$;	$h_g = 20\ (ft)$;	$h_w = 10\ (ft)$;	$s = 5$;
OGWABS4	- $h_a = 10\ (ft)$;	$h_g = 20\ (ft)$;	$h_w = 10\ (ft)$;	$s = 10$;
OGWAC	- $h_a = 10\ (ft)$;	$h_g = 30\ (ft)$;	$h_w = 10\ (ft)$;	
OGWACS3	- $h_a = 10\ (ft)$;	$h_g = 30\ (ft)$;	$h_w = 10\ (ft)$;	$s = 5$;
OGWACS4	- $h_a = 10\ (ft)$;	$h_g = 30\ (ft)$;	$h_w = 10\ (ft)$;	$s = 10$;
OGWBA	- $h_a = 20\ (ft)$;	$h_g = 10\ (ft)$;	$h_w = 10\ (ft)$;	
OGWBAS3	- $h_a = 20\ (ft)$;	$h_g = 10\ (ft)$;	$h_w = 10\ (ft)$;	$s = 5$;
OGWBAS4	- $h_a = 20\ (ft)$;	$h_g = 10\ (ft)$;	$h_w = 10\ (ft)$;	$s = 10$;
OGWBB	- $h_a = 20\ (ft)$;	$h_g = 20\ (ft)$;	$h_w = 10\ (ft)$;	
OGWBBS3	- $h_a = 20\ (ft)$;	$h_g = 20\ (ft)$;	$h_w = 10\ (ft)$;	$s = 5$;
OGWBBS4	- $h_a = 20\ (ft)$;	$h_g = 20\ (ft)$;	$h_w = 10\ (ft)$;	$s = 10$;
OGWBC	- $h_a = 20\ (ft)$;	$h_g = 30\ (ft)$;	$h_w = 10\ (ft)$;	
OGWBCS3	- $h_a = 20\ (ft)$;	$h_g = 30\ (ft)$;	$h_w = 10\ (ft)$;	$s = 5$;
OGWBCS4	- $h_a = 20\ (ft)$;	$h_g = 30\ (ft)$;	$h_w = 10\ (ft)$;	$s = 10$;

Table 4.5B (Continued)

Deviations from the Base Case Parameters

Oil Reservoir - Gas Cap - Aquifer Systems (Cases OGW)**

Case	Variation			
OGWCA	- $h_a = 50\ (ft)$;	$h_g = 10\ (ft)$;	$h_w = 10\ (ft)$;	
OGWCAS3	- $h_a = 50\ (ft)$;	$h_g = 10\ (ft)$;	$h_w = 10\ (ft)$;	$s = 5$;
OGWCAS4	- $h_a = 50\ (ft)$;	$h_g = 10\ (ft)$;	$h_w = 10\ (ft)$;	$s = 10$;
OGWCB	- $h_a = 50\ (ft)$;	$h_g = 20\ (ft)$;	$h_w = 10\ (ft)$;	
OGWCBS3	- $h_a = 50\ (ft)$;	$h_g = 20\ (ft)$;	$h_w = 10\ (ft)$;	$s = 5$;
OGWCBS4	- $h_a = 50\ (ft)$;	$h_g = 20\ (ft)$;	$h_w = 10\ (ft)$;	$s = 10$;
OGWCC	- $h_a = 50\ (ft)$;	$h_g = 30\ (ft)$;	$h_w = 10\ (ft)$;	
OGWCCS3	- $h_a = 50\ (ft)$;	$h_g = 30\ (ft)$;	$h_w = 10\ (ft)$;	$s = 5$;
OGWCCS4	- $h_a = 50\ (ft)$;	$h_g = 30\ (ft)$;	$h_w = 10\ (ft)$;	$s = 10$;

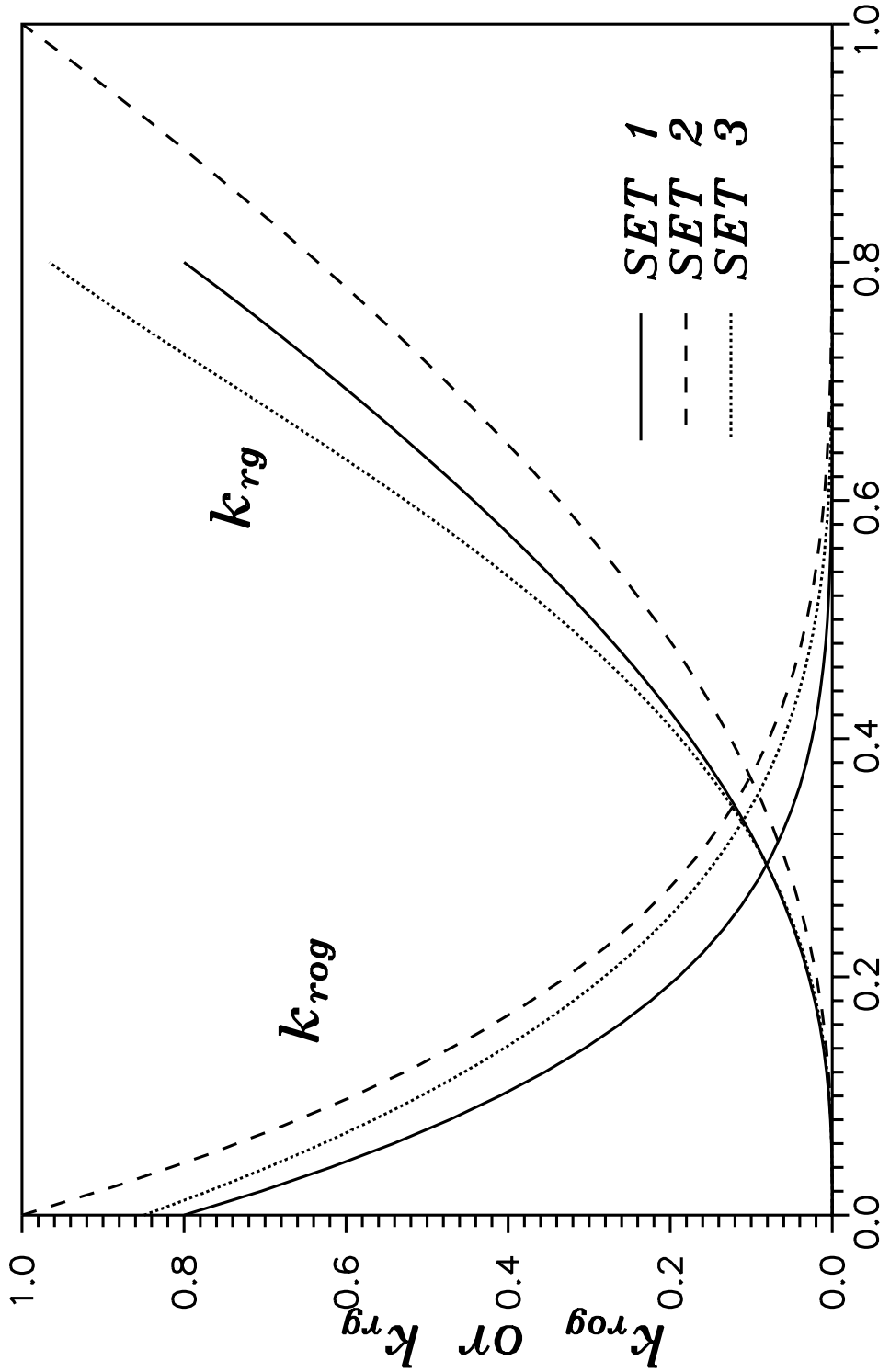

Fig. 4.6 – Two–phase oil–gas relative permeability curves.

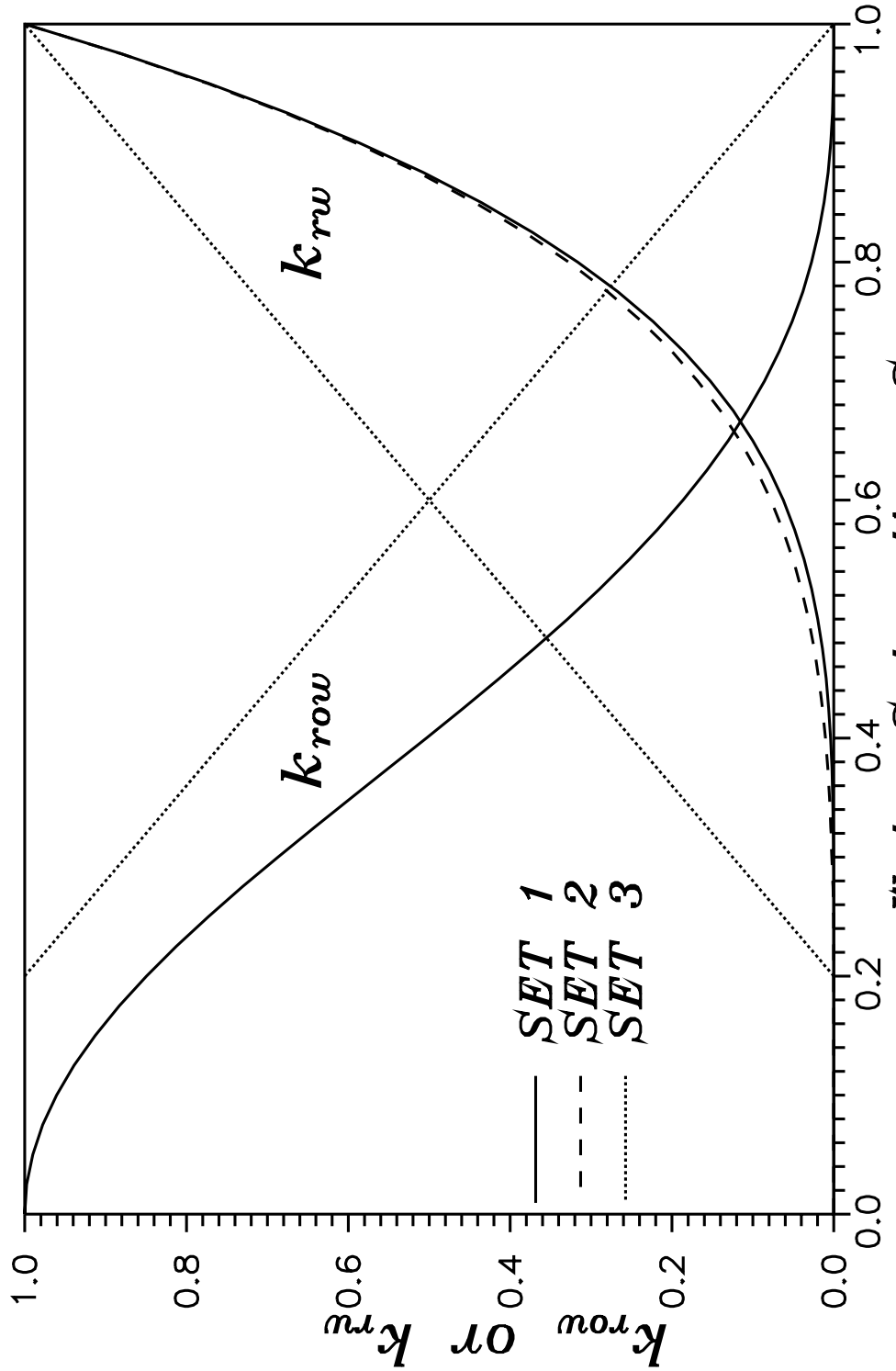

Fig. 4.7 – Two–phase water–oil relative permeability curves.

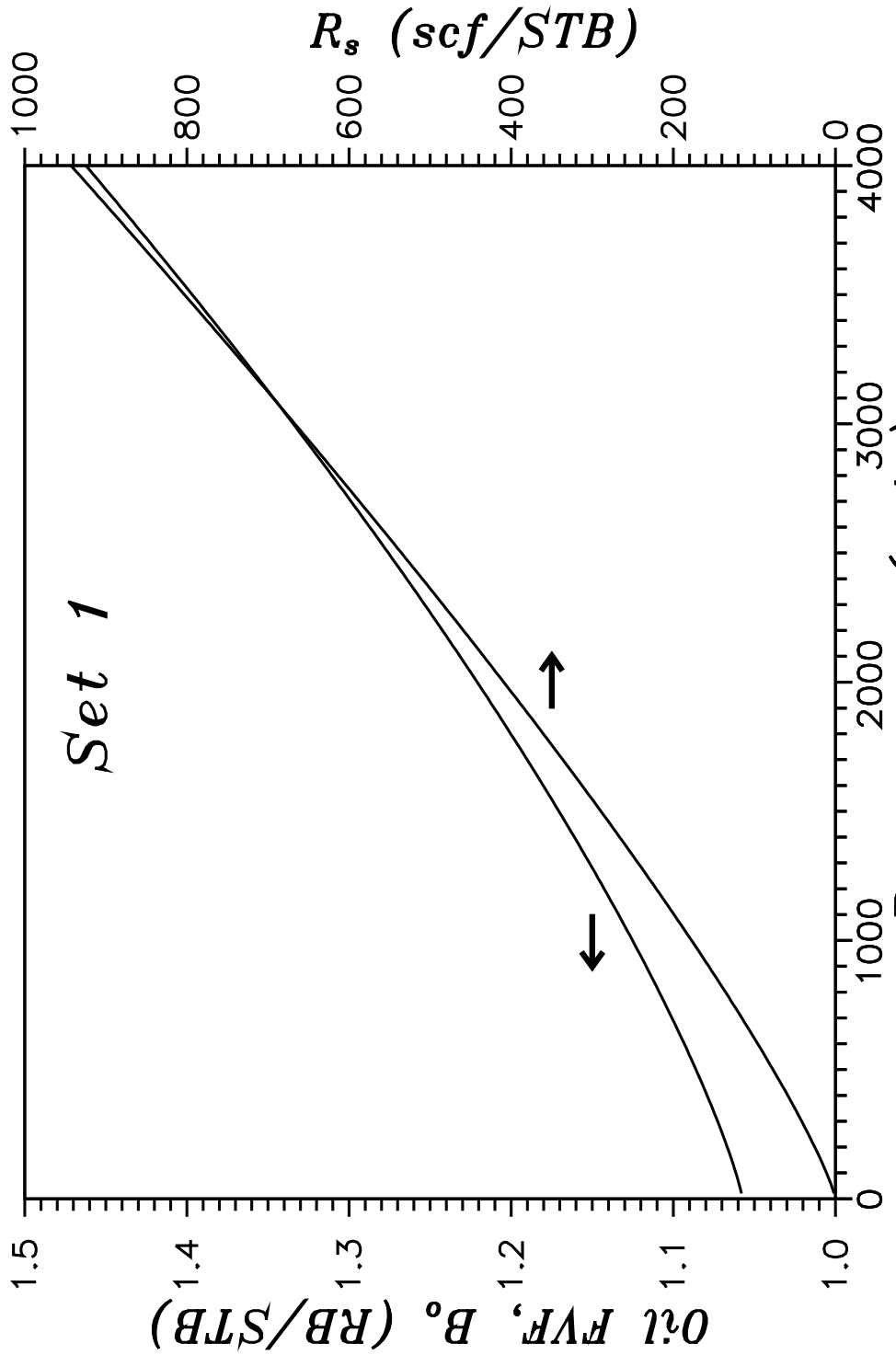

Fig. 4.8 – Oil formation volume factor and solution gas–oil ratio.

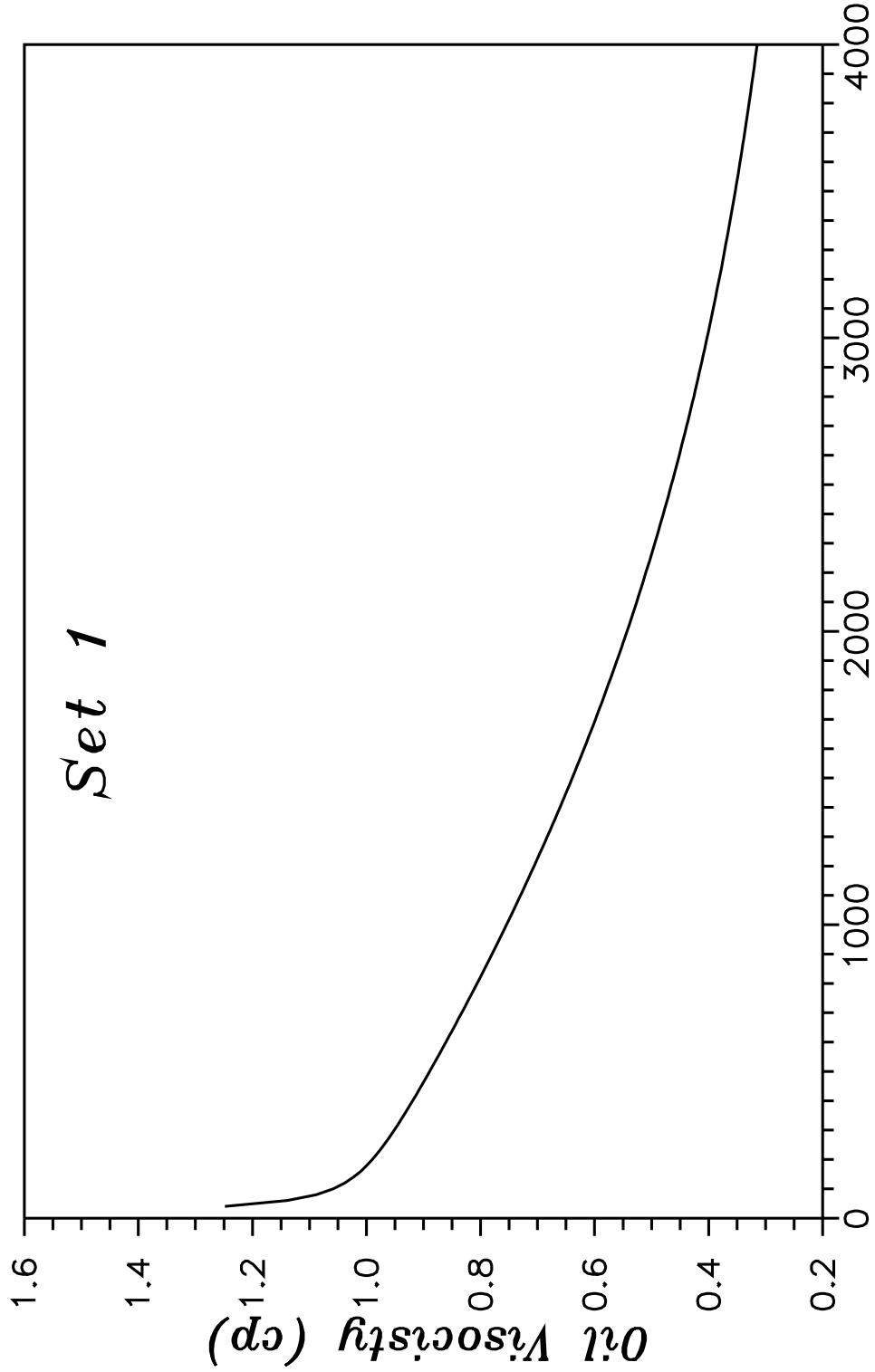

Fig. 4.9 – Oil viscosity for PVT Set 1.

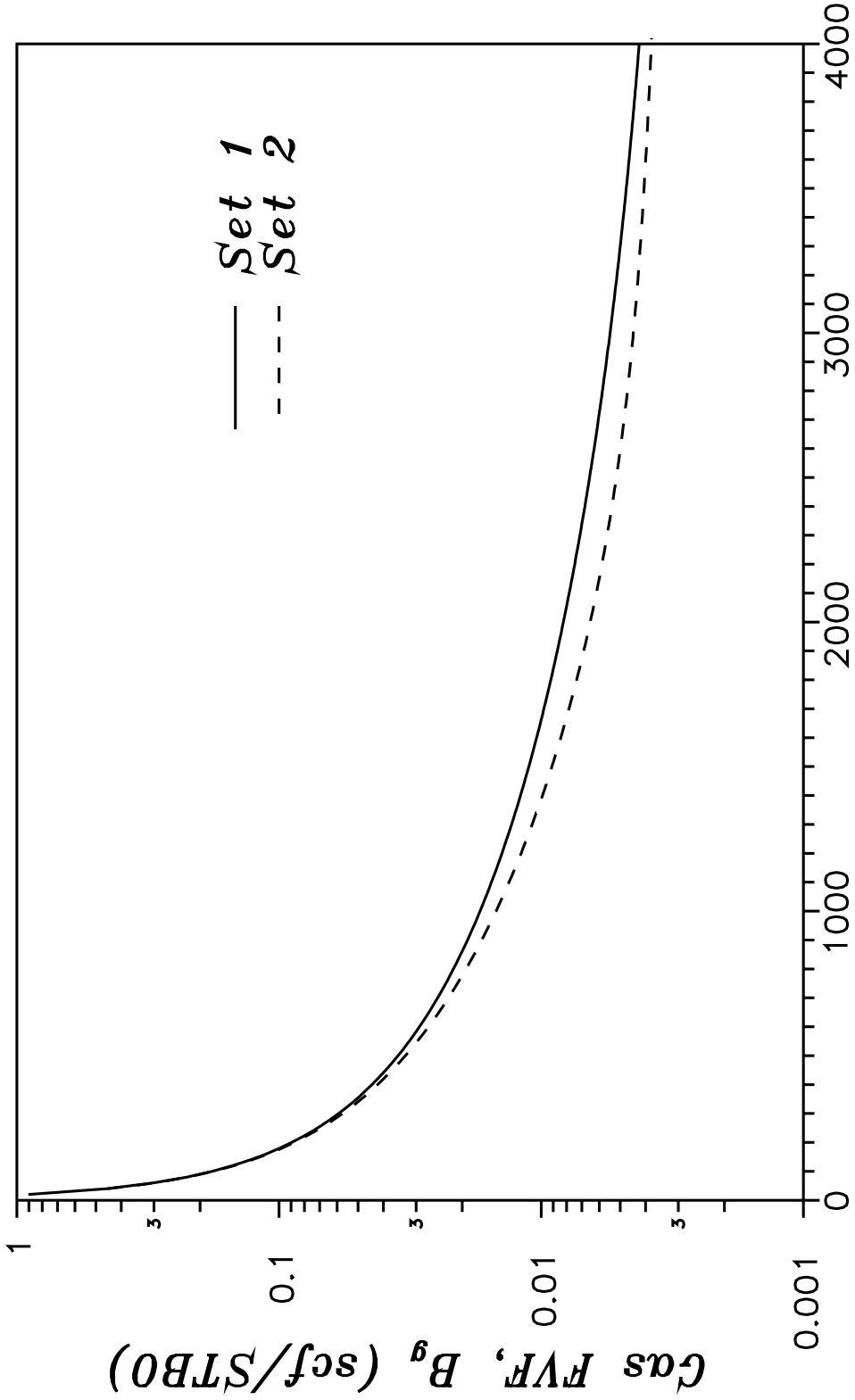

Fig. 4.10 – Gas formation volume factors.

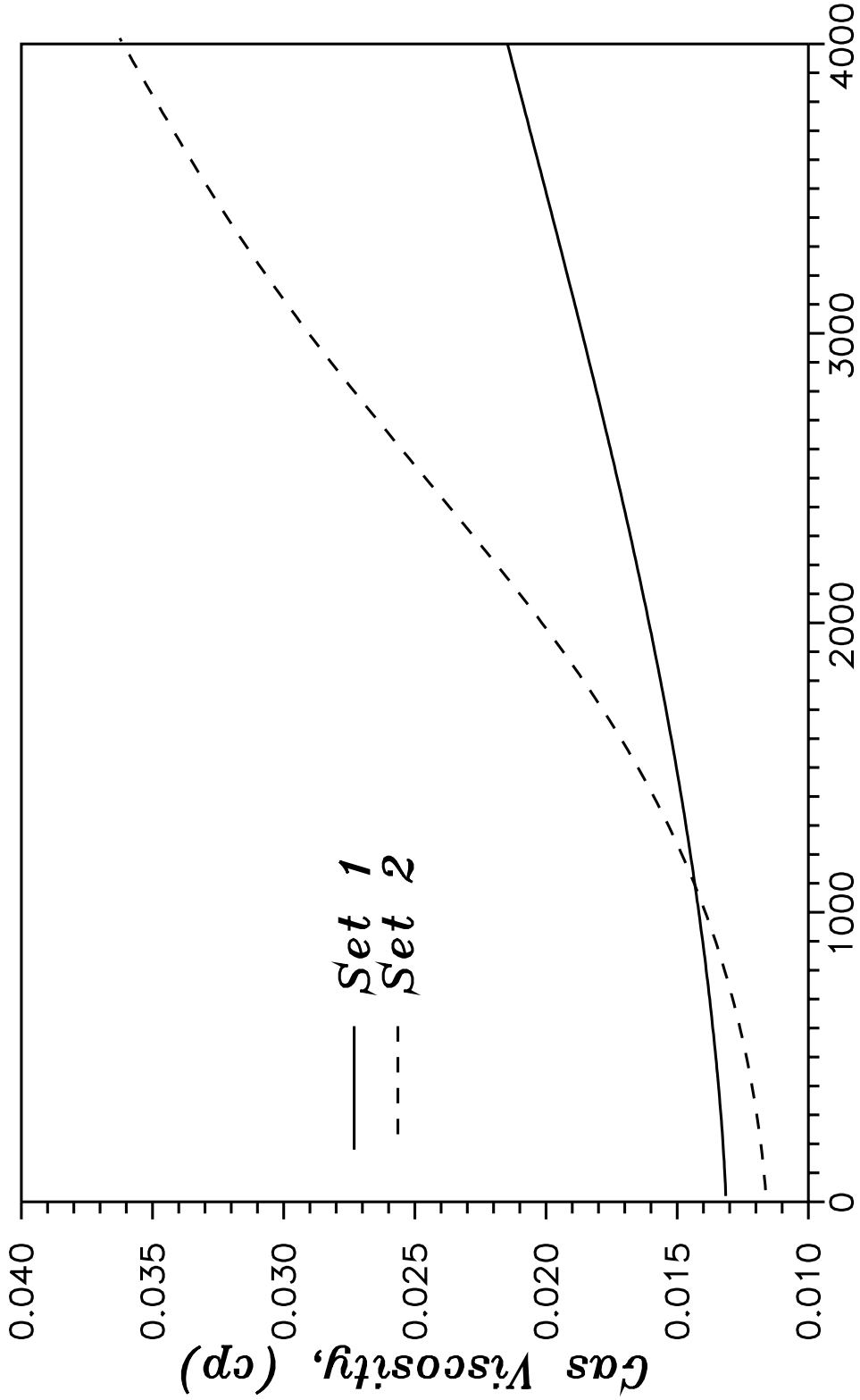

Fig. 4.11 – Set 1 and Set 2 gas viscosities.

where q_t is the total production rate in reservoir barrels per day. The m in Eq. 4.2.1 represents the slope of the semilog straight line portion of a plot of pressure versus logarithm of time, e.g., for drawdown $-2.303 dp_{wf}/d\ln t$. We note that Ref. 30 showed Eq. 4.2.1 is strictly valid only if saturation gradients are negligible.

In their work on pressure transient analysis of two-phase (oil-water) flow problems, including flow to a restricted-entry well, Refs. 23 and 24 made several important contributions to our understanding and interpretation of multiphase pressure transient data. One of their primary contributions was to show that when vertical saturation gradients exist in the reservoir, the total mobility calculated from Eq. 4.2.1 represents a thickness-averaged total mobility in the zone of the reservoir investigated during the test, i.e.,

$$\bar{\lambda}_t = \frac{1}{h}\int_0^h \left(\frac{kk_{ro}}{\mu_o} + \frac{kk_{rw}}{\mu_w}\right) dz \ . \tag{4.2.2}$$

For restricted-entry wells, Refs. 23 and 24 also showed that the thickness-averaged individual phase mobilities could be obtained from pseudoradial flow pressure data if, and only if, the producing water-oil ratio was equal to the in-situ water-oil ratio in the region reflected by pseudoradial flow data. In restricted-entry cases where estimates of individual mobilities can be obtained, the mobility computed from

$$\lambda_l = \frac{162.6 q_l B_l}{mh} \ , \tag{4.2.3}$$

$l = o, w$, gives the thickness-averaged phase mobility defined by

$$\bar{\lambda}_l = \frac{1}{h}\int_0^h \left(\frac{kk_{rl}}{\mu_l}\right) dz \ . \tag{4.2.4}$$

From Eqs. 4.2.1 and 4.2.3 we see that

$$\lambda_t = \lambda_o + \lambda_w \ . \tag{4.2.5}$$

From Eqs. 4.2.2 and 4.2.4 we see that

$$\bar{\lambda}_t = \bar{\lambda}_o + \bar{\lambda}_w \ . \tag{4.2.6}$$

Thus, the results of Refs. 23 and 24 indicate that we can obtain reliable estimates of $\bar{\lambda}_t$ by estimating individual phase mobilities and adding them together even though the estimates of individual phase mobilities may be meaningless.

Another important observation of Refs. 23 and 24 is the fact that if multiphase flow effects are important, then a rapid decline in pressure does not necessarily signify the onset of boundary effects, i.e., when coning of water occurs, there is a resultant decrease in the total mobility, λ_t, adjacent to the open interval which causes a rapid decline in the wellbore pressure (increase in the pressure derivative). Results of this study, and also presented in Ref. 28, indicate that coning itself, i.e., production of the unwanted fluid, is not necessarily required to observe this increase in the pressure derivative. In fact, all that is required is for there to be a "significant" change in the vertical saturation profile in the reservoir, i.e., movement of the oil-water contact (OWC) or the "building" of the water cone. This effect is discussed further in Chapters V and VI.

Analysis of pressure transient data obtained from a restricted-entry well becomes more complicated when solution-gas is present. Most analysis methods for multiphase systems containing solution-gas utilize a pseudopressure function.[31–38] For radial flow to a fully-penetrating well in a solution-gas-drive reservoir, Refs. 31 and 32 showed that the mobilities calculated from drawdown pressure and rate data represent the mobilities at the sandface. Based on this result and the observation by Refs. 23 and 24 that calculated mobilities for restricted-entry oil-water systems represent total-thickness-averaged mobilities, the following question arises: what do the mobilities calculated formally with Eqs. 4.2.1 and 4.2.3 (using

pressure and rate data obtained from a restricted-entry well in a solution-gas system) represent, if anything?

The highly non-linear nature of the mathematical problem describing multiphase flow in the reservoir has to date precluded the development of useful analytic solutions to such problems. Insight into the conditions under which standard semilog analysis techniques can be applied to drawdown pressure transient data obtained from such systems may be gained, however, by examining analytical solutions to analogous problems under single phase flow conditions and considering the fundamental physical properties of the fluid/reservoir system required for the semilog analysis techniques to be applicable. Although it may be inadvisable to do so, to date, procedures for analyzing both gas flow and multiphase flow problems have been derived by trying to correlate the results for the nonlinear cases with standard results for the single-phase flow of a slightly compressible liquid of constant compressibility and constant viscosity. Such correlations frequently employ the use of pseudopressure and/or pseudotime. In an attempt to provide a fundamental theoretical and physical explanation of the multiphase results to be presented here, we then first re-examine single-phase flow.

4.3 Single Phase Liquid Flow

Here, consider the single phase flow of a slightly-compressible liquid of constant compressibility and constant viscosity. We first assume plane radial flow to a completely-penetrating well producing at a constant rate in an infinite reservoir. We define

$$p_D = \frac{kh[p_i - p(r,t)]}{141.2qB\mu} \ , \tag{4.3.1}$$

$$p_{wD} = \frac{kh[p_i - p_{wf}]}{141.2qB\mu} \ , \tag{4.3.2}$$

$$r_D = r/r_w \ , \tag{4.3.3}$$

and

$$t_D = \frac{0.00633kt}{\phi c_t \mu {r_w}^2} \ , \tag{4.3.4}$$

where time, t, is in days. For constant rate production through a line source well, we consider a point $r_{iD} = r_i/r_w$ at some fixed distance from the well. Then if ${t_D}/{r_{iD}}^2 \geq 100$, we know for all $r_D < r_{iD}$,

$$p_D = \frac{1}{2}\ln\left(\frac{4t_D}{e^{\gamma}{r_D}^2}\right) \ , \tag{4.3.5}$$

for $s = 0$, and

$$p_{wD} = \frac{1}{2}\ln\left(\frac{4t_D}{e^{\gamma}}\right) + s \ , \tag{4.3.6}$$

where we assume an infinitesimally thin skin region. Eq. 4.3.5 also indicates that the flow rate through a cylinder of radius r_{iD} is

$$q_D(r_{iD}, t_D) = -\left[r_D \frac{\partial p_D}{\partial r_D}\right]_{r_{iD}} = 1 \ , \tag{4.3.7}$$

where the actual flow rate at the well is also

$$q_D(r_D = 1, t_D) = -\left[r_D \frac{\partial p_D}{\partial r_D}\right]_{r_D=1} = 1 = q_D(r_{iD}, t_D) \ . \tag{4.3.8}$$

Similarly, from Eqs. 4.3.5 and 4.3.6 it follows that

$$\left.\frac{\partial p_D}{\partial t_D}\right|_{r_D} = \frac{\partial p_{wD}}{\partial t_D} \ , \tag{4.3.9}$$

for $r_D \leq r_{iD}$, or

$$\frac{\partial p(r_i, t)}{\partial t} = \frac{\partial p_{wf}}{\partial t} = \frac{\partial p(r, t)}{\partial t} \ , \ r < r_i \ . \tag{4.3.10}$$

Eq. 4.3.8, which is only approximate, indicates that we have a steady-state region for $1 < r_D \leq r_{iD}$. The flow rate at all points in this region is constant and

Eq. 4.3.10 indicates that within this region, $\partial p/\partial t$ is a constant. Eq. 4.3.9 also indicates that for $t_D/{r_{iD}}^2 \geq 100$, the pressure drop $[p(r_i,t) - p_{wf}(t)]$ across this region remains constant.

By using the line source solution, we can see that Eqs. 4.3.8 and 4.3.9 are only approximations, but are extremely good ones. If Eq. 4.3.8 were exact, then we would have a true steady-state region and from the flow equations it would follow that $\partial p_D/\partial t_D = 0$, which is not the case for the well testing problems of interest.

We also know that when Eq. 4.3.5 holds,

$$r\frac{\partial p}{\partial r} = -2t\frac{\partial p}{\partial t} \ . \tag{4.3.11}$$

Eq. 4.3.11 also follows if pressure is a function of a Boltzmann transform, which is the case for the line source solution. For an infinitesimally thin skin $p_D(r_D, t_D)$ for $r_D > 1$ can be correlated in terms of the Boltzmann transform, but $p_{wD} = p_D|_{r_D=1^+} + s$ cannot be correlated. Eq. 4.3.11 still applies, however, at $r = {r_w}^+$, and since $\partial p({r_w}^+, t)/\partial t = \partial p_{wf}/\partial t$, Eq. 4.3.9 applies at all points in the reservoir as well as at the wellbore.

We now extend our arguments to a composite reservoir, with the inner zone $(r < r_i)$ permeability and porosity given respectively by k_1 and ϕ_1, and with the corresponding outer zone $(r \geq r_i)$ values given by k_2 and ϕ_2. If time is sufficiently large so that

$$q = q(r_i) \ , \tag{4.3.12}$$

where q is the production rate in STB, then

$$q = \frac{k_1 h}{141.2\mu B}\left(r\frac{\partial p}{\partial r}\right)_{r=r_w} = \frac{k_1 h}{141.2\mu B}\left(r\frac{\partial p}{\partial r}\right)_{r=r_i^-} = \frac{k_2 h}{141.2\mu B}\left(r\frac{\partial p}{\partial r}\right)_{r=r_i^+} . \tag{4.3.13}$$

Eq. 4.3.13 indicates that when the inner zone behaves like a "steady state" region, the problem is equivalent to having a well of radius, r_i, producing at a rate, q, from the outer zone. Eventually, this well will behave like a line source well and we will have

$$\left(r\frac{\partial p}{\partial r}\right)_{r_i+} = -2t\frac{\partial p(r_i,t)}{\partial t} \ . \tag{4.3.14}$$

When Eq. 4.3.14 applies, Eq. 4.3.13 is equivalent to

$$q = \frac{k_2 h}{141.2\mu B}\left[-2t\frac{\partial p(r_i,t)}{\partial t}\right] \ . \tag{4.3.15}$$

The inner zone then behaves similar to a skin zone and the pressure drop across this zone becomes approximately constant, so Eq. 4.3.10 applies. Then, Eq. 4.3.15 yields

$$q = \frac{k_2 h}{141.2\mu B}\left[-2t\frac{\partial p_{wf}}{\partial t}\right] \ , \tag{4.3.16}$$

which is equivalent to the well-known result that, at late time, a semilog plot of pressure versus time will have a semilog slope of

$$m = \frac{162.6qB\mu}{k_2 h} \ . \tag{4.3.17}$$

Similarly, the "steady-state" zone arguments for a restricted-entry well producing from layer 1 of a two-layer reservoir yield

$$q = \frac{k_1 h_w}{141.2\mu B}\left(r\frac{\partial p}{\partial r}\right)_{r=r_w} = \frac{1}{141.2B}\int_{z=0}^{z=h}\frac{k}{\mu}\left(r\frac{\partial p}{\partial r}\right)_{r=r_i} dz \ . \tag{4.3.18}$$

where h_w is the length of the perforated interval and k_j and h_j, respectively, denote the permeability and thickness of layer j, and we have assumed a uniform-flux wellbore. If we are far enough from the well, we expect to have negligible flow

in the vertical direction, and then $(r\partial p/\partial r)_{r_i}$ is independent of z. In this case, Eq. 4.3.18 becomes

$$q = \frac{k_1 h_w}{141.2\mu B}\left(r\frac{\partial p}{\partial r}\right)_{r=r_w} = \left[\frac{k_1 h_1 + k_2 h_2}{141.2\mu B}\right]\left(r\frac{\partial p}{\partial r}\right)_{r=r_i} . \tag{4.3.19}$$

As previously, when Eq. 4.3.19 holds, the reservoir corresponding to $r \geq r_i$ is effectively produced at a rate, q, by a well of radius, r_i. When we have radial flow, this pseudo-reservoir is equivalent to a homogeneous reservoir with permeability,

$$\overline{k} = \frac{k_1 h_1 + k_2 h_2}{h} \tag{4.3.20}$$

and we should again have

$$\left(r\frac{\partial p}{\partial r}\right)_{r_i+} = -2t\frac{\partial p(r_i, t)}{\partial t} . \tag{4.3.21}$$

Since $q(r_i) = q = \text{constant}$, then

$$-\left(r\frac{\partial p}{\partial r}\right)_{r_w} = -\left(r\frac{\partial p}{\partial r}\right)_{r_i-} \tag{4.3.22}$$

does not vary with time at all times subsequent to the time a "steady-state zone" of radius r_i is achieved. This suggests again that the pressure drop across this zone $(p(r_i, t) - p_{wf})$ becomes constant, so that

$$\frac{\partial p_{wf}}{\partial t} = \frac{\partial p(r, t)}{\partial t} \ , \ r = r_i . \tag{4.3.23}$$

Combining Eqs. 4.3.21 and 4.3.23 and using the result in Eq. 4.3.19 gives the well known result,

$$q = \left[\frac{k_1 h_1 + k_2 h_2}{141.2\mu B}\right]\left(-2t\frac{\partial p_{wf}}{\partial t}\right) . \tag{4.3.24}$$

The preceding results are for drawdown, but for linear problems the buildup response is the superposition of drawdown results so we expect the same computational results should apply, noting, of course, that the Boltzmann transform does not apply for buildup. For buildup problems, it is a zero rate that propagates out into the reservoir as shut-in time increases.

4.4 Single-Phase Gas Flow and the Real Gas Pseudopressure

In extending our "steady-state zone" arguments to the case of real gas flow, we consider the use of real gas pseudopressure. These arguments have previously been presented by Ref. 131 and we note that Refs. 146-148 have used similar arguments in their work on gas condensate reservoirs. We define

$$m(p) = \int_0^p \frac{dp}{\mu_g B_g} \ , \tag{4.4.1}$$

and

$$m_D = \frac{kh[m(p_i) - m(p(r,t))]}{141.2 q_g} \ , \tag{4.4.2}$$

where q_g is the gas production rate at the well in STB/day and B_g is in RB/STB. Similarly, we define

$$m_{wD} = \frac{kh[m(p_i) - m(p_{wf})]}{141.2 q_g} \ , \tag{4.4.3}$$

and

$$t_D = \frac{0.00633kt}{\phi c_{ti} \mu_{g_i} {r_w}^2} \ , \tag{4.4.4}$$

where time, t, is in days, and the compressibility-viscosity product is evaluated at initial conditions. Note, that if we allow connate water in the reservoir, then we would replace the absolute permeability in Eqs. 4.4.2–4.4.4 with the effective gas permeability at connate water saturation and, also, define the total compressibility as

$$c_t = (S_g c_g)_i + (S_{wc} c_w)_i \approx (S_g c_g)_i \ . \tag{4.4.5}$$

We first consider radial flow to a completely-penetrating well, and assume that the mass rate is approximately constant across a zone of radius r_i; thus,

$$q_g = q_g(r_i) \ , \tag{4.4.6}$$

where the flow rate q_g is in STB/day. It follows from Eq. 4.4.6 that

$$q = \frac{kh}{141.2\mu_g B_g}\left(r\frac{\partial p}{\partial r}\right)_{r=r_w} = \frac{kh}{141.2\mu_g B_g}\left(r\frac{\partial p}{\partial r}\right)_{r=r_i} \ . \tag{4.4.7}$$

Arguing as we did in the liquid case, Eq. 4.4.7 indicates that when the inner zone behaves like a "steady state" region, the problem is equivalent to having a well of radius r_i producing at a rate q from the outer zone. Eventually, this well will behave like a line source well, the Boltzmann transform will become applicable, and we will have

$$q = \frac{kh}{141.2\mu_g B_g}\left[-2t\frac{\partial p(r_i,t)}{\partial t}\right] \ . \tag{4.4.8}$$

Eq. 4.4.7 also implies that

$$r\frac{\partial m(p)}{\partial r}\bigg|_{r_w} = r\frac{\partial m(p)}{\partial r}\bigg|_{r\leq r_i} \ . \tag{4.4.9}$$

For this case, we expect $m(p(r_i)) - m(p_{wf})$ becomes constant across the steady-state zone which gives

$$\frac{\partial m(p_{wf})}{\partial t} = \frac{\partial m(p(r_i,t))}{\partial t} \ . \tag{4.4.10}$$

Using Eq. 4.4.10 in Eq. 4.4.8 we have,

$$q = \frac{kh}{141.2}\left[-2t\frac{\partial m(p(r_i,t))}{\partial t}\right] = \frac{kh}{141.2}\left[-2t\frac{\partial m(p_{wf})}{\partial t}\right] \ , \tag{4.4.11}$$

or

$$q = \frac{kh}{141.2(B_g\mu_g)_{p_{wf}}}\left[-2t\frac{\partial p_{wf}}{\partial t}\right] = \frac{kh}{141.2(B_g\mu_g)_{p(r_i)}}\left[-2t\frac{\partial p(r_i,t))}{\partial t}\right] \ . \tag{4.4.12}$$

For a composite reservoir with an absolute permeability k_1 in the inner zone, and permeability k_2 in the outer zone, our argument indicates that at late times, we will have

$$q = \frac{k_2 h}{141.2(B_g \mu_g)_{p_{wf}}} \left[-2t \frac{\partial p_{wf}}{\partial t} \right] . \tag{4.4.13}$$

To verify this result, we consider a radial flow gas case in a "composite" reservoir. The inner zone extends to $r_1 = 56.4\ ft$ and contains single-phase dry gas, i.e., $S_g = 1$. The outer zone extends to $20,000\ ft$ and contains both dry gas and connate water at irreducible water saturation, i.e., the water is immobile. Other pertinent reservoir and fluid information is included in Table 4.6. A 10-day drawdown test is simulated at a constant surface gas rate of 10 $MMscf/day$, followed by a 10-day buildup test.

We begin by checking the validity of Eq. 4.4.10. Figure 4.12 shows the log-derivative of pseudopressure with respect to time both at the sandface and at a radius, $r = 70.71\ ft$, which is in the outer zone of our " composite" reservoir; recall that $r_1 = 56.4$ feet.. The wellbore pseudopressure derivative clearly indicates the composite nature of our reservoir as it attains one constant value at early time, goes through a transition period, then attains a new constant value at late time. At late time, we also note that the wellbore pseudopressure derivative and the pseudopressure derivative in the outer zone of the composite reservoir are nearly identical. Clearly this supports the validity of Eq. 4.4.10.

In the beginning of our discussion on the real gas pseudopressure, we assumed that the mass flow rate was approximately constant across some "steady-state zone" of radius r_i. In Fig. 4.13, we have plotted the instantaneous mass flow rate across several radii in the reservoir. Fig. 4.13 clearly indicates the existence of such a "steady-state" zone, and indeed, at late time, the mass flow rate is constant even out to a radius of 174 ft. Eq. 4.4.12 is thus verified.

Table 4.6

Reservoir and Fluid Parameters - Case WG-1G

$\phi = 0.2$	$k = 20\ (md)$	$p_i = 2500\ (psia)$
$r_w = 0.25\ (ft)$	$r_1 = 56.4\ (ft)$	$r_e = 20,000\ (ft)$
$h = 40\ (ft)$	$h_w = 40\ (ft)$	$q_g = 10\ (MMscf/D)$
$c_w = 1 \times 10^{-6}\ (psi^{-1})$	$\mu_w = 0.8\ (cp)$	$t_p = 10\ (days)$
k_{rg} = Set 2	k_{rw} = Set 2	
B_g = Set 2	μ_g = Set 2	

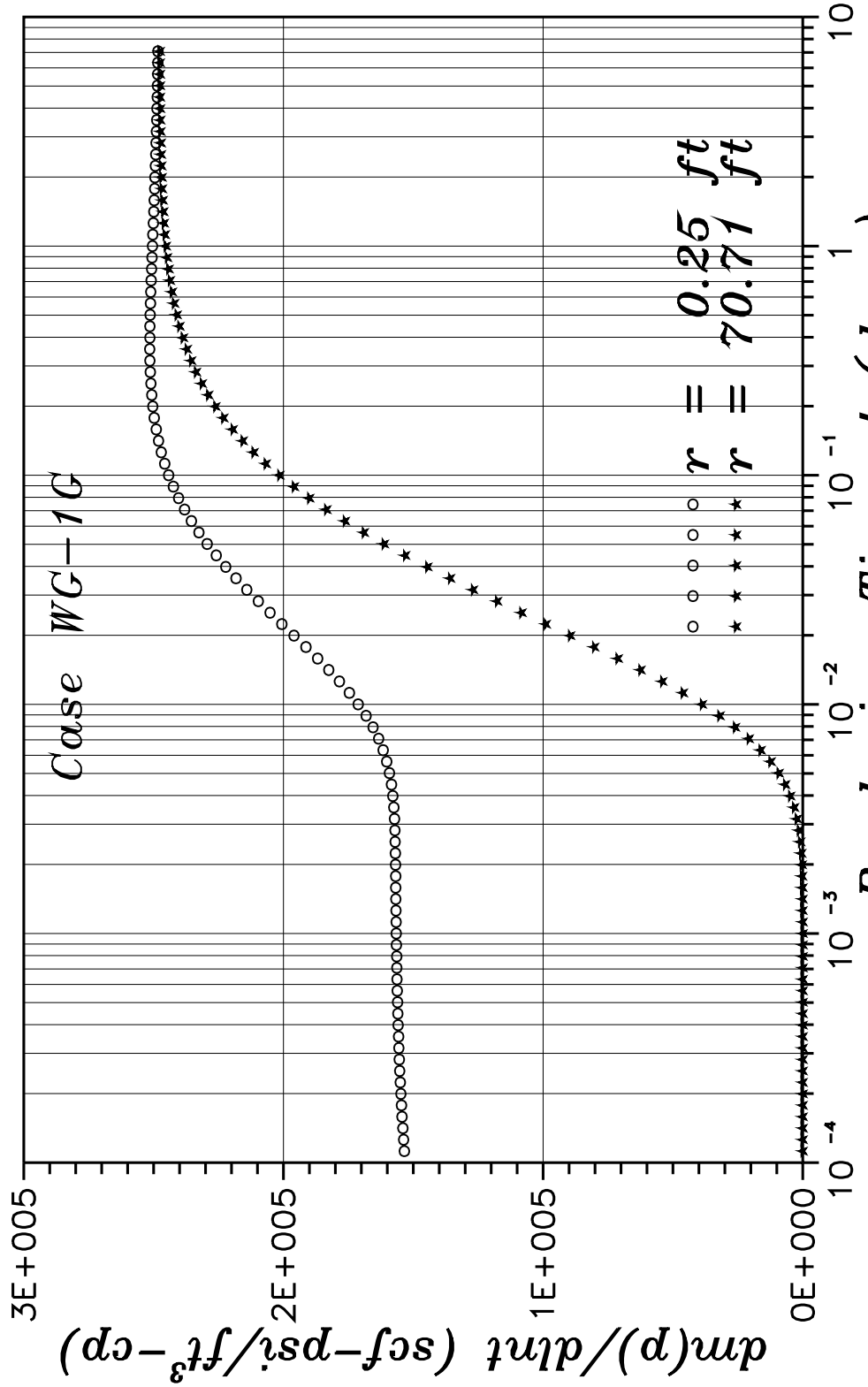

Fig. 4.12 – Diagnostic pseudopressure derivative plot for Case WG-1G.

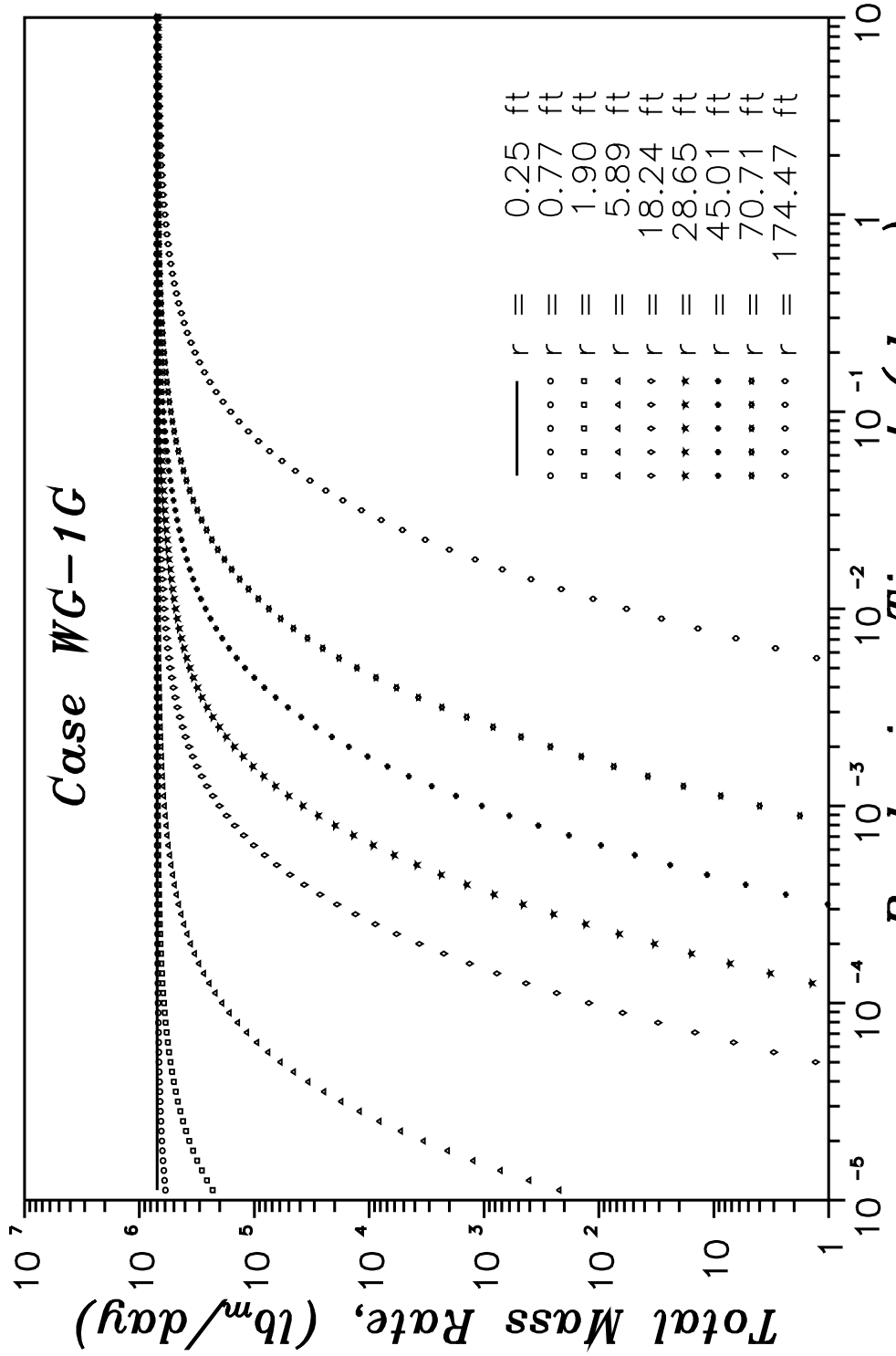

Fig. 4.13 — Total mass flow rate at various radii.

Because of the validity of Eq. 4.4.12, we would, therefore, assume the validity of Eq. 4.4.13. Rearranging Eq. 4.4.13 and substituting effective gas permeability for the absolute permeability, we have

$$\frac{k_{g2}}{\mu_g(p_{wf})} = \frac{70.6 q_g B_g(p_{wf})}{-h dp_{wf}/d\log t} \ . \tag{4.4.14}$$

Figure 4.14 shows the mobility calculated from Eq. 4.4.14, along with the sandface and outer zone mobilities calculated by the simulator. The simulator mobilities are calculated by two methods: method (M1) evaluates the gas viscosity at the initial reservoir pressure, whereas method (M2) evaluates the gas viscosity at the instantaneous wellbore pressure. Method (M2) at $r = r_e$ means that the outer zone value of k_g is used, i.e., $k_g = k_{g2} = k_g(S_w = 1 - S_{wc})$. Figure 4.14 clearly indicates that the gas mobility calculated from Eq. 4.4.14 represents the effective permeability evaluated in the outer region of the reservoir and the gas viscosity evaluated at the wellbore pressure. Since Eq. 4.4.14 is simply a rearrangement of Eq. 4.4.13, this result also indicates the validity of Eq. 4.4.13.

4.5 Multiphase Flow and Fractional Flow Theory

Throughout our discussion on single-phase flow in the previous sections, several assumptions or properties of the analytical solutions have consistently arisen. These include the existence of a "steady-state" zone between the wellbore and some radius, r_i, and for the layered systems, the existence of pseudoradial flow (vertical equilibrium) in the outer region of the reservoir; i.e., at least for $r \geq r_i$.

In the following derivation, we assume a homogeneous and isotropic reservoir and temporarily ignore the effects of gravity and capillary pressure. For the multiphase systems considered in this work, we have assumed Darcy's Law holds individually for each of the phases, i.e.,

$$v_m = -\lambda_m \nabla p \tag{4.5.1}$$

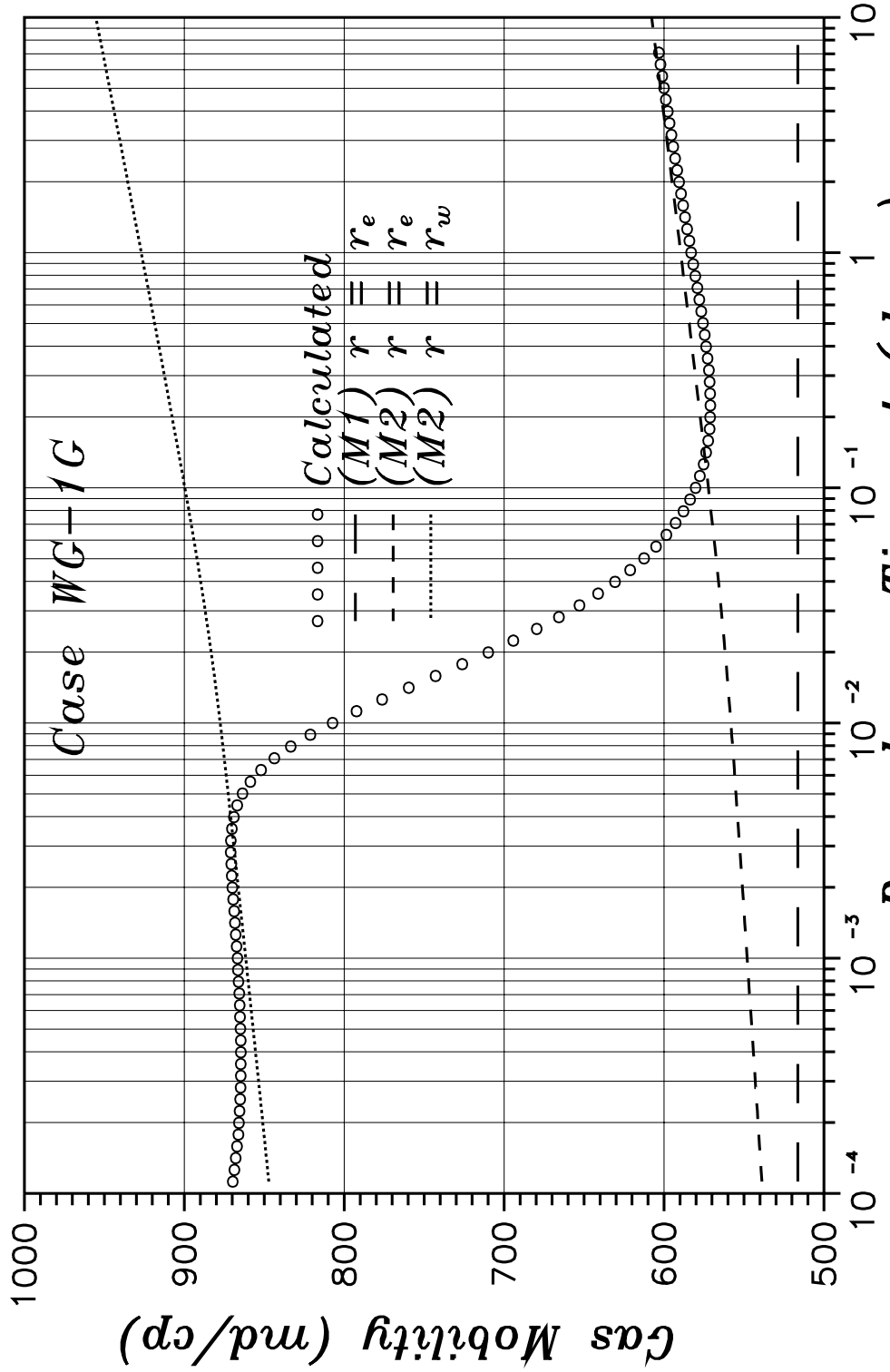

Fig. 4.14 — Gas mobility interpretation plot, Case WG-1G.

where the phase mobility is defined as

$$\lambda_m = \frac{kk_{rm}}{\mu_m} \tag{4.5.2}$$

and the subscript m stands for oil, water or gas. Integrating Eq. 4.5.1 in the theta direction and vertical direction and assuming symmetry in the theta direction we can obtain the volumetric flow rates at any vertical cross-section in the reservoir as

$$q_m = -2\pi r \int_0^h \left(\lambda_m \frac{\partial p}{\partial r} + \lambda_m \frac{\partial p}{\partial z} \right) dz \ . \tag{4.5.3}$$

Under conditions of vertical equilibrium we have $\partial p/\partial z = 0$,or $\partial p/\partial r = f(r)$ only, and so can be removed from under the integrand in Eq. 4.5.3, giving

$$q_m = -2\pi r \frac{\partial p}{\partial r} \int_0^h \lambda_m dz \ . \tag{4.5.4}$$

Multiplying and dividing the right-hand-side of Eq. 4.5.4 by h we obtain

$$q_m = -2\pi h r \frac{\partial p}{\partial r} \frac{1}{h} \int_0^h \lambda_m dz \ . \tag{4.5.5}$$

Recall from Section 4.2 that we have defined the thickness-averaged phase mobilities as

$$\bar{\lambda}_m = \frac{1}{h} \int_0^h \left(\frac{kk_{rm}}{\mu_m} \right) dz \ . \tag{4.5.6}$$

Using Eq. 4.5.6 in Eq. 4.5.5 we have

$$q_m = -2\pi h r \bar{\lambda}_m \frac{\partial p}{\partial r} \ . \tag{4.5.7}$$

Summing the individual flow rates together we obtain

$$q_t = -2\pi h r \bar{\lambda}_t \frac{\partial p}{\partial r} \ , \tag{4.5.8}$$

where the thickness-averaged total mobility, $\bar{\lambda}_t$, is just the sum of the thickness-averaged phase mobilities, i.e.,

$$\bar{\lambda}_t = \bar{\lambda}_o + \bar{\lambda}_w + \bar{\lambda}_g \ . \tag{4.5.9}$$

Finally, solving both Eqs. 4.5.8 and 4.5.7 for $\partial p/\partial r$ and equating, we obtain

$$f_m = \frac{q_m}{q_t} = \frac{\bar{\lambda}_m}{\bar{\lambda}_t} \ . \tag{4.5.10}$$

Equation 4.5.10 states that if vertical equilibrium exists at any cross-section of the reservoir, then the fractional flow rate of each phase across a cylinder of radius r as defined by the volumetric phase flow rates must be equal to the fractional flow rate of that phase as defined by the the thickness-averaged mobilities.

This derivation is readily extended to include the effects of gravity, but only under a very restrictive set of conditions. Inclusion of gravity effects in the foregoing derivation merely requires that we substitute phase potentials for the pressure, and note that under conditions of vertical equilibrium, it is the vertical gradient of the flow potential, not pressure, which must be zero; i.e.,

$$\frac{\partial \Phi_m}{\partial z} = 0 \ , m = o, g, w \ . \tag{4.5.11}$$

Under these conditions, we obtain the same result as before, namely, Eq. 4.5.10.

If we examine the vertical equilibrium condition, Eq. 4.5.11, more closely, however, we see how restrictive this condition really is. Consider for example, an oil-water system in which both fluids co-exist at some location in the reservoir and both fluids are mobile. If vertical equilibrium exists at this location in the reservoir, then Eq. 4.5.11 states

$$\frac{\partial p}{\partial z} + \gamma_o = 0 = \frac{\partial p}{\partial z} + \gamma_w \ , \tag{4.5.12a}$$

or, simplifying, we obtain

$$\gamma_o = \gamma_w \qquad (4.5.12b)$$

where in field units, the phase gravities are defined as

$$\gamma_m = \frac{\rho_m g}{144 g_c} \ , \ m = o, w, g \ . \qquad (4.5.12c)$$

Because Eq. 4.5.12b is not generally satisfied for most oil-water systems and for reservoirs in which capillary pressure effects are negligible, we can state that vertical equilibrium can exist in a multiphase reservoir only if the mobil fluids are fully segregated. Since we know already that the fluids in the reservoirs we are about to investigate will migrate towards the well, the question is not whether or not vertical equilibrium exists, but rather is how close are we to vertical equilibrium and will it affect our results. More so than for comparing pressure gradients within the reservoir, Equation 4.5.10 provides us with a little better physical sense of whether or not vertical equilibrium exists within the reservoir and perhaps provides us a better method for quantifying the closeness to vertical equilibrium. We will utilize Eq. 4.5.10 throughout this study as an indication of where in the reservoir vertical equilibrium may exist and, as important, to identify where it does not exist.

Central to many of the arguments we put forth to explain the pressure response obtained for the multiphase reservoir systems investigated in this study is the classical fractional flow theory, i.e., Buckley-Leverett[117] theory. We, therefore, review the classical theory and examine some of the physical consequences when the assumptions incorporated in the theory approximately hold.

Major assumptions which have typically been incorporated into fractional flow solutions include[118]: (i) one dimensional flow in a homogeneous and isotropic

porous reservoir, (ii) the fluids are incompressible, (iii) gravity and capillarity are negligible, (iv) no fingering, (v) Darcy's law applies, (vi) local equilibrium exists, (vii) the initial distribution of fluids is uniform and (viii) at most, two phases are flowing. Reference 123 notes that even if the fluids are compressible, compressibility effects are negligible if $c\Delta p < 0.01$. Under these assumptions and for the case of water displacing oil in a linear reservoir, the continuity equation for the water phase can be expressed as

$$\frac{\partial S_w}{\partial t} + \frac{q_t}{A\phi}\frac{df_w}{dS_w}\frac{\partial S_w}{\partial x} = 0 \ , \tag{4.5.13}$$

and the velocity of lines of constant saturation follows directly as

$$\left(\frac{dx}{dt}\right)_{S_w} = \frac{q_t}{A\phi}\frac{df_w}{dS_w} \ . \tag{4.5.14a}$$

Equation 4.5.14a states that the velocity of a constant saturation S_w is equal to a constant $(q_t/A\phi)$ times the derivative or slope of the fractional flow curve at that saturation. A dimensionless saturation velocity, or specific velocity[123] for that saturation, may be obtained from Eq. 4.5.14a by dividing through by $(q_t/A\phi)$, giving

$$\hat{v}_{S_w} = \frac{A\phi}{q_t}\left(\frac{dx}{dt}\right)_{S_w} = \left(\frac{df_w}{dS_w}\right)_{S_w} \ . \tag{4.5.14b}$$

It is well known (e.g., see Ref. 119) that direct integration of Eq. 4.5.14 may result in the physically unreal solution of saturation being triple-valued at some locations within the reservoir. Many authors (e.g., Ref. 118-121) have shown through the use of the method of characteristics that the true physical interpretation to the triple-value lies in the formation of a saturation "shock" when characteristics of constant saturation intersect; i.e., through the simultaneous use of the method of characteristics and the concept of shock formation, solutions to

the fractional flow equations are obtained for which the saturation is uni-valued at all locations within the reservoir. The interpretation of a saturation shock is that it represents a discontinuity in the saturation at the location of the shock front. Though under the displacement process in porous media this saturation "shock" must in reality be a finite region of rapid saturation transition[121] since some dissipation (e.g., diffusion, dispersion, compressibility and capillary pressure) is always present, we will use the term to distinguish between saturation discontinuities caused through the displacement process itself, and those that merely exist in the reservoir due to gravity and capillary segregation and equilibrium. Reference 123 notes that when such dissipative effects are present, the shocks are smeared or spread out around the shock front position, but that the position of the shock remains unaltered.

Through material balance considerations across the saturation shock, the velocity of the shock or saturation discontinuity may be expressed as

$$v_{\Delta S_w} = \left(\frac{dx}{dt}\right)_{S_w} = \frac{q_t}{A\phi}\left(\frac{f_{w+} - f_{w-}}{S_{w+} - S_{w-}}\right) , \qquad (4.5.15a)$$

where the subscripts - and + refer to values ahead of (downstream direction), and behind (upstream direction) the shock, respectively. Equation 4.5.15a states that the velocity of the saturation shock is equal to a constant $(q_t/A\phi)$ times the slope of a straight line passing through the points (S_{w-}, f_{w-}) and (S_{w+}, f_{w+}) on the fractional flow curve. Again, a dimensionless velocity or specific velocity may be obtained for the saturation shock by dividing Eq. 4.5.15a through by $(q_t/A\phi)$, thereby obtaining

$$\hat{v}_{\Delta S_w} = \frac{A\phi}{q_t}\left(\frac{dx}{dt}\right)_{S_w} = \left(\frac{f_{w+} - f_{w-}}{S_{w+} - S_{w-}}\right) . \qquad (4.5.15b)$$

Note that Eq. 4.5.14 gives the velocity of lines of constant saturation, whereas Eq. 4.5.15 gives the velocity of the saturation shock; i.e., the particular saturation

S_{w+} that results in material balance being satisfied across the saturation shock. In general, the saturation at which the maximum saturation velocity obtained from Eq. 4.5.14 occurs is not the same as the saturation at which the maximum velocity given by Eq. 4.5.15 occurs; i.e., for a given fractional flow curve and a given downstream saturation (S_{w-}), the maximum velocity calculated from Eq. 4.15.14 will in general not be equal to the maximum velocity (the velocity of the saturation shock) calculated from Eq. 4.5.15. Figure 4.15 shows this more clearly for an oil-water reservoir system to be discussed shortly. Figure 4.15 shows the fractional flow curve for this case with the maximum slope of the fractional flow curve indicated as well as the slope of a tangent line drawn from the downstream fractional flow value and saturation (S_{w-}, f_{w-}) to the upstream fractional flow value and saturation (S_{w+}, f_{w+}). Note that for a given downstream saturation, the maximum specific shock velocity calculated from Eq. 4.5.15b represents the maximum slope for all lines drawn from the downstream saturation and fractional flow value (S_{w-}, f_{w-}) to all other points on the fractional flow curve for which $S_w > S_{w-}$. The point on the fractional flow curve where this line of maximum slope intersects the fractional flow curve represents the conditions at the saturation shock, or the upstream values (S_{w+}, f_{w+}) as indicated in Fig. 4.15.

For a one-dimensional cylindrical (radial) reservoir with a producing well located at the center and displacement occurring in the direction of the well, it is readily shown[122] that the analogous fractional flow equations may be written as

$$\frac{\partial S_w}{\partial t} + \frac{q_t}{2\pi r h \phi}\frac{df_w}{dS_w}\frac{\partial S_w}{\partial r} = 0 \ , \tag{4.5.16}$$

for the continuity equation of water, and

$$\left(\frac{dr}{dt}\right)_{S_w} = \frac{q_t}{2\pi r h \phi}\frac{df_w}{dS_w} \ . \tag{4.5.17a}$$

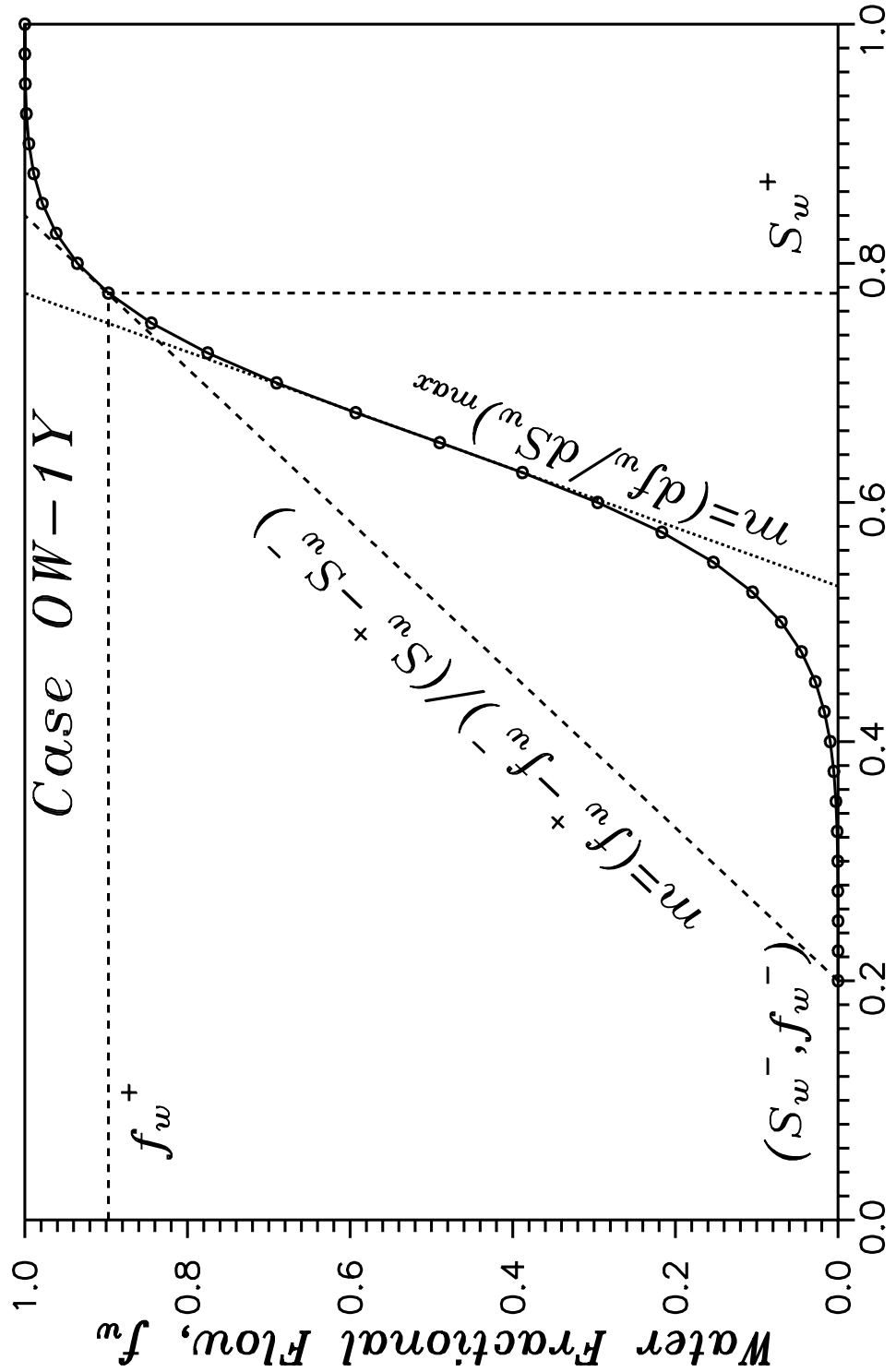

Fig. 4.15 — Fractional flow curve and definitions used in calculation of saturation and front velocities.

for the velocities of lines of constant saturation. As with the linear case, a specific saturation velocity can be obtained from Eq. 4.5.17a by dividing through by $(2\pi rh\phi/q_t)$, resulting in

$$\hat{v}_{S_w} = \frac{2\pi rh\phi}{q_t}\left(\frac{dr}{dt}\right)_{S_w} = \left(\frac{df_w}{dS_w}\right)_{S_w} \quad . \tag{4.5.17b}$$

The velocity of a saturation shock for this radial system can also be obtained as

$$v_{\Delta S_w} = \left(\frac{dr}{dt}\right)_{S_w} = \frac{q_t}{2\pi rh\phi}\left(\frac{f_{w+} - f_{w-}}{S_{w+} - S_{w-}}\right) , \tag{4.5.18a}$$

where, again, the subscripts - and + refer to values ahead of (downstream direction), and behind (upstream direction) the shock, respectively. The shock specific velocity can be expressed as

$$\hat{v}_{\Delta S_w} = \frac{2\pi rh\phi}{q_t}\left(\frac{dr}{dt}\right)_{S_w} = \left(\frac{f_{w+} - f_{w-}}{S_{w+} - S_{w-}}\right) , \tag{4.5.18b}$$

Of importance to us in this current study is the pressure behavior at the producing well in a reservoir undergoing an immiscible displacement. To investigate this, we consider a one-dimensional radial reservoir with a fully-penetrating well located at the center of the reservoir and produced at a constant rate. The reservoir is homogeneous, isotropic and contains only oil and water, with the water initially at irreducible water saturation, i.e., $S_w = 0.2$. The reservoir is 20 feet in height and has an external radius of 100 feet. Both the oil and water are considered to be slightly compressible fluids of constant compressibility and constant viscosity with these properties the same as for the oil-water cases listed in Table 4.1 (except for case OW-1W discussed below). The Set 1, two-phase oil-water relative permeability curves are used for case OW-1X and case OW-1Y, and the Set 3 (straight-line) relative permeability curves are used for cases OW-1W and

OW-1Z. Other differences in these case are as follows: for all of the cases, the outer boundary of the reservoir is modeled as a constant pressure boundary at the initial reservoir pressure of 3600 psia; for case OW-1X, the saturation at the outer boundary is the same as the initial reservoir saturation, i.e., $S_w = 0.2$; for cases OW-1W, OW-1Y and OW-1Z, the outer boundary water saturation is held constant at $S_w = 1.0$.

Given relative permeability curves and the viscosities of oil and water, we can readily calculate the fractional flow curves for each of these cases from

$$f_w(S_w) = \frac{\lambda_w}{\lambda_w + \lambda_o} \ . \tag{4.5.18}$$

Figure 4.16 shows the water fractional flow curves for three different cases: the first case (case OW-1Y) uses the Set 1 relative permeability curves and the viscosities given in Table 4.1 (viscosity ratio of $\mu_o/\mu_w = 1.25$); the second case (case OW-1Z) uses the Set 3 (straight-line) relative permeability curves and the same viscosities; the third case (case OW-1W) uses the Set 3 relative permeability curves and a viscosity ratio of $\mu_o/\mu_w = 0.56$. The fractional flow curve for case OW-1Y has the familiar S-shape typically associated with Buckley-Leverett-type displacements. Note that the fractional flow curve for case OW-1Z is slightly concave downward and does not have an inflection point. This is due to the oil-water viscosity ratio being greater than one and precludes the formation of a saturation shock. For a viscosity ratio equal to one, the fractional flow curve would have been a straight line (recall for this case, straight-line relative permeabilities are being used) and also not form a saturation shock. The fractional flow curve for case OW-1W is everywhere concave upwards and represents the case of forming a complete shock;[123] i.e., a shock can develop over the entire possible saturation range.

Figure 4.17 shows the derivative of the fractional flow curve (i.e., specific velocities of lines of constant saturation), the specific velocities of the shock front

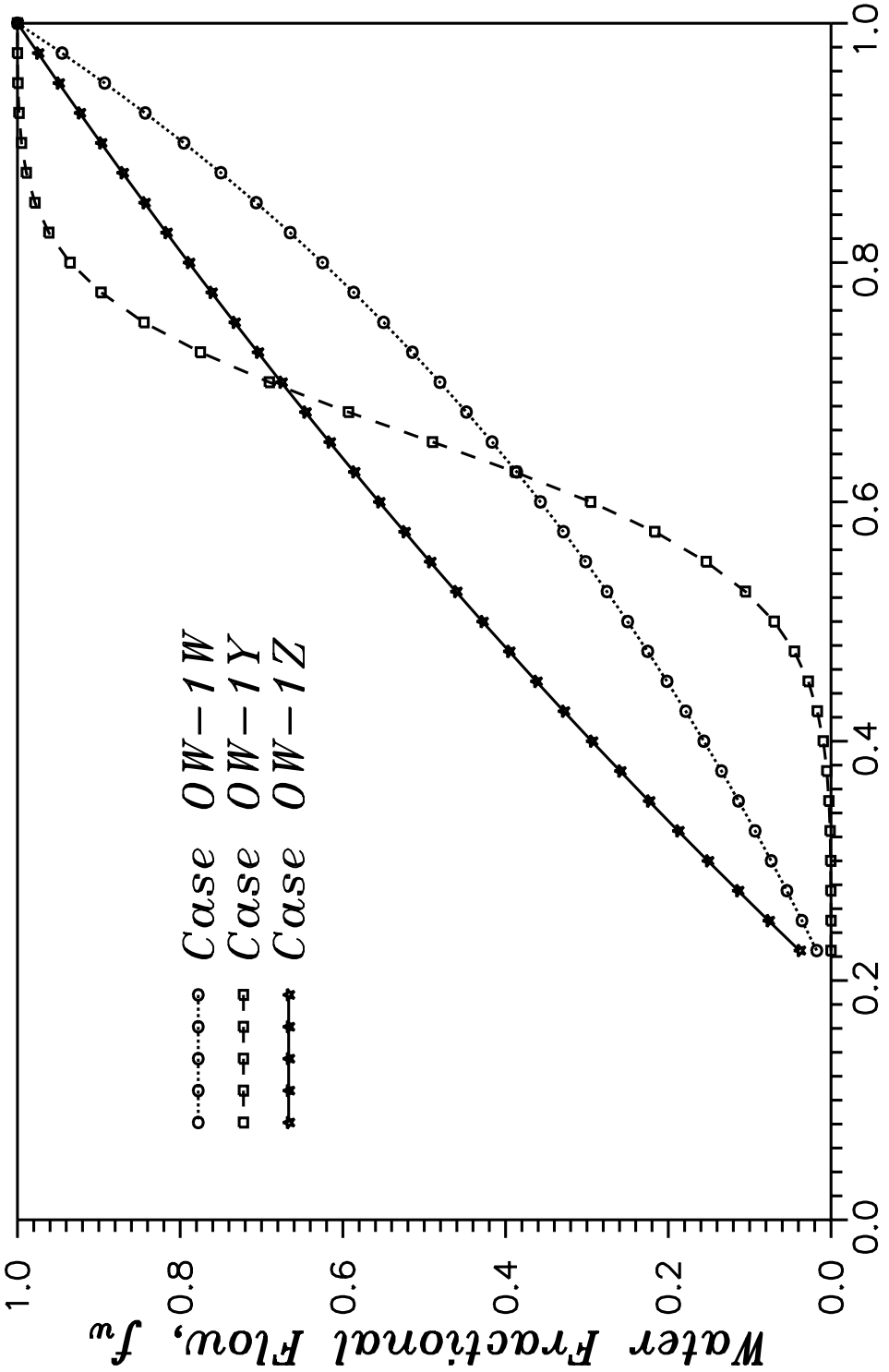

Fig. 4.16 — Fractional flow curves for Cases OW−1Y, OW−1Z and OW−1W.

(Eq. 4.5.15b) and the total relative mobility, λ_{rt}, as a function of water saturation for case OW-1Y. Here, the total relative mobility is defined as

$$\lambda_{rt} = \frac{k_{ro}}{\mu_o} + \frac{k_{rw}}{\mu_w} \ . \tag{4.5.19}$$

Figure 4.17 shows the maximum specific velocity for any saturation occurs at a saturation of $S_w = 0.675$, whereas the maximum specific velocity for a shock front for this case occurs at a saturation of $S_w = 0.775$. Figure 4.17 also shows the minimum total relative mobility occurs at a saturation of $S_w = 0.675$, the same as the maximum saturation velocity. If a shock front actually existed in the reservoir, then material balance considerations across the shock would indicate that the maximum saturation velocity must occur at the shock and is in fact that velocity calculated from Eq. 4.5.15. Because the minimum total mobility occurs at a saturation encompassed by the downstream and upstream values of saturation at the shock, this then implies that the minimum total mobility in this one-dimensional reservoir must also exist at the location of the shock. Note also that behind the shock, the total mobility monotonically increases as the water saturation increases.

Figure 4.18 is similar to Fig. 4.17, except here we show the saturation velocity, velocity of the shock front (Eq. 4.5.15b) and total relative mobility for case OW-1Z. Notice here that the maximum saturation velocity and maximum shock velocity (fictitious shock velocity since no shock will actually form for this case) coincide as we approach the residual water saturation ($S_w = 0.2$). This is also the saturation at which the minimum total relative mobility occurs. Figure 4.18 indicates that the maximum saturation velocity and minimum total relative mobility will always occur at the location of the minimum water saturation existing in the reservoir, and for the simple radial case being considered here, that will always be at the production well. Note that the total relative mobility must

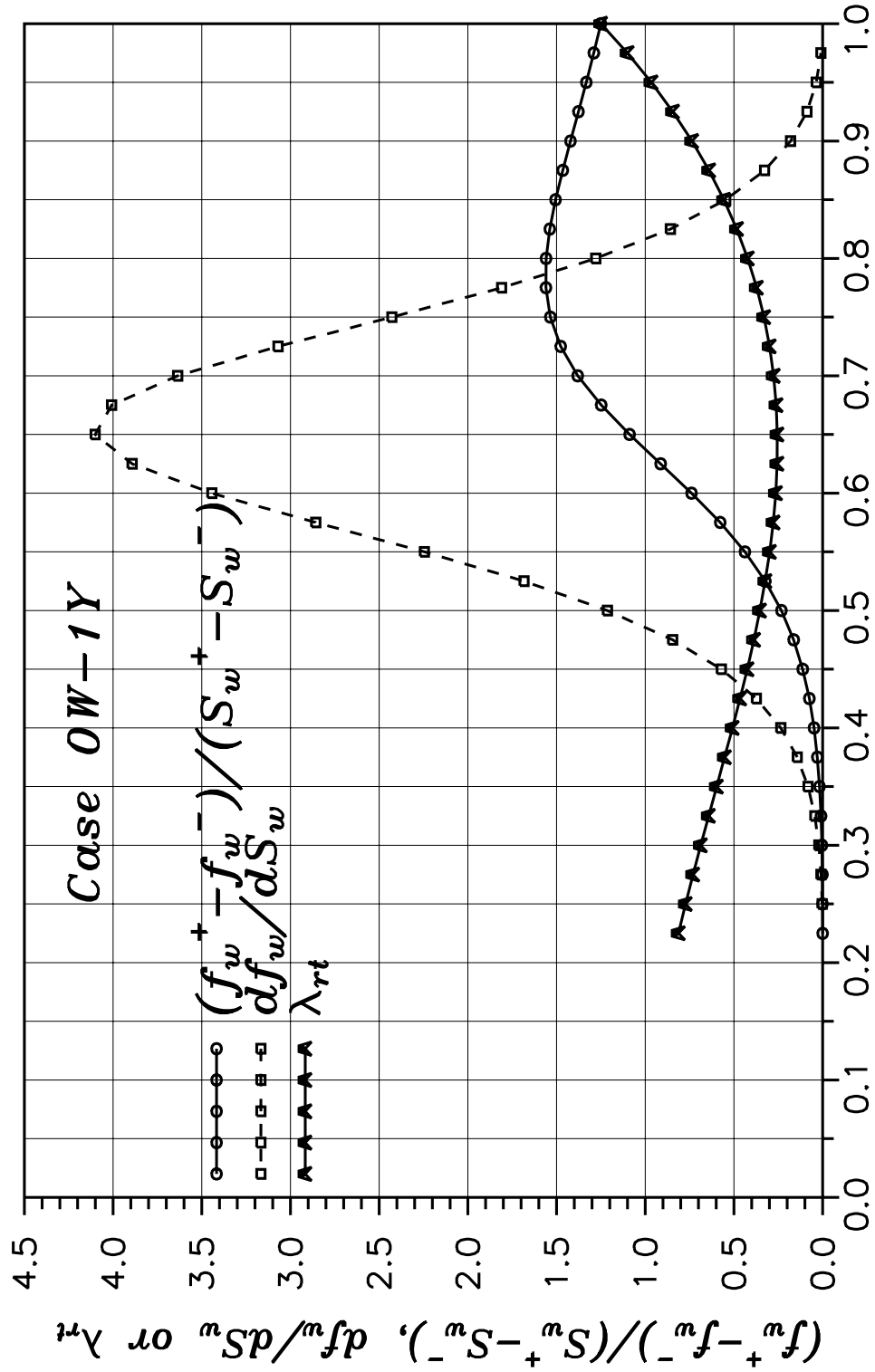

Fig. 4.17 – Relationship between velocity of constant saturation lines and total mobility.

continuously increase as the water saturation increases due to influx from the outer boundary.

Figure 4.19 shows the saturation velocity, velocity of the shock front and the total mobility for case OW-1W. For this case, Fig. 4.19 shows the maximum saturation velocity and maximum shock velocity both occur at the maximum water saturation, which is also the location of the minimum total mobility. Figure 4.18 indicates that the total mobility will decrease for any increase in the water saturation and that the maximum saturation velocity and minimum total relative mobility will always occur at the location of the maximum water saturation existing in the reservoir and for the case being considered here, that will always be at the external radius of the reservoir.

Prior to looking at the pressure response for the producing well, we examine the in-situ flow rates and saturation profiles to insure the assumptions of the fractional flow theory are being approximately met for this case. Figure 4.20 shows the in-situ oil, water and total volumetric flow rates within the reservoir for case OW-1Y at a time of 63.10 days. This figure clearly shows the total reservoir flow rate is essentially constant throughout the reservoir and in fact varies only from 193.47 RB/day at the well to 193.06 RB/day at the outer boundary. For an oil compressibility of $c_o = 1 \times 10^{-5}$ psi^{-1} and the maximum pressure drop of 574 psi for this case, $c_o \Delta p = 0.005$ which is below the value of 0.01 indicated by Ref. 123 to be necessary for compressibility effects to be negligible. Note that this compressibility and pressure drop results in a change in the oil density of approximate 0.5 percent from the initial density.

Figure 4.21 shows the saturation profile in the reservoir at various times for case OW-1Y. Here we clearly see the sharp saturation front typically associated with Buckley-Leverett[117] theory and consistent with the concept or formation of

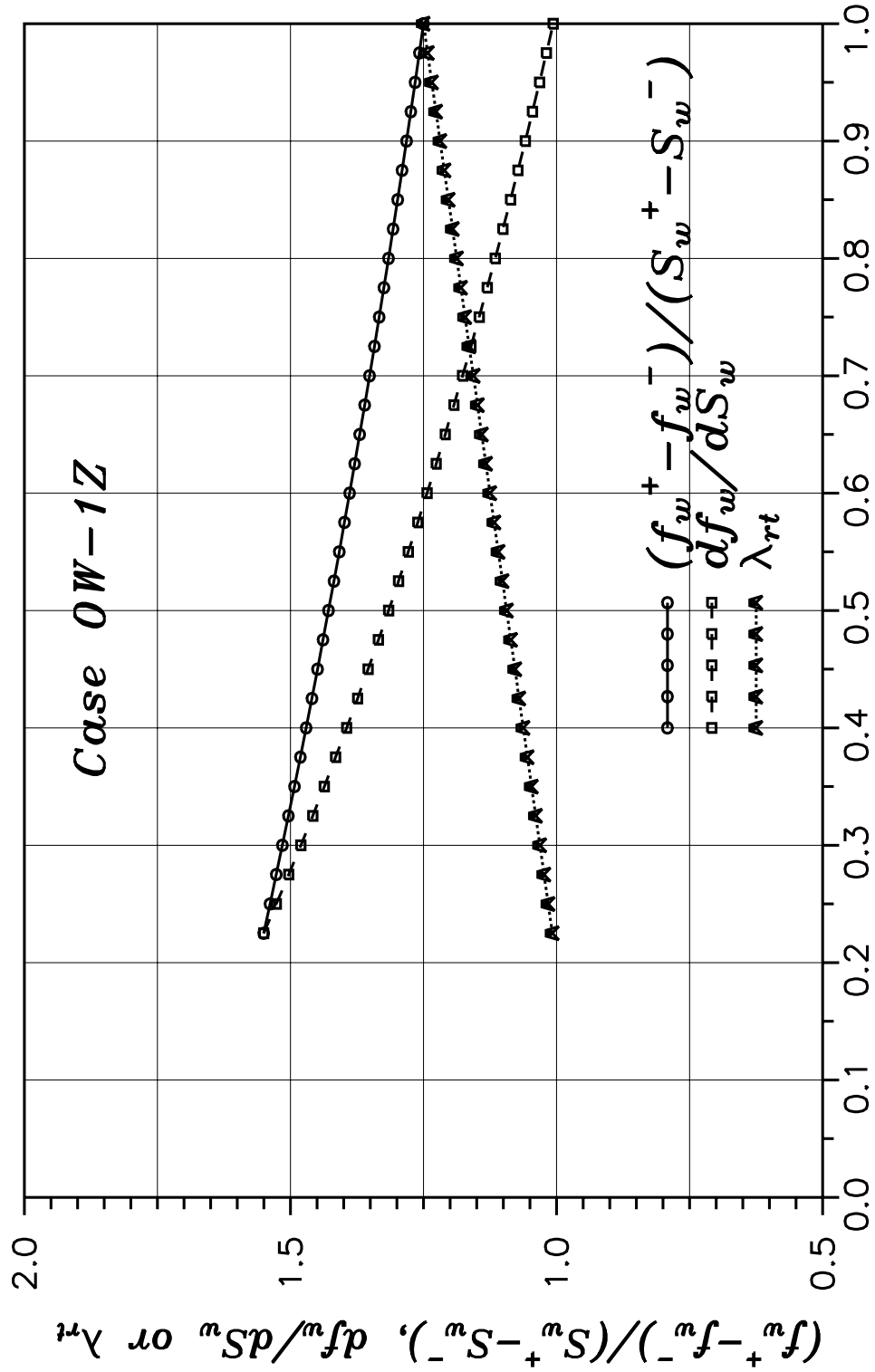

Fig. 4.18 – Relationship between velocity of constant saturation lines and total mobility.

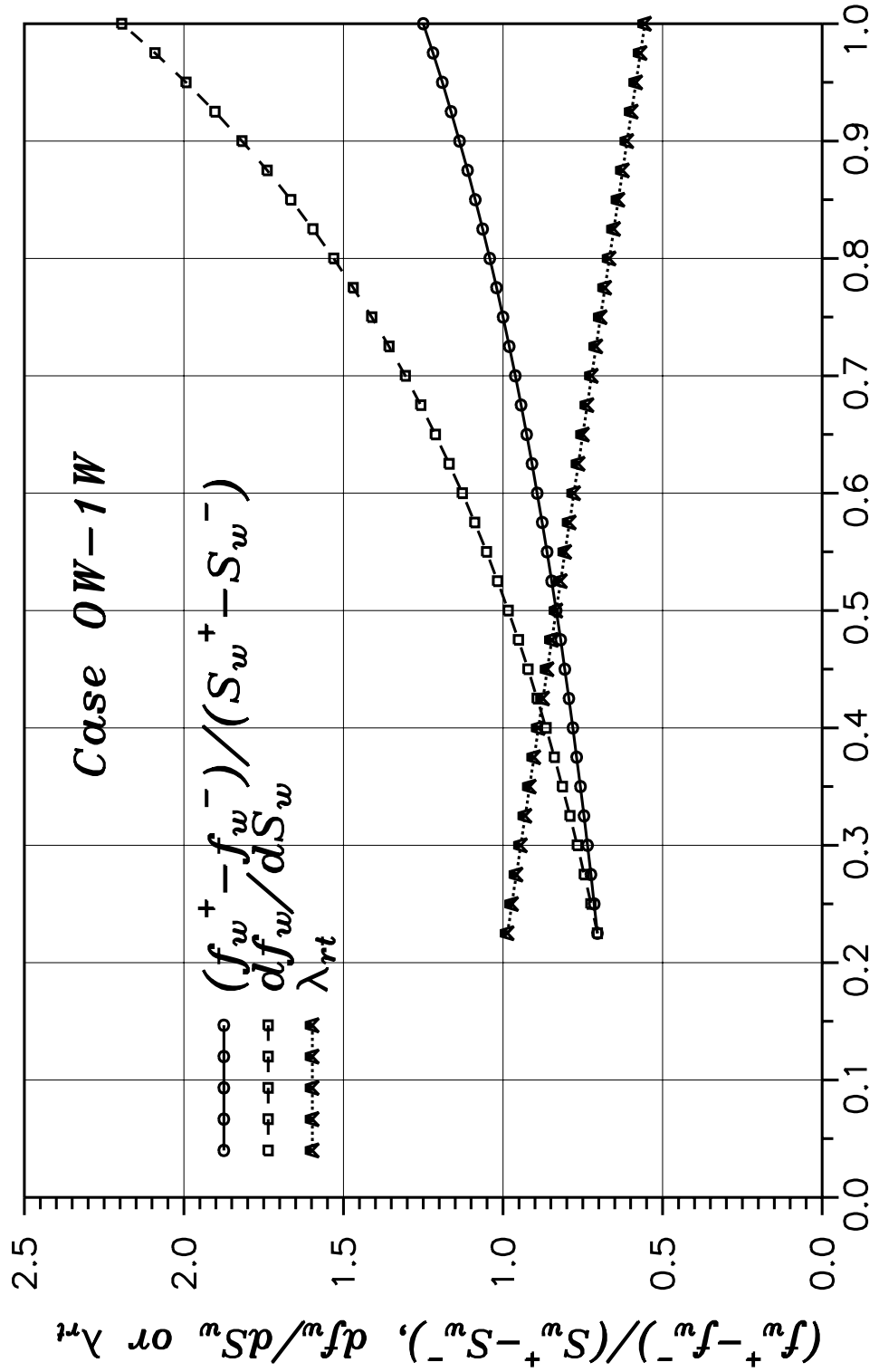

Fig. 4.19 — Relationship between velocity of constant saturation lines and total mobility.

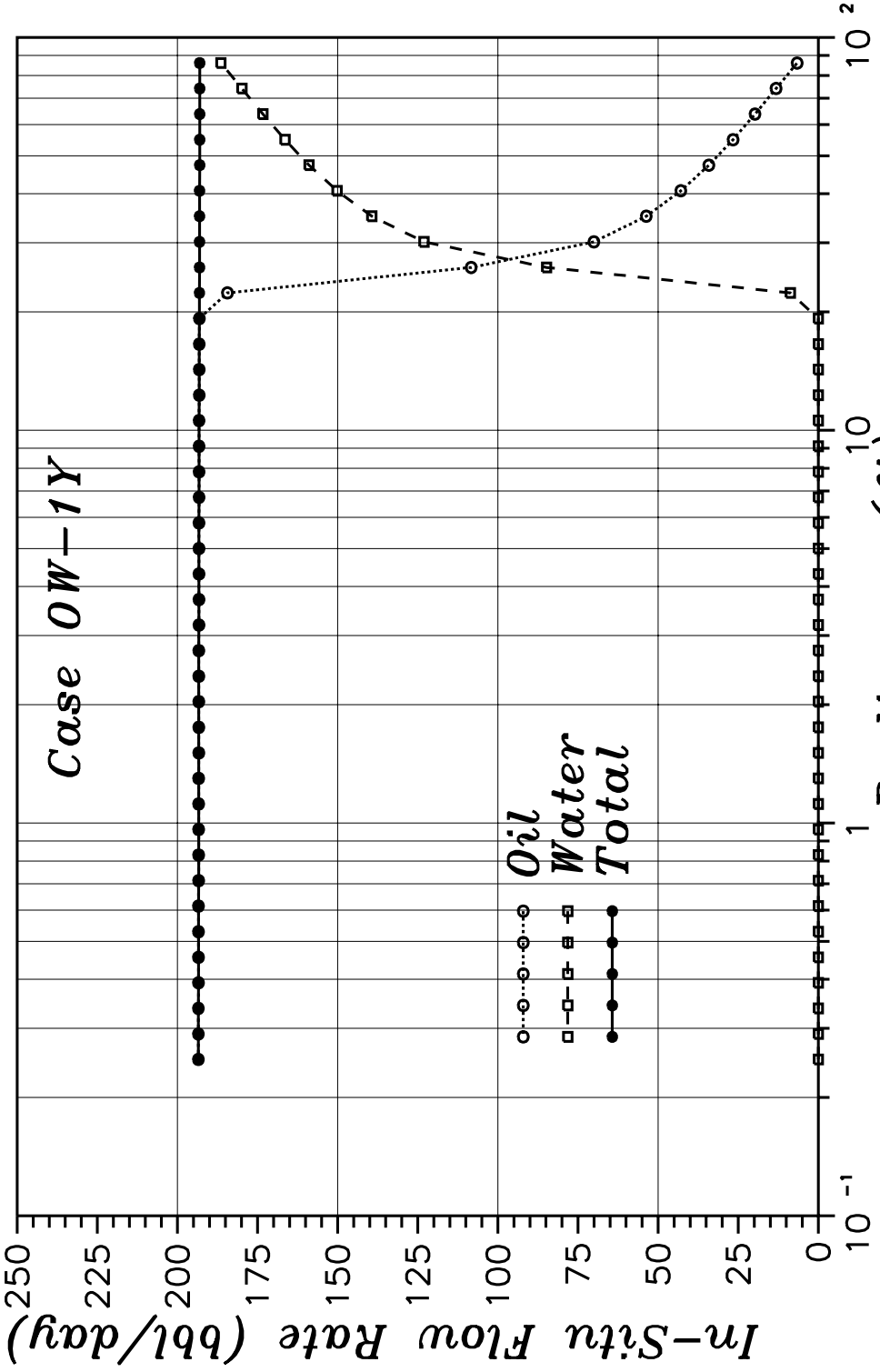

Fig. 4.20 – In-situ flow rates for Case OW-1Y.

a saturation shock. Notice that the water saturation at the trailing edge of the saturation front is $S_w \approx 0.73$, which is slightly less than the front saturation ($S_w = 0.775$) predicted by fractional flow theory (see Fig. 4.15). As noted earlier, we expect there to be some smearing or spreading our of the the saturation front around the shock front position due to various dissipative effects. For the particular case being examined here, we attribute the slight difference in the predicted and simulated front saturation to be due to the effects of numerical dispersion in our simulator. For the numerical approximations incorporated in our simulator, i.e., fully-implicit time approximations with upstream weighting of relative permeabilities, Ref. 47 has shown that the numerical dispersion effects are directly proportional to the time step size and the size of the grid blocks. In other words, the effects of numerical dispersion can be minimize by reducing the time step size and the grid block size. Numerical results not shown indicate that we could indeed reduce the difference between the predicted and simulated saturation at the saturation front by decreasing the time step size used and increasing the number of radial grids employed; i.e., reducing the grid block size. Because we are primarily interested in the pressure behavior of the producing well under these immiscible displacement processes, the current accuracy obtained using 40 radial grid blocks and a maximum time step size of 0.1 days (.01 days near water breakthrough) was considered to be sufficient for our purposes.

Unlike case OW-1Y, the saturation profile for case OW-1Z (Fig. 4.22) shows no sharp saturation fronts, and in fact, shows the saturation increasing at nearly the same rate throughout much of the reservoir. A similar saturation profile was reported by Ref. 122 for a conceptually similar problem. As discuss before, fractional flow theory also predicts that a sharp saturation front will not develop for this case.

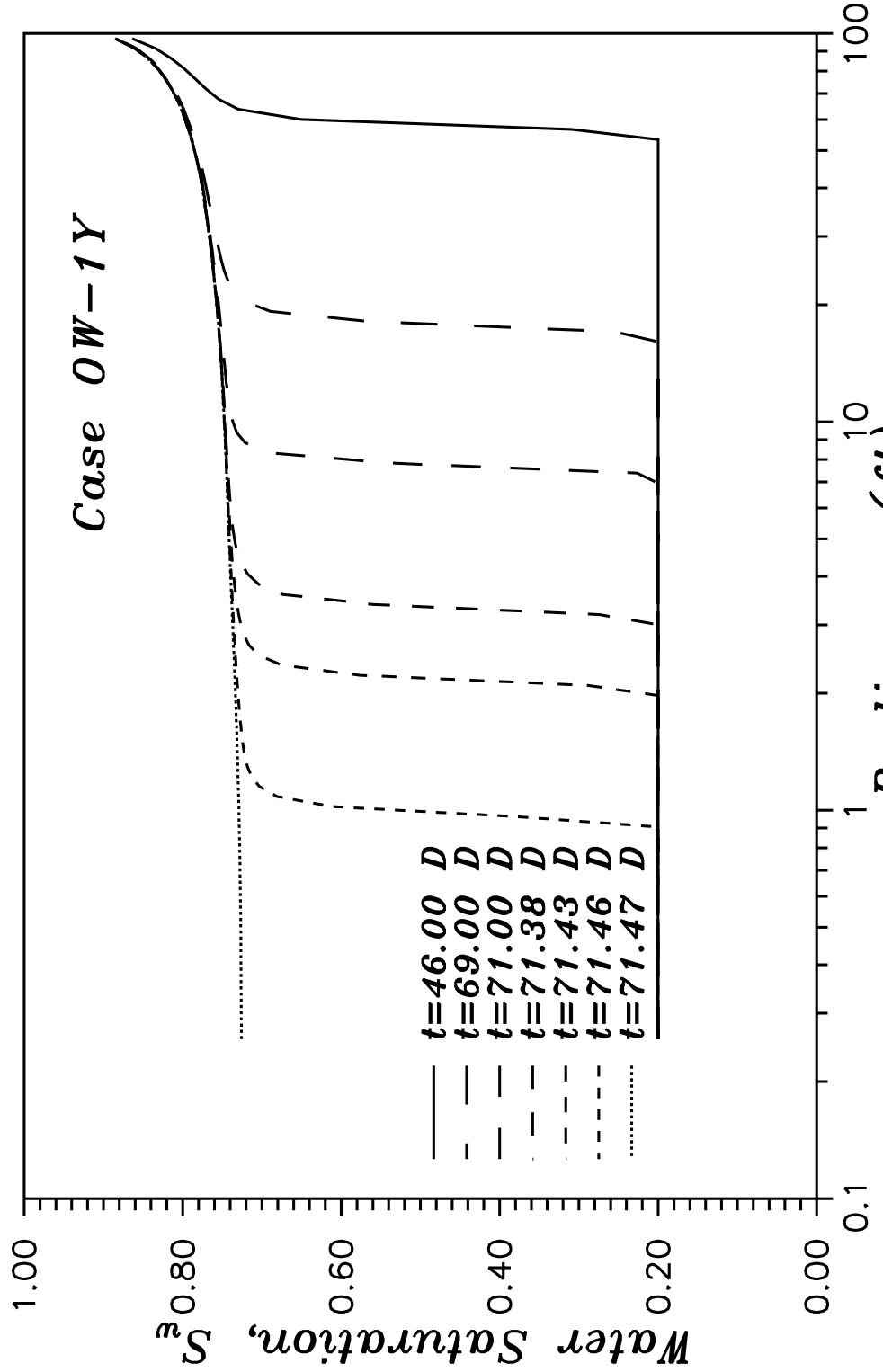

Fig. 4.21 – Saturation profile at various times for Case OW-1Y.

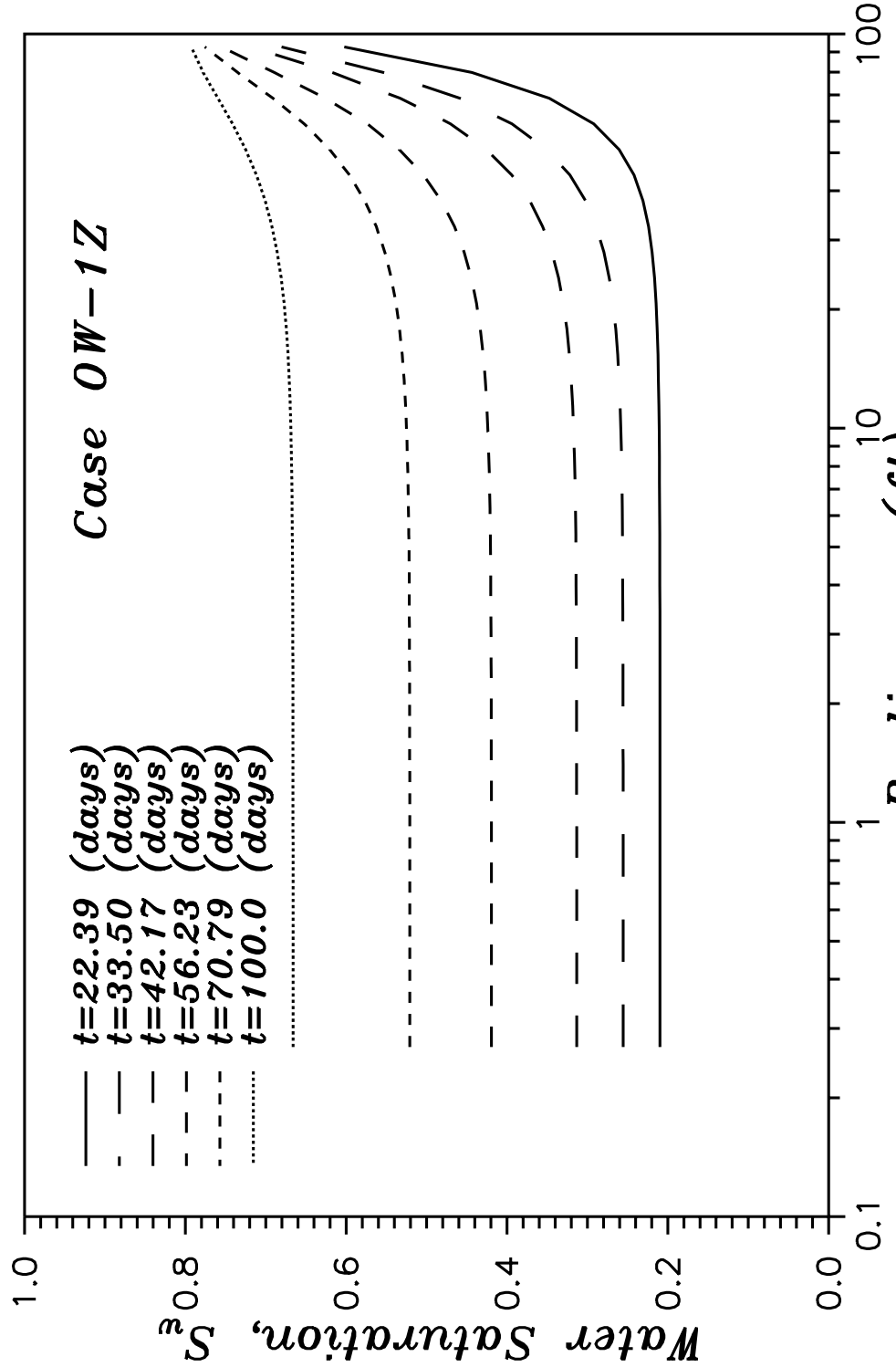

Fig. 4.22 – Saturation profile at various times for Case OW-1Z.

The logarithmic derivatives of the wellbore pressure with-respect-to producing time for each of the cases OW-1W, OW-1X, OW-1Y and OW-1Z are shown in Fig. 4.23. Figure 4.23 shows that the log-derivative of the wellbore pressure for each of the cases is approximately constant until the constant pressure outer boundary is "felt," at which time the derivatives for all of the cases show a dramatic falloff. The log-derivative of pressure for case OW-1X continues to decrease, monotonically decreasing towards zero. The log-derivative of the wellbore pressure for case OW-1Z also continues to decrease, becoming quite negative before monotonically increasing towards zero. For cases OW-1Y and OW-1W, Fig. 4.23 shows the log-derivative of the wellbore pressure initially falls off rapidly once the outer boundary is felt, but as the water begins to influx into the reservoir and the saturation front begins to form, the log-derivative begins to increase. The log-derivative of the wellbore pressure for these two cases continues to increase until water breakthrough at the producing well. Following water breakthrough, the log-derivative monotonically decreases toward zero for case OW-1W. For case OW-1Y, the log-derivative of the wellbore pressure becomes negative following water breakthrough and then monotonically increases towards zero.

Reference 149 recently presented a derivation for the drawdown pressure transient response in a one-dimensional, infinite, radial gas condensate reservoir produced under a constant molar rate from a fully-penetrating well. That derivation showed that the drawdown pressure derivative (with respect to producing time) was a function of the time rate of change in the total molar flow rate in the reservoir and the time rate of change in a total mobility-density product. Reference 149 also showed that the theoretical results could be used to explain the difference between the drawdown and buildup responses. The resultant theoretical expression obtained by Ref. 149 provides a basis for explaining the results obtained above. To fully understand the pressure responses for these oil-water cases, we

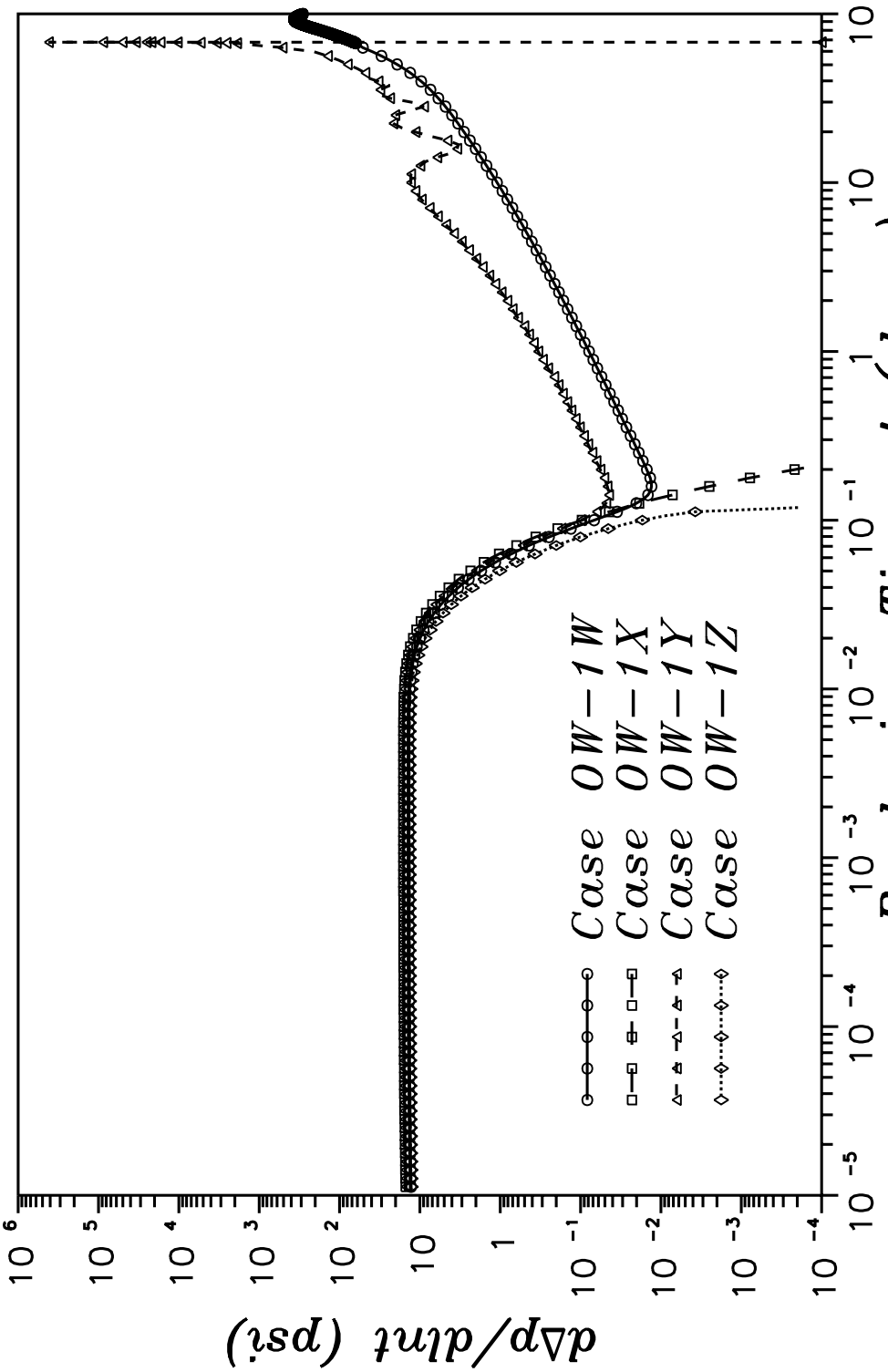

Fig. 4.23 – Pressure derivative response for different fractional flow curves.

utilize a similar derivation here to obtain the pressure derivative response for a fully-penetrating well, centrally located in a finite one-dimensional radial reservoir of radial extent r_e with the outer boundary maintained at a constant pressure and saturation. The only real difference between this derivation and the derivation of Ref. 149 is that we consider the total reservoir volumetric flow rate, whereas Ref. 149 considered the total reservoir molar flow rate. It can be readily shown, however, that the end result of the two derivations are equivalent. For the purposes of the derivation to be presented here, we consider the reservoir to be homogeneous, isotropic and of uniform thickness throughout. Though heterogeneous reservoirs are not considered here, they may be readily included in the derivation as shown by Ref. 149.

We begin the derivation by assuming, as we have throughout this work, that Darcy's Law is valid at every point in the reservoir. Under this assumption, we can express the total reservoir flow rate at any point in the reservoir as

$$q_t(r,t) = C_2 kh \lambda_{rt}(r,t) r \frac{\partial p(r,t)}{\partial r} \quad , \tag{4.5.20}$$

where C_2 is a units conversion factor given by $C_2 = 2\pi(1.127 \times 10^{-3})$ and λ_{rt} is the total relative mobility defined for three-phase systems by

$$\lambda_{rt} = \frac{k_{ro}}{\mu_o} + \frac{k_{rw}}{\mu_w} + \frac{k_{rg}}{\mu_g} \; . \tag{4.5.21}$$

Solving Eq. 4.5.20 for the pressure gradient, integrating the resultant expression from the wellbore radius to the external radius of the reseroir and recalling that the pressure at the outer boundary of the reservoir is at a constant pressure equal to the initial reservoir pressure (i.e., $p(r_e) = p_i$), we obtain

$$\Delta p(t) = p_i - p_{wf}(t) = \frac{1}{C_2 kh} \int_{r_w}^{r_e} \left[\frac{q_t(r',t)}{\lambda_{rt}(r',t)} \right] \frac{dr'}{r'} \quad . \tag{4.5.22}$$

Equation 4.5.22 is a completely general expression for the wellbore pressure response at any time. Note that Eq. 4.5.22 is equally valid for single or multiphase reservoir systems. We will refer to Eq. 4.5.22 as the general pressure response equation.

Lastly, differentiating Eq. 4.5.22 with-respect-to the natural logarithm of time, we obtain the following expression for the log-derivative of the wellbore pressure:

$$\frac{d\Delta p(t)}{d\ln t} = \frac{-dp_{wf}(t)}{d\ln t} = \frac{t}{C_2 kh}\int_{r_w}^{r_e}\left[\frac{1}{\lambda_{rt}(r',t)}\frac{\partial q_t(r',t)}{\partial t} - \frac{q_t(r',t)}{{\lambda_{rt}}^2(r',t)}\frac{\partial \lambda_{rt}(r',t)}{\partial t}\right]\frac{dr'}{r'} \quad . \tag{4.5.23}$$

Equation 4.5.23 indicates that the wellbore pressure response is a function of the time rate of change in the total volumetric flow rate and the time rate of change in the total relative mobility over the entire reservoir. We note that an identical expression could be obtained for the wellbore pressure response for a fully-penetrating well in an infinite acting, 1-D radial homogeneous and isotropic reservoir. We will refer to Eq. 4.5.23 as the general pressure derivative equation.

We now seek to explain the pressure derivative responses shown in Fig. 4.23 through the use of the general pressure derivative equation (Eq. 4.5.23) and the fluid and rock properties for each case. Recall that case OW-1X conceptually represents the single-phase, constant pressure boundary problem, with only the oil phase being mobile. The pressure response for this case OW-1X monotonically decreases to zero once the constant pressure boundary was "felt" at the wellbore. This is precisely what one would expect based on single-phase flow theory. Note that only the oil phase is mobile for this case and we, therefore, have

$$\frac{\partial \lambda_{rt}(r,t)}{\partial t} = 0 \quad . \tag{4.5.24}$$

Utilizing Eq. 4.5.24, we can simplify Eq. 4.5.23 to obtain

$$\frac{d\Delta p(t)}{d\ln t} = \frac{-dp_{wf}(t)}{d\ln t} = \frac{t}{C_2 k h \lambda_{rt}} \int_{r_w}^{r_e} \left[\frac{\partial q_t(r',t)}{\partial t}\right] \frac{dr'}{r'} \quad . \tag{4.5.25}$$

Equation 4.5.25 indicates that the wellbore pressure derivative response for this single-phase problem is only a function of how the flow rate in the reservoir changes with-respect-to time. During early time, or until true steady-state is reached, the flow rate in the reservoir will continue to increase and we will have

$$\frac{\partial q_t(r,t)}{\partial t} > 0 \quad , \quad t < t_{ss} \quad . \tag{4.5.26}$$

By Eq. 4.5.25, the result of Eq. 4.5.26 indicates that the log-derivative of the wellbore pressure will remain positive until true steady-state is reached; i.e.,

$$d\Delta p(t)/d\ln t > 0 \quad , \quad t < t_{ss} \quad . \tag{4.5.27}$$

Now note that at late time the flow rate in the reservoir will approach the sandface flow rate,

$$q_t(r,t) \rightarrow q_t(r_w,t) = \text{constant} \quad , \quad t \rightarrow t_{ss} \quad , \tag{4.5.28}$$

or

$$\frac{\partial q_t(r,t)}{\partial t} \rightarrow 0 \quad , \quad t \rightarrow t_{ss} \quad , \tag{4.5.29}$$

which, by Eq. 4.5.25, indicates that the log-derivative of the wellbore pressure will approach zero

$$\frac{d\Delta p(t)}{d\ln t} \rightarrow 0 \quad , \quad t \rightarrow t_{ss} \quad . \tag{4.5.30}$$

All or these results are consistent with what we know concerning single-phase solutions for constant pressure boundary problems.

The pressure derivative for case OW-1Z shows a similar response to that of case OW-1X, though we mention that $d\Delta p(t)/d\ln t$ actually becomes quite negative (i.e., the wellbore pressure is increasing). Recall that case OW-1Z is the case for which a saturation shock or front cannot develop within the reservoir and also the case for which the total mobility must continually increase as water influxes into the reservoir and the water saturation increases. If we consider only the late-time period for which the volumetric flow rate has become approximately constant across the entire reservoir (i.e., $\partial q_t(r,t)/\partial t = 0$), the general pressure derivative equation (Eq. 4.5.23) can be simplified to obtain

$$\frac{d\Delta p(t)}{d\ln t} = \frac{-dp_{wf}(t)}{d\ln t} = \frac{q_t t}{C_2 kh}\int_{r_w}^{r_e}\left[-\frac{1}{{\lambda_{rt}}^2(r',t)}\frac{\partial \lambda_{rt}(r',t)}{\partial t}\right]\frac{dr'}{r'} \quad . \tag{4.5.31}$$

Equation 4.5.31 indicates that once the flow rate has become constant across the entire reservoir, the wellbore pressure derivative response will become a function only of the total relative mobility profile and the time-rate of change in the total relative mobility. As mentioned previously and also shown in Fig. 4.18, the total relative mobility for this case must increase for any increase in the water saturation and we, therefore, have

$$\frac{\partial \lambda_{rt}(r,t)}{\partial t} > 0 \quad , \; t < t_{ss} \; . \tag{4.5.32}$$

Utilizing this result in Eq. 4.5.31, we see that the log-derivative of the wellbore pressure drop must in fact become negative (the wellbore pressure must increase) once the reservoir flow rate has become approximately constant across the entire reservoir. Note also for this case that the total relative mobility will continue to increase until the reservoir has been completely flooded with water (see Fig. 4.18), i.e., $S_w = 1 - S_{or}$. This result and Eq. 4.5.31 then tell us that the log-derivative of the wellbore pressure drop will continue to be negative and not reach zero until true steady-state is reached (nothing changes with time) and this cannot be achieved until the reservoir has been 100 percent flooded with water.

For cases OW-1Y and OW-1W, Fig. 4.23 shows $d\Delta p/d\ln t$ initially falls off rapidly once the outer boundary is felt, but as the water begins to influx into the reservoir and the saturation front begins to form, $d\Delta p(t)/d\ln t$ begins to increase. To fully understand this pressure behavior, let us divide the reservoir into three regions where we define the first region as that part of the reservoir between the wellbore and the leading edge of the saturation front ($r_w \leq r \leq r_f^-$), the second region we define to be that part of the reservoir encompassing the saturation front ($r_f^- < r < r_f^+$) and the third region we define as that part of the reservoir from the trailing edge of the saturation front to the outer radius of the reservoir ($r_f^+ \leq r \leq r_e$). With these definitions and considering only the "late-time" period for which the volumetric flow rate has become approximately constant across the entire reservoir (i.e., $\partial q_t(r,t)/\partial t = 0$), the general pressure derivative equation (Eq. 4.5.23) can be simplified and expanded to obtain

$$\frac{d\Delta p(t)}{d\ln t} = \frac{q_t t}{C_2 kh}\left\{ \int_{r_w}^{r_f^-} \left[-\frac{1}{{\lambda_{rt}}^2(r',t)} \frac{\partial \lambda_{rt}(r',t)}{\partial t} \right] \frac{dr'}{r'} + \int_{r_f^-}^{r_f^+} \left[-\frac{1}{{\lambda_{rt}}^2(r',t)} \frac{\partial \lambda_{rt}(r',t)}{\partial t} \right] \frac{dr'}{r'} + \int_{r_f^+}^{r_e} \left[-\frac{1}{{\lambda_{rt}}^2(r',t)} \frac{\partial \lambda_{rt}(r',t)}{\partial t} \right] \frac{dr'}{r'} \right\} . \qquad (4.5.33)$$

Now note in that part of the reservoir ahead of the saturation front, the total mobility is unchanged and we have $\partial \lambda_{rt}(r,t)/\partial t = 0$ for $r < r_f^-$. Equation 4.5.33 can, therefore, be simplified to

$$\frac{d\Delta p(t)}{d\ln t} = \frac{q_t t}{C_2 kh}\left\{ \int_{r_f^-}^{r_f^+} \left[-\frac{1}{{\lambda_{rt}}^2(r',t)} \frac{\partial \lambda_{rt}(r',t)}{\partial t} \right] \frac{dr'}{r'} + \int_{r_f^+}^{r_e} \left[-\frac{1}{{\lambda_{rt}}^2(r',t)} \frac{\partial \lambda_{rt}(r',t)}{\partial t} \right] \frac{dr'}{r'} \right\} . \qquad (4.5.34)$$

The question now arises as to how do the two integrals in Eq. 4.5.34 relate to one another; i.e., what are the relative contributions of each? For the moment,

let us concentrate on case OW-1Y. Recall for case OW-1Y that the minimum total mobility occurs at the saturation front and the total mobility increases with increasing water saturation behind the front; or, in other words,

$$\frac{\partial \lambda_{rt}(r,t)}{\partial t} < 0 \quad , r_f^- < r < r_f^+ \tag{4.5.35}$$

and

$$\frac{\partial \lambda_{rt}(r,t)}{\partial t} > 0 \quad , r_f^+ \leq r \leq r_e \quad . \tag{4.5.36}$$

Note that by Eq. 4.5.35, the first integral will be positive, whereas by Eq. 4.5.36, the second integral will be negative. Because $d\Delta p(t)/d\ln t$ for case OW-1Y is positive for all times up to water breakthrough, then clearly the first integral must dominate. Note that if an actual saturation shock existed in the reservoir, then

$$\frac{\partial \lambda_{rt}(r,t)}{\partial t} = -\infty \quad , r = r_f \ . \tag{4.5.37}$$

Though we do not have a true shock here, we suspect that because of the sharp saturation profile exhibited for this case (see Fig. 4.21) that the first integral will dominate. Note that simply due to the fact that we are dealing with a radial reservoir system with flow towards the well, the velocity of fluids must increase as they approach the well; i.e.,

$$v = \frac{q_t}{2\pi r h} \quad . \tag{4.5.38}$$

Also, note that if the velocity of the saturation front approximately satisfies the Buckley-Leverett[117] theory, then we have

$$v_{\Delta S_w} = \left(\frac{dr}{dt}\right)_{S_w} = \frac{q_t}{2\pi r_f h \phi}\left(\frac{f_{w+} - f_{w-}}{S_{w+} - S_{w-}}\right) \tag{4.5.39}$$

which indicates that

$$\lim_{r \to 0} v_{\Delta S_w} = \infty \tag{4.5.40}$$

which implies that

$$\lim_{r_f \to 0} \frac{\partial \lambda_{rt}(r,t)}{\partial t} = -\infty \quad , r = r_f \ . \tag{4.5.41}$$

Equation 4.5.41 also appears to be strongly supported by the physical evidence exhibited in Fig. 4.23, which shows $d\Delta p/d\ln t$ becomes extremely large just prior to water breakthrough ($r_f = r_w$), approaching 10^6 psi.

As added evidence for the dominance of the first integral over the second integral, the derivative of the total relative mobility with-respect-to time ($\partial \lambda_{rt}(r,t)/\partial t$) was calculated at several radii over the course of the well test. Figure 4.24 shows the results of these calculations which can be summarized as follows: First, the magnitude of $\partial \lambda_{rt}(r,t)/\partial t$ when the saturation front passes a particular radius ($r_f^- < r < r_f^+$) is much greater (typically greater than 2 orders of magnitude) than the magnitude of the derivative behind the front ($r \geq r_f^+$). This difference in the magnitude of the derivative at different times causes the a plot of the derivative versus time to appear like an impulse function (as shown in Fig. 4.24). Second, as the saturation front progresses towards the well (moving in order from Fig. 4.24a to Fig. 4.24c), the magnitude of the mobility derivative increases substantially; e.g., for case OW-1Y, Fig. 4.24 shows the the mobility derivative increases by three orders of magnitude in moving from a radius of 56.6 feet (Fig. 4.24a) to a radius of 0.285 feet (Fig. 4.24c).

Based on the above discussion and numerical results, Eq. 4.5.34 can clearly be further simplified to obtain

$$\frac{d\Delta p(t)}{d\ln t} = \frac{q_t t}{C_2 kh} \int_{r_f^-}^{r_f^+} \left[-\frac{1}{{\lambda_{rt}}^2(r',t)} \frac{\partial \lambda_{rt}(r',t)}{\partial t} \right] \frac{dr'}{r'} \quad . \tag{4.5.42}$$

Until water breakthrough occurs at the well, Eq. 4.5.42 indicates that $d\Delta p(t)/d\ln t$ will vary in a manner directly related to how $\partial \lambda_{rt}(r,t)/\partial t$ at the saturation front

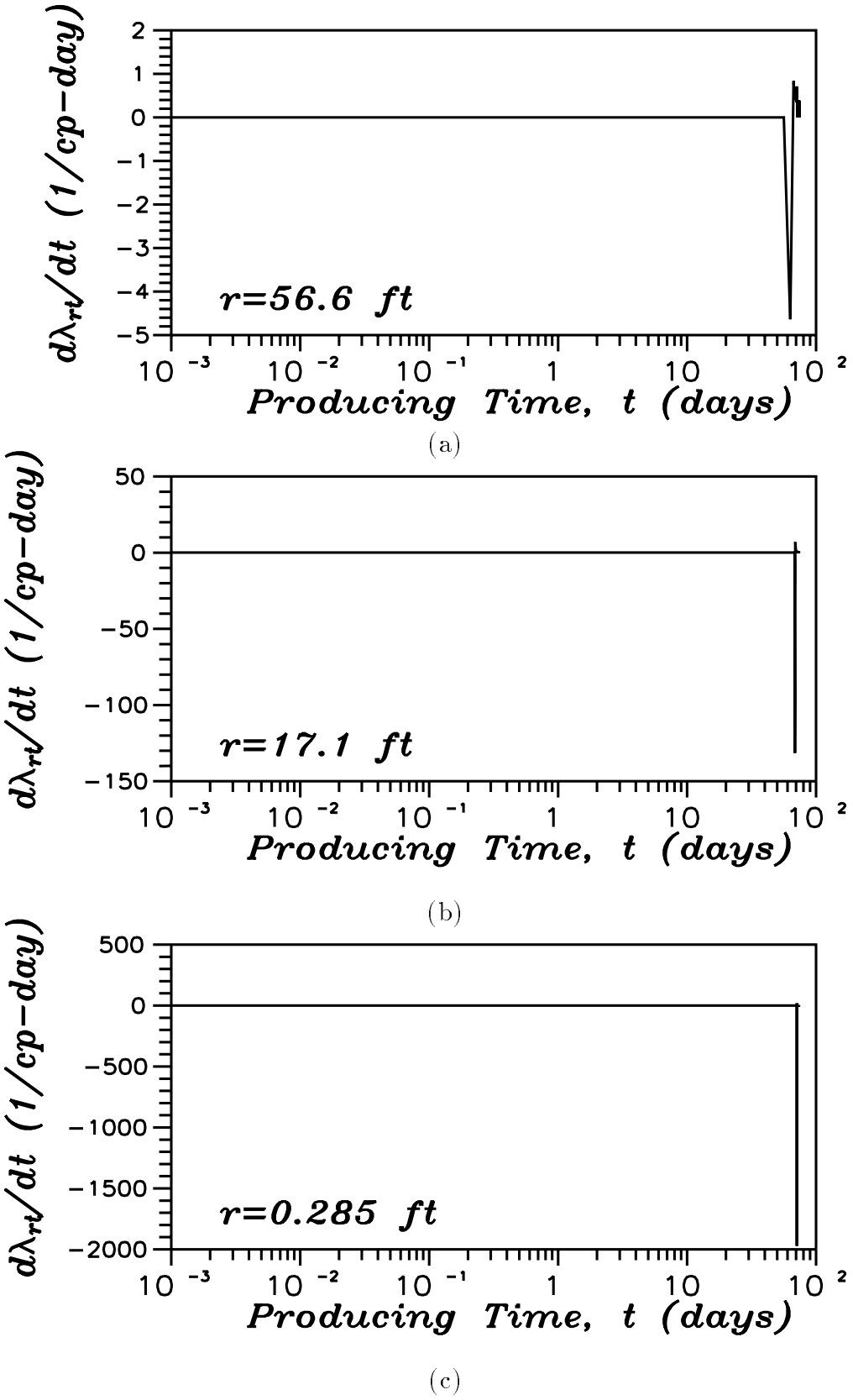

Figure 4.24 - Effect of radius on the time derivative of the total relative mobility.

varies. In other words, since the time derivative of the total relative mobility is negative (Eq. 4.5.35) then by Eq. 4.5.42, the log-derivative of the wellbore pressure drop with-respect-to time must be be positive; i.e.,

$$\frac{d\Delta p(t)}{d\ln t} > 0 \quad , r_f > r_w \quad . \tag{4.5.43}$$

Because $\partial\lambda_{rt}(r,t)/\partial t$ increases as the saturation front moves towards the well (i.e., as the time, t increases), then Eq. 4.5.42 indicates that $d\Delta p(t)/d\ln t$ must also increase as the time increases. Both of these results are clearly displayed in Fig. 4.23 for case OW-1Y.

Once the saturation front has passed (i.e., water breakthrough occurs), then the pressure behavior should once again follow the general pressure derivative equation simplified for the constant flow rate across the reservoir; i.e.,

$$\frac{d\Delta p(t)}{d\ln t} = \frac{-dp_{wf}(t)}{d\ln t} = \frac{q_t t}{C_2 kh}\int_{r_w}^{r_e}\left[-\frac{1}{{\lambda_{rt}}^2(r',t)}\frac{\partial\lambda_{rt}(r',t)}{\partial t}\right]\frac{dr'}{r'} \quad . \tag{4.5.44}$$

Now, however, the total relative mobility must increase anywhere in the reservoir where the water saturation increases and we have

$$\partial\lambda_{rt}(r,t) > 0 \quad , r_w \le r \le r_e \quad , \tag{4.5.45}$$

which by Eq. 4.5.44, indicates that the log-derivative of the wellbore pressure drop must be less than zero until true steady-state is reached in the reservoir; i.e.,:

$$\frac{d\Delta p(t)}{d\ln t} < 0 \quad , t < t_{ss} \quad . \tag{4.5.46}$$

Returning now to case OW-1W, recall that the general pressure derivative equation was simplified above (Eq. 4.5.34) to obtain

$$\frac{d\Delta p(t)}{d\ln t} = \frac{q_t t}{C_2 kh}\left\{ \int_{r_f^-}^{r_f^+} \left[-\frac{1}{{\lambda_{rt}}^2(r',t)} \frac{\partial \lambda_{rt}(r',t)}{\partial t} \right] \frac{dr'}{r'} + \int_{r_f^+}^{r_e} \left[-\frac{1}{{\lambda_{rt}}^2(r',t)} \frac{\partial \lambda_{rt}(r',t)}{\partial t} \right] \frac{dr'}{r'} \right\} \quad . \tag{4.5.47}$$

For case OW-1W, recall that the total mobility must continually decrease for any increase in the water saturation (see Fig. 4.19) and, therefore, the time derivative of the total relative mobility must be negative; i.e.,

$$\frac{\partial \lambda_{rt}(r,t)}{\partial t} < 0 \quad , \quad r > r_f^- \quad , \quad t < t_{ss} \quad . \tag{4.5.48}$$

Based on Eq. 4.5.48, Eq. 4.5.47 tells us that the log-derivative of the wellbore pressure drop must be non-zero and positive for all times up to steady-state:

$$\frac{d\Delta p(t)}{d\ln t} > 0 \quad , t < t_{ss} \quad . \tag{4.5.49}$$

Furthermore, since a sharp saturation front will also develop for case OW-1W, the arguments made above for case OW-1Y concerning the relative magnitudes of the two integrals in the pressure derivative equation are also valid for case OW-1W and the pressure derivative equation can be written as follows up to the time of water breakthrough at the well:

$$\frac{d\Delta p(t)}{d\ln t} = \frac{q_t t}{C_2 kh} \int_{r_f^-}^{r_f^+} \left[-\frac{1}{{\lambda_{rt}}^2(r',t)} \frac{\partial \lambda_{rt}(r',t)}{\partial t} \right] \frac{dr'}{r'} \quad . \tag{4.5.50}$$

Similar to case OW-1Y, we expect the log-derivative of the wellbore pressure drop, $d\Delta p(t)/d\ln t$, to increase as the saturation front progresses towards the well, which is precisely what is shown in Fig. 4.23. Unlike case OW-1Y, however, once

water breakthrough occurs, the total relative mobility in the reservoir continues to decrease, meaning that the partial derivative of the total relative mobility with-respect-to time is a negative quantity; i.e.,

$$\frac{\partial \lambda_{rt}(r,t)}{\partial t} < 0 \quad , \quad t < t_{ss} \quad . \tag{4.5.51}$$

By Eq. 4.5.44, then, the log-derivative of the wellbore pressure drop will continue to be a positive quantity, at least up to steady-state:

$$\frac{d\Delta p(t)}{d \ln t} > 0 \quad , \quad t < t_{ss} \quad . \tag{4.5.52}$$

Before leaving this chapter, we comment on the "wiggles" in the log-derivative of the wellbore pressure drop exhibited in Fig. 4.23 for case OW-1Y. These "wiggles" in the logarithmic pressure derivative are a consequence of the fact that we are simulating the reservoir using a discrete grid system and as such, are unable to propagate the sharp saturation front continuously from grid block to grid block; i.e., for large grid blocks, the grid block must "fill up" with water before the saturation "shock" can develop and propagate to the next grid block. Figure 4.25 shows a crossplot of $d\Delta p(t)/d \ln t$ versus time and $(1/{\lambda_{rt}}^2)\partial \lambda_{rt}/\partial t$ versus time for the outermost four grid blocks used in the simulation ($59.1 \leq r \leq 92.7$ ft). Figure 4.25 shows an almost perfect correlation between successive peaks in the pressure derivative humps and successive peaks (note negative quantity) in the mobility derivative function for the neighboring grid blocks. After the magnitude of the mobility derivative function reaches a maximum, it (the magnitude) begins to decrease and Fig. 4.25 shows a corresponding decrease in the log-derivative of the wellbore pressure drop. Now note that the valleys in the pressure derivative humps correspond almost exactly to the times at which the mobility derivative

function for neighboring grid blocks intersect one another. These points of intersection represent the times at which the mobility derivative function in that region of the reservoir begins to decrease again (the magnitude of the mobility derivative function increases as it becomes more negative), and correspondingly, we see the log-derivative of the wellbore pressure drop begins increasing again.

4.6 Summary

Reservoir and fluid descriptions have been presented for each of the reservoir systems investigated in this study. A literature review of previous works concerning the analysis of pressure transient data for multiphase systems has also been presented.

A theoretical analysis of the single-phase solution for liquids has shown the existence of a "steady-state" zone in the inner region of the reservoir. Similarly, a theoretical analysis and numerical investigation of single-phase gas flow has shown the validity of our "steady-state" zone arguments and the computational equations derived based on those arguments.

For multiphase flow cases, an expression has been derived which shows that vertical equilibrium exists in the reservoir if, and only if, the fractional flow rate of each phase as defined by the volumetric flow rates is the same as that calculated from the total thickness averaged mobilities existing at the same radius in the reservoir; i.e.,

$$f_m|_r = \frac{\bar{\lambda}_m}{\bar{\lambda}_t}\Big|_r = \frac{q_m}{q_t}\Big|_r \ . \tag{4.6.1}$$

For multiphase reservoir systems in which gravity effects are also included and capillary pressure effects are assumed negligible, we have shown that vertical equilibrium can exist in the reservoir only if (i) all fluids have the same density, or (ii) all mobile fluids are fully segregated.

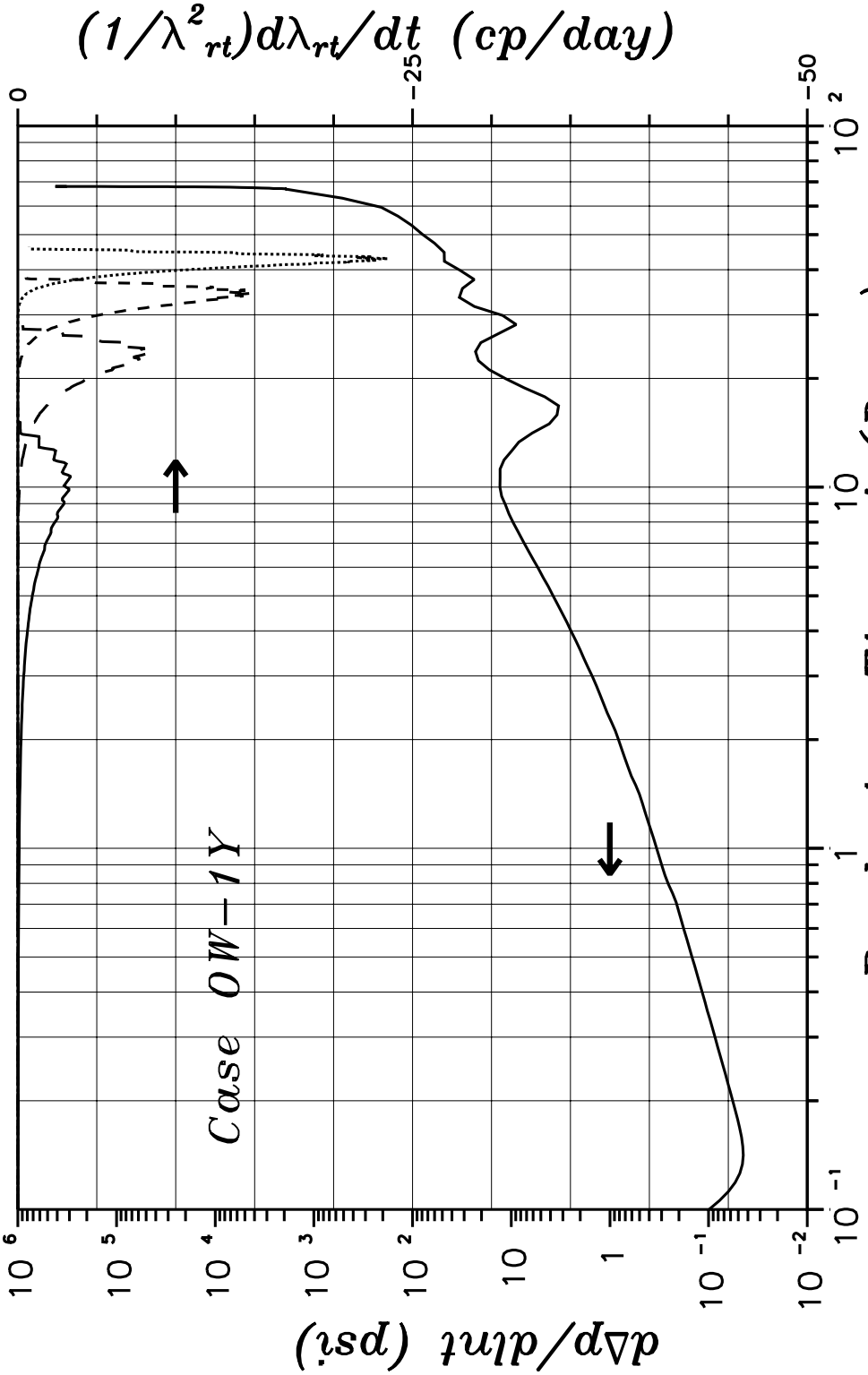

Fig. 4.25 – Crossplot of pressure derivative and total mobility derivative function.

A recently developed theoretical expression[149] for the pressure response in a reservoir containing a constant pressure outer boundary (either at infinity or at a fixed radius) has been used in conjunction with fractional flow theory and detailed numerical simulations to examine the pressure behavior of a fully-penetrating well producing an edge-water drive oil reservoir containing a constant pressure outer boundary. Three separate cases having distinctly different fractional flow curves were examined in detail and include a case for which a sharp saturation front or "shock" cannot develop (case OW-1Z - fractional flow curve concave downward everywhere), a case for which a sharp saturation front or "shock" can develop at every saturation (case OW-1W - fractional flow curve concave up everywhere), and a case for which a sharp saturation front or "shock" can develop over a certain saturation range (case OW-1Y - typical "S" shaped fractional flow curve).

For case OW-1W (no saturation front), the theoretical expression of Ref. 149 was used to obtain an expression which shows that once the constant pressure outer boundary was "felt" by the wellbore and once the volumetric flow rate across the reservoir has stabilized, the log-derivative of the wellbore pressure drop, $d\Delta p(t)/d\ln t$, must in fact become negative and will subsequently increase monotonically to zero. It was also shown that $d\Delta p(t)/d\ln t$ cannot be zero until the reservoir has been completely flooded with water ($S_o = S_{or}$) and the total relative mobility, λ_{rt}, ceases to change.

For the two cases in which a sharp saturation front develops in the reservoir (cases OW-1W and OW-1Y), the expression of Ref. 149 was used in conjunction with fractional flow theory and detailed numerical results to obtain an expression which shows that the log-derivative of the wellbore pressure drop is dominated by the time rate of change in the total relative mobility across the saturation front; i.e.,

$$\frac{d\Delta p(t)}{d\ln t} = \frac{q_t t}{C_2 kh}\int_{r_f^-}^{r_f^+}\left[-\frac{1}{{\lambda_{rt}}^2(r',t)}\frac{\partial\lambda_{rt}(r',t)}{\partial t}\right]\frac{dr'}{r'} \quad . \tag{4.6.2}$$

Furthermore, because the time derivative of the total relative mobility across the saturation front is negative for both of these cases and because the magnitude of this derivative must increase as the velocity of the saturation front increases as it progresses towards the well, Eq. 4.6.2 indicates that not only must $d\Delta p(t)/d\ln t$ be a positive quantity, but it must be an increasing positive quantity up to the time of breakthrough; i.e., $d\Delta p(t)/d\ln t$ will be both positive and increasing up to water breakthrough at the well.

Following water breakthrough, the general expression of Ref. 149 was used to show that $d\Delta p(t)/d\ln t$ will remain positive for case OW-1W until true steady-state is reached; i.e., until the reservoir has been completely flooded with water ($S_o = S_{or}$) and the fluid saturations no longer change with time. For case OW-1Y, it was shown that following water breakthrough, $d\Delta p(t)/d\ln t$ must become negative and will approach zero only as the fluid saturations cease to change.

CHAPTER V

CONSTANT PRESSURE BOUNDARY ASSUMPTION

In this chapter, we discuss the applicability of modeling a gas cap or aquifer as a constant pressure boundary. We do not, however, discuss methods for the analysis of systems containing constant pressure boundaries. Through a series of examples in which a constant pressure boundary is placed within the gas cap or aquifer, we show that the pressure response (pressure derivative) obtained from such systems is fundamentally different from the pressure response predicted by single-phase analytical solutions.

Note that we are not making an argument for or against the possible existence of a constant pressure boundary. Clearly, there are situations in which an aquifer or gas cap could physically maintain an approximately constant pressure; e.g., gas injection into a gas cap for pressure maintenance or an aquifer near to and hydrodynamically connected to a large body of water such as an ocean. The arguments to be presented are merely related to the fact that the pressure response obtained from a pressure transient test in a multiphase reservoir with a constant pressure boundary is fundamentally different from the pressure response which would be obtained from a single-phase reservoir with a constant pressure boundary.

5.1 Background Information

As discussed in the Chapter I, many investigators have used a constant pressure boundary assumption to model the effects of a gas cap or aquifer, e.g., see

Refs. 21 and 5-8. A common characteristic of all analytical solutions incorporating a constant pressure boundary condition is that as soon as the constant pressure boundary is "felt" by the wellbore, the pressure derivative decreases monotonically towards zero, at least for single-phase solutions. For constant pressure upper or lower boundaries, this then precludes the existence of a pseudoradial flow regime in the reservoir and a constant pressure derivative (semilog straight line) indicative of that flow regime.

Refs. 23-26 and Ref. 28 showed by numerical simulation that for oil reservoir - aquifer systems[23−26,28] and for oil reservoir - gas cap systems[25,26,28], an approximate semilog straight line was obtained indicative of pseudoradial flow. Similarly, Ref. 27 showed through numerical simulations of a horizontal well producing a water reservoir overlain by a gas cap and an oil reservoir overlain by a gas cap, that a constant pressure derivative (semilog straight line) was obtained at late time, again suggesting pseudoradial flow. Note that each of the references just mentioned utilized no-flow upper and lower boundaries in their simulations. In this current study, we show an extensive set of drawdown (Chapter VI) and buildup (Chapter VII) examples for a variety of two and three-phase reservoir systems (with no-flow upper and lower boundaries) in which the pressure derivative became approximately constant, suggesting pseudoradial flow. It is important to note, however, that even though we were able to provide a physical interpretation of the mobility computed from the drawdown apparent semilog straight line and Eqs. 4.6.1 and 4.6.2, we were unable to provide a fundamental methodology for converting this calculated mobility into one of the more common average mobilities normal to the primary flow direction; i.e., mobility at the sandface or total thickness averaged mobility. It is also important to note that the results for every two-dimensional case discussed in Chapter VI and Chapter VII failed to show the pressure derivative falling to zero as would be expected if the aquifer or

gas cap could truly be represented by an analogous single-phase constant pressure boundary.

5.2 Drawdown

5.2.1 Oil-Water Systems

The first cases we consider are oil-water systems. Referring to Fig. 4.1 and Table 4.1, the oil-water systems we examine are OW-4B, OW-3X, OW-3Y and OW-4Z. All four cases consist of a 40 foot oil reservoir with only the top ten feet perforated. For case OW-4B, a 20 foot water zone underlays the oil zone and the bottom boundary is closed, i.e., a no-flow boundary. In case OW-3X, the lower boundary is located at the bottom of the oil zone, is modeled as a constant pressure boundary (at initial pressure) and is considered to have the same fluid saturations as initially in the oil zone. This case conceptually represents the single-phase analytical solution to the problem and we see that fluid influx into the reservoir across the lower boundary will be entirely oil. Case OW-3Y is identical to case OW-3X except the fluid saturation at the lower boundary is specified as 100 percent water. For this case, the fluid influx into the reservoir will be entirely water. Lastly, case OW-4Z includes a 20 ft. water zone below the oil zone and a constant pressure boundary (at initial pressure and 100 percent water saturation) beneath the water zone. Cases OW-2B and OW-3B are included in the figures merely for reference or comparison purposes. Recall that case OW-2B represents a 40 foot oil reservoir with closed boundaries and a fully-penetrating well. Case OW-3B is the same except for a restricted-entry well instead of fully-penetrating. For each of these cases, a 10 day constant rate drawdown test was simulated and followed by a 10 day simulated buildup test.

Figure 5.1 shows the drawdown pressure derivative response obtained for each of these reservoir systems. First, we note that the pressure derivative for case

OW-4B becomes essentially constant at late time, indicating a semilog straight line and suggestive of pseudoradial flow in the reservoir. For case OW-3X, we see the typical pressure derivative response commonly associated with a constant pressure boundary, i.e., the log-derivative of the wellbore pressure drop decreases monotonically towards zero. For case OW-3X, this is precisely what we would expect based on single-phase theory.

Though the drawdown pressure derivative responses for cases OW-3Y and OW-4Z initially fall off rapidly after "feeling" the constant pressure boundary, there are significant differences from the response of case OW-3X. First, we note that the pressure response for case OW-4Z is substantially delayed in time due to the increased thickness in the whole reservoir (both oil and water zones); i.e., the constant pressure boundary is located 60 feet below the top of the reservoir for case OW-4Z and only 40 feet below the top for cases OW-3X and OW-3Y. The consequence of this effect is that any attempt to match this pressure response to single-phase analytical solutions necessarily requires that the location of the constant pressure boundary be part of the solution. Figure 5.1 does show that if the location of the constant pressure boundary is the same for both the single phase case and the multiphase case, then the pressure response will be the same, at least for a short period following the constant pressure boundary being felt; e.g., the pressure responses shown in Fig. 5.1 for cases OW-3X and OW-3Y are nearly identical up to a producing time of 0.3 days.

The second, and most obvious difference between the pressure responses, is the fact that $\partial \Delta p / \partial \ln t$ for cases OW-3Y and OW-4Z reverse and instead of decreasing, begin to increase. In Chapter IV we showed similar pressure responses for a one-dimensional radial reservoir with a constant pressure outer boundary and water influx into the reservoir. This current problem is directly analogous, with the exception that water influx and displacement now occur primarily in the vertical

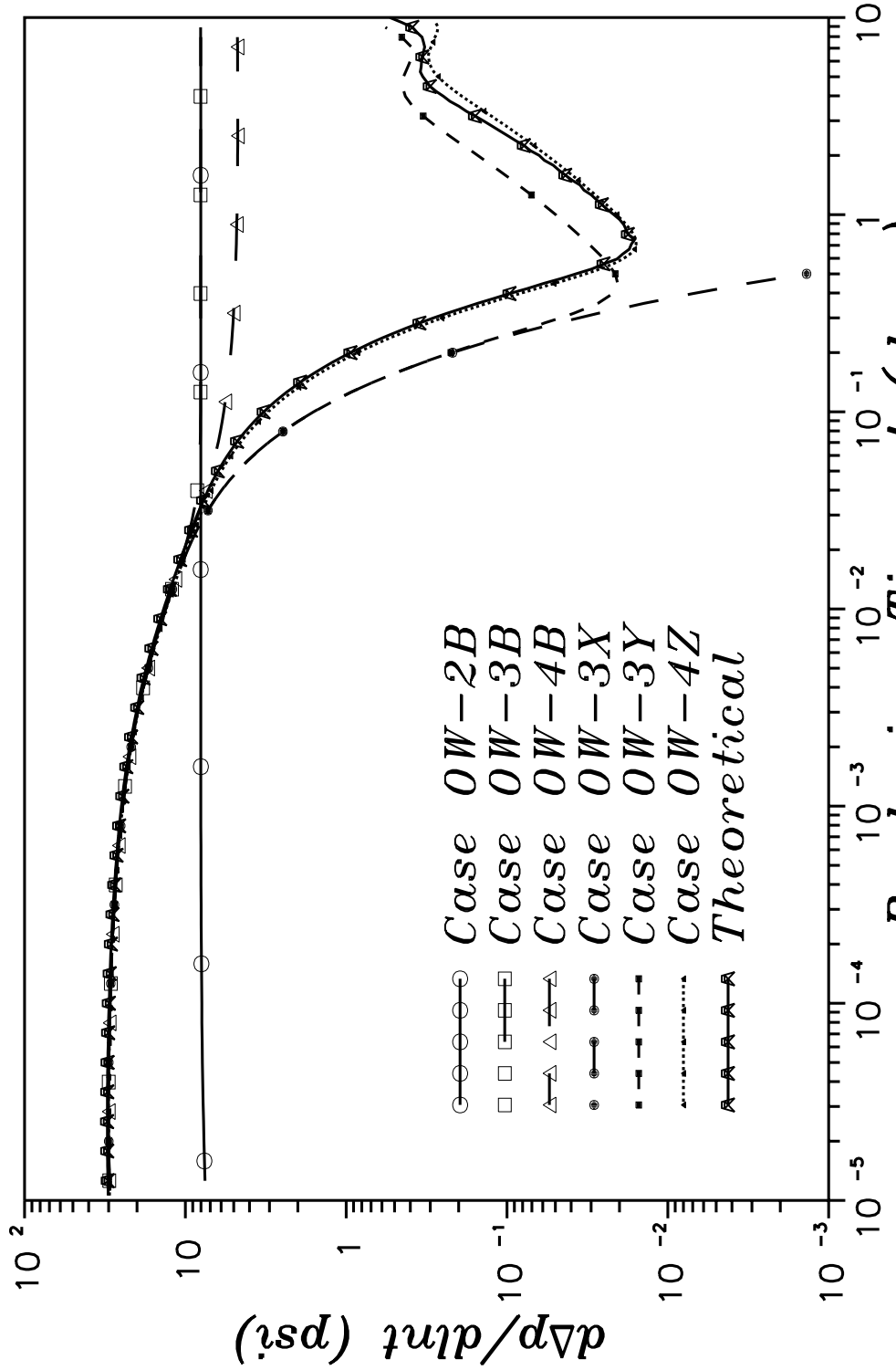

Fig. 5.1 – Comparison of pressure derivative responses for various constant pressure lower boundary reservoir systems.

direction. Note that the relative permeability curves and PVT properties for the current oil-water cases are the same as those used for the one-dimensional oil-water cases discussed in Chapter IV in conjunction with fractional-flow theory. The fractional flow curve for these cases, then, is the same as for the one-dimensional case OW-1Y discussed in Chapter IV and shown in Fig. 4.15. The derivative of the fractional flow curve and the total mobility for this system as a function of water saturation are shown in Fig. 4.16. Recall for case OW-1Y that a sharp saturation front or "shock" was predicted to develop in the reservoir as water influxed across the outer boundary. Note again that when we use the term "shock" here, we are simply using the term to distinguish between a sharp saturation front which develops in the reservoir due to a displacment process from a sharp saturation interface which exists in the reservoir due to the initial equilibrium forces. For the current cases (OW-3Y and OW-4Z), then, we suspect that a sharp saturation front or "shock" will develop in the vicinity of the oil-water contact as water displaces the oil.

To see the analogy between case OW-1Y of the previous chapter and cases OW-3Y and OW-4Z, we first examine the assumptions under which the one-dimensional Buckley-Leverett problem was derived to see if the same assumptions approximately hold for the current problems; i.e., to see if the conditions are such that a sharp saturation front or "shock" will form. Figure 5.2 shows the in-situ volumetric flow rate at the sandface and across the lower boundary for cases OW-3Y and OW-4Z. The flow rate across the lower boundary was calculated simply as the vertical flow rate across the lower boundary at each radius, integrated across the radial extent of the reservoir. Here we see that by 0.2 days for case OW-3Y and by 0.4 days for case OW-4Z, the in-situ volumetric flow rates have become constant and equal across both the sandface and the lower boundary.

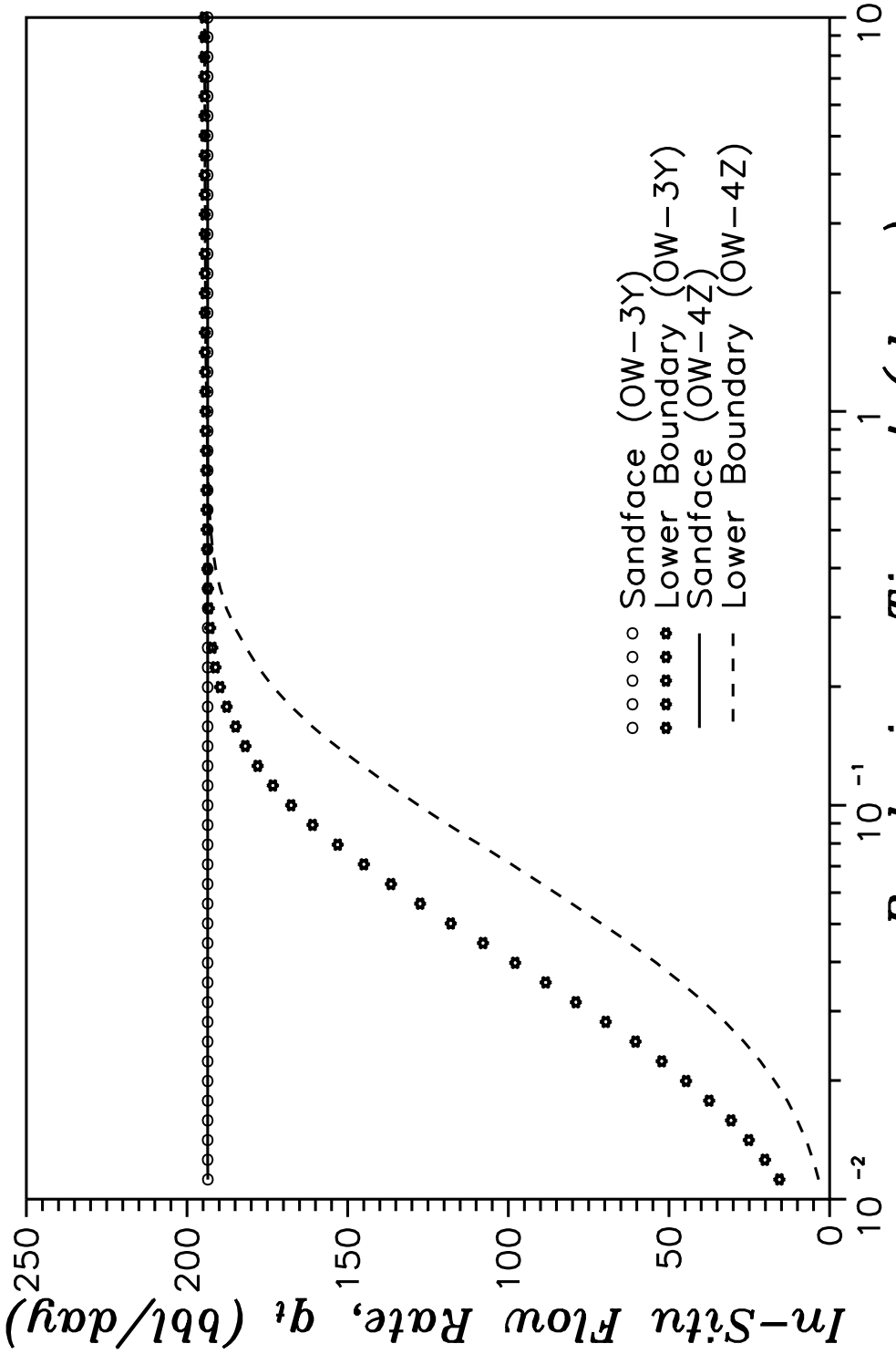

Fig. 5.2 – Comparison of in-situ reservoir flow rates at the sandface and across the lower boundary.

Next, we examine the saturation profiles in the reservoir. Figure 5.3 shows the vertical saturation profile for case OW-4Z at various times and for the first radial grid block. Figure 5.4 shows the radial saturation profile for case OW-4Z at various times and for the first vertical grid block above the original oil-water contact. The vertical saturation profile shown in Fig. 5.3 has the typical sharp saturation profile associated with Buckley-Leverett-type displacements and predicted by fractional-flow theory. Figure 5.4 shows that this saturation front extends approximately 40 feet out into the reservoir and that this saturation front appears to be moving at an approximately constant vertical velocity across this 40 feet.

In Chapter IV, we showed for case OW-1Y that the conditions for the formation of a sharp saturation front or "shock" were being approximately satisfied. Under those conditions, we derived an expression from a theoretical equation developed by Ref. 149 to show that once the volumetric flow rate across the reservoir had stabilized and up until the time of water breakthrough at the well, the log-derivative of the wellbore pressure drop was a function of the total relative mobility and the time rate of change in the total relative mobility across the saturation front. We also presented theoretical arguments supported by numerical results which showed that the log-derivative of the wellbore pressure drop, $d\Delta p(t)/d\ln t$, would remain positive and actually increase up to the time of water breakthrough as the saturation front progressed towards the well. The analysis for cases OW-3Y and OW-4Z is slightly more complicated due to the fact that the displacement, and flow in general, occurs across two dimensions.

There are a variety of ways we can incorporate vertical flow into our analysis and here we proceed in a simple piecewise manner. Let us consider the reservoir to be infinite acting in the radial direction. Let us further assume that Darcy's Law holds at every point in the reservoir. Under these conditions, we can write the

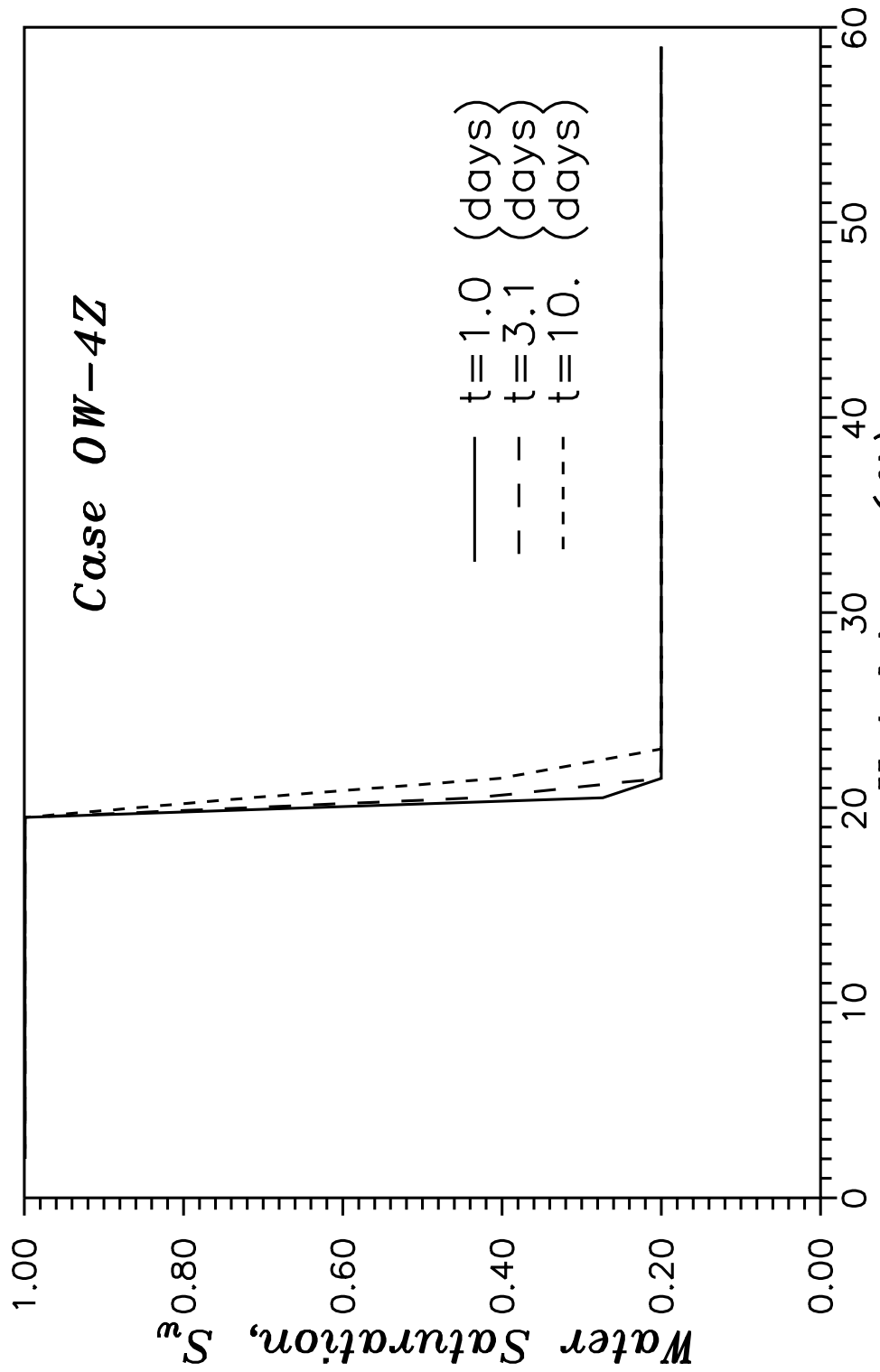

Fig. 5.3 – Vertical saturation profile at various times for Case OW–4Z.

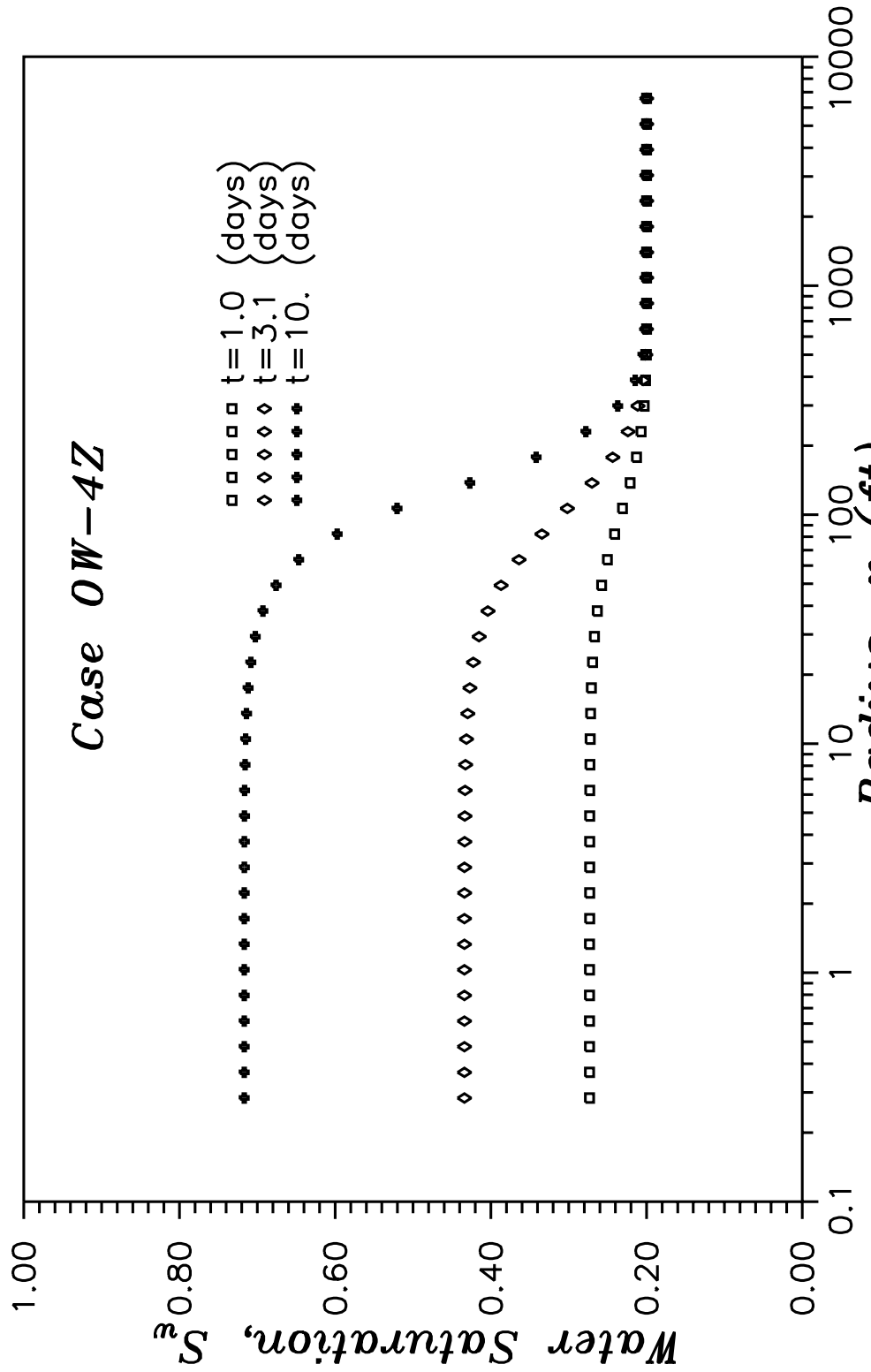

Fig. 5.4 – Radial saturation profile at various times for Case OW–4Z.

theoretical expression of Ref. 149 (Eq. 4.5.23 in Chapter IV) in a more general form to account for the vertical location dependence; i.e., using the radial form of Darcy's Law, the log-derivative of the pressure drop at any point in the reservoir can be expressed as

$$\frac{\partial \Delta p}{\partial \ln t} = -\frac{\partial p(r,z,t)}{\partial \ln t} = \frac{t}{c_1 k}\int_r^\infty \frac{\partial}{\partial t}\left[\frac{v_t(r',z,t)}{\lambda_{rt}(r',z,t)}\right]dr' \quad , \tag{5.2.1}$$

where c_1 is a units conversion factor given by $c_1 = 6.328 \times 10^{-3}$. Because here we are concerned with multidimensional flow, it is appropriate to consider fluid velocities rather than the volumetric flow rates as were used in Chapter IV for the the one-dimensional radial problem. Here, we have defined the total fluid velocity simply as the sum of the individual phase velocities, or

$$v_t(r,z,t) = v_o(r,z,t) + v_w(r,z,t) \quad . \tag{5.2.2}$$

Let us now consider vertical flow in the reservoir and proceed to derive the vertical form of the theoretical expression of Ref. 149. Darcy's law for vertical flow in the reservoir can be written

$$v_{zt}(r,z,t) = c_1 k_z\left[\lambda_{ro}(r,z,t)\frac{\partial \Phi_o(r,z,t)}{\partial z} + \lambda_{rw}(r,z,t)\frac{\partial \Phi_w(r,z,t)}{\partial z}\right] \quad , \tag{5.2.3}$$

where the derivative of the phase potentials are defined as

$$\frac{\partial \Phi_m(r,z,t)}{\partial z} = \frac{\partial p(r,z,t)}{\partial z} + \gamma_m(r,z,t) \quad , m = o,w,g \quad , \tag{5.2.4}$$

and the phase gravities are defined simply as $\gamma_m = \rho_m g/144 g_c$. Here, we note that because of how we have defined the velocity (Eq. 5.2.3) and the coordinate system, the velocity will be negative if flow is in the positive z-direction; i.e., if flow is from the bottom of the reservoir ($z = 0$) towards the top of the reservoir

$z = h$. Using Eq. 5.2.4 in Eq. 5.2.3 and solving for the vertical pressure gradient, we obtain

$$\frac{\partial p(r,z,t)}{\partial z} = \frac{1}{c_1 k_z}\frac{v_{zt}(r,z,t)}{\lambda_{rt}(r,z,t)} - \frac{(\lambda_{ro}(r,z,t)\gamma_o(r,z,t) + \lambda_{rw}(r,z,t)\gamma_w(r,z,t))}{\lambda_{rt}(r,z,t)} \quad . \tag{5.2.5}$$

Integrating Eq. 5.2.5 with-respect-to the vertical direction from any vertical location to the lower boundary and using the fact that the lower boundary has been held at a constant pressure equal to the initial pressure at that location (i.e., $p(z=0,t) = p(z=0,t=0) = p_i(z=0)$), we obtain

$$\begin{aligned}\Delta p(r,z,t) =& p_i(z=0) - p(r,z,t) \\ =& \frac{1}{c_1 k_z}\int_z^0 \left[\frac{v_{zt}(r,z',t)}{\lambda_{rt}(r,z',t)}\right] dz' \\ &- \int_z^0 \left[\frac{(\lambda_{ro}(r,z',t)\gamma_o(r,z',t) + \lambda_{rw}(r,z',t)\gamma_w(r,z',t))}{\lambda_{rt}(r,z',t)}\right] dz' \end{aligned} \tag{5.2.6}$$

Simply reversing the limits of integration on the right-hand-side of Eq. 5.2.6 we obtain

$$\begin{aligned}\Delta p(r,z,t) =& p_i(z=0) - p(r,z,t) \\ =& -\frac{1}{c_1 k_z}\int_0^z \left[\frac{v_{zt}(r,z',t)}{\lambda_{rt}(r,z',t)}\right] dz' \\ &+ \int_0^z \left[\frac{(\lambda_{ro}(r,z',t)\gamma_o(r,z',t) + \lambda_{rw}(r,z',t)\gamma_w(r,z',t))}{\lambda_{rt}(r,z',t)}\right] dz' \end{aligned} \tag{5.2.7}$$

If we now take the derivative of Eq. 5.2.7 with-respect-to the natural logarithm of time, we have

$$\frac{\partial \Delta p}{\partial \ln t} = -\frac{\partial p(r,z,t)}{\partial \ln t}$$

$$= -\frac{t}{c_1 k_z}\int_0^z \frac{\partial}{\partial t}\left[\frac{v_{zt}(r,z',t)}{\lambda_{rt}(r,z',t)}\right]dz'$$

$$+t\int_0^z \frac{\partial}{\partial t}\left[\frac{(\lambda_{ro}(r,z',t)\gamma_o(r,z',t)+\lambda_{rw}(r,z',t)\gamma_w(r,z',t))}{\lambda_{rt}(r,z',t)}\right]dz' \quad (5.2.8)$$

Note that Eqs. 5.2.1 and 5.2.8 both provide expressions for the log-derivative of the pressure at any point in the reservoir; i.e., for any given point in the reservoir, both Eqs. 5.2.1 and 5.2.8 provide equally valid expressions for the derivative of the pressure at that point with-respect-to the natural logarithm of time. The only assumptions used in the derivation of Eqs. 5.2.1 and 5.2.8 are that Darcy's Law is valid at every point in the reservoir, the reservoir is infinite acting in the radial direction (or constant pressure outer boundary) and the lower boundary maintains a constant pressure equal to the initial pressure at that location. As such, Eqs. 5.2.1 and 5.2.8 are both equally valid for multiphase flow as they are for single phase flow, and both are equally valid for buildup as they are for drawdown. Note that neither Eq. 5.2.1 nor Eq. 5.2.8 represent complete solutions to the reservoir problems considered here, but they do provide us with the functional relationship between parameters which allows us to explain the observed pressure responses.

Because Eqs. 5.2.1 and 5.2.8 are both valid at any point in the reservoir, let us select a point next to the perforated interval in our reservoir at a height equal to our wellbore datum level; i.e., at (r_w^+, z_{wb}). The reason for selecting r_w^+ instead of r_w is simply due to Eq. 5.2.8 not being strictly valid at r_w. Provided

r_w^+ is sufficiently close to r_w, then $p(r,z,t) \approx p_{wf}(t, z_{wb})$ and we can express Eq. 5.2.8 as

$$\frac{\partial \Delta p}{\partial \ln t} \approx - \frac{\partial p_{wf}(z_{wb},t)}{\partial \ln t}$$

$$\approx - \frac{t}{c_1 k_z} \int_0^{z_{wb}} \frac{\partial}{\partial t}\left[\frac{v_{zt}}{\lambda_{rt}}\right] dz'$$

$$+ t \int_0^{z_{wb}} \frac{\partial}{\partial t}\left[\frac{(\lambda_{ro}\gamma_o + \lambda_{rw}\gamma_w)}{\lambda_{rt}}\right] dz' \quad . \tag{5.2.9}$$

Without loss of generality and in order to simplify the nomenclature we have dropped the location and time dependence designations for each of the parameters in Eq. 5.2.9. It should be understood that each of the parameters generally depend on the radial, r, and vertical, z, location and time, t.

To simplify our discussion that follows, let us define the gravity term as

$$G(r,z,t) = c_1 k_z [\lambda_{ro}(r,z,t)\gamma_o(r,z,t) + \lambda_{rw}(r,z,t)\gamma_w(r,z,t)] \quad , \tag{5.2.10}$$

which also gives

$$\frac{\partial G}{\partial t} = c_1 k_z \left[\lambda_{ro}\frac{\partial \gamma_o}{\partial t} + \gamma_o \frac{\partial \lambda_{ro}}{\partial t} + \lambda_{rw}\frac{\partial \gamma_w}{\partial t} + \gamma_w \frac{\partial \lambda_{rw}}{\partial t}\right] \quad . \tag{5.2.11}$$

Using Eqs. 5.2.10 and 5.2.11 in Eq. 5.2.9 and expanding the derivatives, we obtain

$$\frac{\partial \Delta p}{\partial \ln t} \approx - \frac{\partial p_{wf}(z_{wb},t)}{\partial \ln t}$$

$$\approx \frac{t}{c_1 k_z} \int_0^{z_{wb}} \left\{ \frac{1}{{\lambda_{rt}}^2}\left[v_{zt} - G\right]\frac{\partial \lambda_{rt}}{\partial t} - \frac{1}{\lambda_{rt}}\left[\frac{\partial v_{zt}}{\partial t} - \frac{\partial G}{\partial t}\right]\right\} dz' \quad . \tag{5.2.12}$$

Note that we have taken the minus sign inside the first integral here and then combined the integrals. Equation 5.2.12 indicates that in addition to the direct dependence on the total velocity, v_{zt}, the gravity term, G, and the inverse total relative mobility, λ_{rt}, the log-derivative of the wellbore pressure drop is also a function of the time rate of change of each of these terms.

We henceforth refer to Eq. 5.2.12 as the vertical form of Ref. 149's theoretical expression for the log-derivative of the wellbore pressure drop. Using numerical values for the vertical velocity, total relative mobility and gravity term output by our simulator for each vertical grid block along the first radial grid block for each time step, Eq. 5.2.12 was evaluated for case OW-4Z. The result is shown in Fig. 5.1 as the curve marked "Theoretical." Except for a slight deviation at very late time, Fig. 5.1 shows an excellent match between $\partial\Delta p/\partial \ln t$ calculated from Eq. 5.2.12 and $\partial\Delta p/\partial \ln t$ calculated directly from the wellbore pressures output by our simulator. The late-time difference is most probably due to our using a simple first-order backward difference approximation for the property time derivatives in Eq. 5.2.12.

Having established the numerical validity of Eq. 5.2.12, we can proceed to examine the individual contributions of the terms inside the integral of Eq. 5.2.12. Similar to what was done for case OW-1Y in the previous chapter, let us define $z_f^-(r)$ as the leading edge (downstream side) of the saturation front and $z_f^+(r)$ as the trailing edge (upstream side) of the saturation front for cases OW-3Y and OW-4Z. Note that initially the trailing edge of the saturation front will just be the oil-water contact and because only single phase water exists below the oil-water contact, we, therefore, have

$$\frac{\partial \lambda_{rt}(r,z,t)}{\partial t} = 0 \quad , \; z \leq z_{owc} \tag{5.2.13}$$

and

$$\frac{\partial \lambda_{rm}(r,z,t)}{\partial t} = 0 \quad , \; z \leq z_{owc} \quad , m = o, w \quad . \tag{5.2.14}$$

Furthermore, because only single phase oil exists for $z > z_f^-$, then the mobility does not change in this region of the reservoir and we have

$$\frac{\partial \lambda_{rt}(r,z,t)}{\partial t} = 0 \quad , \; z > z_f^- \tag{5.2.15}$$

and

$$\frac{\partial \lambda_{rm}(r,z,t)}{\partial t} = 0 \quad , \; z > z_f^- \quad , m = o, w \quad . \tag{5.2.16}$$

If pressure changes are small across the reservoir or fluid compressibilities are small, then we can express the derivative of the gravity term as

$$\frac{\partial G}{\partial t} = c_1 k_z \left[\gamma_o \frac{\partial \lambda_{ro}}{\partial t} + \gamma_w \frac{\partial \lambda_{rw}}{\partial t} \right] \quad . \tag{5.2.17}$$

By Eqs. 5.2.14 and 5.2.16, however, the time derivatives of the individual phase mobilities are zero in the single-phase regions of the reservoir and in these regions we then obtain

$$\frac{\partial G}{\partial t} = 0 \quad , \; z \leq z_{owc} \; , \; z > z_f^- \quad . \tag{5.2.18}$$

As we have already shown (Fig. 5.2), the total volumetric flow rate across the two open boundaries (sandface and lower boundary) of the reservoir are equal and unchanging (flow is one-dimensional across any of the boundaries and so volumetric flow rates may appropriately be used). Numerical results not shown also indicate that the total fluid flow rates across any horizontal plane in the reservoir have essentially stabilized by 0.5 days; i.e.,

$$\frac{\partial v_{zt}(r,z,t)}{\partial t} = 0 \quad . \tag{5.2.19}$$

Note that Eq. 5.2.19 does not say that the vertical velocity is independent of position, only that it becomes independent of time.

Based on Eqs. 5.2.13–5.2.19, Eq. 5.2.12 can be expressed

$$\frac{\partial \Delta p}{\partial \ln t} \approx -\frac{\partial p_{wf}(z_{wb},t)}{\partial \ln t}$$

$$\approx \frac{t}{c_1 k_z}\int_{z_{owc}}^{\bar{z_f}} \left\{ \frac{1}{{\lambda_{rt}}^2}\left[v_{zt}-G\right]\frac{\partial \lambda_{rt}}{\partial t} + \frac{1}{\lambda_{rt}}\left[\frac{\partial G}{\partial t}\right]\right\} dz' \quad . \qquad (5.2.20)$$

Equation 5.2.20 simply states that once the total fluid flow rate in the vertical direction has stabilized, $d\Delta p(t)/d\ln t$ will depend on how λ_{rt} and G vary over that part of the reservoir where multiple phases are mobile.

By the same arguments made for case OW-1Y in the previous chapter, we know that the change in the total relative mobility (and similarly the phase mobilities) across the saturation front, $z_f^+ < z < \bar{z_f}$, will dominate the mobility derivative term (and the gravity term) and we can, therefore, write Eq. 5.2.20 as

$$\frac{\partial \Delta p}{\partial \ln t} \approx -\frac{\partial p_{wf}(z_{wb},t)}{\partial \ln t}$$

$$\approx \frac{t}{c_1 k_z}\int_{z_f^+}^{\bar{z_f}} \left\{ \frac{1}{{\lambda_{rt}}^2}\left[v_{zt}-G\right]\frac{\partial \lambda_{rt}}{\partial t} + \frac{1}{\lambda_{rt}}\left[\frac{\partial G}{\partial t}\right]\right\} dz' \quad . \qquad (5.2.21)$$

Equation 5.2.21 represents the late-time (for this case, $t > 0.5$ days) pressure response for the curent oil-water case and will remain valid as long as the assumptions incorporated in it development hold; i.e., as long as the lower boundary is at a constant pressure, Darcy's Law holds at every point in the reservoir, and the vertical total fluid velocity, v_{zt}, does not change with time along the vertical slice of the reservoir. Equation 5.2.21 indicates that variations in the log-derivative of the wellbore pressure drop will depend upon how the phase mobilities (included in

the total relative mobility, λ_{rt}, and the gravity term, G) change with time across the saturation front.

In Chapter IV, we showed that the derivative of the total relative mobility across the saturation front will be a negative quantity for the phase mobilities used for case OW-1Y. Since the same rock and fluid properties are used here for cases OW-3Y and OW-4Z, then the time derivative of the total relative mobility across the saturation front will also be a negative quantity for these cases. As noted previously, the total fluid velocity in the vertical direction will be a negative quantity when flow is from the bottom of the reservoir towards the well, which is the case here. Since the gravity term, G, is a positive quantity (see Eq. 5.2.10) and is subtracted from the velocity, then the first group of terms inside the integral of Eq. 5.2.21 must be a positive quantity. By the same arguments as for the derivative of the total relative mobility, the time derivative of the gravity term will be a negative quantity across the saturation front. For example, if we examine Eq. 5.2.17, we see that the derivatives of the phase mobilities are multiplied by the phase gravities. If the phase gravities were equal, then the derivative of the gravity term would simply be the total relative mobility scaled by the phase gravities and the constant $c_1 k_z$. Because the phase gravities are in general not equal to one another, then a secondary effect of their presence is to shift the saturation at which the minimum in the gravity term will occur; i.e., the saturation at which the minimum in the gravity term occurs will not in general coincide with the saturation at which the minimum in the total relative mobility occurs. Additionally, for the specific values of reservoir parameters used for these oil-water cases ($k_z = 5$ md), the constant $c_1 k_z$ is numerically equal to 0.0316. This means that not only will the gravity term be much less (several orders of magnitude) than the total relative mobility, but the derivative of the gravity term will be several orders of magnitude less than the derivative of the total relative mobility.

Figure 5.5 shows the relationship between the total relative mobility, the gravity term, G, and the derivatives of these two parameters with-respect-to water saturation. As discussed above, Figure 5.5 shows that the gravity term is much smaller in magnitude than the total relative mobility and in fact, the gravity term and it's derivative can barely be distinguished from zero on the plot. Numerical calculations show the maximum value for the gravity term is $G = 0.0172$ and the maximum value for the derivative of the gravity term with-respect-to water saturation is $\partial G/\partial S_w = 0.0781$. These values compare with a maximum value for the total relative mobility of $\lambda_{rt} = 1.25$ and a maximum value for the derivative of the total relative mobility with-respect-to water saturation of $\partial \lambda_{rt}/\partial S_w = 5.687$.

In the context of explaining the increasing log-derivative of the wellbore pressure exhibited for cases OW-3Y and OW-4Z (Fig. 5.1), let us examine the group of terms inside the integral of Eq. 5.2.21 in slightly more detail. Clearly, if the this group of terms were positive, then the log-derivative of the pressure drop would also be positive. Let us, then, examine under what condition this group of terms will be a positive quantity. First, we have

$$\left\{ \frac{1}{{\lambda_{rt}}^2} \left[v_{zt} - G \right] \frac{\partial \lambda_{rt}}{\partial t} + \frac{1}{\lambda_{rt}} \left[\frac{\partial G}{\partial t} \right] \right\} > 0 \quad . \tag{5.2.22}$$

Multiplying through by λ_{rt} we obtain

$$\left\{ \frac{1}{\lambda_{rt}} \left[v_{zt} - G \right] \frac{\partial \lambda_{rt}}{\partial t} + \frac{\partial G}{\partial t} \right\} > 0 \quad . \tag{5.2.23}$$

Without introducing any significant error for the current cases (as justified by the results shown in Fig. 5.5), let us consider as a limiting value of the gravity term as $G = C\lambda_{rt}$, where C is a constant such that $0 < C < 1$. We, therefore, also have

$$\frac{\partial G}{\partial t} = C \frac{\partial \lambda_{rt}}{\partial t} \quad . \tag{5.2.24}$$

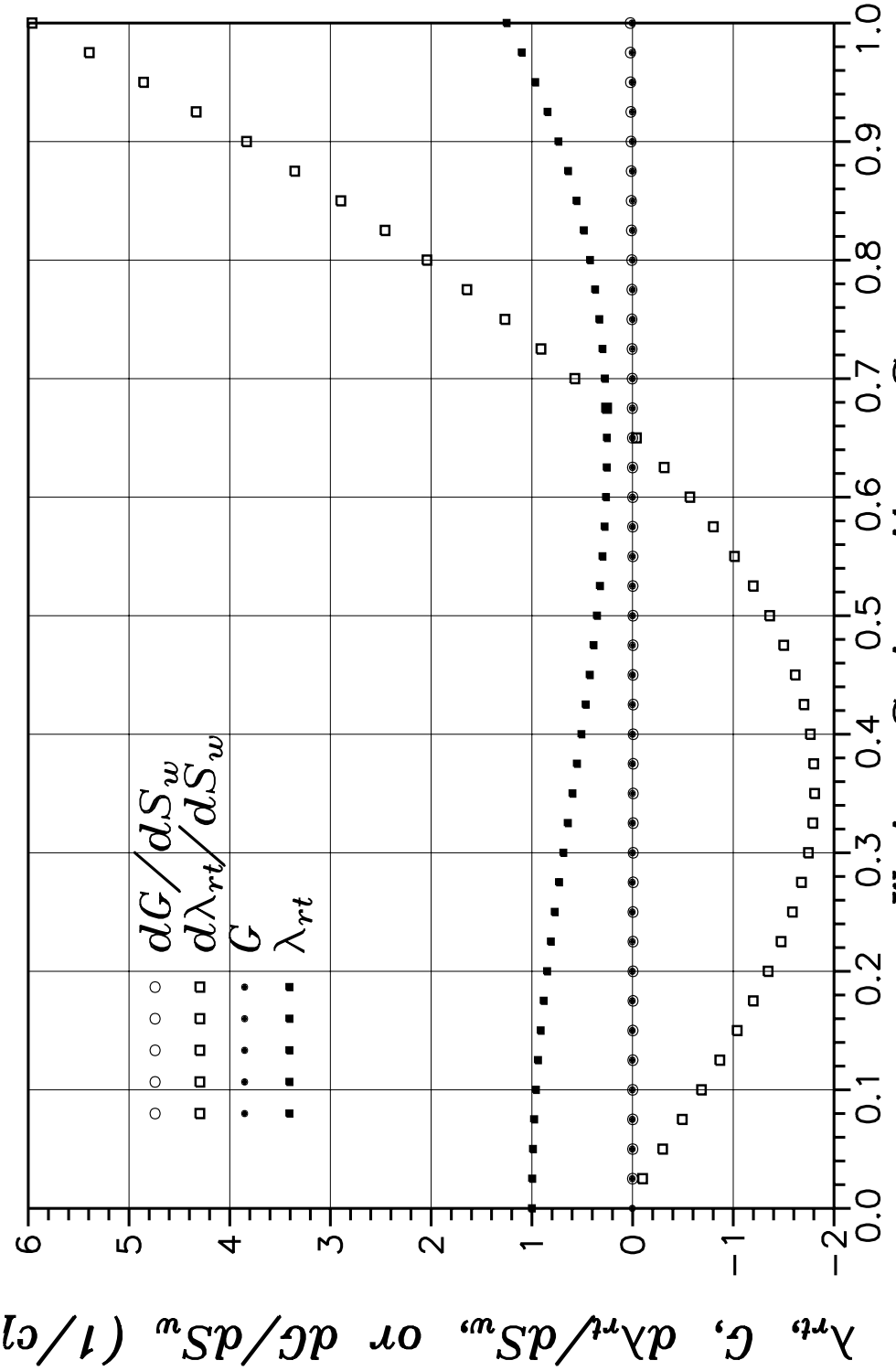

Fig. 5.5 – Total relative mobility, gravity term and derivatives.

Using Eq. 5.2.24 in Eq. 5.2.23 and simplifying we obtain

$$\left\{\frac{1}{\lambda_{rt}}\left[v_{zt}-G\right]\frac{\partial\lambda_{rt}}{\partial t}+C\frac{\partial\lambda_{rt}}{\partial t}\right\}>0 \quad . \tag{5.2.25}$$

Multiplying Eq. 5.2.25 through by λ_{rt} and dividing through by $\partial\lambda_{rt}/\partial t$ we have

$$v_{zt}-G+C\lambda_{rt}<0 \quad . \tag{5.2.26}$$

Note that because $\partial\lambda_{rt}/\partial t$ is a negative value, then we had to switch our inequality. Now, by using our definition for the limiting form of the gravity term ($G=C\lambda_{rt}$) we finally obtain

$$v_{zt}<0 \quad . \tag{5.2.27}$$

Equation 5.2.27 simply tells us that the only condition for the late-time log-derivative of the pressure drop to be positive is for v_{zt} to be a negative quantity or, in other words, for flow to be from the bottom of the reservoir towards the well. As already shown, this is precisely the situation for cases OW-3Y and OW-4Z. In other words, as long as flow is from the bottom of the reservoir towards the well and prior to water breakthrough, then the log-derivative of the wellbore pressure drop must remain non-zero and positive.

If we now re-examine Eq. 5.2.21, we see that as long as the integral term is a constant or, at the worst, decreases at a rate slower than the time increases, then the log-derivative of the wellbore pressure drop must increase. For strictly linear flow, we expect the velocity of fluids towards the well to be a constant. For multi-dimensional flow towards a centrally located well, however, the flow will be convergent towards the well and we, therefore, expect the fluid velocities in both the radial and vertical directions to increase as we approach the well. That this has to be so can easily be seen by simply drawing an analogy with the well.

As you move along the well, more and more fluid enters the well, and so the total volumetric flow rate in the well increases. Since the well is of a fixed cross-sectional area, the total fluid velocity then must increase. In a similar manner, as you move down along the inner boundary, more and more fluid enters the first radial grid block from the radial direction along this boundary. Since fluid can only leave the grid block from the upper face, the total volumetric rate leaving the grid block must increase (assuming minimal storage in the grid block). Since the cross-sectional area of the upper face of the grid block is fixed, the total fluid velocity must increase to accommodate the increased volumetric flow. Examining Eq. 5.2.21 again, we see that with an increase in the total vertical velocity as the saturation front progresses towards the well, the value of the integral term must increase and, therefore, the log-derivative of the wellbore pressure drop must also increase.

As with the one-dimensional case OW-1Y discussed in Chapter IV, then, we would also expect the log-derivative of the wellbore pressure drop for cases OW-3Y and OW-4Z to continue to increase until breakthrough of the saturation shock occurs. This is essentially the case, but the physics are slightly more complicated than in the one-dimensional case. Figure 5.6 shows an extended plot (much longer drawdown period) of the log-derivative of the pressure drop for case OW-4Z along with the log-derivative for case OW-4B for reference. At approximately 400 days, Fig. 5.6 shows the log-derivative or the wellbore pressure drop beginning to decline. This is the time at which the saturation shock has reached the lower-most perforation. Not until the average total mobility across all of the perforations has reached a minimum does the log-derivative go to zero (actually it becomes negative as the wellbore pressure begins to increase). As shown in Fig. 5.6, this occurs at a producing time of approximately 1000 days. Recall from Chapter IV that we

showed $\partial\lambda_{rt}(r,z,t)/\partial t$ is a positive quantity behind the saturation front. By Eq. 5.2.12, then, the log-derivative of the wellbore pressure drop will be negative.

5.2.2 Water-Gas Systems

In this section we examine the pressure response for various water reservoir-gas cap systems. The reason for examining such systems is due to the similarities between these cases and cases involving an oil reservoir overlain by a gascap, but without the complexities of mass transfer between the phases. By examining the pressure response for these cases, then, we hope to be able to separate the effects of mobility changes near the gascap due to coning from the effects of mass transfer. Referring to Fig. 4.4 and Table 4.4, the water-gas systems we examine include cases WG-4B, WG-3X, WG-3Y, WG-4Z and WG-4Za. All five cases consist of a 40 foot water reservoir with only the bottom ten feet perforated. For case WG-4B, a 20 foot gascap overlays the water zone and the upper boundary is closed, i.e., a no-flow boundary. For case WG-3X, the upper boundary is located at the top of the water zone, is modeled as a constant pressure boundary (at initial pressure) and is considered to be 100 percent water. This case conceptually represents the single-phase analytical solution to the problem and fluid influx into the reservoir across the upper boundary will be entirely water. Case WG-3Y is identical to case WG-3X except the fluid saturation at the upper boundary is specified as 80 percent gas (water is at residual water saturation). For this case, the fluid influx into the reservoir will be entirely gas. Case WG-4Z includes a 20 ft. gascap above the water zone and a constant pressure boundary (at initial pressure and gas saturation) above the gascap. Lastly, case WG-4Za is identical to case WG-4Z except gravity effects are not included; i.e., the initial pressure is everywhere equal to 3600 psia. Case WG-2B is included in the figure merely for reference or comparison purposes. Recall that case WG-2B represents a 40 foot water reservoir with closed boundaries and a partially-penetrating well. For each of these cases,

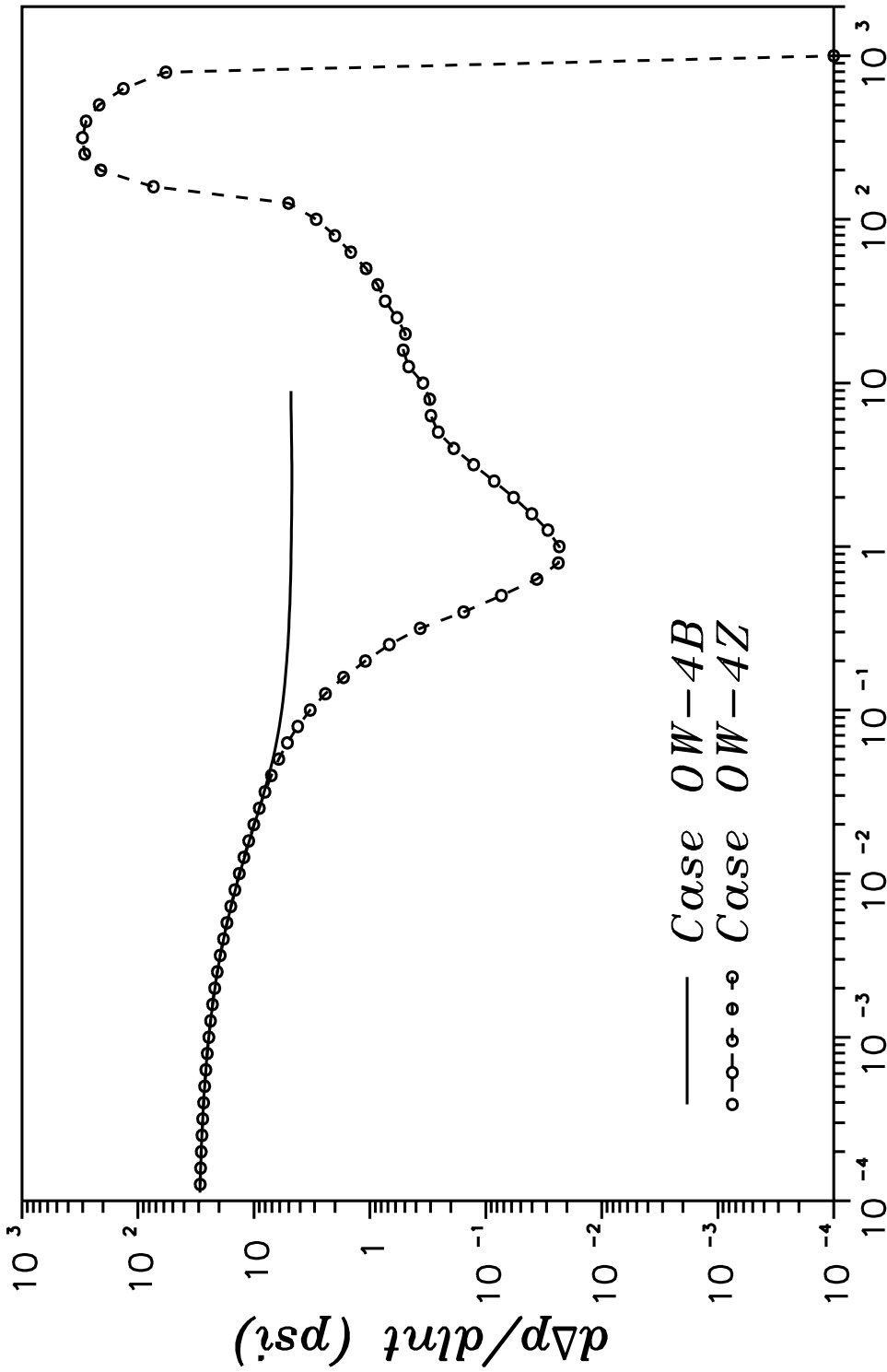

Fig. 5.6 – Pressure derivative response for oil reservoir–aquifer systems.

a 10 day constant rate drawdown test was simulated and followed by a 10 day buildup test.

The drawdown logarithmic derivatives of the wellbore pressure response for these reservoir systems are shown in Fig. 5.7. As expected, the single-phase case (WG-3X) shows the typical pressure derivative response commonly associated with a constant pressure boundary, i.e., the log-derivative of the wellbore pressure drop monotonically decreases towards zero.

The log-derivative of the drawdown pressure responses for the multiphase cases WG-3Y and WG-4Z, however, again show a marked difference from the single phase case; i.e., after the initial rapid decline in the derivative after "feeling" the constant pressure boundary, the derivative increases. As with the oil-water cases discussed above, the pressure response for case OW-4Z is delayed in time (as compared to the response obtained for case WG-3Y) due to the increased thickness in the whole reservoir (both water and gas zones). Note, however, that the difference between cases WG-3Y and WG-4Z is much less than the difference between the oil-water cases OW-3Y and OW-4Z. This is simply due to the diffusivity for the gas phase being much greater than the diffusivity was for the water phase of the previous cases; i.e., the speed of propagation of a pressure transient is proportional to the diffusivity. Because of the high mobility in the gas cap and, therefore, the short time required for a pressure transient to transverse it, the pressure derivatives for cases WG-3Y and WG-4Z very quickly become nearly identical. Unlike the oil-water cases discussed above in which it was shown that the location of the constant pressure boundary would necessarily have to be part of the solution in any attempt to match the early time pressure response with single-phase constant pressure boundary solutions, the current cases imply that many different reservoir descriptions (gas-cap thicknesses) can result in nearly identical pressure responses, rendering the match to the single-phase solution non-unique. Another

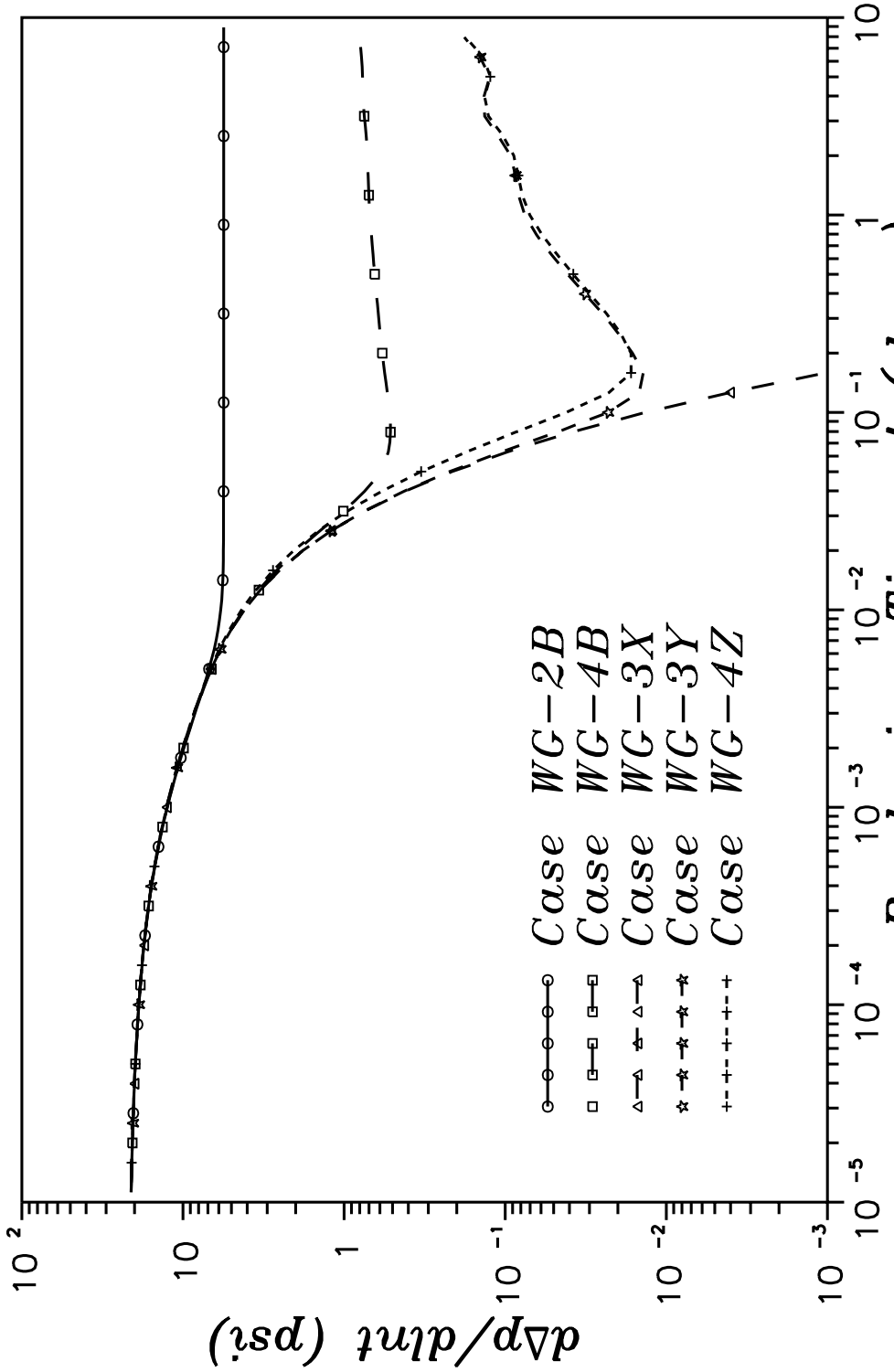

Fig. 5.7 – Comparison of pressure derivative responses for various constant pressure upper boundary reservoir systems.

way of viewing this result is that any attempt to match the pressure response to single-phase solutions necessarily requires the constant pressure boundary be located near the gas-water contact.

As with the oil-water cases discussed in the previous section, the increase in $d\Delta p(t)/d\ln t$ for cases WG-3Y and WG-4Z is due to the decrease in the total mobility near the sharp saturation front or "shock" which develops due to gas influx in the reservoir near the gas-water contact and which propagates towards the well. Prior to developing a theoretical expression similar to that derived in the previous section, we again examine the assumptions underlying the fractional flow theory as they pertain to the current problem.

Figure 5.8 shows the total relative mobility, velocity of lines of constant saturation and the velocity of a saturation shock as a function of gas saturation for the water-gas system being investigated. The gas viscosity used in the mobility calculations was calculated at the initial pressure of the original gas-water contact. Note that the pressure at this location only changes 0.3 psi during the entire test for case WG-4Z. Here we see that the minimum total relative mobility is approximately $\lambda_{rt} \approx 0.8$ cp^{-1} and occurs at a gas saturation of approximately 12 percent, the maximum specific velocity for a line of constant saturation occurs at a gas saturation of approximately 17 percent and the maximum specific shock velocity occurs at a gas saturation of approximately 25 percent. These specific velocities were calculated using the equations developed from fractional flow theory in Chapter IV. Recall that the maximum specific shock velocity represents the specific velocity that a saturation shock would actually propagate should a shock develop in the reservoir.

Figure 5.9 shows the in-situ volumetric flow rate at the sandface and across the upper boundary for cases WG-3Y and WG-4Z. Here we see the in-situ volumetric flow rates across the upper boundary has reached 97% of the sandface

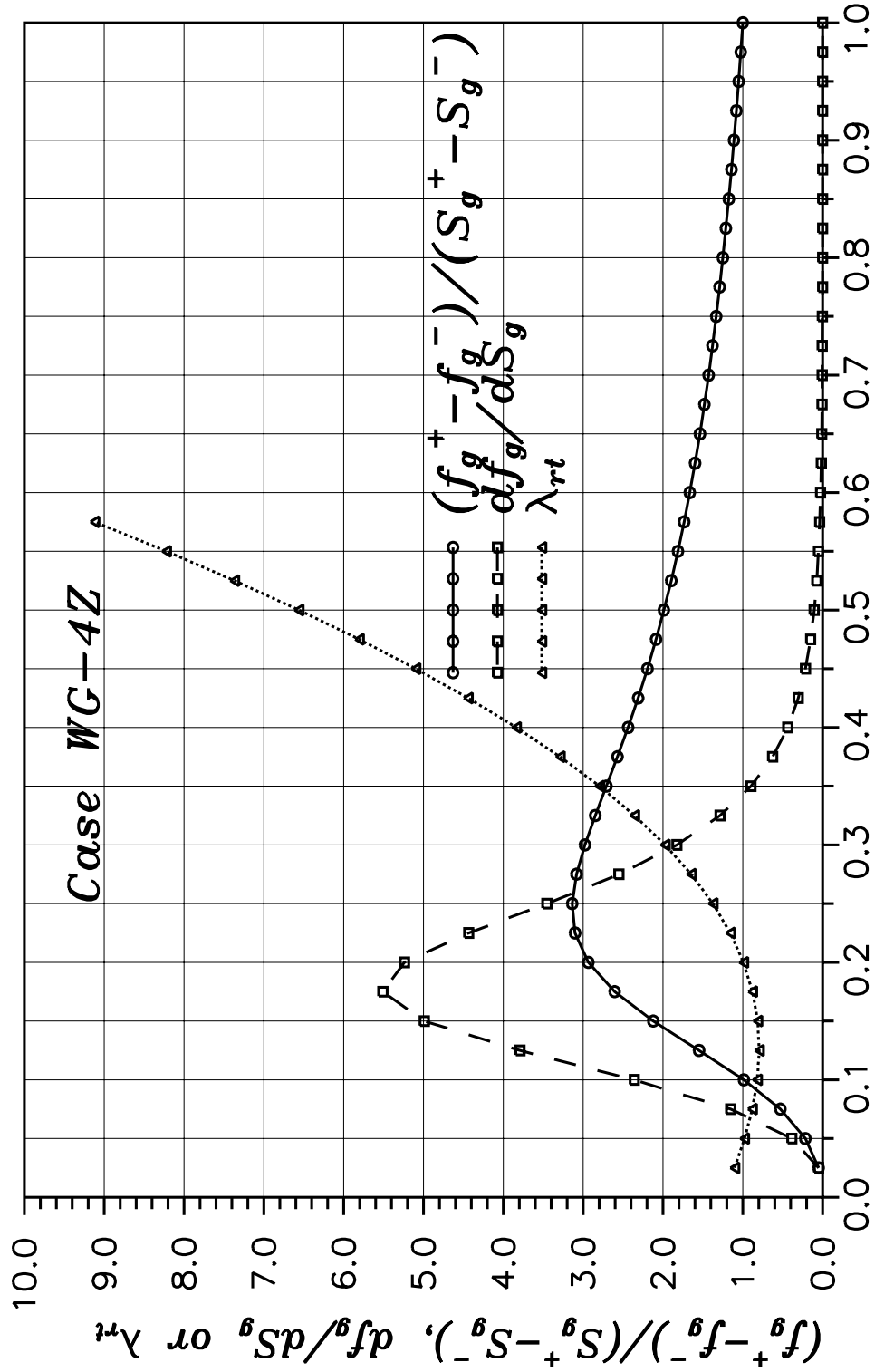

Fig. 5.8 — Relationship between velocity of constant saturation lines and total mobility.

volumetric rate by 0.1 days and 99% by 0.5 days; i.e., the in-situ volumetric flow rates have become constant and equal across both the sandface and the lower boundary. Numerical results not shown indicate that the total fluid flow rate across any cross-section (either radial or vertical) has also stabilized by this time.

Lastly, Fig. 5.10 shows the vertical gas saturation profile in the first radial grid block for various times during the drawdown. Figure 5.10 clearly shows the sharp saturation front, or "shock", which develops in the reservoir as gas influxes into the reservoir and propagates towards the well. As mentioned above, the saturation at the saturation shock predicted by fractional flow theory is $S_g = 0.25$. We have also indicated this saturation on Fig. 5.10 to show that there is a small amount of dispersion across the saturation front apparent from our numerical results. None-the-less, the existence of this sharp saturation front allows us to now consider developing a theoretical expression for the log-derivative of the wellbore pressure drop similar to that derived in the previous section for the oil-water constant pressure boundary cases.

Following the same procedure as used in the previous section, an expression for the log-derivative of the wellbore pressure drop is readily derived to obtain

$$\frac{\partial \Delta p}{\partial \ln t} \approx - \frac{\partial p_{wf}(z_{wb},t)}{\partial \ln t}$$

$$\approx \frac{-t}{c_1 k_z} \int_{z_f^-}^{z_f^+} \left\{ \frac{1}{{\lambda_{rt}}^2} \left[v_{zt} - G \right] \frac{\partial \lambda_{rt}}{\partial t} + \frac{1}{\lambda_{rt}} \left[\frac{\partial G}{\partial t} \right] \right\} dz' \quad , \qquad (5.2.28)$$

where

$$\Delta p = p_i(z=h) - p(r_w^+, z=z_{wb}, t) \approx p_i(z=h) - p_{wf}(z=z_{wb},t) \quad . \qquad (5.2.29)$$

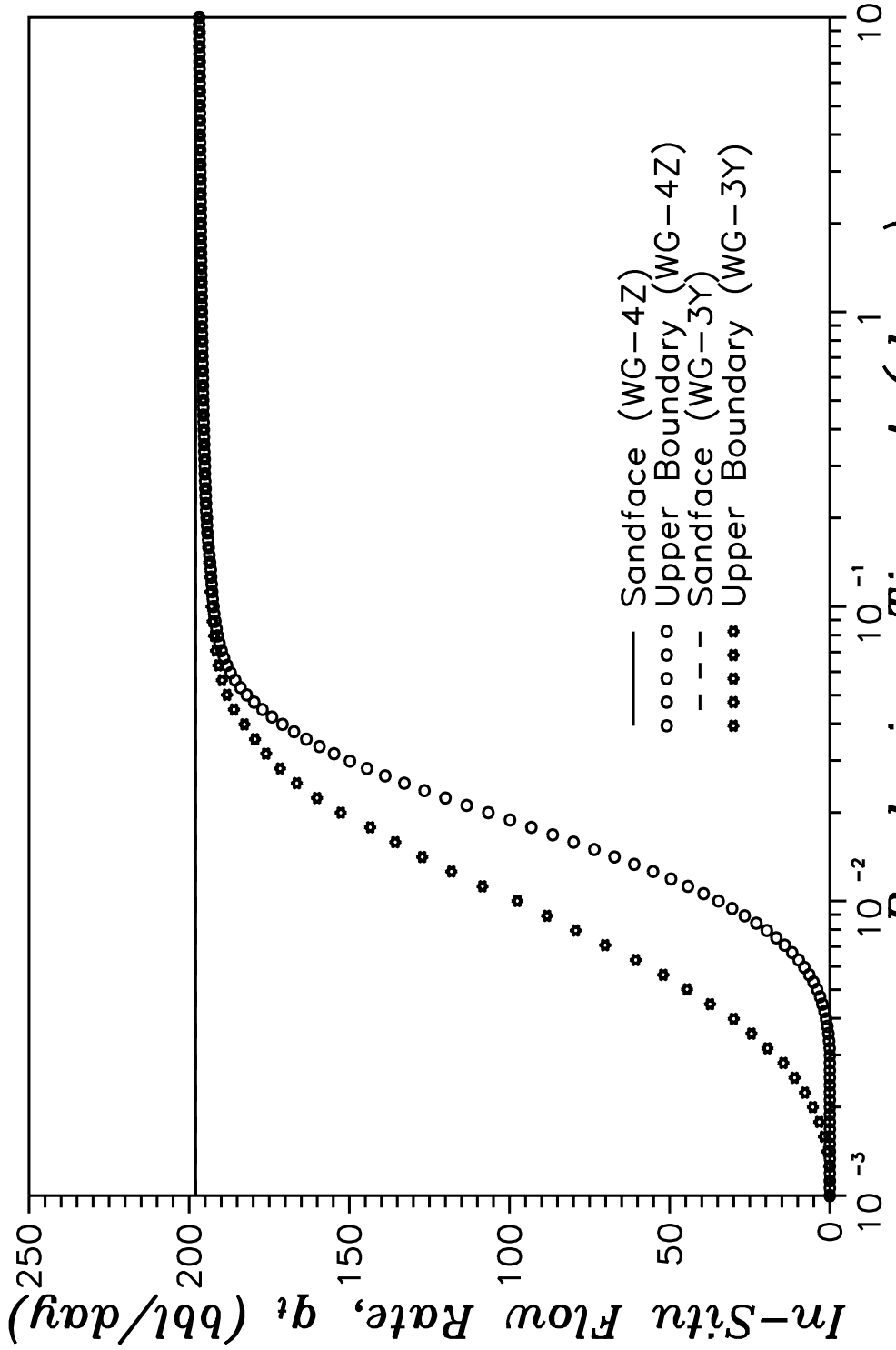

Fig. 5.9 – Comparison of in-situ reservoir flow rates at the sandface and across the upper boundary.

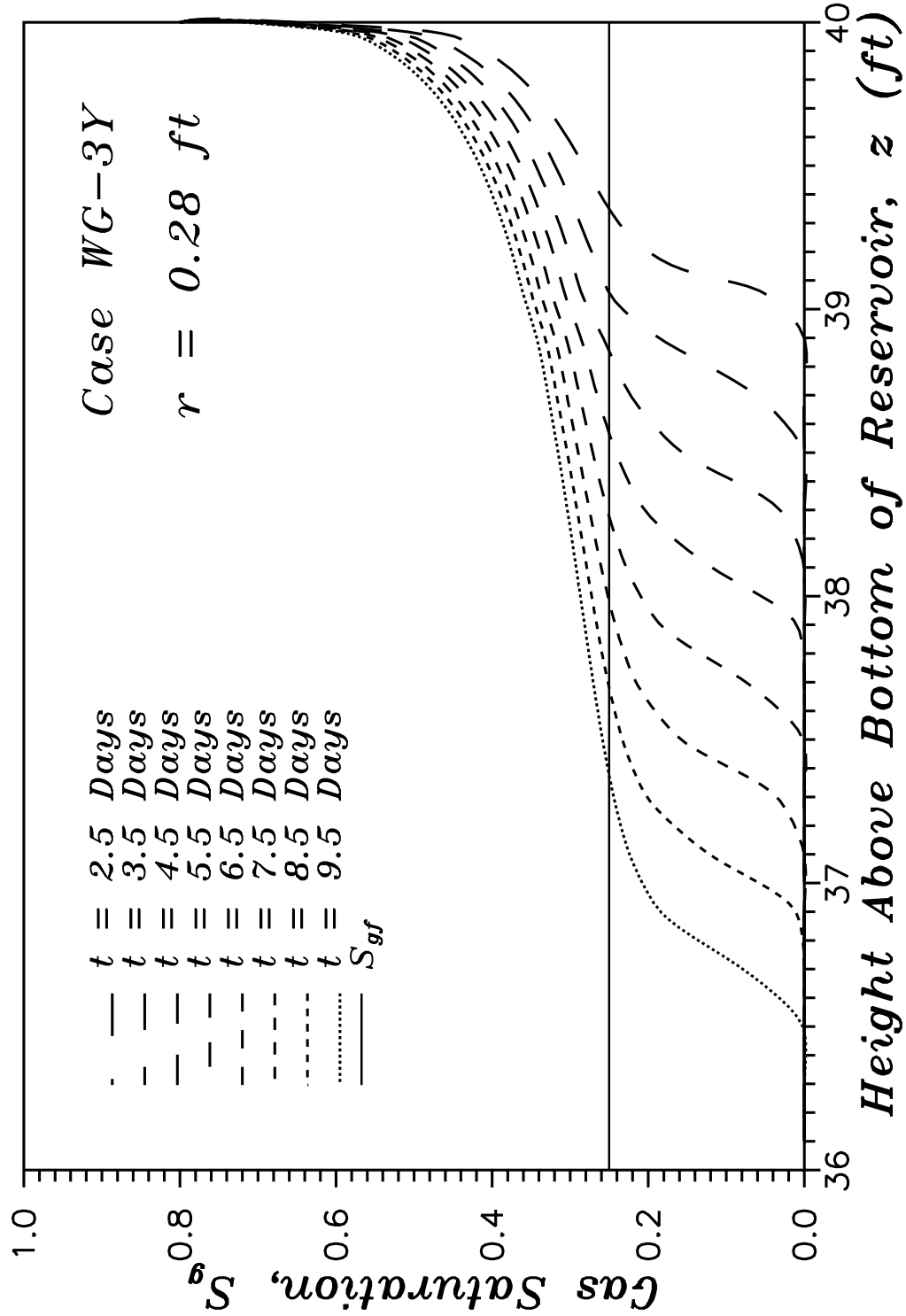

Fig. 5.10 – Vertical saturation profiles near inner boundary indicate formation of a sharp saturation front.

Here, the total fluid vertical velocity is defined simply as the sum of the water and gas phase velocities. The gravity term, G, is given here as

$$G(r,z,t) = c_1 k_z[\lambda_{rg}(r,z,t)\gamma_g(r,z,t) + \lambda_{rw}(r,z,t)\gamma_w(r,z,t)] \quad , \qquad (5.2.30)$$

and the limits of integration are the leading edge of the saturation front, z_f^-, and the trailing edge of the saturation front, z_f^+. Equation 5.2.29 indicates that the log-derivative of the wellbore pressure drop depends on the total fluid vertical velocity, the total relative mobility, the gravity term, and how these parameters change with-respect-to time across the sharp saturation front which develops.

Unlike the oil-water cases discussed in the previous sections, additional simplifications of Eq. 5.2.28 can only be partially justified due to the presence of the highly compressible and low viscosity gas phase. Due to the high compressibility of the gas phase, the derivative of the gravity term can only be simplified if pressure changes are small such that $\partial\gamma_g/\partial t$ is also small. Changes in the gas phase relative mobility in the single phase gas region can likewise only be neglected if pressure changes are small such that variations in the gas-phase viscosity can be neglected. Recall we previously noted that the pressure change at the gas-water contact only varied by 0.3 psi over the duration of the well test for case WG-4Z. Numerical calculations show the maximum value for the gravity term is $G = 0.0585$ and the maximum value for the derivative of the gravity term with-respect-to gas saturation is $\partial G/\partial S_g = -0.1142$. These values compare with a maximum value for the total relative mobility of $\lambda_{rt} = 29.81$ and a maximum value for the derivative of the total relative mobility with-respect-to gas saturation of $\partial\lambda_{rt}/\partial S_g = -58.23$; i.e., the total relative mobility and it's derivative are several orders of magnitude greater than the gravity term and it's derivative, respectively, for the current water-gas systems.

Another complication in Eq. 5.2.28 for the current cases is that both the velocity term and gravity term are positive quantities. This means that the gravity term and velocity term tend to negate the effect of each other, reducing the overall effect of the time derivative of the total relative mobility and, thus, increasing the relative contribution of the time derivative of the gravity term on the pressure derivative. Note that the time derivative of both the total relative mobility and the gravity term are negative quantities across the saturation front. Provided then that the total fluid velocity, v_{zt}, remains greater than the gravity term, G, then the entire term inside the integral of Eq. 5.2.28 must be a negative quantity and, therefore, the log-derivative of the wellbore pressure drop must be positive.

As discussed in the previous section, the total fluid velocity in both the vertical and radial directions must increase as we move towards the well. So, while the total fluid velocity term in Eq. 5.2.28 will increase as the saturation front moves towards the well, the gravity term, G will remain fixed and so the overall contribution from the mobility derivative will increase, causing the log-derivative of the wellbore pressure drop to increase also. Thus, the increasing derivative exhibited in Fig. 5.7.

5.2.3 Oil-Gas Systems

Here we examine the pressure response for various oil reservoir - gascap systems. Referring to Fig. 4.4 and Table 4.4, the oil-gas systems we examine include cases OG-5B, OG-3X, OG-3Y and OG-5Z. Each of the four cases consist of a 40 foot oil reservoir with only the bottom ten feet perforated. For case OG-5B, a 20 foot gascap overlays the oil zone and the upper boundary is closed, i.e., a no-flow boundary. The upper boundary is located at the top of the oil zone for case OG-3X and is modeled as a constant pressure boundary (at initial pressure) and is considered to be 100 percent oil (with it's associated solution gas). Note that this

case **does not** conceptually or physically represent the single-phase analytical solution to the problem, though it is probably the closest we can get and still maintain some of the true physics of the problem; i.e., though the reservoir is initially single phase for this example, we will see that the reservoir very quickly becomes two-phase in the near well region or the reservoir. Note also that the bubble point for this fluid at the upper boundary is fixed at a constant value. Fluid influx into the reservoir across the upper boundary then is single-phase oil plus its associated solution gas. Case OG-3Y is identical to case OG-3X except the fluid saturation at the upper boundary is specified as 80 percent gas (water is at residual water saturation and considered incompressible). For this case, the fluid influx into the reservoir will be entirely gas. Case OG-5Z includes a 20 ft. gascap above the oil zone and a constant pressure boundary (at initial pressure and gas saturation) above the gascap. Case OG-5B is included in the following figures merely for reference or comparison purposes. For each of these cases, a 10 day constant rate drawdown test was simulated and followed by a 10 day buildup test.

The drawdown logarithmic derivative of the wellbore pressure response for each of these reservoir systems is shown in Fig. 5.11. As compared to the oil-water and water-gas cases discussed previously, Fig. 5.11 shows that the constant pressure boundary has much less relative effect on the pressure response for oil-gas systems; i.e., the pressure derivatives for the oil-gas cases do not show the rapid decline once the constant pressure boundary is "felt". In fact, only a slight displacement in the derivative is seen as compared to the closed boundary case (OG-5B). Also note that the log-derivative of the wellbore pressure drop is an order of magnitude larger at late time ($t > 0.1$ days) for the current cases than it was for the water-gas cases of the previous section.

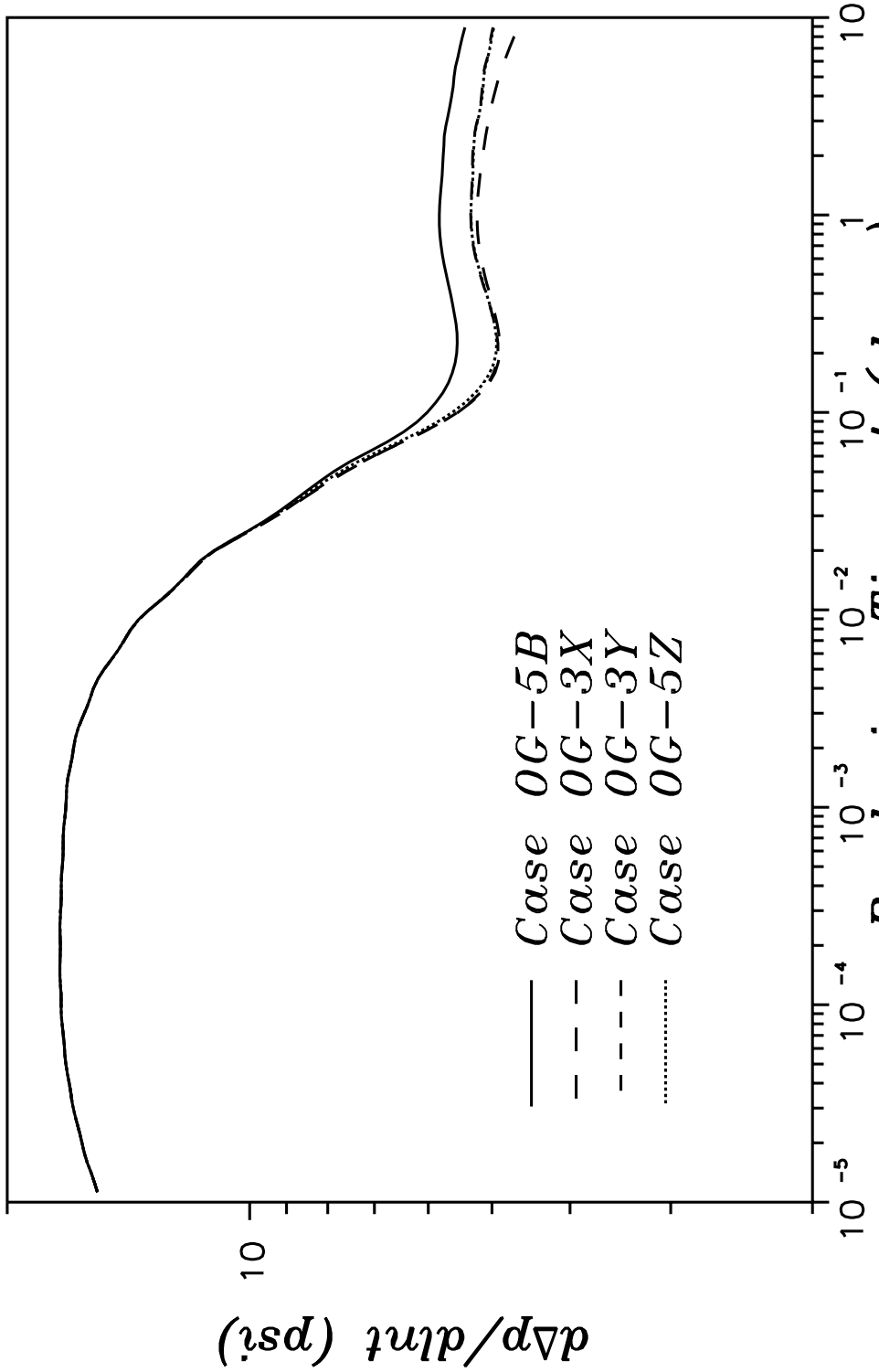

Fig. 5.11 – Comparison of pressure derivative responses for various constant pressure upper boundary reservoir systems.

For cases OG-3Y and OG-5Z, changes in the total mobility near the gas-oil contact are of the same order of magnitude as changes in the total mobility near the gas-water contact for the water-gas systems discussed in the previous section. This implies that the pressure response observed here is dominated by changes in the total mobility near the open interval of the wellbore. Figure 5.12 shows the vertical gas saturation profile in the first radial grid block at the end of the drawdown period for cases WG-4Z, OG-3X and OG-5Z. Note that the changes in the saturation, and therefore the total mobility, at the top of the reservoir is much smaller for case OG-3X than for either WG-4Z and OG-5Z. Changes in the saturation, and therefore the total mobility, near the perforations are, however, nearly identical for cases OG-3X and OG-5Z. This implies that the small difference seen in the pressure derivative between case OG-3X and cases OG-3Y and OG-5Z is due to the changes in the total mobility near the original gas-oil contact. This is in keeping with the results we report in Chapter VI for the closed boundary gascap cases and the results of the previous section. Clearly, there are no circumstances under which the pressure responses shown (Fig. 5.11) could be approximated by single-phase analytical solutions for slightly compressible fluids.

To understand why the log-derivative of the wellbore pressure drop is dominated by changes in the total relative mobility near the open interval of the wellbore, we again make use of the vertical form of Ref. 149's theoretical expression for the wellbore pressure drop. For the current oil-gas reservoir systems in which the upper boundary is held at a constant pressure boundary, we can express the log-derivative of the pressure drop adjacent to the wellbore as

$$\frac{\partial \Delta p}{\partial \ln t} \approx - \frac{\partial p_{wf}(z_{wb}, t)}{\partial \ln t}$$

$$\approx \frac{-t}{c_1 k_z} \int_{z_{wb}}^{h} \left\{ \frac{1}{{\lambda_{rt}}^2} \left[v_{zt} - G \right] \frac{\partial \lambda_{rt}}{\partial t} - \frac{1}{\lambda_{rt}} \left[\frac{\partial v_{zt}}{\partial t} - \frac{\partial G}{\partial t} \right] \right\} dz' \quad . (5.2.30)$$

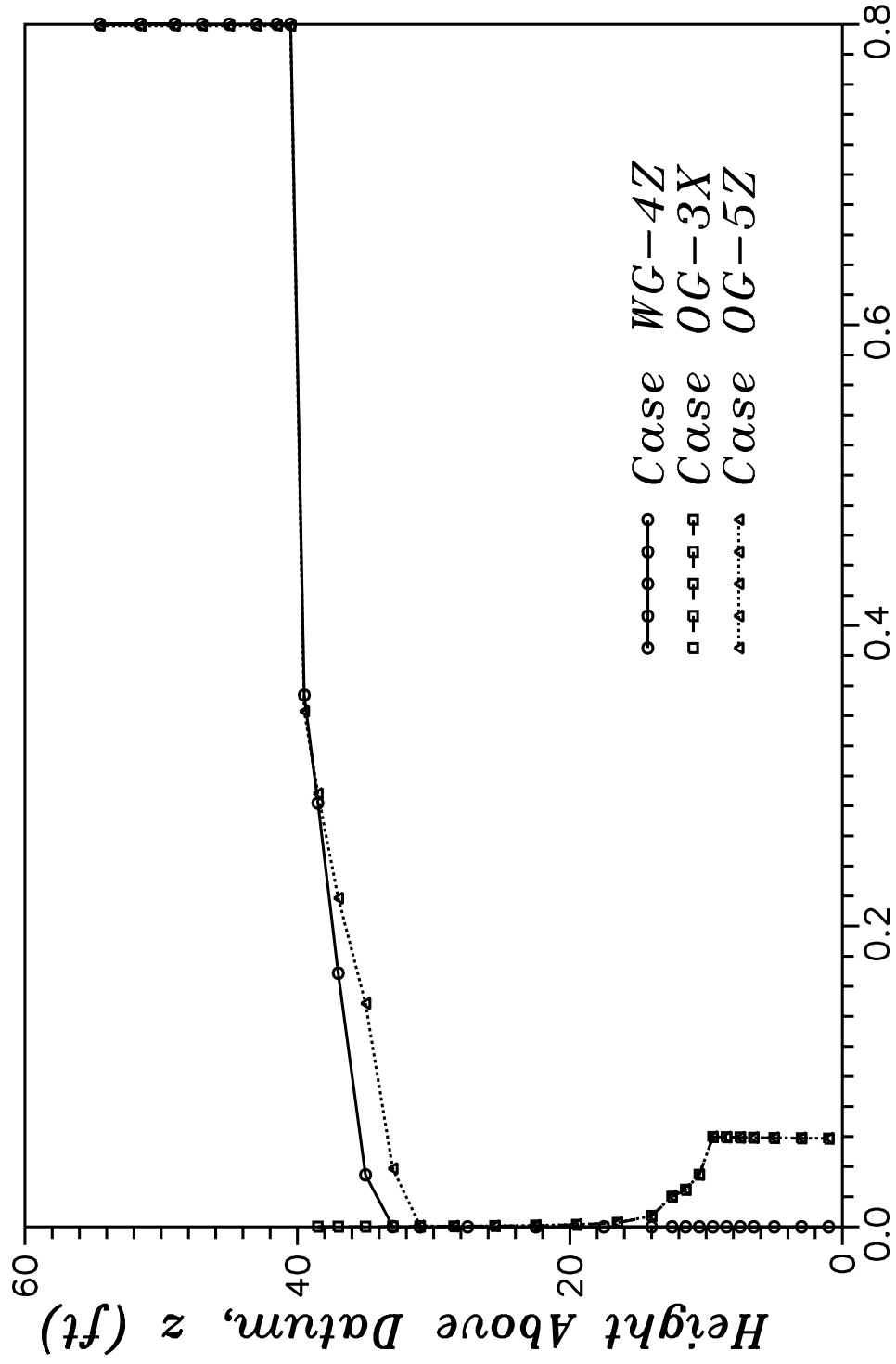

Fig. 5.12 – Comparison of vertical saturation profiles for various constant pressure upper boundary reservoir systems.

Here, we are integrating from the wellbore reference height to the top of the reservoir (where the constant pressure boundary is located). Also, the total relative mobility is given here by

$$\lambda_{rt} = \lambda_{ro} + \lambda_{rg} = \frac{k_{ro}}{\mu_o} + \frac{k_{rg}}{\mu_g} \tag{5.2.31}$$

and the gravity term, G, is given by

$$G(r,z,t) = c_1 k_z [\lambda_{ro}(r,z,t)\gamma_o(r,z,t) + \lambda_{rg}(r,z,t)\gamma_g(r,z,t)] \quad . \tag{5.2.32}$$

Similar to the oil-water and water-gas systems discussed in previous sections, the volumetric flow rate and, therefore, the total fluid velocity becomes essentially constant ($\partial v_{zt}/\partial t = 0$) very quickly once the constant pressure boundary has been "felt" at the sandface. As such, Eq. 5.2.30 can be simplified to obtain

$$\begin{aligned} \frac{\partial \Delta p}{\partial \ln t} &\approx - \frac{\partial p_{wf}(z_{wb},t)}{\partial \ln t} \\ &\approx \frac{-t}{c_1 k_z} \int_{z_{wb}}^{h} \left\{ \frac{1}{{\lambda_{rt}}^2} \left[v_{zt} - G \right] \frac{\partial \lambda_{rt}}{\partial t} + \frac{1}{\lambda_{rt}} \left[\frac{\partial G}{\partial t} \right] \right\} dz' \quad . \end{aligned} \tag{5.2.33}$$

Simply by examining Fig. 5.12, one may surmize that since changes in the gas saturation are much greater near the gas cap than near the sandface, the time rate of change in the total relative mobility will be much greater near the gas cap than near the sandface. As an example, we consider case OG-5Z and calculate the mobility derivatives over the duration of the drawdown both at the sandface and near the gas cap. At a producing time of 0.26 days, which is the time at which the magnitude of the mobility derivative reaches a maximum in the first vertical grid block (at first radial grid block) below the gas cap, $\partial \lambda_{rt}/\partial t = -0.027$ (cp-day)$^{-1}$ near the gas cap and $\partial \lambda_{rt}/\partial t = -0.003$ (cp-day)$^{-1}$ near the perforated

interval of the wellbore; i.e., the magnitude of the mobility derivative near the gas cap is an order of magnitude (actually, 9 times) greater than the mobility derivative near the wellbore. By similarity, the relative difference between the derivative of the gravity term, $\partial G/\partial t$, near the gas cap and near the wellbore is also an order of magnitude. Note that at initial conditions of pressure, numerical calculations show the maximum value for the gravity term is $G = 0.0468$ and the maximum value for the derivative of the gravity term with-respect-to gas saturation is $\partial G/\partial S_g = 0.133$. These values compare with a maximum value for the total relative mobility of $\lambda_{rt} = 23.85$ and a maximum value for the derivative of the total relative mobility with-respect-to gas saturation of $\partial \lambda_{rt}/\partial S_g = 58.2$; i.e., the total relative mobility and it's derivative are several orders of magnitude greater than the gravity term and it's derivative, respectively, for the current oil-gas systems.

The only way for changes in the mobility near the sandface to dominate the effect on the wellbore pressure drop then is for the term $v_{zt} - G$ to be much greater near the sandface than near the gas-oil contact. Numerical calculations show the gravity term, G, to be of the same order of magnitude both at the sandface and near the gas cap. This leads us finally to the conclusion that v_{zt} must be much greater near the sandface than near the gas cap in order for the derivative of the wellbore pressure drop to be affected more by changes in fluid and rock properties near the sandface, then near the gas cap. This is indeed the situation for case OG-5Z, which exhibits a total vertical velocity of 0.625 ft/day near the sandface and a total vertical velocity of only 0.013 ft/day near the gas cap. This means that the vertical fluid velocity near the perforations is over 48 times greater than the vertical fluid velocity near the gas cap. This is an order and a half magnitude difference in the total velocity. This explains why the log-derivative of the wellbore pressure drop is dominated by changes in the mobility near the wellbore, versus those changes which occur far from the well.

5.3 Buildup

In this section, we examine the buildup pressure response for those constant pressure boundary cases discussed in the previous sections. We note here that the pressure response signatures we discuss in this section may not be observable in practice due to the small absolute value of the measured pressure changes. None-the-less, the observed pressure responses are important in that they point to several important physical processes which occur in the reservoir during the buildup period of the well test.

5.3.1 Oil-Water Systems

Here we examine the pressure buildup response for the constant pressure lower boundary oil-water cases discussed in Section 5.2.1. Figure 5.13 shows the logarithmic derivative of the wellbore pressure response with respect to Agarwal equivalent time for various oil-water systems. The no-flow lower boundary cases OW-2B and OW-4B are included for reference purposes. As expected, the pressure derivative for case OW-3X monotonically decreases to zero once the constant pressure lower boundary is felt. Recall that case OW-3X conceptually represents the single phase analytical solution to the problem.

Figure 5.13 shows the pressure derivative for both cases OW-3Y and OW-4Z falling off rapidly once the constant pressure boundary is felt. At approximately 0.6 days for case OW-3Y and 0.9 days for case OW-4Z, however, the pressure derivative increases and generally stabilizes. This result was unexpected for the buildup period. After much analysis of the data for these problems, it was determined that the reason for this increase was related to a complex set of processes related to the effects of gravity and the constant pressure boundary on the multiphase

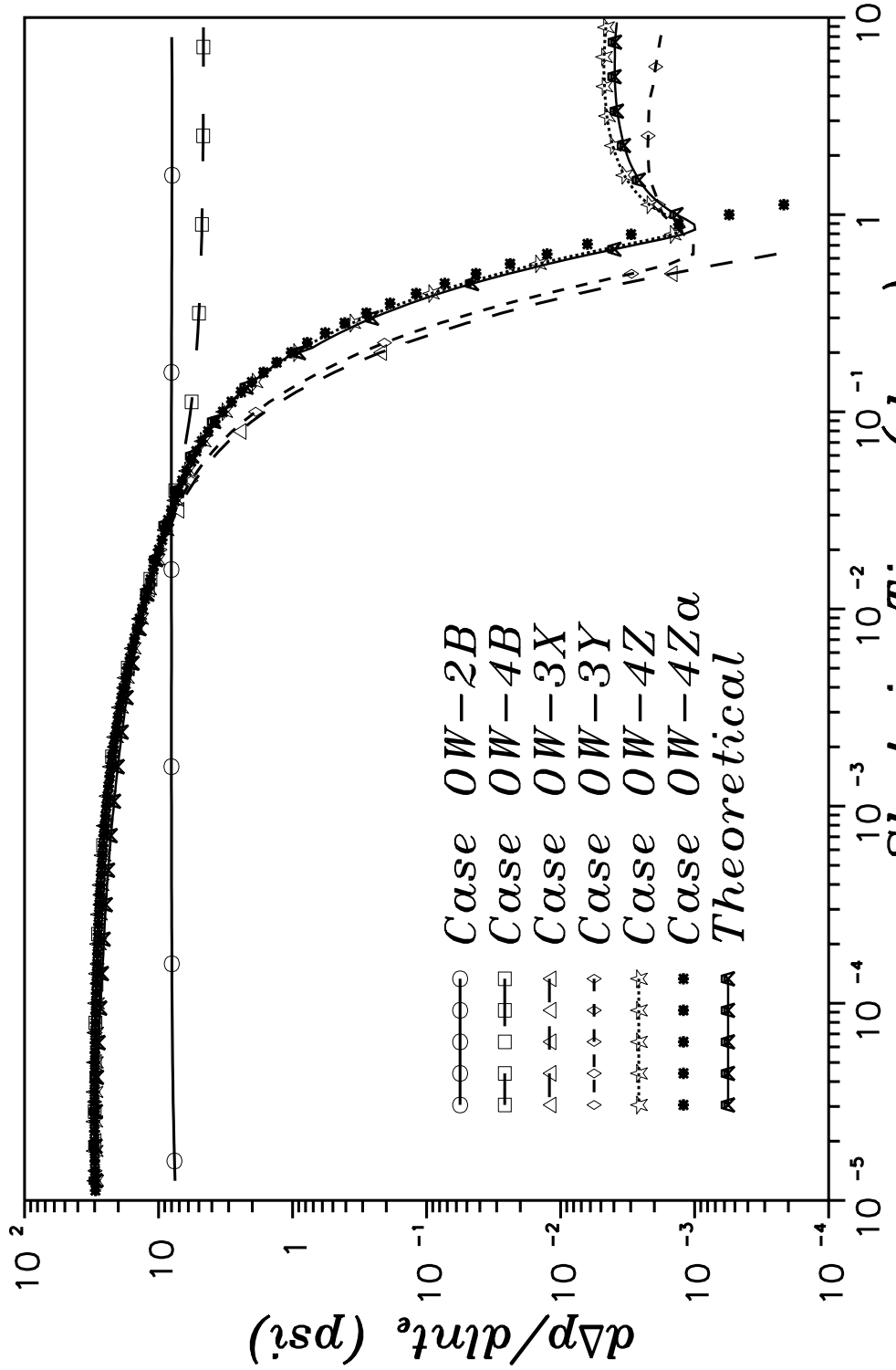

Fig. 5.13 — Comparison of pressure derivative responses for various constant pressure lower boundary reservoir systems.

system. To show that this response is related to the effects of gravity, case OW-4Za was run without including gravity effects in the model. Figure 5.13 shows the pressure derivative for case OW-4Za monotonically decreases to zero.

The physical manifestation of the effects of gravity on these oil-water systems is varied and interesting to note. First, we note that during the buildup, the reservoir pressure in the water zone near the sandface increases to values above the original reservoir pressure at those locations; e.g., at $\Delta t = 10$ days, the pressure at $z = 19.5$ feet is 3611.529 psia, versus the initial pressure of 3611.526 psia. Though the difference in these pressures is small in magnitude, it is very important when considering the physical processes occurring in the reservoir. This result indicates that through a production process only, followed by a buildup period, the reservoir pressure may increase above the initial reservoir pressure at certain locations.

In previous sections, various versions of a theoretical expression developed by Ref. 149 were used to partially explain the drawdown pressure response observed for various constant pressure boundary reservoir systems. It was noted previously that those theoretical expressions were equally valid for buildup as for drawdown. As such, we present without again going into the details of the derivation an expression for the buildup pressure response for the current oil-water reservoir systems:

$$\frac{\partial \Delta p}{\partial \ln \Delta t} \approx \frac{\partial p_{ws}(z_{wb}, \Delta t)}{\partial \ln \Delta t}$$

$$\approx \frac{\Delta t}{c_1 k_z} \int_0^{z_{wb}} \left\{ \frac{1}{\lambda_{rt}} \left[\frac{\partial v_{zt}}{\partial \Delta t} - \frac{\partial G}{\partial \Delta t} \right] - \frac{1}{{\lambda_{rt}}^2} \left[v_{zt} - G \right] \frac{\partial \lambda_{rt}}{\partial \Delta t} \right\} dz' \quad .(5.3.1)$$

Note that the right-hand-side of Eq. 5.3.1 is just the negative of the right-hand-side of Eq. 5.2.12 and with the producing time, t, replaced by the shut-in time,

Δt. Recall that the total relative mobility for the current systems is given by

$$\lambda_{rt} = \lambda_{ro} + \lambda_{rw} = \frac{k_{ro}}{\mu_o} + \frac{k_{rw}}{\mu_w} \tag{5.3.2}$$

and the gravity term, G, is given by

$$G = c_1 k_z [\lambda_{ro}\gamma_o + \lambda_{rw}\gamma_w] \quad . \tag{5.3.3}$$

Using numerical values for the vertical velocity, total relative mobility and gravity term output by our simulator for each vertical grid block along the first radial grid block for each time step, Eq. 5.3.1 was evaluated for case OW-4Z. The result is shown in Fig. 5.1 as the curve marked "Theoretical." Fig. 5.1 shows an excellent match between $\partial \Delta p / \partial \ln t$ calculated from Eq. 5.3.1 and $\partial \Delta p / \partial \ln t$ calculated directly from the wellbore pressures output by our simulator. We have thus numerically verified the correctness of Eq. 5.3.1.

In Section 5.2.1 we showed that the time rate of change in the total relative mobility was a negative quantity across the saturation front which developed in the reservoir and that the total fluid velocity was a negative quantity if flow was from the bottom of the reservoir towards the well. During the buildup test and until the induced pressure transient from shutting in the well has reached the two-phase region of the reservoir, the second group of terms inside the integral will then continue to be a negative quantity. Near the perforations, this term will be zero since the reservoir is single-phase oil and $\partial \lambda_{rt} / \partial \Delta t = 0$. Also near the perforations, $\partial G / \partial \Delta t = 0$, again because near the perforations the reservoir is single-phase oil. Recall, none-the-less, that $\partial G / \partial \Delta t$ will be small even in the two-phase region of the reservoir. During late-time of the drawdown test, it was reported that the total fluid velocity was essentially constant. Ahead of the pressure transient, then,

$\partial v_{zt}/\partial \Delta t$ will continue to be zero. Near the perforations, however, the total fluid velocity will decrease substantially (become less negative) during early-time in the buildup period. This means that $\partial v_{zt}/\partial \Delta t$ will be a positive quantity behind the leading edge of the pressure transient and, therefore, the first group of terms inside the integral will be a positive quantity. The dominance of the first group of terms over the second group of terms is what leads to the positive log-derivative of the wellbore pressure drop at early time. Even if the magnitude of the second group of terms inside the integral were of the same order as the first group of terms, their total contribution to the pressure derivative would still be an order of magnitude less than the first group of terms since the multiphase region is more than an order of magnitude less in size than the single phase region.

Of more interest in analyzing the derivative behavior is the late-time pressure response for the current cases. As the total fluid velocity in the two-phase region of the reservoir decreases, so must the derivative of the total relative mobility decrease. This combination of reduced values results in the second group of terms inside the integral becoming negligibly small. Similar to the total relative mobility, the derivative of the gravity term, G, in Eq. 5.3.1 also becomes negligibly small. This leaves the derivative of the total fluid velocity as the only parameter left to influence the pressure derivative.

During the buildup, the gravity forces act to reverse the vertical flow direction of the fluids in the reservoir. At 0.84 days, the flow direction in both the oil zone and in the transition zone generated due to the production of fluids is vertically upward. In the water zone near the well, however, the flow direction has reversed and the water begins to flow downwards and back out into the reservoir. Part of this result is due to the increased pressure (now above the initial reservoir pressure) discussed above. Figure 5.14 shows the total vertical flow rate of fluids across the reservoir as a function of vertical location and shut-in time. Figure 5.14

shows that at a shut-in time of 0.84 days, the flow direction in the water zone has switched from upward to downward flow. Note that the majority of the downward flow is in the near wellbore region of the reservoir.

Note that even though the direction of vertical total fluid velocity has changed from upward flow to downward flow, the sign of the derivative of the fluid velocity will remain positive since the change in the total velocity remains in the same direction; i.e., the total velocity continues to become less negative, or more positive. Figure 5.15 shows the log-derivative with-respect-to shut-in time of the vertical total fluid velocity at two vertical locations in the reservoir, $z = 46$ feet and $z = 21$ feet. The vertical location $z = 46$ feet is just below the lowermost perforation and the vertical location $z = 21$ feet is within the two-phase region of the reservoir. The vertical velocities used to calculate these derivatives were calculated along the innermost radial grid block of the reservoir. Figure 5.15 shows that the total vertical velocity decreases rapidly (derivative increases rapidly) in the region of the reservoir behind the pressure transient introduced by shutting in the well. As the velocity continues to decrease and approach zero, the log-derivative falls off rapidly. At 0.84 days, Fig. 5.15 shows the log-derivative of the vertical velocity begins to increase again. As noted above, this is precisely the time at which the total fluid velocity changes direction. Recall in Chapter IV that we showed that in the absence of capillary pressure, vertical equilibrium (zero vertical flow) can exist in a reservoir containing multiple fluid phases only if the phases were fully segregated. An examination and comparison of Fig. 5.15 with the log-derivative of the wellbore pressure drop for case OW-4Z shown in Fig. 5.13 supports our conclusion that the derivative of the wellbore pressure drop is reflecting the changes in (derivative of) the total fluid velocity.

Lastly, we observe that our oil-water reservoir system was initially in gravity equilibrium. Because the reservoir pressure has increased above the initial pressure

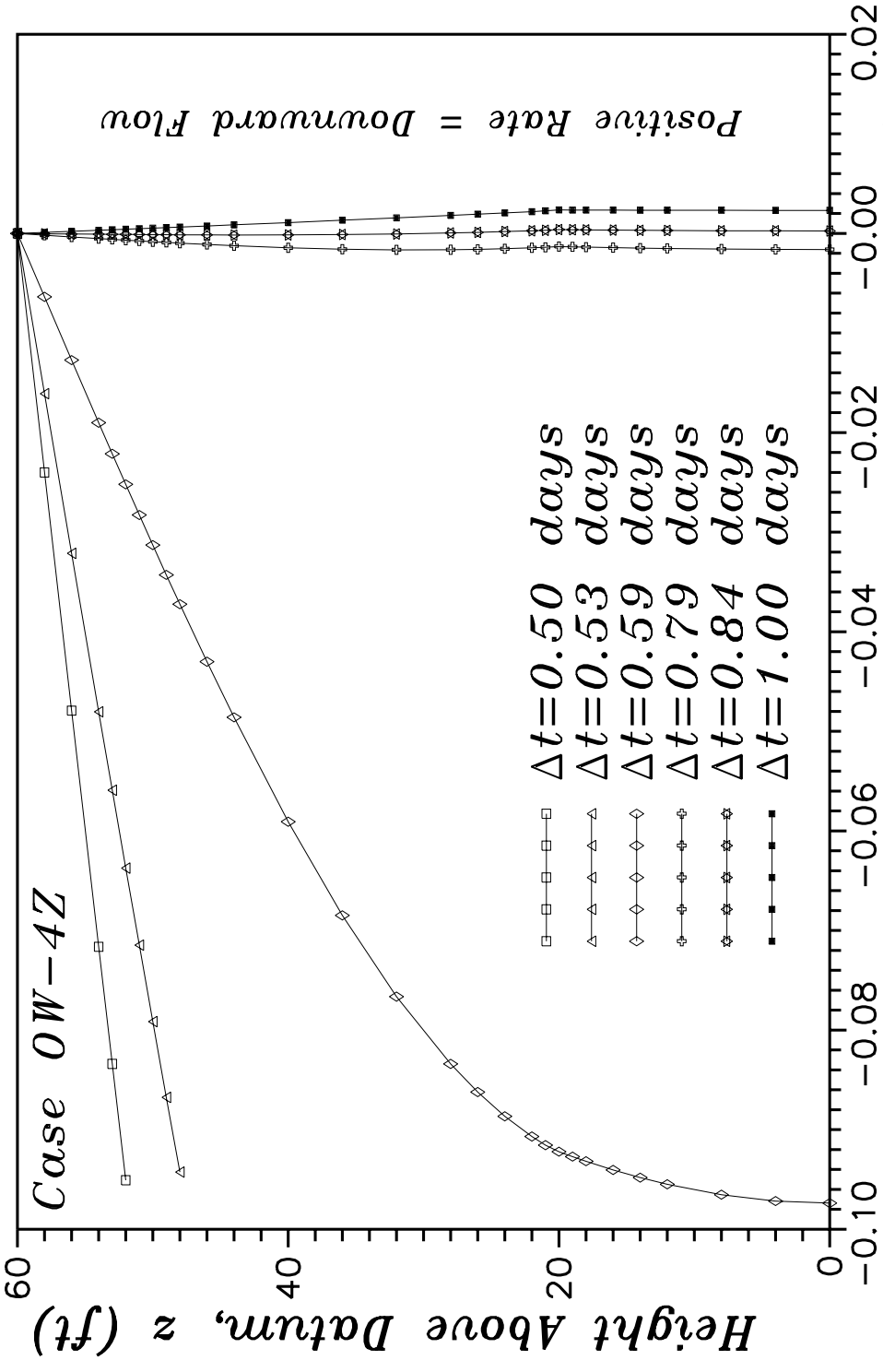

Fig. 5.14 – In-situ reservoir vertical flow rate as a function of shut-in time.

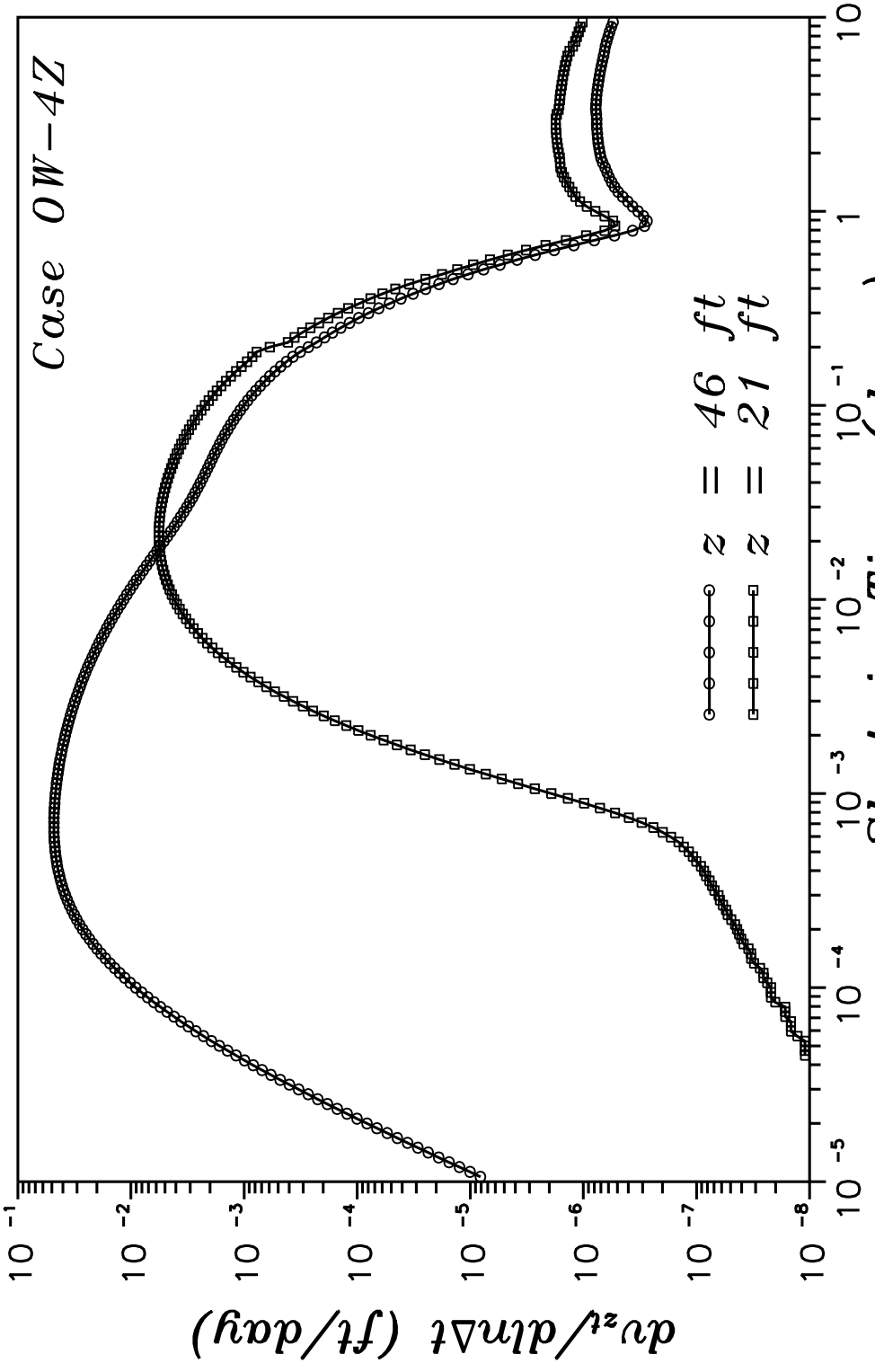

Fig. 5.15 – Log–derivative of vertical velocity as a function of shut–in time.

in the water zone, and the location of our constant pressure boundary has not changed, then our constant pressure boundary has become a sink and fluids will flow towards the boundary and out of our reservoir domain. Figure 5.16, which shows the total volumetric influx rate as a function of shut-in time, shows this to be exactly the case. At a shut-in time of approximately 0.84 days, the gross fluid influx into our reservoir has become negative, i.e., the fluid flow is out of the reservoir. Note also that this occurs precisely at the same time as the other phenomena discussed above.

5.3.2 Water-Gas Systems

Here we examine the buildup pressure response for those water-gas, constant pressure upper boundary cases discussed in Section 5.2.2. Figure 5.17 shows the log-derivative with respect to equivalent time of the wellbore shut-in pressure plotted as a function of shut-in time for cases WG-4B, WG-4X, WG-4Y, WG-4Z and WG-4Za. Recall that case WG-4B has a closed (no-flow) upper boundary and is included for reference purposes only. Also recall that case WG-3X is a single phase water reservoir with a constant pressure upper boundary and $S_w = 1.0$ at the upper boundary. As would be expected based on single phase flow theory, the pressure derivative for case WG-3X monotonically decreases to zero.

For cases WG-3Y and WG-4Z, Fig. 5.17 shows the log-derivative of the shut-in pressure decreases dramatically once the constant pressure boundary is felt. At a shut-in time of approximately 0.2 days, however, the derivatives for these two cases begin to increase. This response is similar to that reported in the previous section for the oil-water cases OW-3Y and OW-4Z, and as such, we suspect this response is due to the effects of gravity on the gas-water system. To verify this, case WG-4Za was run with the gravity option turned off in our simulator. Figure 5.17 shows the log-derivative of the shut-in wellbore pressure

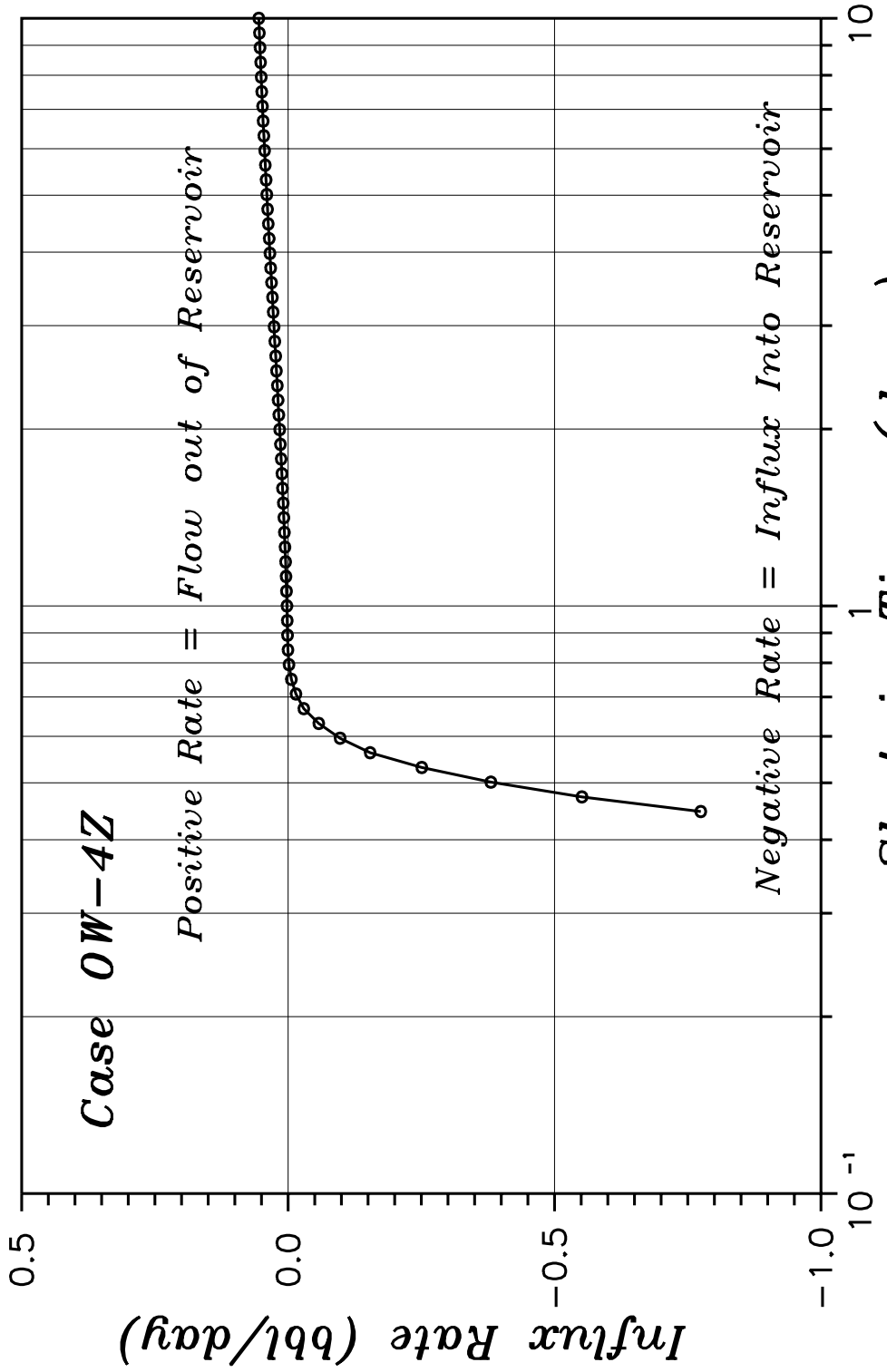

Fig. 5.16 – Water influx rate across the lower boundary.

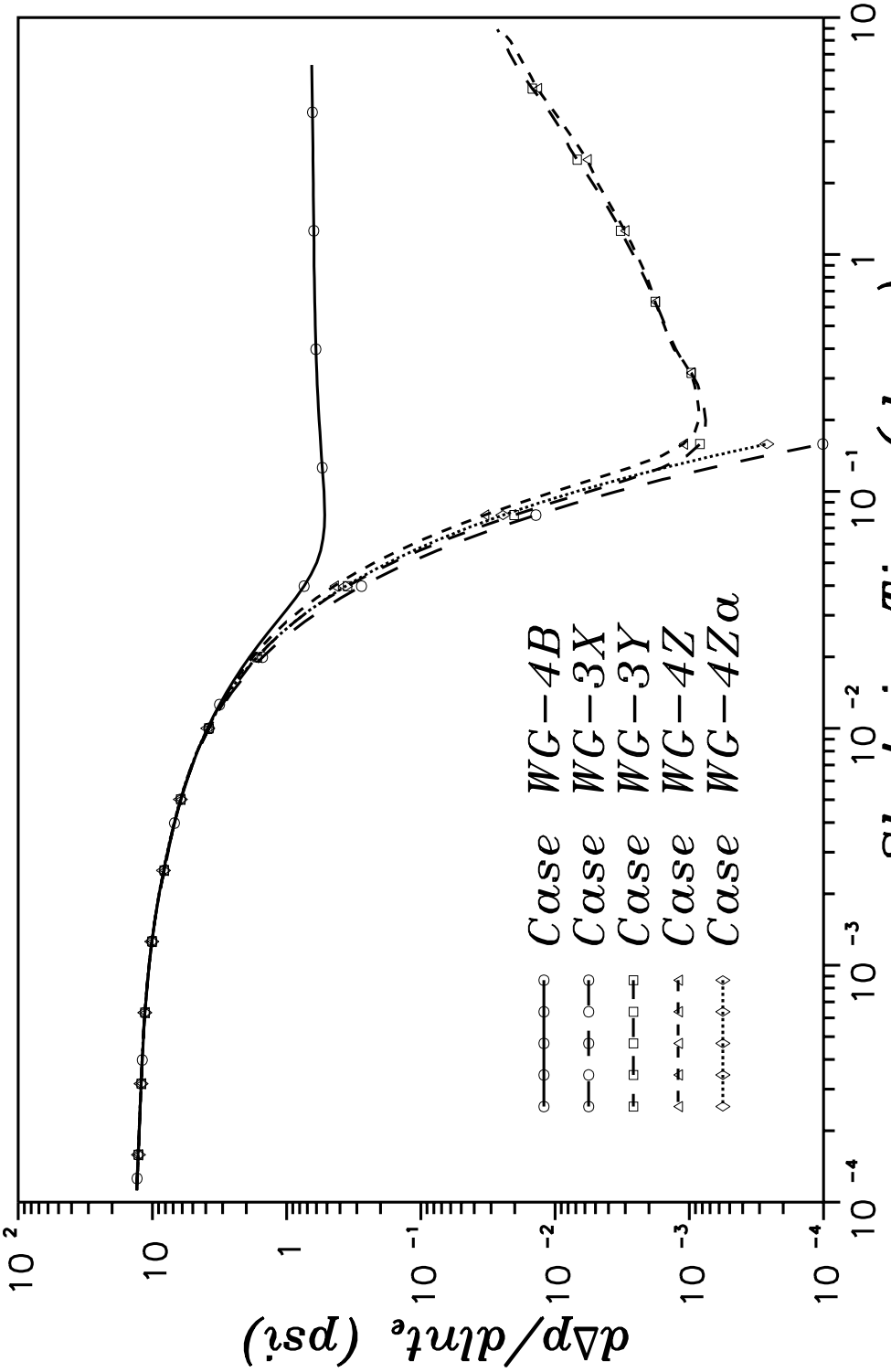

Fig. 5.17 – Comparison of pressure derivative responses for various constant pressure upper boundary reservoir systems.

for case WG-4Za monotonically decreases to zero, thus verifying that the increase in the log-derivative for cases WG-3Y and WG-4Z is due to the effects of gravity on our system. We also note that similar to the one-dimensional cases discussed in Chapter IV, the log-derivative of the shut-in wellbore pressure here exhibits a unit slope. Again, we have not fully investigated what physical significance, if any, this unit slope implies.

As with the oil-water cases noted above, the physical manifestation of the effects of gravity on these gas-water systems is complex and varied. Analogous to the oil-water cases, the pressure at the original gas-water contact during the buildup increases above the original reservoir pressure at that location. Figure 5.18 is a plot of the grid block pressure just above the original gas-water contact and near the inner boundary versus shut-in time. Also include in Fig. 5.18 is the initial pressure at that location. Figure 5.18 clearly shows the pressure at this location increases above the initial pressure at that location at a shut-in time of approximately 0.035 days. We note here that the difference between this pressure and the initial pressure, though still small, is much greater than for the oil-water cases discussed in the previous section. This result is important and directly related to the physical processes occurring in the reservoir.

Figure 5.19 shows the vertical gas saturation profile near the original gas-water contact as a function of shut-in time for case WG-4Z. Figure 5.19 clearly indicates that phase redistribution (gas percolation) occurs in the reservoir during the buildup, with the gas saturation decreasing below $z = 38.7$ feet and increasing above; e.g., the gas saturation decreases from $S_g = 0.16$ to $S_g = 0.13$ at $z = 37.0$ feet and increases from $S_g = 0.35$ to $S_g = 0.39$ at $z = 39.5$ feet. Figure 5.20, which shows the vertical phase and total flow rates in the reservoir at a shut-in time of $\Delta t = 10$ days for case WG-4Z, also provides clear evidence of phase redistribution in the reservoir, with the water flowing downward and gas flowing

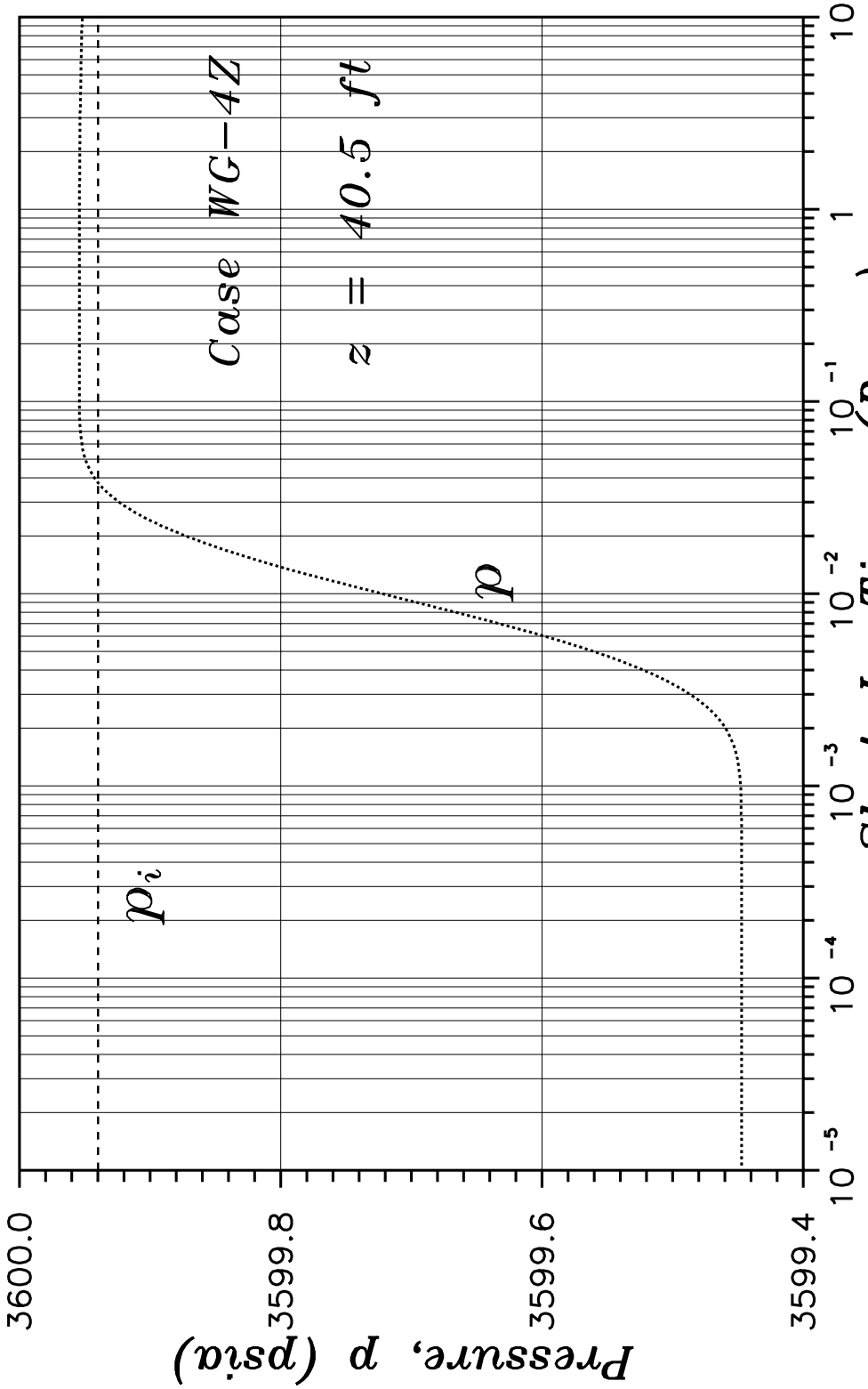

Fig. 5.18 — Comparison of initial pressure and pressure during buildup in the gas cap.

upward. Analogous to phase redistribution in the wellbore (though on a larger time scale), phase redistribution in the reservoir appears capable of causing reservoir pressures to increase to values greater than the initial reservoir pressure.

A variety of physical consequences arise due to the phase redistribution and increased pressure in that region of the reservoir. First, we note that because the reservoir pressure has increased above the initial pressure in the gas zone for case WG-4Z (in the developed gas-water transition zone for case WG-3Y) and the location of our constant pressure boundary has not changed, then our constant pressure boundary has become a sink and gas flows towards the boundary and out of the reservoir domain. Figure 5.21, which shows the gas influx rate into the reservoir for case WG-4Z, indicates that gas begins to flow out of the reservoir at approximately $\Delta t = 0.11$ days.

We also note that because of the increased pressure in the gas zone near the inner boundary, the potential exists for the gas to flow radially back out into the reservoir. Figure 5.22 shows the in-situ reservoir flow rates of gas, water and combined gas and water for case WG-4Z at a shut-in time of $\Delta t = 1.0$ day. Though the rates are small, Fig. 5.22 clearly shows the gas phase flowing away from the inner boundary and back out into the reservoir.

The question now arises as to how these physical phenomena affect the buildup pressure response. As in the previous section, an expression based the theoretical work of Ref. 149 can be obtained for the buildup pressure response for the current water-gas reservoir systems:

$$\frac{\partial \Delta p}{\partial \ln \Delta t} \approx \frac{\partial p_{ws}(z_{wb}, \Delta t)}{\partial \ln \Delta t}$$

$$\approx \frac{\Delta t}{c_1 k_z} \int_{z_{wb}}^{h} \left\{ \frac{1}{{\lambda_{rt}}^2} \left[v_{zt} - G \right] \frac{\partial \lambda_{rt}}{\partial \Delta t} - \frac{1}{\lambda_{rt}} \left[\frac{\partial v_{zt}}{\partial \Delta t} - \frac{\partial G}{\partial \Delta t} \right] \right\} dz' \quad . (5.3.4)$$

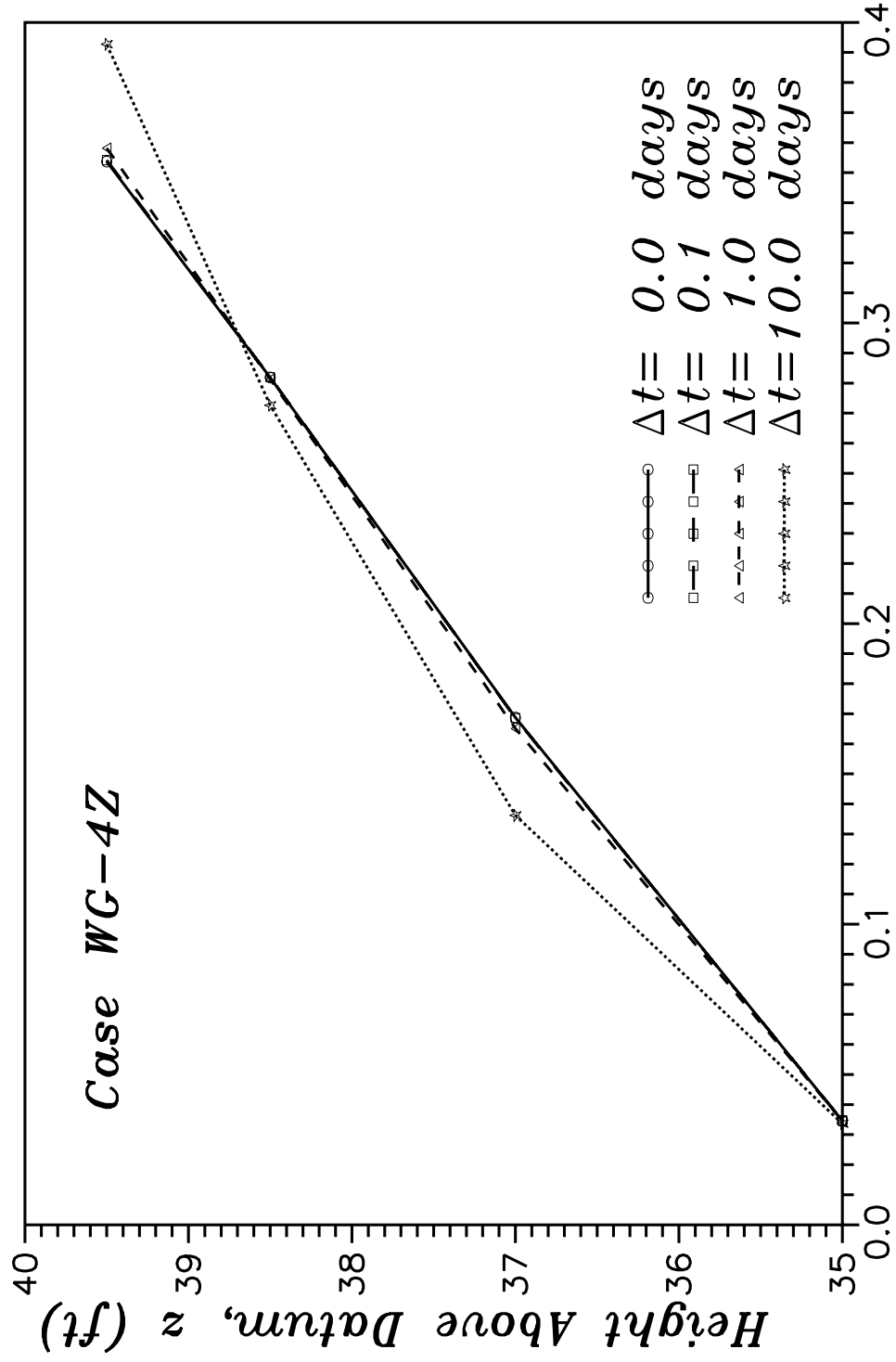

Fig. 5.19 — Gas saturation as a function of vertical position and shut-in time.

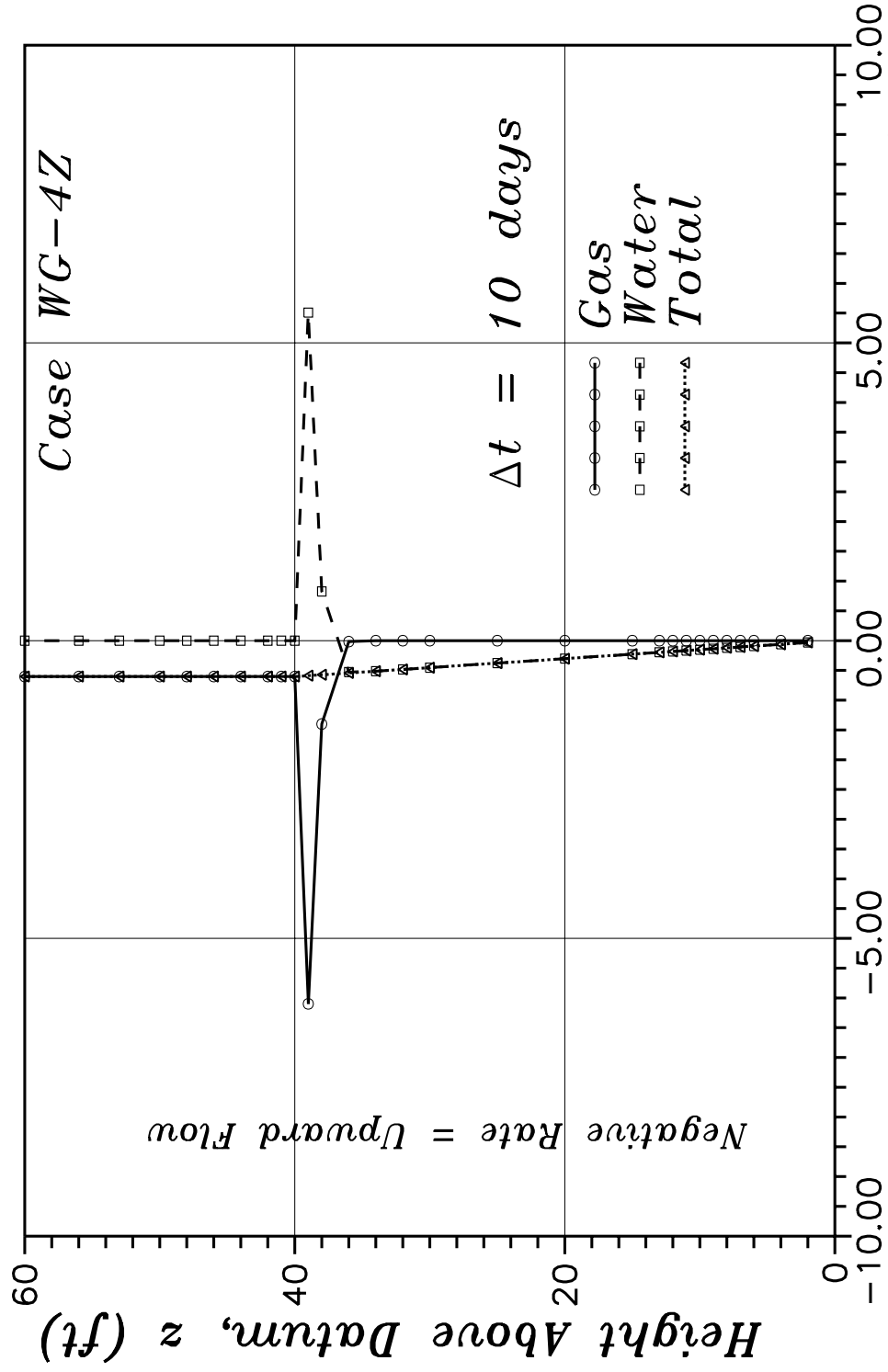

Fig. 5.20 – In-situ vertical flow rates as a function of vertical location.

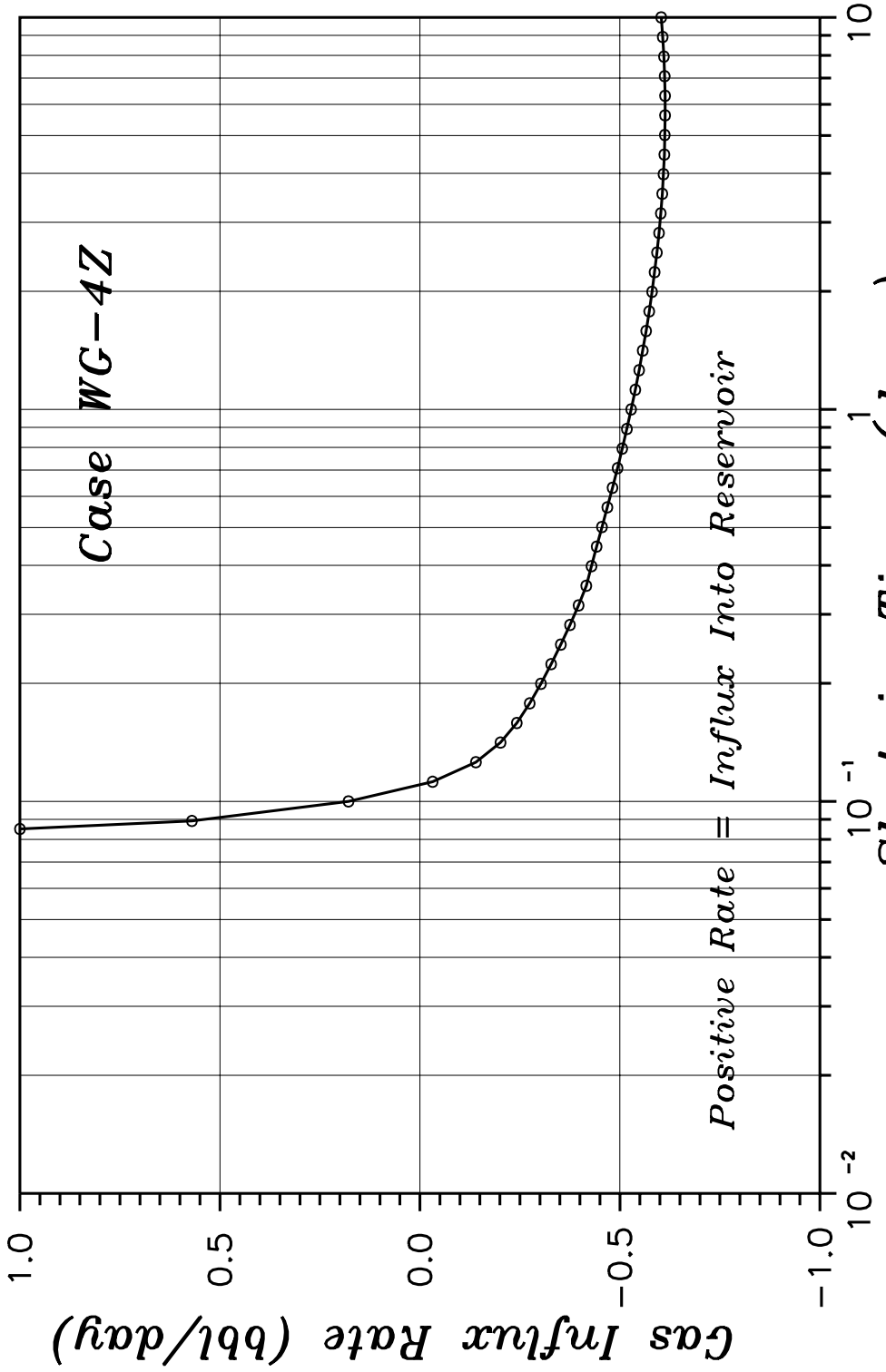

Fig. 5.21 – Gas influx rate across the constant pressure upper boundary.

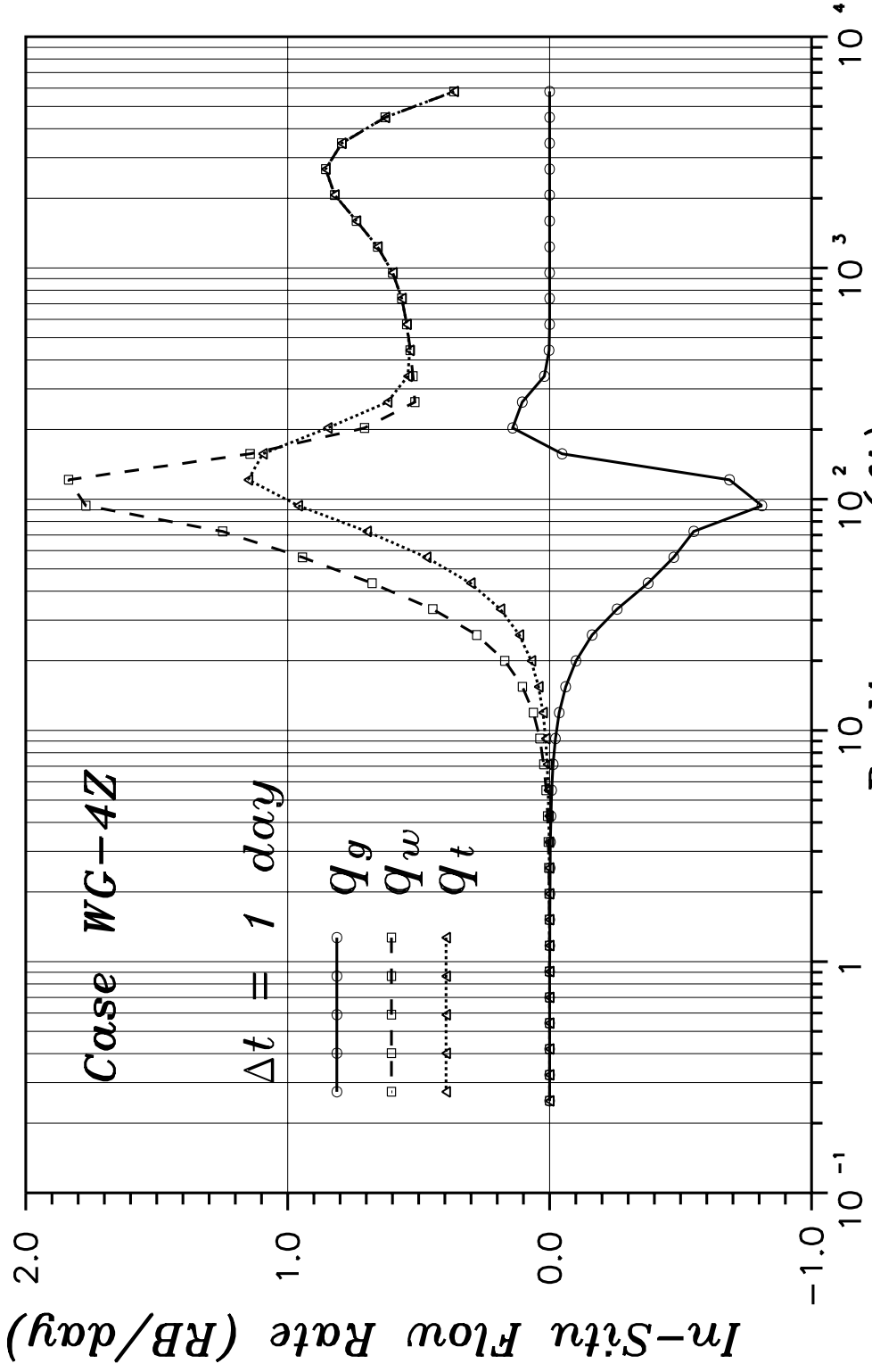

Fig. 5.22 – In-situ radial phase and total flow rates.

Here, the total relative mobility is given by

$$\lambda_{rt} = \lambda_{rw} + \lambda_{rg} = \frac{k_{rw}}{\mu_w} + \frac{k_{rg}}{\mu_g} \tag{5.3.5}$$

and the gravity term, G, is given by

$$G = c_1 k_z [\lambda_{rw}\gamma_w + \lambda_{rg}\gamma_g] \quad . \tag{5.3.6}$$

As before, we concern ourselves here with providing an explanation for the late-time pressure response observed in Fig. 5.17; i.e., the increasing log-derivative of the shut-in wellbore pressure. Again, we note that the first group of terms inside the integral of Eq. 5.3.4 will be zero everywhere except in the two-phase region of the reservoir. Because of the significant amount of phase redistribution occurring during the buildup period, $\partial\lambda_{rt}/\partial\Delta t$ and $\partial G/\partial\Delta t$ may still be significant in the two-phase region of the reservoir. Table 5.1 shows values of the various parameters in Eq. 5.3.4 at several vertical locations and at a shut-in time of 5.01 days. Items to note in Table 5.1 include the fact that the gravity term, G, is at least an order of magnitude greater than the total vertical velocity at each of these locations. This means that the term $[v_{zt} - G]$ will be a negative quantity at each location. Note also that, depending on the location, $\partial\lambda_{rt}/\partial\Delta t$ and $\partial G/\partial\Delta t$ may be either positive or negative. This is a consequence of the gas saturation decreasing in some grid blocks and increasing in others. Note that variations in the total relative mobility are significant across the various vertical locations shown. Considering the mobility-squared term in the denominator of the first group of terms, this has a significant impact on the relative contributions of the two groups of terms; e.g., consider at $z = 37$ feet, $1/{\lambda_{rt}}^2 = 1.49$, whereas at $z = 39.5$ feet, $1/{\lambda_{rt}}^2 = 0.09$. This is a full order of magnitude difference. Lastly, we note that because the derivative of the total vertical velocity is a positive quantity everywhere, then the contribution

to the pressure derivative from the single phase regions of the reservoir will be a negative quantity. The net result of each of these variations with location is that the only specific statement we can make concerning Eq. 5.3.4 is that the contribution from the multiphase region must be positive and greater than the contribution from the single phase regions of the reservoir (must be true since the log-derivative of the shut-in pressure is positive).

5.3.3 Oil-Gas Systems

In this section we examine the pressure buildup response for the oil-gas constant pressure upper boundary cases discussed in Section 5.2.3. The logarithmic derivative of the wellbore pressure with respect to equivalent time is plotted as a function of shut-in time in Fig. 5.23 for each of the cases OG-5B, OG-3X, OG-3Y and OG-5Z. The pressure responses for these cases look quite similar to those for the water-gas cases discussed in the previous section and shown in Fig. 5.16, and as such, we expect the underlying physics responsible for the pressure responses to also be similar. Figure 5.23 shows the pressure derivative for case OG-3X monotonically decreasing towards zero for the values of the derivative shown; the derivative for case OG-3X actually reverses and begins to increase at a shut-in time of approximately 1 day, but at this time it is approximately equal to 5×10^{-5} psi. Based on the discussion in the previous sections, this suggests that the effect of phase redistribution near the perforated interval is minimal for the values of gas saturation developed during the drawdown for this case. Analogous to the water-gas cases WG-3Y and WG-4Z discussed in the previous section, the pressure derivatives for cases OG-3Y and OG-5Z decrease rapidly once the constant pressure boundary is felt, but then reverse and increase at a constant rate (unit slope) once phase redistribution in the reservoir becomes significant.

Figure 5.24 shows the reservoir pressure as a function of shut-in time at a location just above the original gas-oil contact and near the inner boundary. As

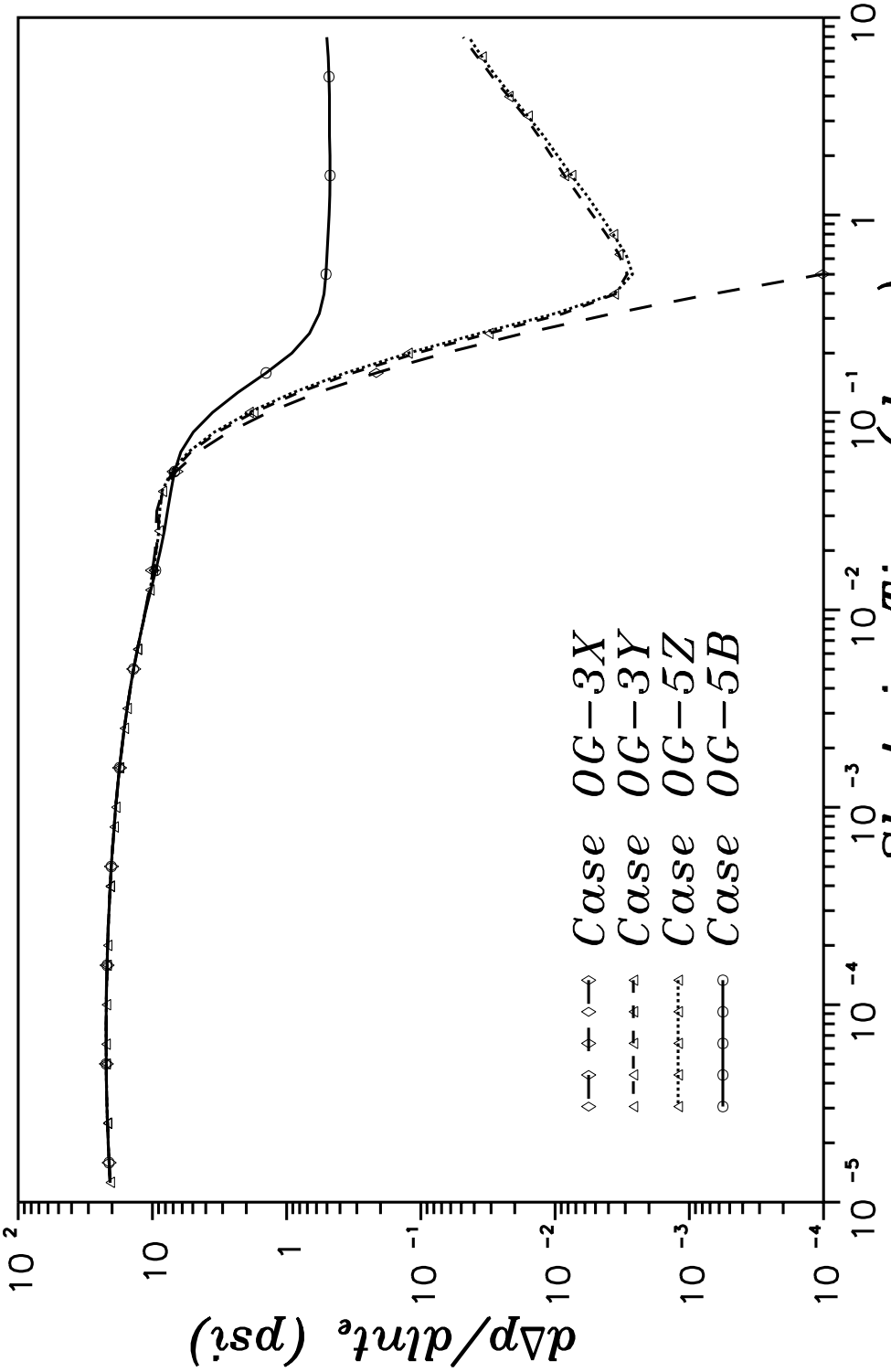

Fig. 5.23 – Comparison of pressure derivative responses for various constant pressure upper boundary reservoir systems.

with the water-gas cases, Fig. 5-24 shows that one of the consequences of the phase redistribution in the reservoir is that the pressure increases above the initial reservoir pressure at this location.

Along with the total flow rate in the vertical direction, Figure 5.25 shows the in-situ vertical flow rates for both the oil and gas phases as a function of vertical location at a shut-in time of $\Delta t = 0.25$ days. Numerical results indicate this to be the time at which the total vertical flow rate becomes positive (upward flow) for all radial cross-sections (vertical locations) in the reservoir. Figure 5.25 clearly shows the phase redistribution occurring in the reservoir, with, for example, the gas phase at $z = 39$ feet flowing upwards at a rate just over 20 RB/day and the oil phase at $z = 39$ feet flowing downward at a rate just under 20 RB/day.

As in the previous section, an expression based the theoretical work of Ref. 149 can be readily obtained for the buildup pressure response for the current oil-gas reservoir systems and can be expressed as

$$\frac{\partial \Delta p}{\partial \ln \Delta t} \approx \frac{\partial p_{ws}(z_{wb}, \Delta t)}{\partial \ln \Delta t}$$

$$\approx \frac{\Delta t}{c_1 k_z} \int_{z_{wb}}^{h} \left\{ \frac{1}{{\lambda_{rt}}^2} \left[v_{zt} - G \right] \frac{\partial \lambda_{rt}}{\partial \Delta t} - \frac{1}{\lambda_{rt}} \left[\frac{\partial v_{zt}}{\partial \Delta t} - \frac{\partial G}{\partial \Delta t} \right] \right\} dz' \quad . (5.3.7)$$

Here, the total relative mobility is given by

$$\lambda_{rt} = \lambda_{ro} + \lambda_{rg} = \frac{k_{ro}}{\mu_o} + \frac{k_{rg}}{\mu_g} \tag{5.3.8}$$

and the gravity term, G, is given by

$$G = c_1 k_z [\lambda_{ro} \gamma_o + \lambda_{rg} \gamma_g] \quad . \tag{5.3.9}$$

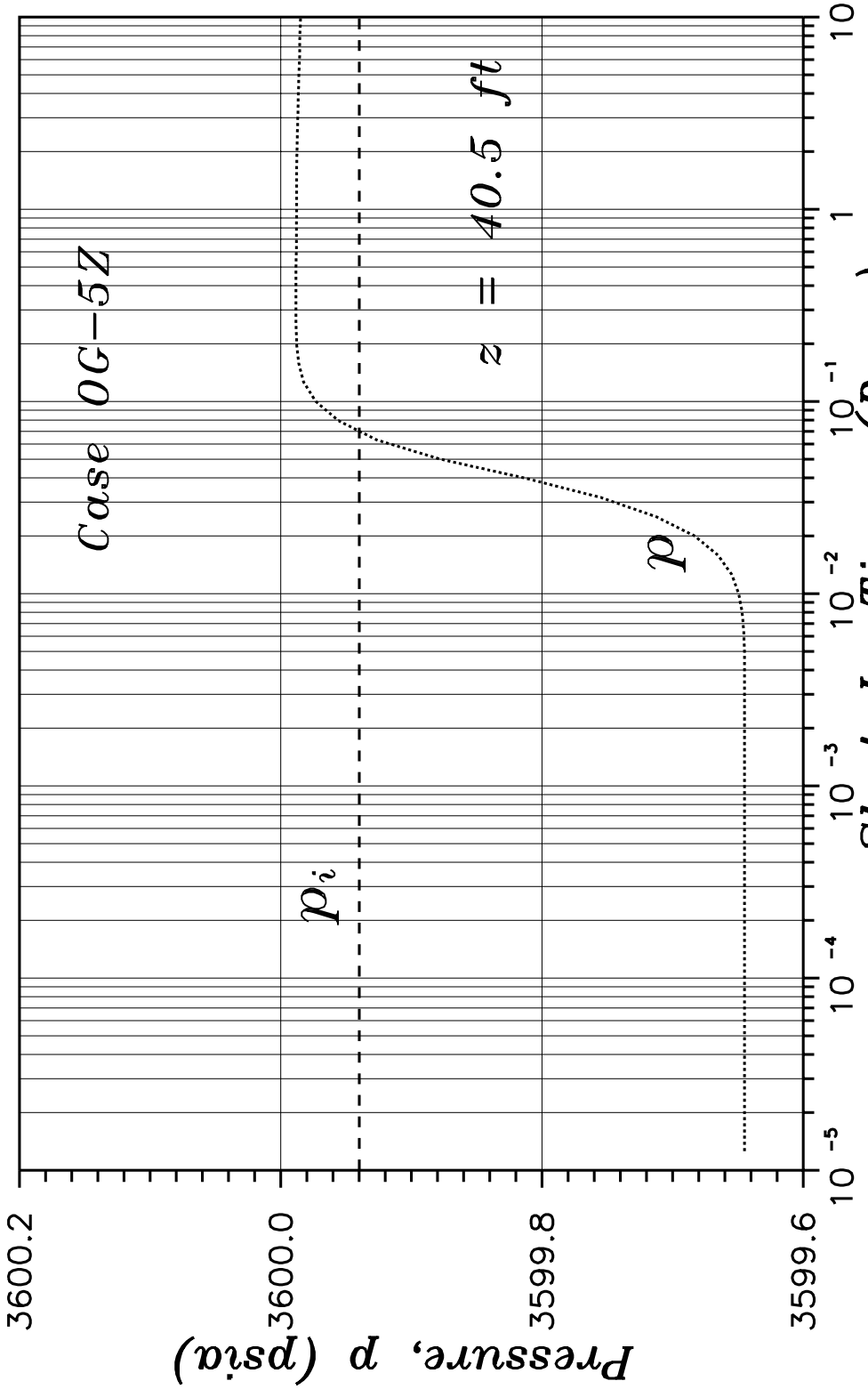

Fig. 5.24 — Comparison of initial pressure and pressure during buildup in the gas cap.

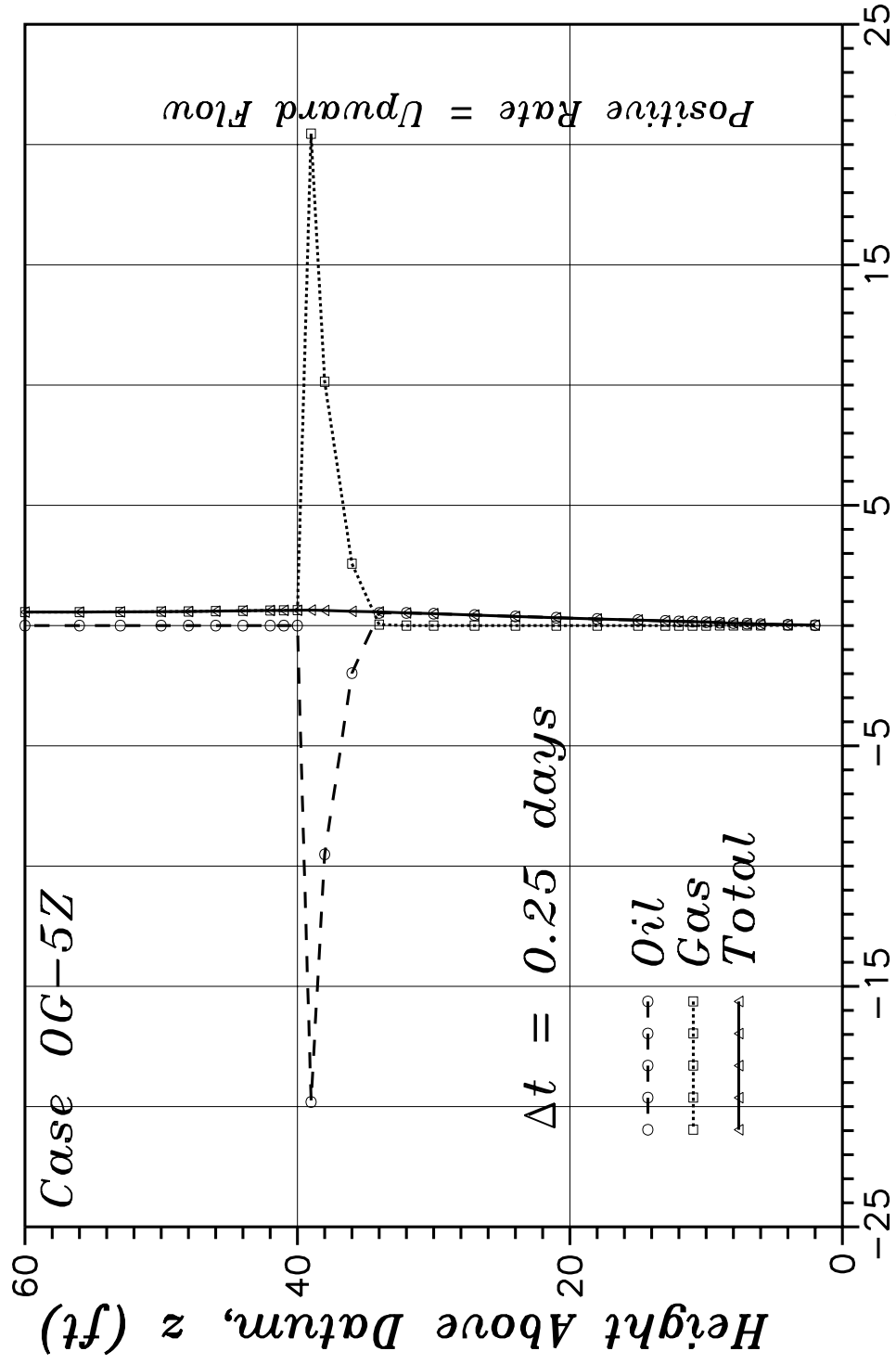

Fig. 5.25 – In-situ vertical flow rates as a function of vertical location.

Here, we concern ourselves with providing an explanation for the late-time pressure response observed in Fig. 5.23 for case OG-5Z; i.e., the increasing log-derivative of the shut-in wellbore pressure. Similar to the water-gas cases discussed in the previous section, it is very difficult to generalize the relative effects of each of the individual parameters in Eq. 5.3.7. Table 5.2 gives values of the various parameters in Eq. 5.3.7 at several vertical locations and at a shut-in time of 5.01 days. As noted previously, any significant phase redistribution which occurs during the buildup period may lead to significant variations in $\partial\lambda_{rt}/\partial\Delta t$ and $\partial G/\partial\Delta t$ over the two-phase region of the reservoir. In fact, an examination of Table 5.2 shows $\partial\lambda_{rt}/\partial\Delta t$ varies by some 3 orders of magnitude just in the upper 6.5 feet of the two-phase region; i.e., from $z = 33$ feet to $z = 39.5$ feet. For case OG-5Z, we note that the reservoir remains two-phase oil and gas adjacent to the well perforations. We also note through an examination of Table 5.2 that $\partial\lambda_{rt}/\partial\Delta t$ is generally much smaller near the perforations than in the two-phase region of the reservoir near the gas cap. This is probably due to the changes in the mobility near the perforations being mainly due to changes in the viscosities with pressure and and changes in the relative permeabilities caused by changes in the saturations caused by gas redissolving in the oil. Near the gas cap, where changes in pressure are small, changes in the phase relative mobilities is due primarily to the flow of the different phases. Additional results indicative of the complexities involved here is the sign of $\partial\lambda_{rt}/\partial\Delta t$ as a function of depth. Table 5.2 shows the derivative of the total relative mobility is negative at $z = 10.5$ feet, positive at $z = 33$ feet, negative again at $z = 37$ feet and, finally, positive again at $z = 38.5$ feet. A similar complexity is observed for the derivative of the gravity term, $\partial G/\partial\Delta t$.

Since fluid flow has reversed at late-time and is in the positive vertical direction, the total vertical velocity is a negative quantity. Subtracting the positive quantity, G for this velocity, then, results in a negative quantity. This means that

changes in the total relative mobility in those regions of the reservoir where the total relative mobility is increasing will tend to make the pressure derivative less positive and changes in the total relative mobility in those regions of the reservoir where the total relative mobility is decreasing will tend to make the pressure derivative more positive.

We note from Table 5.2 that variations in the total relative mobility are significant across the various vertical locations shown. Again considering the mobility-squared term in the denominator of the first group of terms in Eq. 5.3.7, this has a significant impact on the relative contributions of the two groups of terms; e.g., at $z = 35$ feet, $1/{\lambda_{rt}}^2 = 0.53$, whereas at $z = 39.5$ feet, $1/{\lambda_{rt}}^2 = 0.021$. This is a full order of magnitude difference.

Finally, we note that merely because of the relative magnitudes of the parameters in Eq. 5.3.7 near the perforations and in the single-phase regions of the reservoir, the majority of the contribution to the pressure derivative comes from the multiphase region of the reservoir.

Lastly, we examine Fig. 5.26 which shows the total vertical flow rate as a function of shut-in time for various vertical locations in the reservoir for case OG-5Z; i.e., at $z = 11$ feet (just above the perforated interval), at $z = 36$ feet (just below the region of the reservoir where most of the phase redistribution is occurring) and at $z = 60$ feet (the location of the constant pressure upper boundary). Figure 5.26 shows that by a shut-in time of 0.25 days, the vertical flow rate has becomes positive (upward) at each of these vertical locations. Note that this means our constant pressure upper boundary has now become a sink and fluids are leaving our reservoir across this boundary.

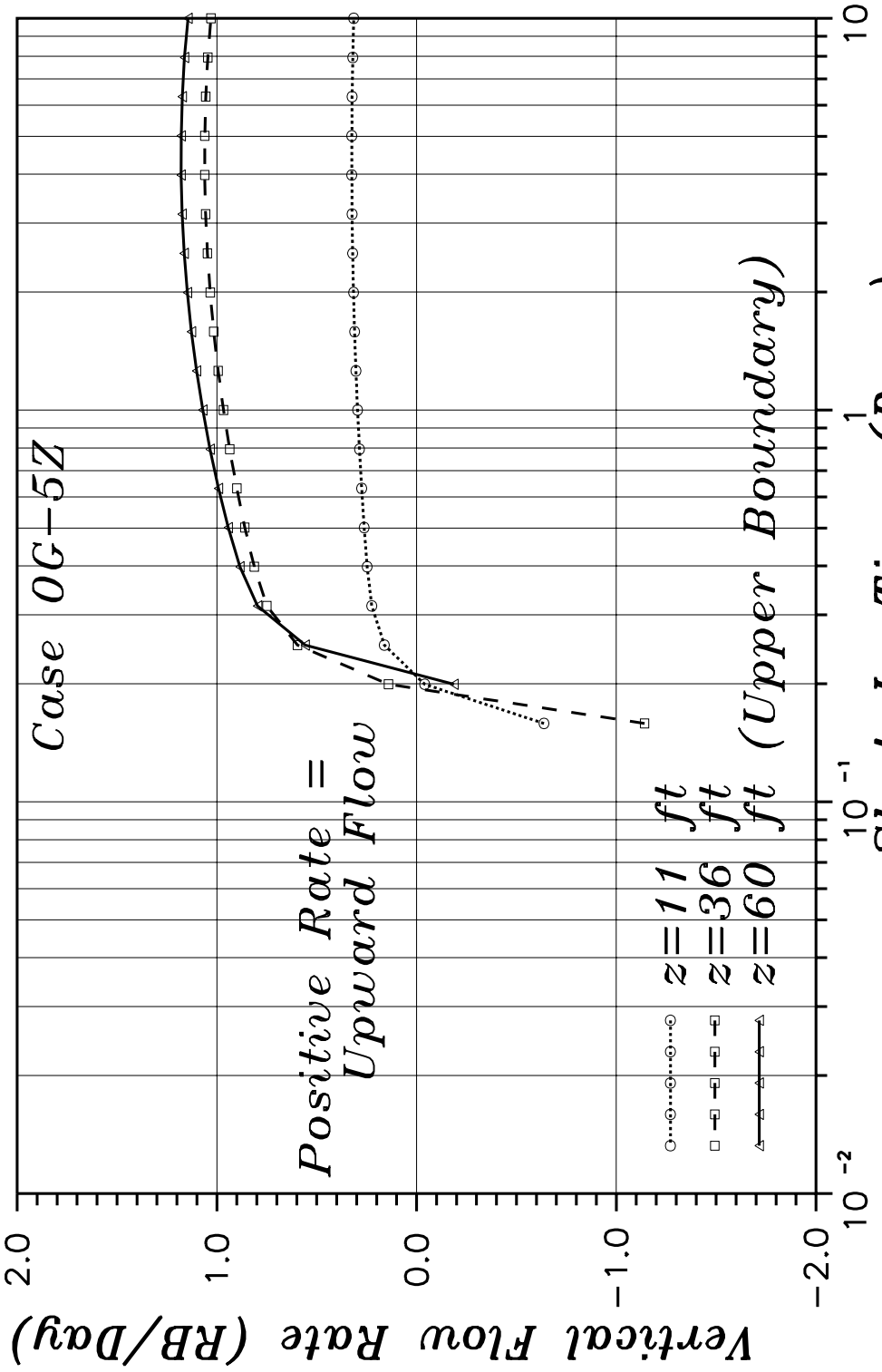

Fig. 5.26 – In-situ total vertical flow rate as a function of shut-in time and vertical location.

5.4 Summary

In this chapter we have examined the applicability of modeling a gas cap or aquifer as a constant pressure boundary. Through a series of numerical examples, we have shown that the pressure response obtained from multiphase reservoir systems containing a constant pressure boundary is fundamentally different from the pressure response predicted by single-phase constant pressure boundary solutions. In particular, we have shown that following an initial rapid decline in the pressure derivative once the constant pressure boundary is felt, the pressure derivative for each of the multiphase reservoir cases investigated actually increases.

With the aid of a vertical form of the theoretical expression developed by Ref. 149 and in conjunction with fractional flow theory, we have shown that for drawdown, the underlying reason for this increase in the log-derivative of the wellbore pressure drop is due to the time-rate of change in the total relative mobility over the two-phase region of the reservoir. Also related to the fractional flow theory, we have shown that the log-derivative of the wellbore pressure drop will continue to increase until breakthrough of the saturation front at the wellbore.

For the oil-water cases investigated, we have shown that any attempt to match the pressure response to single-phase constant pressure boundary solutions necessarily requires that the location of the constant pressure boundary be part of the solution. For the water-gas cases investigated we have shown that the pressure response shows little sensitivity to the location of the constant pressure boundary in the gas cap and as such, any match of the pressure response prior to the time the pressure derivative begins to increase may be non-unique.

For the oil-gas constant pressure boundary cases examined, the drawdown pressure derivative exhibited an approximate semilog straight line, indicating that

the pressure response was dominated by the changes in the mobility at the sandface. Under no circumstances could the pressure response for these cases be interpreted as or matched to single-phase constant pressure boundary solutions. With the aid of numerical results and the vertical form of Ref. 149's theoretical expression for the log-derivative of the wellbore pressure drop, we have shown that the primary reason for the wellbore pressure response being dominated by changes in the total relative mobility near the perforations is due to a much greater velocity of the fluids in that region.

For pressure buildup tests, we have shown that the underlying reason for the increase in the pressure derivative is due to gravity effects, and in particular, phase redistribution in the reservoir. We do note that the magnitude of the these pressure changes during the late time buildup period are at the limit of our ability to measure in the field, and as such, may not be observable in practice.

None-the-less, several other physical phenomena occurring in the reservoir during the buildup period have been identified and include: (i) phase redistribution may result in reservoir pressures which are greater at some locations than they were initially, prior to the drawdown; (ii) because the location of the constant pressure boundary modeled in these cases was fixed, and because of the phase redistribution effects, the constant pressure boundary may act like a "sink" with fluids flowing out of the reservoir; (iii) also due to the phase redistribution effects, it is possible for fluids to flow back into the reservoir in the high mobility layer; (iv) and, the increasing pressure derivative for the water-gas and oil-gas cases exhibited a unit slope during the buildup. We have not been able to associate a clear meaning to the unit slope other than its direct relationship to the phase redistribution occurring in the reservoir during the buildup.

CHAPTER VI
DRAWDOWN BEHAVIOR

This chapter concerns itself with the analysis of drawdown pressure transient data obtained from a restricted-entry well under multiphase flow conditions. Conditions under which semilog analysis of drawdown pressure transient data can be performed and procedures for that analysis are discussed. Much of the material presented in this chapter is also intended to lay a foundation for the analysis of buildup pressure transient data discussed in Chapter VII. Reservoir systems investigated include oil reservoirs underlain by an aquifer, gas reservoirs underlain by an aquifer, oil reservoirs overlain by a gas cap, water reservoirs overlain by a gas cap and oil reservoirs overlain by a gas cap and underlain by an aquifer.

6.1 Two-Phase Oil-Water Systems

In this section, we examine semilog analysis of drawdown pressure data obtained from a restricted-entry well in oil reservoir - aquifer systems. A reservoir schematic of the oil-water systems investigated here was shown previously in Fig. 4.1 and reservoir and fluid properties were listed in Tables 4.1A and 4.1B. For each of the systems investigated, the logarithmic derivative of the pressure drop was calculated and plotted versus producing time. In addition, as per the work of Refs. 23 and 24, individual thickness averaged phase mobilities and total mobilities were calculated from, respectively,

$$\bar{\lambda}_l = \frac{70.6 q_l B_l}{hd\Delta p/d\ln t}\ ,\ l = o, w \tag{6.1.1}$$

and

$$\bar{\lambda}_t = \bar{\lambda}_o + \bar{\lambda}_w \ , \tag{6.1.2}$$

where $\Delta p = p_i - p_{wf}$ and $\bar{\lambda}_l$ is interpreted as

$$\bar{\lambda}_l = \frac{1}{h}\int_0^h \left(\frac{kk_{rl}}{\mu_l}\right) dz \ . \tag{6.1.3}$$

Note that if an early time semilog straight line is apparent, then the phase and total mobilities adjacent to the perforated interval may potentially be calculated using Eqs. 6.1.1–6.1.2 by replacing h with h_w. Because this early time semilog straight line will rarely be observed in practice due to wellbore storage and skin effects or it simply occurs too early, we concentrate in this work on the late time semilog straight line.

Figure 6.1 is a semilog plot of the log-derivative of the wellbore pressure versus producing time for all of the zero-skin cases (the skin cases are discussed in Chapter VIII). The pressure derivatives shown in Fig. 6.1 exhibit the classic restricted-entry response, i.e., a fairly constant log-derivative at very early time reflecting radial flow over the perforated interval in the near well region, a dramatic falloff in the derivative during a transition period and finally, what appears as an approximately constant derivative at late time suggestive of pseudoradial flow across the entire reservoir thickness.

Based on the semi-log plot of the pressure derivative, Eqs. 6.1.1 and 6.1.2 were used to calculate total thickness averaged mobilities for each of the oil-water systems. The average of the last three points on each derivative curve were used to estimate the thickness averaged mobilities. These values are shown in the second column of Table 6.1. The initial total thickness averaged mobilities existing in the reservoir are included in column one of Table 6.1 and were obtained directly

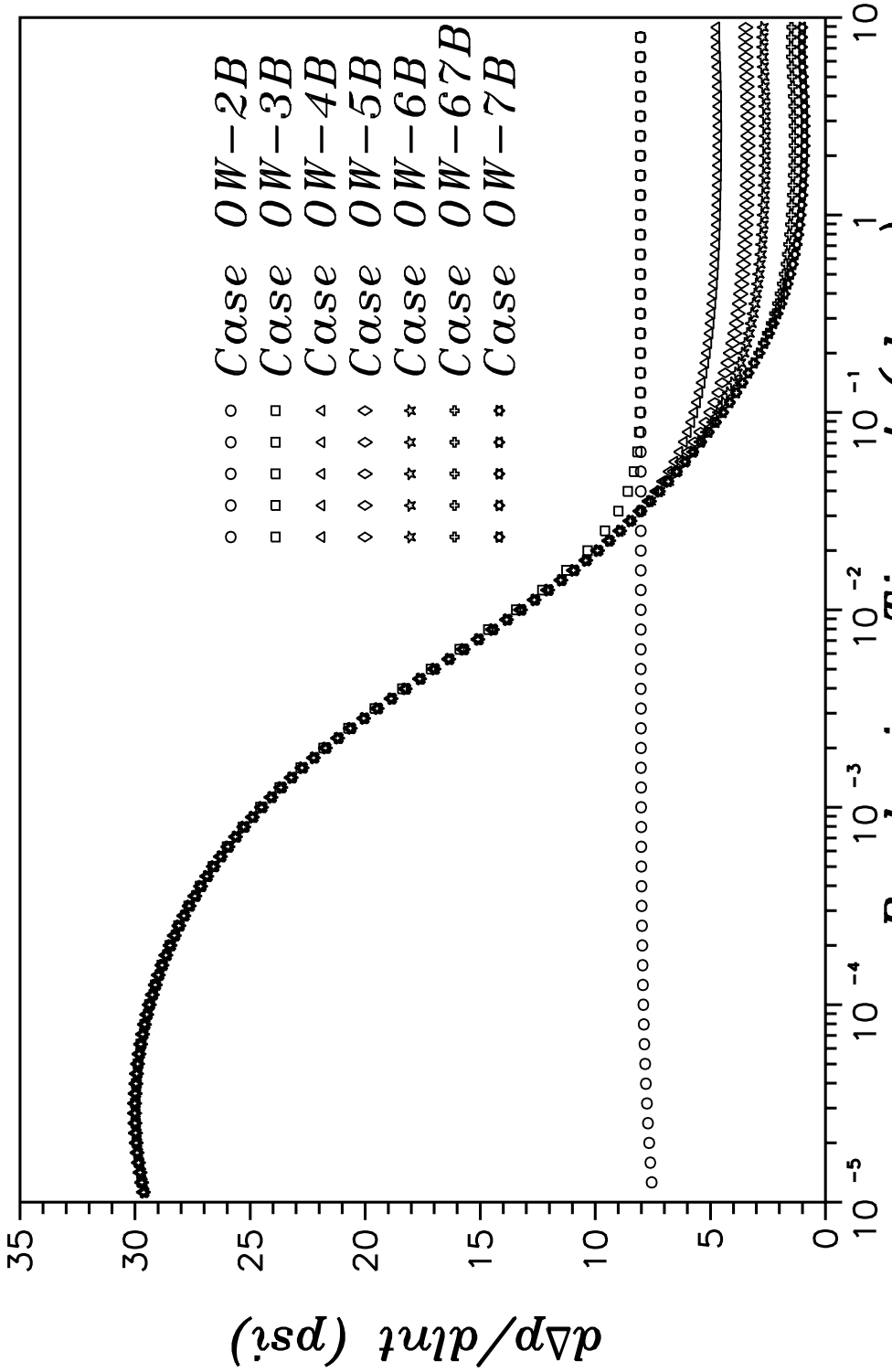

Fig. 6.1 — Semilog drawdown pressure derivative plot.

from our simulator. The results shown indicate there can be significant deviation between the calculated mobilities and the initial mobilities in the reservoir; e.g., the calculated total mobility for case OW-7B differs from the initial total thickness averaged mobility by 24.8 percent.

To understand this difference, we re-examine the pressure derivative for these cases, except this time on a log-log plot (Fig. 6.2). Unlike the semi-log plot in which the log-derivative of pressure appeared to be constant, Fig. 6.2 indicates that the log-derivative of the wellbore pressure is in fact not constant during late time. Figure 6.2 shows that the pressure derivative becomes almost constant for a short period, then increases. This increase in the derivative is not due to boundary effects because the reservoir is still infinite-acting. The increase is not due to the coning of water because no water is being produced. In the previous chapter we saw that changes in the total mobility near the original oil-water contact could cause the pressure derivative to increase, even for constant pressure boundary cases. This is also the reason for the increase in the derivative for the current cases; e.g., the water saturation in the first vertical grid block above the original oil-water contact increases from $S_w = 0.2$ to $S_w = 0.68$ during the drawdown period for case OW-5B, and the corresponding total relative mobility $(k_{ro}/\mu_o + k_{rw}/\mu_w)$ in the same grid block decreases from 0.85 cp^{-1} to 0.26 cp^{-1} (see Fig. 6.3).

A natural question at this point in the discussion may be what about the calculated mobility for that part of the pressure derivative curve which appears to be approximately constant? Eqs. 6.1.1 and 6.1.2 were again used to calculate a total mobility for each time corresponding to the approximately constant pressure derivative and the maximum calculated mobility is reported in the third column of Table 6.1; percent differences between these calculated mobilities and the initial thickness averaged mobilities are shown in column four of Table 6.1. Though the

Table 6.1

Drawdown Semilog Analysis Results: Oil-Water Systems

Case	Simulator $\bar{\lambda}_t$ (md/cp)	Calculated $\bar{\lambda}_t$ (last) (md/cp)	Calculated $\bar{\lambda}_t$ (max) (md/cp)	Percent Deviation
OW-2B	42.47	42.48	42.48	-0.02
OW-2BS3	42.47	42.48	42.48	-0.02
OW-2BS4	42.47	42.48	42.47	0.00
OW-3B	42.47	42.47	42.47	0.01
OW-3BS3	42.47	42.55	42.46	0.02
OW-3BS4	42.47	42.75	42.46	0.02
OW-4B2	49.05	47.53	48.33	1.46
OW-4B2S3	49.05	47.71	48.42	1.28
OW-4B2S4	49.05	48.16	48.69	0.73
OW-5B	52.34	49.22	50.71	3.11
OW-5BS3	52.34	49.49	50.86	2.83
OW-5BS4	52.34	50.14	51.25	2.08
OW-5P	52.34	36.74	50.74	3.06
OW-5S	52.34	46.85	49.90	4.668
OW-6B	54.31	49.80	51.89	4.46
OW-6BS3	54.31	50.14	52.07	4.12
OW-6BS4	54.31	50.98	52.55	3.24
OW-67B	58.05	48.30	52.14	10.18
OW-7B	59.57	44.77	49.96	16.13
OW-7BS3	59.57	45.50	49.96	16.13
OW-7BS4	59.57	47.49	51.28	13.92
OW-7O	59.57	45.21	50.11	15.88
OW-7P	59.57	24.62	49.40	17.07
OW-7Q	59.57	43.57	48.55	18.50
OW-7S	59.57	38.72	45.71	23.27

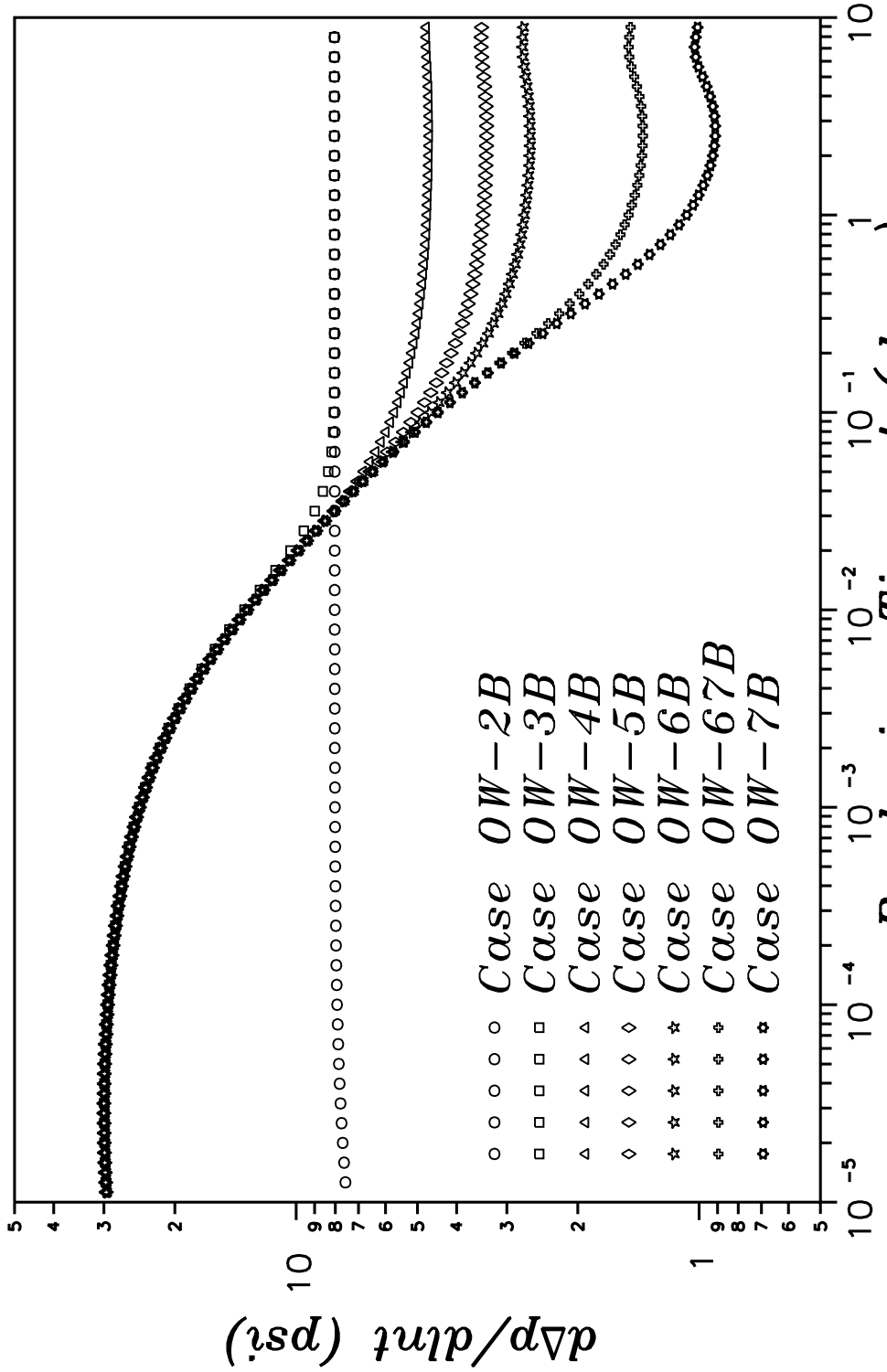

Fig. 6.2 — Diagnostic drawdown pressure derivative plot for oil—water cases.

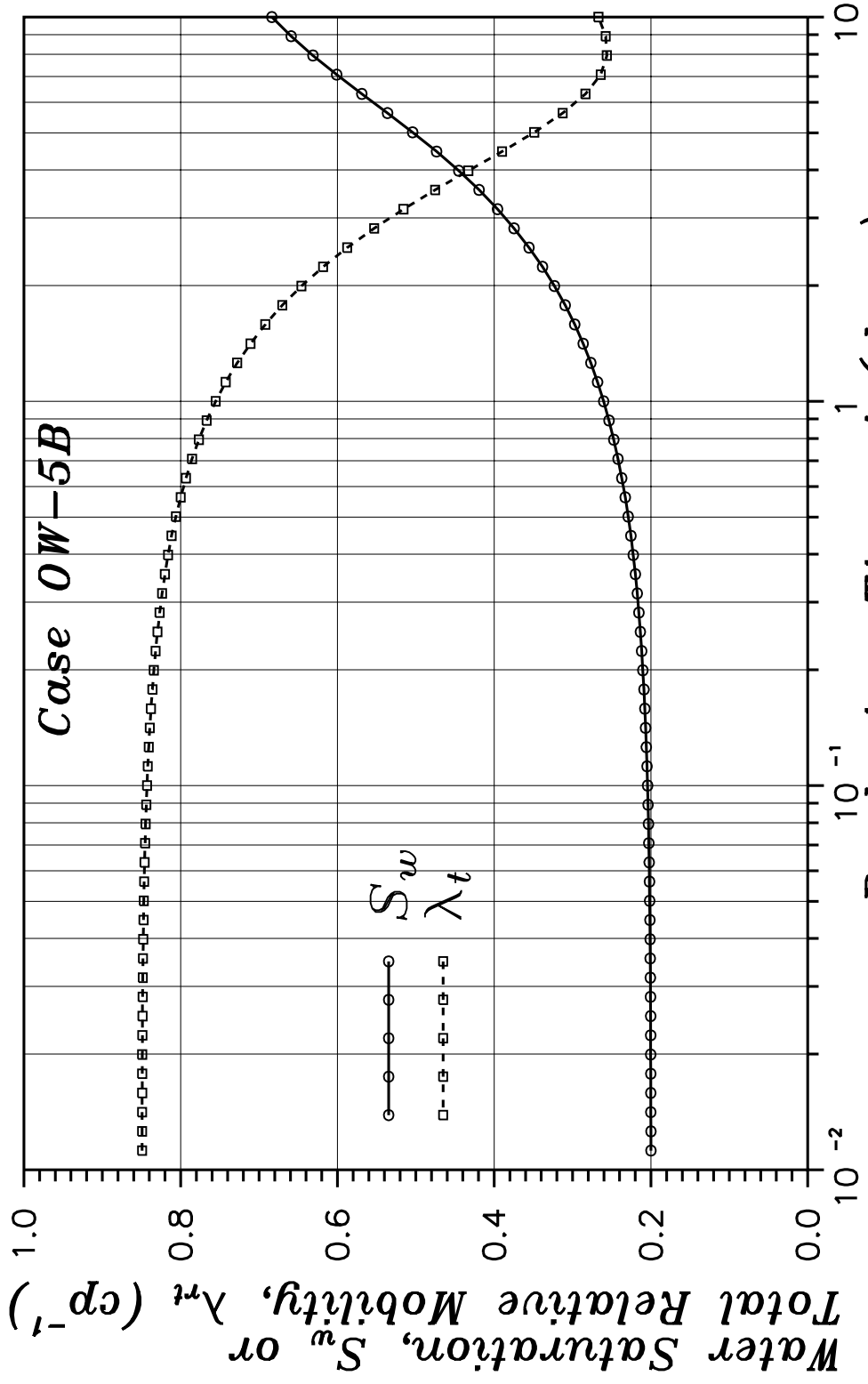

Fig. 6.3 — Water saturation and total relative mobility near oil—water contact as a function of producing time.

difference between the initial reservoir total mobility and the calculated mobilities is much smaller than calculated previously, there are still significant differences; e.g., for case OW-7B there is a 16 percent difference.

As discussed above, we know that the total mobility changes near the oil-water contact in the inner region of the reservoir due to building of a water cone, and, here, we have been comparing the mobility calculated formally from Eqs. 6.1.1 and 6.1.2 to the initial thickness-averaged total mobility which existed in the reservoir at time equal to zero. If an analytical solution to the current problem existed, then we would have a clear interpretation of what the mobility formally calculated from Eq. 6.1.1 and 6.1.2 actually represents. Unfortunately, there exists no such solution. While it would be helpful if an expression similar to that developed by Ref. 149 could be used to explain the results observed here, we have no such expression for the multidimensional cases presented here. We do postulate, however, that the pressure derivative will be influenced in a similar manner; i.e., in addition to other parameters, such as the permeability, reservoir thickness, etc., we suspect that the log-derivative of the wellbore pressure drop will be influence by $\partial\lambda_{rt}(r,z,t)/\partial t$ and $\partial q_t(r,z,t)/\partial t$.

Alternatively, one may ask under what conditions would the total mobility calculated from Eqs. 6.1.1 and 6.1.2 give the initial thickness-averaged total mobility (which after production begins, exists only in the outer region of the reservoir). This question seeks to place the multiphase analysis in the same framework as the single-phase solutions discussed in Chapter IV; i.e., as with many other works on multiphase pressure transient analysis, we ask under what conditions the multiphase case will follow or match analogous single-phase solutions? For single-phase reservoirs, and in single-phase regions of a multiphase reservoir, $\partial\lambda_{rt}(r,z,t)/\partial t$ will be equal to zero (provided changes in viscosities are small). In the inner

region of the reservoir for the current oil-water cases (where the water cone develops), flow is predominately in a vertical direction. Under this senario, another way of showing that the relative mobilities are (are not) changing is though the concept of vertical equilibrium. For instance, if vertical equilibrium exists, then there is no vertical flow and $\partial\lambda_{rt}(r,z,t)/\partial t$ will be zero in that region of the reservoir. Recall from Chapter IV that one of the assumptions required to obtain the thickness-averaged permeability in a single-phase layered reservoir was that vertical equilibrium (pseudoradial flow) exist beyond some radius in the reservoir. A second property of single-phase solutions included the existence of a "steady-state" zone between the wellbore and some radius, r_i, in the outer region of the reservoir. Note that in order for the pressure derivative for the single-phase reservoir systems to not be influence by vertical flow, this "steady-state" zone must extend out in the reservoir at least to the point where vertical equilibrium exists. In other words, the pressure derivative for the single-phase slightly-compressible, constant viscosity, constant compressibility, liquid reservoir system is only influenced by what occurs or exists ahead of the "steady-state" zone.

Figure 6.4 shows the total cross-sectional mass rate, surface volumetric rate and reservoir volumetric rate for case OW-5B as a function of radius at a producing time of 2.51 days. The producing time of 2.51 days for this case corresponds to the time for which the calculated mobility differs the least from the initial thickness averaged total mobility. Figure 6.4 shows that while the reservoir and surface volumetric rates are essentially constant out to a distance just over 100 feet, the mass rate is only constant out to a distance of approximately 30 feet. Note that for single-phase flow, a constant surface rate in the reservoir implies a constant mass rate, or vice a versa. Generally speaking, however, there is no such general relationship between the in-situ surface rate and the in-situ mass rate for reservoirs producing under multiphase flow conditions. Because the two fluids for

these oil-water cases are "slightly compressible" fluids, we expect there to be little difference in the reservoir and surface volumetric rates, no matter which fluids are being produced. Because of the significant difference in the densities of the two fluids, however, we expect that if the volumetric proportion of each phase flowing differs significantly throughout the reservoir, then the mass rate will also differ significantly. This is the case here, with radial flow in the near well region ($r \leq 30$ feet) dominated by the oil phase and flow in the outer region of the reservoir a mixture of the two phases. Clearly, if we employ the term "steady state" to imply a constant mass rate (does not change with-respect-to time) across some region of the reservoir, then this requirement is satisfied only in the near wellbore region. If we employ the term "steady state" to imply a constant reservoir volumetric rate (does not change with-respect-to time) across some region of the reservoir, then the "steady-state" zone will be much larger.

The second assumption we wish to examine is the existence of pseudoradial flow (vertical equilibrium) in the reservoir. Recall in Chapter IV, we derived an expression for multiphase flow cases which showed that vertical equilibrium exists in the reservoir if, and only if, the fractional flow rate of each phase as defined by the in-situ volumetric flow rates is the same as that calculated from the thickness-averaged total mobilities existing at the same radius in the reservoir; i.e.,

$$f_m|_r = \left.\frac{\bar{\lambda}_m}{\bar{\lambda}_t}\right|_r = \left.\frac{q_m}{q_t}\right|_r , m = o, w \ , \tag{6.1.4}$$

where q_m and q_t are in reservoir volumes. Figure 6.5 shows the fractional flow rates calculated from both the phase flow rates and the thickness averaged mobilities as a function of radius. The solid and dashed horizontal lines represent the mobility-calculated fractional flow rates and the open symbols represent the rate-calculated fractional flow rates. The total in-situ volumetric flow rate is also included in Fig. 6.5 for reference and note that we have indicated the radius at which this flow rate

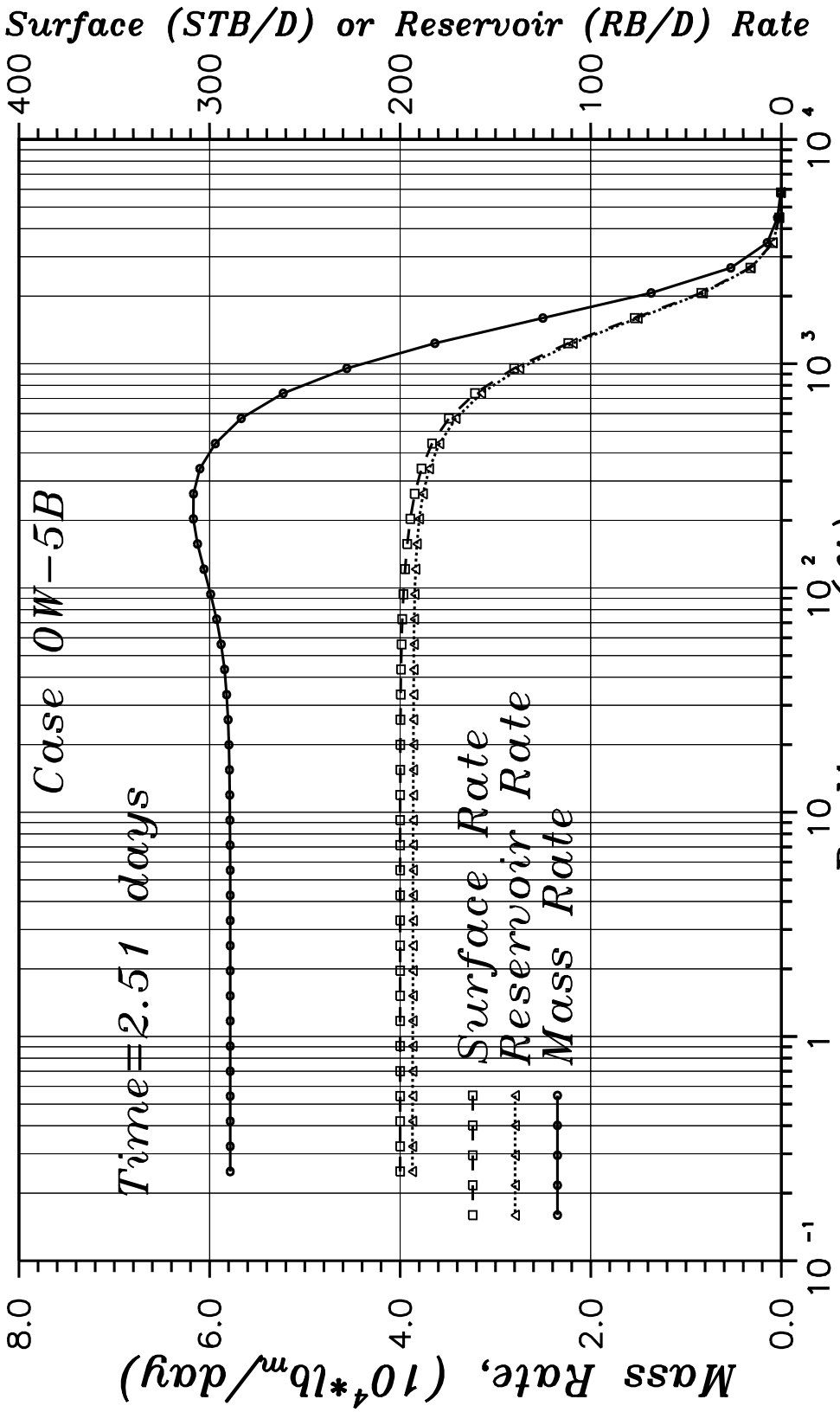

Fig. 6.4 — Mass and volumetric rates as a function of radius.

is equal to 98 percent of the sandface flow rate. Figure 6.5 shows that pseudoradial flow (vertical equilibrium) exists in the reservoir for $700 \leq r \leq 2000$ feet. Figure 6.5 then suggests that the fluid mobilities near the oil-water contact must be changing in the region of the reservoir $r < 700$ feet. What this indicates, then, is that the assumptions required for semilog analysis techniques to provide us with the initial thickness-averaged total mobility are not being satisfied for the current cases.

While the above analysis tends to indicate that the fundamental assumptions required for semilog analysis of the late time drawdown pressure data do not hold for the oil-water cases considered here, there may potentially still be some hope of obtaining a meaningful interpretation of the mobilities calculated formally using Eqs. 6.1.1 and 6.1.2. In examining the calculated mobilities shown in Table 6.1, we notice that the deviation from the initial total thickness averaged mobilities increases almost linearly as the thickness of our reservoir increases, or correspondingly, the aquifer thickness increases. Figure 6.6 shows the percent deviation of the calculated mobility from the initial thickness averaged plotted against the aquifer thickness. As can be seen, there is an excellent correlation between the aquifer thickness and the percent deviation in the calculated (Eqs. 6.1.1 and 6.1.2) thickness-average total mobility and the initial value for the thickness-averaged total mobility. This result makes intuitive sense when one considers the relative amounts of oil and water flowing in the reservoir; i.e., if pseudoradial flow exists in the outer region of the reservoir (as it does for each of the cases considered here), then proportionately more water than oil must be flowing for the thicker aquifer cases. Because the inner boundary is a no-flow boundary, that water flowing towards the inner boundary must flow upwards into the oil zone. Because more water is flowing for the thicker aquifer cases, then more water must be flowing up into the the oil zone near the inner boundary. In fact, at the inner

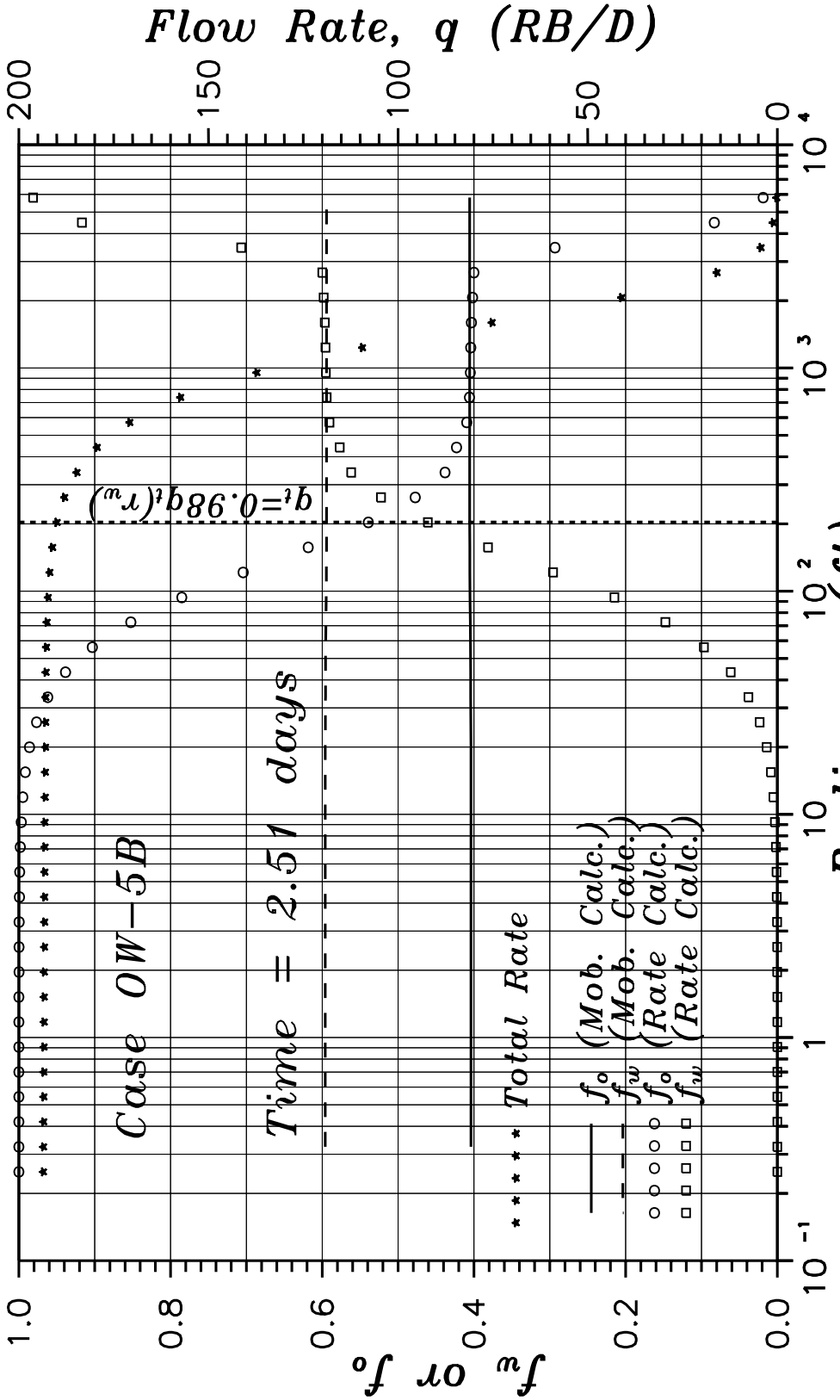

Fig. 6.5 — Comparison of fractional flow rates as an indicator of vertical equilibrium.

boundary and in the first vertical grid block above the oil-water contact, results show the water saturation has increased to 0.657 for case OW-4B and 0.696 for case OW-7B.

This result is encouraging in that it provides some hope of being able to correlate a calculated mobility with the actual thickness-averaged mobilities existing in the reservoir. If estimates for the thickness of the oil and water zone are available from, for example, well logs, then one may be able to use simulation results to perform a sensitivity analysis on the calculated mobility. Bases on the simulation results, then, one may be able to estimate the approximate error between the pressure-transient calculated thickness-averaged total mobility from the actual thickness-averaged mobility. Note, however, there are many other reservoir and fluid properties that might also effect this correlation (e.g., vertical permeability, fluid mobilities, production rate, etc.) and much more work is necessary before a truly useful method could be developed.

As a preliminary to future work, however, we do comment on the effect of several of these parameters on the calculated mobilities. Case OW-7O is identical to case OW-7B except, in case OW-7O, gravity effects were not included in the model. Table 6.1 indicates a minimal effect on the calculated mobility as compared to case OW-7B. For cases OW-5P and OW-7P the vertical permeability was increased to 50 md (same as horizontal permeability) from the 5 md used for cases OW-5B and OW-7B, respectively. For these cases, the results are varied, with the calculated mobility for case OW-5P appearing to be slightly more accurate and the calculated mobility for case OW-7P appearing to be slightly less accurate. For case OW-7Q, the perforated interval was increased to 20 feet (penetration ratio doubled over that for case OW-7B) and resulted in a slight decrease in the relative accuracy. We also note that the relative error for this case does not follow the correlation for the other cases, possibly indicating that the distance from the

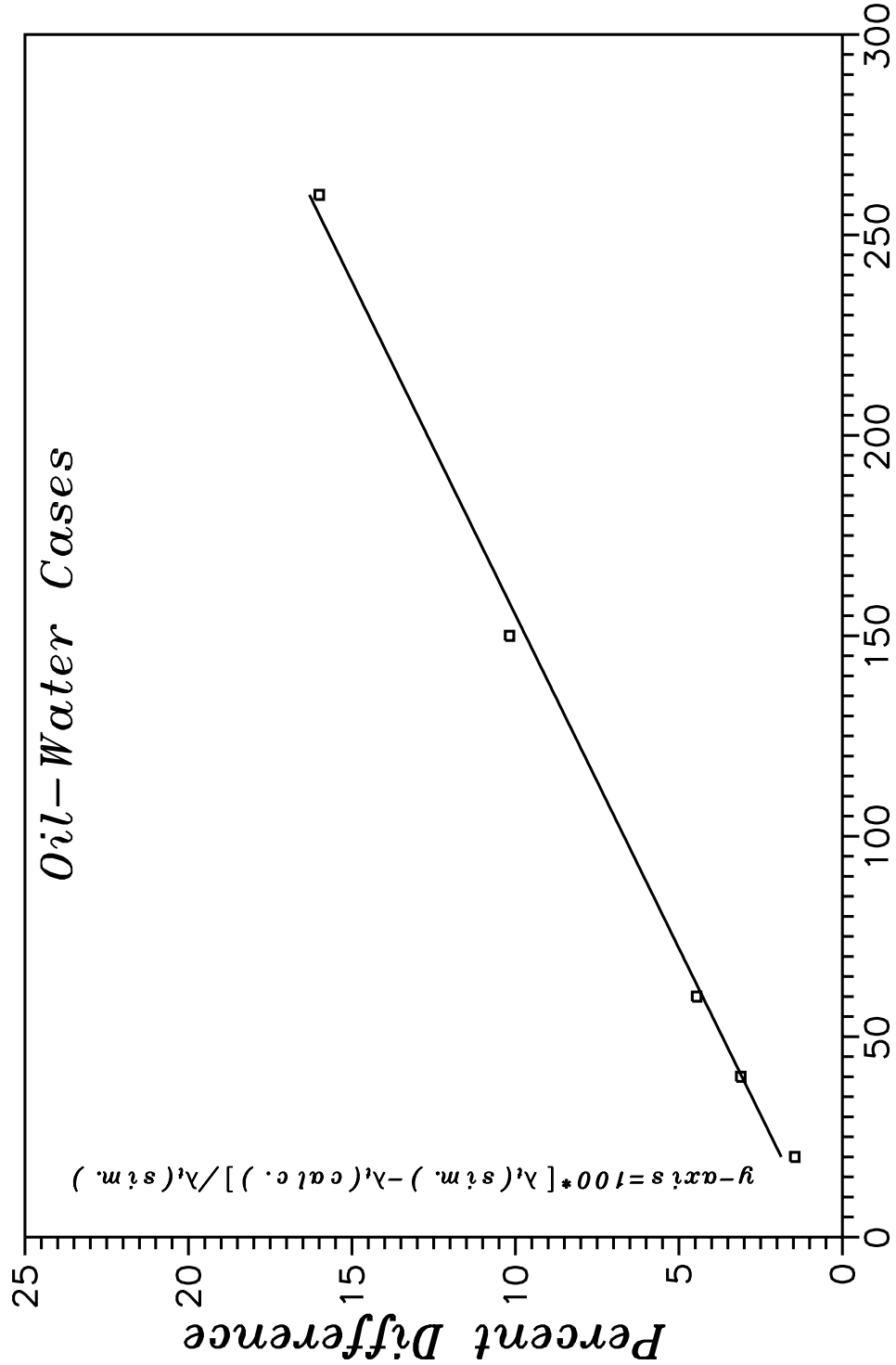

Fig. 6.6 – Correlation between relative difference in calculated mobility and initial mobility.

bottom of the perforated interval to the original oil-water contact may somehow be a correlating parameter here, though no additional cases were run to examine this possibility. For cases OW-5S and OW-7S, the production rate was doubled over that of cases OW-5B and OW-7B and resulted in calculated mobilities which deviate substantially more from the initial thickness averaged mobilities. The reason for this increased deviation is due an increase in the movement of water near the oil-water contact. Case OW-5B, for example, exhibits a water saturation of $S_w = 0.68$ and $S_w = 0.32$ in the first two grid blocks above the oil-water contact at the inner boundary. Case OW-5S, on the other hand, exhibits a water saturation of $S_w = 0.78$ and $S_w = 0.69$ in the first two grid blocks above the oil-water contact at the inner boundary; i.e., the water saturation in this region of the reservoir is substantially higher for case OW-5S than for OW-5B.

6.2 Two-Phase Gas-Water Systems

Here, we wish to examine the cases of a restricted-entry well in a gas reservoir and a restricted-entry well in a gas reservoir underlain by an aquifer. A vertical cross-section of the reservoir with the lower boundary and fluid saturations indicated for each of the gas reservoir - aquifer systems considered are shown in Fig. 4.2 of Chapter IV. Other pertinent fluid and physical property data are included in Table 4.2 for the "base case" (Case GW-2B), along with the deviations from the base case parameters for each of the other gas-water systems considered. Aquifers of 5, 10, 20, and 60 ft are considered. A 10-day drawdown at a constant surface gas production rate of 10 ($MMscf/D$) followed by a 10-day buildup were simulated for each of the cases.

Figure 6.7 shows the the log-derivative of flowing pressure with respect to producing time and Fig. 6.8 shows the log-derivative of the real gas pseudopressure with respect to producing time for each of the zero-skin gas-water cases. For the

restricted-entry cases the drawdown pressure derivative plot (Fig. 6.7) does not indicate a well-defined late time (pseudoradial flow) semilog straight line, which suggests analysis should be done in terms of pseudopressure. The drawdown (Fig. 6.8) pseudopressure derivative plots, however, indicate rather well-defined late time semilog straight lines. Also note from both Figures 6.7 and 6.8 that it is difficult to distinguish one case from another. This result indicates that the effect of the water zone on the derivatives is small and possibly negligible. We discuss this possibility in more detail below.

In analyzing drawdown data by semilog methods and in the absence of wellbore storage effects, Reynolds et al.[124] and others[38,125] have shown that the pseudotime function introduced by Agarwal[126] (or additionally Scott's[127] normalized time) should not be used. In Chapter IV we showed that for a single-phase gas reservoir with a fully-penetrating well, the gas mobility could be calculated from drawdown pressure data using

$$\lambda_g = \frac{k_g}{\mu_g(p_{wf})} = \frac{70.6 q_g B_g(p_{wf})}{h d\Delta p/d\ln t} \ , \tag{6.2.1}$$

where we note that the viscosity and formation volume factor are evaluated at the flowing wellbore pressure. Note that Eq. 6.2.1 is equivalent to the more common equation utilized to calculate the effective gas permeability in a single-phase gas reservoir; i.e.,

$$k_g = \frac{-70.6 q_g}{h dm(p_{wf})/d\ln t} \ , \tag{6.2.2}$$

where the wellbore pseudopressure is defined as

$$m(p_{wf}) = \int_{p_{wf}}^{p_i} \frac{dp}{\mu_g B_g} \ . \tag{6.2.3}$$

Figure 6.9 shows the instantaneous values of total mobility calculated from Eq. 6.2.1 using the drawdown pressure data for Case GW-3B, and also, the values of

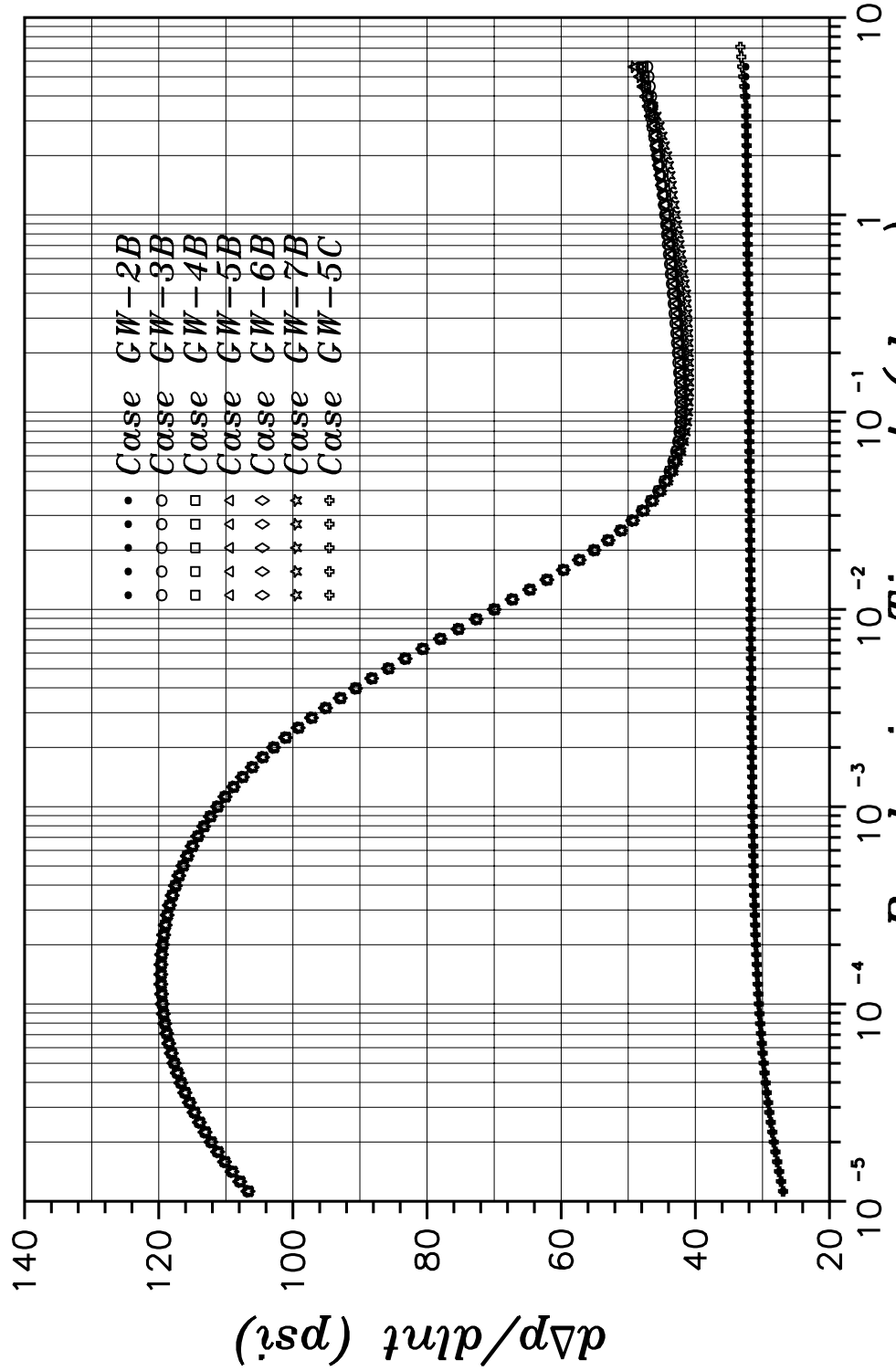

Fig. 6.7 – Diagnostic drawdown pressure derivative plot (Gas–Water).

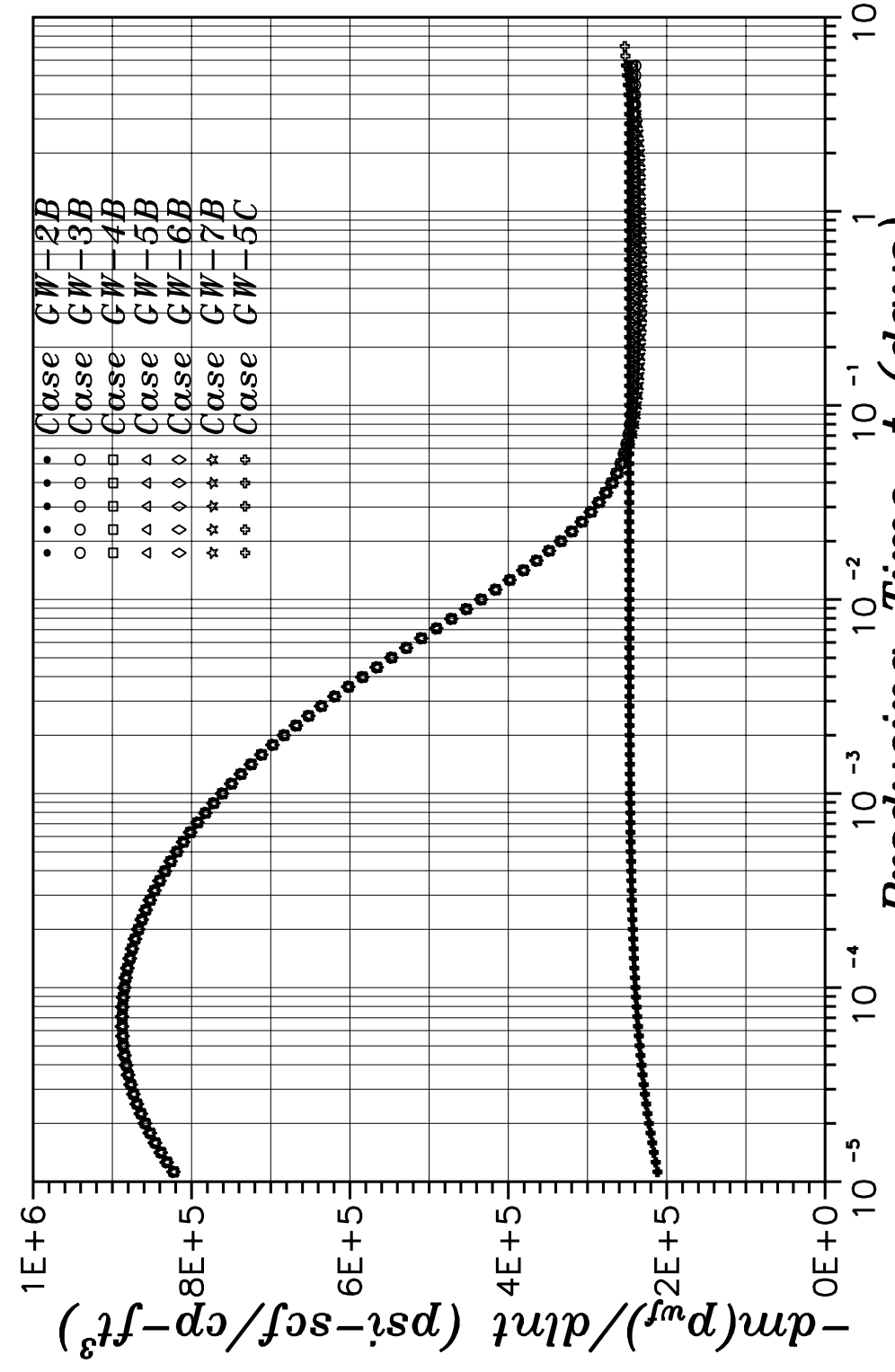

Fig. 6.8 — Diagnostic drawdown pseudopressure derivative plot (Gas–Water).

the total mobility calculated by the simulator using method (M2), i.e., effective permeabilities evaluated in the outer region of the reservoir and the PVT properties evaluated at the wellbore pressure,

$$\bar{\lambda}_g(sim.) = \frac{kk_{rg}(S_{g_i})}{\mu_g(p_{wf})} \ . \tag{6.2.4}$$

Although there is some discrepency, the match between the calculated mobility and the simulator values is really quite good, differing by less than 3 percent. None the less, we check our assumption of the existence of a "steady-state" region in the reservoir by plotting (Fig. 6.10) the total mass flow rate across various radii in the reservoir. Here, we see that there is indeed a rather well-developed "steady-state zone" within the reservoir, extending at least 157 ft into the reservoir.

Next, we examine Case GW-7B, a 40 ft thick gas reservoir underlain by a 60 ft aquifer. Only the top ten feet of the reservoir is perforated. For this case, since we are only producing one phase (gas), while there are two mobile phases in the reservoir, we conjecture by analogy with Eq. 4.3.24 and the single phase gas cases that Eq. 6.2.1 should give us the total thickness averaged mobility, i.e.,

$$\bar{\lambda}_t = \frac{k_g h_g}{\mu_g(p_{wf})h} + \frac{k_w h_w}{\mu_w(p_{wf})h} = \frac{-70.6 q_g B_g(p_{wf})}{h dp_{wf}/d\ln t} \ , \tag{6.2.5}$$

where h_g is the thickness of the gas zone and h_w is the thickness of the water zone.

Figure 6.11 shows the instantaneous values of total-thickness-averaged mobility calculated from Eq. 6.2.5, i.e., from

$$\bar{\lambda}_t = \frac{-70.6 q_g B_g(p_{wf})}{h dp_{wf}/d\ln t} \ , \tag{6.2.6}$$

along with values of the total-thickness-averaged mobilities calculated from simulator data using method (M2) (viscosities evaluated at p_{wf}) for various radii in

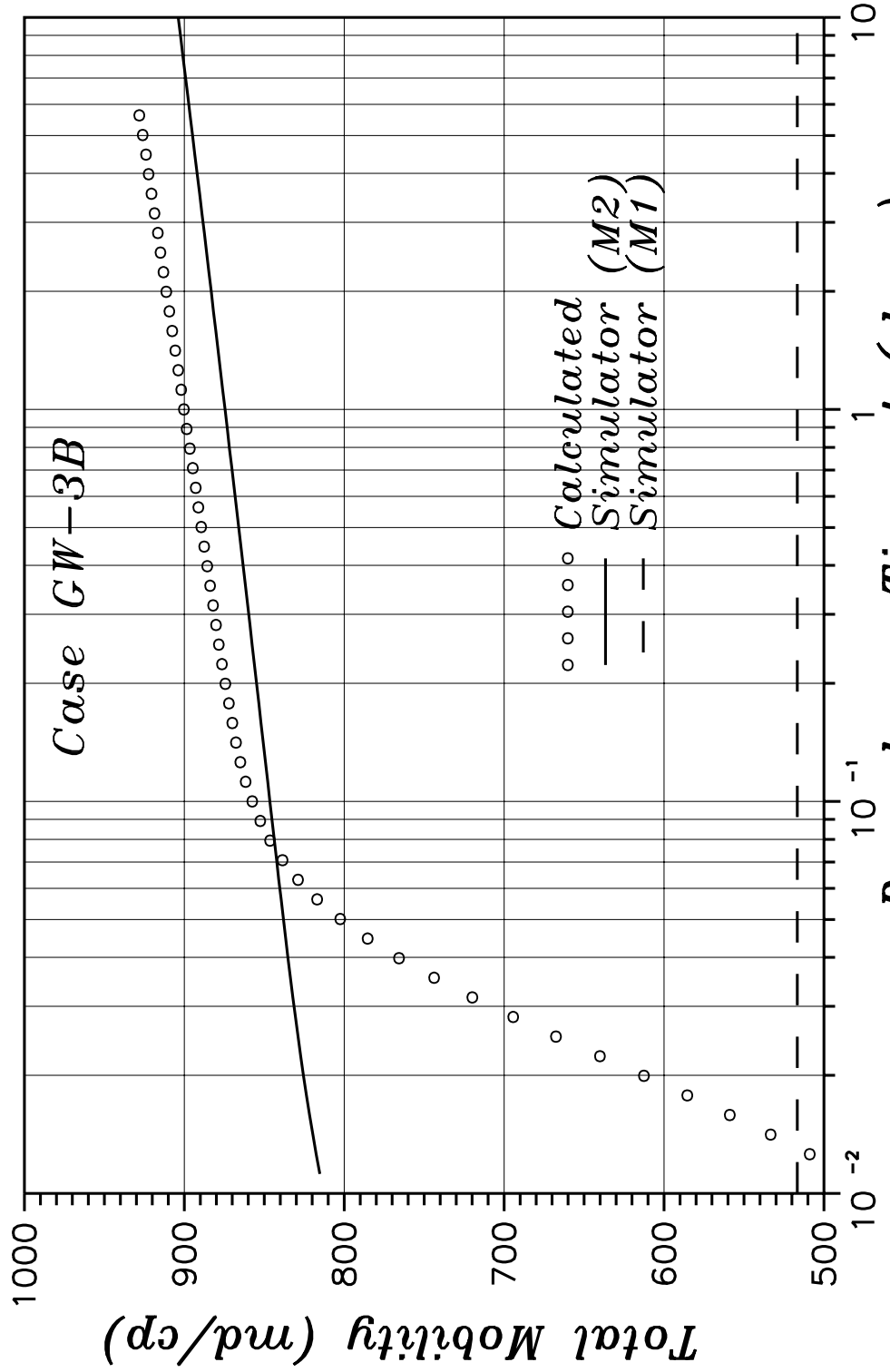

Fig. 6.9 – Total mobility interpretation plot (Case GW-3B).

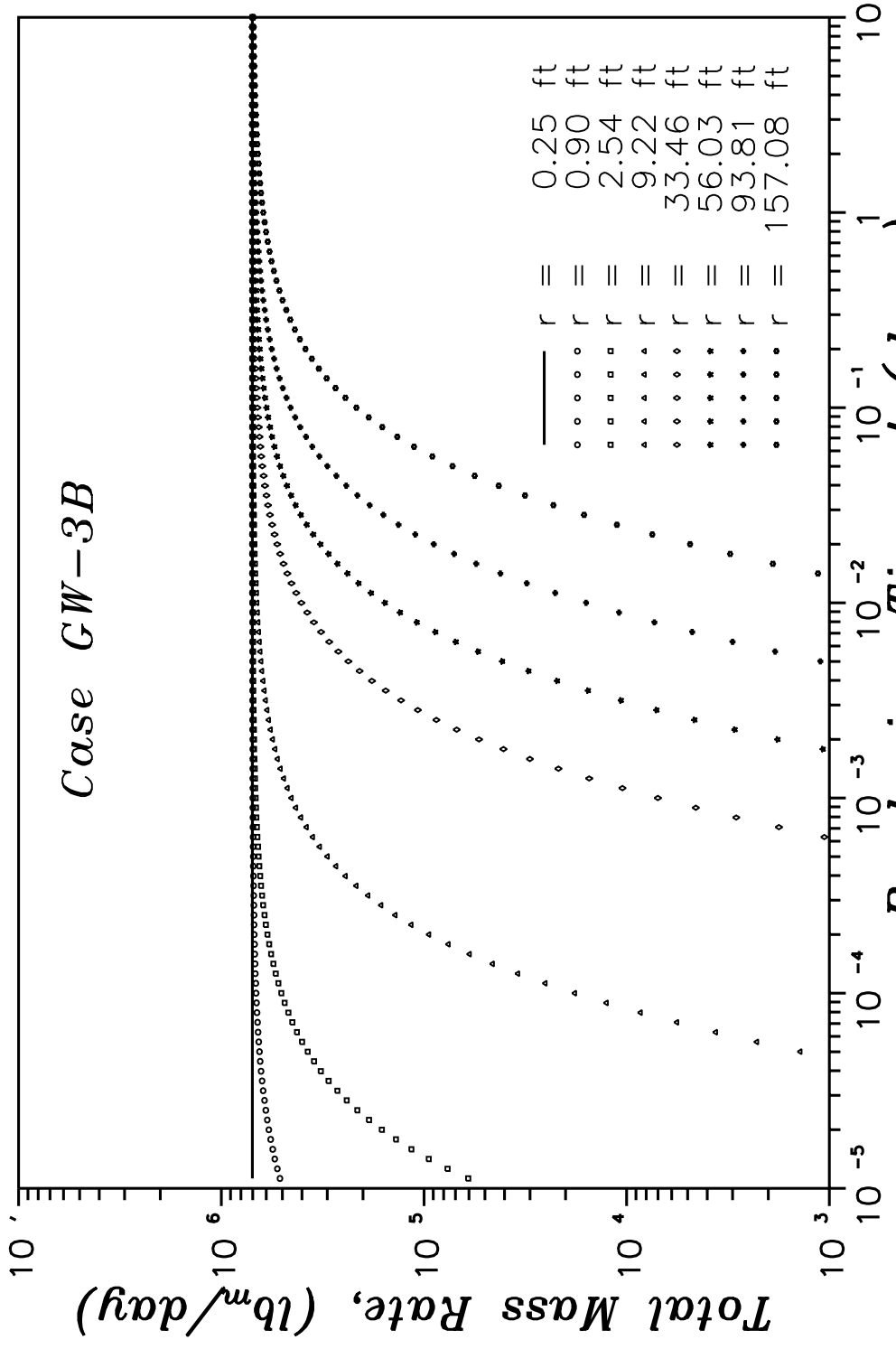

Fig. 6.10 — Total mass flow rate comparison plot (Case GW-3B).

the reservoir. This plot again clearly indicates that the PVT properties should be evaluated at the wellbore pressure. We also note that at approximately 0.5 $days$, water begins to "cone" towards the well. This is clearly indicated in the figure by the simulator output mobilities for $r = 0.28\ ft$ and $r = 38.0\ ft$. As coning (building of the water cone) becomes significant, the calculated total mobility decreases analogous to results for oil-water systems discussed in the previous section.

This vertical movement of water can also be seen if we examine the total mass rate across various cross-sections of the reservoir. Figure 6.12 is a slightly expanded plot of the total mass flow rate in the reservoir across various radii. At approximately 0.5 $days$, we note that there exists a higher total mass flow rate out in the reservoir than there is at the sandface. This makes intuitive sense in that at reservoir conditions the water mass density is approximately 3.7 times larger than the gas mass density. When water begins to move vertically upward (building a cone), we have the more dense water displacing the less dense gas. Out in the reservoir, the water mass flow rate must increase to continue supplying the water for building the cone.

Next, we examine two cases (GW-6C and GW-6B) which are similar to one another, and hope to show that in the outer region of the reservoir both cases behave nearly identical. Case GW-6C is a commingled reservoir 60 ft thick, with a 40 ft layer containing gas and irreducible (immobile) water, and a 20 ft layer containing only water. This reservoir is produced at a constant surface gas rate ($q_g = 10\ MMscf/D$) from a fully-penetrating well. The different zones for case GW-6B, which was discussed above, are in vertical communication with one another. Recall that the reservoir for case GW-6B is produced at a constant surface gas rate of $q_g = 10\ MMscf/D$ from a restricted-entry well perforated only in the top ten feet of the reservoir.

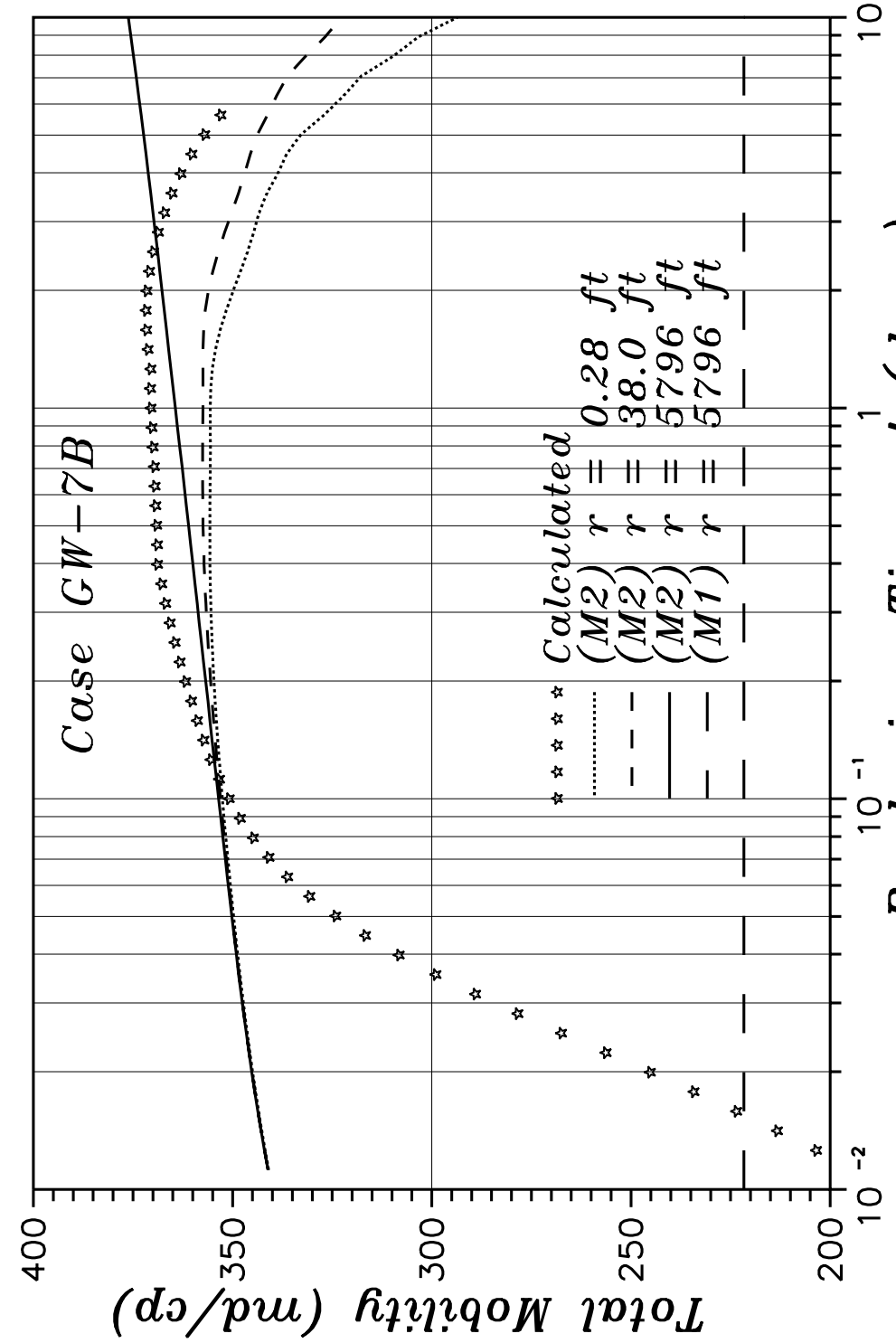

Fig. 6.11 — Total mobility drawdown interpretation plot (Case GW-7B).

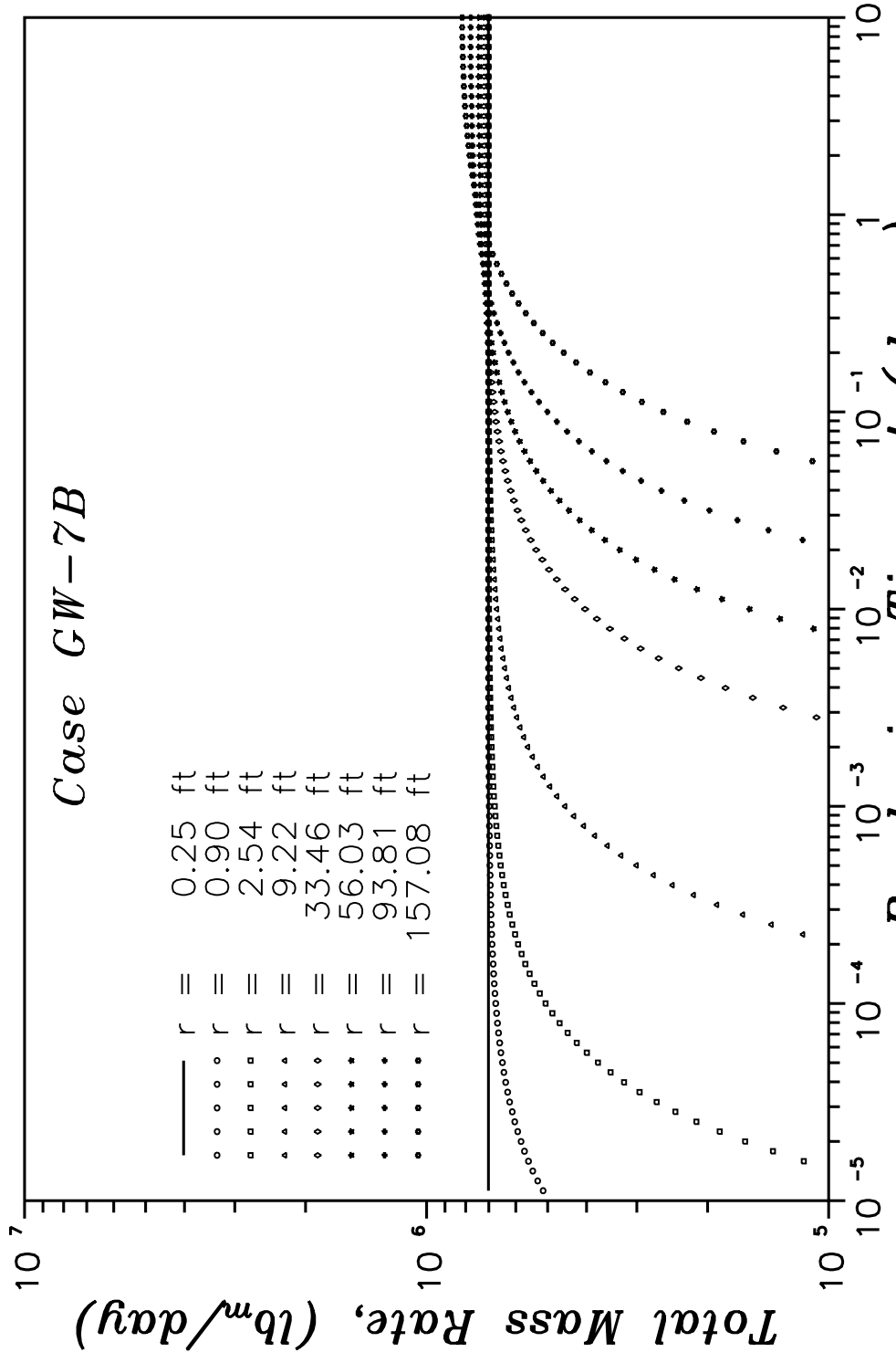

Fig. 6.12 — Total mass flow rate comparison plot (Case GW-7B).

The initial thickness averaged total mobility for both cases is 352.8 (md/cp). For case GW-6C, we apply Eq. 6.2.1 to each layer individually (gas rate and gas properties replaced with water rate and water properties for layer 2) with h replaced by the thickness of the layer, add the results and divide by h to obtain the total-thickness-averaged mobility. Eq. 6.2.5 is applied for case GW-6B. Results for the two cases are shown in Figs. 6.13 and 6.14, respectively. The reported simulator values for method M2 were evaluated at the initial saturation, but with pvt properties evaluated at the wellbore pressure. Fig. 6.13 shows the total mobility for Case GW-6C varying from 397.5 (md/cp) at 0.01 $days$ to 434.5 (md/cp) at 10 $days$. For Case GW-6B, we see in Fig. 6.14 that the calculated mobility varies from 572.6 (md/cp) at 0.1 day, to 610.8 (md/cp) at 10 $days$.

Since the vertical fluid distributions, reservoir dimensions and horizontal permeabilities are the same for both cases at initial conditions, the total thickness averaged mobilities are the same for both cases also. The total mobilities calculated from pressure transient analysis, however, are completely different for each of the cases, and are only reconciled if we consider the evaluation of the PVT properties at the wellbore pressure (shown in Figs. 6.13 and 6.14 as solid lines).

Even though the total-thickness-averaged mobility calculated for Case GW-6C was quite accurate, we should note that the individual phase mobilities were not quite so accurate. For instance, the total thickness averaged water mobility was calculated as 7.4 (md/cp) at a producing time of 1 day as compared to the true value of 8.33 (md/cp). This is probable due to the fact that the reservoir was produced at a constant surface gas rate, and therefore, the water production rate was varying (increasing) during the entire production period. Because of the commingled nature of this case, we should be able to evaluate the individual layers independently, and thereby use a form of rate-normalization to evaluate the water

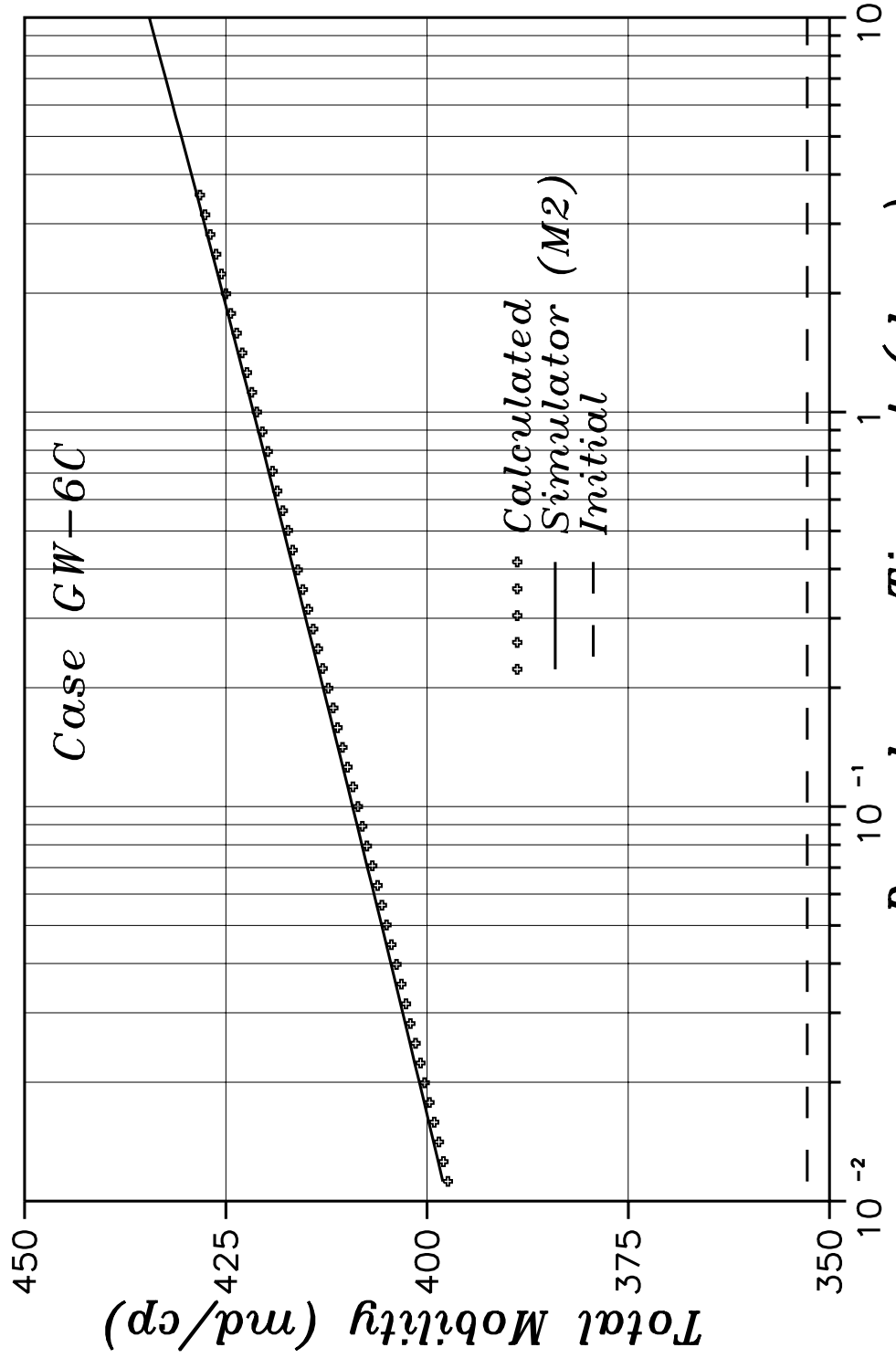

Fig. 6.13 – Drawdown total mobility interpretation plot (Case GW-6C).

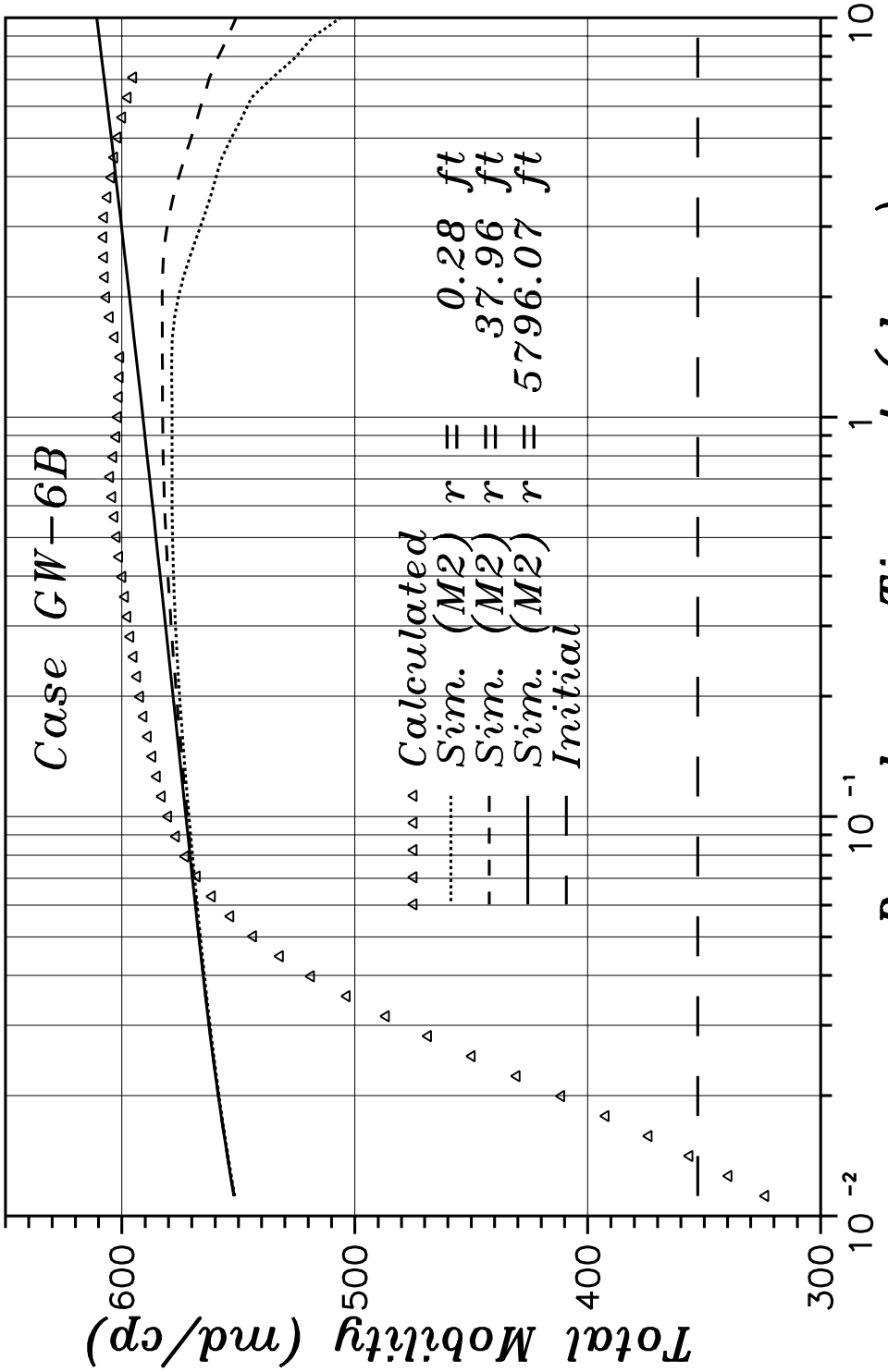

Fig. 6.14 — Drawdown total mobility interpretation plot (Case GW-6B).

layer. To do so, we define an instantaneous rate normalized water pseudopressure as

$$\overline{m}(p_{wf}) = \frac{\int_{p_{wf}}^{p_i} \frac{dp}{B_w \mu_w}}{q_w(t)} \ , \tag{6.2.7}$$

and then calculate the effective water permeability in the water zone as

$$k_w = \frac{70.6}{h_w d\overline{m}(p_{wf})/d\ln t} \ , \tag{6.2.8}$$

where here, h_w represents the thickness of the water layer. Using Eqs. 6.2.7 and 6.2.8, we calculated an effective water permeability in the water zone of 20 (md), which is exactly equal to the true value. We also note that the thickness averaged gas mobility for this case represents 97.6 percent of the total thickness averaged mobility. Because of this, one could probably ignore the water completely and still obtain a reasonable estimate of the thickness averaged mobility or thickness averaged effective gas permeability, e.g., ignoring the contribution from the water, Eq. 6.2.5 can be modified as

$$\bar{k}_g = \frac{k_g h_g}{h} = \frac{-70.6 q_g B_g(p_{wf}) \mu_g(p_{wf})}{h dp_{wf}/d\ln t} \ . \tag{6.2.9}$$

Utilizing Eq. 6.2.9, we calculated a thickness averaged effective gas permeability of 8.32 (md). This compares with the actual initial thickness averaged effective gas permeability of 8.47 (md), a 1.8 percent difference.

In Table 6.2 we show the total thickness averaged mobilities output from our simulator (method M2) and calculated using Eq. 6.2.5 at a producing time of 0.1 days. Recall that for method M2, the output simulator mobilities are evaluated using the initial fluid saturations and the pvt fluid properties evaluated at the prevailing wellbore pressure. Note that there is nothing magic about the time 0.1 days chosen for the comparison. We have simply chosen this time as a reference

point for these cases so that a simple comparison can be made without having to show a complete time plot comparing the mobilities. The calculated mobilities shown in Table 6.2 exhibit a similar trend to the calculated mobilities in the previous section; i.e., the percent deviation from the "actual" mobility existing in the reservoir increases with the thickness of the aquifer.

Figure 6.15 shows the percent deviation of the calculated mobilities from the mobilities output from our simulator plotted against the aquifer thickness. Three sets of cases are plotted in this figure: cases GW-*B at 0.1 days, cases GW-*B at 1 day, and cases GW-*B2 at 0.1 days. Recall that cases GW-*B2 are identical to cases GW-*B except for the production rate is only 1 MMscf/day instead of 10 MMscf/day. Figure 6.15 shows a linear trend for each of these sets of data, though each have a slightly different slope. Based on similar results discussed in the previous section, this figure suggests a similar explanation for these results; i.e., the thicker the aquifer, then there must be proportionately more water flowing in the outer region of the reservoir where pseudoradial flow exists. Since the inner boundary is closed in the water zone, this water must flow vertically near the inner boundary. The increased vertical movement of water near the inner boundary results in a reduction in the total mobility near the gas-water contact, which results in an increase in the wellbore pressure derivative, and a decrease in the mobility calculated from Eq. 6.2.5. This decreasing total mobility is readily apparent on Fig. 6.14.

Lastly, we wish to examine the underlying assumptions (at least for single-phase) for semilog analysis of these systems. First, we examine the mass flow rates for each system. Figure 6.16 shows the total mass rates for both cases GW-6B and GW-6C as a function of radius at producing times of 1 day and 10 days. Recall that case GW-6C had a fully-penetrating well and that the reservoir was commingled; i.e., no flow between the layer containing gas and the layer containing

Table 6.2

Drawdown Semilog Analysis Results: Gas-Water Systems

Case	Simulator $\bar{\lambda}_t$ (md/cp)	Calculated $\bar{\lambda}_t$ (md/cp)	Percent Deviation
GW-2B	601.4	601.9	0.09
GW-2BS3	530.7	530.9	0.05
GW-2BS4	537.2	537.5	0.05
GW-3B2	540.4	539.2	0.22
GW-3B	846.5	859.9	1.59
GW-3BS3	568.5	567.5	0.18
GW-3BS4	598.9	598.9	0.01
GW-4B2	480.4	481.2	0.17
GW-4B	752.4	767.6	2.03
GW-4B2S3	505.3	506.4	0.21
GW-4B2S4	532.3	534.4	0.40
GW-5B2	432.3	435.2	0.65
GW-5B	677.1	692.9	2.33
GW-5BS3	454.8	457.4	0.57
GW-5BS4	479.0	482.7	0.77
GW-5C	481.1	481.5	0.09
GW-6B2	360.3	364.8	1.27
GW-6B	564.2	581.3	3.03
GW-6BS3	379.0	383.4	1.17
GW-6BS4	399.2	404.7	2.37
GW-6C	409.3	408.6	0.16
GW-7B2	216.2	221.2	2.33
GW-7B	338.5	352.7	4.18
GW-7BS3	227.4	232.5	2.23
GW-7BS4	239.5	245.4	2.43
GW-7C	240.6	240.8	0.10

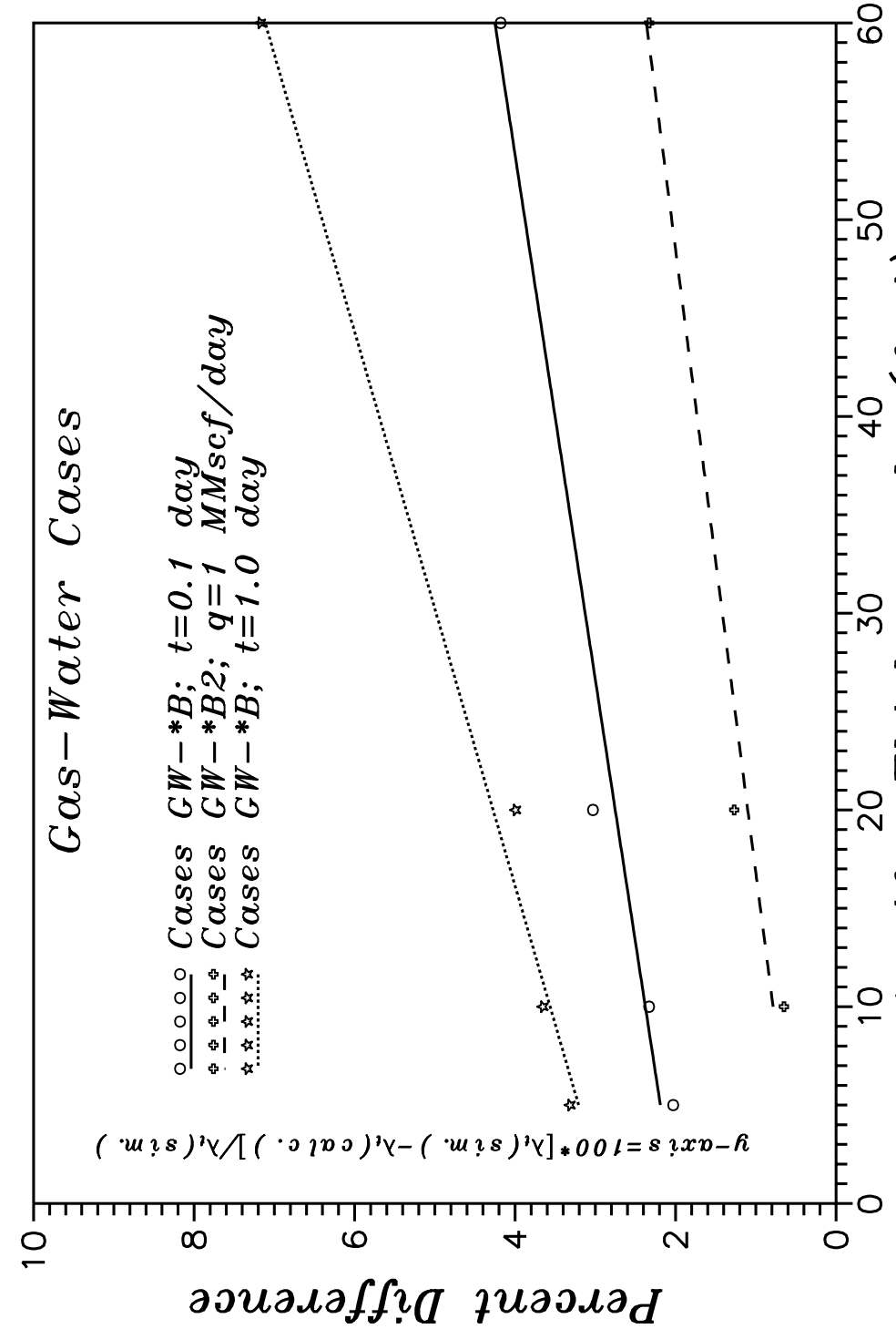

Fig. 6.15 – Correlation between relative difference in calculated and simulator mobility with thickness of aquifer.

water. While both cases exhibit a zone of constant mass rate over some region close to the wellbore, there is a significant difference between the two in this region (approximately 9 percent). This is the region of the reservoir where the water cone is being built for case GW-6B, i.e., water flow is primarily vertical, whereas for case GW-6C, the water zone is open to flow and flow is purely radial. Further out in the reservoir, Fig. 6.16 shows the mass rate for case GW-6B increasing, approaching the mass rate of case GW-6C.

Figure 6.17 shows the percent difference between the mass rates for these two cases as a function of radius. At a producing time of 10 days, Fig. 6.17 shows there is a region of the reservoir, $150 \leq r \leq 500$ feet, for which the difference between the two cases is less than two percent. This suggests the existence of pseudoradial flow in this section of the reservoir.

Indeed, if we examine (Fig. 6.18) the fractional flow rate of each phase as calculated from the thickness-averaged mobilities in the reservoir versus the fractional flow of each phase as calculated from the reservoir volumetric flow rates, we see that the fractional flow rates become equal for each calculation method at a radius of approximately 150 feet; i.e., pseudoradial flow (vertical equilibrium) exists in the reservoir in the region $150 \leq r \leq 3500$ feet.

These results indicate that while vertical equilibrium exists in the reservoir in the region $150 \leq r \leq 3500$ feet, a "steady-state" zone (constant mass rate) only exists in the region $r_w \leq r \leq 30$ feet. This means that the pressure response for these cases are being influenced by vertical flow in the reservoir. Since the mobility computation equation (Eqs. 6.2.5) assumes that vertical equilibrium exists in the region of the reservoir influencing the pressure derivative, then it should be no surprise that our computed mobilities are in error.

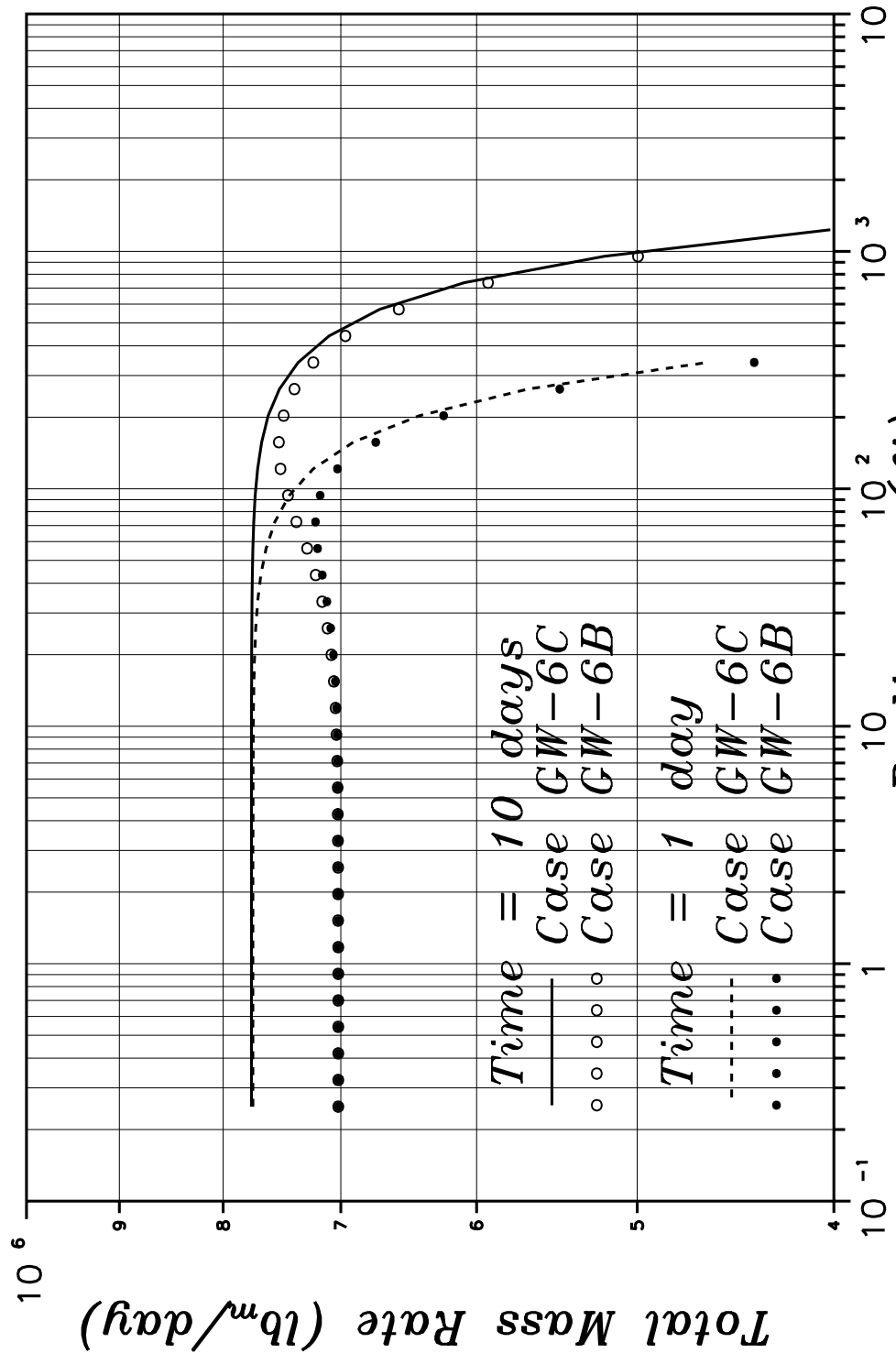

Fig. 6.16 – Comparison of in-situ mass flow rates for restricted-entry case versus comingled fully-penetraing case.

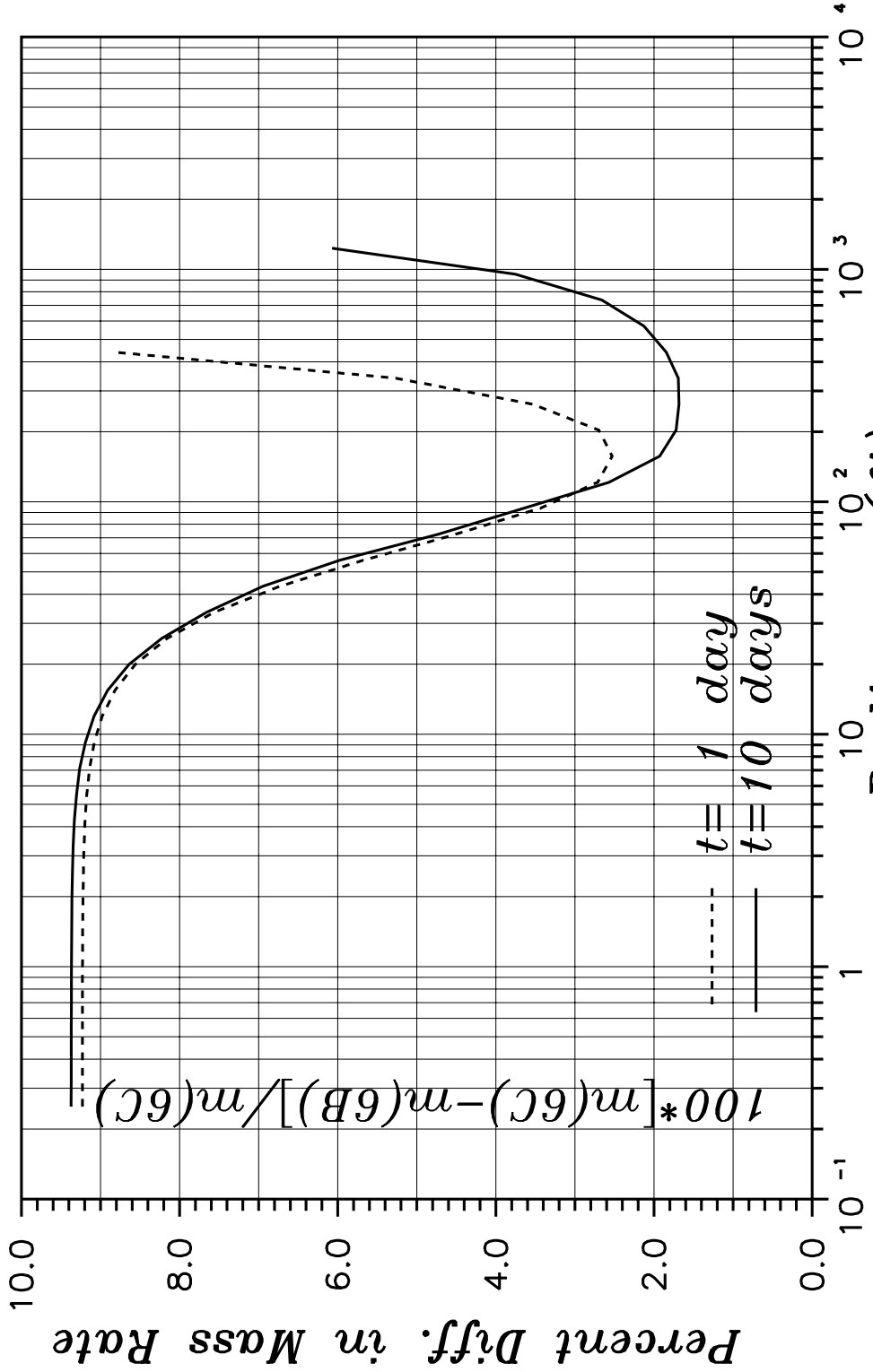

Fig. 6.17 — Percent difference in mass flow rates at various times for cases GW−6B and GW−6C.

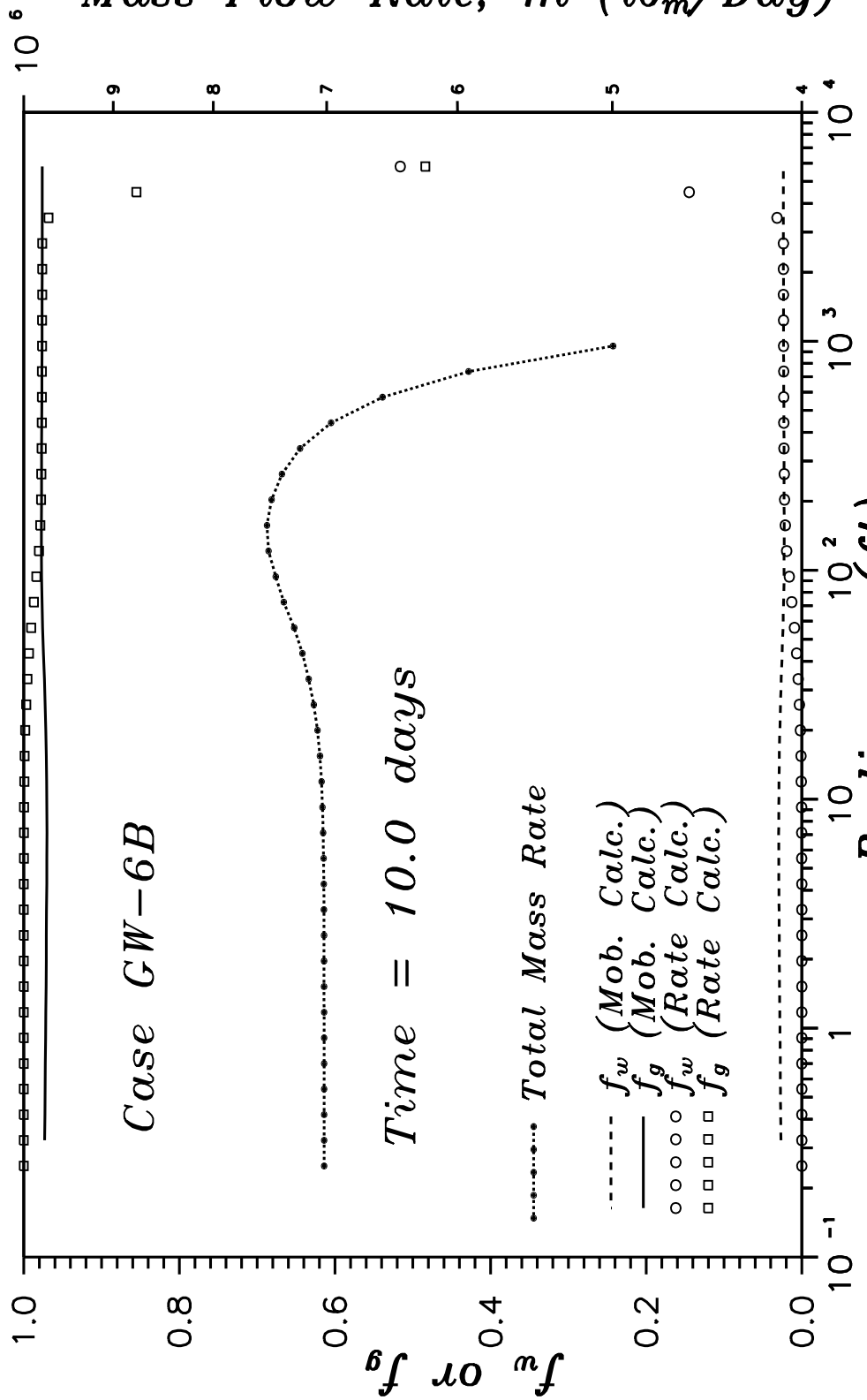

Fig. 6.18 — Comparison of fractional flow rates as an indicator of vertical equilibrium.

6.3 Two-Phase Water-Gas Systems

In this section we examine a series of water reservoirs overlain by a gas cap and produced at a constant water rate from a restricted-entry well. We consider these cases as a prelude to investigating the drawdown behavior of an oil reservoir overlain with a gas cap (discussed in the next section). For the current cases, our analysis should be simplified since we do not need to consider mass transfer between the phases. Also, analysis of these analogous water reservoir - gas cap cases will hopefully provide us with information that will enable us to distinguish between mass transfer effects and flow effects on the pressure transient response for the oil reservoir - gas cap cases.

A vertical cross-section of the reservoir with the upper boundary and fluid saturations indicated for each of the water reservoir - gas cap systems considered are shown in Fig. 4.4 of Chapter IV. Other pertinent fluid and physical property data are included in Tables 4.4A and 4.4B for the "base case" (Case WG-1B), along with the deviations from the base case parameters for each of the other water-gas systems considered. Gas caps of 0, 10, 20, 25 and 30 feet are considered. A 10-day drawdown at a constant surface water production rate of 200 (STB/D) followed by a 10-day buildup are simulated for each of the cases.

For each of the systems investigated, the logarithmic derivative of the pressure drop was calculated and plotted versus producing time. A thickness-averaged total mobility was calculated from

$$\bar{\lambda}_l = \frac{70.6 q_l B_l}{h d\Delta p/d\ln t} \ , \ l = g, w \tag{6.3.1}$$

where the thickness-averaged total mobility is interpreted to represent the sum of the individual phase thickness-averaged mobilities,

$$\bar{\lambda}_t = \bar{\lambda}_g + \bar{\lambda}_w \ . \tag{6.3.2}$$

The pressure derivative responses for each of the zero-skin cases are shown if Fig. 6.19. Fig. 6.19 shows that only for the single phase water cases (WG-1B and WG-2B) are well-defined late time (pseudoradial flow) semilog straight lines indicated; i.e., constant log-derivative of pressure. In the previous section we interpreted the increasing pressure derivative as an indication that analysis should be performed in terms of pseudopressure. For the current cases, however, we are producing water (with a compressibility of $3 \times 10^{-6}\ psi^{-1}$) and the change in pressure near the original gas-water contact is small. The use of a water pseudopressure, then, would have minimal impact on the analysis for these cases; the derivative of a water pseudopressure would still exhibit the non-constant (increasing) behavior exhibited by the pressure derivative.

Based on the results of the previous two sections, we speculate that the increasing pressure derivative is due to multiphase effects. In particular, we speculate that the increasing derivative is due to movement of gas across the original gas-water contact towards the well and a decrease in the total mobility at this location. Figure 6.20 shows the gas saturation and total relative mobility ($k_{rg}/\mu_g + k_{rw}/\mu_w$) for case WG-5B as a function of producing time for three vertical locations just below the original gas-water contact and near the inner boundary. Figure 6.20 indicates changes in the total mobility becomes significant at approximately the same time as the pressure derivative begins to increase.

Based on this observation, we utilized Eq. 6.3.1 to calculate thickness-averaged total mobilities for each of the cases at the producing time where the pressure derivative reaches a minimum (just begins to increase). The results of these calculations are shown in column 3 of Table 6.3. Also included in Table 6.3 are the initial thickness-averaged total mobility (column 2), the percent deviation of the calculated mobility from the initial thickness-averaged mobility (column 4), the initial thickness-averaged mobility adjusted to account for the wellbore

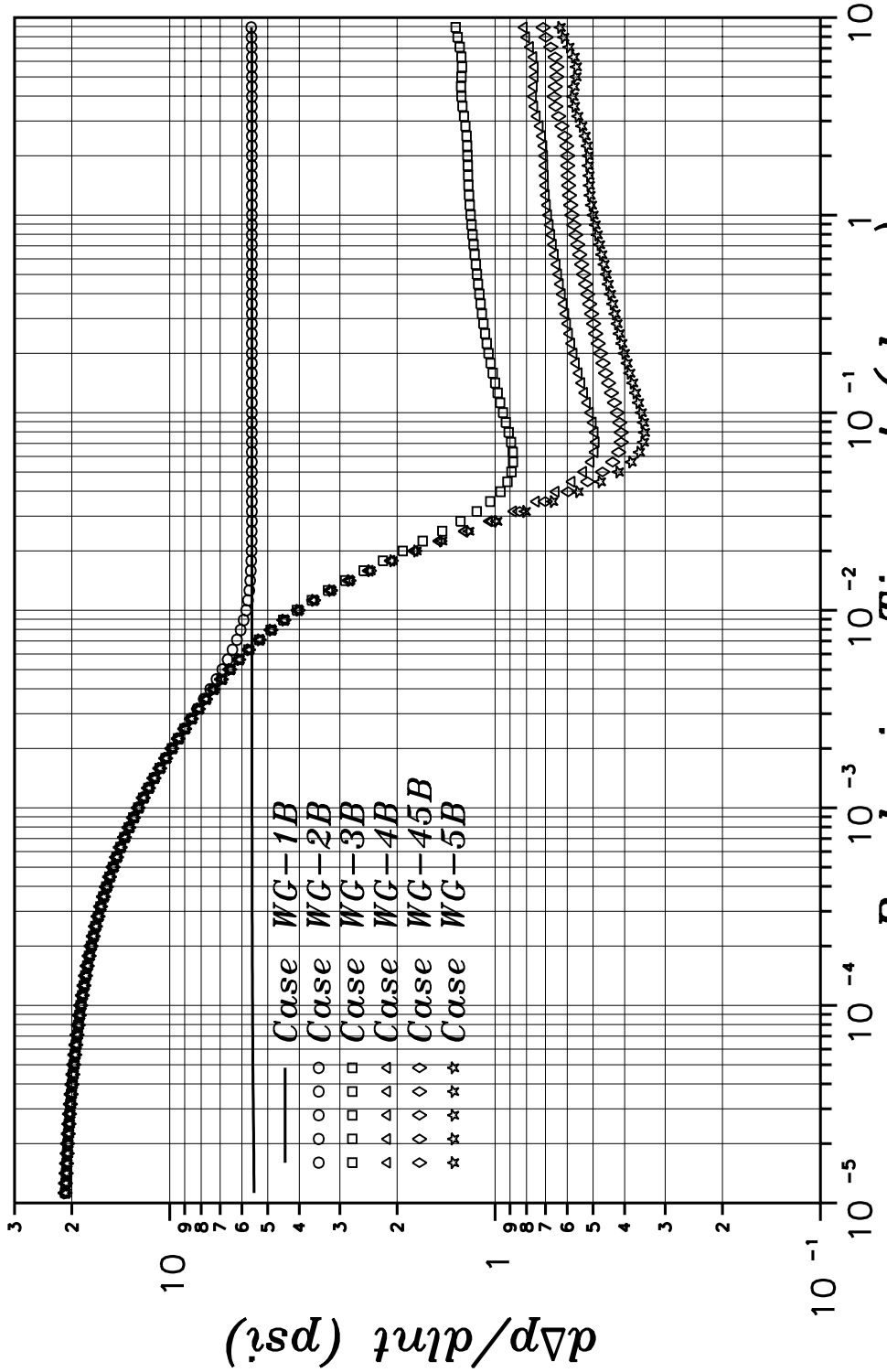

Fig. 6.19 – Diagnostic drawdown pressure derivative plot (Water–Gas).

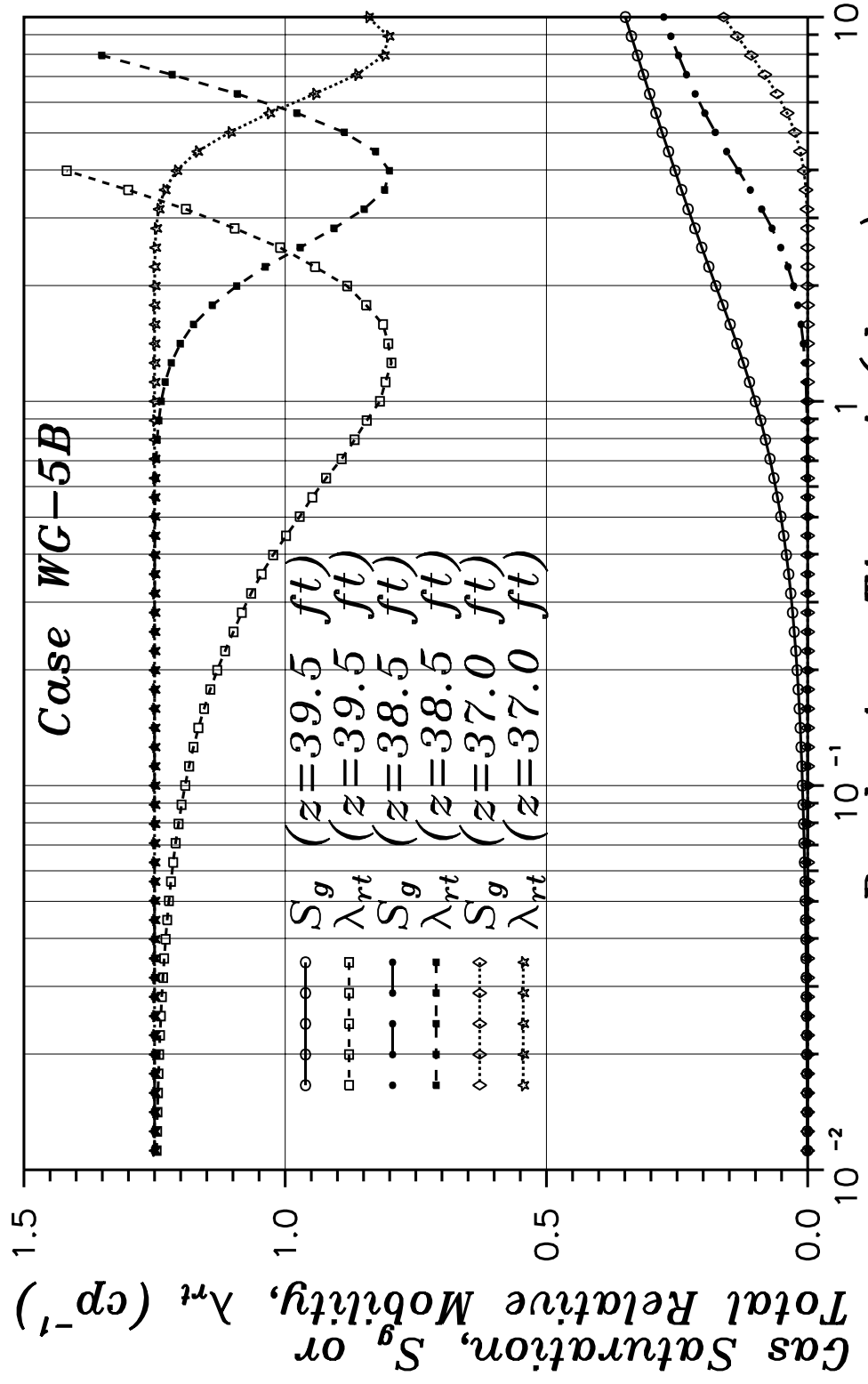

Fig. 6.20 — Gas saturation and total relative mobility near gas–water contact as a function of producing time.

pressure (column 5), i.e., $\bar{\lambda}_t = k[k_{rg}/\mu_g(p_{wf}) + k_{rw}/\mu_w(p_{wf})]$, and, lastly, the percent deviation of the calculated mobility from the modified initial thickness-averaged mobility (column 6). The first item worth noting in Table 6.3 is the fact that the calculated mobilities are independent of the skin factor (see cases ****-S3 and ****-S4, which represent cases with input skin factors of $s = 5$ and $s = 10$, respectively). Because of the increased pressure drop at the well due to the skin factor, this result then implies that the PVT properties are essentially independent of pressure over that pressure range; e.g., since only water is being produced, the only PVT property which shows up in our calculation equation (Eq. 6.3.1) is the water phase formation volume factor. Recall from Table 4.4 that the water compressibility for the current cases is only $c_w = 3 \times 10^{-6}$ psi^{-1}, which results in a minimal change in the water formation volume factor over the course of the well test. This result in turn implies analysis can be performed in terms of pressure only; i.e., there is no need to consider analysis based on pseudopressure, even though we have gas in our system.

In the previous two sections, we have shown that the deviation of the calculated mobilities from the thickness-averaged total mobility existing in the reservoir correlate extremely well with aquifer thickness. For the current cases, then, we suspect that the deviation in the calculated mobilities will correlate with the thickness of the gas cap. While the deviations in Table 6.3 can be shown to correlate extremely well with the gas cap thickness, the trend of the correlation is opposite from that reported in the previous sections; i.e., instead of the deviation increasing with an increase in the gas cap, the deviation decreases. We also note that the deviations reported in Table 6.3 are much larger than the deviations reported in previous sections, though we have no basis for expecting them to be similar in magnitude.

Table 6.3

Drawdown Semilog Analysis Results: Water-Gas Systems

Case	Simulator $\bar{\lambda}_t(p_i)$ (md/cp)	Calculated $\bar{\lambda}_t$ (md/cp)	Percent Deviation	Simulator $\bar{\lambda}_t(p_{wf})$ (md/cp)	Percent Deviation
WG-1B	62.5	62.5	0.0	62.5	0.0
WG-1BS3	62.5	62.5	0.0	62.5	0.0
WG-1BS4	62.5	62.5	0.0	62.5	0.0
WG-2B	62.5	62.5	0.0	62.5	0.0
WG-2BS3	62.5	62.5	0.0	62.5	0.0
WG-2BS4	62.5	62.5	0.0	62.5	0.0
WG-3B	239.1	317.5	32.8	248.2	27.9
WG-3B2S3	239.1	317.5	32.8	259.4	22.4
WG-3B2S4	239.1	317.6	32.8	273.1	16.3
WG-4B	357.2	470.2	31.6	371.9	26.4
WG-4BS3	357.2	470.4	31.7	390.6	20.4
WG-4BS4	357.2	470.4	31.7	413.5	13.8
WG-45B	402.6	525.3	30.5	419.5	25.2
WG-5B	441.5	572.5	29.7	460.3	24.4
WG-5BS3	441.5	572.7	29.7	484.4	18.2
WG-5BS4	441.5	572.7	29.7	513.7	11.5

In addition to the differences noted above, observe that the calculated mobilities reported in Table 6.3 are larger than the simulator values. This implies that the pressure derivative is smaller than that necessary to calculate the proper mobilities. In the past, people probably would have attributed this to "pressure maintenance" due to the gas cap, and in a sense, this is the probable cause here. For multilayered reservoirs, Ref. 19 showed that the time to the beginning of the semilog straight line for single phase systems is strongly affected by ω, the ratio of the porosity-compressibility product for the open interval divided by the thickness averaged value; i.e.,

$$\omega = \frac{\phi_1 c_{t1} h_1}{\overline{\phi c_t} h} \ , \tag{6.3.3}$$

where

$$\overline{\phi c_t} = \frac{1}{h} \int_0^h \phi c_t dz \ . \tag{6.3.4}$$

For small ω, Ref. 19 showed that the derivative of p_{wD} falls below the theoretical value of 1.151 for a period before returning to the correct slope; e.g., see Figs. 5.13 and 5.14 of Ref. 19. For case WG-5B, we have $c_{t1} = 3 \times 10^{-6}$ and $\bar{c}_t = 6.129 \times 10^{-5}$ which gives us $\omega = 0.028$ (ϕ is a constant for this case). This is indeed a small value for ω, and so we suspect that the minimum pressure derivative for the cases shown in Fig. 6.19 are below the "proper" value representing pseudoradial flow.

To verify this conjecture, we run another case (WG-5D) similar to case WG-5B in which we have reduced the porosity in the gas cap from 0.2 to 0.01. This results in an increase in ω from 0.028 to 0.457. This change in ω should be large enough for us to verify our conjecture above. Figure 6.21 shows a comparison of the pressure derivatives for case WG-5B and WG-5D. Figure 6.21 shows the late-time pressure derivative for case WG-5D is indeed much higher than for case WG-5B. We also note that the maximum calculated mobility (from Eq. 6.3.1) for case WG-5D is 393 md/cp. This value is now less than the thickness-averaged

total mobility in the reservoir. This result tends to support our conjecture above that at late time the pressure derivative for cases with a small ω will initially fall below the value representative of pseudoradial flow. Simply as a side note since the question will be asked, we note that the sharp increase in the derivative at late time for case WG-5D is due to boundary effects. Because of the decrease in the porosity in the gas cap, we have essentially reduced the time to boundary dominated flow by an order of magnitude.

In examining Fig. 6.21 further, we note that the pressure derivatives for both cases become similar at approximately 1 day. Based on this observation, we recalculated the thickness-averaged total mobilities (Eq. 6.3.1) at a producing time of 1 day, with the results shown in Table 6.4. Columns 3 and 4 of Table 6.4 show the percent deviation of the calculated mobility from the initial thickness-averaged mobility and the thickness-averaged mobility modified based on the wellbore pressure, respectively. These results are more in line with results reported in previous sections in that the deviation from the simulator values increase with an increase in the gas cap thickness. In fact, if we examine Fig. 6.22, which shows the percent deviation plotted as a function of the gas cap thickness, we again obtain a straight line correlation.

In Section 5.2.2 of Chapter 5 we showed for water reservoirs overlain by a gas cap and a constant pressure upper boundary that an increasing pressure derivative could be directly attributed to the movement of a saturation front or "shock" across the original gas-water contact and towards the well. Part of that discussion revolved around a recent theoretical development by Ref. 149 that showed the log-derivative with-respect-to producing time of the wellbore pressure drop was in part dependent upon the time rate of change in the total relative mobility in the two-phase region of the reservoir. Part of that discussion also revolved around the validity of the assumptions incorporated into the classical

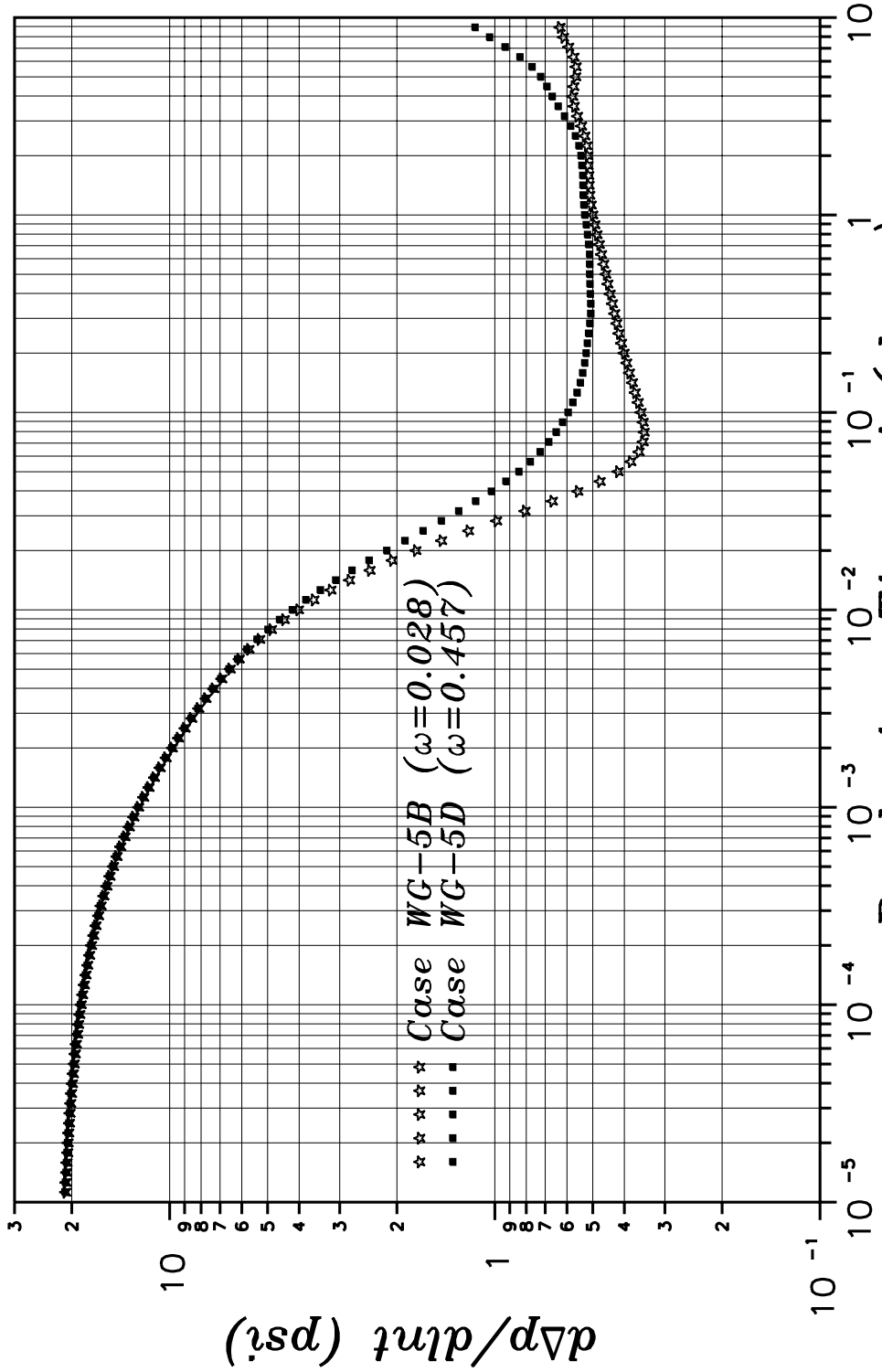

Fig. 6.21 — Effect of ω on the drawdown pressure derivative.

Table 6.4

Drawdown Semilog Analysis Results: Water-Gas Systems

Case	Calculated $\bar{\lambda}_t(1\ day)$ (md/cp)	Percent Deviation	Percent Deviation
WG-3B	235.1	1.68	5.27
WG-3BS3	235.1	1.66	9.36
WG-3BS4	235.1	1.65	13.90
WG-4B	336.1	5.91	9.63
WG-4BS3	336.3	5.87	13.92
WG-4BS4	336.3	5.86	18.67
WG-45B	370.7	7.91	11.64
WG-5B	398.1	9.83	13.52
WG-5BS3	398.1	9.79	17.77
WG-5BS4	398.3	9.77	22.47

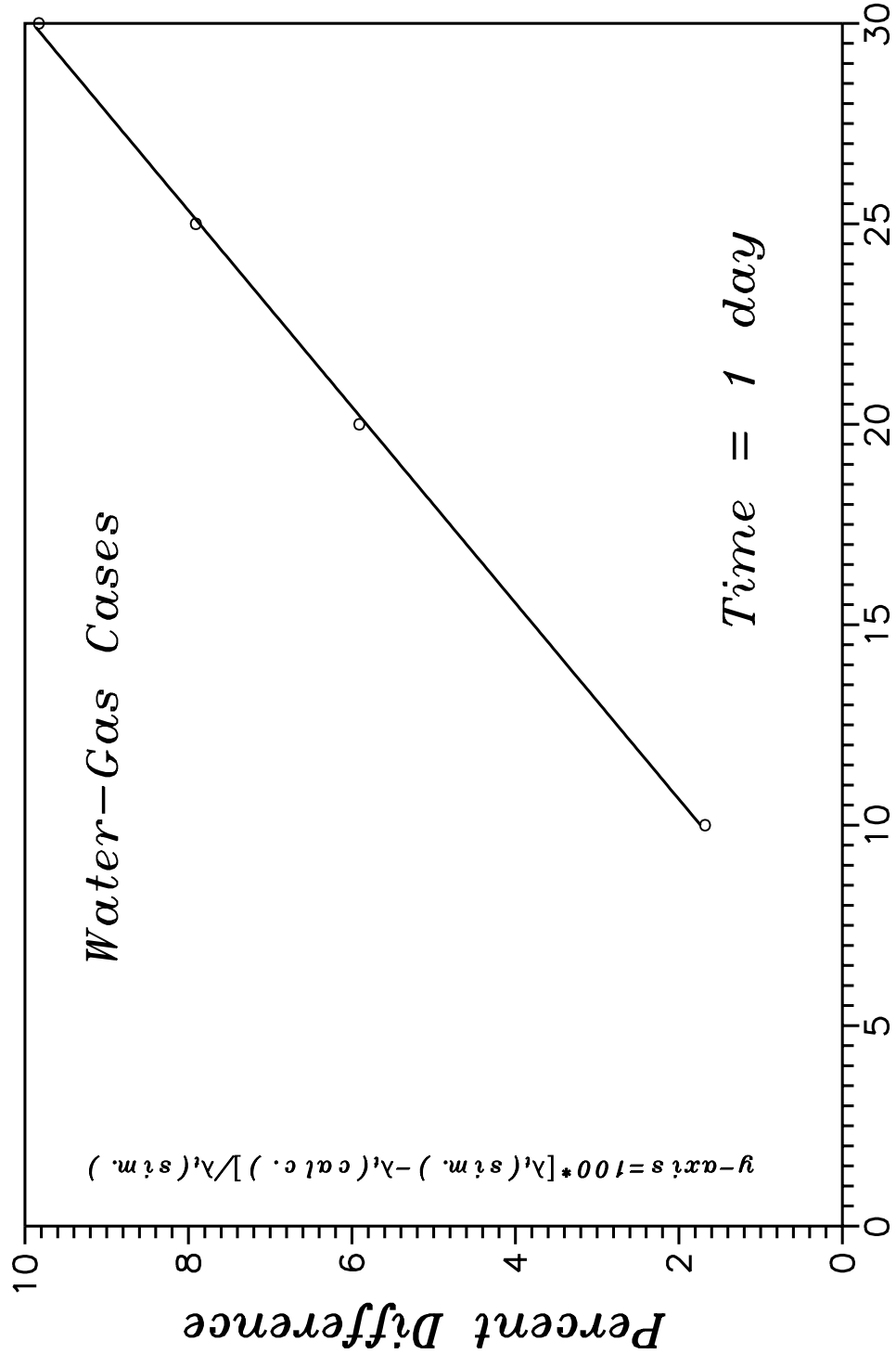

Fig. 6.22 – Correlation between relative difference in calculated and simulator mobilities.

Buckley-Leverett[117] theory on fractional flow; i.e., we showed that if conditions were such that a sharp saturation front or "shock" were to develop, then the contribution of the time-derivative of the total relative mobility to the time-derivative of the wellbore pressure drop would be dominated by the time-rate of change in the total relative mobility across the saturation front. Two common assumptions for the development of the sharp saturation front or shock include: (i) a constant reservoir volumetric flow rate across the reservoir, and (ii) the fluids are incompressible. For the current cases (water reservoir overlain by a gas cap, but no constant pressure upper boundary), these assumptions can be shown to be at least approximately satisfied. The pressure near the original water-gas contact ($z = 39.5\ ft$), for example, only decreases from 3600.18 psia to 3597.0 psia over the course of the drawdown test. Clearly, even for gases this change in pressure will have an insignificant effect on the gas density. At the sandface, the pressure decreases from 3611.03 psia to 3382.27 psia over the entire drawdown test. Because the compressibility of water for these cases is only $c_w = 3 \times 10^{-6}\ psi^{-1}$, this pressure drop results in an insignificant 0.07 percent decrease in the water density near the sandface.

Unlike the cases discussed in Section 5.2.2, the volumetric flow rate across the gas-water contact ($q_z = 186.25\ bbl/day$) never achieves the volumetric flow rate at the sandface ($q_r = 197.98\ bbl/day$). Note here that we are comparing a vertical flow rate with a radial flow rate. What is important to our current discussion, however, is a comparison of the vertical flow rates across the reservoir. In this regard, we examine the total vertical flow rate at the top of the perforations ($q_z = 194.97\ bbl/day;\ z = 10\ ft$), at a vertical height of $z = 30\ ft$ ($q_z = 189.16\ bbl/day$) and across the original gas-water contact ($q_z = 186.25\ bbl/day;\ z = 40\ ft$). Here, we see that the vertical flow rate varies by some 4.5 percent from the top of the perforations to the original gas-water contact, but more importantly, the vertical

flow rate varies by only 1.5 percent in the region 30 $ft \leq z \leq 40$ ft. These results point to the fact that, at least locally in the vicinity of the original gas-water contact, the conditions for the formation of a sharp saturation front or "shock" are being approximately satisfied.

In Section 5.2.2 we showed that the wellbore pressure response exhibited a direct relationship to the movement of this saturation front. Here, we again show a direct relationship between the wellbore pressure response and the movement of a saturation front or "shock". Figure 6.23 is a crossplot of the calculated total thickness averaged mobility obtained from the wellbore pressure response and Eq. 6.3.1 and the total relative mobility ($\lambda_{rt} = k_{rg}/\mu_g + k_{rw}/\mu_w$) at three vertical locations near the gas-water contact. Recall from Section 5.2.2 that the total relative mobility at a saturation "shock" for these cases was shown to be approximately $\lambda_{rt} \approx 0.8$ cp^{-1}. Examining the total relative mobility curves shown in Fig. 6.23, we see the mobility at each subsequent vertical location decreases to this same minimum mobility as the saturation shock passes each discrete grid block. Once the shock has passed the grid block, the total mobility increases again. Because of the discrete nature of our finite difference discretization of the reservoir, we note that the propagation of the saturation shock appears discontinuous in Fig. 6.23; however, the actual arrival time of the saturation shock at each grid block should be approximately correct provided numerical dispersion effects are small. The important point to note here is how the calculated mobility appears to track the movement of the minimum mobility at the saturation shock; i.e., as the mobility at each grid block reaches a minimum, a local minimum is observed in the calculated mobility. Another way of stating this is that each local minima or maxima on the calculated mobility curve corresponds almost exactly to either the time the relative mobility reaches a minimum at one of the vertical grid blocks, or

the time at which the relative mobility curves for two adjacent vertical grid blocks intersect.

Before leaving this section, we wish to examine the underlying assumptions for semilog analysis for these systems. Figure 6.24 shows the total mass rate at various cross-sections in the reservoir as a function of producing time for case WG-5B. Here, we see that the total mass rate at each radii becomes approximately constant with respect to producing time, however, at radii greater than approximately 30 feet, the rates decrease with increasing radius. This again makes intuitive sense since for these cases, we have a less dense fluid (gas) displacing a more dense fluid (water). Also, vertical equilibrium or pseudoradial flow are more closely approximated farther out in the reservoir, which means on a proportional basis of the volumetric flow rates more gas should be flowing and thus a lower total mass rate.

Lastly, we examine the fractional flow of each phase as calculated from the thickness-averaged mobilities in the reservoir versus the fractional flow of each phase as calculated from the reservoir volumetric flow rates; i.e.,

$$f_m|_r = \frac{\bar{\lambda}_m}{\bar{\lambda}_t}\Big|_r = \frac{q_m}{q_t}\Big|_r \ , m = g, w \ , \tag{6.3.5}$$

Recall that under flowing conditions, vertical equilibrium in the reservoir is indicated only when the mobility and rate calculated fractional flow rates are equal. Figure 6.25 shows these fractional flow rates as a function of radius at a producing time of 10 days. Also included in Fig. 6.25 is the total in-situ mass flow rate and the in-situ total volumetric flow rate normalized by the total volumetric flow rate at the sandface, i.e., $q_t(r)/q_t(r_w)$, at a producing time of 10 days From Fig. 6.25 we see that at the end of the drawdown ($t = 10\ days$) pseudoradial flow (vertical equilibrium) exists in the reservoir in the region $500\ ft \leq r \leq 3000\ ft$. Examining the total in-situ mass rate, however, Fig. 6.25 shows that a "steady-state"

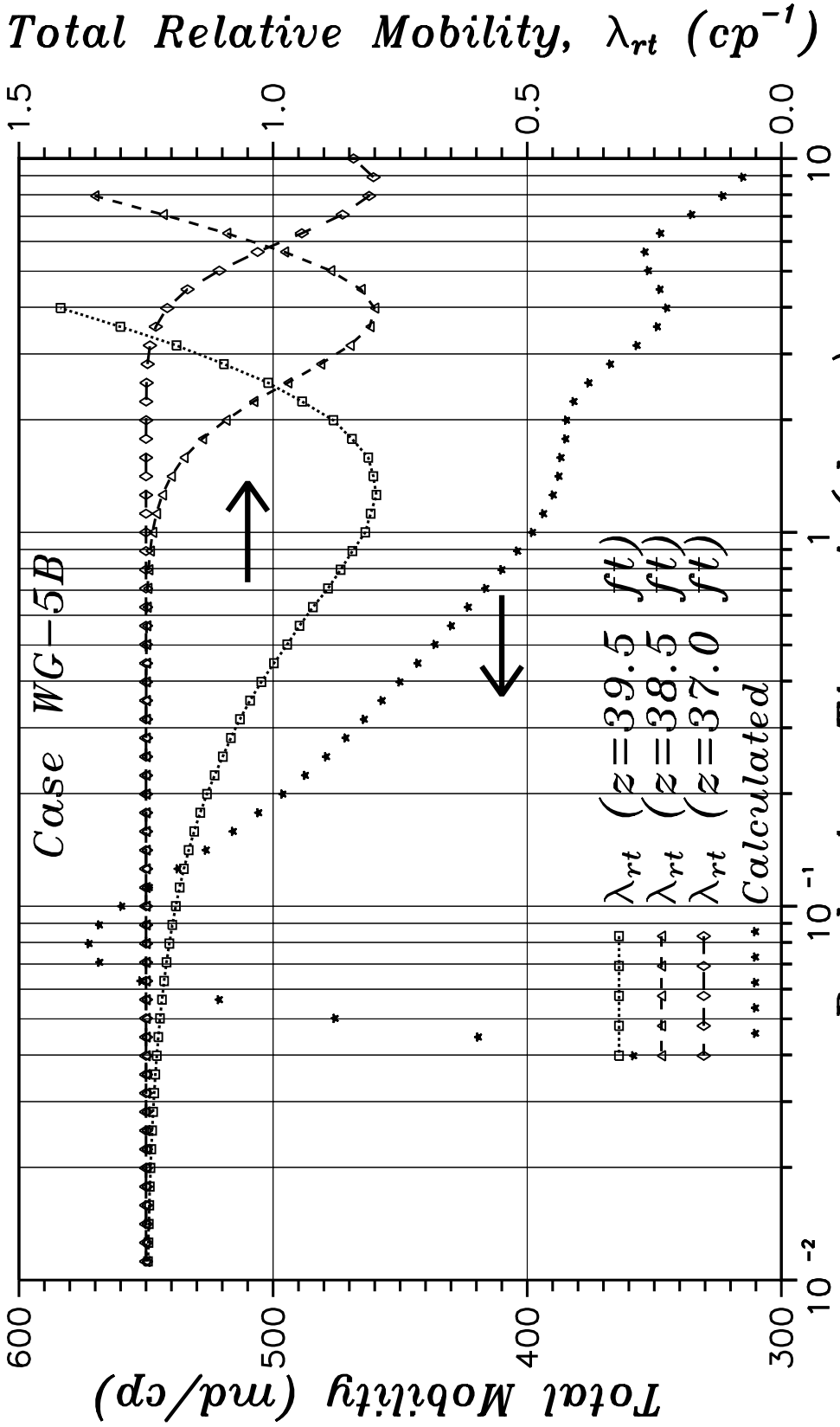

Fig. 6.23 — Relationship between calculated mobility and movement of saturation shock near gas—water contact.

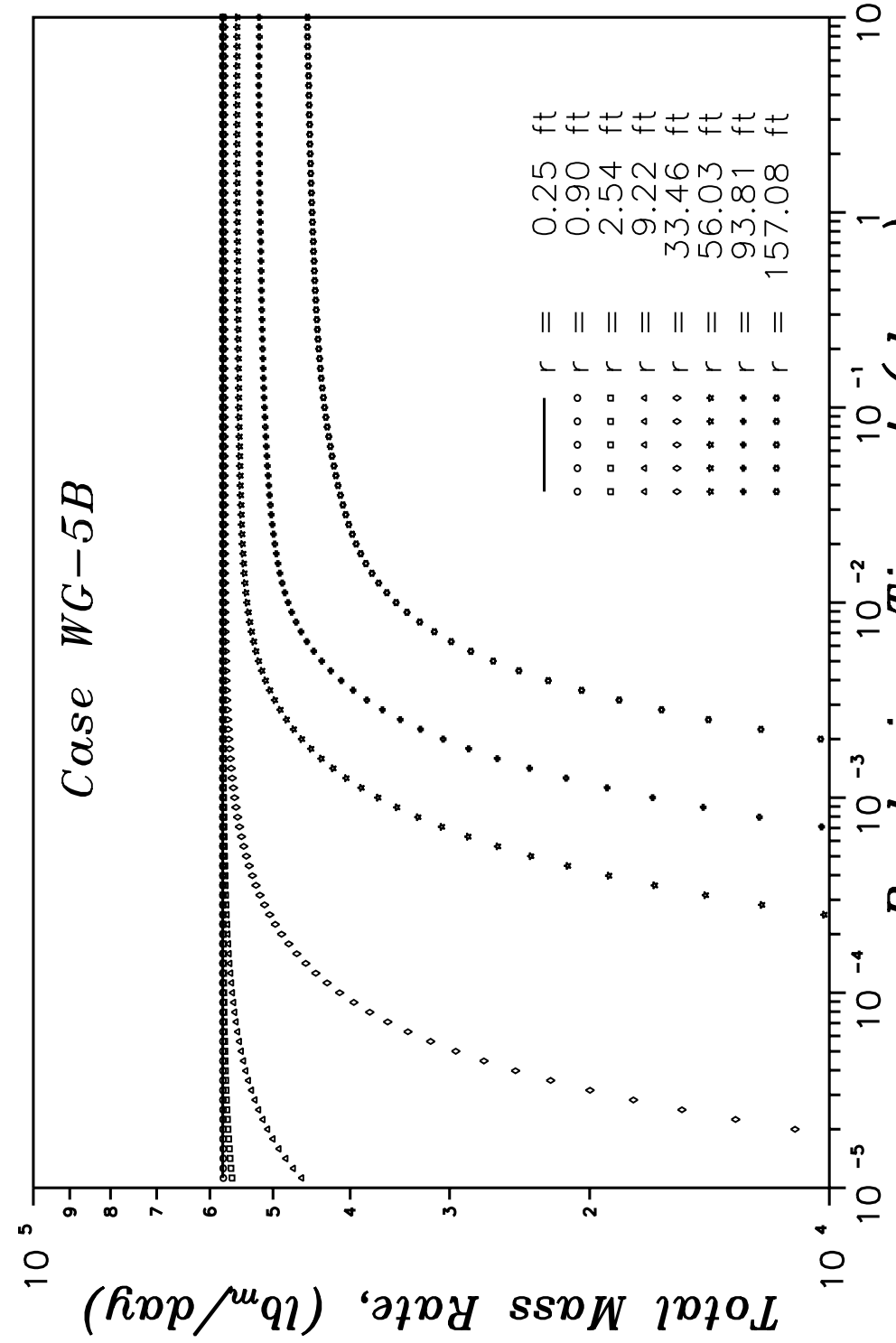

Fig. 6.24 — Total mass flow rate comparison plot (Case WG-5B).

zone (constant mass rate) exists only out to a radius of approximately 30 feet. Figure 6.25 also shows that the total in-situ volumetric flow rate is approximately constant (to within 2 percent) out to a radius of approximately 500 feet. If we define the "steady-state" region based on the mass rates, then we clearly do not satisfy the properties of the single-phase solutions (constant rate out to at least the beginning of the pseudoradial flow region). If we define the "steady-state" region based on the in-situ total volumetric rates, then both assumptions required at least for single-phase problems are being satisfied. Because of the difference in our calculated thickness-averaged mobility from the initial thickness-averaged total mobility, we can, therefore, state that if the total volumetric flow rate is the proper rate to use to define a "steady-state" zone, then the two required properties of a "steady-state" zone and pseudoradial flow beyond the "steady-state" zone are clearly not sufficient conditions for semilog analysis to provide estimates of the initial thickness-averaged total mobilities.

6.4 Two-Phase Oil-Gas Systems

In this section we examine a series of oil reservoirs overlain by a gas cap and produced at a constant oil rate from a restricted-entry well. A vertical cross-section of the reservoir with the upper boundary and initial fluid saturations indicated for each of the reservoir systems examined are shown in Fig. 4.3 of Chapter IV. Other pertinent fluid and physical property data are included in Tables 4.3A and 4.3B for the "base case" (Case OG-2B), along with the deviations from the base case parameters for each of the other oil-gas systems considered. Gas caps of 0, 10, 20 and 30 feet are considered. A 10-*day* drawdown at a constant surface oil production rate of 200 (STB/D) followed by a 10-*day* buildup are simulated for each of the cases. Only the drawdown data are examined in this section; the buildup data are examined in Chapter VII.

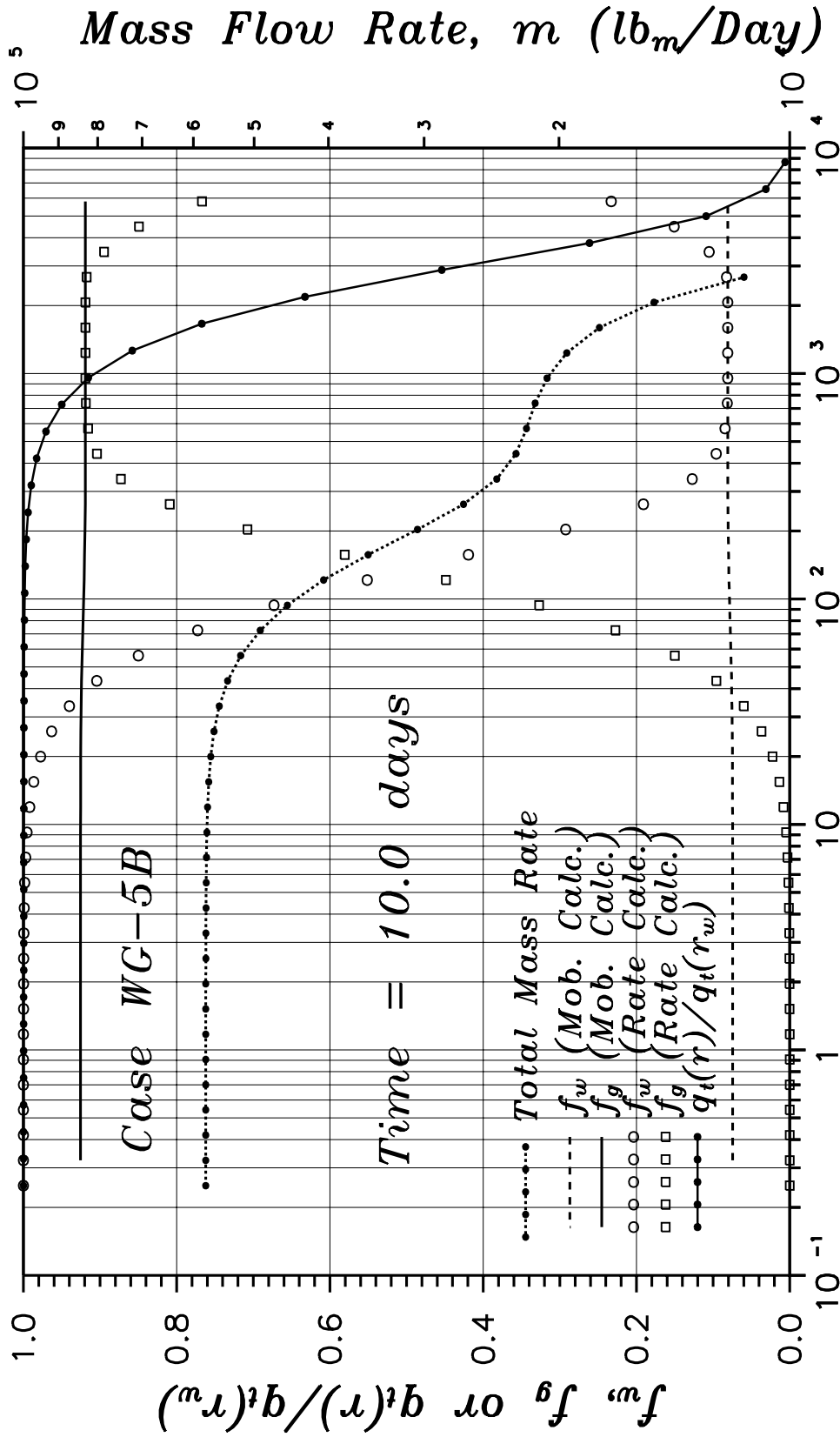

Fig. 6.25 – Comparison of fractional flow rates as an indicator of vertical equilibrium (pseudoradial flow).

As briefly discussed in Chapter IV, the analysis of pressure transient data obtained from a restricted-entry well becomes more complicated when solution-gas is present. Ignoring the possible effects of gravity and capillary pressure, and considering only fully-penetrating wells, Refs. 31 and 32 independently showed that the mobilities calculated from drawdown pressure transient data and rate data represent the mobilities at the sandface. Actually, they showed that effective phase permeabilities at the sandface could be obtained from

$$kk_{ro} = \frac{70.6 q_o B_o \mu_o}{hd\Delta p/d\ln t} \tag{6.4.1}$$

and

$$kk_{rg} = \frac{70.6 q_{gf} B_g \mu_g}{hd\Delta p/d\ln t} \tag{6.4.2}$$

where q_{gf} is the free gas production rate at the sandface and the PVT properties are evaluated at the wellbore pressure. Obviously, if viscosity as a function of pressure is known, then Eqs. 6.4.1 and 6.4.2 can be rearranged to obtain

$$\bar{\lambda}_o|_{r_w} = \frac{70.6 q_o B_o}{hd\Delta p/d\ln t} \tag{6.4.3}$$

and

$$\bar{\lambda}_g|_{r_w} = \frac{70.6 q_{gf} B_g}{hd\Delta p/d\ln t}\ . \tag{6.4.4}$$

References 31 and 32 both assumed the Boltzmann transform to be valid for their one-dimensional reservoirs, thus allowing saturation to be considered a unique function of pressure. Under these conditions, it is easily shown that Eqs. 6.4.1-6.4.4 fall out directly from the appropriate inner boundary condition for those systems; e.g., for a constant surface oil rate, from,

$$q_o = 2\pi(1.127\times 10^{-3}) h \frac{kk_{ro}}{B_o\mu_o} r \frac{\partial p}{\partial r}|_{r_w}\ . \tag{6.4.5}$$

We note here that the validity of Eqs. 6.4.1 through 6.4.4 are entirely dependent upon the validity of the assumptions incorporated into their development, i.e., all variables correlate uniquely with the Boltzmann transform, thereby providing a basis for saturation to be considered a unique function of pressure.

Reference 128 (129) points out, however, that saturation is not in general a unique function of pressure. For the two-dimensional reservoir systems considered in this work (in which gravity effects are also considered), one need only consider the initial reservoir conditions to show that saturation is not a unique function of pressure; e.g., for all $z \leq z_{goc}$,

$$S_o = 1 - S_{wc} \ , \tag{6.4.6}$$

and

$$p(r, z, t = 0) = p(r, z = 0, t = 0) - \int_0^z \gamma_o dz \ . \tag{6.4.7}$$

At first glance, one is tempted to consider saturation to be a unique function of the oil phase potential, since the initial condition requires the potentials to be equal throughout the reservoir. Any attempt to show this, however, is destined to fail due to the fact that the fluids at depth are more undersaturated than the fluids near the top of the reservoir (near the gas-oil contact). In other words, a 10 psi decrease in the pressure (potential) may be required to drop below the bubble point at the bottom of the reservoir, whereas only a fraction of a psi pressure drop may be required near the top of the reservoir. This lack of a unique relationship between saturation and pressure, then, precludes the use of a multiphase pseudopressure akin to those defined by Refs. 31-38 to analyze our results, and we therefore limit our discussion and analysis to the use of standard semilog analysis techniques in terms of pressure.

Figure 6.26 shows the logarithmic derivative of the wellbore pressure with-respect-to producing time for several of the reservoir systems investigated. Figure 6.26 shows the classic pressure derivative response for production from a restricted-entry well, i.e., a fairly constant early-time derivative, a rapid decline in the derivative, followed by a second flattening of the derivative at late time. Notice that the derivative for case OG-2B (fully-penetrating well) shows a continuous increase, whereas the late-time derivatives for the restricted-entry cases show an increase followed by a decrease. Though we have been unable to conclusively isolate the root cause for this behavior, we very briefly discuss this apparent disparity later in this section.

In the previous sections on other multiphase reservoir systems we have shown that the best estimates of the mobilities calculated from the drawdown pressure and rate data do not directly correspond to the sandface values or total thickness averaged values. It is not clear then what, if anything, the mobilities obtained formally with Eqs. 6.4.3, 6.4.4 and

$$\bar{\lambda}_t = \bar{\lambda}_o + \bar{\lambda}_g \tag{6.4.8}$$

represent. We therefore begin our analysis by examining the fully-penetrating well example (case OG-2B).

Figure 6.27 shows the total mobility at the sandface as output by our simulator along with the total mobilities calculated using Eqs. 6.4.3, 6.4.4 and 6.4.8 for both cases OG-2B and OG-2C; case OG-2C is identical to case OG-2B except for gravity effects were ignored in the simulation. Figure 6.27 shows that, though delayed in time, the calculated mobility for case OG-2B eventually matches the simulator value for the sandface mobility. It should be noted that at early- to middle-time, there is a significant variation in the sandface gas saturation as a

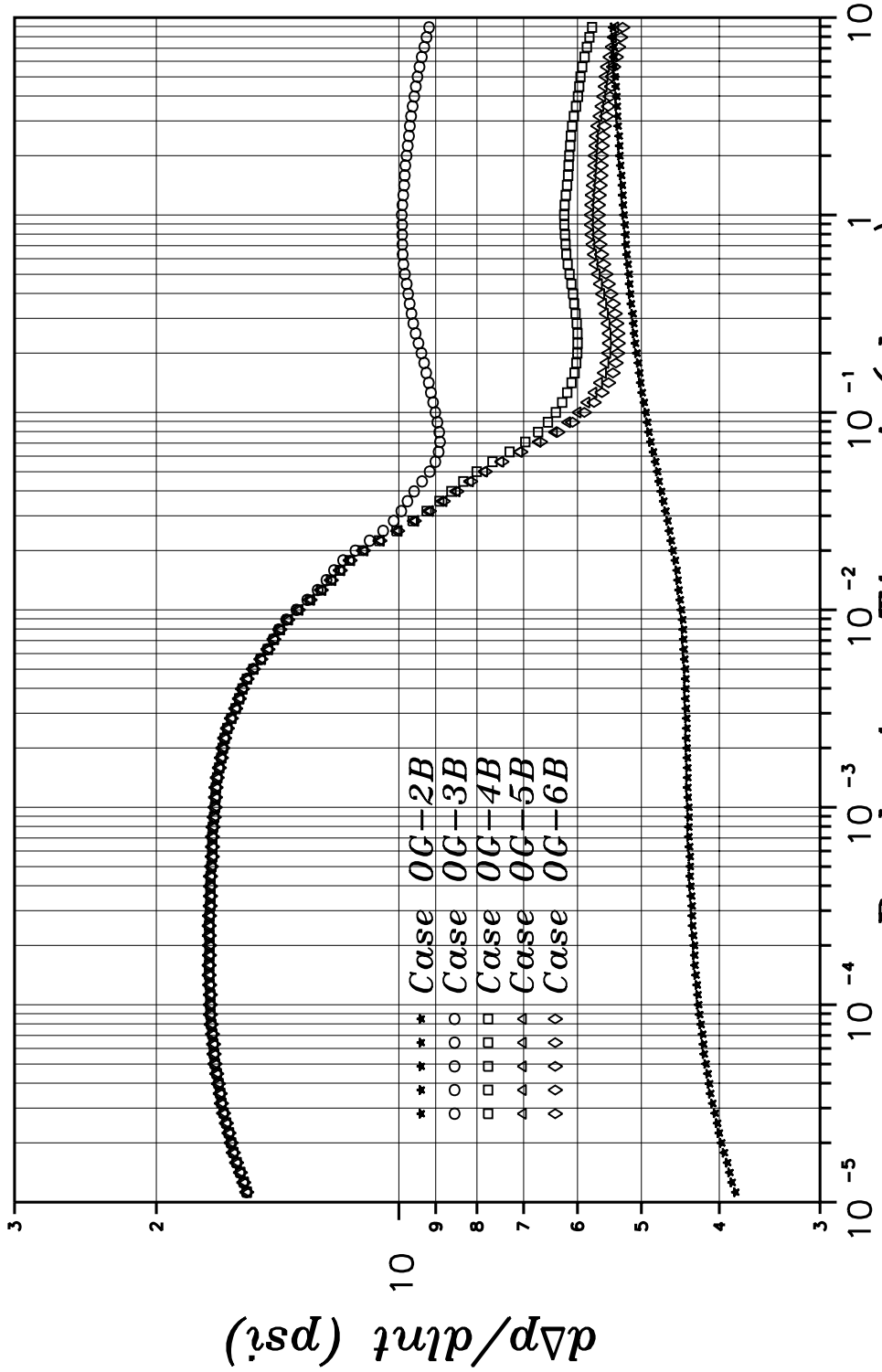

Fig. 6.26 – Diagnostic drawdown pressure derivative plot (Oil–Gas).

function of depth for case OG-2B, but these saturations become approximately equal at the same time the calculated mobilities begin to match the simulator values for the sandface mobility. This early- to middle-time variation in the gas saturation has a variety of effects on calculated mobilities for cases OG-2B. Note from Fig. 6.27 that the thickness-averaged total mobilities at the sandface (as output by our simulator) appear to be nearly identical for both of these cases. For case OG-2B, however, the total mobility drops rapidly near the top of the perforations and decreases more slowly near the bottom of the perforations; i.e., this vertical variation in the total mobilities is masked in the thickness-averaged mobilities.

Recall also from Chapters IV and V we discussed a theoretical expression developed by Ref. 149 for the wellbore pressure derivative in reservoir systems which were either semi-infinite in extent of contained a constant pressure boundary. The theoretical expression of Ref. 149 shows the wellbore pressure derivative to be a function of both how the volumetric rate changes with-respect-to time and how the total relative mobility changes with-respect-to time across the reservoir. Note that no similar analytical expression exists for a closed boundary reservoir system. We do postulate, however, that the functional dependence of the variables will be similar for the closed boundary cases. Since the initial pressure at the top of the reservoir for case OG-2B is the same as the initial pressure for case OG-2C, we would expect the rate of change in the total relative mobility at the top of the reservoir for case OG-2B to be similar to that for case OG-2C. At the bottom of the reservoir for case OG-2B, however, the initial pressure is some 12 psi greater than for case OG-2C, and we expect the rate of change in the total relative mobility will be less. In fact, since the fluids at the bottom of the reservoir for case OG-2B are initially above the bubble-point pressure by 12 psi, the initial rate of change in the total relative mobility will be strictly due to changes in the oil-phase viscosity

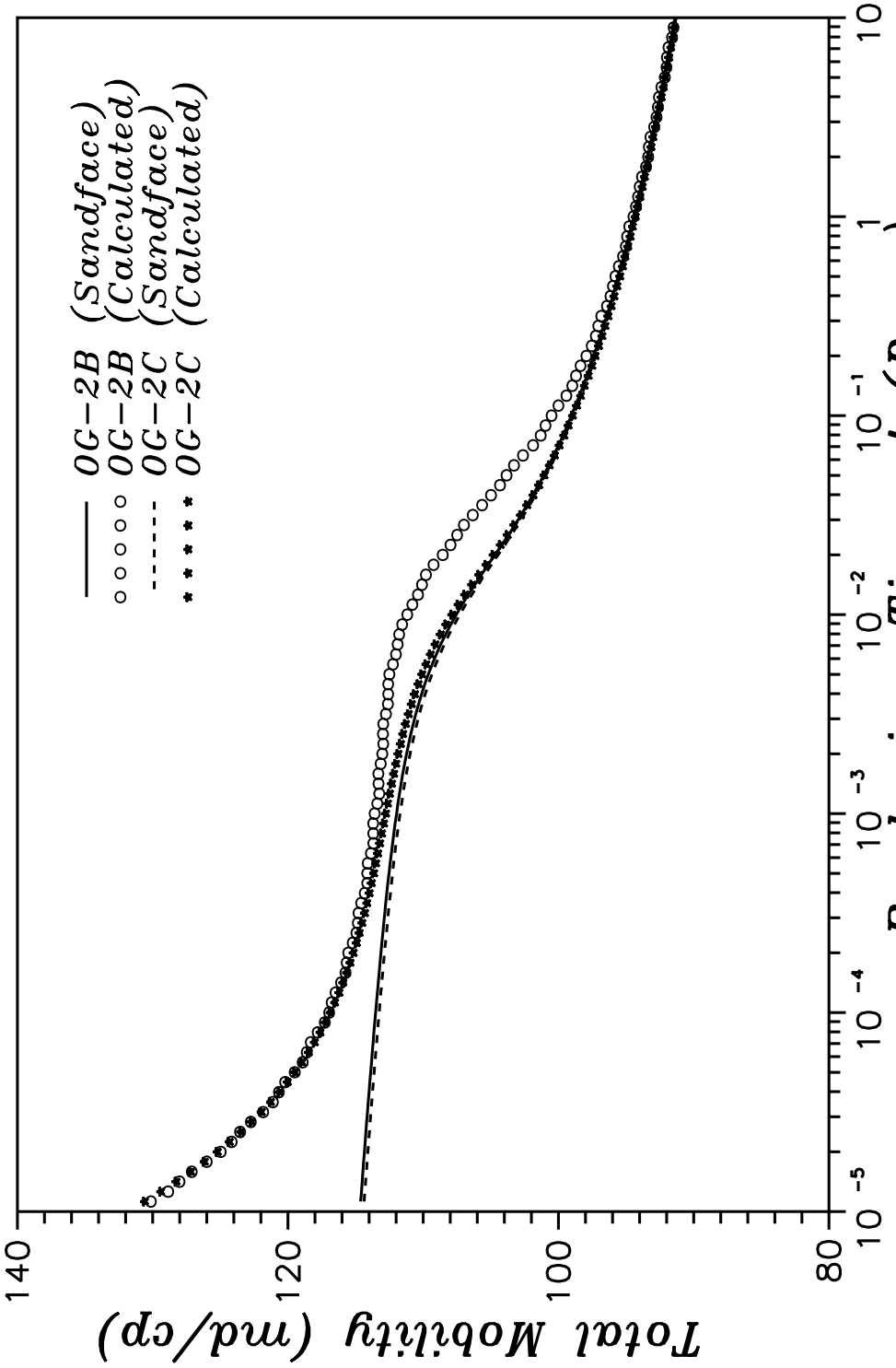

Fig. 6.27 – Comparison of calculated mobilities with sandface mobilities for fully-penetrating well examples.

due to pressure changes. On average, then, the time-rate of change in the total relative mobility across the sandface will be less for case OG-2B than for case OG-2C. By the theoretical expression of Ref. 149, this then would lead to the pressure-derivative being less for case OG-2B than for case OG-2C. By Eqs. 6.4.3, 6.4.4 and 6.4.8, we, therefore, expect the calculated total mobility to be greater for case OG-2B than for case OG-2C, which is precisely what is shown in Fig. 6.27.

At late time, the saturation becomes approximately equal across the sandface for case OG-2B and the time-rate of change in the total relative mobility also becomes approximately equal. While it is difficult, if not impossible, to prove due to the non-linear nature of this problem, it would appear that if the saturation at the sandface is changing with time, then it must be independent of the vertical direction (at the sandface) in order for Eqs. 6.5.3 and 6.5.4 to be applicable for reservoir systems in which gravity affects are not negligible.

For all of the oil-gas cases considered in this section, mobilities calculated using Eqs. 6.4.3 and 6.4.4, $\bar{\lambda}_t$, are shown in Table 6.5 along with the initial thickness-averaged total mobilities, $\bar{\lambda}_t(p_i)$, the total mobilities at the sandface, $\bar{\lambda}_t(p_{wf})$, at the end of the drawdown and the percent deviation of the calculated mobilities from the sandface values output from our simulator. While Table 6.5 clearly shows that the calculated mobilities do not even remotely appear to resemble the thickness-averaged total mobilities, the comparison with the simulator sandface values is far from good, with the difference between the calculated values and the sandface values varying by as much as 54 percent for one of the skin cases (OG-6BS4).

In the previous sections, we have shown that the deviation between the calculated mobilities and the simulator values correlated extremely well with the thickness of the aquifer or gas cap. For those cases, however, it was clear that our

Table 6.5

Drawdown Semilog Analysis Results: Oil-Gas Systems

Case	Simulator $\bar{\lambda}_t(p_i)$ (md/cp)	Simulator $\bar{\lambda}_{t1}(p_{wf})$ (md/cp)	Calculated $\bar{\lambda}_t$ (md/cp)	Percent Deviation
OG-2B	116.01	91.39	91.49	-0.1
OG-2BS3	116.01	84.59	82.54	2.4
OG-2BS4	116.01	80.27	76.42	4.3
OG-3B	116.01	76.83	54.77	28.7
OG-3BS3	116.01	67.64	42.30	37.5
OG-3BS4	116.01	61.78	35.38	42.7
OG-3C	116.01	76.35	53.92	29.4
OG-4B	485.51	77.26	69.90	9.5
OG-4BS3	485.51	67.99	48.15	29.2
OG-4BS4	485.51	62.09	37.97	38.9
OG-5B	731.86	77.31	62.03	19.8
OG-5BS3	731.86	68.03	41.93	38.4
OG-5BS4	731.86	62.13	32.78	47.2
OG-6B	907.86	77.33	54.50	29.5
OG-6BS3	907.86	68.05	36.56	46.3
OG-6BS4	907.86	62.15	28.48	54.2

calculated mobilities represented something approaching the thickness-averaged total mobility. None-the-less, we examine this phenomena for the current cases. In Fig. 6.28, we have plotted the percent deviation between the calculated total mobility (Eqs. 6.4.3, 6.4.4 and 6.4.8) and the sandface values output by our simulator. Values for cases OG-4B, OG-5B and OG-6B are shown for several producing times as a function of the gas cap thickness. Once again, we see there is an excellent correlation.

Next, we examine the flow rates and fraction flow profiles in the reservoir. Figure 6.29 shows the total mass rate and fractional flow profiles at a producing time of 10 days. The mass rate is seen to be constant only out to a radius of approximately 20 feet, where it drops off sharply, levels off slightly at approximately 500 feet and then sharply declines again for $r > 1000$ feet. Clearly, if we use the term "steady-state" to indicate a zone of constant mass rate, then a "steady-state" zone exists only in the region, $r_w \leq r \leq 20$ feet. If, on the other hand, the term "steady-state" is used to indicate a zone of constant reservoir volumetric rate, then Fig. 6.29 indicates that a "steady-state" zone exists (to within 2 percent) out to a radius of approximately 260 feet. In either case, Fig. 6.29 shows that this "steady-state" zone does not extend out to the point in the reservoir where vertical equilibrium exists; i.e., the pressure response at the well will be influenced by vertical flow ahead of the "steady-state" zone and prior to the region of the reservoir under vertical equilibrium.

Based on our previous discussions on the fractional flow rates and their relationship to vertical equilibrium, Fig. 6.29 shows that as we move away from the wellbore in the region $r_w \leq r \leq 10$ feet, we move further away from vertical equilibrium. For $r > 10$ feet, the reservoir goes through a large transition zone in which it approaches closer and closer to vertical equilibrium, until, at approximately $r = 600$ feet, Fig. 6.29 shows vertical equilibrium exists in the reservoir.

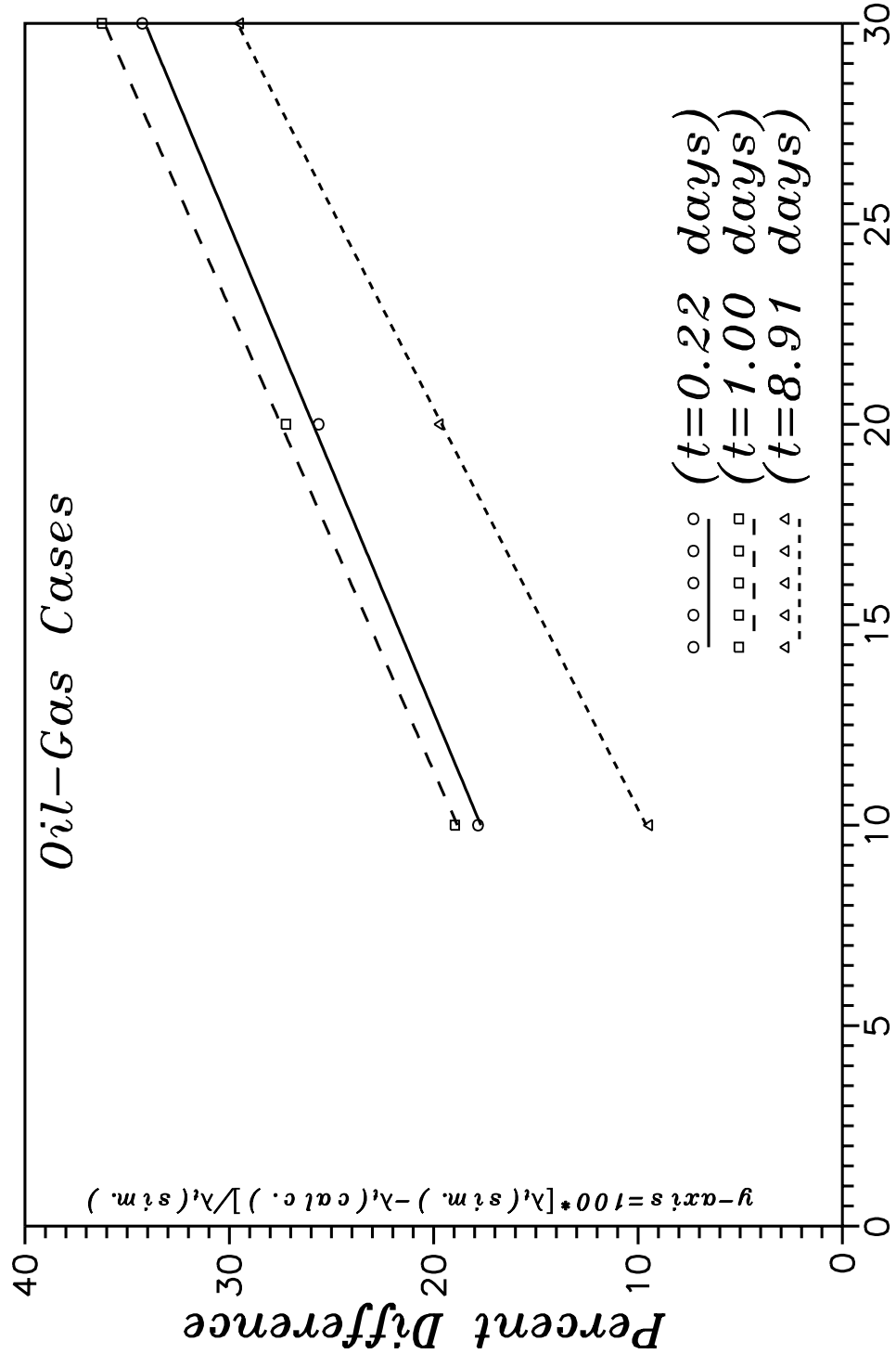

Fig. 6.28 – Correlation between relative difference in calculated and simulator mobilities.

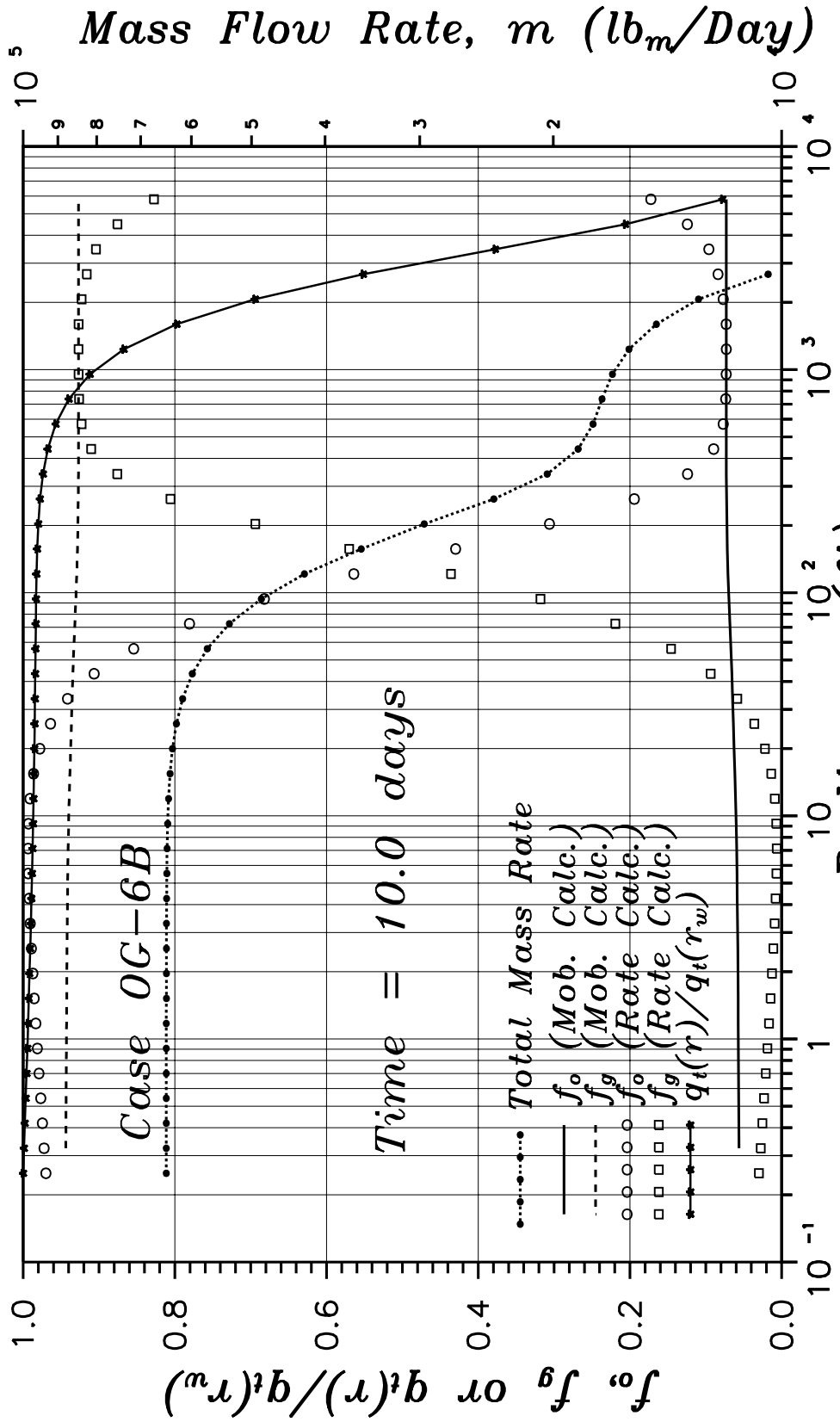

Fig. 6.29 — Comparison of fractional flow rates as an indicator of vertical equilibrium (pseudoradial flow).

As note above, this then indicates that the wellbore pressure response will be influenced by vertical flow in the region of the reservoir, $260 \leq r \leq 600$ feet.

Lastly, we return to the pressure derivatives for these cases (Fig. 6.26) and examine the increasing and decreasing behavior of the derivative. Though nearly every rock and fluid property as a function of time and location were examined in an attempt to explain this behavior, no conclusive, all encompassing observations were obtained. We limit our discussion here to case OG-3B, though the discussion is equally applicable for all of the cases discussed in this section.

Before reporting on actual results, we note that the initial increase in the pressure derivative at late time ($0.1 \leq t \leq 1.0$ days) cannot be attributed to the movement of a saturation front at the fluid contact since case OG-3B exhibits this same behavior, yet has no gas cap (fluid contact) across which the front would initially develop

In examining the pressure derivatives for cases OG-3B through OG-6B, we note that the pressure derivative reaches a peak at a producing time of 1.0 day for all four cases. If a rock or fluid property (or combination thereof) were solely responsible for the observed pressure response, we should expect that such a property would exhibit a similar or inverse response, showing a maximum or minimum at $t = 1.0$ days. In examining the physical properties and in-situ flow rates, it was found that no properties immediately adjacent to the open interval exhibited such behavior. When we examined the first vertical grid block above the perforated interval, however, both the in-situ flowing gas-oil ratio and total relative mobility exhibited some sort of local minimum or maximum at this time.

The in-situ flowing gas-oil ratio at this location is plotted in Fig. 6.30 as a function of producing time. Whereas the late-time pressure derivatives exhibited a maximum at $t = 1.0$ days, the vertical flowing gas-oil ratio shows a minimum

occurring at approximately 0.5 days. It would appear extremely unlikely, however, that a 0.3 percent increase in the flowing gas-oil ratio (from 1.0 to 10.0 days) could account for an approximately 10 percent decrease in the pressure derivative.

The second property which exhibited a sharp change in the neighborhood of 1.0 day producing time is the total mobility in the region just above the perforated interval. Figure 6.31 shows the total relative mobility at this location and also at the sandface. Here we note that in the time frame $0.1 \leq t \leq 1.0$ days, the total relative mobility just above the open interval is decreasing at a much faster rate than the total relative mobility across the open interval. Near a producing time of 1.0 days, the total mobility above the perforated interval begins to decrease at a much higher rate than at the sandface and thereafter decreases at a just slightly faster rate than the sandface mobility. One could argue that if the total mobility at the sandface controls the pressure response due to radial flow in solution gas systems, then the total mobility at heights just above the perforated interval (bottom perforated reservoir) should control the pressure response due to vertical flow in the reservoir, at least in the near-well region. There is some justification for this argument based on previous works[16–19] on single-phase flow in multilayered reservoirs. In those works, it was found that the pressure response was most dependent on the value of the permeability in the perforated layer and the layer immediately adjacent to the perforated layer.

In addition to the single-phase multilayer argument discussed above, one may also make some heuristic arguments based on the work of Ref. 149 and the results of Chapter V of this work. Recall from Chapter V that we showed via the vertical form of the theoretical expression of Ref. 149 that $\partial \Delta p / \partial \ln t$ for a restricted-entry well in a multiphase, solution-gas reservoir system with a constant pressure upper boundary was highly dependent upon the time-rate of change in the total relative mobility ($\partial \lambda_{rt} / \partial \ln t$) in the neighborhood of the well. Recall also

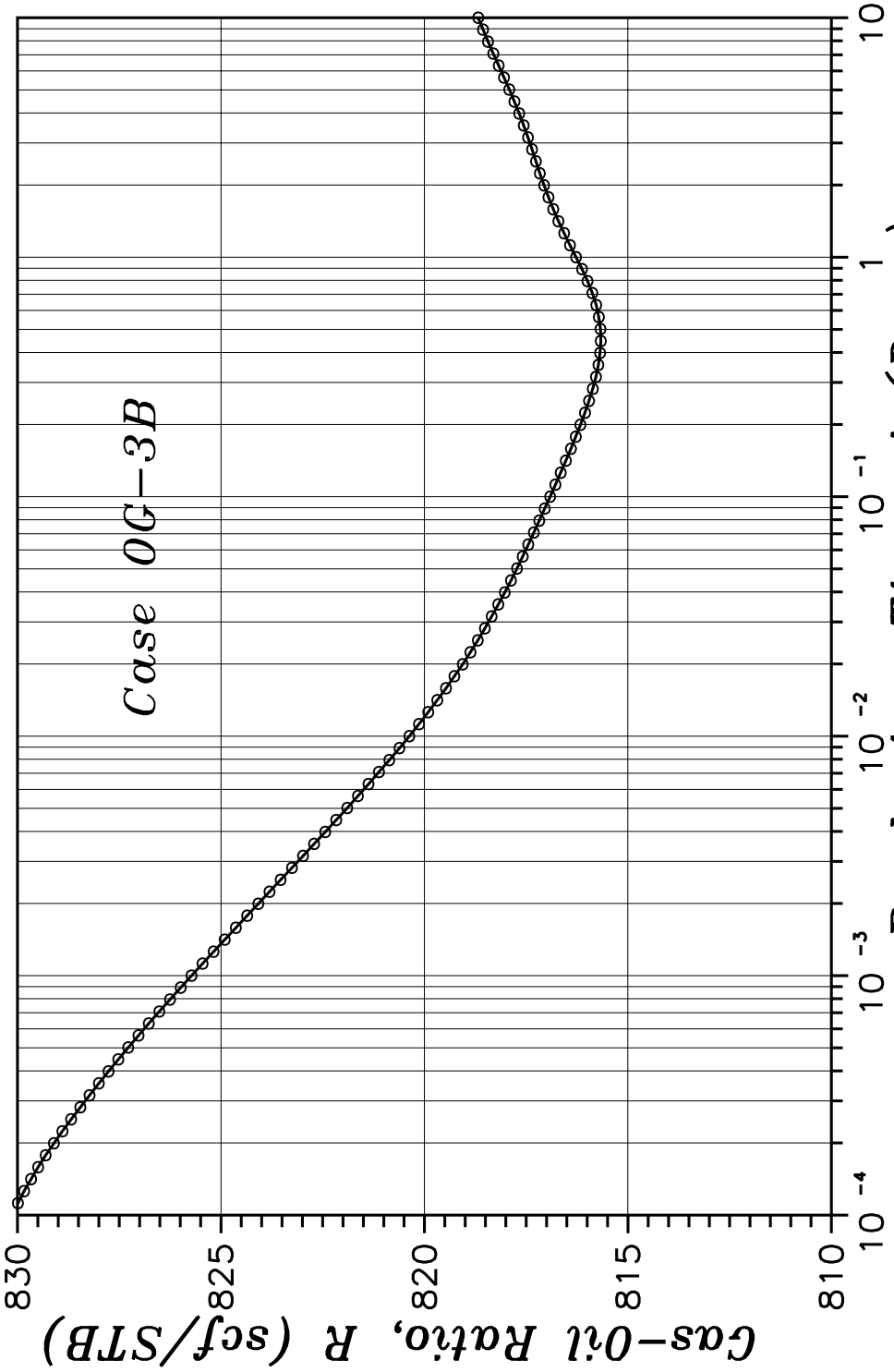

Fig. 6.30 — Flowing gas—oil ratio above perforated interval.

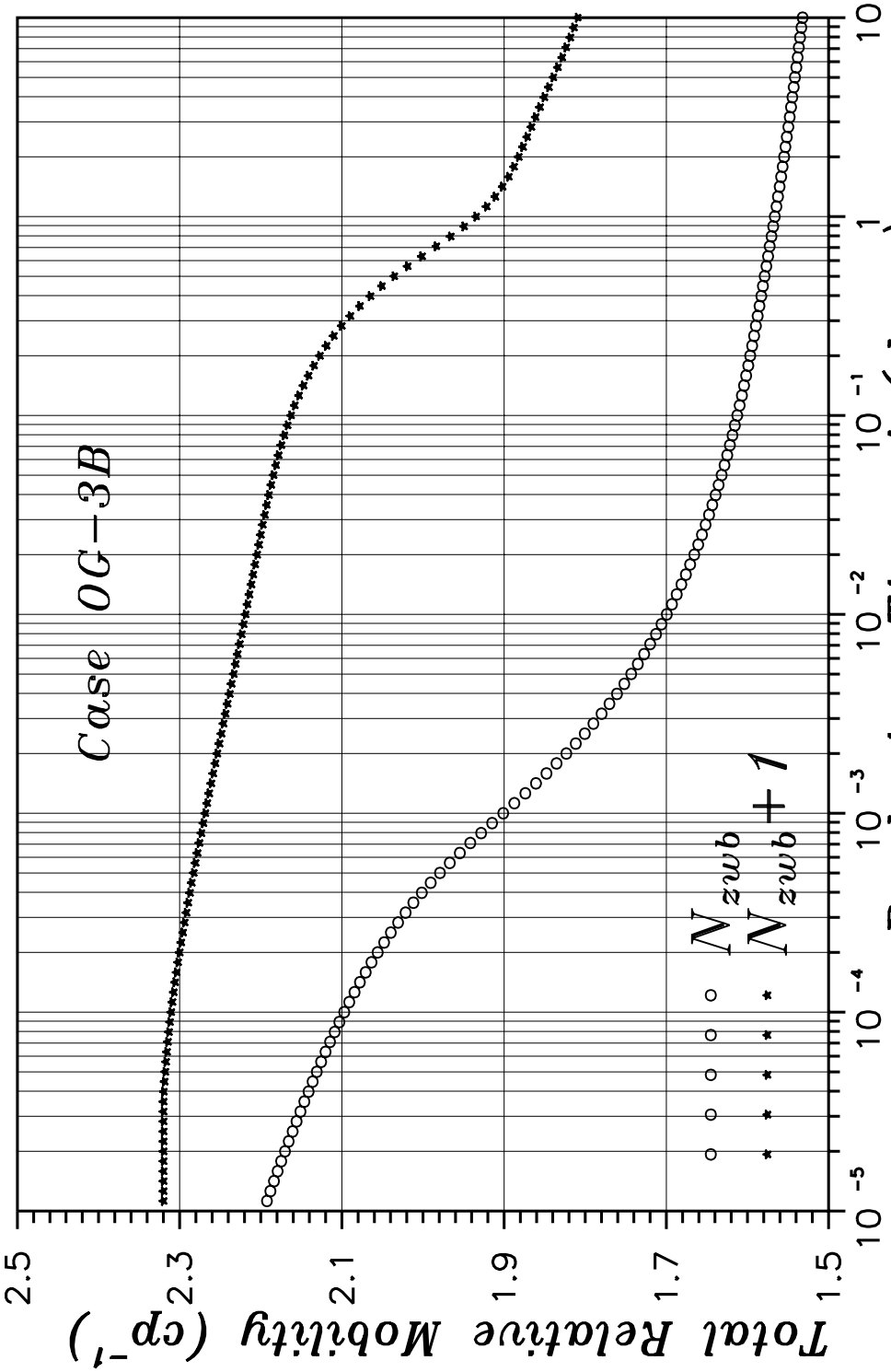

Fig. 6.31 — Total relative mobility at sandface and just above the open interval.

that the reason for this strong dependence was due to the convergent nature of the flow near the well and the fact that in the theoretical expression of Ref. 149, $\partial\lambda_{rt}/\partial \ln t$ is multiplied by the vertical velocity over that part of the reservoir. Recall again that no similar analytical expression exists for a closed boundary reservoir system. None-the-less, if we postulate that the functional dependence of $\partial\Delta p/\partial \ln t$ on the rock and fluid parameters will be similar in nature for the current reservoir systems as for the constant pressure upper boundary, solution-gas systems investigated in Chapter V, then one would expect the time-derivative of the total relative mobility to exhibit an increasing (in absolute magnitude), followed by a decreasing, signature. This is precisely the response indicated in Fig. 6.31 and more clearly expressed in Fig. 6.32, where the logarithmic derivative with-respect-to producing time of the total relative mobility, both at the perforated interval and just above the perforated interval, are plotted as a function of producing time for case OG-3B.

As mentioned previously, almost every fluid and rock property were examined as a function of time and location in an attempt to fully explain the pressure derivative behavior observed for the cases presented in this section. Though the arguments presented above are clearly not as theoretically rigorous as we would like, they are supported by the numerical results already presented (above and in Chapter V), and in a loose sense, the observations of Refs. 16-19 in their use of only the vertical permeabilities in layers near the perforated interval.

6.5 Three-Phase Oil-Gas-Water Systems

In this section we examine pressure transient data for a series of oil reservoirs overlain by a gas cap, underlain by an aquifer (water zone) and produced at a constant oil rate from a restricted-entry well. A vertical cross-section of the reservoir with the upper boundary and initial fluid saturations indicated for each

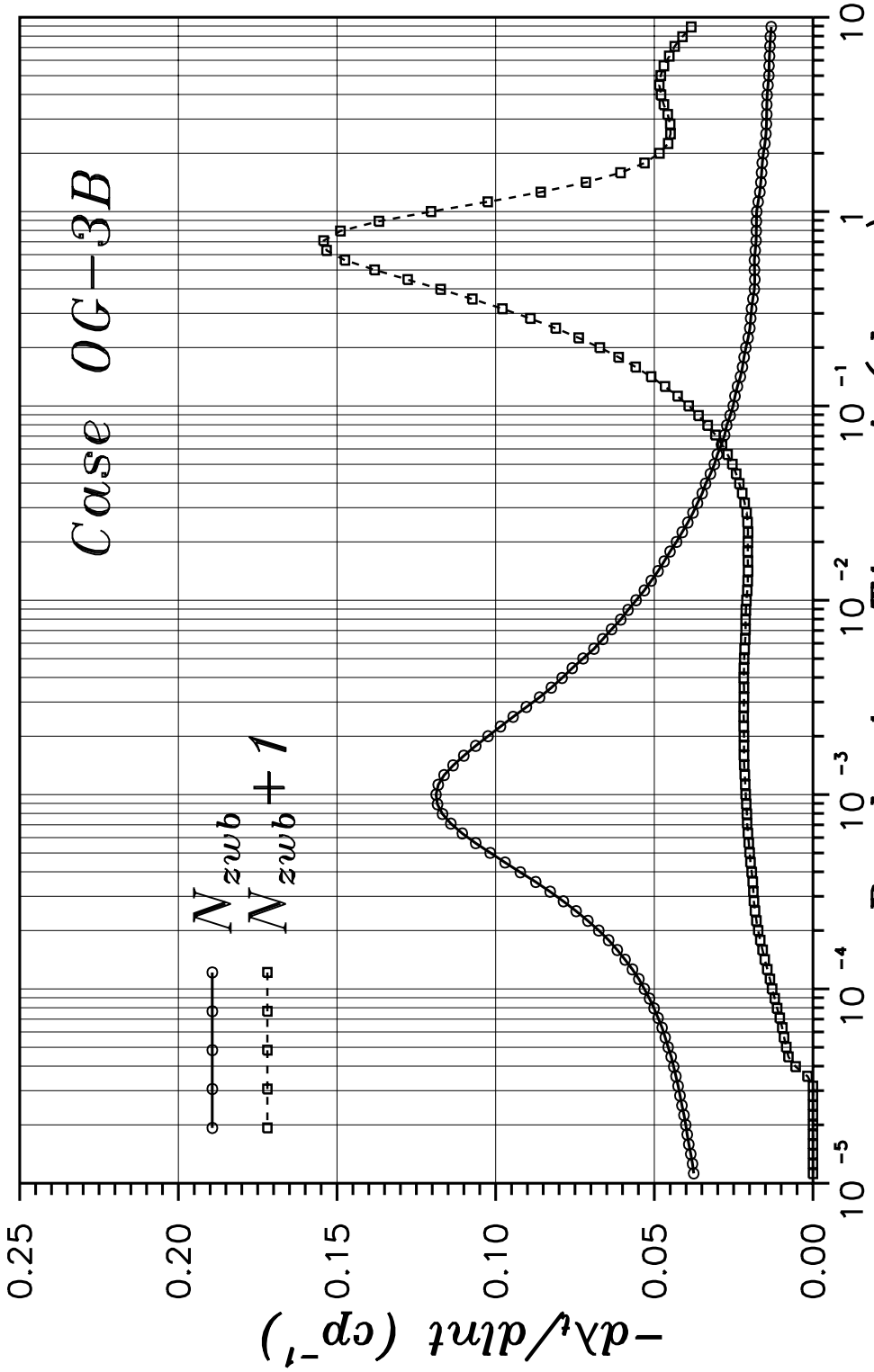

Fig. 6.32 — Derivative of relative mobility at sandface and just above the open interval.

of the reservoir systems examined are shown in Fig. 4.5 of Chapter IV. Other pertinent fluid and physical property data are included in Tables 4.5A and 4.5B for the "base case" (Case OGW), along with the deviations from the base case parameters for each of the other three-phase systems considered. All of the cases considered here assume a 70 ft thick oil zone perforated only in the center 10 ft. Gas caps of 0, 10, 20 and 30 feet are considered in conjunction with aquifers of 0, 10, 20 and 50 feet. A 10-day drawdown at a constant surface oil production rate of 200 (STB/D) followed by a 10-day buildup are simulated for each of the cases. Here, we only examine the drawdown data; the buildup data are examined in *Chapter VII.*

Based on the results of the previous sections and consistent with the analysis methods provided for the two-phase systems, we consider the use of the following equation for the analysis of drawdown pressure and rate data for three-phase reservoir systems:

$$\bar{\lambda}_t = \frac{70.6(q_o B_o + q_w B_w + q_{gf} B_g)}{hd\Delta p/d\ln t} \ , \tag{6.5.1}$$

where the PVT properties are assumed to be evaluated at the prevailing wellbore pressure and q_{gf} if the free gas production rate at the sandface; i.e.,

$$q_{gf} = q_o[R(t) - R_s(p_{wf})] \ . \tag{6.5.2}$$

Diagnostic log-log pressure derivative plots for the drawdown are shown in Figures 6.33 and 6.34. Figure 6.33 shows the derivative obtained for the base case (OGW) and three cases in which the reservoir has a 30 ft thick gas cap and various sized aquifers; i.e., 10 ft (case OGWAC), 20 ft (case OGWBC) and 50 ft (case OGWCC) aquifers. Figure 6.34, on the other hand, shows the pressure derivative for the base case (case OGW) and three cases in which the reservoir has

a 50 ft aquifer and various sized gas caps; i.e., 10 ft (case OGWCA), 20 ft (case OGWCB) and 30 ft (case OGWCC) gas caps.

There are several items worth noting on these derivative plots. Similar to the two-phase solution-gas systems investigated in the previous section, the late-time derivative response for these systems exhibit an increasing and decreasing behavior. As with the solution-gas reservoir systems considered in the previous section, one could argue that if the total mobility at the sandface controls the pressure response due to radial flow in solution gas systems, then the total mobility at heights just above and below the perforated interval should control the pressure response due to vertical flow in the reservoir, at least in the near-well region. Once again, there is some justification for this argument based on previous works[16–19] on single-phase flow in multilayered reservoirs. For multilayered reservoirs in which the perforated interval was in a central layer (away from the upper or lower boundaries), those references found that the pressure response was most dependent on the permeability values of the perforated layer and the layers immediately adjacent to the perforated layer. Heuristic arguments based on the work of Ref. 149 and the results reported in Chapter V, can also be used to justify this argument. Since, however, this argument is the same as that presented in the previous section, it is not repeated here.

Though a prolonged semilog straight line (constant derivative) is not apparent in Figs. 6.33 and 6.34, we proceed with our calculation of a total mobility from our conjectured equation (Eq. 6.5.1). In addition to the mobilities calculated formally with Eq. 6.5.1 (at $t = 8.91$ days), Table 6.6 also lists the initial total thickness averaged total mobilities, the sandface mobilities near the end of the drawdown (8.91 days) and the percent deviation between the calculated mobilities and the sandface values. As can be seen, the mobilities calculated using Eq. 6.5.1

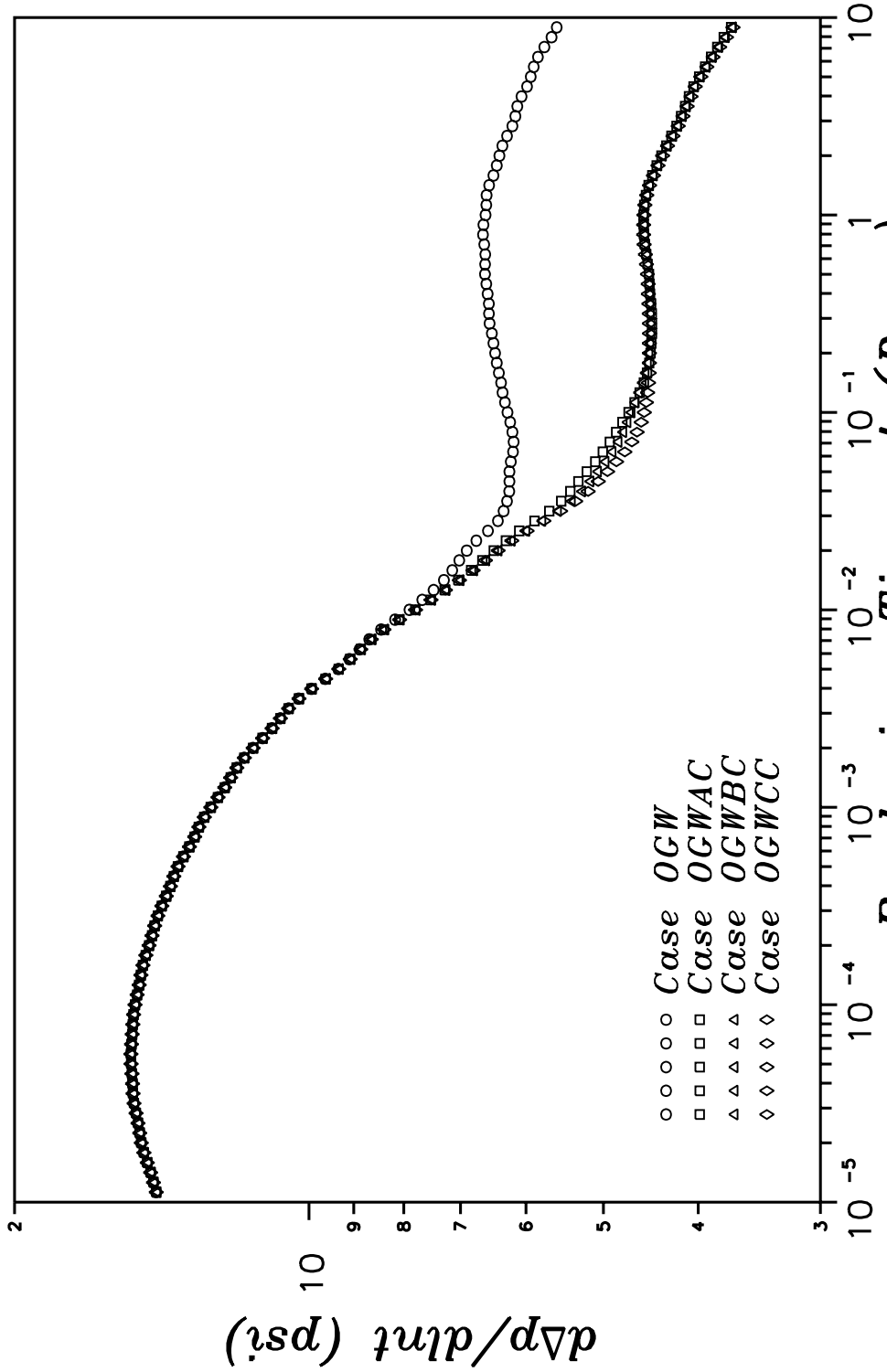

Fig. 6.33 – Diagnostic drawdown pressure derivative plot for three–phase oil–gas–water cases.

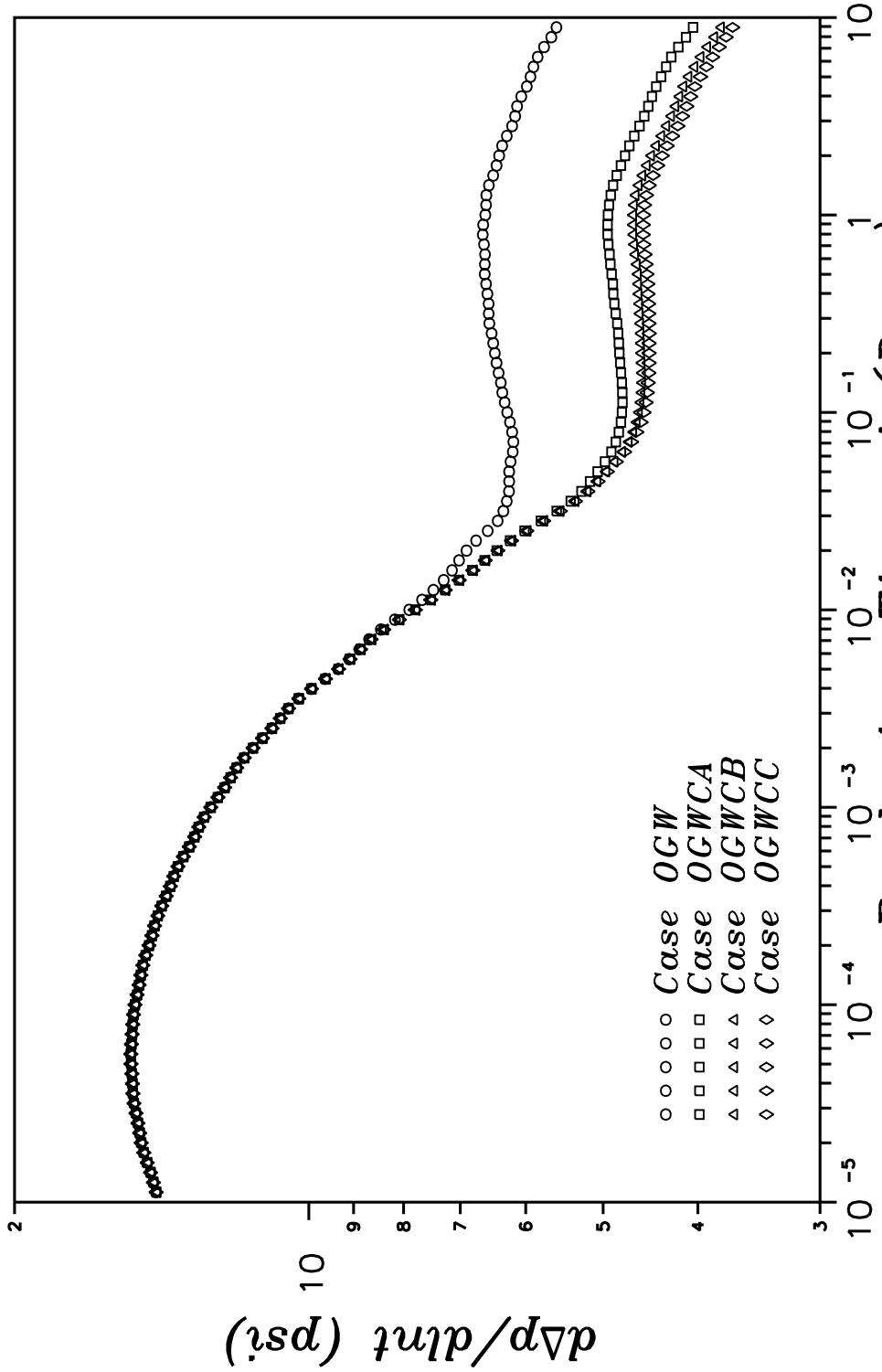

Fig. 6.34 – Diagnostic drawdown pressure derivative plot for three–phase oil–gas–water cases.

are significantly lower than either the initial thickness-averaged total mobilities or the sandface total mobilities.

In keeping with our analysis in the previous sections, we again examine the relationship between the deviation in the mobilities and the aquifer and gas cap thicknesses to see if there is a correlation. Figures 6.35 and 6.36 show the percent difference between the calculated mobility and sandface mobility for each of the zero-skin aquifer cases and gas cap cases; i.e., all zero-skin cases except case OGW at a producing time of 8.91 days. Figure 6.35 shows the percent difference between the calculated mobility and sandface mobility plotted as a function of the aquifer thickness. Figure 6.36 shows the percent difference between the calculated mobility and sandface mobility plotted as a function of the gas cap thickness.

The first observation concerning the data exhibited in Figs. 6.35 and 6.36 is the excellent correlation between the relative difference in the mobilities and the thickness of the aquifer or thickness of the gas cap. Figures 6.35 and 6.36 appear to exhibit six correlations, one for each size of aquifer and one for each size of gas cap; i.e., for each size aquifer (Fig. 6.36), the difference in mobilities shows an excellent correlation with an increase in the gas cap size and for each size gas cap (Fig. 6.35), the differences in mobilities show an excellent correlation with an increase in the aquifer size. The reason for obtaining different correlations for for different sized aquifers (or alternatively, different sized gas caps) is due to the difference in the water mobility (in the aquifer) and the gas mobility (in the gas cap); e.g., an increase in the aquifer size results in a decrease in the thickness-averaged total mobility, $\bar{\lambda}_t$, whereas an increase in the gas cap size results in an increase in the total $\bar{\lambda}_t$. Note that even though increasing the size of the aquifer or the size of the gas cap results in opposite effects on the thickness-averaged total mobility, both result in an increased deviation between the calculated mobility (Eq. 6.5.1) and the sandface total mobility. In previous sections, we have noted that an increase

Table 6.6

Drawdown Semilog Analysis Results: Oil-Gas-Water Systems

Case	Simulator $\bar{\lambda}_t(p_i)$ (md/cp)	Simulator $\bar{\lambda}_{t1}(p_{wf})$ (md/cp)	Calculated $\bar{\lambda}_t$ (md/cp)	Percent Deviation
OGW	123.17	85.45	54.14	36.64
OGWS3	123.17	75.62	38.18	49.51
OGWS4	123.17	69.35	31.37	54.77
OGWAA	275.83	85.67	54.14	36.80
OGWAAS3	275.83	75.80	37.17	50.96
OGWAAS4	275.83	69.52	29.35	57.79
OGWAB	404.06	85.70	52.34	38.93
OGWABS3	404.06	75.83	35.16	53.63
OGWABS4	404.06	69.54	27.49	60.46
OGWAC	508.99	85.72	49.33	42.45
OGWACS3	508.99	75.84	32.77	56.79
OGWACS4	508.99	69.56	25.50	63.35
OGWBA	254.46	85.67	48.94	42.88
OGWBAS3	254.46	75.80	33.55	55.74
OGWBAS4	254.46	69.52	26.47	61.92
OGWBB	372.98	85.71	47.71	44.33
OGWBBS3	372.98	75.83	32.03	57.77
OGWBBS4	372.98	69.54	25.03	64.01
OGWBC	471.76	85.72	45.26	47.20
OGWBCS3	471.76	75.85	30.06	60.37
OGWBCS4	471.76	69.56	23.38	66.39
OGWCA	210.09	85.68	38.19	55.43
OGWCAS3	210.09	75.81	26.07	65.61
OGWCAS4	210.09	69.53	20.53	70.47
OGWCB	306.38	85.71	37.75	55.96
OGWCBS3	306.38	75.84	25.28	66.66
OGWCBS4	306.38	69.56	19.74	71.62
OGWCC	389.85	85.73	36.33	57.62
OGWCCS3	389.85	75.85	24.10	68.23
OGWCCS4	389.85	69.56	18.74	73.06

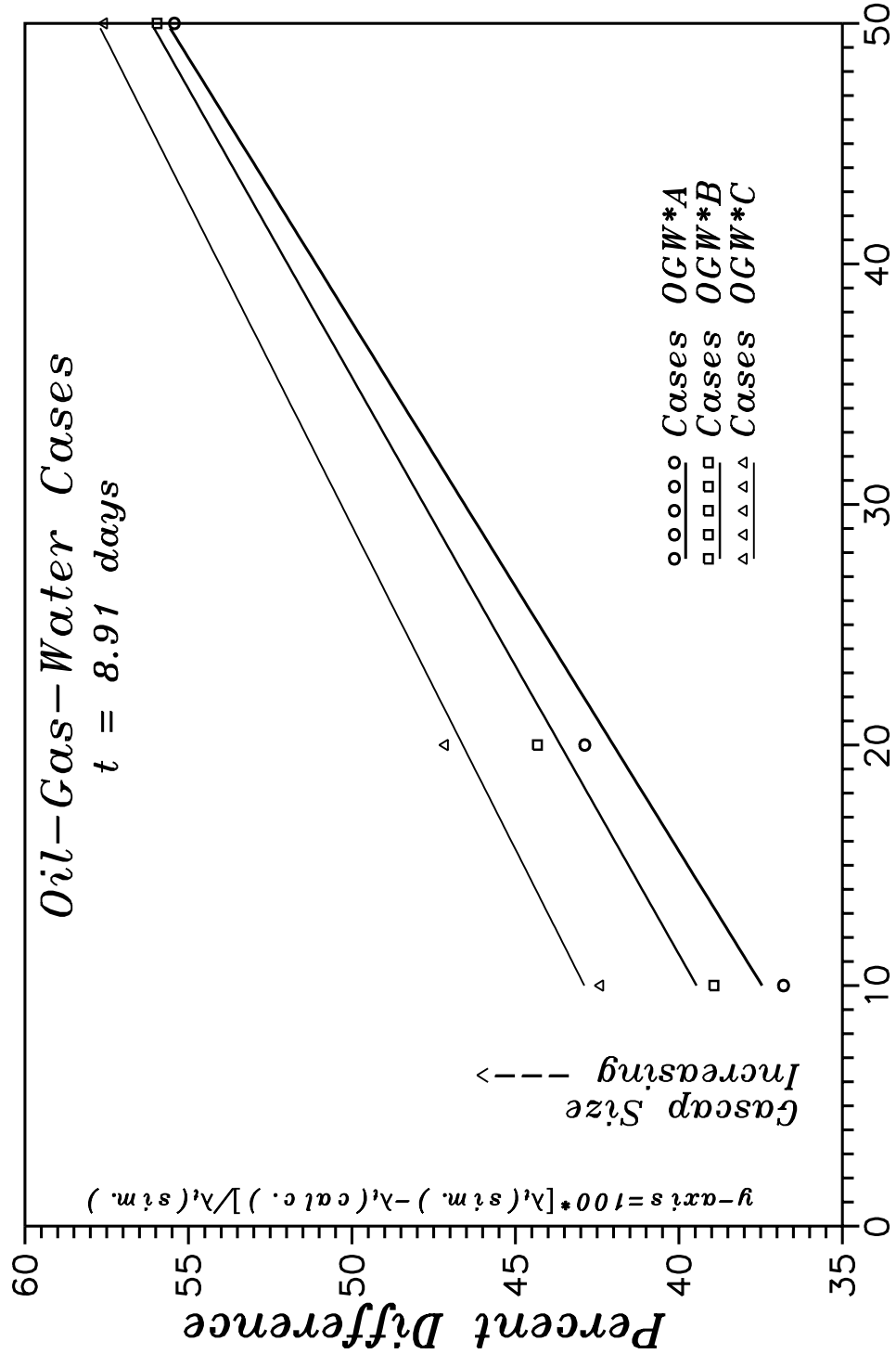

Fig. 6.35 – Correlation between relative difference in calculated and simulator mobilities.

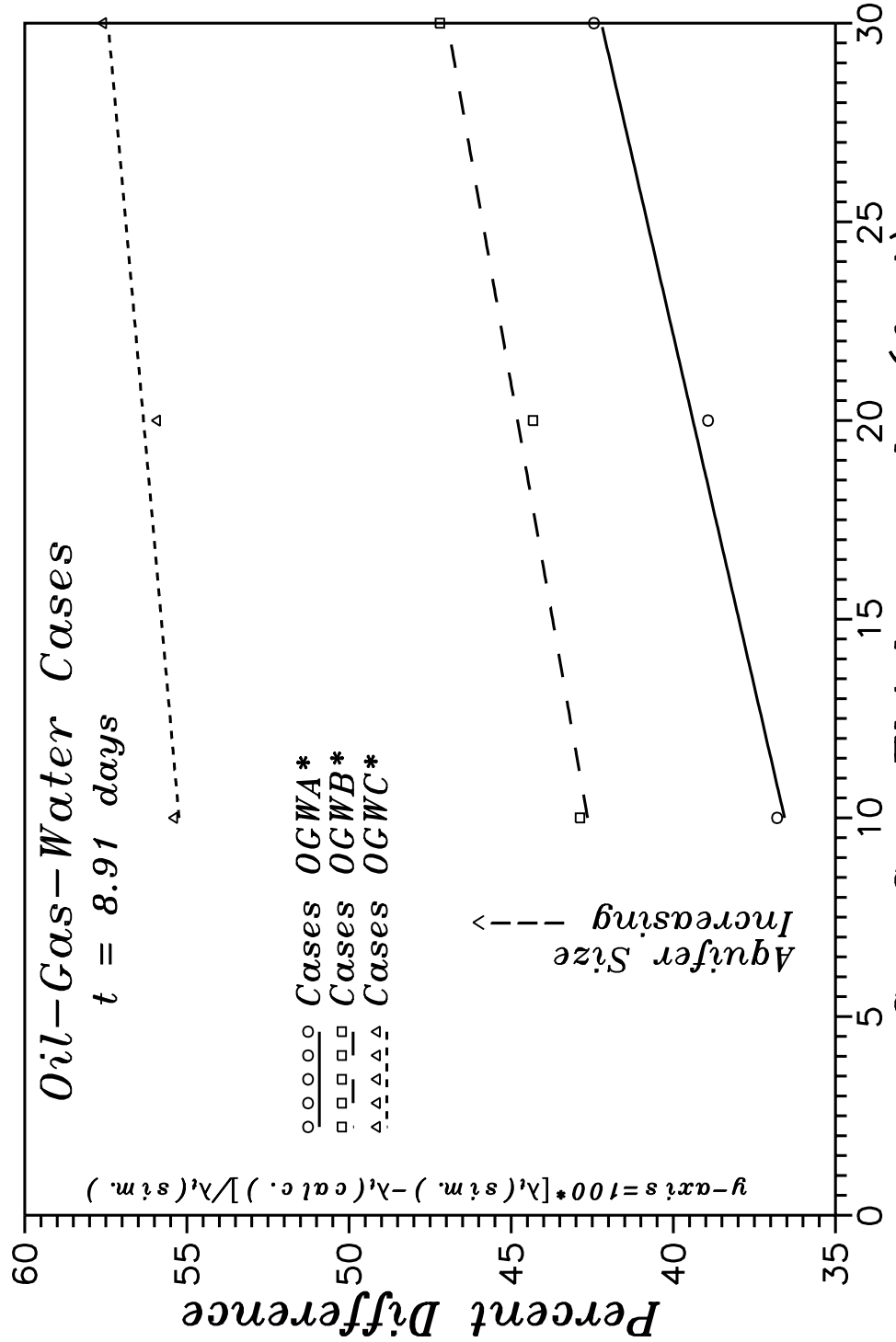

Fig. 6.36 – Correlation between relative difference in calculated and simulator mobilities.

in the gas cap size or in the aquifer size results in an increase in the "coning" behavior of the reservoir system; i.e., for larger aquifers or gas caps, the water or gas cone, respectively, will develop faster with the fluid saturations changing more rapidly in the neighborhood of the original fluid contacts. Recall that the reason for this increased coning behavior is due to the fact that as the aquifer size or gas cap size increases, then for a given production rate the fractional flow of water or gas, respectively, at any cross-section of the reservoir must increase. Because the inner boundary is closed in the aquifer or gas cap, the fluids begin to flow vertically as they approach the inner boundary and the vertical flow rates will increase.

Lastly, we examine the total mass rate, total volumetric flow rate and fraction flow rate profiles in the reservoir. Figure 6.37 shows the total reservoir volumetric flow rate normalized by the sandface rate ($q_t(r)/q_t(r_w)$), the total mass flow rate and fractional flow rate profiles at a producing time of 10 days for case OG-WCC. Figure 6.37 shows the total radial mass rate for this case is approximately constant out to a radius of 20 to 30 feet, where it falls off sharply. A "steady-state" zone based on the total mass rate, therefore, exists only in the region $r_w \leq r \leq 30$ feet. If based on the reservoir volumetric flow rate, a "steady-state" zone exist in the reservoir over the region $r_w \leq r \leq 300$ feet, or ten times that based on the total mass rate.

As with the oil-gas cases discussed in the previous section, the fractional flow rates shown in Fig. 6.37 indicate that as we move away from the wellbore in the region $r_w \leq r \leq 10$ feet, we move further away from vertical equilibrium. For $r > 10$ feet, Fig. 6.37 indicates that a large transition zone exists in which the reservoir approaches closer and closer to vertical equilibrium as we move out into the reservoir. Not until we reach $r = 1000$ feet, can we say that the reservoir is approximately in vertical equilibrium. So, once again, the "steady-state" region

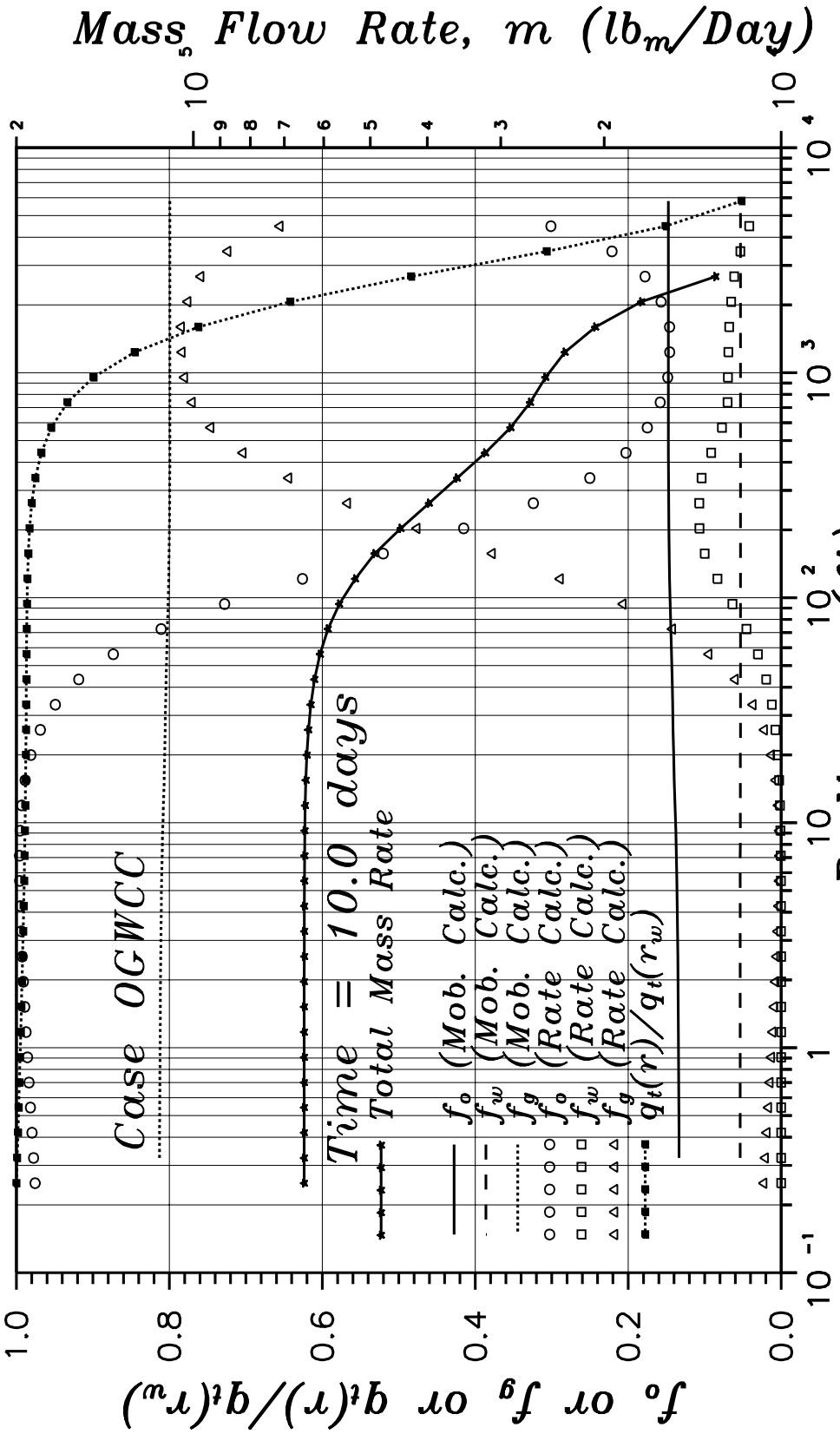

Fig. 6.37 — Comparison of fractional flow rates as an indicator of vertical equilibrium (pseudoradial flow).

in the reservoir does not extend out in the reservoir to the point where vertical equilibrium exists. This then implies that the wellbore pressure response is being influenced by vertical flow in that region of the reservoir ahead of the "steady-state" zone and before the zone of vertical equilibrium; i.e., at least over the region $300 \leq r \leq 1000$ feet.

6.6 Summary

An extensive array of two-phase and three-phase reservoirs systems have been used to investigate the applicability of semilog analysis techniques to drawdown pressure transient and rate data obtained from a restricted-entry well under multiphase flow conditions. Reservoir systems investigated include oil reservoirs underlain by an aquifer, gas reservoirs underlain by an aquifer, oil reservoirs overlain by a gas cap, water reservoirs overlain by a gas cap and oil reservoirs overlain by a gas cap and underlain by an aquifer.

For oil-water systems, Refs. 23 and 24 observed that if multiphase flow effects are important, then a rapid decline in pressure does not necessarily signify the onset of boundary effects, i.e., when coning of water occurs, there is a resultant decrease in the total mobility adjacent to the open interval which causes a rapid decline in the wellbore pressure (increase in the pressure derivative). Results presented here (for each of the two-phase and three-phase reservoir systems considered) and in Ref. 28 indicate that coning itself, i.e., production of the unwanted fluid, is not necessarily required to observe this increase in the pressure derivative. In fact, all that is required is for there to be a "significant" change in the vertical saturation profile in the reservoir, i.e., movement of the fluid contact or the "building" of the water or gas cone.

For the non-solution gas systems, changes in the wellbore pressure derivative have been shown to coincide (correlate) directly with changes in the total

mobility near the fluid contacts. For solution gas reservoir systems, the pressure derivative is so dominated by changes in the total mobility near the open interval that changes in the derivative due to changes in the mobility at the fluid contacts are difficult, if not impossible, to observe. For these solution-gas reservoir systems, we have shown that much of the pressure derivative behavior can be attributed to vertical flow near the sandface and changes in the total mobility which occur just above or below the perforations.

Unlike one-dimensional radial reservoir systems in which previous authors (e.g., Refs. 31-34) have suggested the use of a multiphase pseudopressure based on a unique functionality between saturation and pressure, we note that saturation is neither a unique function of pressure or phase potential for the reservoir systems (two-dimensional cross-sections) considered here. All multiphase analysis presented in this work are then presented in terms of pressure only.

Using the transient pressure and rate data, a total mobility was formally calculated for each of these reservoir systems using the following equation:

$$\bar{\lambda}_t = \frac{70.6(q_o B_o(p_{wf}) + q_w B_w(p_{wf}) + q_{gf} B_g(p_{wf}))}{h d\Delta p/d\ln t} \,. \qquad (6.6.1)$$

For a fully-penetrating well in a solution-gas-oil reservoir in which gravity effects are included and the saturation at the sandface changes with time, we have presented arguments and numerical results which show that the saturation must be independent of the vertical direction at the sandface before Eq. 6.6.1 will become applicable; i.e., provide accurate estimates of the thickness-averaged total mobility at the sandface. Furthermore, for reservoir fluids in which the viscosity and formation volume factors are functions of pressure, we have shown that the proper interpretation of the mobilities calculated from Eq. 6.6.1 is one in which all PVT properties are evaluated at the prevailing wellbore pressure.

For data obtained from a restricted-entry well in all of the reservoir systems except the gas reservoir - aquifer systems, Eq. 6.6.1 greatly underpredicted the actual mobilities existing in the reservoir. For the gas reservoir - aquifer systems, the calculated mobilities were slightly overpredicted. For reservoir systems not containing solution gas, the calculated mobilities were found to more closely approximate the thickness-averaged total mobility. For reservoir systems containing solution gas, the calculated mobilities were found to more closely approximate the total mobility averaged over the open interval at the sandface.

For the gas reservoir - aquifer systems investigated, we have shown that ignoring the presence of water in the system results in negligible error; i.e., accurate estimates of the thickness-averaged effective gas permeability can be obtained by utilizing the real gas pseudopressure only.

For all of the reservoir systems considered in this chapter, we have shown that while a "steady-state" region exists in the reservoir between the well and some point out in the reservoir, this zone does not extend to that region of the reservoir where vertical equilibrium (pseudoradial flow) exists. This means that the wellbore pressure is influenced by vertical flow in that region ahead of the steady-state zone and behind the region of vertical equilibrium.

For all of the multiphase reservoir systems investigated, we have shown that the percent deviation between the mobilities calculated formally with Eq. 6.6.1 and the mobilities existing in the reservoir correlate extremely well with the thickness of of the aquifer (for those cases containing an aquifer) and with the thickness of the gas cap (for those cases containing a gas cap). This result provides us with hope that accurate estimates of in-situ fluid mobilities may eventually be obtained from drawdown pressure and rate data, though we have yet to be able to obtain these ourselves.

Lastly, for water - gas cap cases, we have shown that the dimensionless porosity-compressibility-thickness product, i.e.,'

$$\omega = \frac{\phi_1 c_{t1} h_1}{\overline{\phi c_t} h} \ , \tag{6.6.2}$$

is an important correlating parameter in the interpretation of the pressure transient data.

CHAPTER VII
BUILDUP ANALYSIS

This chapter concerns itself with the analysis of buildup pressure transient data obtained from a restricted-entry well under multiphase flow conditions. Conditions under which semilog analysis of the buildup pressure transient data can be performed and procedures for that analysis are discussed. The reservoir systems investigated are the same as in the previous chapter and again include oil reservoirs underlain by an aquifer, gas reservoirs underlain by an aquifer, oil reservoirs overlain by a gas cap, water reservoirs overlain by a gas cap and oil reservoirs both overlain by a gas cap and underlain by an aquifer.

The theoretical basis for analysis of buildup pressure data arises naturally from the superposition of two constant-rate drawdown solutions. From a theoretical standpoint, however, we know that superposition is valid only for linear initial-boundary-value problems. Because the multiphase systems considered in this work represent nonlinear initial-boundary-value problems, an *a priori* assumption concerning the application of standard superposition results cannot be made. Instead, it will be necessary to examine detailed numerical results for each of the different multiphase reservoir systems investigated to (i) ascertain the applicability of superposition based on the accuracy of reservoir parameters estimated from equations based on the validity of superposition, and (ii) provide a physical explanation justifying the application of superposition.

Recall from the previous chapter that all of the multiphase reservoir systems exhibited pseudoradial flow (vertical equilibrium) in the outer regions of the

reservoir. If vertical equilibrium at this location (call it r_i) should be maintained during the buildup and should we be able to propagate a no-flow "steady-state" region out into the reservoir to this point, then we speculate that superposition should be approximately valid; i.e., under these conditions (vertical equilibrium at r_i and a no-flow "steady-state" region for $r \leq r_i$), then the reservoir in the region $r \leq r_i$ should simply behave like a fully-penetrating line-source well of radius r_i.

In the following sections, we examine this argument for (ii) above in more detail as it relates to each of the individual cases. For (i) above, we examine the accuracy of mobility estimates obtained from equations based on superposition as well as various linearization schemes used in conjunction with superposition; e.g., pseudo-equivalent time based on a pseudo shut-in time or a normalized shut-in time.

7.1 Two-Phase Oil-Water Systems

In this section we examine the buildup pressure data for those oil-water reservoir systems discussed in Section 6.1 and for which a cross-sectional schematic of the reservoir is shown in Fig. 4.1. The fluid properties and other pertinent reservoir data for these cases are included in Tables 4.1A and 4.1B.

As background information, we note that Refs. 23 and 24 showed that buildup data could often be analyzed by semilog analysis even in cases where drawdown data did not exhibit a well-defined pseudoradial flow semilog straight line because of coning. Though they did not consider equivalent time, their results clearly indicate that the thickness-averaged total mobility for such systems can be calculated from

$$\bar{\lambda}_t = \frac{70.6[q_o B_o(p_{ws}) + q_w B_w(p_{ws})]}{hd\Delta p/d\ln t_e} , \qquad (7.1.1)$$

where equivalent time, t_e is defined as

$$t_e = \frac{t_p \Delta t}{t_p + \Delta t} \ , \tag{7.1.2}$$

Δp is defined as

$$\Delta p = p_{ws} - p_{wf,s} \ , \tag{7.1.3}$$

p_{ws} is the shut-in wellbore pressure and $p_{wf,s}$ is the flowing wellbore pressure at the instant of shut-in.

In Fig. 7.1, we have plotted the logarithmic derivative with-respect-to equivalent time of the shut-in pressure ($d\Delta p / d \ln t_e$) versus shut-in time (Δt). Fig. 7.1 shows the classic restricted-entry pressure response, i.e., an approximately constant log-derivative of the shut-in pressure at early time (indicative of radial flow adjacent to the open interval), a sharp drop in the derivative during a transition period, and lastly, a fairly constant derivative at late time (suggestive of pseudoradial flow in the reservoir). Because the early time constant derivative is often masked by wellbore storage and skin effects, we neglect that part of the derivative curve for the time being and concentrate on the late time derivative. Note that all of the cases except cases OW-67B and OW-7B exhibit well defined late time constant derivatives (semilog straight lines) suggestive of pseudoradial flow. Results not shown indicate that the reason for not seeing a constant derivative for cases OW-67B and OW-7B is simply that the simulated well test was not conducted over a sufficiently long time to reach the pseudoradial flow period.

For each of the oil-water cases investigated, Eq. 7.1.1 was used to estimate a thickness-averaged total mobility. Results from these calculations are shown in Table 7.1 along with the initial thickness-averaged total mobility existing in the reservoir and the percent deviation between these two mobilities. Clearly, Eq.

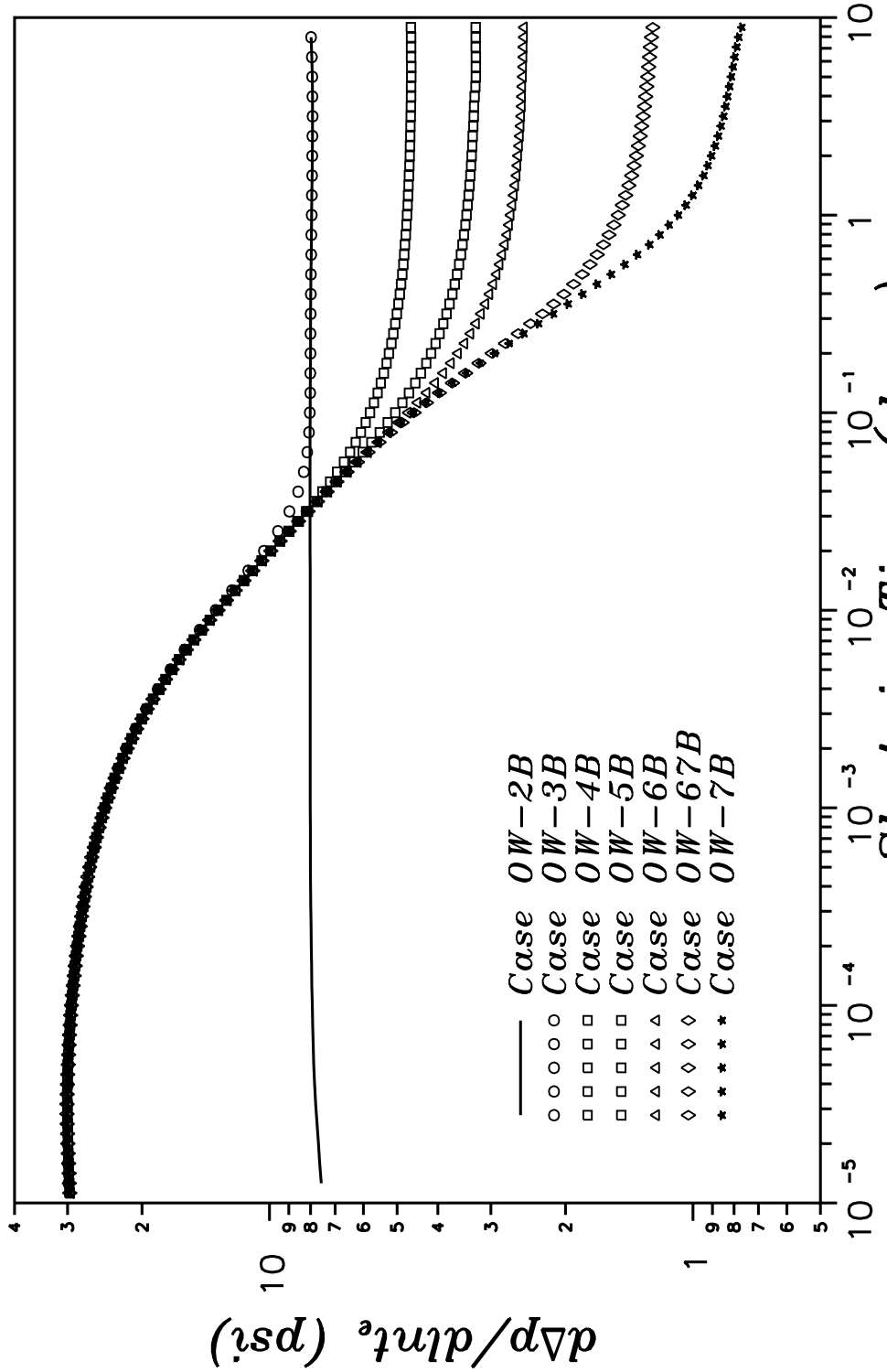

Fig. 7.1 — Diagnostic buildup pressure derivative plot (oil–water).

7.1.1 provides excellent approximations to the thickness-averaged total mobilities existing in the outer region of the reservoir. These results tend to support the validity of using the superposition based Eq. 7.1.1 for the analysis of buildup pressure data in oil-water systems.

While the results obtained from Eq. 7.1.1 strongly support the use of this superposition based analysis method, we still seek to provide a physical interpretation as to why superposition appears to hold for these cases. In the introduction to this chapter, we postulated that if vertical equilibrium existed in the outer region of the reservoir ($r \geq r_i$), and if a no-flow "steady-state" region propagated out into the reservoir to this point, then the reservoir at that location should behave like a fully-penetrating line-source well of radius r_i and superposition should be approximately valid. Figure 7.2 shows our indicators of vertical equilibrium (cross-sectional fractional flow rates) and well as a normalized cross-sectional mass flow rate at a shut-in time of 8.9 days. Figure 7.2 clearly shows the mobility and rate calculated fractional flow rates become equal for the region of the reservoir $r \geq 200$ feet; i.e., vertical equilibrium exists in the reservoir for $r \geq 200$ feet. Note that over that region of the reservoir in which vertical equilibrium does not exist ($r < 200$ feet) the radial flow rate is extremely small. In comparing the region of vertical equilibrium for the drawdown (Fig. 6.5) with the region of vertical equilibrium for the buildup (Fig. 7.2), we note that the vertical equilibrium region is much larger and occurs at a smaller radius for the buildup than for the drawdown. This result is probably due to the greater influence of gravity on the system in the absence of active production. Figure 7.2 also clearly shows that, within one percent, the no-flow "steady-state" zone has propagated out to a radius of approximately $r \approx 400$ feet.

Unlike the drawdown results presented in the previous chapter, the results discussed above show that the no-flow "steady-state" zone has propagated out

Table 7.1

Buildup Semilog Analysis Results: Oil-Water Systems

Case	Simulator $\bar{\lambda}_t$ (md/cp)	Calculated $\bar{\lambda}_t$ (md/cp)	Percent Deviation
OW-2B	42.47	42.71	0.6
OW-2BS3	42.47	42.71	0.6
OW-2BS4	42.47	42.71	0.6
OW-3B	42.47	42.71	0.6
OW-3BS3	42.47	42.71	0.6
OW-3BS4	42.47	42.71	0.6
OW-4B	49.05	48.99	0.1
OW-4BS3	49.05	49.00	0.1
OW-4BS4	49.05	49.00	0.1
OW-5B	52.34	52.10	0.4
OW-5BS3	52.34	52.30	0.1
OW-5BS4	52.34	52.30	0.1
OW-5P	52.34	52.25	0.2
OW-5S	52.34	51.78	1.1
OW-6B	54.31	53.97	0.6
OW-6BS3	54.31	54.00	0.6
OW-6BS4	54.31	54.00	0.6
OW-67B	58.05	57.68	0.6
OW-7B	59.57	59.18	0.7
OW-7BS3	59.57	57.60	3.3
OW-7BS4	59.57	57.60	3.3
OW-7O	59.57	58.85	1.2
OW-7P	59.57	59.61	0.1
OW-7Q	59.57	58.84	1.2
OW-7S	59.57	58.55	1.7

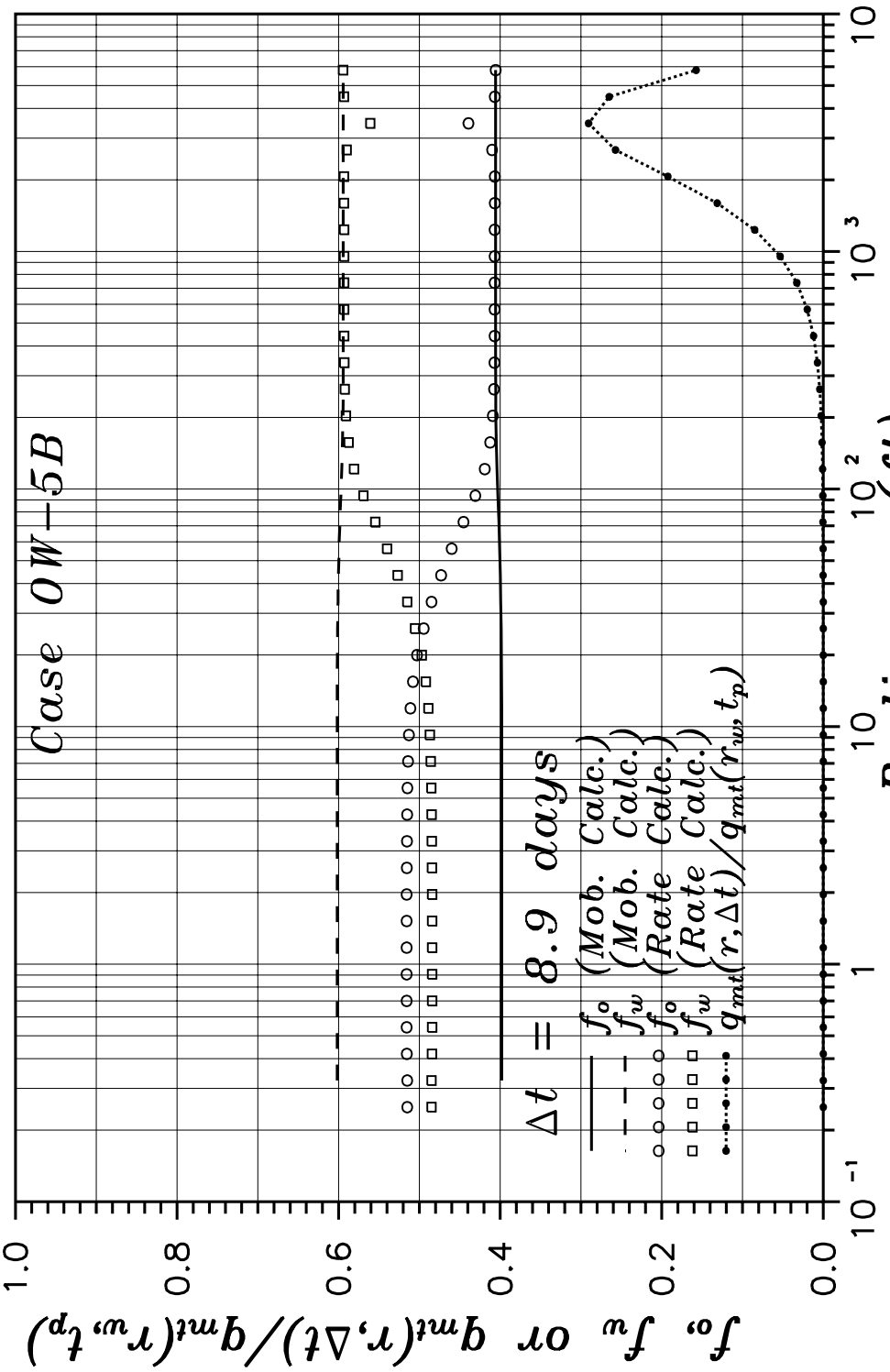

Fig. 7.2 – Comparison of fractional flow rates as an indicator of vertical equilibrium.

to the region of the reservoir under vertical equilibrium. Because changes in the wellbore pressure are only influenced by what occurs ahead of this no-flow "steady-state" zone, the wellbore pressure response can not be influenced by vertical flow. We have speculated throughout this work that these same two conditions are a necessary (but not sufficient) condition for the application of semilog analysis techniques. The fact that these conditions were not met during the drawdown phase of the pressure transient test and the results from semilog analysis techniques for those cases were substantially in error tends to support the concept of these two conditions being required to hold for the application of semilog analysis techniques to pressure transient data.

Lastly, Figure 7.3 shows the logarithmic derivatives of the drawdown and buildup pressures, both at the sandface and in the outer region of the reservoir ($r =$ 340 feet). Two aspects of Fig. 7.3 are important in relation to the above arguments concerning the existence of a "steady-state" zone and the validity of superposition based analysis techniques. First, we note that (as discussed in Chapter IV) if a steady-state zone exists, then the log-derivative of pressure should be a constant across that zone. Figure 7.3 clearly shows the late-time buildup log-derivative of the wellbore pressure approaching and becoming equal to the log-derivative of the buildup pressure at $r = 340$ feet. This result is just one more piece of information confirming the existence of a "steady-state" region between the well and some location substantially out in the reservoir.

In pressure transient analysis, the buildup pressure response is typically considered to be the superposition of two drawdown solutions. Provided the proper time scales are selected for both solutions (drawdown and buildup), the derivatives of those solutions should also be equal. For our case then, if superposition is valid, then the equivalent time log-derivative of the buildup pressure when plotted as a function of equivalent time should overlay the log-derivative

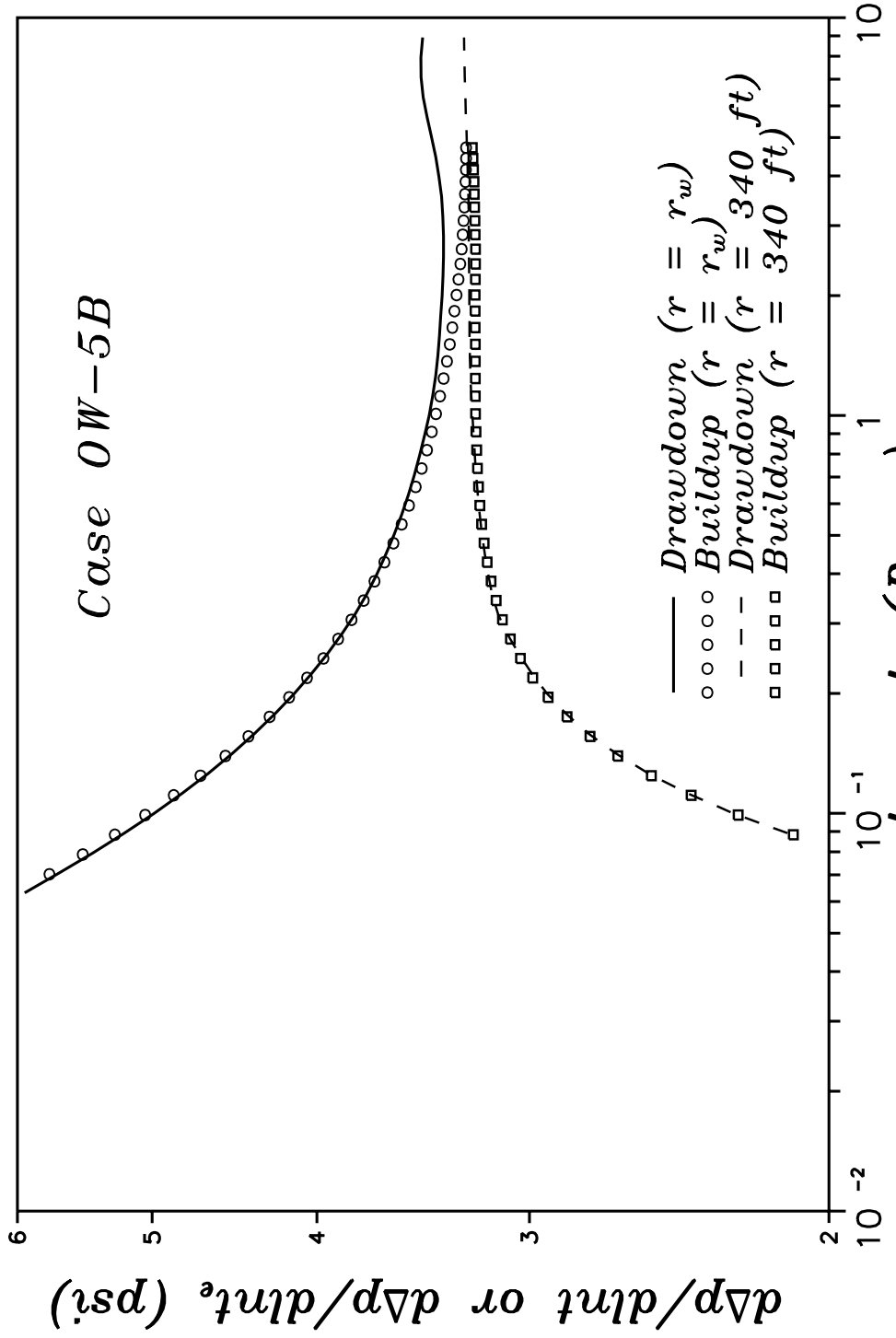

Fig. 7.3 – Comparison of pressure derivatives at the sandface and in the outer region of the reservoir.

of the drawdown pressure plotted as a function of producing time; e.g., once the logarithmic approximation to the exponential integral function becomes valid for the single-phase line-source solution (linear problem), we know that

$$\frac{-dp_{wf}}{d\ln t} = \frac{dp_{ws}}{d\ln t_e} = \frac{1}{2} \ . \tag{7.1.4}$$

In examining Fig. 7.3, we see that the drawdown and buildup pressure derivatives for locations out in the reservoir ($r = 340$ feet) do indeed overlay one another. For the wellbore pressure derivatives, however, we have a mixed response. During early time, the drawdown and buildup pressure derivatives overlay one another and at late time they do not. The early time behavior is not surprising for this case since in the near well region (above the oil-water contact), the reservoir is single-phase oil (considered to be a slightly compressible fluid of constant compressibility and constant viscosity for these oil-water cases). Until the pressure transient during the buildup is influenced by the water in the system or some other boundary; then, we expect the pressure transient response should approximately satisfy the analytical solution[108] to the single-phase oil restricted-entry problem. At late time, however, the wellbore drawdown and buildup pressure derivatives deviate from one another, indicating that superposition of drawdown wellbore pressure responses is not valid. In the previous chapter we showed that the increase in the drawdown pressure derivative was due to multiphase flow effects (building of a water cone). The fact that the buildup pressure derivative does not show the increase in the pressure derivative that the drawdown does re-enforces the drawdown interpretation that the increase in the drawdown derivative was due to movement of the water phase near the oil-water contact and the subsequent decrease in the total relative mobility at that point. Because the fluids are not flowing, or are flowing at such a small rate, near the oil-water contact at late-times during the buildup, then the effect on the wellbore pressure response is minimal.

7.2 Two-Phase Gas-Water Systems

This section concerns itself with the analysis of buildup pressure data for those gas-water reservoir systems discussed in Section 6.2 and for which a cross-sectional schematic of the reservoir with initial saturation profiles is shown in Fig. 4.2. The fluid properties and other pertinent reservoir data for these cases are included in Tables 4.2A and 4.2B.

For buildup analysis of radial dry gas reservoirs, Ref. 124 presented two Horner time ratios, one based on a normalized shut-in time and one based on shut-in pseudotime, that yielded an accurate analysis of buildup data. In analyzing buildup pressure data obtained from a restricted-entry well in a gas reservoir - aquifer system, we consider here both the conventional equivalent time, Eq. 7.1.2, and a Horner time ratio based on a shut-in pseudotime, where an equivalent-pseudotime, t_{ae}, is defined as

$$t_{ae} = \frac{t_p \Delta t_a}{t_p + \Delta t} \ , \tag{7.2.1}$$

with pseudo-shut-in time defined by

$$\Delta t_a = \int_0^{\Delta t} \frac{dt}{\mu_g c_t} \ . \tag{7.2.2}$$

Results presented previously in Refs. 28 and 131 suggest that either of the following equations could be used to obtain a reasonable estimate of the total-thickness-averaged mobilities for gas-water systems producing only gas:

$$\bar{\lambda}_t = \frac{70.6 q_g B_g(p_{ws})}{h d\Delta p / d \ln t_e} \ , \tag{7.2.3}$$

or,

$$\bar{\lambda}_t = \frac{70.6 q_g B_g(p_{ws})}{h d\Delta p / d \ln t_{ae}} \ , \tag{7.2.4}$$

where Δp is defined by Eq. 7.1.3. Prior to examining the validity (accuracy) of these equations, however, we first examine the pressure derivatives for these cases.

Figure 7.4 shows the log-derivative of the shut-in pressure with-respect-to equivalent time plotted as a function of shut-in time. Approximately constant log-derivatives are seen at both early-times and late-times, with a sharp transition zone between the two. Unlike the drawdown results which did not exhibit well defined late-time semilog straight lines (constant log-derivatives of the wellbore pressure), the buildup results appear to display rather well developed semilog straight lines. Whereas the drawdown results suggested that pseudopressure may be required to analyze the results, the buildup data suggests that analysis of pressure data alone may be sufficient to perform the analysis; i.e., the constant late-time log-derivative of the shut-in pressure suggests that changes in fluid properties during this time are minimal and analysis may be performed in terms of pressure only.

Next, we examine the thickness-averaged total mobilities calculated directly using Eqs. 7.2.3 and 7.2.4. Figure 7.5 shows these mobilities for case GW-5B, along with the thickness-averaged total mobilities output by our simulator. The simulator thickness-averaged total mobilities in the outer zone of the reservoir were calculated by two methods, one of which evaluates the gas viscosity at the initial reservoir pressure, p_i, (shown by the dashed line) and one which evaluates the gas viscosity at the instantaneous wellbore shut-in pressure, p_{ws} (shown by the solid line). Both methods use the effective permeabilities evaluated at initial saturation conditions. In a practical sense, there is little difference between the mobilities calculated using either of Eq. 7.2.3 or 7.2.4. Note that the results of Fig. 7.5 indicate that $\bar{\lambda}_t$ estimated from either of Eqs. 7.2.3 or 7.2.4 approximately satisfy

$$\bar{\lambda}_t = \frac{1}{h}\int_0^h \left(\frac{k k_{rg}}{\mu_g(p_{ws})} + \frac{k k_{rw}}{\mu_w(p_{ws})} \right) dz \ , \tag{7.2.5}$$

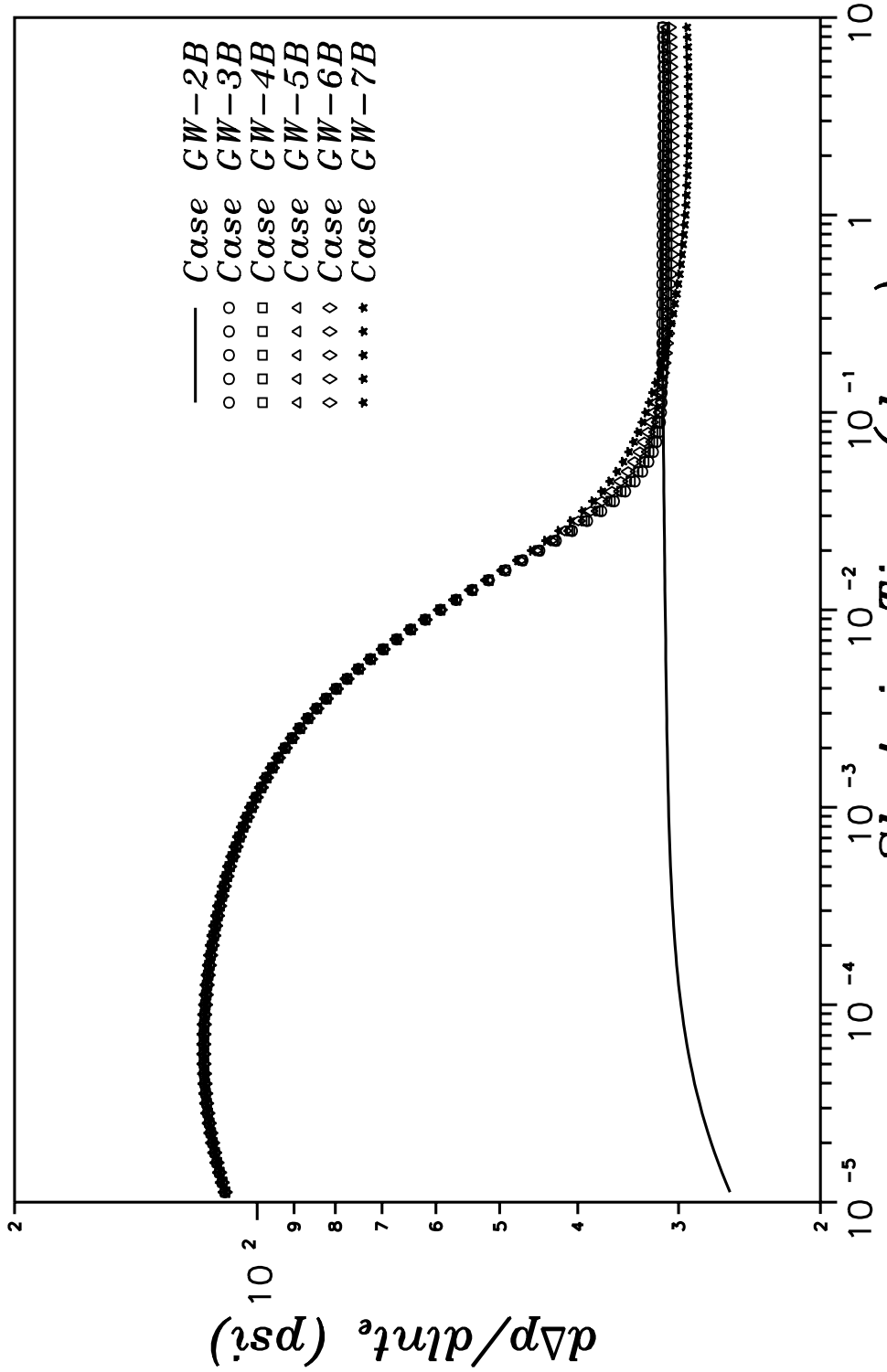

Fig. 7.4 – Diagnostic buildup pressure derivative plot (gas–water).

where kk_{rg} and kk_{rw} correspond to the region in the outer part of the reservoir where pseudoradial flow occurs, but viscosities are evaluated at the wellbore shut-in pressure, p_{ws}. For single-phase radial flow, this result would follow directly from the fact that the dimensionless real-gas pseudopressure function approximately satisfies the standard semilog equation.

Table 7.2 contains a complete list of the calculated (both Eqs. 7.2.3 and 7.2.4) thickness-averaged total mobilities, the actual thickness-averaged total mobility (viscosity evaluated at the wellbore shut-in pressure) and the percent deviation of each of the calculated mobilities from the actual mobility. The results shown in Table 7.2 clearly indicate that either of Eqs. 7.2.3 or 7.2.4 provide excellent approximations to the thickness-average total mobility. One would be hard pressed to assert that one method or the other (Eqs. 7.2.3 or 7.2.4) provides more accurate results. Indeed, if we consider only the high-rate ($q_g = 10$ MMscf/day) zero-skin cases, the results are mixed; i.e., the calculation based on equivalent time (Eq. 7.2.3) appears to be slightly more accurate for cases GW-2B and GW-3B, whereas the calculation based on pseudo-equivalent time (Eq. 7.2.4) appears to be slightly more accurate for the cases containing a water zone (cases GW-4B to GW-7B). Results shown for the low-rate ($q_g = 1\ MMscf/day$) cases indicate equivalent-time based calculations (Eq. 7.2.3) are slightly more accurate for most cases. Recall that cases with non-zero skin factors are designated as **-**S3 for those cases with a skin of $s = 5$ and **-**S4 for those cases with a skin of $s = 10$.

In keeping with the arguments presented in the introduction to this chapter, we examine the state of the reservoir during the buildup to provide a physical justification for the use of superposition based analysis methods for this non-linear problem. Figure 7.6 shows the mobility and rate calculated fractional flow rates as a function of radius near the end of the buildup test. The mobility and rate calculated fractional flow rates clearly become equal for the region of the reservoir

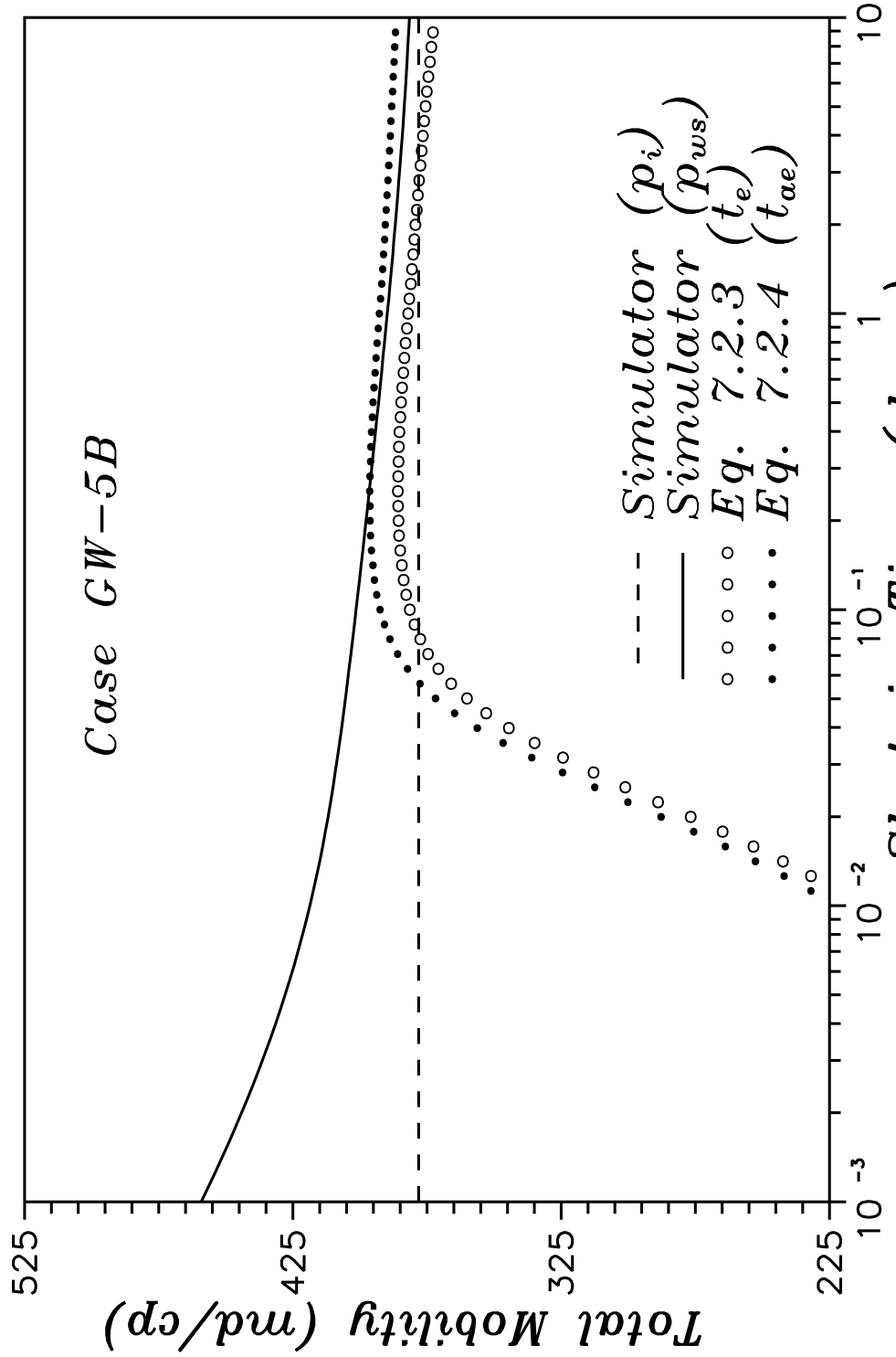

Fig. 7.5 – Comparison of calculated and simulator mobilities.

Table 7.2

Buildup Semilog Analysis Results: Gas-Water Systems

Case	Simulator $\bar{\lambda}_t(p_{wf})$ (md/cp)	Calculated $\bar{\lambda}_t(t_e)$ (md/cp)	Percent Deviation	Calculated $\bar{\lambda}_t(t_{ae}))$ (md/cp)	Percent Deviation
GW-2B	471.09	463.02	1.71	480.52	2.01
GW-2BS3	467.07	466.87	0.04	468.70	0.35
GW-2BS4	467.07	466.87	0.04	468.70	0.35
GW-3B	471.09	463.01	1.72	480.55	2.01
GW-3B2	467.07	466.86	0.04	468.70	0.35
GW-3BS3	467.07	466.86	0.04	468.70	0.35
GW-3BS4	467.07	466.86	0.05	468.70	0.35
GW-4B	421.52	411.91	2.28	427.47	1.41
GW-4B2	417.95	417.82	0.03	419.45	0.36
GW-4BS3	417.95	417.82	0.03	419.45	0.36
GW-4BS4	417.95	417.82	0.03	419.45	0.36
GW-5B	381.85	372.76	2.38	386.76	1.29
GW-5B2	378.65	378.58	0.02	380.05	0.37
GW-5BS3	378.65	378.58	0.02	380.05	0.37
GW-5BS4	378.65	378.58	0.02	380.05	0.37
GW-6B	322.33	314.56	2.41	326.24	1.21
GW-6B2	319.70	319.69	0.00	320.92	0.38
GW-6BS3	319.70	319.69	0.00	320.92	0.38
GW-6BS4	319.70	319.69	0.00	320.91	0.38
GW-7B	203.45	198.47	2.45	205.54	1.02
GW-7B2	201.82	201.57	0.12	202.31	0.24
GW-7BS3	201.82	201.29	0.26	202.03	0.11
GW-7BS4	201.82	201.57	0.12	202.30	0.24

$r \geq 150$ feet; i.e., vertical equilibrium exists in the reservoir for $r \geq 150$ feet. Figure 7.6 also shows the no-flow "steady-state" zone has, to within two percent, propagated out to a radius of approximately $r \approx 200$ feet; i.e., the mass rate at $r = 200$ feet is less that two percent of the mass production rate which existed at the this location at the end of the drawdown period. Note that at a radius of $r = 340$ feet, the mass rate is only 5 percent of the producing mass rate at the instant of shut-in. Because the flow rate is only varying significantly in the region of the reservoir where vertical equilibrium exists and because the flow rate is negligible in the inner region of the reservoir, the wellbore pressure response should not be influence by flow in the vertical direction. Clearly, if the region of the reservoir, $r \leq 150\ ft$, is at "steady-state" and vertical equilibrium exists in the reservoir for $r \geq 150\ ft$, then the reservoir in the region $r \leq 150\ ft$ should behave like a line source well of radius $r_w = 150\ ft$. For such a reservoir system, the only non-linearities which arise are due to the non-linearities involved with the pressure dependent fluid properties, e.g., ρ_g, μ_g, etc. Because of the location ($r = 150\ ft$), however, the pressure changes are small and effects of the nonlinearities should be negligible, or at the worst, tolerable, (see, for example, Fig. 7.5 which shows the total mobility, with viscosities evaluated at the wellbore pressure, varying by a mere 2.5 percent in the time range $0.1 \leq \Delta t \leq 10$ days).

7.3 Two-Phase Water-Gas Systems

In this section, we consider the analysis of pressure data obtained from a restricted-entry well located in a water reservoir overlain by a gas cap. Analysis of drawdown pressure data was discussed in Section 6.3. A cross-section of the reservoir along with the initial fluid saturation profiles are shown in Fig. 4.4. Fluid properties and other pertinent reservoir data for these cases are included in Tables 4.4A and 4.4B.

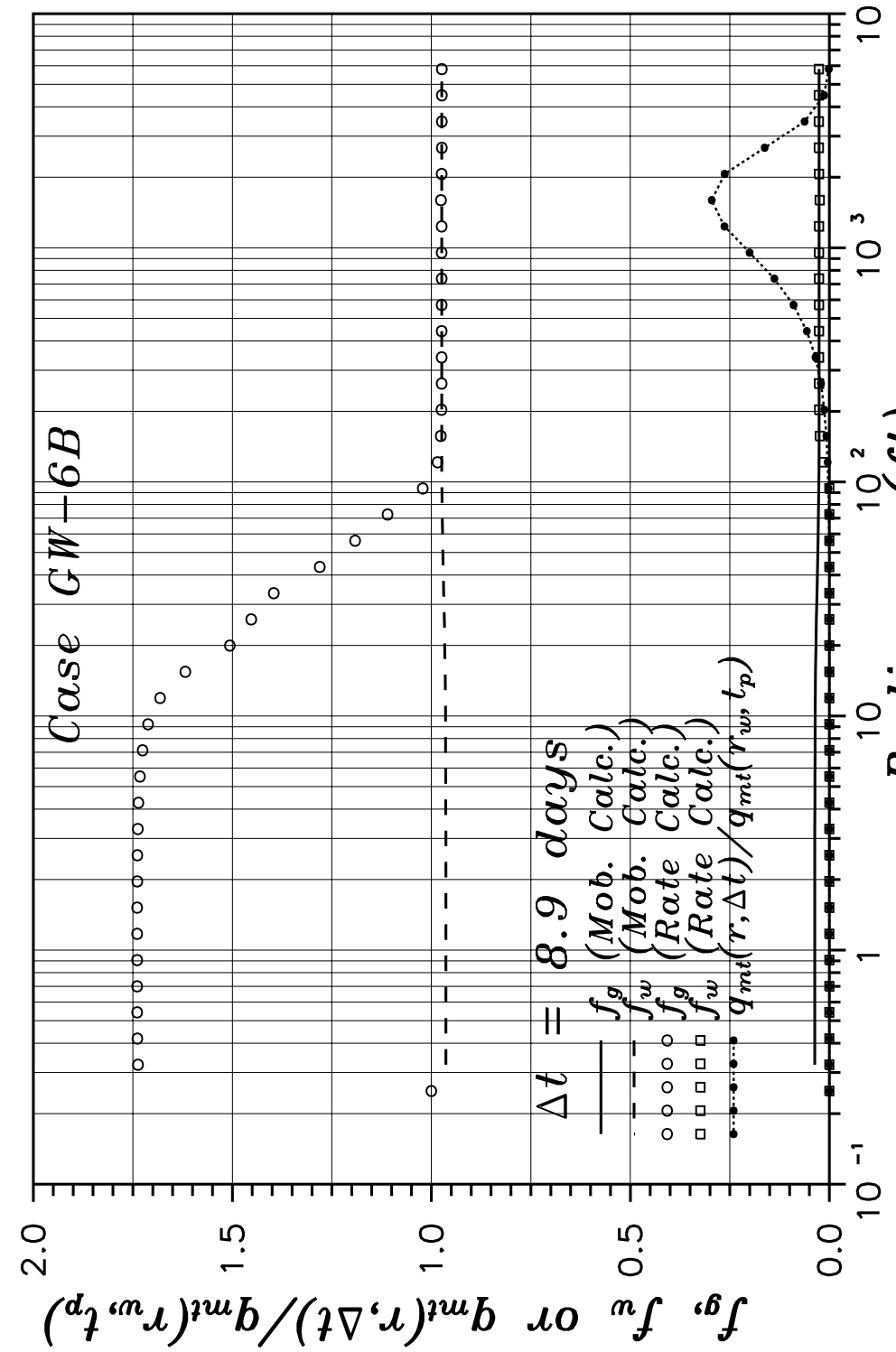

Fig. 7.6 – Comparison of fractional flow rates as an indicator of vertical equilibrium.

Based on the results of the previous sections, the drawdown results (Section 6.3) and the results of Ref. 132, we conjecture that the thickness-averaged total mobility can be obtained by

$$\bar{\lambda}_t = \frac{70.6[q_w B_w(p_{ws}) + q_g B_g(p_{ws})]}{hd\Delta p/d\ln t_e} \tag{7.3.1}$$

during buildup. Prior to examining results based on this equation, however, we examine the log-derivative of the shut-in wellbore pressure.

Figure 7.7 shows the log-derivative (with-respect-to equivalent time) of the shut-in wellbore pressure plotted as a function of shut-in time for these cases. Note that a constant pressure derivative is seen only for the fully-penetrating case (WG-1B), which also happens to be single-phase water. Due to the small compressibility of the water, the duration of the early-time semilog straight line for the restricted-entry cases is to short to be seen on this diagnostic plot.

Concentrating on the late-time data, we see that only the single-phase cases WG-1B and WG-2B exhibit well defined semilog-straight lines (constant derivatives). The late-time derivatives for each of the restricted-entry cases containing a gas cap exhibit a minimum, followed by a monotonically increasing log-derivative of wellbore pressure; all except case WG-5D which is discussed below. There are actually two separate reasons for the increasing derivative, one of which was discussed in Chapter VI, Section 6.3. Recall from the previous chapter, we showed that the log-derivative of the wellbore pressure was strongly affected by ω, the ratio of the porosity-compressibility product for the open interval divided by the thickness averaged value, where ω was defined as

$$\omega = \frac{\phi_1 c_{t1} h_1}{\overline{\phi c_t} h} \tag{7.3.2}$$

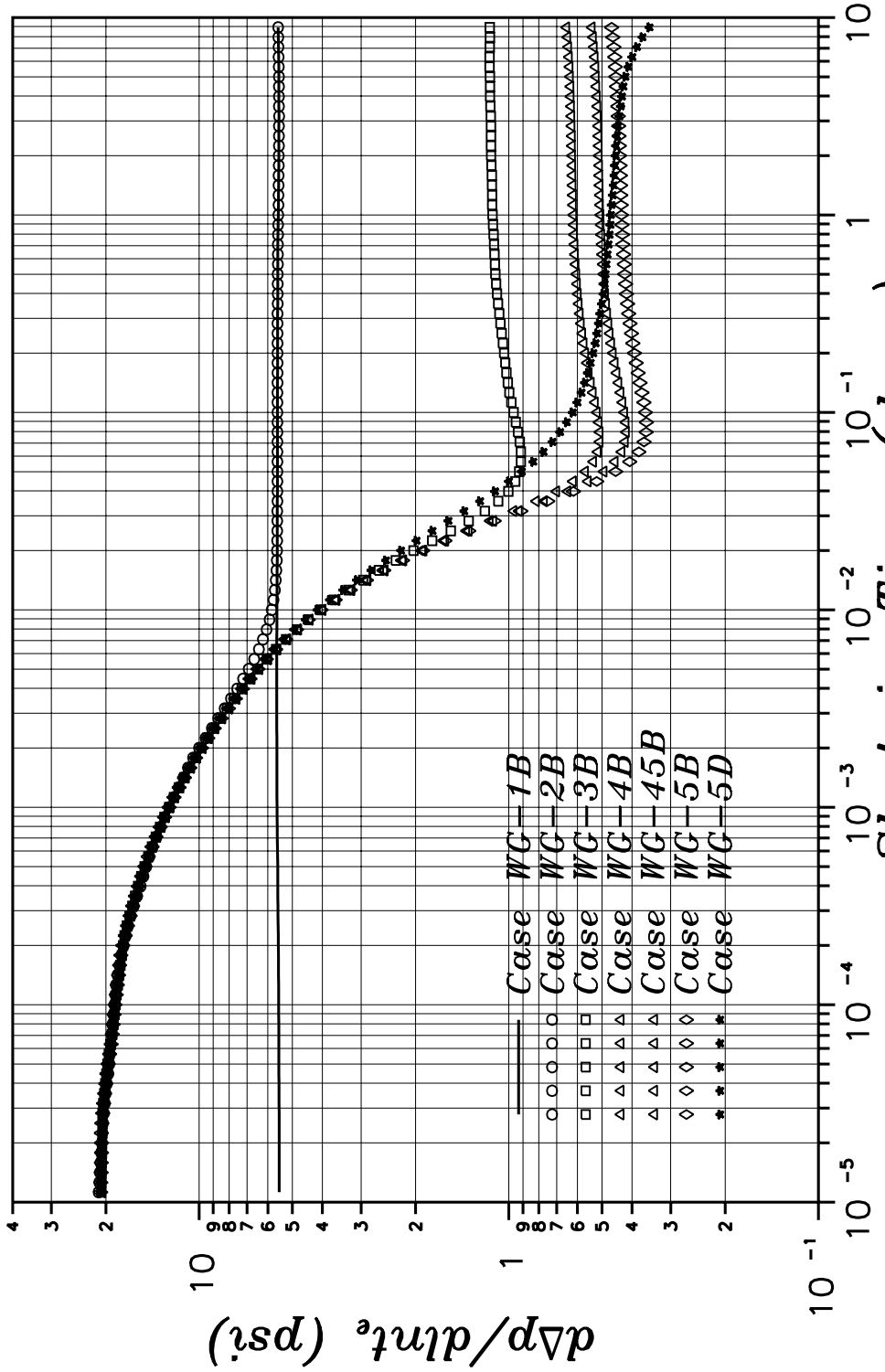

Fig. 7.7 – Diagnostic buildup pressure derivative plot (water-gas).

and

$$\overline{\phi c_t} = \frac{1}{h}\int_0^h \phi c_t dz \ . \tag{7.3.3}$$

Also recall that we showed for a small ω, the log-derivative of the flowing wellbore pressure could fall below the "correct" value before returning to the proper semilog slope. If superposition holds for the current cases, we should expect the buildup log-derivative of wellbore pressure with-respect-to equivalent time to also exhibit this behavior. Because the log-derivative will be less than the "correct" value, we should expect mobilities calculated using Eq. 7.3.1 to be greater than the true value of mobility existing in the reservoir. Figure 7.7 also shows the log-derivative for case WG-5D, which as you will recall is identical to case WG-5B except for the porosity in the gas cap was decreased to 0.01, resulting in a value of ω equal to 0.4566, more than an order of magnitude larger than for the other reservoir systems. Values of ω for the other cases are include in Table 7.3 discussed below. As a side note, we state that the sharp decline in the pressure derivative at the end of the buildup for case GW-5D is due to boundary effects; the decrease in the porosity in the gas cap has essentially reduced the time to boundary-dominated flow by an order of magnitude.

For each of the zero-skin cases, Table 7.3 shows the initial value of the thickness-averaged total mobility (output by simulator), the thickness-averaged total mobilities calculated using Eq. 7.3.1, and the percent deviation between the two. For this exercise, we utilized the minimum pressure derivative exhibited by each of the cases (near 0.1 days shut-in time) in the calculation of the thickness-averaged total mobilities. The results shown in Table 7.3 tend to support our conjecture concerning the effect of ω on our interpretation of where the semilog straight line begins (constant log-derivative of the shut-in pressure). That is, for small values of ω, the beginning time of the pseudoradial-flow semilog straight line

is delayed. This result was also reported by Ref. 19 for multilayer reservoirs. We also note that the percent deviations reported in Table 7.3 correlate extremely well with $1/\omega$. The implications of this result are not pursued further in this study, but rather, it is suggested that they be investigated in future work related to segregated multiphase reservoirs.

Table 7.4 contains a complete list of the calculated (Eq. 7.3.1) thickness-averaged total mobilities, the actual thickness-averaged total mobilities (viscosity evaluated at the wellbore shut-in pressure) and the percent deviation between the two. Here, we have used the log-derivative of the shut-in pressure at a shut-in time of approximately 5 days in our calculations. The reason for using the value of the derivative at this time follows from a close examination of the derivative data which indicates that for shut-in times greater that 5 days, the log-derivative of shut-in pressure begins to increase. As discussed in Chapter V, the reason for this increase is phase redistribution in the reservoir. The results shown in Table 7.4 indicate that Eq. 7.3.1 provides excellent approximations to the thickness-averaged total mobility, provided we are on the "correct" semilog straight line as discussed above.

7.4 Two-Phase Oil-Gas Systems

In this section we discuss the analysis of buildup pressure transient data for oil reservoirs overlain by a gas cap. Drawdown analysis for such systems was discussed in Section 6.4. A cross-sectional schematic of the various reservoir - gas cap configurations is show in Fig. 4.3. Fluid properties and other pertinent reservoir data for these cases are included in Tables 4.3A and 4.3B.

In our analysis of buildup pressure data for reservoir systems containing solution-gas and having been produced at a constant surface oil rate, we consider three different methods for calculating the total mobility in the reservoir and

Table 7.3

Buildup Semilog Analysis Results: Water-Gas Systems

Mobilities Affected by Small Values of ω

Case	ω	Simulator $\bar{\lambda}_t(p_i)$ (md/cp)	Calculated $\bar{\lambda}_t(p_{ws})$ (md/cp)	Percent Deviation
GW-3B	0.0220	239.31	305.80	27.79
GW-4B	0.0121	357.22	453.01	26.81
GW-45B	0.0099	402.59	508.84	26.39
GW-5B	0.0083	441.47	555.16	25.75

Table 7.4

Buildup Semilog Analysis Results: Water-Gas Systems

Case	Simulator $\bar{\lambda}_t(p_{ws})$ (md/cp)	Calculated $\bar{\lambda}_t$ (md/cp)	Percent Deviation
WG-1B	62.50	63.19	1.10
WG-2B	62.50	63.19	1.10
WG-2BS3	62.50	63.19	1.10
WG-2BS4	62.50	63.19	1.10
WG-3B	238.92	242.74	1.60
WG-3BS3	238.92	242.75	1.61
WG-3BS4	238.92	242.76	1.61
WG-4B	356.50	363.64	2.02
WG-4BS3	356.50	363.71	2.02
WG-4BS4	356.50	363.74	2.03
WG-45B	401.72	406.34	1.15
WG-5B	440.48	442.16	0.38
WG-5BS3	440.48	442.26	0.40
WG-5BS4	440.48	442.25	0.40

discuss the ramifications of each. Each of the methods considers the use of a different gas production rate in the calculation of the total mobility. The first method (Method 1) utilizes the gas flow rate at the instant of shut-in,

$$\bar{\lambda}_t = \frac{70.6[q_o B_o(p_{ws}) + q_{gf}(t_p) B_g(p_{ws})]}{hd\Delta p/d\ln t_e} \ , \tag{7.4.1}$$

the second method (Method 2) utilizes the producing gas-oil ratio, R, at the instant of shut-in,

$$\bar{\lambda}_t = \frac{70.6\{q_o B_o(p_{ws}) + q_o[R(t_p) - R_s(p_{ws})] B_g(p_{ws})]}{hd\Delta p/d\ln t_e} \tag{7.4.2}$$

and the third method (Method 3) utilizes the drawdown free gas production rate versus pressure relationship,

$$\bar{\lambda}_t = \frac{70.6[q_o B_o(p_{ws}) + q_{gf}(p_{ws}) B_g(p_{ws})]}{hd\Delta p/d\ln t_e} \ , \tag{7.4.3}$$

where here we have defined the free gas rate to be used in the buildup calculations as

$$q_{gf}(p_{ws}) = q_o[R(p_{wf}) - R_s(p_{wf})] \ , \tag{7.4.4}$$

for $p_{ws} = p_{wf}$; i.e., given a relationship between the producing gas-oil ratio and the flowing pressure (assumed measured during the drawdown), we determine the free gas rate to use in Eq. 7.4.3 by interpolating in this relationship at the current shut-in pressure and subtracting the solution gas-oil ratio at the current shut-in pressure. The thickness-averaged total mobility, $\bar{\lambda}_t$, is interpreted to be defined by

$$\bar{\lambda}_t = \frac{1}{h}\int_0^h \left(\frac{kk_{ro}}{\mu_o(p_{ws})} + \frac{kk_{rg}}{\mu_g(p_{ws})}\right) dz \tag{7.4.5}$$

and

$$\bar{\lambda}_t = \bar{\lambda}_o + \bar{\lambda}_g \ . \tag{7.4.6}$$

Consider now two solution-gas-drive reservoirs (cases OG-1B and OG-1BS4), identical in all respects save for a thin skin zone (s=10 for case OG-1BS4), being produced at a constant surface oil rate from a fully-penetrating well. Note for this case and all other cases with a positive skin considered in this study, the skin zone extends out to a radius of 0.54166 feet, meaning that the skin zone is approximately 0.29 feet thick. Because of the increased pressure drop at the well for the reservoir with the skin zone (case OG-1BS4),the gas saturation at the sandface will be higher and, therefore, the free gas production rate will be higher than for the undamaged reservoir. At the end of the drawdown period, the sandface gas saturation for case OG-1B is $S_g = 0.035$ and for case OG-1BS4 is $S_g = 0.054$. Correspondingly, the free gas production rate at the end of the drawdown period is $q_{gf} = 1.8 \times 10^3 \ scf/day$ for case OG-1B and $q_{gf} = 7.1 \times 10^3 \ scf/day$ for case OG-1BS4. At a small distance away from the wellbore, however, the pressure and saturation profiles during the drawdown are the same (see Fig. 7.8) for both reservoirs. If we were to use Eq. 7.4.1 (Method 1) to calculate the total mobilities in each reservoir (for which we obtain identical late time pressure derivatives), we would clearly obtain a higher mobility for the reservoir with the skin zone due to the higher free gas production rate at the instant of shut-in. This result clearly indicates a problem with the use of Eq. 7.4.1 to estimate the thickness-averaged total mobility; i.e., because a "steady-state" no-flow zone develops quickly near the sandface and because the actual total mobility in the outer region of the reservoir is the same for both cases, then a valid method for estimating the total mobility must give the same value for both cases. As we will show below, the converse of this statement is not necessarily true; i.e., that a method provides the same

calculated values for the mobilities for both of these reservoirs does not mean that the method is correct.

Figure 7.9 shows the total mobilities calculated using Eq. 7.4.1 for cases OG-1B and OG-1BS4. Also included on Fig. 7.9 are the total mobilities (with viscosities evaluated at the shut-in wellbore pressure) existing in the outer region of the reservoir for each case. These simulator values for the total mobility represent the largest values for the total mobility based on our interpretation of what mobilities we are actually calculating. Figure 7.9 reconfirms that the actual mobilities existing in the outer region of the reservoir are the same for the two cases. More importantly, however, are the following two facts: (i) the mobilities calculated by Eq. 7.4.1 (Method 1) differ significantly as discussed above, and (ii) at late time, the mobilities calculated by Eq. 7.4.1 are larger in magnitude than any mobility existing in the reservoir (for case OG-1BS4, significantly larger). These two facts suggest that Eq. 7.4.1 is not "theoretically" correct and should not be used. Thus, we searched for a method to improve the reliability of Eq. 7.4.1.

As pointed out by Ref. 133, the second method (Eq. 7.1.2) may give results that are clearly incorrect from a physical viewpoint. Consider, for example, the calculation of the gas phase mobility from the following equation:

$$\bar{\lambda}_g = \frac{70.6 q_o [R(t_p) - R_s(p_{ws})] B_g(p_{ws})]}{h \partial p_{ws} / \partial \log t_e} \ . \tag{7.4.7}$$

If the dissolved gas-oil ratio becomes greater than the producing gas-oil ratio at shut-in, Eq. 7.4.7 will give a negative gas mobility, a physical impossibility. In using this method to calculate mobilities, or rather, effective permeabilities, Ref. 36 simply sets the gas mobility (effective permeability) equal to zero whenever it is calculated to be negative (refer to this method as Method 2B). If we set $R(t_p) - R_s(p_{ws})$ to zero whenever it becomes negative, then computations shown

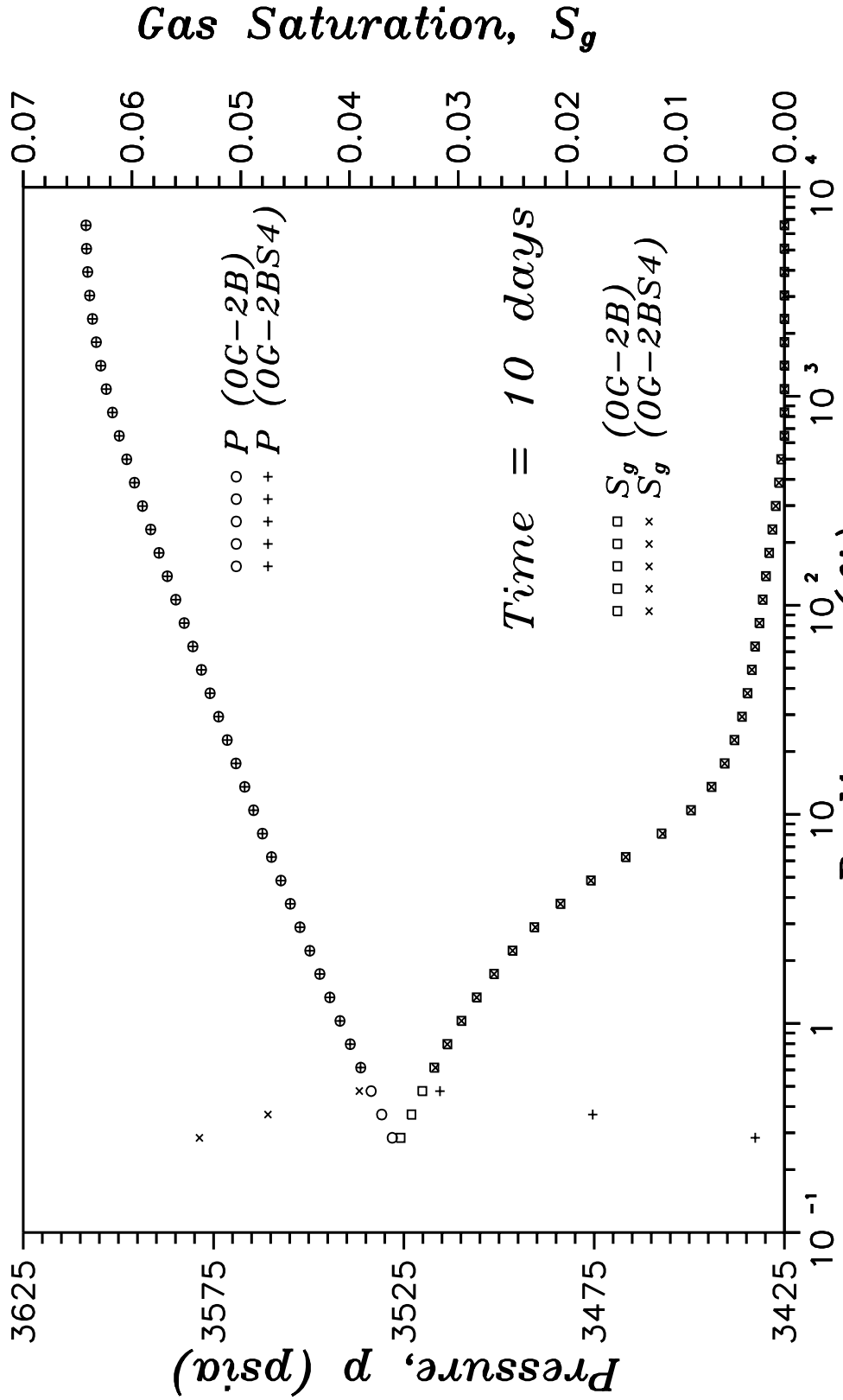

Fig. 7.8 – Comparison of radial pressure and saturation profiles for solution–gas systems with and without skin.

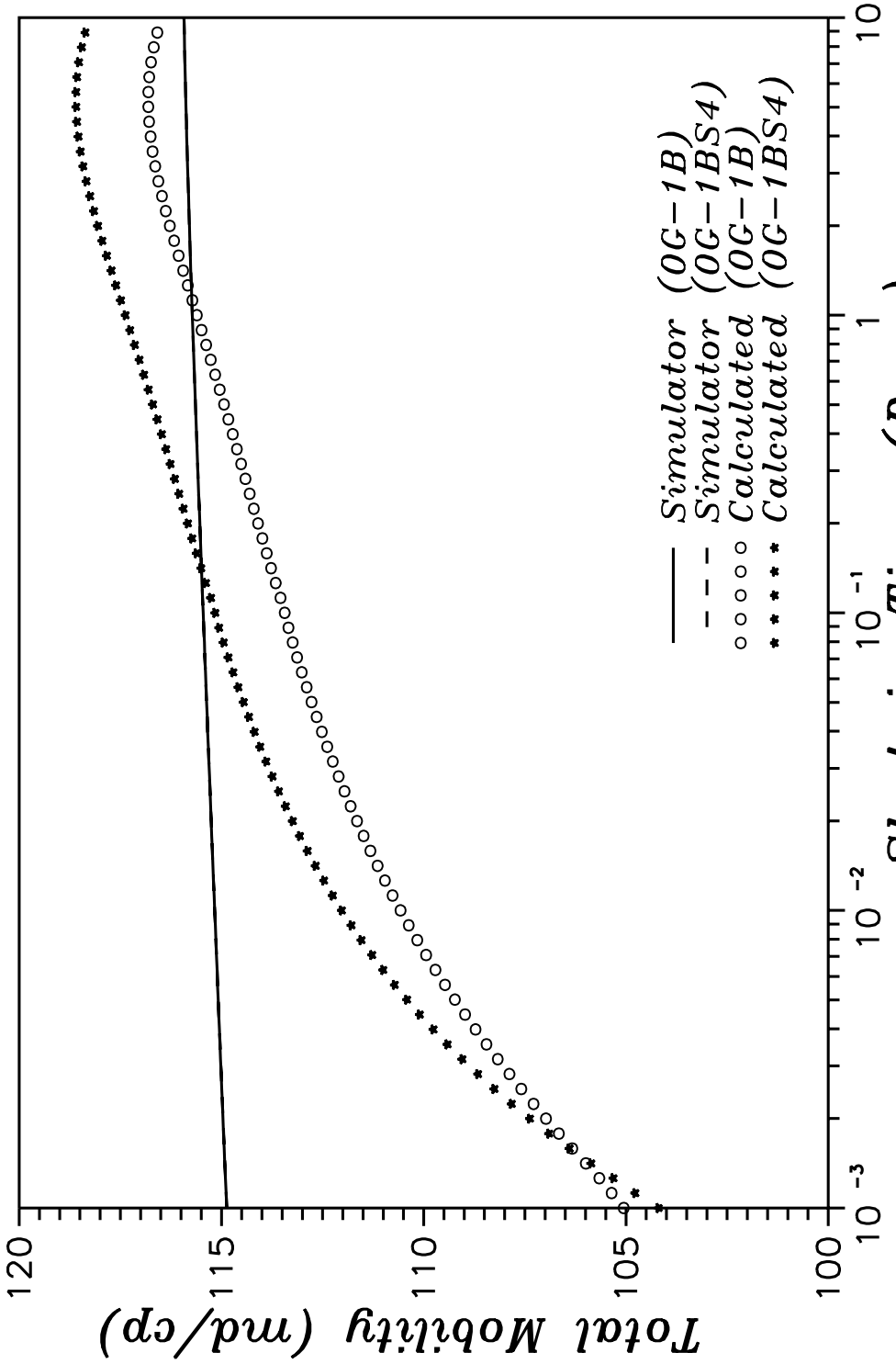

Fig. 7.9 – Comparison of actual and calculated total mobilties using Eq. 7.1.1.

below indicate Eqs. 7.4.2 and 7.4.3 provide nearly identical results. Prior to examining detailed calculations for all of the two-phase oil-gas cases investigated here, we examine the log-derivative of the shut-in wellbore pressure.

Figure 7.10 shows the log-derivative (with-respect-to equivalent time) of the shut-in wellbore pressure plotted as a function of shut-in time for these cases. There are several noteworthy items apparent on this plot; first, we note that a fairly well developed semilog straight line (constant derivative) suggestive of pseudoradial flow is apparent over at least a portion of the late-time data; second, we note there is an obvious "hump" during the transition period (beginning at approximately 0.02 days) in the derivative data for those cases with a gas cap; and third, we note the sharp rise in the derivative data at late time for cases OG-2B and OG-3B (cases with no gas cap, but including the effects of gravity). Each of these phenomena will be discussed in turn, beginning with the apparent pseudoradial flow period.

Table 7.5 contains the thickness-averaged total mobilities estimated by each of the methods discussed above, along with the "actual" thickness-averaged total mobility (at initial conditions) output by our simulator. Values of the calculated mobilities represent the maximum values calculated during the apparent pseudoradial flow period. Results shown in Table 7.5 clearly indicate the mobility calculated by Method 1 (Eq. 7.4.1) increases with increasing skin factor, and in general, these values are higher than the "actual" mobility in the reservoir. Results obtained using Methods 2, 2B and 3 are quite similar both in value and in they appear unaffected by changes in the skin factor. Note, however, the mobilities calculated using Method 2 (Eq. 7.4.2) are always less than the mobilities obtained from Method 3 (Eq. 7.4.3). As discussed above, this is due to negative gas mobilities obtained using the second method. If we set $R(t_p) - R_s(p_{ws})$ to

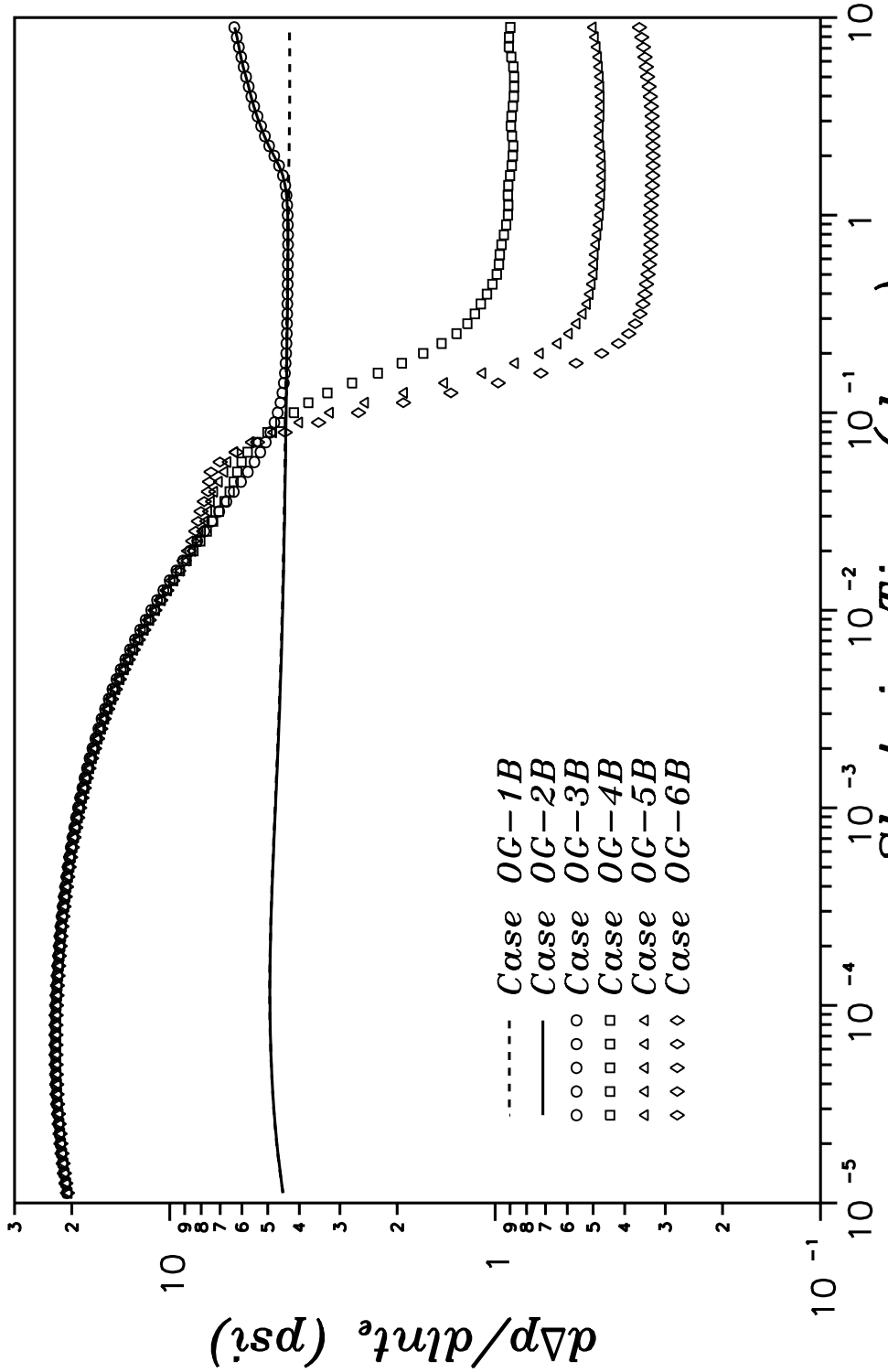

Fig. 7.10 — Diagnostic buildup pressure derivative plot (oil—gas).

zero in Eq. 7.4.2 whenever it becomes negative (Method 2B), then Eqs. 7.4.2 and 7.4.3 give nearly identical results.

Generally speaking, the results presented in Table 7.5 are quite good, with the deviation from the simulator values on the order of one percent for the non-gas cap cases and one to six percent for the gas cap cases. Some of this deviation can be attributed to the effects of gravity, i.e., phase redistribution in the reservoir as discussed in Chapter V. Recall from Chapter IV that we showed in the absence of capillary pressure, vertical equilibrium can exist in a multiphase reservoir only under the restricted conditions of equal phase densities or complete segregation of the phases. Recall also that vertical equilibrium, as well as a no-flow "steady-state" zone, are implicitly implied in all of the analysis methods presented in this study. Figure 7.11 shows in-situ fractional flow rates for both the oil and gas phases calculated from both the thickness-averaged total mobilities and the cross-sectional volumetric phase flow rates. Also shown in Fig. 7.11 is the normalized total mass rate defined by

$$q_{mt,\mathrm{norm}}(r,\Delta t) = \frac{q_{mt}(r,\Delta t)}{q_{mt}(r_w,t_p)} \ , \tag{7.4.8}$$

where q_{mt} is the cross-sectional mass rate. Figure 7.11 clearly shows the reservoir fluids in the region $400 \leq r \leq 4000\ ft$ to be approximately in vertical equilibrium. Note also that the "no-flow steady-state" zone has propagated out to a radius of $500\ ft$ (to within 5 percent). Under these conditions, we expect semilog analysis techniques to be approximately valid for these solution gas cases.

One is tempted to assume at later times during the buildup, the no-flow region will propagate out into the region exhibiting vertical equilibrium. Such is not the case, however, as both of these processes are dynamically linked to one another; i.e., as the radial flow component diminishes (no-flow zone propagates

Table 7.5

Buildup Semilog Analysis Results: Oil-Gas Systems

Thickness-Averaged Total Mobility

Case	Simulator $\bar{\lambda}_t(p_i)$ (md/cp)	Method 1 $\bar{\lambda}_t(p_{ws})$ (md/cp)	Method 2 $\bar{\lambda}_t(p_{ws})$ (md/cp)	Method 2B $\bar{\lambda}_t(p_{ws})$ (md/cp)	Method 3 $\bar{\lambda}_t(p_{ws})$ (md/cp)
OG-1B	116.01	116.81	115.43	116.19	116.19
OG-1BS3	116.01	117.86	115.43	116.19	116.19
OG-1BS4	116.01	118.60	115.43	116.19	116.19
OG-2B	116.01	115.41	114.13	114.80	114.80
OG-2BS3	116.01	116.27	114.13	114.80	114.80
OG-2BS4	116.01	117.17	114.13	114.80	114.80
OG-3B	116.01	118.19	114.05	114.83	114.83
OG-3BS3	116.01	122.39	114.04	114.82	114.83
OG-3BS4	116.01	126.89	114.03	114.82	114.83
OG-4B	485.50	468.83	452.80	455.74	455.74
OG-4BS3	485.50	485.60	452.99	455.94	455.96
OG-4BS4	485.50	503.87	453.55	456.42	456.45
OG-5B	731.86	721.07	696.64	700.97	700.97
OG-5BS3	731.86	746.82	696.91	701.25	701.27
OG-5BS4	731.86	774.82	697.55	701.90	701.95
OG-6B	907.86	894.76	864.52	869.84	869.84
OG-6BS3	907.86	927.30	865.39	870.73	870.77
OG-6BS4	907.86	961.89	866.04	871.38	871.45

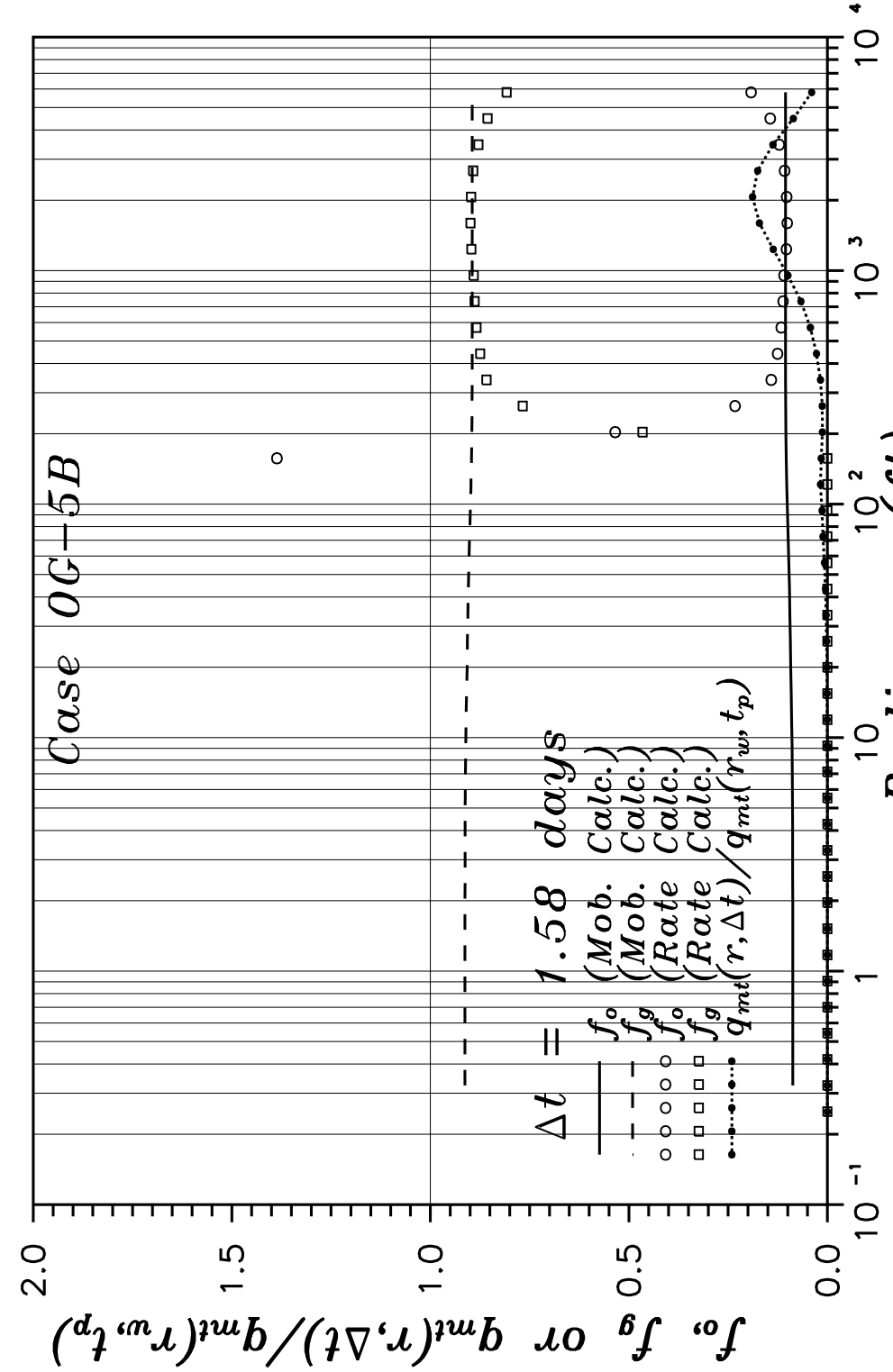

Fig. 7.11 — Comparison of fractional flow rates as an indicator of vertical equilibrium.

outwards), the vertical flow components begin to dominate and vertical equilibrium is lost. This is in keeping with our discussion in Chapter IV concerning the conditions required for vertical equilibrium to exist. Additional reasons for the deviation between the calculated and simulator values are discussed below.

Next, we examine the underlying causes of the sharp rise in the late-time derivative data for cases OG-2B and OG-3B. We note that neither case is overlain by a gas cap and gravity effects are included for all simulated cases except case OG-1B; i.e., for case OG-1B, only one vertical grid block was used. Because of the absence of gravity for case OG-1B, one is tempted to associate the sharp rise in the derivative for cases OG-2B and OG-3B to gravity effects, i.e., phase redistribution. Another difference exists between cases OG-1B and OG-2B, however, which we will show has much more to do with this phenomena. The initial pressure used for case OG-1B is $p_i = 3600.0001\ psia$ (just above the bubble-point pressure of $p_b = 3600\ psia$), whereas the initial pressure for case OG-2B varies from $3600.0001\ psia$ at the top of the reservoir to $3611.0916\ psia$ at the bottom of the reservoir. Case OG-1B was, therefore, rerun with an initial pressure of $3608.6741\ psia$ (the initial pressure at the wellbore datum depth of case OG-2B). Call this case OG-1C.

Figure 7.12 shows the log-derivative (w.r.t. equivalent time) of the shut-in wellbore pressure as a function of shut-in time for case OG-1C, along with the derivatives for cases OG-1B, OG-2B and OG-3B. Also included in Fig. 7.12 are results for cases OG-1C and OG-3B obtained from the commercial simulator, Eclipse[110]. Results obtained from the Eclipse simulator are included merely to verify this phenomena is not due to an error in the coding of our simulator.

Not only does Fig. 7.12 show an increase in the pressure derivative for case OG-1C, but the sharpness and magnitude of this increase were totally unexpected. The result of this experiment clearly indicates that the rise in the derivative at

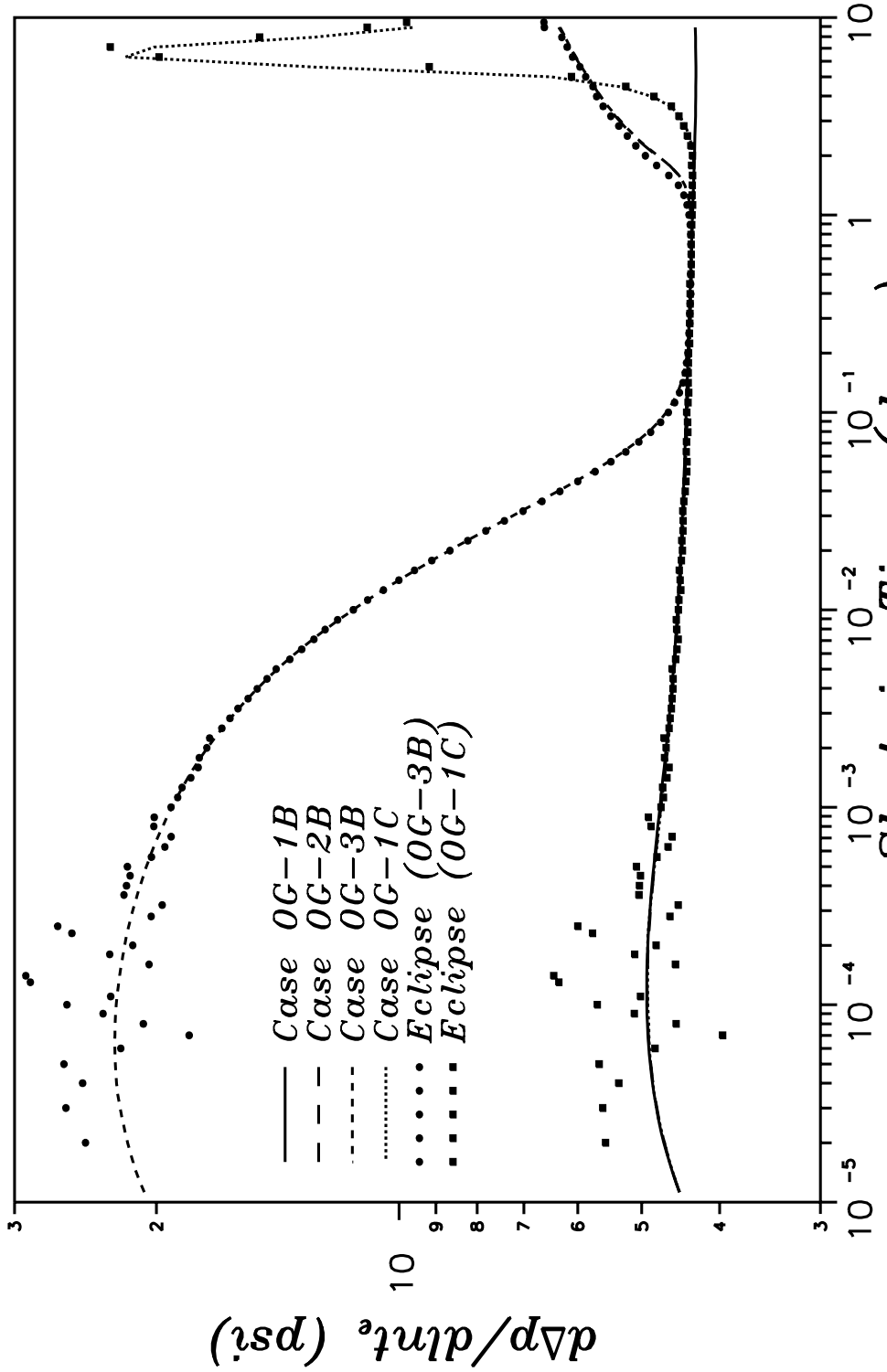

Fig. 7.12 – Effect of degree of undersaturation and comparison of results with Eclipse simulator.

late time is in some way related to the degree of undersaturation of the original reservoir system. One consequence of a higher degree of undersaturation is the fact that for the same pressure drawdown, less gas will evolve from solution. Less gas evolution also implies that changes in the bubble-point pressure for the reservoir fluids over the duration of the drawdown will probably be less. This result then implies that it will be much easier to collapse the free gas during the buildup period; i.e., redissolve a significant amount of the free gas existing at the instant of shut-in. While the collapse of the gas phase is the physical process occurring in the reservoir during the buildup, it is most likely the change in compressibility occurring with that collapse that is reflected in the pressure derivative.

Reference 101 made similar arguments concerning the complete redissolution of gas during a simulated pressure buildup test; i.e., an increase in the pressure derivative, followed by a decrease was due to collapse of the free gas saturation. Reference 35 later showed (again simulated data) that an increase in the pressure derivative may be possible if the pressure rises above the bubble-point pressure during the afterflow dominated flow period of the buildup. Reference 27 presented both simulated data and field data which exhibit an increase (followed by a decrease) in the pressure derivative. This increase in the pressure derivative was attributed to re-solution of some of the gas and a corresponding decrease in time in the overall fluid compressibility. Results presented by Ref. 27 were for a horizontal well in a solution gas reservoir overlain by a gas cap. Finally, Ref. 134 presented field data for a pressure buildup test in which this phenomenon of a sharply increasing pressure derivative, followed by a decline in the derivative is clearly visible in the pressure derivative data. Again, Ref. 134 attributed this phenomenon to the complete re-dissolution of the gas phase within the drainage area.

Reference 134 also history matched the field test with a simulator, which was then used to conduct a sensitivity study on the effect of the bubble-point pressure on the buildup test behavior. Though in their study the bubble-point pressure was varied, it is in fact the difference between the bubble-point pressure and the initial pressure which is of importance. Their sensitivity analysis showed that there is a limited range of saturation pressures and, therefore, degrees of undersaturation for which this phenomenon will occur, with the upper limit being those cases in which the wellbore pressure does not fall below the initial bubble-point pressure during the drawdown period. Though a lower limit was not mentioned, a reasonable assumption would be that the lower limit is slightly above the initial bubble-point pressure. That this is true follows if one considers a reservoir initially at the bubble-point pressure and produced for a period of time and shut in for a buildup test. Because the reservoir was initially at the bubble-point pressure, the entire region of the reservoir encompassed by the radius of investigation must be two phase (any drop in pressure will result in gas evolution). During the buildup test, fluids flow towards the lower pressure near the well, thus decreasing the pressure in the outer region of the reservoir, and, therefore, causing additional gas to evolve from the oil. In this manner, a reservoir initially at the bubble-point cannot redissolve all of the free gas during a buildup test, and the pressure derivative phenomenon discussed above will not be observed.

In light of the results of Ref. 134, well tests were simulated for five additional one-dimensional solution gas reservoir systems (cases OG-1D to OG-1H). While the initial bubble-point pressure was the same (3600 psia) for each of these cases, the initial reservoir pressure varied from $3600.0001 \leq p_i \leq 3660\ psia$. A one day drawdown test followed by a 10 day buildup test were simulated for each case. Figure 7.13 shows the logarithmic derivative (w.r.t. equivalent time) of the shut-in wellbore pressure, plotted as a function of shut-in time, for each of these cases

and Fig. 7.14 shows the wellbore shut-in pressure plotted as a function of shut-in time. Figure 7.13 shows that as the initial degree of undersaturation increases, the "hump" in the pressure derivative occurs earlier in time during the shut-in period and the magnitude of the disturbance is less. This makes intuitive sense; since for the more undersaturated systems less gas will evolve during the drawdown period and the two-phase region will be restricted to the near-wellbore region of the reservoir, re-dissolution of the gas phase should occur at earlier times. Note that results indicate that no two-phase grid block at the end of the drawdown period returns to single phase for case OG-1D.

The most probable explanation for the variation in the magnitude of the derivative "hump" is related to the volume of the reservoir affected by the collapse of the gas phase and the variation in the fluid compressibility which occurs when passing through the saturation pressure. Figure 7.15 is a crossplot of the radial extent of the two-phase region and the logarithmic pressure derivative, both plotted as a function of the shut-in time. Results shown in Fig. 7.15 clearly show a correlation between the start of the pressure derivative increase and the time at which the gas phase first collapses completely at the outer reaches of the two-phase region of the reservoir. These results provide strong support for the arguments presented above. Concerning the magnitude of the pressure derivative increase, we note that for case OG-1E, the gas phase collapses completely over a region of the reservoir encompassing a radius of approximately 250 feet ($5.5 \leq r \leq 260\ ft$). For case OG-1G, on the other hand, the gas phase collapse occurs only over a region of the reservoir encompassing a radius of approximately 10 feet ($2.5 \leq r \leq 12\ ft$). This means that the volume of the reservoir affected for case OG-1E is nearly 500 times that for case OG-1G. At the same time, however, we note that the majority of the gas collapse occurs over a 0.22 day time window for case OG-1E and only a 10^{-3} day time window for case OG-1G. If our speculation concerning the

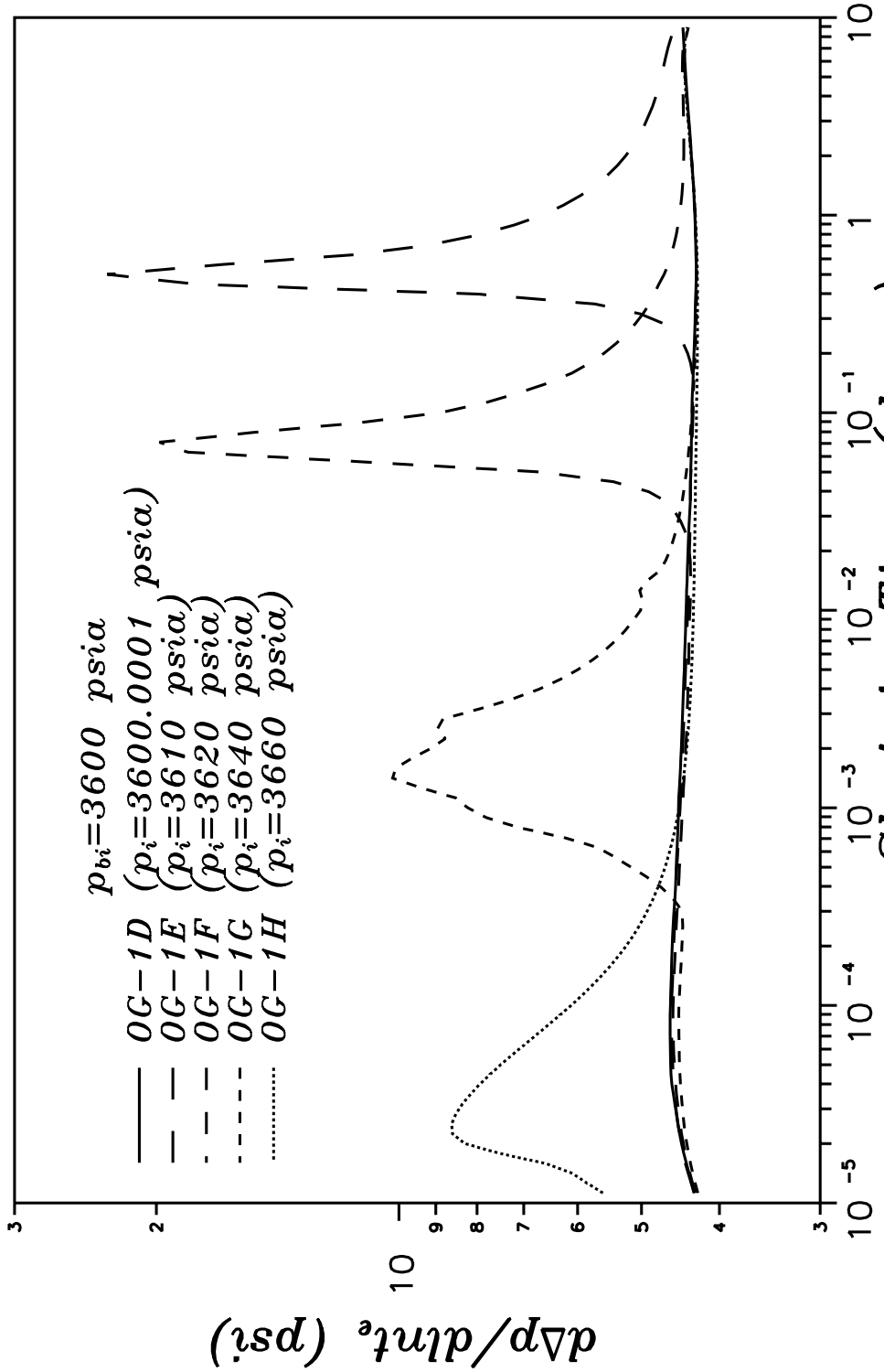

Fig. 7.13 — Effect of initial degree of undersaturation on buildup pressure derivative response.

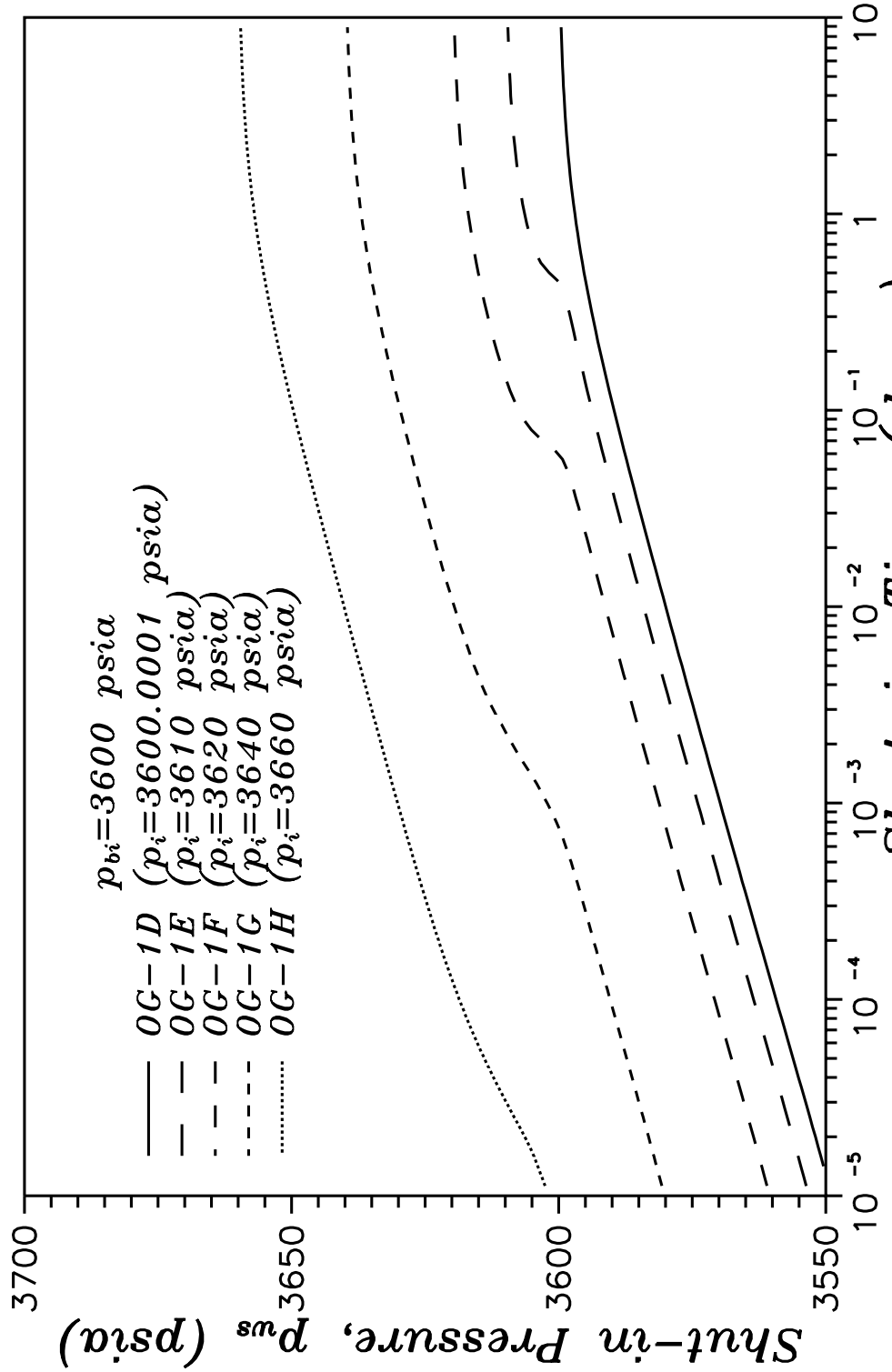

Fig. 7.14 – Effect of initial degree of undersaturation on buildup pressure response.

magnitude of the pressure derivative "hump" is true, then one might speculate that the magnitude of the increase is proportional to the volume of the reservoir affected divided by the time frame over which the gas phase collapses. Under this speculation, then one may naively postulate a relationship between the different cases as

$$\frac{d\Delta p}{d\ln t_e}\Big|_1 = \frac{V_1 \Delta t_2}{V_2 \Delta t_1}\frac{d\Delta p}{d\ln t_e}\Big|_2 \tag{7.4.9}$$

Using the numbers presented above for cases OG-1E and OG-1G in Eq. 7.4.9 results in

$$\frac{d\Delta p}{d\ln t_e}\Big|_{OG-1E} = 2.27\frac{d\Delta p}{d\ln t_e}\Big|_{OG-1G} \ . \tag{7.4.10}$$

For a naive speculation, Eq. 7.4.10 does a pretty good job of matching the actual results indicated by Figs. 7.13 through 7.15.

While the results and discussion presented above clearly indicate that the physical process occurring in the reservoir at the time corresponding to the "hump" in the pressure derivative is the collapse of the gas phase, the underlying connection between the pressure derivative and actual physical property changes which occur upon redissolution of the gas phase have not been addressed. We note that the gas saturation existing in that region of the reservoir which experiences complete collapse of the gas phase is quite small and there is an insignificant variation in the total mobility in that region as the gas phase collapses. This leaves the compressibility of the reservoir fluids and their variation as phase boundaries are crossed as the only physical properties which may be affecting the pressure derivative. As for changes in the fluid compressibility which occur when crossing a saturation pressure, Ref. 101 alluded to significant system compressibility decreases around and in the wellbore upon complete redissolution of the gas phase and how "the transient responses become sharper", apparently referring to the fact that a pressure transient will travel faster through a less compressible fluid,

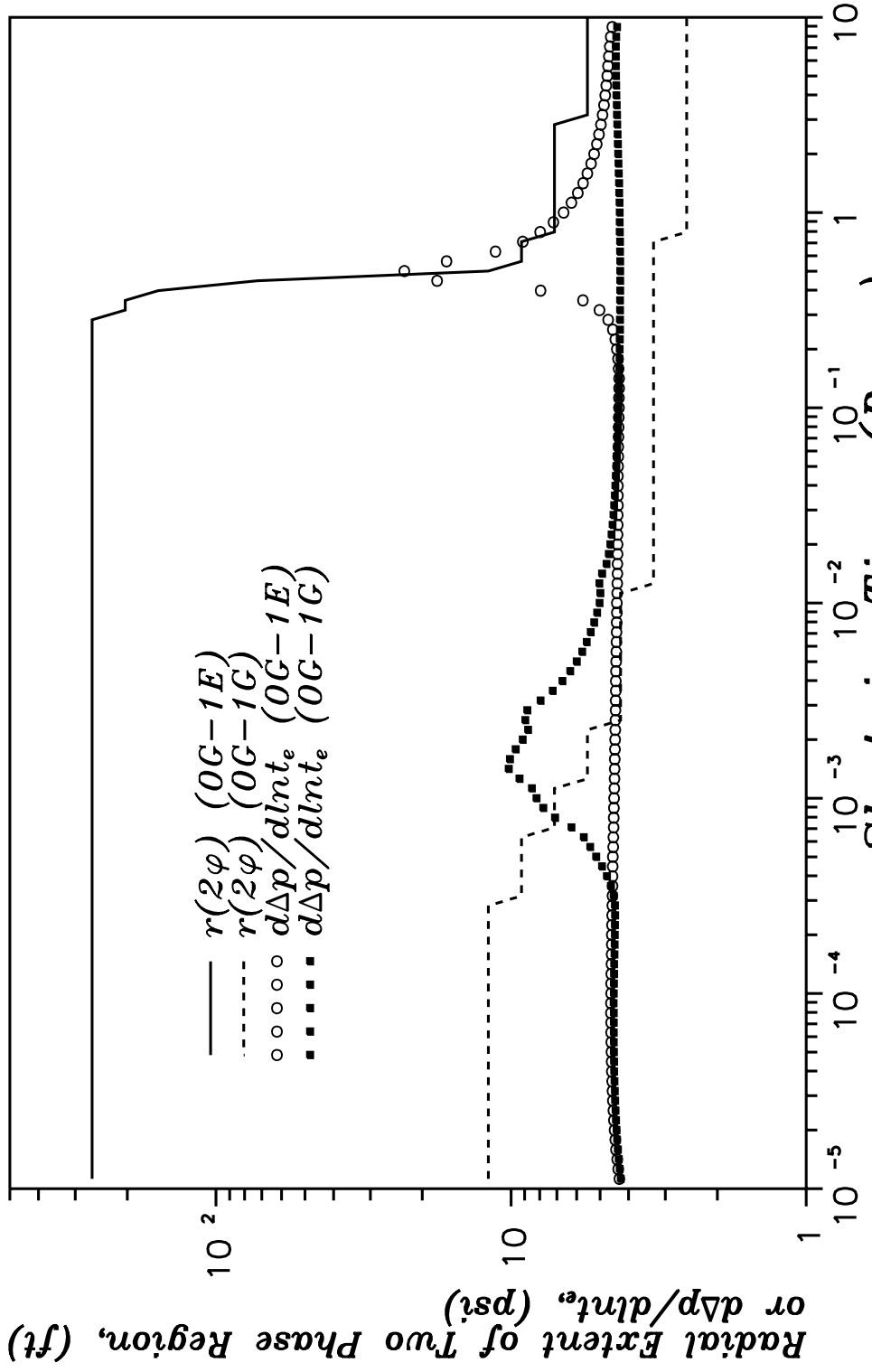

Fig. 7.15 – Comparison of two–phase region size and correlation of pressure derivative response with collapse of gas phase.

all other factors being the same. For all of the current cases, we note there also is a significant decrease in the system compressibility upon collapse of the gas saturation, although we note that a significant gas saturation remains in the near well region, with complete collapse of the gas saturation occurring predominately away from the wellbore.

The decrease in the fluid compressibility becomes apparent if we examine the formation volume factors utilized for the reservoir fluids considered in this study. Throughout this work, we have assumed the slope of the oil formation volume factor versus pressure relationship to be a constant above the bubble-point pressure, i.e.,

$$\frac{dB_o}{dp} = \text{constant} \ \ (RB/STB \cdot psia) \ , p \geq p_b \ . \tag{7.4.11}$$

Numerically, we have used a value of $dB_o/dp = 1.0 \times 10^{-5} \ (RB/STB \cdot psia)$ throughout. Above the bubble-point pressure, B_o represents the total system formation volume factor. Below the bubble-point pressure, there are several definitions available for defining the total system formation volume factor. One such definition is the differential total volume factor, defined by Ref. 135 as

$$B_{td} = B_{od} + R_{L,st}\frac{B_g}{5.615} \tag{7.4.12}$$

where, B_{td} is defined as the total volume factor at pressure p, B_{od} is the differential oil formation volume factor at pressure p, $R_{L,st}$ is the gas liberated by differential liberation from the bubble point pressure to the pressure p and B_g is the gas formation volume factor. Utilizing Eq. 7.4.12 and the physical properties presented in Chapter IV, we find that the slope of the total formation volume factor versus pressure relationship just below the bubble point pressure is $dB_{td}/dp = 1.002 \times 10^{-4} \ (RB/STB \cdot psia)$. This is an order of magnitude (10 times) greater than the slope above the bubble point. Because the total formation

volume factor and the oil formation volume factor must be equal at the bubble point, this implies that the total system compressibility is an order of magnitude less above the bubble point than below the bubble point; i.e., below the bubble point, we have

$$c_t = -\frac{1}{B_{td}}\frac{dB_{td}}{dp} \tag{7.4.13}$$

and above the bubble point

$$c_{tb} = -\frac{1}{B_o}\frac{dB_o}{dp} \ . \tag{7.4.14}$$

Solving Eqs. 7.4.13 and 7.4.14 for the formation volume factors and utilizing the fact that $B_t = B_o$ at the bubble point, we can equate the resulting equations to obtain

$$\frac{1}{c_t}\frac{dB_{td}}{dp} = \frac{1}{c_{tb}}\frac{dB_o}{dp} \ . \tag{7.4.15}$$

Finally, solving Eq. 7.4.15 for c_{tb}, we obtain

$$c_{tb} = c_t \frac{dB_o}{dp} \Big/ \frac{dB_{tb}}{dp} \ . \tag{7.4.16}$$

Substituting our values for dB_{td}/dp and dB_o/dp into Eq. 7.4.16 we obtain a compressibility above the bubble point of $c_{tb} = 0.0998 c_t$, a full order of magnitude less than the compressibility below the bubble point.

Clearly, such a dramatic change (discontinuity) in any physical property must have a significant effect on the wellbore pressure response observed during a well test. To investigate this phenomenon further, well tests were simulated for six additional one-dimensional solution gas reservoir systems (cases OG-1I to OG-1M). The initial pressure was the same (3608.7 psia) for each of these reservoir systems, as was the initial bubble point pressure (3600 psia). The only difference between the cases was a variation in the slope of the formation volume factor

versus pressure relationship above the bubble point pressure; i.e., dB_{td}/dp was varied over the range $5 \times 10^{-6} \leq dB_{td}/dp \leq 1 \times 10^{-4}\ RB/STB \cdot psia$. Figure 7.16 shows the logarithmic derivative (w.r.t. equivalent time) of the shut-in wellbore pressure as a function of shut-in time for each of these six cases. Based on the results presented in Fig. 7.16, we conclude that the effect of increasing the slope of the formation volume factor above the bubble point (compressibility of undersaturated oil increases) in relation to the slope of the total formation volume factor for the saturated fluids (compressibility of saturated oil and gas) is to reduce the magnitude of the "hump" in the pressure derivative data. In fact, when the slope of the undersaturated formation volume factor is set equal to the slope of the saturated total formation volume factor, the "hump" in the pressure derivative data disappears completely. Note that compressibility of an undersaturated oil is highly unlikely to ever come close to the total compressibility of it's associated saturated fluid system. In fact, according to Ref. 136, it is rare when the compressibility of an undersaturated oil is ever greater than $2.5 \times 10^{-5}\ psi^{-1}$. Calculations performed using the correlation of Ref. 137 for calculating the oil formation volume factor above the bubble point indicate a value of $2.2 \times 10^{-5}\ psi^{-1}$ would be obtained for the reservoir fluid properties utilized in this study, indicating again that the compressibility of the undersaturated system is approximately an order of magnitude less than the compressibility of the corresponding saturated system.

Concerning the "hump" observed in the pressure derivative during the transition period for those cases containing a gas cap (see cases OG-4B, OG-5B and OG-6B in Fig. 7.10), we note that it can be shown to result precisely for the same reasons (collapse of the free gas saturation and the resultant order of magnitude decrease in the system compressibility) as discussed above for the non-gas cap cases. During the drawdown, gas in the gas cap expands downward, displacing oil and helping to maintain the reservoir pressure. Because of this pressure maintenance, less gas is released from solution and the actual volume of the reservoir

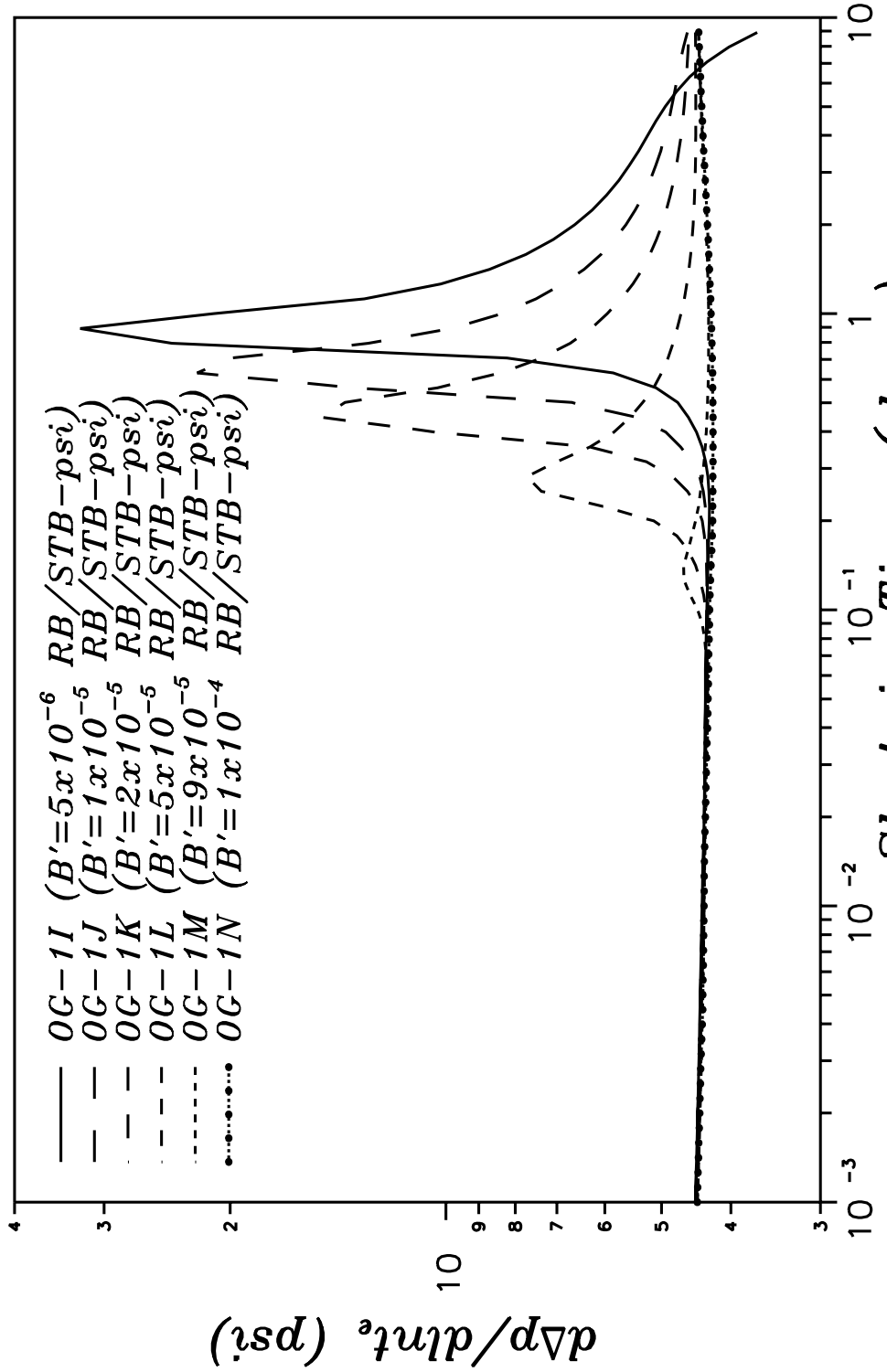

Fig. 7.16 – Effect of slope of oil formation volume factor versus pressure relationship on the pressure derivative response.

which drops below the bubble-point pressure during the drawdown is much less than the corresponding reservoir without a gas cap. Due to the decreased gas release, the bubble-point pressure also remains closer to the original bubble point. During the subsequent buildup period, then, the increase in the pressure required to completely collapse the gas phase in certain regions of the reservoir is smaller in magnitude and, therefore, occurs earlier in time.

Whereas the reservoir systems without a gas cap exhibited an increase in the derivative, the gas-cap cases mearly show a deflection in the derivative during the buildup. Most likely, this is a reflection of the fact that the total system compressibility is much higher for those cases with a gas cap and, therefore, the effect of the decrease in the compressibility during the buildup is less overall. As discussed previously, the volume of the two-phase region which converts back to single phase appears to also be related to the magnitude of "hump" in the derivative. Because the volume of the two-phase region which develops is smaller for the gas cap cases, we therefore expect the magnitude of the derivative "hump" to be smaller.

Note that the results discussed above concerning the collapse of the gas phase all imply that it may be possible to obtain reasonably accurate estimates of the in-situ bubble-point pressure from a pressure buildup test. For example, the wellbore pressure at the time at which the derivative "hump" first appears was at most 7 psi less than the original bubble-point pressure of the system. Examining the pressure derivative more closely, we find that the wellbore pressure at the time of the peak in the derivative "hump" for the one-dimensional systems investigated is extremely close (1-2 psi) to the original bubble-point pressure. At the time the derivative "hump" begins to decrease rapidly again for the restricted-entry cases, the wellbore pressure is again extremely close (1-2 psi) to the original bubble-point pressure. This possibility is not pursued further in this work, but it recommended

that field examples which exhibit the pressure derivative "hump" be obtained and analyzed in conjunction with the reported fluid properties for those reservoir.

Lastly, we comment on the apparent limited evidence (Refs. 27, 35, 101 and 134) supporting the above observations and interpretations concerning the pressure derivative "hump". First, we note that most publications in the literature dealing with well test analysis for solution-gas reservoir systems only consider reservoir systems initially at the bubble point pressure. As shown above, the "hump" in the derivative data will not be seen for such cases. Second, we note that for initially slightly undersaturated reservoir systems, the phenomenon occurs quite early during the buildup test and, therefore, may be masked by wellbore storage and skin effects. Third, we note that buildup tests are generally of short duration in comparison to the total production time. This, then, may result in insufficient time for the pressure to build up enough to completely collapse a significant amount of gas in the reservoir. Fourth, Ref. 101 cites several studies concerning supersaturation in porous media, as well as one reference concerning residual solubility hysteresis[137]. The results of Ref. 137 indicate that because of capillary pressure phenomenon, there is a residual solubility hysteresis in porous media; i.e., some of the gas will never dissolve during reservoir repressurization. If some of the gas will never re-dissolve during repressurization, then there is a question concerning how the system compressibility will be affected during a buildup test in which the reservoir pressure increases above the initial bubble-point pressure. The field data presented by Refs. 27 and 134 appear to suggest that either (i) not all porous media will experience this hysteresis effect, or (ii) that the compressibility changes occur in spite of the hysteresis effect. Surely, other possible reasons exist for the limited amount of field data exhibiting the phenomenon discussed above. To this end, we note other operating parameters have not been investigated fully and include such items as the effect of the production rate, oil gravity, solution gas-oil

ratio and gas gravity, among others. Further investigation of these or additional parameters is beyond the scope of this work and are recommended for future study.

7.5 Three-Phase Oil-Gas-Water Systems

This section concerns itself with the analysis of buildup pressure transient data obtained from a restricted-entry well in a three-phase reservoir (oil reservoir overlain by a gas cap and underlain by an aquifer). Analysis of drawdown pressure transient data for these systems was discussed in Section 6.5. A cross-sectional schematic of the reservoir with initial saturation profiles is shown in Fig. 4.5. Fluid properties and other pertinent reservoir data for these cases are included in Tables 4.5A and 4.5B. A 70 foot oil zone is considered with gas caps ranging in size from 0-30 feet and aquifers ranging in size from 0-50 feet. The well is completed only over the center 10 feet of the oil zone.

In the previous section, four different methods (three methods and one variant) were considered for calculating the thickness-averaged total mobility for two-phase, oil-gas, reservoir systems. Theoretical and physical arguments, supported by numerical results, indicated that only two of these methods provide results which did not violate the fundamental physics of the problem, or our understanding of those physics. Because the arguments presented in the previous section are generally applicable to any reservoir system containing solution-gas, we suspect that they should also hold for the three-phase reservoir systems considered here. In fact, numerical results which will not be presented show exactly that.

Based on the results of the previous section and the results discussed above, we only consider two methods here. As before, we note that the difference in these methods results from the use of a different gas production rate in the calculation of the thickness-averaged total mobility. The first method we consider is the variant

of the second method considered in the previous section (Method 2B). Recall that this method utilizes the producing gas-oil ratio, R, at the instant of shut-in, except we set $R(t_p) - R_s(p_{ws})$ to zero whenever it becomes negative. Modified to include water, Method 2B becomes

$$\bar{\lambda}_t = \frac{70.6\{q_o B_o(p_{ws}) + q_o[R(t_p) - R_s(p_{ws})]B_g(p_{ws}) + q_w B_w(p_{ws})\}}{hd\Delta p/d\ln t_e} \quad . \tag{7.5.1}$$

Method 3, which utilizes the drawdown free gas production rate versus pressure relationship, can be expressed as

$$\bar{\lambda}_t = \frac{70.6[q_o B_o(p_{ws}) + q_{gf}(p_{ws})B_g(p_{ws}) + q_w B_w(p_{ws})]}{hd\Delta p/d\ln t_e} \ , \tag{7.5.2}$$

Recall that $q_{gf}(p_{ws})$ is defined as

$$q_{gf}(p_{ws}) = q_o[R(p_{wf}) - R_s(p_{wf})] \ , \tag{7.5.3}$$

for $p_{wf} = p_{ws}$. For each of the three-phase reservoir systems considered, the thickness-averaged total mobility, $\bar{\lambda}_t$, is interpreted to be defined by

$$\bar{\lambda}_t = \frac{1}{h}\int_0^h \left(\frac{kk_{ro}}{\mu_o(p_{ws})} + \frac{kk_{rg}}{\mu_g(p_{ws})} + \frac{kk_{rw}}{\mu_w(p_{ws})}\right)dz \tag{7.5.4}$$

or, alternatively,

$$\bar{\lambda}_t = \bar{\lambda}_o + \bar{\lambda}_g + \bar{\lambda}_w \ . \tag{7.5.5}$$

Equation 7.5.4 states that we interpret the mobilites calculated formally using Eqs. 7.5.1 or 7.5.2 as representing the thickness-averaged total mobilities in the outer region of the reservoir with the effective phase permeabilities being evaluated at that location and the phase viscosities evaluated at the prevailing shut-in wellbore pressure. Prior to discussing the results of calculations performed using Eqs. 7.5.1

and 7.5.2, we examine the buildup pressure derivatives obtained for each of the simulated well tests.

The log-derivatives (with-respect-to equivalent time) of the shut-in wellbore pressures plotted as a function of shut-in time are shown if Fig. 7.17 for each of the zero-skin, three-phase cases considered. Similar to the gas cap cases discussed in the previous section, those cases with a gas cap (all except cases OGW and OGW2), all show a distinctive "hump" in the derivative during the middle-time or transition region of the diagnostic plot. As discussed in the previous section, this "hump" in the derivative is a result of the complete collapse of the gas phase and the corresponding step decline in the total fluid compressibility over some region of the reservoir. Note that at late time, all of the cases except case OGW exhibit rather well defined semilog straight lines (constant derivatives). Cases OGW and OGW2 are discussed later in this section. As would be expected, an increase in the gas cap thickness results in a much larger decline in the pressure derivative than does an equal thickness increase in the size of the aquifer; e.g., compare the difference in the derivative between cases OGWAA and OGWAB and compare the difference in the derivative between cases OGWAA and OGWBA.

Table 7.6 contains the thickness-averaged total mobilities calculated from pseudoradial flow buildup pressure data using each of Eqs. 7.5.1 and 7.5.2 along with the "actual" thickness-averaged total mobility output by our simulator for each of the three-phase reservoir systems investigated. Note that the simulator values of the thickness-averaged total mobility reported are at the initial reservoir conditions. Because fairly well defined late-time semilog straight lines are apparent for each of the cases, an average of the log-derivative over the time frame $1.0 \leq \Delta t \leq 10.0$ days was used in all calculations for each of the cases. The percent deviation of the calculated thickness-averaged total mobility from the true value is also reported. Note that even though the water production rate is included in

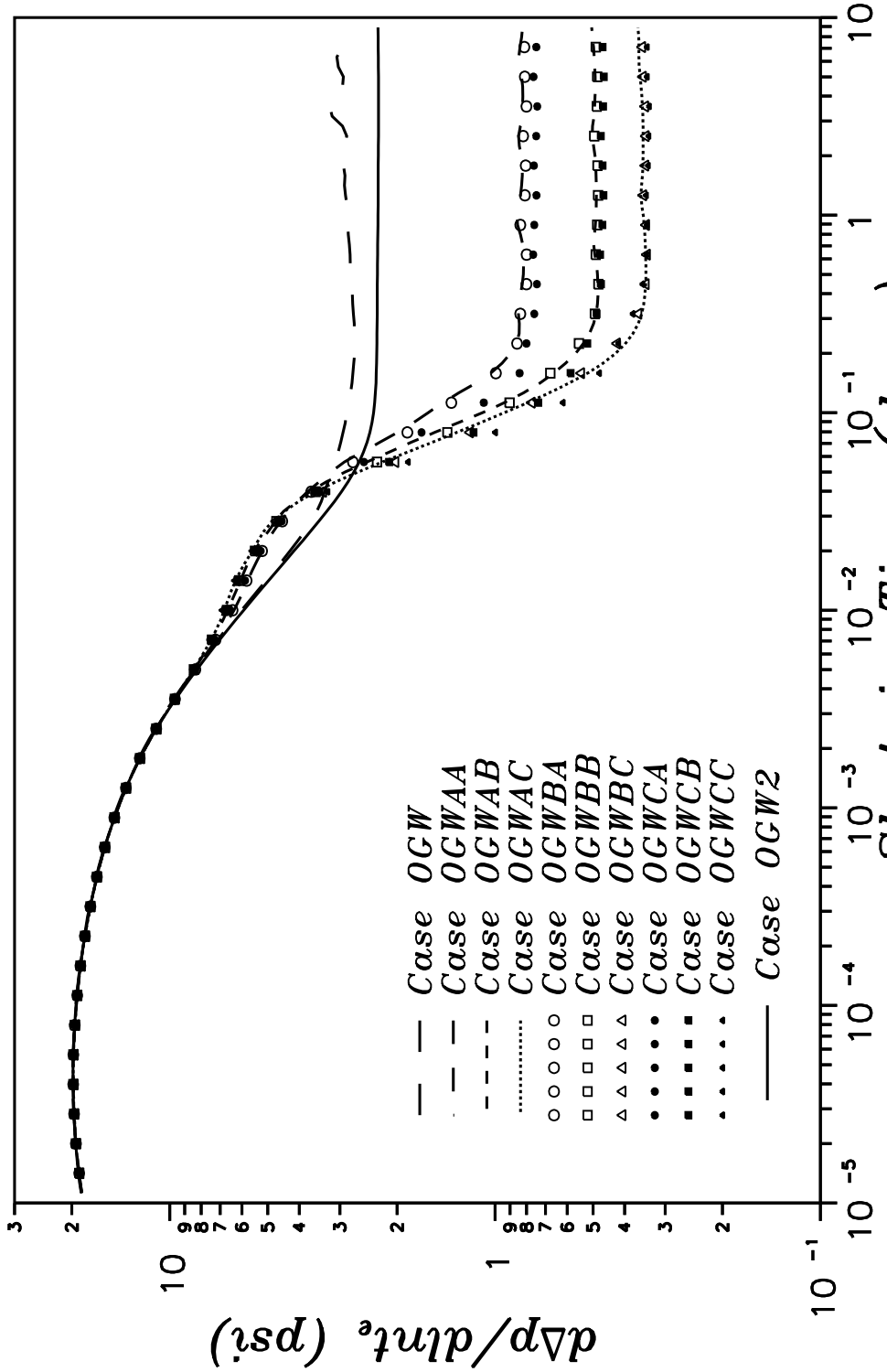

Fig. 7.17 — Diagnostic buildup pressure derivative plot (oil–gas–water).

Eq. Eqs. 7.5.1 and 7.5.2, no water was produced in any of the cases considered. Even though no water is produced at the well, water may have a non-zero mobility in the outer part of the reservoir and we hope Eqs. 7.5.1 and 7.5.2 provide an approximation to the three-phase thickness-averaged total mobility given by Eq. 7.5.5. Results shown in Table 7.6 show that Eq. 7.5.1, modified to set $R(t_p) - R_s(p_{ws})$ to zero whenever it becomes negative, provides nearly identical estimates for the thickness-averaged total mobilities as those obtained from Eq. 7.5.2. In general, the thickness-averaged total mobilities obtained from either Eq. 7.5.1 or 7.5.2 are in excellent agreement with the "actual" values obtained from our simulator. The large error in the estimated thickness-averaged total mobilities for cases OGW, OGWS3 and OGWS4 are discussed later.

Though difficult to make a definitive statement, it appears there is a general trend to more accurate approximations to the thickness-averaged total mobility as the thickness of either the gas cap or the aquifer increases. That the accuracy improves as the thickness of the aquifer increases makes sense in that the total mobility in the water zone is invariant (a constant). Addition of a larger aquifer, then, implies that the "linearity" of the problem should also increase, thereby increasing the theoretical validity of Eqs. 7.5.1 and 7.5.2. As discussed earlier, presence of a gas cap (or increased size of a gas cap) tends to help maintain the reservoir pressure, thereby reducing the amount of gas coming out of solution during drawdown and the resultant problems which arise when the gas redissolves during the buildup; i.e., the step change in the total compressibility when the gas phase completely collapses. Another effect of the reduced amount of free gas is that the effects of phase redistribution are also reduced during the buildup.

The poor estimate obtained for the thickness-averaged total mobility for case OGW is readily explained based on the results of the previous section and the discussions presented above. First, we note that the oil reservoir for case

Table 7.6

Buildup Semilog Analysis Results: Oil-Gas-Water Systems

Case	Simulator $\bar{\lambda}_t$ (md/cp)	Method 2B $\bar{\lambda}_t$ (md/cp)	Method 3 $\bar{\lambda}_t$ (md/cp)	Percent Deviation
OGW	123.17	96.29	96.29	21.8
OGWS3	123.17	96.29	96.29	21.8
OGWS4	123.17	96.30	96.30	21.8
OGW2	123.17	124.48	124.48	-1.1
OGWAA	275.83	265.26	265.26	3.8
OGWAAS3	275.83	265.29	265.29	3.8
OGWAAS4	275.83	265.42	265.43	3.8
OGWAB	404.06	402.94	402.94	0.3
OGWABS3	404.06	403.01	403.01	0.3
OGWABS4	404.06	403.35	403.35	0.2
OGWAC	508.99	510.61	510.61	-0.3
OGWACS3	508.99	510.72	510.73	-0.3
OGWACS4	508.99	511.33	511.35	-0.5
OGWBA	254.46	245.30	245.30	3.6
OGWBAS3	254.46	245.33	245.34	3.6
OGWBAS4	254.46	245.46	245.47	3.5
OGWBB	372.98	371.51	371.51	0.4
OGWBBS3	372.98	371.58	371.59	0.4
OGWBBS4	372.98	371.90	371.92	0.3
OGWBC	471.76	472.51	472.51	-0.2
OGWBCS3	471.76	472.61	472.62	-0.2
OGWBCS4	471.76	473.20	473.21	-0.3
OGWCA	210.09	204.19	204.21	2.8
OGWCAS3	210.09	204.21	204.22	2.8
OGWCAS4	210.09	204.33	204.33	2.7
OGWCB	306.38	304.58	304.58	0.6
OGWCBS3	306.38	304.65	304.65	0.6
OGWCBS4	306.38	304.93	304.95	0.5
OGWCC	389.85	388.91	388.91	0.2
OGWCCS3	389.85	389.00	389.00	0.2
OGWCCS4	389.85	389.49	389.51	0.1

OGW is neither overlain by a gas cap nor underlain by an aquifer. Results not shown indicate that the volume of the reservoir that falls below the bubble-point presure during the drawdown is much larger for this case than for those cases in which a gas cap or aquifer exist. As per our arguments in the previous section and again above, a large fraction of this volume undergoes a complete collapse of the gas phase during the ensuing buildup period with a corresponding decrease in the total fluid compressibility in that region. To show this more conclusively, an example identical in all respects to case OGW except the value of dB_o/dp above the bubble point was increased to 1.0×10^{-4} $(RB/STB \cdot psia)$ from the original 1.0×10^{-5} $(RB/STB \cdot psia)$ was run and the results compared. Figure 7.16 shows that case OGW2 exhibits a substantially better semilog straight line than does case OGW. The results in Table 7.6 also show that mobility estimates obtained for case OGW2 are substantially more accurate; differing by a mere 1.1 percent as compared to the 21.8 percent deviation for case OGW.

Lastly, we examine the underlying assumptions (vertical equilibrium and existence of a no-flow "steady-state" zone) incorporated in Eqs. 7.5.1 and 7.5.2 to ascertain their validity for the three-phase reservoir systems investigated. Figure 7.18 shows in-situ fractional flow rates for each of the three phases (oil, gas and water) calculated from both the thickness-averaged total mobilities and the cross-sectional volumetric phase flow rates output by our simulator. Also shown in Fig. 7.18 is the normalized total mass rate defined by

$$q_{mt,\mathrm{norm}}(r, \Delta t) = \frac{q_{mt}(r, \Delta t)}{q_{mt}(r_w, t_p)} \ , \tag{7.5.6}$$

where q_{mt} is the cross-sectional total mass rate. Figure 7.18 shows that at a shut-in time of 1 day, vertical equilibrium approximately exists in the region $400 \leq r \leq 2000$ ft of the reservoir. The "steady-state" region of the reservoir, on the other hand, extends only out to a radius of 300 feet (to approximately 5 percent); at

$r = 400\ ft$, the total mass rate is approximately 12 percent that of the producing mass rate at the instant of shut-in. Based on these results, one might expect our calculated thickness-averaged total mobilities to be more in error than they are.

To understand why our results are not more in error, we briefly examine the work of Ref. 145. Oliver[145] presented a single-phase perturbation solution to the diffusion equation for the case of a well situated in an infinite reservoir where the permeability was an arbitrary function of radial position. The most important aspect of Oliver's solution is that it provided an explicit weighting or kernel function defining how the permeabilities are averaged to obtain the observed pressure response. Reference 145 noted that 98 percent of the permeability contribution to the wellbore pressure response comes from within the radii $0.12\sqrt{t_D} \leq r_D \leq 2.34\sqrt{t_D}$. This means that permeabilities at radii greater than $2.34\sqrt{t_D}$ and less than $0.12\sqrt{t_D}$ add essentially no contribution to the average permeability. This also means that the region (volume) of the reservoir affecting the pressure response grows with time and moves out into the reservoir with time. If we assume the pressure response for our problem similarly reflects the properties of the reservoir (and fluids) over some volume of the reservoir which expands with time and moves out into the reservoir with time, then we can visualize that if the non-vertical equilibrium exists only over the inner part of this volume, then its effect on the total pressure response should be small as it will be averaged with the rest of the volume which exists under conditions of vertical equilibrium. For example: just for the sake of argument, suppose Oliver's kernel function were directly applicable to our current problem. Furthermore, let us suppose that the radial extent of the no-flow steady-state zone represents the inner radii for which the kernel function indicates some contribution is being made to the pressure response; i.e., $r_D = 0.12\sqrt{t_D}$ corresponds to the radius of 300 feet where we have approximately achieved a "steady-state" zone. Under these conditions, the radius

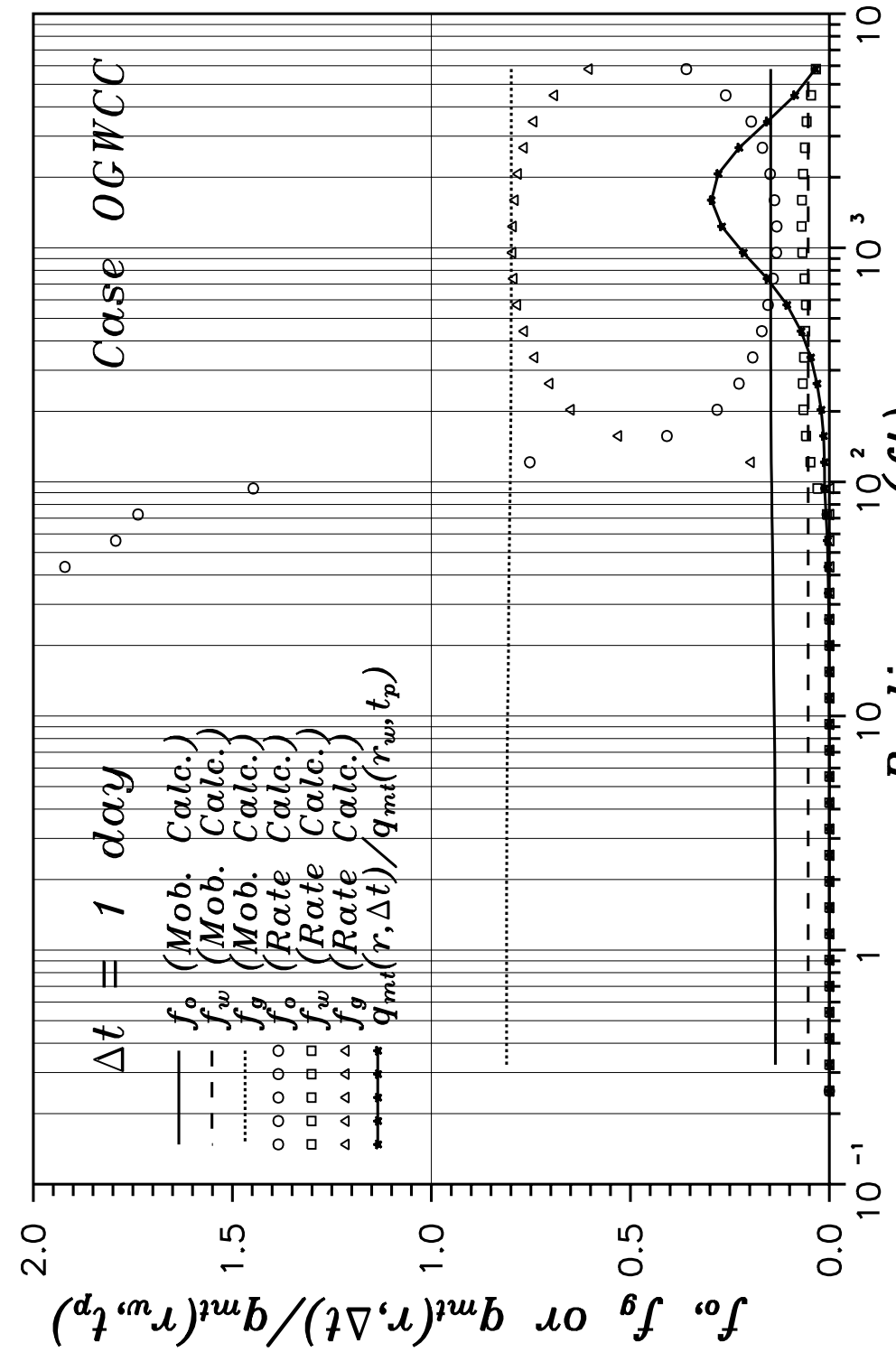

Fig. 7.18 — Comparison of fractional flow rates as an indicator of vertical equilibrium.

where vertical equilibrium exists ($r = 400$ feet) would correspond to a dimensionless radius equal to $r_D = 0.16\sqrt{t_D}$. Under these conditions it becomes clear that the vast majority of the contribution to the pressure response is due to that part of the reservoir under vertical equilibrium.

7.6 Summary

In this chapter we have investigated the applicability of semilog analysis techniques to buildup pressure transient data obtained from a restricted-entry well previously produced under a constant rate and multiphase flow conditions. The same extensive array of two-phase and three-phase reservoirs systems investigated in Chapter VI were used.

The buildup pressure data for nearly all of the cases examined in this chapter exhibited approximate semilog straight lines indicative of pseudoradial flow in the reservoir. This result also supports our conclusions in Chapter V concerning the fact that the common practice of approximating a gas cap or aquifer as a constant pressure boundary cannot be justified.

For nearly all of the cases examined, including those cases in which the drawdown pressure data was uninterpretable, standard Horner analysis of the pseudoradial flow pressure buildup data provided an excellent approximation to the thickness-averaged total mobility in the outer region of the reservoir. For each of the reservoir systems, a thickness-averaged total mobility was formally calculated using the following equation:

$$\bar{\lambda}_t = \frac{70.6(q_o B_o(p_{ws}) + q_w B_w(p_{ws}) + q_{gf}(p_{ws}) B_g(p_{ws}))}{hd\Delta p/d\ln t_e} \,, \tag{7.6.1}$$

where the total mobility $\bar{\lambda}_t$ was interpreted to be

$$\bar{\lambda}_t = \frac{1}{h}\int_0^h \left(\frac{kk_{ro}}{\mu_o(p_{ws})} + \frac{kk_{rg}}{\mu_g(p_{ws})} + \frac{kk_{rw}}{\mu_w(p_{ws})}\right) dz \tag{7.6.2}$$

and kk_{ro}, kk_{rg} and kk_{rw} correspond to the region in the outer part of the reservoir where pseudoradial flow exists, but viscosities are evaluated at the wellbore shut-in pressure. In Eq. 7.6.1, equivalent time, t_e is defined as

$$t_e = \frac{t_p \Delta t}{t_p + \Delta t} \ , \tag{7.6.3}$$

Δp is defined as

$$\Delta p = p_{ws} - p_{wf,s} \ , \tag{7.6.4}$$

p_{ws} is the shut-in wellbore pressure and $p_{wf,s}$ is the flowing wellbore pressure at the instant of shut-in.

For the two-phase gas-water systems investigated, an alternative Horner time ratio based on a shut-in pseudotime was also considered, where an equivalent-pseudotime, t_{ae}, was defined as

$$t_{ae} = \frac{t_p \Delta t_a}{t_p + \Delta t} \ , \tag{7.6.5}$$

with pseudo-shut-in time defined by

$$\Delta t_a = \int_0^{\Delta t} \frac{dt}{\mu_g c_t} \ . \tag{7.6.6}$$

Equation 7.6.1 was then used with t_e replaced by t_{ae}. In a practical sense, there was little difference between the mobilities calculated using Eq. 7.6.1 with either t_e or t_{ae}. Note that the mobilities calculated using Eq. 7.6.1 were in excellent agreement with the "actual" mobilities input into the simulator. This result was in spite of the fact that production during the drawdown period was purposely set to an extremely high rate to insure a large pressure change during the simulated well test; i.e., conditions under which analysis based on a real gas pseudopressure is usually recommended for single phase gas reservoirs.

As in the previous chapter, pressure transient data was analyzed for several water reservoirs overlain by a gas cap due to the similarity to an oil reservoir overlain by a gas cap (without the complications of mass transfer between the phases) and in hopes of identifying parameters contributing to the pressure transient behavior. Similar to the drawdown behavior for such systems, the buildup pressure transient data exhibited a slightly increasing log-derivative of the shut-in pressure. It was shown that this increasing derivative was related to ω, the ratio of the porosity-compressibility product of the open interval divided by the thickness-averaged value, where

$$\omega = \frac{\phi_1 c_{t1} h_1}{\overline{\phi c_t} h} \tag{7.6.7}$$

and

$$\overline{\phi c_t} = \frac{1}{h} \int_0^h \phi c_t dz \ . \tag{7.6.8}$$

Also similar to the drawdown, we showed for a small ω, the log-derivative of the shut-in wellbore pressure could fall below the "correct" value before returning to the proper semilog slope.

For reservoir systems containing solution gas, four different methods for estimating the thickness-averaged total mobility were considered, differing only in the gas production rate utilized in Eq. 7.6.1. The first method utilized the gas flow rate at the instant of shut-in, $q_{gf}(t_p)$. This method was shown to be theoretically inconsistent with the actual physics of the problem; i.e., the methods results in predicted mobilities significantly greater than ever exists in the reservoir. The second method utilized the producing gas-oil ratio, R, at the instant of shut-in; i.e.,

$$q_{gf}(p_{ws}) = q_o[R(t_p) - R_s(p_{ws})] \ . \tag{7.6.9}$$

This method was also shown to fail in instances when the solution gas-oil ratio becomes greater than the producing gas-oil ratio at the instant of shut-in; by Eq. 7.6.9, this situation indicates a negative gas flow rate. An alternative to this method was also considered where the free gas production rate predicted by Eq. 7.6.9 was simply set equal to zero whenever it became negative. Results for the thickness-averaged total mobility then became nearly identical to the results obtained from the fourth method. The forth method utilized the drawdown free gas production rate versus pressure relationship; i.e.,

$$q_{gf}(p_{ws}) = q_o[R(p_{wf}) - R_s(p_{wf})] \ , \tag{7.6.9}$$

for $p_{wf} = p_{ws}$; i.e., the free gas rate utilized in the mobility calculations is an interpolated value from the measured drawdown free gas rate - wellbore pressure relationship. Results obtained for the thickness-averaged total mobilities using these methods were generally quite good.

For solution-gas reservoir systems initially above the bubble-point pressure, we have shown that a sharp increase in the pressure derivative may appear for fully-penetrating reservoir systems and a significant deviation in the derivative may arise in the case of a restricted-entry well. As has been discussed in the literature, this phenomenon is related to the collapse of the gas phase in some region of the reservoir during the buildup period. More importantly, however, we have shown that this pressure response is fundamentally related to the step change in the total fluid compressibility which occurs when the bubble-point pressure is crossed. This existence of this phenomenon implies that it may be possible in some cases to determine the original bubble-point pressure of the reservoir fluids from a pressure buildup test.

Lastly, we have shown that the fundamental assumptions incorporated into our semilog analysis techniques, i.e., the existence of vertical equilibrium in the

reservoir and the existence of a "no-flow steady-state" region between the wellbore and the location of the reservoir where vertical equilibrium exists are at the worst approximately satisfied and in most cases, satisfied extremely well. This is in contrast to the drawdown results for which no case exhibited a "steady-state" region extending out to the location in the reservoir where vertical equilibrium exists. Because the drawdown results were greatly in error and the buildup results were quite accurate, this again implies that these two assumptions must be satisfied (necessary conditions) in order for semilog analysis of pressure transient data (either drawdown or buildup) to be valid.

CHAPTER VIII
RESTRICTED-ENTRY PSEUDOSKIN CORRELATION

In this chapter, we examine the calculation of the pseudoskin factor caused by partial penetration in a reservoir with multiple flowing phases. Only the total skin factor, which is a linear combination of the mechanical skin factor due to damage or stimulation and the pseudoskin factor due to partial penetration, can be obtained directly from semilog analysis of pseudoradial flow pressure data. In order to obtain the true mechanical skin factor, an independent estimate of the pseudoskin factor due to restricted entry is required.

Though a detailed examination of the literature on this topic was presented earlier in Chapter I, we reiterate some of the more important assumptions prevalent in the pseudoskin correlation to be presented and the physical basis for its development. When horizontal saturation gradients are negligible and during the course of production there is negligible change in the vertical saturation profile, then the multiphase flow situation should be analogous to single-phase flow in a layered reservoir. Refs. 16-21 discuss procedures or solutions that can be used to estimate the pseudoskin factor caused by restricted-entry in layered reservoirs; the results of Refs. 20 and 21 are restricted to two-layer reservoirs. Note that this would restrict the analogy of single-phase flow in a two-layer reservoir to a completely gravity segregated reservoir containing only two-phases. In reality, multiphase reservoirs generally have a transition zone separating segregated phases and in solution-gas systems, vertical and horizontal saturation gradients can develop rapidly within the reservoir. In trying to draw an analogy between multiphase and

single phase reservoirs, it would then seem appropriate to draw that analogy with the single-phase multilayer reservoirs. This provided the motivation for Refs. 16-19 which have developed methods for computing the restricted-entry pseudoskin factor in single-phase multilayer reservoirs.

The physical similarities between the single-phase multilayered reservoirs and multiphase single-layer reservoirs also provides the motivation for extending the single-phase multilayer pseudoskin factor correlations of Ref. 19 (also in Refs. 16 and 18) to the multiphase systems considered in this work. A multiphase analog to the correlation of Ref. 17 is also considered but only in a cursory manner.

8.1 Multiphase Pseudoskin Correlation

For single-phase homogeneous flow to a restricted-entry well, it is well known[2,3,9,16] that the skin factor computed from the pseudoradial flow semilog straight line represents a total skin factor, s_t given by

$$s_t = \frac{s}{b} + s_b \ , \tag{8.1.1}$$

where s denotes the mechanical skin factor, s_b the pseudoskin factor due to restricted entry and $b = h_w/h$ is the penetration ratio.

For single-phase flow to a restricted-entry well in a multilayer reservoir, Refs. 16 and 18 showed that the penetration ratio, b, in Eq. 8.1.1 should be replaced by a multilayer analog termed the dimensionless open interval flow capacity, f_1, and defined as

$$f_1 = \frac{k_1}{\bar{k}} \frac{h_w}{h} \ , \tag{8.1.2}$$

where, k_1 is the permeability of the reservoir adjacent to the perforated interval, $\bar{k}$ is the thickness-averaged total permeability defined as

$$\bar{k} = \frac{1}{h} \int_0^h k(z) dz \quad , \tag{8.1.3}$$

h_w is the thickness of the open interval and h is the total reservoir thickness.

In extending the single-phase multilayer pseudoskin correlation of Refs. 16 and 18, we consider here (also in Ref. 28) a purely analogous multiphase definition for the dimensionless open interval flow capacity; i.e., we consider a definition for f_1 in which we merely replace the absolute permeability by the total fluid mobility:

$$f_1 = \frac{\bar{\lambda}_{t1}}{\bar{\lambda}_t}\frac{h_w}{h} \ , \tag{8.1.4}$$

where $\bar{\lambda}_{t1}$ represents the thickness averaged total mobility adjacent to the open interval and $\bar{\lambda}_t$ is total-thickness-averaged mobility. We note that Ref. 20 was probably the first work to consider this analogy, at least for simple oil-water systems.

Furthermore, in all formulas of Refs. 16 and 18-19, we replace $\bar{k}$ by $\bar{\lambda}_t$ and $\bar{k}^*_z$ by

$$\bar{\lambda}^*_z = \frac{h}{(k_z/k)[h_w/\bar{\lambda}_{t1} + (h-h_w)/\bar{\lambda}_{t2}]} \ , \tag{8.1.5}$$

where $\bar{\lambda}_{t1}$ is the thickness averaged total mobility adjacent to the open interval and $\bar{\lambda}_{t2}$ is the thickness averaged mobility for $z = h_w$ to $z = 2h_w$ provided that the z-coordinate is oriented so that the perforated interval of the wellbore corresponds to $z = 0$ to $z = h_w$. For the multilayer case in which one of the center layers is open to flow, the analogous multiphase definition of $\bar{\lambda}^*_z$ is

$$\bar{\lambda}^*_z = \frac{h}{(k_z/k)[h_w/\bar{\lambda}_{t1} + (h-z_2)/\bar{\lambda}_{t2} + z_1/\bar{\lambda}_{t3}]} \ , \tag{8.1.6}$$

where $\bar{\lambda}_{t1}$ is the thickness averaged total mobility adjacent to the open interval, $\bar{\lambda}_{t2}$ is the thickness averaged mobility for the h_w (ft) immediately above the perforated interval, $\bar{\lambda}_{t3}$ is the thickness averaged mobility for the h_w (ft) immediately below the perforated interval, z_1 is the distance from the bottom of the reservoir to

the lower-most perforation and z_2 is the vertical distance from the bottom of the reservoir to the upper-most perforation.

Note that the original[19] single-phase forms of Eqs. 8.1.5 and 8.1.6 were actually modifications of the derived analytical expressions for $\bar{k}_z^*$. Numerical results presented by Ref. 19 showed that the vertical permeability of the third layer away from the perforated interval had little influence on the value of the calculated pseudoskin; i.e., the calculated pseudoskin factor was most influenced by the vertical permeability of the layers immediately adjacent to the perforated layer. Reference 19, therefore, modified their definition of $\bar{k}_z^*$ and reported that the single-phase forms of Eqs. 8.1.5 and 8.1.6 provided the best results; i.e., when used in the pseudoskin calculations, they resulted in the best estimates of the pseudoskin factor.

For all of the reservoir systems considered in this study, however, we have assumed:

$$\bar{\lambda}_{t1} = \bar{\lambda}_{t2} = \bar{\lambda}_{t3} \ . \tag{8.1.7}$$

There are several reasons for making this assumption: first, we currently have no method available to us for determining $\bar{\lambda}_{t2}$ or $\bar{\lambda}_{t3}$ directly from the well test data; second, because of the small penetration ratio and the large offset of the perforated interval from the fluid contacts, Eq. 8.1.7 is an excellent approximation, at least for the non-solution-gas reservoir systems investigated; third, for the solution-gas reservoir systems examined in this study, the difference between $\bar{\lambda}_{t1}$, $\bar{\lambda}_{t2}$ and $\bar{\lambda}_{t3}$ was less than a few percent, with $\bar{\lambda}_{t1} < \bar{\lambda}_{t2} \approx \bar{\lambda}_{t3}$. The net effect of this result and assumption 8.1.7, as seen from application of Eqs. 8.1.8 through 8.1.12 below, is that the estimated pseudoskin factor will be insignificantly greater than would have been predicted had assumption 8.1.7 not been made.

Under the conditions of Eq. 8.1.7, Eqs. 8.1.5 and 8.1.6 degenerate to

$$\bar{\lambda}_z^* = (k_z/k)\bar{\lambda}_{t1} \ . \tag{8.1.8}$$

We also have,

$$\bar{h}_D^* = \frac{h}{r_w}\sqrt{\frac{\bar{\lambda}_t}{\bar{\lambda}_z^*}} \ , \tag{8.1.9}$$

and

$$\tilde{h}_{w_D} = \frac{C' f_1(1-f_1)\bar{h}_D^*}{\exp(C_1)} \ , \tag{8.1.10}$$

where

$$C_1 = 0.481 + 1.01 f_1 - 0.838 f_1^2 \tag{8.1.11}$$

and C' is a function of the location of the open interval.[16–19] For those cases where the perforated interval is adjacent to the upper or lower boundary, $C' = 2$. For other cases, C' can be obtained from the correlation of Fig. 6 of Ref. 16 or Fig. 4.9 of Ref. 19. Reference 17 provided an explicit formula to determine C' so that the computed value of C' will cause the correlation of Ref. 19 to give the same value of pseudoskin as the correlation of Ref. 17. This point is discussed further below.

After making the modifications noted above, the expression for the pseudoskin factor is identical to that of Refs. 16, 18 and 19:

$$s_b = \left(\frac{1-f_1}{f_1}\right)\ln(\tilde{h}_{w_D}) \ . \tag{8.1.12}$$

For each of the reservoir systems considered here, Hawkins'[44] formula is used to incorporate a skin zone into the simulator, i.e.,

$$s = \left(\frac{k}{k_s} - 1\right)\ln\left(\frac{r_s}{r_w}\right) \ , \tag{8.1.13}$$

and the vertical permeability in the skin zone is approximated by

$$\left(\frac{k_{zs}}{k_z}\right) = \left(\frac{k_s}{k}\right) . \tag{8.1.14}$$

The total skin factor, s_t, is computed from pseudoradial flow pressure data by the following equation:

$$s_t = 1.151\left[\frac{\Delta p_{ws}(1\text{hr})}{m} - \log\left(\frac{\bar{\lambda}_t}{\phi \bar{c}_t r_w^2}\right) + 3.2274\right] , \tag{8.1.15}$$

where $m = dp_{ws}/d\log t_e$ is the slope of the pseudoradial flow semilog straight line, $\bar{c}_t$ is the initial thickness-averaged total compressibility given by

$$\bar{c}_t = \frac{1}{h}\int_0^h (c_o S_o + c_g S_g + c_w S_w + c_r) dz , \tag{8.1.16}$$

and $\Delta p_{ws}(1\text{hr}) = p_{ws}(\Delta t = 1 \text{ hr}) - p_{wf,s}$.

According to the above equations, the restricted-entry pseudoskin factor is estimated from Eqs. 8.1.4 and 8.1.9-8.1.12, the total skin factor is estimated from Eq. 8.1.15 and lastly, the mechanical damage skin is calculated as

$$s = (s_t - s_b) \times f_1 \quad . \tag{8.1.17}$$

Using Ref. 19's multilayer definitions for f_1, $\bar{k}$ and $\bar{k}_z^*$, Ref. 17 modified the single-layer pseudoskin correlation of Ref. 10 to obtain a pseudoskin correlation for multilayer reservoirs. The correlation of Ref. 17 may be expressed as

$$s_{b,d} = \left(\frac{1-f_1}{f_1}\right)\ln\left(\frac{\pi \bar{h}_D^*}{2}\right) + \frac{1}{f_1}\ln\left[\frac{f_1}{2+f_1}\left(\frac{\bar{A}-1}{\bar{B}-1}\right)^{1/2}\right] , \tag{8.1.18}$$

where

$$\bar{A} = \frac{1}{f_2 + 0.25 f_1} \quad , \tag{8.1.19}$$

$$\bar{B} = \frac{1}{f_2 + 0.75 f_1} \tag{8.1.20}$$

and

$$f_2 = \frac{\bar{k}_2 \bar{h}_2}{\bar{k} h} \quad . \tag{8.1.21}$$

In Eq. 8.1.21, $\bar{k}_2$ is the thickness-averaged permeability above the perforated interval and $\bar{h}_2$ is the distance from the top of the perforated interval to the top of the reservoir. Equation 8.1.18 is readily modified for multiphase reservoir systems by utilizing the multiphase definitions for f_1 and $\bar{h}_D^*$ presented above and also replacing the the permeabilities in the definition for f_2 by the appropriate thickness-averaged total mobilities. As noted previously, we assume in all of our calculations that $\bar{\lambda}_{t2} = \bar{\lambda}_{t1}$.

As mentioned above, Ref. 17 presented a correlation for the C' of Ref. 19. Equating the right hand sides of Eqs. 8.1.18 and 8.1.12 and using Eq. 8.1.10, Ref. 17 obtained the following correlation for C':

$$C' = \frac{\pi \exp(C_1)}{2 f_1 (1 - f_1)} \left[\frac{f_1}{2 + f_1} \left(\frac{\bar{A} - 1}{\bar{B} - 1} \right)^{1/2} \right]^{\frac{1}{1 - f_1}} \quad . \tag{8.1.22}$$

Obviously, the mere equating of Eqs. 8.1.18 and 8.1.12 assumes that both equations will provide the same value for the pseudoskin. Indeed, for the cases investigated in which the perforated interval is adjacent to one of the upper or lower boundaries, it will be shown that the values of the pseudoskin obtained from each of these correlations are nearly identical and the value of C' obtained from Eq. 8.1.22 is almost exactly equal to the value of 2.0 obtained from Fig. 4.9 of Ref. 19.

For reservoir-well configurations in which the perforated interval is vertically located away from the upper or lower boundaries, however, the values of C' obtained from Eq. 8.1.22 are consistently larger in value (as much as 25 percent) than those obtained from Fig. 4.9 of Ref. 19. While this appears to be a large difference, we note that C' appears in the calculation of $\tilde{h}_{w_D}$ which appears inside a logarithm term in Eq. 8.1.12. If this value for C' is then used in the correlation of Ref. 19, the net result is that the 25 percent deviation in C' only results in an approximate 5 percent deviation in the estimated value of the pseudoskin obtained from the correlation of Ref. 19; i.e., the value of the pseudoskin obtained from the correlation of Ref. 19 using C' obtained from Eq. 8.1.22 will deviate by approximately 5 percent from the value of pseudoskin obtained from the correlation of Ref. 19 using C' obtained from Fig. 4.9 of Ref. 19. Specific examples of these differences are included below in Section 8.2 along with the actual results obtained from the multiphase correlation presented above.

8.2 Numerical Results

In this section, we present results for the skin factors calculated formally using Eqs. 8.1.4 and 8.1.9-8.1.12 to estimate the pseudoskin factor, Eq. 8.1.15 to estimate the total skin factor and, lastly, Eq. 8.1.17 to obtain the mechanical damage skin. No corrections to the open interval mobility or flowing wellbore pressure at the instant of shut-in are performed; i.e., the actual measured flowing wellbore pressure at the instant of shut-in is utilized as is the calculated open interval total mobility. Recall that the open interval total mobility is calculated from the same equations as the thickness-averaged total mobilities, with the exceptions that the open interval thickness is substituted for the reservoir thickness and the slope of the semilog straight line is the slope (log-derivative of the wellbore pressure) of the early-time semilog straight line. Tables 8.1 - 8.4 contain some of the required

and calculated parameters necessary to estimate the various skin factors for a variety of the two-phase oil-water, gas-water and oil-gas reservoir systems and the three-phase oil-gas-water reservoir systems investigated in this work. Along with the calculated and actual (simulator) values of the thickness-averaged total mobilities, Tables 8.5 - 8.8 contain the estimated pseudoskin factors, total skin factors and damage skin factors for each of these systems, as well as the actual value of damage skin input into our simulator.

Results shown in Table 8.5 indicate that our method for the calculation of the pseudoskin and damage skin provide accurate estimates of the pseudoskin and damage skin for the oil-water systems investigated. This is probably due to the fact that the viscosities for the oil-water cases were held constant and variations in the vertical and horizontal saturation distributions were minimal over the course of the transient tests; i.e., these cases approximately satisfy the assumptions under which the pseudoskin correlation and total skin factor equation were derived. The maximum error in the damage skin factor is only 6.8 percent (Case OW-7BS3) for these systems.

Results for the gas-water cases (Table 8.6) are somewhat mixed depending upon the gas production rate during the drawdown test. For those cases produced at the lower rate of 1 MMscf/Day the results are quite accurate with a maximum error of 6 percent for case GW-3BS3. The accuracy of the calculations for these cases again arises due to minimal change in the fluid saturations and fluid properties (e.g., gas viscosity) over the course of the well test. For the high production rate cases (cases GW-*B), Table 8.6 shows a significant error in the calculated skin factor; e.g., the calculated damage skin factor for case GW-3B is 1.89 versus the input value of $s = 0$. The reason for this error is predominately due to variations in the fluid properties due to large pressure changes at the sandface (i.e., the gas viscosity) and the corresponding variation in the open interval total mobility.

Table 8.1
Parameters for Skin Calculations: Oil-Water Systems

Case	Δp(1 hr) (psi)	m (psi)	$\bar{\lambda}_{t1}$ (md/cp)	f_1	C_1	$\bar{\lambda}^*_z$	$\bar{h}^*_{_D}$	$\tilde{h}_{w_D}$
OW-2B†	98.8	18.37	42.47	n/a	n/a	n/a	n/a	n/a
OW-2BS3	180.0	18.37	42.47	n/a	n/a	n/a	n/a	n/a
OW-2BS4	261.3	18.37	42.47	n/a	n/a	n/a	n/a	n/a
OW-3B	322.9	18.37	42.47	0.249	0.680	4.247	507.4	96.0
OW-3BS3	649.5	18.37	42.47	0.249	0.680	4.247	507.4	96.0
OW-3BS4	976.5	18.37	42.47	0.249	0.680	4.247	507.4	96.0
OW-4B	324.4	10.67	42.47	0.144	0.609	4.247	815.1	109.6
OW-4BS3	651.8	10.67	42.47	0.144	0.609	4.247	815.2	109.6
OW-4BS4	978.7	10.67	42.47	0.144	0.609	4.247	815.2	109.6
OW-5B	326.9	7.52	42.47	0.102	0.575	4.247	1120.8	115.4
OW-5BS3	652.7	7.58	42.47	0.102	0.575	4.247	1123.0	115.3
OW-5BS4	979.7	7.65	42.47	0.102	0.575	4.247	1123.0	115.3
OW-6B	326.4	5.91	42.47	0.079	0.555	4.247	1425.9	118.7
OW-6BS3	653.9	5.81	42.47	0.079	0.555	4.247	1426.3	118.6
OW-6BS4	980.8	5.81	42.47	0.079	0.555	4.247	1426.3	118.6
OW-67B	328.7	2.86	42.47	0.039	0.519	4.247	2800.8	124.2
OW-7B	329.8	1.77	42.47	0.024	0.505	4.247	4479.5	126.3
OW-7BS3	657.1	1.82	42.47	0.025	0.505	4.247	4419.3	127.8
OW-7BS4	983.9	1.82	42.47	0.025	0.505	4.247	4419.3	127.8
OW-7O	329.8	1.78	42.47	0.024	0.505	4.247	4467.0	126.6
OW-7P	259.1	1.75	42.47	0.024	0.505	42.47	1421.7	39.8

† - Wells for cases OW-2B* are fully-penetrating.

Table 8.2
Parameters for Skin Calculations: Gas-Water Systems

Case	$\Delta p(1\text{ hr})$ (psi)	m (psi)	$\bar{\lambda}_{t1}$ (md/cp)	f_1	C_1	$\bar{\lambda}^*_z$	$\bar{h}^*_{_D}$	$\tilde{h}_{w_D}$
GW-2B†	340.5	72.28	547.6	n/a	n/a	n/a	n/a	n/a
GW-2BS3	65.9	7.12	473.1	n/a	n/a	n/a	n/a	n/a
GW-2BS4	97.0	7.12	473.2	n/a	n/a	n/a	n/a	n/a
GW-3B	1174.9	72.28	646.4	0.349	0.731	161.6	270.8	59.2
GW-3BS3	236.2	7.12	479.5	0.257	0.685	119.9	315.8	60.7
GW-3BS4	359.7	7.12	479.8	0.257	0.685	119.9	315.8	60.7
GW-4B	1175.1	72.22	646.4	0.349	0.731	161.6	287.4	62.8
GW-4BS3	236.2	7.07	479.4	0.255	0.684	119.9	336.1	64.4
GW-4BS4	359.8	7.07	479.8	0.255	0.684	119.9	336.0	64.4
GW-5B	1175.7	71.82	646.3	0.347	0.730	191.6	303.8	66.3
GW-5BS3	236.3	7.02	479.4	0.253	0.683	119.9	355.4	67.9
GW-5BS4	359.8	7.02	479.8	0.253	0.683	119.9	355.3	67.9
GW-6B	1177.2	70.92	646.1	0.342	0.729	161.5	334.9	72.8
GW-6BS3	236.3	6.93	479.4	0.250	0.681	119.9	392.0	74.4
GW-6BS4	359.8	6.93	479.7	0.250	0.681	119.9	391.8	74.4
GW-7B	1182.5	67.42	645.3	0.325	0.721	161.3	443.7	94.7
GW-7BS3	236.6	6.60	479.3	0.238	0.674	119.8	518.4	95.9
GW-7BS4	360.1	6.59	479.6	0.238	0.674	119.9	518.6	95.9
GW-3B2	111.7	7.12	479.1	0.257	0.685	119.8	315.9	60.7
GW-4B2	111.7	7.07	479.1	0.255	0.684	119.8	336.2	64.4
GW-5B2	111.8	7.02	479.1	0.253	0.683	119.8	355.6	67.9
GW-6B2	111.8	6.93	479.0	0.250	0.681	119.8	392.1	74.4
GW-7B2	112.1	6.59	478.9	0.238	0.674	119.7	519.0	95.9

† - Wells for cases GW-2B* are fully-penetrating.

Table 8.3
Parameters for Skin Calculations: Oil-Gas Systems

Case	$\Delta p(1\text{ hr})$ (psi)	m (psi)	$\bar{\lambda}_{t1}$ (md/cp)	f_1	C_1	$\bar{\lambda}^*_z$	$\bar{h}^*_{_D}$	$\tilde{h}_{w_D}$
OG-1B†	55.6	9.859	100.97	n/a	n/a	n/a	n/a	n/a
OG-1BS3	112.6	9.844	97.58	n/a	n/a	n/a	n/a	n/a
OG-1BS4	172.9	9.859	95.97	n/a	n/a	n/a	n/a	n/a
OG-2B†	55.3	9.977	101.15	n/a	n/a	n/a	n/a	n/a
OG-2BS3	112.2	9.977	97.76	n/a	n/a	n/a	n/a	n/a
OG-2BS4	172.6	9.977	96.20	n/a	n/a	n/a	n/a	n/a
OG-3B	219.5	9.975	87.49	0.1905	0.643	8.7	579.7	94.0
OG-3BS3	503.4	9.975	86.88	0.1892	0.642	8.7	581.7	93.9
OG-3BS4	821.0	9.975	87.05	0.1895	0.642	8.7	581.1	93.9
OG-4B	222.9	2.013	88.05	0.0386	0.519	8.8	1438.9	63.6
OG-4BS3	505.6	2.012	87.71	0.0385	0.519	8.8	1442.0	63.5
OG-4BS4	821.7	2.010	87.89	0.0385	0.519	8.8	1441.3	63.5
OG-5B	223.0	1.091	88.10	0.0210	0.502	8.8	2140.7	53.2
OG-5BS3	505.5	1.090	87.80	0.0209	0.502	8.8	2144.9	53.1
OG-5BS4	821.4	1.089	88.00	0.0209	0.502	8.8	2143.5	53.1
OG-6B	223.0	0.753	88.12	0.0145	0.495	8.8	2782.0	48.4
OG-6BS3	505.4	0.753	87.84	0.0144	0.495	8.8	2787.8	48.3
OG-6BS4	821.3	0.752	88.04	0.0144	0.495	8.8	2785.7	48.3

† - Wells for cases OG-1B* and OG-2B* are fully-penetrating.

Table 8.4
Parameters for Skin Calculations: Oil-Gas-Water Systems

Case	$\Delta p(1\text{ hr})$ (psi)	m (psi)	$\bar{\lambda}_{t1}$ (md/cp)	f_1	C_1	$\bar{\lambda}^*_z$	$\bar{h}^*_D$	$\tilde{h}_{w_D}$
OGW2	180.0	5.257	99.67	0.1144	0.586	10.0	989.5	56.4
OGW	179.7	6.743	99.53	0.1477	0.612	10.0	870.9	60.0
OGWS3	433.8	6.743	97.91	0.1453	0.610	9.8	878.1	59.8
OGWS4	715.6	6.742	98.57	0.1462	0.611	9.9	875.2	59.9
OGWAA	182.5	1.908	99.81	0.0418	0.522	10.0	1855.9	44.6
OGWAAS3	436.0	1.908	98.28	0.0412	0.521	9.8	1870.3	44.3
OGWAAS4	717.3	1.906	99.08	0.0415	0.521	9.9	1863.3	44.4
OGWAB	182.7	1.135	99.82	0.0248	0.506	10.0	2541.3	37.4
OGWABS3	436.2	1.135	98.36	0.0244	0.505	9.8	2560.5	37.2
OGWABS4	717.4	1.134	99.18	0.0246	0.505	9.9	2550.9	37.3
OGWAC	182.8	0.825	99.83	0.0178	0.499	10.0	3146.8	33.7
OGWACS3	436.2	0.825	98.39	0.0175	0.498	9.8	3170.1	33.5
OGWACS4	717.4	0.823	99.22	0.0176	0.499	9.9	3158.7	33.6
OGWBA	182.3	1.867	99.82	0.0407	0.521	10.0	1983.0	46.4
OGWBAS3	435.9	1.866	98.29	0.0401	0.520	9.8	1998.4	46.1
OGWBAS4	717.1	1.865	99.09	0.0404	0.520	9.9	1990.8	46.3
OGWBB	182.6	1.118	99.83	0.0244	0.505	10.0	2684.2	39.0
OGWBBS3	436.1	1.118	98.36	0.0241	0.505	9.8	2704.4	38.7
OGWBBS4	717.2	1.116	99.19	0.0243	0.505	9.9	2694.3	38.9
OGWBC	182.7	0.816	99.83	0.0176	0.499	10.0	3302.2	35.0
OGWBCS3	436.1	0.816	98.40	0.0174	0.498	9.8	3326.6	34.8
OGWBCS4	717.2	0.814	99.23	0.0175	0.498	9.9	3314.7	34.9
OGWCA	182.2	1.756	99.82	0.0376	0.518	10.0	2352.0	51.2
OGWCAS3	435.7	1.755	98.31	0.0370	0.517	9.8	2370.0	50.9
OGWCAS4	716.9	1.754	99.12	0.0373	0.518	9.9	2360.9	51.1
OGWCB	182.4	1.067	99.83	0.0234	0.504	10.0	3093.2	43.1
OGWCBS3	435.9	1.067	98.38	0.0231	0.504	9.8	3116.3	42.9
OGWCBS4	717.0	1.065	99.21	0.0232	0.504	9.9	3104.8	43.0
OGWCC	182.5	0.789	99.84	0.0171	0.498	10.0	3744.8	38.7
OGWCCS3	435.9	0.789	98.41	0.0169	0.498	9.8	3772.3	38.4
OGWCCS4	717.0	0.787	99.24	0.0170	0.498	9.9	3758.9	38.5

Estimates of the pseudoskin factor and damage skin factor for the oil-gas (Table 8.7) and three-phase (Table 8.8) reservoir systems deviate substantially from the input skin factors. The maximum error in the damage skin factors for these systems is 48.6 percent for case OG-1BS3. For these solution gas cases, variations in both the saturation profile and the pressure dependent fluid properties combine to affect the skin calculations. Because of the relatively small pressure change during the test, it would appear that the saturation variations which occur due to gas coming out of solution have a much more significant impact on the calculations than do variations in the fluid viscosities.

It is noted here that a method for correcting the errors in the damage skin and pseudoskin calculations resulting from non-linearities due to multiphase flow effects and due to variations in the fluid properties has been developed by Ref. 150. This method has also been shown to work exceptionally well for gas condensate reservoirs. This method is not pursued further in this work, but rather is presented in Ref. 150. If the reader is interested in obtaining more accurate skin factor estimates for multiphase reservoir systems, it suggested that he or she investigate the method presented in Ref. 150.

8.3 Modified Method of Ref. 17

In this section we only briefly examine the pseudoskin factors and damage skin factors obtained from the multiphase analog to the pseudoskin method of Ref. 17 expressed by Eq. 8.1.18–8.1.21. Table 8.9 shows a comparison of the pseudoskin factors and damage skin factors obtained from the method used in the previous section along with the pseudoskin factors and damage skin factors obtained from the multiphase analog correlation of Ref. 17. Table 8.9 shows that the pseudoskin factors (and subsequently, the damage skin factors) are nearly identical for those cases in which the perforated interval is adjacent to a reservoir boundary. For

those cases in which the perforated interval is located away from the upper or lower boundary (e.g., case OGWCCS4), the correlation of Ref. 17 appears to be slightly more accurate, or at the least, results in values of pseudoskin factors that are approximately 6 percent greater that those obtained from the modified correlation of Ref. 19.

8.4 Summary

In this chapter we have presented two correlations for estimating the pseudoskin factor due to restricted-entry in multiphase reservoirs. These correlations were shown to provide reasonably accurate results for oil-water reservoir systems and for gas-water reservoir systems in which the gas production rate is low, i.e., small pressure drawdown. For gas-water reservoirs produced at a high rate and for reservoirs containing solution-gas, it has been shown that these correlations may be significantly in error if not modified.

Table 8.9

Comparison of Pseudoskin Correlation Results

Case	s_t (Eq. 8.1.15)	s_b (Eq. 8.1.12)	s_{b2} (Eq. 8.1.18)	s (Eq. 8.1.17) (Use s_b)	s (Eq. 8.1.17) (Use s_{b2})	s (Input)
OW-5BS4	141.01	42.02	41.99	10.05	10.10	10
GW-5BS4	53.29	12.43	12.46	10.34	10.33	10
OG-5BS4	861.64	186.14	188.32	14.11	14.07	10
OGWCCS4	1043.56	211.31	223.85	14.14	13.94	10

Table 8.5
Skin Calculation Results: Oil-Water Systems

Case	$\lambda_t(Sim.)$ (md/cp)	$\lambda_t(Calc.)$ (md/cp)	s_t (Eq. 8.1.15)	s_b (Eq. 8.1.12)	s (Eq. 8.1.17)	s (Sim.)
OW-2B	42.47	42.71	0.01	n/a	0.01	0
OW-2BS3	42.47	42.71	5.10	n/a	5.10	5
OW-2BS4	42.47	42.71	10.19	n/a	10.19	10
OW-3B	42.47	42.71	14.00	13.80	0.05	0
OW-3BS3	42.47	42.71	34.52	13.80	5.15	5
OW-3BS4	42.47	42.71	55.01	13.80	10.24	10
OW-4B	49.05	48.99	28.61	27.81	0.12	0
OW-4BS3	49.05	49.00	63.92	27.81	5.22	5
OW-4BS4	49.05	49.00	99.17	27.81	10.31	10
OW-5B	52.34	52.10	43.52	41.85	0.17	0
OW-5BS3	52.34	52.30	92.60	42.02	5.13	5
OW-5BS4	52.34	52.30	141.01	42.02	10.05	10
OW-6B	54.31	53.97	57.01	55.92	0.09	0
OW-6BS3	54.31	54.00	122.99	55.95	5.27	5
OW-6BS4	54.31	54.00	187.73	55.95	10.36	10
OW-67B	58.05	57.68	125.44	119.60	0.23	0
OW-7B	59.57	59.18	208.06	197.43	0.25	0
OW-7BS3	59.57	57.60	409.79	192.51	5.34	5
OW-7BS4	59.57	57.60	616.99	192.51	10.43	10
OW-7O	59.57	58.85	206.84	196.40	0.25	0
OW-7P	59.57	59.61	163.22	151.44	0.28	0

Table 8.6
Skin Calculation Results: Gas-Water Systems

Case	$\lambda_t(Sim.)$ (md/cp)	$\lambda_t(Calc.)$ (md/cp)	s_t (Eq. 8.1.15)	s_b (Eq. 8.1.12)	s (Eq. 8.1.17)	s (Sim.)
GW-2B	471.09	480.52	-0.25	n/a	-0.25	0
GW-2BS3	467.07	468.70	4.99	n/a	4.99	5
GW-2BS4	467.07	468.70	10.01	n/a	10.01	10
GW-3B	471.09	480.55	13.04	7.61	1.89	0
GW-3BS3	467.07	468.70	32.52	11.89	5.30	5
GW-3BS4	467.07	468.70	52.50	11.89	10.44	10
GW-4B	421.52	427.47	13.06	7.73	1.86	0
GW-4BS3	417.95	419.45	32.87	12.17	5.28	5
GW-4BS4	417.95	419.45	52.90	12.16	10.39	10
GW-5B	381.85	386.76	13.17	7.90	1.83	0
GW-5BS3	378.65	380.05	33.05	12.44	5.22	5
GW-5BS4	378.65	380.05	53.29	12.43	10.34	10
GW-6B	322.33	326.24	13.43	8.24	1.78	0
GW-6BS3	319.70	320.92	33.57	12.93	5.16	5
GW-6BS4	319.70	320.91	54.08	12.92	10.29	10
GW-7B	203.45	205.54	14.49	9.45	1.64	0
GW-7BS3	201.82	202.03	35.54	14.60	4.98	5
GW-7BS4	201.82	202.30	57.16	14.61	10.13	10
GW-3B2	467.07	468.70	12.39	11.90	0.13	0
GW-4B2	417.95	419.45	12.51	12.18	0.08	0
GW-5B2	378.65	380.05	12.64	12.45	0.05	0
GW-6B2	319.70	320.92	12.89	12.95	-0.01	0
GW-7B2	201.82	202.31	13.87	14.64	-0.18	0

Table 8.7
Skin Calculation Results: Oil-Gas Systems

Case	$\lambda_t(Sim.)$ (md/cp)	$\lambda_t(Calc.)$ (md/cp)	s_t (Eq. 8.1.15)	s_b (Eq. 8.1.12)	s (Eq. 8.1.17)	s (Sim.)
OG-1B	116.01	116.19	0.75	n/a	0.75	0
OG-1BS3	116.01	116.19	7.43	n/a	7.43	5
OG-1BS4	116.01	116.19	14.45	n/a	14.45	10
OG-2B	116.01	114.80	0.65	n/a	0.65	0
OG-2BS3	116.01	114.80	7.22	n/a	7.22	5
OG-2BS4	116.01	114.80	14.59	n/a	14.59	10
OG-3B	116.01	114.83	19.59	19.31	0.05	0
OG-3BS3	116.01	114.83	52.35	19.47	6.22	5
OG-3BS4	116.01	114.83	89.00	19.43	13.18	10
OG-4B	485.50	455.74	121.24	103.33	0.69	0
OG-4BS3	485.50	455.96	282.96	103.75	6.89	5
OG-4BS4	485.50	456.45	464.27	103.66	13.89	10
OG-5B	731.86	700.97	228.96	185.71	0.91	0
OG-5BS3	731.86	701.27	527.25	186.35	7.11	5
OG-5BS4	731.86	701.95	861.64	186.14	14.11	10
OG-6B	907.86	869.84	334.25	264.13	1.01	0
OG-6BS3	907.86	870.77	766.54	265.12	7.23	5
OG-6BS4	907.86	871.45	1250.44	264.77	14.22	10

Table 8.8
Skin Calculation Results: Oil-Gas-Water Systems

Case	$\lambda_t(Sim.)$ (md/cp)	$\lambda_t(Calc.)$ (md/cp)	s_t (Eq. 8.1.15)	s_b (Eq. 8.1.12)	s (Eq. 8.1.17)	s (Sim.)
OGW2	123.17	124.48	33.63	31.22	0.28	0
OGW	123.17	96.29	25.04	23.64	0.21	0
OGWS3	123.17	96.29	68.41	24.07	6.44	5
OGWS4	123.17	96.30	116.53	23.90	13.54	10
OGWAA	275.83	265.26	104.01	87.02	0.71	0
OGWAAS3	275.83	265.29	256.97	88.29	6.94	5
OGWAAS4	275.83	265.43	427.09	87.67	14.08	10
OGWAB	404.06	402.94	179.12	142.57	0.91	0
OGWABS3	404.06	403.01	436.17	144.51	7.12	5
OGWABS4	404.06	403.35	721.92	143.54	14.22	10
OGWAC	508.99	510.61	248.81	194.38	0.97	0
OGWACS3	508.99	510.73	602.38	196.94	7.10	5
OGWACS4	508.99	511.35	997.03	195.69	14.14	10
OGWBA	254.46	245.30	106.34	90.49	0.64	0
OGWBAS3	254.46	245.34	262.79	91.81	6.85	5
OGWBAS4	254.46	245.47	436.51	91.16	13.94	10
OGWBB	372.98	371.51	181.82	146.30	0.87	0
OGWBBS3	372.98	371.59	442.75	148.28	7.09	5
OGWBBS4	372.98	371.92	733.52	147.29	14.22	10
OGWBC	471.76	472.51	251.45	198.44	0.93	0
OGWBCS3	471.76	472.62	608.91	201.05	7.08	5
OGWBCS4	471.76	473.21	1007.90	199.78	14.12	10
OGWCA	210.09	204.21	113.31	100.75	0.47	0
OGWCAS3	210.09	204.22	279.65	102.18	6.57	5
OGWCAS4	210.09	204.33	464.35	101.46	13.54	10
OGWCB	306.38	304.58	190.62	157.03	0.79	0
OGWCBS3	306.38	304.65	464.02	159.16	7.03	5
OGWCBS4	306.38	304.95	768.72	158.09	14.19	10
OGWCC	389.85	388.91	260.02	209.91	0.86	0
OGWCCS3	389.85	389.00	630.85	212.66	7.05	5
OGWCCS4	389.85	389.51	1043.56	211.31	14.14	10

CHAPTER IX

CONCLUSIONS AND RECOMMENDATIONS

Here we summarize the results and main conclusions presented throughout this work. Opportunities for future research in the areas of multiphase pressure transient analysis and reservoir simulation are also discussed.

As part of this work, a comprehensive, fully-implicit, variable bubble-point/variable dew-point, coning simulator has been developed. A detailed description of the mathematical and numerical formulation of the simulator has been presented. As part of that formulation, a detailed and rigorous discussion on the treatment of variable bubble-point and variable dew-point problems and the variable substitution logic required for their efficient treatment has been presented and a simple iterative method developed which (i) corrects both the bubble-point (dew-point) pressure and the hydrocarbon saturations when phase boundaries are crossed, (ii) is convergent and (iii) results in no oscillations between Newton iterations.

Validation of the simulator results was obtained through a comparison with results obtained from an extensive array of analytical solutions, published data and other numerical simulators, both research and commercial, for an extensive array of one-dimensional and two-dimensional single-phase, two-phase and three-phase reservoir systems. In all cases, an excellent match (comparison) was obtained between the results obtained from these other sources and the simulator developed in this work.

As part of the development of the simulator discussed above, a sparse direct solver [93] and three conjugate gradient-type iterative methods, GMRES(k)[49–51], Orthomin(k)[48] and Bi-CGSTAB[52] (and it's variant Bi-CGSTAB-P[52]) for the solution of nonsymmetric systems of linear equations have been fully implemented in our simulator. Preconditioning options for the iterative methods include block-symmetric-Gauss-Seidel incomplete factorization (BSGS), block-incomplete-LU decomposition (BILU), and a domain decomposition preconditioner (partition matrix method) based on the Bramble et al.[90] preconditioner. Additionally, for the domain decomposition overall preconditioner, options are included for using either BSGS or BILU preconditioning for the subdomains and one of four (BSGS of A_{33}, BILU of A_{33}, A_{33} and M_{M2}[45,46]) preconditioners for the Schur complement.

Through the use of a series of test matrices, various aspects of the iterative methods and preconditioners have been investigated.. The primary results of this investigation are as follows.

(i) For type of problem and typical size of problem considered in this work, the preconditioned conjugate gradient-type iterative methods incorporated in our simulator are between 1.5 and 2.4 orders of magnitude faster than the direct solution method incorporated in our simulator.

(ii) Without preconditioning and with full orthogonalization, method GMRES appears to be a more robust iterative method than Orthomin, Bi-CGSTAB or Bi-CGSTAB-P for the nonsymmetric linear systems investigated; i.e., GMRES converges, whereas Orthomin, Bi-CGSTAB and Bi-CGSTAB-P do not.

(iii) The effect of the number of orthogonalizations used is much greater for GMRES(k) than for Orthomin(k); i.e., as k is increased, the convergence

rate for GMRES(k) improves more significantly than for Orthomin(k). This may be due in part to the restarting of the iterative process for GMRES(k).

(iv) For the test problems considered, Orthomin(k) required preconditioning and greater than five orthogonalizations to converge.

(v) Based purely on the convergence rate (number of iterations), preconditioned methods Bi-CGSTAB and Bi-CGSTAB-P slightly outperformed methods GMRES(k) and Orthomin(k).

(vi) Based on computational efficiency (CPU time), method GMRES(k) significantly outperforms methods Orthomin(k) and Bi-CGSTAB-P, and almost doubles the performance of method Bi-CGSTAB.

(vii) For the problems considered in this work, the BILU preconditioner greatly outperformed the BSGS preconditioner; i.e., resulted in a much improved convergence rate (reduced number of iterations) for the iterative method. It is interesting to note that this occurs even though the l_2-norm of the preconditioned residual is always less for the first few iterations for the BSGS preconditioned system.

(viii) The effect of domain decomposition grid ordering on standard BILU preconditioned iterative methods is to decrease the convergence rate (increase the number of iterations).

(ix) Four preconditioners for the Schur complement have been examined in conjunction with the use of a domain decomposition technique as the overall preconditioner and include the BSGS approximation to A_{33}, the BILU approximation to A_{33}, the matrix A_{33} itself and Meurant's[91,92] simplified preconditioner, M_{M2}. Results clearly show Meurant's preconditioner performs the best for each of the test problems considered, with little difference between the other three Schur complement preconditioners.

(x) Though certain partitionings of the reservoir domain resulted in the domain decomposition preconditioned iterative method requiring less iterations that the BILU preconditioned iterative method, this partitioning could not be determined *a priori*. Even with the improved convergence rate, the domain decomposition method was computationally more expensive (required more CPU time) than the BILU preconditioned method.

A theoretical analysis of the single-phase pressure transient solution for liquid systems has shown the existence of a "steady-state" zone in the inner region of the reservoir. Similarly, a theoretical analysis and numerical investigation of single-phase gas flow has shown the validity of our "steady-state" zone arguments and the computational equations derived based on those arguments. We note that Ref. 131 has previously used these arguments and Refs. 146-148 have used similar arguments in their work on gas condensate reservoirs.

For multiphase flow cases, an expression has been derived which shows that vertical equilibrium exists in the reservoir if, and only if, the fractional flow rate of each phase as defined by the volumetric flow rates is the same as that calculated from the total thickness averaged mobilities existing at the same radius in the reservoir; i.e.,

$$f_m|_r = \frac{\bar{\lambda}_m}{\bar{\lambda}_t}\Big|_r = \frac{q_m}{q_t}\Big|_r \ . \tag{9.1}$$

For multiphase reservoir systems in which gravity effects are also included and capillary pressure effects excluded, we have shown that vertical equilibrium can exist in the reservoir only if (i) all fluids have the same density, or (ii) all mobile fluids are fully segregated.

A recently developed theoretical expression[149] for the pressure response in a reservoir containing a constant pressure outer boundary (either at infinity or at a

fixed radius) has been used in conjunction with fractional flow theory and detailed numerical simulations to examine the pressure behavior of a fully-penetrating well producing an edge-water drive oil reservoir containing a constant pressure outer boundary. Three separate cases having distinctly different fractional flow curves were examined in detail and include a case for which a sharp saturation front or "shock" cannot develop (case OW-1Z - fractional flow curve concave downward everywhere), a case for which a sharp saturation front or "shock" can develop at every saturation (case OW-1W - fractional flow curve concave up everywhere), and a case for which a sharp saturation front or "shock" can develop over a certain saturation range (case OW-1Y - typical "S" shaped fractional flow curve).

For case OW-1W (no saturation front), the theoretical expression of Ref. 149 was used to obtain an expression which shows that once the constant pressure outer boundary was "felt" by the wellbore and once the volumetric flow rate across the reservoir has stabilized, the log-derivative of the wellbore pressure drop, $d\Delta p(t)/d\ln t$, must in fact become negative and will subsequently increase monotonically to zero. It was also shown that $d\Delta p(t)/d\ln t$ cannot be zero until the reservoir has been completely flooded with water ($S_o = S_{or}$) and the total relative mobility, λ_{rt}, ceases to change.

For the two cases in which a sharp saturation front develops in the reservoir (cases OW-1W and OW-1Y), the expression of Ref. 149 was used in conjunction with fractional flow theory and detailed numerical results to obtain an expression which shows that the log-derivative of the wellbore pressure drop is dominated by the time rate of change in the total relative mobility across the saturation front; i.e.,

$$\frac{d\Delta p(t)}{d\ln t} = \frac{q_t t}{C_2 kh} \int_{r_f^-}^{r_f^+} \left[-\frac{1}{{\lambda_{rt}}^2(r',t)} \frac{\partial \lambda_{rt}(r',t)}{\partial t} \right] \frac{dr'}{r'} \quad . \tag{9.2}$$

Furthermore, because the time derivative of the total relative mobility across the saturation front is negative for both of these cases and because the magnitude of this derivative must increase as the velocity of the saturation front increases as it progresses towards the well, Eq. 9.2 indicates that not only must $d\Delta p(t)/d\ln t$ be a positive quantity, but it must be an increasing positive quantity up to the time of breakthrough; i.e., $d\Delta p(t)/d\ln t$ will be both positive and increasing up to water breakthrough at the well.

Following water breakthrough, the general expression of Ref. 149 was used to show that $d\Delta p(t)/d\ln t$ will remain positive for case OW-1W until true steady-state is reached; i.e., until the reservoir has been completely flooded with water ($S_o = S_{or}$) and the fluid saturations no longer change with time. For case OW-1Y, it was shown that following water breakthrough, $d\Delta p(t)/d\ln t$ must become negative and will approach zero only as the fluid saturations cease to change.

The applicability of modeling a gas cap or aquifer as a constant pressure boundary has been thoroughly investigated. Through a series of numerical examples, we have shown that the pressure response obtained from multiphase reservoir systems containing a constant pressure boundary is fundamentally different from the pressure response predicted by single-phase constant pressure boundary solutions. In particular, we have shown that following an initial rapid decline in the pressure derivative once the constant pressure boundary is felt, the pressure derivative for each of the multiphase reservoir cases investigated actually increases.

With the aid of a vertical form of the theoretical expression developed by Ref. 149 and in conjunction with fractional flow theory, we have shown that for drawdown, the underlying reason for this increase in the log-derivative of the well-bore pressure drop is due to the time-rate of change in the total relative mobility over the two-phase region of the reservoir. Also related to the fractional flow

theory, we have shown that the log-derivative of the wellbore pressure drop will continue to increase until breakthrough of the saturation front at the wellbore.

For the constant-pressure boundary oil-water cases investigated, we have shown that any attempt to match the pressure response to single-phase constant pressure boundary solutions necessarily requires that the location of the constant pressure boundary be part of the solution. For the water-gas cases investigated we have shown that the pressure response shows little sensitivity to the location of the constant pressure boundary in the gas cap and as such, any match of the pressure response prior to the time the pressure derivative begins to increase may be non-unique.

For the oil-gas constant pressure boundary cases examined, the drawdown pressure derivative exhibited an approximate semilog straight line, indicating that the pressure response was dominated by the changes in the mobility at the sandface. Under no circumstances could the pressure response for these cases be interpreted as or matched to single-phase constant pressure boundary solutions. With the aid of numerical results and the vertical form of Ref. 149's theoretical expression for the log-derivative of the wellbore pressure drop, we have shown that the primary reason for the wellbore pressure response being dominated by changes in the total relative mobility near the perforations is due to a much greater velocity of the fluids in that region.

For the pressure buildup tests simulated in these constant-pressure boundary reservoirs, we have shown that the underlying reason for the increase in the pressure derivative is due to gravity effects, and in particular, phase redistribution in the reservoir. We do note that the magnitude of the these pressure changes during the late time buildup period are at the limit of our ability to measure in the field, and as such, may not be observable in practice.

None-the-less, several other physical phenomena occurring in the reservoir during the buildup period have been identified and include: (i) phase redistribution may result in reservoir pressures which are greater at some locations than they were initially, prior to the drawdown; (ii) because the location of the constant pressure boundary modeled in these cases was fixed, and because of the phase redistribution effects, the constant pressure boundary may act like a "sink" with fluids flowing out of the reservoir; (iii) also due to the phase redistribution effects, it is possible for fluids to flow back into the reservoir in the high mobility layer; (iv) and, the increasing pressure derivative for the water-gas and oil-gas cases exhibited a unit slope during the buildup. We have not been able to associate a clear meaning to the unit slope other than its apparent direct relationship to the phase redistribution occurring in the reservoir during the buildup. This has not been fully investigated in this work and represents and opportunity for future researchers to investigate.

An extensive array of two-phase and three-phase reservoirs systems have been used to investigate the applicability of standard semilog analysis techniques to drawdown pressure transient and rate data obtained from a restricted-entry well under multiphase flow conditions. Reservoir systems investigated include oil reservoirs underlain by an aquifer, gas reservoirs underlain by an aquifer, oil reservoirs overlain by a gas cap, water reservoirs overlain by a gas cap and oil reservoirs overlain by a gas cap and underlain by an aquifer.

For oil-water systems, Refs. 23 and 24 observed that if multiphase flow effects are important, then a rapid decline in pressure does not necessarily signify the onset of boundary effects, i.e., when coning of water occurs, there is a resultant decrease in the total mobility adjacent to the open interval which causes a rapid decline in the wellbore pressure (increase in the pressure derivative). Results presented here (for each of the two-phase and three-phase reservoir systems

considered) and in Ref. 28 indicate that coning itself, i.e., production of the unwanted fluid, is not necessarily required to observe this increase in the pressure derivative. In fact, all that is required is for there to be a "significant" change in the vertical saturation profile in the reservoir, i.e., movement of the fluid contact or the "building" of the water or gas cone.

For the non-solution gas systems, changes in the wellbore pressure derivative have been shown to coincide (correlate) directly with changes in the total mobility near the fluid contacts. For solution gas reservoir systems, the pressure derivative is so dominated by changes in the total mobility near the open interval that changes in the derivative due to changes in the mobility at the fluid contacts are difficult, if not impossible, to observe. For these solution-gas reservoir systems, we have shown that much of the pressure derivative behavior can be attributed to vertical flow near the sandface and changes in the total mobility which occur just above or below the perforations.

Unlike one-dimensional radial reservoir systems in which previous authors (e.g., Refs. 31-34) have suggested the use of a multiphase pseudopressure based on a unique functionality between saturation and pressure, we note that saturation is neither a unique function of pressure or phase potential for the reservoir systems (two-dimensional cross-sections) considered here. All multiphase analysis presented in this work are then presented in terms of pressure only.

Using the transient pressure and rate data, a total mobility was formally calculated for each of these reservoir systems using the following equation:

$$\bar{\lambda}_t = \frac{70.6(q_o B_o + q_w B_w + q_{gf} B_g)}{h d\Delta p/d\ln t} \ . \tag{9.3}$$

For a fully-penetrating well in a solution-gas-oil reservoir in which gravity effects are included and the saturation at the sandface changes with time, we have presented arguments and numerical results which show that the saturation must be

independent of the vertical direction at the sandface before Eq. 9.3 will become applicable; i.e., provide accurate estimates of the thickness-averaged total mobility at the sandface. Furthermore, for reservoir fluids in which the viscosity and formation volume factors are functions of pressure, we have shown that the proper interpretation of the mobilities calculated from Eq. 9.3 is one in which all PVT properties are evaluated at the prevailing wellbore pressure.

For data obtained from a restricted-entry well in all of the reservoir systems investigated except the gas reservoir - aquifer systems, Eq. 9.3 greatly underpredicted the actual mobilities existing in the reservoir. For the gas reservoir - aquifer systems, the calculated mobilities were slightly overpredicted. For reservoir systems not containing solution gas, the calculated mobilities were found to more closely approximate the thickness-averaged total mobility in the outer region of the reservoir. For reservoir systems containing solution gas, the calculated mobilities were found to more closely approximate the total mobility averaged over the open interval at the sandface.

For the gas reservoir - aquifer systems, we have shown that ignoring the presence of water in the system results in negligible error; i.e., accurate estimates of the total-thickness-averaged effective gas permeability can be obtained by utilizing the real gas pseudopressure only.

For all of the reservoir systems considered, we have shown that while during drawdown a "steady-state" region exists in the reservoir between the well and some point out in the reservoir, this zone does not extend to that region of the reservoir where vertical equilibrium (pseudoradial flow) exists. This means that the wellbore pressure is influenced by vertical flow in that region ahead of the steady-state zone and behind the region of vertical equilibrium.

For all of the multiphase reservoir systems investigated, we have shown that the percent deviation between the mobilities calculated formally with Eq. 9.3 and the mobilities existing in the reservoir correlate extremely well with the thickness of of the aquifer (for those cases containing an aquifer) and with the thickness of the gas cap (for those cases containing a gas cap). This result provides us with hope that accurate estimates of in-situ fluid mobilities may eventually be obtained from drawdown pressure and rate data, though we have yet to be able to obtain these ourselves.

For water reservoir - gascap cases, we have shown that the dimensionless porosity-compressibility-thickness product, i.e.,'

$$\omega = \frac{\phi_1 c_{t1} h_1}{\overline{\phi c_t} h} \ , \tag{9.4}$$

is an important correlating parameter in the interpretation of the pressure transient data.

In Chapter VII we have investigated the applicability of semilog analysis techniques to buildup pressure transient data obtained from a restricted-entry well previously produced under a constant rate and multiphase flow conditions. The same extensive array of two-phase and three-phase reservoirs systems investigated for the drawdown pressure transient analysis Chapter VI were used.

The buildup pressure data for nearly all of the cases examined exhibited approximate semilog straight lines indicative of pseudoradial flow in the reservoir. This result supports our conclusions in Chapter V concerning the fact that the common practice of approximating a gas cap or aquifer as a constant pressure boundary cannot be justified.

For nearly all of the cases examined, including those cases in which the drawdown pressure data was uninterpretable, standard Horner analysis of the

pseudoradial flow pressure buildup data provided an excellent approximation to the thickness-averaged total mobility in the outer region of the reservoir. For each of the reservoir systems, a thickness-averaged total mobility was formally calculated using the following equation:

$$\bar{\lambda}_t = \frac{70.6(q_o B_o(p_{ws}) + q_w B_w(p_{ws}) + q_{gf}(p_{ws}) B_g(p_{ws}))}{h d\Delta p / d \ln t_e} \ , \tag{9.5}$$

where the thickness-averaged total mobility $\bar{\lambda}_t$ was interpreted to be

$$\bar{\lambda}_t = \frac{1}{h} \int_0^h \left(\frac{k k_{ro}}{\mu_o(p_{ws})} + \frac{k k_{rg}}{\mu_g(p_{ws})} + \frac{k k_{rw}}{\mu_w(p_{ws})} \right) dz \tag{9.6}$$

and kk_{ro}, kk_{rg} and kk_{rw} correspond to the region in the outer part of the reservoir where pseudoradial flow exists, but viscosities are evaluated at the wellbore shut-in pressure. In Eq. 9.5, equivalent time, t_e is defined as

$$t_e = \frac{t_p \Delta t}{t_p + \Delta t} \ , \tag{9.7}$$

Δp is defined as

$$\Delta p = p_{ws} - p_{wf,s} \ , \tag{9.8}$$

p_{ws} is the shut-in wellbore pressure and $p_{wf,s}$ is the flowing wellbore pressure at the instant of shut-in.

For the two-phase gas-water systems investigated, an alternative Horner time ratio based on a shut-in pseudotime was also considered, where an equivalent-pseudotime, t_{ae}, was defined as

$$t_{ae} = \frac{t_p \Delta t_a}{t_p + \Delta t} \ , \tag{9.9}$$

with pseudo-shut-in time defined by

$$\Delta t_a = \int_0^{\Delta t} \frac{dt}{\mu_g c_t} \ . \tag{9.10}$$

Equation 9.5 was then used with t_e replaced by t_{ae}. In a practical sense, there was little difference between the mobilities calculated using Eq. 9.5 with either t_e or t_{ae}. Note that the mobilities calculated using Eq. 9.5 were in excellent agreement with the "actual" mobilities input into the simulator and existing in the outer region of the reservoir. This result was in spite of the fact that production during the drawdown period was purposely set to an extremely high rate to insure a large pressure change during the simulated well test; i.e., conditions under which analysis based on a real gas pseudopressure is usually recommended for single phase gas reservoirs.

As in Chapter VI, pressure transient data were analyzed for several water reservoirs overlain by a gas cap due to the similarity to an oil reservoir overlain by a gas cap (without the complications of mass transfer between the phases) and in hopes of identifying parameters contributing to the pressure transient behavior. Similar to the drawdown behavior for such systems, the buildup pressure transient data exhibited a slightly increasing log-derivative of the shut-in pressure. It was shown that this increasing derivative was related to ω, the ratio of the porosity-compressibility product of the open interval divided by the thickness-averaged value, where

$$\omega = \frac{\phi_1 c_{t1} h_1}{\overline{\phi c_t} h} \tag{9.11}$$

and

$$\overline{\phi c_t} = \frac{1}{h} \int_0^h \phi c_t dz \ . \tag{9.12}$$

Also similar to the drawdown, we showed for a small ω, the log-derivative of the shut-in wellbore pressure could fall below the "correct" value before returning to the proper semilog slope. We also note note that the percent deviation in the calculated and "actual" thickness-averaged total mobilities reported in Table 7.3 correlate extremely well with $1/\omega$. The implications of this result were not pursued in this study, but rather, it is suggested that they be investigated in future work related to segregated multiphase reservoirs.

For reservoir systems containing solution gas, four different methods for estimating the thickness-averaged total mobility were considered, differing only in the gas production rate utilized in Eq. 9.5. The first method utilized the gas flow rate at the instant of shut-in, $q_{gf}(t_p)$. This method was shown to be theoretically inconsistent with the actual physics of the problem; i.e., the method results in predicted mobilities significantly greater than ever exists in the reservoir. The second method utilized the producing gas-oil ratio, R, at the instant of shut-in; i.e.,

$$q_{gf}(p_{ws}) = q_o[R(t_p) - R_s(p_{ws})] \ . \tag{9.13}$$

This method was also shown to fail in instances when the solution gas-oil ratio becomes greater than the producing gas-oil ratio at the instant of shut-in; by Eq. 9.13, this situation indicates a negative gas flow rate. An alternative to this method was also considered where the free gas production rate predicted by Eq. 9.13 was simply set equal to zero whenever it became negative. Results for the thickness-averaged total mobility then became nearly identical to the results obtained from the fourth method. The forth method utilized the drawdown free gas production rate versus pressure relationship; i.e.,

$$q_{gf}(p_{ws}) = q_o[R(p_{wf}) - R_s(p_{wf})] \ , \tag{9.14}$$

for $p_{ws} = p_{wf}$. Results obtained for the thickness-averaged total mobilities using these methods were generally quite good.

For solution-gas reservoir systems initially above the bubble-point pressure, we have shown that a sharp increase in the pressure derivative may appear for fully-penetrating reservoir systems and a significant deviation in the derivative may arise in the case of a restricted-entry well. As has been discussed in the literature, this phenomena is related to the collapse of the gas phase in some region of the reservoir during the buildup period. More importantly, however, we have shown that this pressure response is fundamentally related to the step change in the total fluid compressibility which occurs when the bubble-point pressure is crossed. The existence of this phenomena implies that it may be possible in some cases to determine the original bubble-point pressure of the reservoir fluids from a pressure buildup test. We note that other operating parameters have not been investigated fully as they relate to this phenomena and include such items as the effect of the production rate, oil gravity, solution gas-oil ratio and gas gravity, among others. Further investigation of these or additional parameters is strongly recommended for future study.

We have shown that the fundamental assumptions incorporated into our semilog analysis techniques, i.e., the existence of vertical equilibrium in the reservoir and the existence of a "no-flow steady-state" region between the wellbore and the location of the reservoir where vertical equilibrium exists are at the worst approximately satisfied and in most cases, satisfied extremely well. This is in contrast to the drawdown results for which no case exhibited a "steady-state" region extending out to the location in the reservoir where vertical equilibrium exists. Because the drawdown results were greatly in error and the buildup results were quite accurate, this again implies that these two assumptions must be

satisfied (necessary conditions) in order for semilog analysis of pressure transient data (either drawdown or buildup) to be valid.

Lastly, we have presented two correlations for estimating the pseudoskin factor due to restricted-entry in multiphase reservoirs. These correlations were shown to provide reasonably accurate results for oil-water reservoir systems and for gas-water reservoir systems in which the gas production rate is low, i.e., small pressure drawdown. For gas-water reservoirs produced at a high rate and for reservoirs containing solution-gas, it has been shown that these correlations may be significantly in error if not modified.

A method for correcting these errors in the damage skin and pseudoskin calculations resulting from non-linearities due to multiphase flow effects and due to variations in the fluid properties was developed by this author as part of this work. This method has also been shown to work exceptionally well for gas condensate reservoirs. This method is not, however, pursued further in this work, but rather is presented in Ref. 150. If the reader is interested in obtaining more accurate skin factor estimates for multiphase reservoir systems, it suggested that he or she investigate the method presented in Ref. 150.

NOMENCLATURE

Variable	Definition (Oilfield Units in Parenthesis)
a	transmissibility area terms defined by Eqs. 2.4.37-2.4.39, (ft)
A	Jacobian matrix; or,
	area, (ft^2)
$\tilde{A}$	permuted Jacobian matrix
b	r.h.s. vector - residuals of the primary equations; or,
	penetration ratio, h_w/h
$\tilde{b}$	permuted r.h.s. vector - residuals of the primary equations
B_g	gas formation volume factor, (RB/STB)
B_o	oil formation volume factor, (RB/STB)
B_{od}	differential oil formation volume factor, (RB/STB)
B_t	total fluid formation volume factor, (RB/STB)
B_w	water formation volume factor, (RB/STB)
C	preconditioned matrix A; or,
	Schur complement
C'	correlating parameter for pseudoskin correlation
c_1	units conversion factor, $(0.006328\ ft^2 \cdot cp/[md \cdot psi \cdot day])$; or,
	correlating parameter for pseudoskin correlation, Eq. 8.1.11
c_2	units conversion factor, $(5.6146\ scf/STB$ or $ft^3/RB)$
C_p	cost of algorithm, $T_p \cdot P$
$\hat{c}$	element of Given's rotation
c_f	rock compressibility, (psi^{-1})

c_g	gas phase compressibility, (psi^{-1})
c_o	oil phase compressibility, (psi^{-1})
c_t	total compressibility, (psi^{-1})
c_{tb}	total compressibility above the bubble-point pressure, (psi^{-1})
c_w	water phase compressibility, (psi^{-1})
d	preconditioned r.h.s. vector b
D	block diagonal of matrix A
e_1	first unitary vector $\{1, 0, 0, \ldots, 0\}^T$
E	relative error
E_p	efficiency of algorithm, S_p/P
f_m	fractional flow rate of phase m
f_w	fractional flow rate of water
f_1	dimensionless open interval flow capacity (Eqs. 6.1.8 and 6.1.9)
f_2	dimensionless flow capacity of layer 2 (Eq. 8.1.21)
F	block diagonal of BILU preconditioner matrix
g	gravitational constant, $(32.2\ ft/s^2)$
g_c	conversion factor for gravitational constant $(32.174\ lb_f \cdot s^2/lb_m \cdot ft)$
G	gravity term defined by Eq. 5.2.10 or its equivalent
h	reservoir thickness, (ft) or
	element of upper Hessenberg matrix H
h_D	dimensionless thickness, Eq. 3.1.11
$\bar{h}^*_D$	(Eq. 6.4.15)
h_w	length of perforated zone, (ft)
h_{w_1}	vertical location of bottom of perforated zone, (ft)
h_{w_2}	vertical location of top of perforated zone, (ft)
$\tilde{h}_{w_D}$	dimensionless parameter defined by Eq. 8.1.10
i	discrete radial grid index
I	identity matrix

J	Jacobian matrix
k	number of orthogonalizations; or,
	horizontal permeability, (md); or,
	discrete vertical grid index; or,
	iteration level
$[k]$	permeability tensor, (md)
k_h	horizontal permeability, (md)
k_r	relative permeability
k_{rg}	relative permeability to gas
k_{ro}	relative permeability to oil
k_{rw}	relative permeability to water
k_s	absolute permeability in skin zone, (md)
$\bar{k}_t$	thickness-averaged absolute permeability, (md)
k_z	vertical permeability, (md)
k_{zs}	vertical permeability in skin zone, (md)
$\bar{k}_z^*$	dimensionless vertical permeability (Eq. 6.4.14)
L	strictly lower block triangular part of A
m	slope of semilog straight line portion of plot of
	pressure versus logarithm of time (or equivalent time) (psi)
M	Schur complement preconditioner
$m(p)$	real gas pseudopressure, $(psi \cdot scf/cp \cdot ft^3)$
m_t	total mass rate, (lb_m/day)
m_{wD}	dimensionless real gas pseudopressure at the wellbore
$\overline{m}_t$	total molar rate, $(lbmole/day)$
n	order of matrix A
	or, time level
N_r	number of radial grid points
N_{r1}	number of radial grid points in domain 1

N_T	total number of grid points
N_z	number of vertical grid points
N_{zgoc}	minimum discrete vertical index for which $z_k \geq z_{goc}$
N_{zref}	maximum discrete vertical index for which $z_k \leq z^r$
N_{zowc}	maximum discrete vertical index for which $z_k \leq z_{owc}$
N_{zw_1}	vertical direction discrete index of grid block with lower block boundary located at h_{w_1}
N_{zw_2}	vertical direction discrete index of grid block with upper block boundary located at h_{w_2}
p	pressure, $(psia)$
P	permutation matrix; or, number of processors
p_b	bubble-point pressure, $(psia)$
p_{cog}	gas-oil capillary pressure, (psi)
p_{cow}	oil-water capillary pressure, (psi)
p_d	dew-point pressure, $(psia)$
p_{dl}	lower dew-point pressure, $(psia)$
p_{du}	upper dew-point pressure, $(psia)$
p_D	dimensionless pressure, Eq. 3.1.1
p_g	gas phase pressure, $(psia)$
p_o	oil phase pressure, $(psia)$
p_w	water phase pressure, $(psia)$
p_{wb}	bottomhole wellbore pressure, $(psia)$
p_{wD}	dimensionless flowing wellbore pressure, Eq. 3.1.7
p_{wf}	flowing wellbore pressure, $(psia)$
$p_{wf,s}$	flowing wellbore pressure at the instant of shut-in, $(psia)$
p_{ws}	shut-in wellbore pressure, $(psia)$
q	volumetric flow rate, (RB/day)

Q	overall preconditioner matrix
q_g	volumetric gas flow rate at reservoir conditions, (ft^3/day)
q_{gf}	free gas production rate at the sandface, (ft^3/day)
q_o	volumetric oil flow rate at reservoir conditions, (RB/day)
q_w	volumetric water flow rate at reservoir conditions, (RB/day)
r	radial direction/location,(ft)
	or, residual vector $(r = b - Ax)$
R	permutation matrix
	or, gas-oil ratio, $(scfg/STBO)$
r_D	dimensionless radius, Eq. 3.1.3
r_e	external radius of reservoir, (ft)
$R_{L,st}$	gas liberated by differential liberation from the bubble-point
	pressure to pressure, p, (scf/STB)
r_s	radius extent of skin zone, $(ft$
R_s	solution gas-oil ratio, $(scfg/STBO)$
R_{sb}	solution gas-oil ratio at bubble-point pressure, $(scfg/STBO)$
r_v	oil volatility, $(STBO/scfg)$
r_{vd}	oil volatility at dew-point pressure, $(STBO/scfg)$
r_w	wellbore radius, (ft)
s	mechanical skin factor
$\hat{s}$	element of Given's rotation
s_b	pseudoskin factor
S_p	speedup, T_1/T_p
s_t	total or apparent skin factor
S_g	gas saturation
S_{gc}	critical gas saturation
S_o	oil saturation
S_{or}	residual oil saturation

S_w	water saturation
S_{wc}	connate water saturation
t	time, $(days)$
T_1	cpu time required for best sequential algorithm on a single processors
t_{ae}	equivalent pseudotime, Eq. 7.2.1 $(days \cdot psi/cp)$
t_D	dimensionless time, Eq. 3.1.2
t_e	Agarwal equivalent time, Eq. 7.1.2, $(days)$
t_{int}	time to intersection of drawdown and buildup pressure derivative curves, $(days)$
$\mathcal{T}$	transmissibility term, $(lbmole/psi \cdot day)$
t_p	total producing time, $(days)$
T_p	cpu time required for parallel algorithm on P processors
t_s	time to start of semi-log straight line, $(days)$
Δt	shut-in time, $(days)$
Δt_a	pseudo-shut-in time, Eq. 7.2.2 $(days \cdot psi/cp)$
U	strictly upper block triangular part of matrix A
v	search direction vector
$\vec{v}$	phase velocity, (ft/day)
$v_{\Delta S_w}$	velocity of line of constant saturation
V	discrete grid block volume, (ft^3)
$\vec{x}$	solution vector
$\tilde{x}$	permuted solution vector
x_1	mole fraction component #1 in oil phase
x_2	mole fraction component #2 in oil phase
y	preconditioned solution vector
y_1	mole fraction component #1 in gas phase
y_2	mole fraction component #2 in gas phase
z	vertical direction/position, (ft)

z_1	vertical location of lower-most perforation, (ft)
z_2	vertical location of upper-most perforation, (ft)
z^r	reference vertical location at which reference pressure is defined, (ft)
z_D	dimensionless height, Eq. 3.1.10
z_D	dimensionless location of the perforated interval, Eq. 3.1.12
z_D^*	equivalent average pressure point
z_g	gas compressibility factor
z_{goc}	vertical location of gas-oil contact, (ft)
z_{owc}	vertical location of water-oil contact, (ft)

Greek Symbols

α	grid expansion factor
ε	convergence or error criteria
γ	phase gravity, (psi/ft)
$\overline{\gamma}$	volumetric averaged total fluid gravity, (psi/ft)
Γ_3	boundary between subdomains, (Fig. 2.5)
κ	spectral condition number
λ	phase mobility, (md/cp); or,
	eigenvalue
λ_t	total mobility, (md/cp); or,
$\bar{\lambda}$	thickness-averaged mobility, (md/cp)
$\bar{\lambda}_t$	thickness-averaged total mobility, (md/cp)
λ_r	relative mobility, (cp^{-1})
$\bar{\lambda}_z^*$	see Eq. 6.4.17
μ	viscosity, (cp)
ν	Newton's method iteration level
π	3.1415926535
ρ	mass density, (lb_m/ft^3)

	or,l_2–norm of residual vector
$\overline{\rho}$	molar density, $(lbmole/ft^3)$
ϕ	porosity
Φ	phase potential, (psi)
ω	ratio of the porosity-compressibility product for the open interval divided by the thickness-averaged value
Ω	region (domain)
δ	difference in successive iteration values of unknowns
Δ	difference operator
∇	"del" operator, differential operator

Subscripts

1	hydrocarbon component #1; or, of or belonging to layer 1
2	hydrocarbon component #2; or, of or belonging to layer 2
3	water component
4	wellbore constraint equation
c	capillary or, constant
ex	extrapolated
f	at saturation front
g	gas phase
gc	critical gas
goc	gas-oil contact
h	in horizontal (radial) direction
i	at initial conditions, or, equation index,

	or, discrete index of radial grid location
$i + \frac{1}{2}$	discrete index of radial grid block boundary location
inf	inflection
j	variable index
k	discrete index of vertical grid location
$k + \frac{1}{2}$	discrete index of vertical grid block boundary location
m	phase (oil, gas, or water)
ν	Newton's method iteration level
o	oil phase
og	oil-gas
ow	oil-water
r	relative; or
	radial
w	water phase
	or, wellbore
wb	wellbore
wc	connate water
wf	wellbore flowing
woc	water-oil contact
ws	wellbore shut-in
z	in vertical direction

Superscripts

$+$	upstream side of saturation front
$-$	downstream side of saturation front
a	actual or measured
k	iteration counter
L	Linear

n	discrete index of time; or,
	nonlinear
ν	Newton's method iteration level
r	reference
T	transpose

REFERENCES

1. Muskat, M.: *Physical Principles of Oil Production,* McGraw-Hill Book Co., Inc., New York City (1949) 259-270.

2. Bilhartz, H.L., Jr. and Ramey, H.J., Jr.: "The Combined Effects of Storage, Skin and Partial Penetration on Well Test Analysis," paper *SPE 6753*, presented at the SPE 52^{nd} Annual Technical Conference and Exhibition held in Denver, CO, Oct. 9-12, (1977).

3. Brons, F. and Marting, V.E.: "The Effect of Restricted Fluid Entry on Well Productivity," *J. Pet. Tech.* (February, 1961) 172-174.

4. Nisle, R.G.: "The Effect of Partial Penetration on Pressure Build-Up in Oil Wells," *Pet. Trans., AIME*, Vol. 213, (1958) 85-90.

5. Abbaszadeh, M. and Hegeman, P.: "Pressure Transient Behavior of Slanted Limited-Entry Well In a Reservoir With a Gas Cap and/or Bottomwater Drive," paper *SPE 19045*, SPE, Richardson, TX, (1988).

6. Buhidma, I.M. and Raghavan, R.: "Transient Pressure Behavior of Paritally Penetrating Wells Subject to Bottomwater Drive," *J. Pet. Tech.* (July 1980) 1251-1261.

7. Lockhart, D.L., Ogbe, D.O. and Dehghani, K.: "Single Well Pressure Transient Testing in Prudhoe Bay, Alaska," paper *SPE 18139* presented at the SPE 63^{rd} Annual Technical Conference and Exhibition held in Houston, TX, Oct. 2-5, 1988.

8. Streltsova-Adams, T.D.: "Pressure Transient Analysis for Afterflow-Dominated Wells Producing From a Reservoir With A Gas Cap," *J. Pet. Tech.* (April 1981) 743-754.

9. Odeh, A.S.: "An Equation for Calculating Skin Factor Due to Restricted Entry," *J. Pet. Tech.* (June, 1980) 964-965.

10. Papatzacos, P.: "Approximate Partial-Penetration Pseudoskin for Infinite-Conductivity Wells," *SPE Reservoir Engineering* (May 1987) 227-234.

11. Gringarten, A.C. and Ramey, H.J.Jr.: "An Approximate Infinite Conductivity Solution for a Paritally Penetrating Line-Source Well," *Soc. Pet. Eng. J.*, (April 1975) 140-148.

12. Kuchuk, F.J. and Kirwan, P.A.: "New Skin and Wellbore Storage Type Curves for Partially Penetrating Wells," *SPE Formation Evaluation* (Dec. 1987) 546-554.

13. Odeh, A.S.: "Pseudosteady-State Flow Capacity of Oil Wells With Limited Entry and an Altered Zone Around the Wellbore," *Soc. Pet. Eng. J.* (Aug. 1977) 271-280.

14. Ding, W.: *Analysis of Data From a Restricted-Entry Well,* Ph.D. Dissertation, The University of Tulsa, Tulsa, OK (1989).

15. Kazemi, H. and Seth, M.S.:"Effect of Anisotropy and Stratification on Pressure Transient Analysis of Wells with Restricted Flow Entry," *J. Pet. Tech.* (May 1969) 639-647.

16. Yeh, N. and Reynolds, A.C.: "Computation of the Pseudoskin Factor Caused by a Restricted-Entry Well Completed in a Multilayer Reservoir, *SPE Formation Evaluation*, (June 1989) 253-263.

17. Ding, W. and Reynolds, A.C.: "Computation of the Pseudodskin Factor for a Restricted-Entry Well", paper *SPE 21705*, presented at the SPE Production Operations Symposium held in Oklahoma City, OK, April 7-9, 1991.

18. Yeh, N. and Reynolds, A.: "Analysis of Pressure Data From a Restricted-Entry Well in a Multilayer Reservoir," *SPE Formation Evaluation* (March 1989) 253-263.

19. Yeh, N.: *Well Test Analysis for Restricted-Entry Wells in Multilayer Reservoirs,* PhD dissertation, U. of Tulsa, Tulsa, OK (1986).

20. Reynolds, A.C., Chen, J.C. and Raghavan, R.: "Pseudoskin Factor Caused by Partial Penetration," *J. Pet. Tech.* (Dec. 1984) 2197-2210.

21. Chu, W.C., Chen, J.C., Reynolds, A.C. and Raghavan, R.: "On the Analysis of Well Test Data Influenced by Wellbore Storage, Skin, and Bottomwater Drive," *J. Pet. Tech.* (Nov. 1984) 1991-2001.

22. Thompson, L.G. and Reynolds, A.C.: "Analysis of Variable-Rate Well-Test Pressure Data Using Duhamel's Principle," *SPE Form. Eval.* (Oct. 1986) 453-470.

23. Chu, W.C., Reynolds, A.C. and Raghavan, R.: "Pressure Transient Analysis of Two-Phase Flow Problems," *SPE Form. Eval.* (April 1986) 151-164.

24. Chu, W.C.: *Well Test Analysis for Two-Phase Flow*, PhD dissertation, U. of Tulsa, Tulsa, OK (1981).

25. Al-Khalifah, A.J.A. and Odeh, A.S.: "Well Test Analysis in Gravity-Segregated Reservoirs," paper *SPE 18577*, SPE, Richardson, TX, (1988).

26. Al-Khalifa, A.J. and Odeh, A.S.: "Well Test Analysis in Oil Reservoirs with Gas Caps and/or Water Aquifers," paper *SPE 19842* presented at the SPE 64^{th}

Annual Technical Conference and Exhibition held in San Anatonio, TX, Oct. 8-11, 1989.

27. Rosenzweig, J.J., Korpics, D.C. and Crawford, G.E.: "Pressure Transient Analysis of the JX-2 Horizontal Well, Prudhoe Bay, Alaska," paper *SPE 20610* presented at the SPE 65^{th} Annual Technical Conference and Exhibition held in New Orleans, LA, Sept. 23-26, 1990.

28. Roadifer, R.D. and Reynolds, A.C.: "Estimation of the Pseudoskin Factor Caused by a Restricted-Entry Well Under Multiphase Flow Conditions," paper *SPE 26052* presented at the 1993 SPE Western Regional Meeting held in Anchorage, AK, May 26-28, 1993.

29. Perrine, R.L.: "Analysis of Pressure Buildup Curves," *Drill. and Prod. Prac.,* API (1956) 482-509.

30. Martin, J.C.: "Simplified Equations of Flow in Gas Drive Reservoirs and the Theoretical Foundation of Multiphase Pressure Buildup Analysis," *J. Pet. Tech.,* (Oct. 1959) 321-323.

31. Serra, K., Peres, A. and Reynolds, A.: "Well Test Analysis for Solution-Gas-Drive Reservoirs: Part I - Determination of Relative and Absolute Permeabilities," *SPEJ* (June 1990).

32. Al-Khalifah, A-J.A., Horne, R.N. and Aziz, K.: "In-Place Determination of Reservoir Relative Permeability Using Well Test Analysis," paper *SPE 16774* presented at the SPE 62^{nd} Annual Technical Conference and Exhibition held in Dallas, TX, Sept. 27-30, 1987.

33. Evinger, H.H. and Muskat, M.: "Calculation of Theoretical Productivity Factor," *Trans., AIME* 146 (1942) 126-139.

34. Raghavan, R.: "Well Test Analysis: Wells Producing by Solution Gas Drive," *Soc. Pet. Eng. J.* (Oct. 1977) 369-376.

35. Ayan, C. and Lee, W.J.: "The Effects of Multiphase Flow on the Interpretation of Pressure Buildup Tests," paper *SPE 15537* presented at the SPE 61^{st} Annual Technical Conference and Exhibition held in New Orleans, LA, Oct. 5-8, 1986.

36. Serra, K.V., Peres, A.M.M. and Reynolds, A.C.: "Well Test Analysis for Solution-Gas-Drive Reservoirs: Part II - Buildup Analysis," *SPEJ* (June 1990).

37. Bøe, A., Skjæveland, S. and Whitson, C.: "Two-Phase Pressure Test Analysis," paper *SPE 10224* presented at the 1981 SPE Annual Technical Conference and Exhibition held in San Antonio, TX (Oct. 5-7, 1981).

38. Aanonsen, S.: *Nonlinear Effects During Transient Flow in Reservoirs as Encountered in Well Test Analysis,* Dr. Scient. dissertation, U. of Befgen, Norway (1985).

39. Shank, G.D. and Vestal, C.R.: "Practical Techniques in Two-Pseudocomponent Black Oil Simulation," paper *SPE 15156* presented at the SPE Rocky Mountain Regional Meeting held in Billings, MT, May 19-21, 1986.

40. Stone, H.L.: "Probability Model for Estimating Three-Phase Relative Permeability," *J. Pet. Tech.*, (Feb. 1970) 214-218.

41. Stone, H.L.: "Estimation of Three-Phase Relative Permeability and Residual Oil Data," *J. Can. Pet. Tech.*, (Oct.-Dec. 1973) 53-61.

42. MacDonald, R.C. and Coats, K.H.: "Methods for Numerical Simulation of Water and Gas Coning," *SPEJ,* (Dec. 1970) 425-436.

43. Aziz, K. and Settari, A.: *Petroleum Reservoir Simulation*, Applied Science Publishers Ltd, London, (1979).

44. Hawkins, M.R.,Jr.: "A Note on the Skin Effect," *Trans. AIME* (1956) 356-357.

45. Abou-Kassem, J.H. and Farouq Ali, S.M.: "Appraisal of Steamflood Models," *SPE Paper 13947* presented at the SPE 1985 California Regional Meeting held in Bakersfield, CA, March 27-29, (1985).

46. Blair, B.P. and Weinaug, C.F.: "Solution of Two-Phase Flow Problems Using Implicit-Difference Equations," *Soc. Pet. Eng. J.*, (1960) 417-424.

47. Peaceman, D.W.: *Fundamentals of Numerical Reservoir Simulation*, Elsevier Scientific Publishing Company, Amsterdam, (1977).

48. Vinsome, P.K.W.: "Orthomin, an Iterative Method for Solving Sparse Sets of Simultaneous Linear Equations," paper *SPE 5729*, presented at the Fourth SPE-AIME Symposium on Numerical Simulation of Reservoir Performance held in Los Angeles, CA, Feb. 19-20, 1976.

49. Saad, Y. and Schultz, M.H.: "GMRES - a Generalized Minimum Residual Algorithm for Solving Nonsymmetric Linear Systems," *Report # 254*, Dept. of Computer Science, Yale University, 1983.

50. Saad, Y. and Schultz, M.H.: "Conjugate Gradient-Like Algorithms for Solving Nonsymmetric Linear Systems," *Math. Comp.*, Vol. 44, No. 170, (April 1985) 417-424.

51. Saad, Y. and Schultz, M.H.: "GMRES: A Generalized Minimum Residual Algorithm for Solving Nonsymmetric Linear Systems," *SIAM J. Sci. Statis. Comput.*, Vol. 7, No. 3, (July 1986) 856-869.

52. Van der Vorst, H.A.: "Bi-CGSTAB: A Fast and Smoothly Converging Variant of Bi-CG for the Solution of Nonsymmetric Linear Systems," *SIAM J. Sci. Stat. Comput.* Vol. 13, No. 2, (March 1992) 631-644.

53. Sonneveld, P: "CGS: a Fast Lanczos-type Solver for Nonsymmetric Linear Systems," *SIAM J. Sci. Statist. Comput.*, 10, (1989) 36-52.

54. Betté, S., Díaz, J.C., Jines, W.R. and Steihaug,T.: "A Block Preconditioned Conjugate Gradient-type Iterative Solver for Linear Systems in Thermal Reservoir Simulation," *J. Comp. Phys.*, Vol. 67, No. ?, (Nov. 1986) 37-58.

55. Eisenstat, S.C., Elman, H.C. and Schultz, M.H.: "Variational Iterative Methods for Nonsymmetric Systems of Linear Equations," *SIAM J. Numer. Anal.*, Vol. 20, No. 2, (April 1983) 345-357.

56. Axelsson, O.: "Conjugate Gradient Type Methods for Unsymmetric and Inconsistent Systems of Linear Equations," *Lin. Alg. Appl.*, Vol. 29, (1980) 1-16.

57. Elman, H.C.: *Iterative Methods for Large Sparse Nonsymmetric Systems of Linear Equations,* Ph.D. Thesis, Computer Science Dept., Yale Univ., New Haven, CT, (1982).

58. Jea, K.C. and Young, D.M.: "Generalized Conjugate Gradient Acceleration of Nonsymmetrizable Iterative Methods," *Lin. Alg. Appl.*, 34 (1980) 159-194.

59. Saad, Y.: "Krylov Subspace Methods for Solving Large Unsymmetric Linear Systems," *Math. Comput.*, 37 (1981) 105-126.

60. Saad, Y.: "Practical Use of Some Krylov Subspace Methods for Solving Indefinite and Unsymmetric Linear Systems," *SIAM J. Sci. Statist. Comput.*, 5 (1984) 203-228.

61. Ponting, D.K., Foster, B.A., Naccache, P.F., Nicholas, M.O., Pollard, R.K., Rae, J., Banks, D. and Walsh, S.K.: "An Efficient Fully Implicit Simulator," *Soc. Pet. Eng. J.*, 23 (June 1983) 544-552.

62. Eisenstat, S.C., Elman, H.C. and Schultz, M.H.: "Block-Preconditioned Conjugate-Gradient-Like Methods for Numerical Reservoir Simulation," paper *SPE 13534*, presented at the SPE 1985 Reservoir Simulation Symposium held in Dallas, TX, Feb. 10-13, 1985.

63. Northrup, E.J. and Woo, P.T.: "Application of Preconditioned Conjugate-Gradient-Like Methods in Reservoir Simulation," paper *SPE 13532* presented at the SPE 1985 Reservoir Simulation Symposium held in Dallas, TX, Feb. 10-13, 1985.

64. Simon, H.D.: "Incomplete LU Preconditioning for the Helmholtz Equation," *Report CM-55*, Boeing Computer Services, (June 1984).

65. Roadifer, R.D.: "An Investigation of Domain Decomposition Preconditioned Iterative Solvers for Petroleum Reservoir Coning Simulation," Project Report for CS8243, The University of Tulsa, July 23, 1991.

66. Appleyard, J.R. and Cheshire, I.M.: "Nested Factorization," paper *SPE 12264*, presented at the Seventh SPE Symposium on Reservoir Simulation held in San Francisco, CA, Nov. 15-18, 1983.

67. Watts, J.W. III: "A Conjugate Gradient-Truncated Direct Method for the Iterative Solution of the Reservoir Simulation Pressure Equation," *Soc. Pet. Eng. J.*, (June 1981) 345-353.

68. Behie, A. and Forsyth, P.A. Jr.: "Incomplete Factorization Methods for Fully Implicit Simulation of Enhanced Oil Recovery," *SIAM J. Scient. Stat. Comp.*, **5** (1984) 543-561.

69. Tan, T.B.S. and Letkeman, J.P.: "Application of D4 Ordering and Minimization in an Effective Partial Matrix Inverse Iteration Method," paper *SPE*

10493, presented at the Sixth SPE Symposium on Reservoir Simulation held in New Orleans, LA, Feb. 1-3, 1982.

70. Meijerink, J.A.: "Iterative Methods for the Solution of Linear Equations Based on Incomplete Block Factorization of the Matrix," paper *SPE 12262*, presented at the Seventh SPE Symposium on Reservoir Simulation held in San Francisco, CA, Nov. 15-18, 1983.

71. Wallis, J.R., Kendall, R.P. and Little, T.E.: "Constrained Residual Acceleration of Conjugate Residual Methods," paper *SPE 13536*, presented at the SPE 1985 Reservoir Simulation Symposium held in Dallas, TX, Feb. 10-13, 1985.

72. Dupont, T., Kendall, R.P. and Rachford, H.H. Jr.: "An Approximate Factorization Procedure for Solving Self-Adjoint Elliptic Difference Equations," *SIAM J. Numer. Anal.*, **5** (1968) 559-573.

73. Gustafsson, I.: "A Class of First Order Factorization Methods," *BIT*, **18** (1978) 142-156.

74. Díaz, J.C., Jines, W.R., McDonald, A.E. and Stehaug, T.: "Block Diagonal Scaling for Iterative Methods in Thermal Simulation," *Comm. Appl. Num. Methods*, Vol. 1, (1985) 263-267.

75. Behie, A. and Forsyth, P.A. Jr.: "Practical Considerations for Incomplete Factorization Methods in Reservoir Simulation," paper *SPE 12263*, presented at the Seventh SPE Symposium on Reservoir Simulation held in San Francisco, CA, Nov. 15-18, 1983.

76. Simon, H.D.: "Incomplete LU Preconditioners for Conjugate-Gradient-Type Iterative Methods," paper *SPE 13533*, presented at the SPE 1985 Reservoir Simulation Symposium held in Dallas, TX, Feb. 10-13, 1985.

77. Schwarz, H.A.: *Gesammelte mathematische Abhandlungen*, Springer, Berlin, 2 (1890) 133-134.

78. Concus, P., Golub, G.H. and O'Leary, D.P.: "A Generalized Conjugate Gradient Method for the Numerical Solution of Elliptic Partial Differential Equations," *Proceedings of the Symposium on Sparse Matrix Computations*, J.R. Bunch and D.J. Rose, eds., Academic Press, New York, (1975) 309-332.

79. Bjørstad, P.E. and Widlund, O.B.: "Iterative Methods for the Solution of Elliptic Problems on Regions Partitioned into Substructures," *Technical Report 136*, Courant Institute of Mathematical Sciences, New York Univ., (Sept. 1984).

80. Dryja, M.: "A Capcitance Matrix Method for Dirichlet Problem on Polygonal Region," *Numer. Math.*, **39**, (1982) 51-64.

81. Golub, G.H. and Mayers, D.: "The Use of Pre-Conditioning Over Irregular Regions," Lecture at the Sixth Int. Conf. on Computing Methods in Applied Sciences and Engineering, Versailles, France (Dec. 1983).

82. Bramble, J.H., Pasciak, J.E. and Schatz, A.H.: "An Iterative Method for Elliptic Problems on Regions Partitioned into Substructures," *Math. Comput.*, **46** (1986) 361-370.

83. Przemieniecki, J.S.: "Matrix Structural Analysis of Substructures," *AIAA J.*, **1** (1963) 138-147.

84. Glowinski, R., Periaux, J. and Dinh, Q.V.: "Domain Decomposition Methods for Nonlinear Problems in Fluid Dynamics," *INRIA Report No.147* (1982).

85. Bjørstad, P.E. and Widlund, O.B.: "Solving Elliptic Problems on Regions Partitioned into Substructures," *Elliptic Problem Solvers II*, G. Birkhoff and A. Schoenstadt, eds., Academic Press (1984) 245-256.

86. Killough, J.E. and Wheeler, M.F.: "Parallel Iterative Linear Equation Solvers: An Investigation of Domain Decomposition Algorithms for Reservoir Simulation," paper *SPE 16021*, presented at the Ninth SPE Symposium on Reservoir simulation held in San Antonio, TX, Feb.1-4, 1987.

87. Chan, T.F.: "Analysis of Preconditioners for Domain Decomposition," *SIAM J. Numer. Anal.*, Vol. 24, No. 2, (April 1987) 382-390.

88. Keyes, D.E. and Gropp, W.D.: "A Comparison of Domain Decomposition Techniques for Elliptic Partial Differential Equations and Their Parallel Implementation," *SIAM J. Sci. Stat. Comput.*, Vol. 8, No. 2, (March 1987) 167-202.

89. Chan, T.F. and Resasco, D.C.: "A Framework for the Analysis and Construction of Domain Decomposition Preconditioners," in *Proceedings of the First Symposium on Domain Decomposition Methods for Partial Differential Equations*, R. Glowinski, G.H. Golub, G.A. Meurant and J. Periaux, eds., SIAM, Philadelphia (1988).

90. Bramble, J.H., Pasciak, J.E. and Schatz, A.H.: "The Construction of Preconditioners for Elliptic Problems by Substructures," *Math. Comp.*, **47** (1986) 103-134.

91. Meurant, G.: "Domain Decomposition Versus Block Preconditioning," in *Proceedings of the First Symposium on Domain Decomposition Methods for Partial Differential Equations*, R. Glowinski, G.H. Golub, G.A. Meurant and J. Periaux, eds., SIAM, Philadelphia (1988).

92. Meurant, G.: "Incomplete Domain Decompositioners for the Conjugate Gradient Method," in *Domain Decomposition Methods*, T.F. Chan et al., eds., SIAM (1989) 100-106.

93. Duff, I.S. and Reid, J.K.: "Some Design Features of a Sparse Matrix Code," *ACM Trans. Math. Soft.*, Vol. 5, No. 1 (March 1979) 18-35.

94. Price, H.S. and Coats, K.H.: "Direct Methods in Reservoir Simulation," *Soc. Pet. Eng. J.* (June 1974) 295-308.

95. Eisenstat, S.C., Gursky, M.C., Schultz, M.H. and Sherman, A.H.: *Yale Sparse Matrix Package,* I. The symmetric codes, Report 112, Department of Computer Science, Yale University, New Haven, Conn., (1977)

96. Eisenstat, S.C., Gursky, M.C., Schultz, M.H. and Sherman, A.H.: *Yale Sparse Matrix Package,* II. The nonsymmetric codes, Report 114, Department of Computer Science, Yale University, New Haven, Conn., (1977)

97. Markowitz, H.M.: "The Elimination Form of the Inverse and Its Application to Linear Programming," *Management Sci.*, **3** (1957) 255-269.

98. Steffenson, R.J. and Sheffield, M.: "Reservoir Simulation of a Collapsing Gas Saturation Requiring Areal Variation in Bubble-Point Pressure," paper *SPE 4275* presented at the 3^{rd} Numerical Simulation of Reservoir Performance Symposium of the Society of Petroleum Engineers of AIME held in Houston, TX, Jan. 10-12, (1973).

99. Spillette, A.G., Hillestad, J.G. and Stone, H.L.: "A High-Stability Sequential Solution Approach to Reservoir Simulation," paper *SPE 4542* presented at the SPE-AIME 48^{th} Annual Fall Meeting held in Las Vegas, NV, Sept. 30 - Oct. 3, (1973).

100. Cook, R.E., Jacoby, R.H. and Ramesh, A.B.: "A Beta-Type Reservoir Simulator for Approximating Compositional Effects During Gas Injection," *Soc. Pet. Eng. J.* (OCt. 1974) 471-481.

101. Kazemi, H.: "A Reservoir Simulator for Studying Productivity Variation and Transient Behavior of a Well in a Reservoir Undergoing Gas Evolution," *J. Pet. Tech.*, (Nov. 1975) 1401-1412.

102. Thomas, L.K., Lumpkin, W.B. and Reheis, G.M.: "Reservoir Simulation of Variable Bubble-Point Problems," *Soc. Pet. Eng. J.* (Feb. 1976) 10-16.

103. Stright, D.H., Jr., Aziz, K., Settari, A. and Starratt, F.E.: "Carbon Dioxide Injection Into Bottom-Water, Undersaturated Viscous Oil Reservoirs," *J. Pet. Tech.* (Oct. 1977) 1248-1258.

104. Thomas, G.W.: *Principles of Hydrocarbon Reservoir Simulation,* International Human Resources Development Corporation, Boston (1982).

105. Ammer, J.R., Sams, W.N. and Brummert, A.C.: "An Extended Black Oil Miscible Simulator That Rigorously Treats Variable Bubblepoint Problems," paper *SPE 18533* presented at the SPE Eastern Regional Meeting held in Charleston, WV, Nov. 1-4, (1988).

106. Letkeman, J.P. and Ridings, R.L.: "A Numerical Coning Model," *Soc. Pet. Eng. J.*, **19**, No. 4 (1970) 418-424.

107. Theis, C.V.: "The Relation Between the Lowering of the Piezometric Surface and the Rate and Duration of Discharge of a Well Using Ground-Water Storage," *Trans.*, AGU (1935) 519-524.

108. Gringarten, A.C.: *Unsteady-State Pressure Distributions Created by a Well With a Single Horizontal Fracture, Partial Penetration, or Restricted Entry,* Ph.D. dissertation, Stanford University, Stanford, CA (1971).

109. Serra, K.V.: *Well Testing for Solution Gas Drive Reservoirs*, Ph.D. Dissertation, The University of Tulsa, Tulsa, OK (1988).

110. *ECLIPSE 100 REFERENCE MANUAL*, Version 92A, Intera Information Technologies Limited, Oxfordshire, England (1992).

111. Weinstein, H.G., Chappelear, J.E. and Nolen, J.S.: "Second Comparative Solution Project: A Three-Phase Coning Study," *J. Pet. Tech.* (March 1986) 345-353.

112. Elman, H.C.: "A Stability Analysis of Incomplete LU Factorizations," Math. of Comp., Vol. 47, No. 175 (July 1986) 191-217.

113. Standing, M.B.: "A General Pressure-Volume-Temperature Correlation for Mixtures of California Oils and Greases," *Drill. and Prod. Prac.,* API (1947) 275.

114. Beal, C.: "The Viscosity of Air, Water, Natural Gas, Crude Oil and Its Associated Gases at Oil-Field Temperatures and Pressures," *Trans. AIME*, Vol. 165 (1946) 94-115.

115. Chew, J.N. and Connaly, C.A.,Jr.: "A Viscosity Correlation for Gas-Saturated Crude Oils," *Trans. AIME* Vol. 216 (1959) 23-25.

116. Standing, M.B.: *Volumetric and Phase Behavior of Oil Field Hydrocarbon Systems,* 8^{th} Printing, SPE, Dallas, TX, (1977) 121.

117. Buckley, S.E. and Leverett, M.C.: "Mechanism of Fluid Displacement in Sands," *Trans.*, AIME (1942) **146**, 107-116.

118. Pope, G.A.: "The Application of Fractional Flow Theory to Enhanced Oil Recovery," *SPEJ*, (June 1980) 191-205.

119. Cardwell, W.T., Jr.: "The Meaning of the Triple Value in Noncapillary Buckley-Leverett Theory," *Pet. Trans., AIME* (1959), vol. 216, 271-276.

120. Fayers, F.J. and Perrine, R.L.: "Mathematical Description of Detergent Flooding in Oil Reservoirs," *Pet. Trans. AIME*, vol. 216, (1959) 277-283.

121. Sheldon, J.W., Zondek, B. and Cardwell, W.T., Jr.: "One-Dimensional, Incompressible, Noncapillary, Two-Phase Fluid Flow in Porous Medium," *Pet. Trans., AIME*, Vol. 216, (1959) 290-296.

122. Larsen, L., Kviljo, K. and Litlehamar, T.: "Estimating Skin Decline and Relative Permeabilities From Cleanup Effects in Well Test Data Using Buckley-Leverett Methods," paper *SPE 17566* presented at the SPE International Meeting on Petroleum Engineering held in Tianjin, China, Nov. 1-4, 1988.

123. Lake, L.W.: Enhanced Oil Recovery, Prentice Hall, Englewood Cliffs, N.J., (1989).

124. Reynolds, A.C., Bratvold, R.B. and Ding, W.: "Semilog Analysis of Gas Well Drawdown and Buildup Data," *SPEFE* (Dec. 1987) 657-670.

125. Finjord, J.: "A Study of Pseudotime," paper *SPE 12577* available at SPE headquarters, Richardson, TX.

126. Agarwal, R.G.: "Real Gas Pseudo-Time - A New Function for Pressure Buildup Analysis of MHF Gas Wells," paper *SPE 8279* presented at the 1979 SPE Annual Technical Conference and Exhibition, Sept. 23-26.

127. Scott, J.O.: "Application of a New Method for Determining Flow Characteristics of Fractured Gas Wells in Tight Sands," paper SPE 7931 presented at the 1979 SPE Symposium on Low Permeability Gas Reservoirs, Denver, CO, May 20-22, 1979.

128. Aanonsen, S.: "Application of Pseudotime to Estimate Average Reservoir Pressure," paper *SPE 14256* presented at the 60^{th} Annual Technical Conference

and Exhibition of the Society of Petroleum Engineers held in Las Vegas, NV, Sept. 22-25, 1985.

129. Aanonsen, S.I.: "Nonlinear Effects During Transient Fluid Flow in Reservoirs as Encountered in Well-Test Analysis," *Report No. 79*, Department of Applied Mathematics, The University of Bergen, Bergen, 1985.

130. Haberman, R.: *Elementary Applied Partial Differential Equations,* Prentice-Hall, Inc., Englewood Cliffs, New Jersey (1987).

131. Roadifer, R.D. and Reynolds, A.C.: "Analysis of Well-Test Data From a Restricted-Entry Well Under Multiphase Flow Conditions," The University of Tulsa Petroleum Reservoir Exploitation Projects (TUPREP), Research Report 7 (May 1992).

132. Roadifer, R.D. and Reynolds, A.C.: "Analysis of Well-Test Data From a Restricted-Entry Well Under Multiphase Flow Conditions," The University of Tulsa Petroleum Reservoir Exploitation Projects (TUPREP), Research Report 8 (November 1992).

133. Whitson, C.H.: *Topics on Phase Behavior and Flow of Petroleum Reservoir Fluids,* Thesis for the Degree Doctor of Technical Sciences, U. of Trondheim, (1983).

134. Ayan, C. and Lee, W.J.: "Multiphase Pressure Buildup Analysis: Field Examples," paper *SPE 17412* presented at the SPE California Regional Meeting held in Long Beach, CA, March 23-25, 1988.

135. Amyx, J.W., Bass, D.M. Jr., Whiting, R.L.: *Petroleum Reservoir Engineering*, McGraw-Hill Book Company, New York (1960).

136. Vogel, John L.: personal communication, (1994).

137. Motyakou, V.I., Rafibeili, N.M. and Pagimon, O.P.: "Study of Hysteresis Phenomena in Gas-Oil Systems," *Neft. Khoz.* (1967) **45**, No. 5, 47-50.

138. Prats, M.: "A Method for Determining the Net Vertical Permeability Near a Well From In-Situ Measurements," *J.Pet.Tech.* (May 1970) 637-643.

139. Falade, G.K. and Brigham, W.E.: "The Analysis of Single-Well Pulse Tests in a Finite-Acting Slab Reservoir," paper *SPE 5055B* presented at the SPE-AIME 49^{th} Annual Fall Meeting, Houston, TX, Oct. 6-9, 1974.

140. Raghavan, R. and Clark, K.K.: "Vertical Permeability From Limited Entry Flow Tests in Thick Formations," *Soc. Pet. Eng. J.* (Feb. 1975) 65-73.

141. Peres, A.M.M., Serra, K.V. and Reynolds, A.C.: "Towards a Unified Theory of Well Testing for Nonlinear Radial Flow Problems With Applications to Interference Tests," paper *SPE 18113* presented at the 63^{rd} Annual Technical Conference and Exhibition of the Society of Petroleum Engineers held in Houston, TX, Oct. 2-5, 1988.

142. Slider, H.C.: "Application of Pseudo-Steady-State Flow to Pressure-Buildup Analysis," paper *SPE 1403* presented at the SPE-AIME Regional Meeting, Amarillo, TX, Oct. 27-28, 1966.

143. Slider, H.C.: "A Simplified Method of Pressure Buildup Analysis for a Stabilized Well," *J. Pet. Tech.* (Sept. 1971) 1155-1160.

144. Earlougher, R.C.,Jr.: *Advances in Well Test Analysis*, Society of Petroleum Engineers of AIME, Dallas (1977).

145. Oliver, D.S.: "The Averaging Process in Permeability Estimation From Well-Test Data,' *SPEFE* (Sept. 1990) 319-324.

146. Niu, J.G., Thompson, L.G. and Reynolds, A.C.: "Well Testing and Performance Predictions for Gas Condensate Systems: Modified Isochronal Tests," The University of Tulsa Petroleum Reservoir Exploitation Projects (TUPREP), Research Report 7 (May 1992).

147. Niu, J.G., Thompson, L.G. and Reynolds, A.C.: "Well Testing for Gas Condensate Reservoirs," The University of Tulsa Petroleum Reservoir Exploitation Projects (TUPREP), Research Report 8 (November 1992).

148. Thompson, L.G.: *Personal communication*, (1992).

149. Thompson, L.G. and Reynolds, A.C.: "Well Testing for Gas Condensate Reservoirs," The University of Tulsa Petroleum Reservoir Exploitation Projects (TUPREP), Research Report 11 (September 1994).

150. Roadifer, R.D., Yeh, N.S. and Jones, J.R.: "Accurate Well Condition Estimates Under Multiphase Flow Conditions," paper *SPE 30579* to be presented at the 1995 SPE Annual Technical Conference and Exhibition, Dallas, TX, Oct. 22-25, 1995.

APPENDIX A
ROCK AND FLUID PROPERTIES

In this appendix we present the expressions for all fluid and physical properties, along with their derivatives, required by our numerical model. Afterwards, the relationship between the compositional formulation of the problem employed in this work and the more conventional black oil formulation of the problem is derived. Note that standard oil-field (English) units are used throughout this appendix, and whenever a pressure is designated without a phase subscript, it is assumed to represent the oil phase pressure.

As noted in Chapter II, we assume that the PVT behavior of the hydrocarbon mixture can be represented by two pseudocomponents 1 and 2, where we consider component #1 to represent the lighter hydrocarbon fractions and component #2 the heavier fractions; i.e., we assume that at standard conditions of pressure and temperature ($p_{sc} = 14.7\ psi$: $T_{sc} = 60\ ^oF$) all of component #1 exists in the gas phase and all of component #2 exists in the oil phase. At reservoir conditions, both pseudocomponents can be present in both the oil and gas phases, but are insoluble in the aqueous phase. Water exists only in the aqueous phase.

We assume that the following properties are known functions of their arguments: $B_o(p)$, $R_s(p)$, $\mu_o(p)$, $B_g(p)$, $r_v(p)$, $\mu_g(p)$, $B_w(p)$, $\mu_w(p)$, $k_{rg}(S_g)$, $k_{rog}(S_g)$, $p_{cog}(S_g)$, $k_{rw}(S_w)$, $k_{row}(S_w)$ and $p_{cow}(S_w)$. We also assume that the derivatives of these properties with respect to their arguments are known, or, if tabulated functions, that the derivatives can be represented by a chord slope between successive

entries in the table. For pressures greater than the bubble-point pressure, we require the slope of the oil formation volume factor curve $B_o' = (dB_o/dp)$ and the slope of the oil viscosity curve $\mu_o' = (d\mu_o/dp)$ be known and assume they are constant. For pressures greater than an upper dew-point pressure or less than a lower dew-point pressure, we require the slope of the gas formation volume factor curve $B_g' = (dB_g/dp)$ and the slope of the gas viscosity curve $\mu_g' = (d\mu_g/dp)$ be known and assume they also are constant. The molecular weights (M_1, M_2 and M_w) and mass densities at standard conditions (ρ_{gsc}, ρ_{osc} and ρ_{wsc}) for each of component #1 (gas phase), component #2 (oil phase) and water, respectively, are assumed to be known. For compressible formations, we require the rock compressibility, c_f, a reference porosity, ϕ^r, and a reference pressure, p^r, be known.

A.1 Rock-Fluid Properties

The porosity at any pressure is calculated as

$$\phi(p) = \phi^r[1 + c_f(p - p^r)] \qquad (A-1a)$$

and the derivative w.r.t. pressure as

$$\frac{d\phi}{dp} = \phi^r c_f \ . \qquad (A-1b)$$

As noted in Chapter II, we assume the three-phase oil relative permeability can be represented by any of four correlations[40–43] and is a function of both gas and water saturations, i.e., $k_{ro} = k_{ro}(S_g, S_w)$.

Stone's[40] Method 1

The three-phase oil relative permeability is estimated from Stone's[40] first method as

$$k_{ro} = S_o^* \frac{k_{row}}{(1 - S_w^*)} \frac{k_{rog}}{(1 - S_g^*)} \ , \qquad (A-2a)$$

where

$$S_o^* = \frac{S_o - S_{or}}{1 - S_{wc} - S_{or}} \ , \qquad (A-2b)$$

$$S_w^* = \frac{S_w - S_{wc}}{1 - S_{wc} - S_{or}} \qquad (A-2c)$$

and

$$S_g^* = \frac{S_g}{1 - S_{wc} - S_{or}} \ . \qquad (A-2d)$$

The partial derivatives of the three-phase oil relative permeability w.r.t. gas and water saturation are, respectively,

$$\frac{\partial k_{ro}}{\partial S_g} = S_o^* \frac{k_{row}}{(1 - S_w^*)} \frac{1}{(1 - S_g^*)} \left[\frac{dk_{rog}}{dS_g} - \frac{k_{rog}}{(1 - S_g^*)} \frac{1}{1 - S_{wc} - S_{or}} \right] \qquad (A-2e)$$

and

$$\frac{\partial k_{ro}}{\partial S_w} = S_o^* \frac{k_{rog}}{(1 - S_g^*)} \frac{1}{(1 - S_w^*)} \left[\frac{dk_{row}}{dS_w} - \frac{k_{row}}{(1 - S_w^*)} \frac{1}{1 - S_{wc} - S_{or}} \right] . \qquad (A-2f)$$

Stone's[41] Method 2

The second method developed by Stone[41] can be expressed as

$$k_{ro} = (k_{row} + k_{rw})(k_{rog} + k_{rg}) - (k_{rw} + k_{rg}) \qquad (A-3a)$$

and the required partial derivatives as

$$\frac{\partial k_{ro}}{\partial S_g} = (k_{row} + k_{rw}) \left[\frac{dk_{rog}}{dS_g} + \frac{dk_{rg}}{dS_g} \right] - \frac{dk_{rg}}{dS_g} \qquad (A-3b)$$

and

$$\frac{\partial k_{ro}}{\partial S_w} = \left[\frac{dk_{row}}{dS_w} + \frac{dk_{rw}}{dS_w} \right] (k_{rog} + k_{rg}) - \frac{dk_{rw}}{dS_w} \ . \qquad (A-3c)$$

Method of MacDonald and Coats[42]

MacDonald and Coats[42] presented an expression in which the three-phase oil relative permeability is simply the product of the two-phase oil relative permeabilities:

$$k_{ro} = k_{rog} k_{row} \ . \qquad (A-4a)$$

The partial derivatives follow directly as

$$\frac{\partial k_{ro}}{\partial S_g} = k_{row} \frac{dk_{rog}}{dS_g} \qquad (A-4b)$$

and

$$\frac{\partial k_{ro}}{\partial S_w} = k_{rog} \frac{dk_{row}}{dS_w} \ . \qquad (A-4c)$$

Modified[43] Stone's Method 2

Lastly, we consider a modified version of Stone's second method discussed in Ref. 43. First, let us denote the two-phase (oil-water) oil relative permeability at irreducible water saturation as k_{rowc}, i.e., $k_{rowc} = k_{row}(S_{wc})$. The three-phase oil permeability is then calculated from

$$k_{ro} = k_{rowc} \left[\left(\frac{k_{row}}{k_{rowc}} + k_{rw} \right) \left(\frac{k_{rog}}{k_{rowc}} + k_{rg} \right) - (k_{rw} + k_{rg}) \right] \qquad (A-5a)$$

and the required partial derivatives from

$$\frac{\partial k_{ro}}{\partial S_g} = k_{rowc} \left[\left(\frac{k_{row}}{k_{rowc}} + k_{rw} \right) \left(\frac{1}{k_{rowc}} \frac{dk_{rog}}{dS_g} + \frac{dk_{rg}}{dS_g} \right) - \frac{dk_{rg}}{dS_g} \right] \qquad (A-5b)$$

and

$$\frac{\partial k_{ro}}{\partial S_w} = k_{rowc} \left[\left(\frac{1}{k_{rowc}} \frac{dk_{row}}{dS_w} + \frac{dk_{rw}}{dS_w} \right) \left(\frac{k_{rog}}{k_{rowc}} + k_{rg} \right) - \frac{dk_{rw}}{dS_w} \right] \ . \qquad (A-5c)$$

A.2 PVT Properties

At standard conditions of pressure and temperature, the molar densities of component #1 (gas phase), component #2 (oil phase) and water are, respectively,

$$\overline{\rho}_{gsc} = \frac{\rho_{gsc}}{M_1} \ , \qquad (A-6a)$$

$$\overline{\rho}_{osc} = \frac{\rho_{osc}}{M_2} \qquad (A-6b)$$

and

$$\overline{\rho}_{wsc} = \frac{\rho_{wsc}}{M_w} \ . \qquad (A-6c)$$

A.2.1 Oil Phase Properties

Solution Gas-Oil Ratio (Volumetric)

Below the bubble-point pressure, the solution gas-oil ratio is only a function of the grid block pressure and we have

$p < p_b$

$$R_s = R_s(p) \qquad (A-7a)$$

and

$$\frac{dR_s}{dp} = \frac{dR_s(p)}{dp} \ . \qquad (A-7b)$$

Above the bubble-point pressure, the solution gas-oil ratio is a function only of the bubble-point pressure (i.e., $dR_s/dp = 0$) and we have

$p \geq p_b$

$$R_s = R_{sb}(p_b) = R_s(p)|_{p=p_b} \qquad (A-7c)$$

$$\frac{dR_s}{dp_b} = \left.\frac{dR_s}{dp}\right|_{p=p_b} \qquad (A-7d)$$

Solution Gas-Oil Ratio (Molar)

Using Eqs. A-6a and A-6b, we can convert the volumetric solution gas-oil ratio into a molar solution gas-oil ratio, obtaining for pressures below the bubble-point pressure

$p < p_b$

$$\overline{R}_s = \frac{R_s}{5.615}\frac{\overline{\rho}_{gsc}}{\overline{\rho}_{osc}} \qquad (A-8a)$$

and

$$\frac{d\overline{R}_s}{dp} = \frac{1}{5.615}\frac{\overline{\rho}_{gsc}}{\overline{\rho}_{osc}}\frac{dR_s(p)}{dp} \ . \qquad (A-8b)$$

For pressures greater than the bubble-point pressure, we obtain

$p \geq p_b$

$$\overline{R}_s = \frac{R_{sb}}{5.615}\frac{\overline{\rho}_{gsc}}{\overline{\rho}_{osc}} \qquad (A-8c)$$

$$\frac{d\overline{R}_s}{dp_b} = \frac{1}{5.615}\frac{\overline{\rho}_{gsc}}{\overline{\rho}_{osc}}\frac{dR_s}{dp_b} \ . \qquad (A-8d)$$

Note, $(d\overline{R}_s/dp) = 0$ for $p \geq p_b$ and $\overline{R}_s$ has units (lbmoles of comp. #1)/(lbmole of comp. #2).

Oil Phase Mole Fractions

For the oil phase we require the following mole fraction constraint to hold:

$$x_1 + x_2 = 1 \ , \qquad (A-9a)$$

where the mole fractions of components 1 and 2 in the oil phase can be calculated from

$$x_1 = \frac{\overline{R}_s}{1 + \overline{R}_s} \qquad (A-9b)$$

and

$$x_2 = \frac{1}{1 + \overline{R}_s} \ . \qquad (A-9c)$$

Eq. A-9a can always be used to eliminate either one of x_1 or x_2 or used to relate properties and derivatives of each to one another, e.g., $x_2 = 1 - x_1$. It is easily shown that the derivatives of the mole fractions with respect to pressure and bubble-point pressure can therefore be written as

$p < p_b$

$$\frac{dx_1}{dp} = \left(\frac{1 - x_1}{1 + \overline{R}_s}\right)\frac{d\overline{R}_s}{dp} \ , \qquad (A-9d)$$

$$\frac{dx_2}{dp} = -\frac{dx_1}{dp} \ , \qquad (A-9e)$$

$p \geq p_b$

$$\frac{dx_1}{dp_b} = \left(\frac{1 - x_1}{1 + \overline{R}_s}\right)\frac{d\overline{R}_s}{dp_b} \qquad (A-9f)$$

and

$$\frac{dx_2}{dp_b} = -\frac{dx_1}{dp_b} \ . \qquad (A-9g)$$

For $p \geq p_b$ we also note that

$$\frac{dx_1}{dp} = 0 \qquad (A-9h)$$

and

$$\frac{dx_2}{dp} = 0 \ . \qquad (A-9i)$$

Oil Phase Molecular Weight

Having expressions for the mole fractions in the oil phase, the molecular weight for the oil phase can be calculated directly from

$$M_o = x_1 M_1 + (1 - x_1) M_2 \ , \qquad (A - 10a)$$

and the derivatives w.r.t pressure and bubble-point pressure calculated from

$p < p_b$

$$\frac{dM_o}{dp} = (M_1 - M_2)\frac{dx_1}{dp} \qquad (A - 10b)$$

and

$p \geq p_b$

$$\frac{dM_o}{dp} = 0 \qquad (A - 10c)$$

and

$$\frac{dM_o}{dp_b} = (M_1 - M_2)\frac{dx_1}{dp_b} \ . \qquad (A - 10d)$$

Oil Formation Volume Factor

The oil formation volume factor, B_o, can be a function of pressure only or a function of both the pressure and the bubble-point pressure, depending on whether we are below or above the bubble-point pressure, respectively. Below the bubble-point pressure we have

$p < p_b$

$$B_o = B_o(p) \qquad (A-11a)$$

and

$$\frac{dB_o}{dp} = \frac{dB_o(p)}{dp} \ . \qquad (A-11b)$$

For pressures above the bubble-point pressure we have

$p \geq p_b$

$$B_o = B_o(p)|_{p=p_b} + B'_o(p - p_b) \ , \qquad (A-11d)$$

$$\frac{\partial B_o}{\partial p} = B'_o \qquad (A-11e)$$

and

$$\frac{\partial B_o}{\partial p_b} = \left.\frac{dB_o}{dp}\right|_{p=p_b} - B'_o \ . \qquad (A-11e)$$

Oil Phase Mass Density

Expressions for the oil phase mass density and its derivatives can now be written as

$$\rho_o = \frac{1}{B_o}\left(\rho_{osc} + \frac{R_s \rho_{gsc}}{5.615}\right) \ , \qquad (A-12a)$$

$$\frac{\partial \rho_o}{\partial p} = \frac{1}{B_o}\left(\frac{\rho_{gsc}}{5.615}\frac{dR_s}{dp} - \rho_o \frac{dB_o}{dp}\right) \ , \qquad (A-12b)$$

and

$$\frac{\partial \rho_o}{\partial p_b} = \frac{1}{B_o}\left(\frac{\rho_{gsc}}{5.615}\frac{dR_s}{dp_b} - \rho_o \frac{dB_o}{dp_b}\right) \ . \qquad (A-12c)$$

Note that for $p < p_b$, Eq. A-12b actually represents a total derivative, i.e., $(d\rho_o/dp) = (\partial\rho_o/\partial p)$, and Eq. A-12c is not applicable.

Oil Phase Molar Density

The oil phase molar density and its derivatives also follow directly and are easily shown to be equal to

$$\overline{\rho}_o = \frac{\rho_o}{M_o} \ , \qquad (A-13a)$$

$$\frac{\partial \overline{\rho}_o}{\partial p} = \frac{1}{M_o}\left(\frac{\partial \rho_o}{\partial p} - \overline{\rho}_o \frac{dM_o}{dp}\right) \qquad (A-13b)$$

and

$$\frac{\partial \overline{\rho}_o}{\partial p_b} = \frac{1}{M_o}\left(\frac{\partial \rho_o}{\partial p_b} - \overline{\rho}_o \frac{dM_o}{dp_b}\right) . \qquad (A-13c)$$

Again, note that Eq. A-13b actually represents a total derivative for $p < p_b$ and Eq. A-13c will not be applicable.

Oil Phase Viscosity

Below the bubble-point pressure, the oil phase viscosity is a function only of pressure and we have

$p < p_b$

$$\mu_o = \mu_o(p) \qquad (A-14a)$$

and

$$\frac{d\mu_o}{dp} = \frac{d\mu_o(p)}{dp} \ . \qquad (A-14b)$$

Above the bubble-point pressure, the oil viscosity is a function of both the pressure and the bubble-point pressure and we have

$p \geq p_b$

$$\mu_o = \mu_o(p)|_{p=p_b} + \mu_o'(p - p_b) \ , \qquad (A-14c)$$

$$\frac{\partial \mu_o}{\partial p} = \mu_o' \qquad (A-14d)$$

and

$$\frac{\partial \mu_o}{\partial p_b} = \left.\frac{d\mu_o}{dp}\right|_{p=p_b} - \mu_o' \ . \qquad (A-14e)$$

A.2.2 Gas Phase Properties

Gas-Liquid Content - Oil Volatility (Volumetric)

Within the two-phase hydrocarbon region, i.e., when the pressure is less than the upper dew-point pressure and greater than the lower dew-point pressure, the oil volatility is a function only of the grid block pressure and we have

$p_{dl} < p < p_{du}$

$$r_v = r_v(p) \qquad (A-15a)$$

and

$$\frac{dr_v}{dp} = \frac{dr_v(p)}{dp} \ . \qquad (A-15b)$$

Where single-phase gas exists, the oil volatility is a function only of the dew-point pressure (i.e., $dr_v/dp = 0$) and we have

$p \geq p_{du}$ **or** $p \leq p_{dl}$

$$r_v = r_{vd}(p_d) = r_v(p)|_{p=p_d} \qquad (A-15c)$$

$$\frac{dr_v}{dp_d} = \left.\frac{dr_v}{dp}\right|_{p=p_d} \qquad (A-15d)$$

Gas-Liquid Content - Oil Volatility (Molar)

Using Eqs. A-6a and A-6b, we convert the volumetric gas-liquid content into a molar gas-liquid content, obtaining for saturated hydrocarbon systems

$p_{dl} < p < p_{du}$

$$\overline{r}_v = 5.615 r_v \frac{\overline{\rho}_{osc}}{\overline{\rho}_{gsc}} \qquad (A-16a)$$

and

$$\frac{d\overline{r}_v}{dp} = 5.615 \frac{\overline{\rho}_{osc}}{\overline{\rho}_{gsc}} \frac{d\overline{r}_v}{dp} \ . \qquad (A-16b)$$

For pressures greater than the upper dew-point pressure or less than the lower dew-point pressure, we obtain

$p \geq p_{du}$ **or** $p \leq p_{dl}$

$$\overline{r}_v = 5.615 r_{vd} \frac{\overline{\rho}_{osc}}{\overline{\rho}_{gsc}} \qquad (A-16c)$$

$$\frac{d\overline{r}_v}{dp_d} = 5.615 \frac{\overline{\rho}_{osc}}{\overline{\rho}_{gsc}} \frac{dr_v}{dp_d} \ . \qquad (A-16d)$$

Note, $(d\overline{r}_v/dp) = 0$ for $p \geq p_{du}$ and $p \leq p_{dl}$ and $\overline{r}_v$ has units (lbmoles of comp. #2)/(lbmole of comp. #1).

Gas Phase Mole Fractions

The following mole fraction constraint holds for the gas phase:

$$y_1 + y_2 = 1 \ , \qquad (A-17a)$$

where the mole fractions of components 1 and 2 in the gas phase can be calculated from

$$y_1 = \frac{1}{1+\overline{r}_v} \qquad (A-17b)$$

and

$$y_2 = \frac{\overline{r}_v}{1+\overline{r}_v} \ . \qquad (A-17c)$$

Eq. A-17a can always be used to eliminate either one of y_1 or y_2 and can be used to relate properties and derivatives of each to one another, e.g., $y_2 = 1 - y_1$. The derivatives of the mole fractions with respect to pressure and dew-point pressure can be calculated directly from

$p_{dl} < p < p_{du}$

$$\frac{dy_1}{dp} = -\left(\frac{1}{1+\overline{r}_v}\right)^2 \frac{d\overline{r}_v}{dp} \ , \qquad (A-17d)$$

$$\frac{dy_2}{dp} = -\frac{dy_1}{dp} \ , \qquad (A-17e)$$

$p \geq p_{du}$ **or** $p \leq p_{dl}$

$$\frac{dy_1}{dp_d} = -\left(\frac{1}{1+\overline{r}_v}\right)^2 \frac{d\overline{r}_v}{dp_d} \ , \qquad (A-17f)$$

and

$$\frac{dy_2}{dp_d} = -\frac{dy_1}{dp_d} \ . \qquad (A-17g)$$

For $p \geq p_{du}$ or $p \leq p_{dl}$ we also note that

$$\frac{dy_1}{dp} = 0 \qquad (A-17h)$$

and

$$\frac{dy_2}{dp} = 0 \ . \qquad (A-17i)$$

Gas Phase Molecular Weight

Having expressions for the mole fractions in the gas phase, the molecular weight for the gas phase can be calculated from

$$M_g = y_1 M_1 + (1 - y_1) M_2 \ , \qquad (A-18a)$$

and the derivatives w.r.t pressure and dew-point pressure calculated from

$p_{dl} < p < p_{du}$

$$\frac{dM_g}{dp} = (M_1 - M_2)\frac{dy_1}{dp} \qquad (A-18b)$$

and

$p \geq p_{du}$ **or** $p \leq p_{dl}$

$$\frac{dM_g}{dp} = 0 \qquad (A-18c)$$

and

$$\frac{dM_g}{dp_d} = (M_1 - M_2)\frac{dy_1}{dp_d} \ . \qquad (A-18d)$$

Gas Formation Volume Factor

The gas formation volume factor, B_g, is a function of pressure only when two hydrocarbon phases co-exist and a function of both the pressure and the dew-point pressure when only an undersaturated gas phase exists. Within the saturated (two-phase) region we have

$p_{dl} < p < p_{du}$

$$B_g = B_g(p) \qquad (A-19a)$$

and

$$\frac{dB_g}{dp} = \frac{dB_g(p)}{dp} \ . \qquad (A-19b)$$

In the undersaturated gas region, we have

$p \geq p_{du}$ **or** $p \leq p_{dl}$

$$B_g = B_g(p)|_{p=p_d} + B_g'(p - p_d) \ , \qquad (A-19c)$$

$$\frac{\partial B_g}{\partial p} = B_g' \qquad (A-19d)$$

and

$$\frac{\partial B_g}{\partial p_d} = \left.\frac{dB_g}{dp}\right|_{p=p_d} - B_g' \ . \qquad (A-19e)$$

Gas Phase Mass Density

Expressions for the gas phase mass density and its derivatives can now be written as

$$\rho_g = \frac{1}{B_g}\left(\rho_{gsc} + 5.615 r_v \rho_{osc}\right) \ , \qquad (A-20a)$$

$$\frac{\partial \rho_g}{\partial p} = \frac{1}{B_g}\left(5.615\rho_{osc}\frac{dr_v}{dp} - \rho_g\frac{dB_g}{dp}\right) \ , \qquad (A-20b)$$

and

$$\frac{\partial \rho_g}{\partial p_d} = \frac{1}{B_g}\left(5.615\rho_{osc}\frac{dr_v}{dp_d} - \rho_g\frac{dB_g}{dp_d}\right) \ , \qquad (A-20c)$$

Note that for $p_{dl} < p < p_{du}$, Eq. A-20b actually represents a total derivative, i.e., $(d\rho_g/dp) = (\partial\rho_g/\partial p)$, and Eq. A-20c is not applicable.

Gas Phase Molar Density

The gas phase molar density and its derivatives also follow directly and are easily shown to be equal to

$$\overline{\rho}_g = \frac{\rho_g}{M_g} \ , \qquad (A-21a)$$

$$\frac{\partial \overline{\rho}_g}{\partial p} = \frac{1}{M_g}\left(\frac{\partial \rho_g}{\partial p} - \overline{\rho}_g \frac{dM_g}{dp}\right) \qquad (A-21b)$$

and

$$\frac{\partial \overline{\rho}_g}{\partial p_d} = \frac{1}{M_g}\left(\frac{\partial \rho_g}{\partial p_d} - \overline{\rho}_g \frac{dM_g}{dp_d}\right) \ . \qquad (A-21c)$$

Again, note that Eq. A-21b actually represents a total derivative for $p_{dl} < p < p_{du}$ and Eq. A-21c will not be applicable.

Gas Phase Viscosity

For saturated hydrocarbon systems, the gas phase viscosity is a function only of pressure and we have

$p_{dl} < p < p_{du}$

$$\mu_g = \mu_g(p) \qquad (A-22a)$$

and

$$\frac{d\mu_g}{dp} = \frac{d\mu_g(p)}{dp} \ . \qquad (A-22b)$$

Within the undersaturated gas region, the gas viscosity is a function of both the pressure and the dew-point pressure and we have

$p \geq p_{du}$ **or** $p \leq p_{dl}$

$$\mu_g = \mu_g(p)|_{p=p_d} + \mu_g'(p - p_d) \ , \qquad (A-22c)$$

$$\frac{\partial \mu_g}{\partial p} = \mu_g' \qquad (A-22d)$$

and

$$\frac{\partial \mu_g}{\partial p_d} = \left.\frac{d\mu_g}{dp}\right|_{p=p_d} - \mu_g' \ . \qquad (A-22e)$$

A.2.3 Water Phase Properties

As mentioned at the begining of this appendix, it is assumed that the water formation volume factor and viscosity as a function of pressure are known, as well as the density at standard conditions and the molecular weight. Given these quantities, we can calculate the water mass density as

$$\rho_w = \frac{\rho_{wsc}}{B_w} \qquad (A-23a)$$

and the derivative w.r.t. pressure as

$$\frac{d\rho_w}{dp} = -\frac{\rho_w}{B_w}\frac{dB_w}{dp} \ . \qquad (A-23b)$$

The molar water density and its derivative w.r.t. pressure follow directly as

$$\overline{\rho}_w = \frac{\rho_w}{M_w} \qquad (A-24a)$$

and

$$\frac{d\overline{\rho}_w}{dp} = \frac{1}{M_w}\frac{d\rho_w}{dp} \ . \qquad (A-24b)$$

A.3 Relationship Between Compositional and Conventional Black Oil Formulations

We begin our derivation by considering the "light" hydrocarbon component (component #1) and the expression $x_1\overline{\rho}_o$. Using Eqs. A-13a, A-10a and A-9a we have

$$x_1\overline{\rho}_o = x_1\left[\frac{\rho_o}{x_1M_1 + x_2M_2}\right] . \qquad (A-25a)$$

Using the definitions for x_1 and x_2 (Eqs. A-9b and A-9c) in Eq. A-25a and simplifying we obtain

$$x_1\overline{\rho}_o = \overline{R}_s\left[\frac{\rho_o}{\overline{R}_sM_1 + M_2}\right] . \qquad (A-25b)$$

Now considering just the denominator of Eq. A-25b and using Eq. A-8a to replace $\overline{R}_s$ we have

$$\begin{aligned}\overline{R}_sM_1 + M_2 &= \frac{R_s\rho_{gsc}M_2}{5.615\rho_{osc}} + M_2 \\ &= M_2\left[\frac{R_s}{5.615}\frac{\rho_{gsc}}{\rho_{osc}} + 1\right] \\ &= \frac{M_2}{\rho_{osc}}\left[\frac{R_s\rho_{gsc}}{5.615} + \rho_{osc}\right] \\ &= \frac{M_2}{\rho_{osc}}\rho_oB_o \qquad (A-25c)\end{aligned}$$

Substituting Eq. A-25c into Eq. A-25b, we obtain

$$\begin{aligned}x_1\overline{\rho}_o &= \overline{R}_s\left[\frac{\rho_o\rho_{osc}}{M_2\rho_oB_o}\right] \\ &= \frac{\overline{R}_s\rho_{osc}}{M_2B_o} \qquad (A-25d)\end{aligned}$$

Finally, using the definitions for $\overline{R}_s$ (Eq. A-8a), $\overline{\rho}_{osc}$ (Eq. A-6b) and $\overline{\rho}_{gsc}$ (Eq. A-6a) in Eq. A-25d, we obtain

$$\begin{aligned}x_1\overline{\rho}_o &= \frac{R_s\rho_{gsc}M_2\rho_{osc}}{5.615\rho_{osc}M_1M_2B_o} \\ &= \left(\frac{\rho_{gsc}}{M_1}\right)\left[\frac{R_s}{5.615B_o}\right] \qquad (A-25e)\end{aligned}$$

In a similar manner, we consider the expression $y_1\overline{\rho}_g$ and use Eqs. A-21a, A-18a and A-17a to obtain

$$y_1\overline{\rho}_g = \frac{\rho_g}{M_1 + \overline{r}_v M_2} \ . \qquad (A-26a)$$

Again, considering only the denominator of Eq. A-26a and substituting Eq. A-16a for $\overline{r}_v$ we obtain

$$\begin{aligned} M_1 + \overline{r}_v M_2 &= M_1 + 5.615 r_v M_2 \frac{\rho_{osc}}{\rho_{gsc}} \frac{M_1}{M_2} \\ &= M_1 \left[1 + 5.615 r_v \frac{\rho_{osc}}{\rho_{gsc}} \right] \\ &= \left(\frac{M_1}{\rho_{gsc}} \right) [\rho_{gsc} + 5.615 r_v \rho_{osc}] \ . \end{aligned} \qquad (A-26b)$$

Multiplying Eq. A-20a by B_g and substituting the result into Eq. A-26b, we obtain

$$M_1 + \overline{r}_v M_2 = \rho_g B_g \left(\frac{M_1}{\rho_{gsc}} \right) \ . \qquad (A-26c)$$

Finally, using Eq. A-26c in Eq. A-26a we obtain

$$y_1\overline{\rho}_g = \left(\frac{\rho_{gsc}}{M_1} \right) \left(\frac{1}{B_g} \right) \ . \qquad (A-26d)$$

Similar to component #1, let us consider the expression $x_2\overline{\rho}_o$ for the "heavy" hydrocarbon component (component #2), and let us use Eqs. A-13a, A-10a and A-9a to obtain

$$x_2\overline{\rho}_o = x_2 \left[\frac{\rho_o}{x_1 M_1 + x_2 M_2} \right] \ . \qquad (A-27a)$$

Using the definitions for x_1 and x_2 (Eqs. A-9b and A-9c) in Eq. A-27a and simplifying we have

$$x_1\overline{\rho}_o = \left[\frac{\rho_o}{\overline{R}_s M_1 + M_2} \right] \ . \qquad (A-27b)$$

Substituting the result derived in Eq. A-25c into Eq. A-27b, we obtain

$$x_1\overline{\rho}_o = \left(\frac{\rho_{osc}}{M_2}\right)\left(\frac{1}{B_o}\right) . \qquad (A-27c)$$

Also, let us derive an equivalent expression for $y_2\overline{\rho}_g$ using Eqs. A-21a, A-18a and A-17a:

$$y_2\overline{\rho}_g = \overline{r}_v\left[\frac{\rho_g}{M_1 + \overline{r}_v M_2}\right] . \qquad (A-28a)$$

Substituting the results obtained in Eq. A-26c into Eq. A-28a, we obtain

$$y_2\overline{\rho}_g = \overline{r}_v\frac{\rho_{gsc}}{M_1 B_g} . \qquad (A-28b)$$

Finally, substituting the definition for $\overline{r}_v$ (Eq. A-16a) into Eq. A-28b, we obtain

$$\begin{aligned} y_2\overline{\rho}_g &= \left[\frac{5.615 r_v \rho_{osc} M_1}{\rho_{gsc} M_2}\right]\left[\frac{\rho_{gsc}}{M_1 B_g}\right] \\ &= \left(\frac{\rho_{osc}}{M_2}\right)\left(\frac{5.615 r_v}{B_g}\right) . \end{aligned} \qquad (A-28c)$$

Recall also that for water we have

$$\overline{\rho}_w = \left(\frac{\rho_{wsc}}{M_w}\right)\left(\frac{1}{B_w}\right) . \qquad (A-29)$$

Substituting Eqs. A-25e and A-26d into Eq. 2.3.29, substituting Eqs. A-27c and A-28c into Eq. 2.3.30 and substituting Eq. A-29 into Eq. 2.3.31, we obtain (using oil field units) respectively, for component #1

$$c_1\left(\frac{\rho_{gsc}}{M_1}\right)\nabla\cdot\left[\frac{[k]R_s\lambda_{ro}}{5.615B_o}(\nabla p_o + \rho_o g\nabla z) + \frac{[k]\lambda_{rg}}{B_g}(\nabla(p_o + p_{cog}) + \rho_g g\nabla z)\right]$$

$$= \left(\frac{\rho_{gsc}}{M_1}\right)\frac{\partial}{\partial t}\left\{\phi\left[\frac{(1-S_w-S_g)R_s}{5.615B_o}+\frac{S_g}{B_g}\right]\right\}, \qquad (A-30)$$

for component #2

$$c_1\left(\frac{\rho_{osc}}{M_2}\right)\nabla\cdot[\frac{[k]\lambda_{ro}}{B_o}(\nabla p_o+\rho_o g\nabla z)+\frac{[k]r_v\lambda_{rg}}{B_g}(\nabla(p_o+p_{cog})+\rho_g g\nabla z)]$$

$$= \left(\frac{\rho_{osc}}{M_2}\right)\frac{\partial}{\partial t}\left\{\phi\left[\frac{(1-S_w-S_g)}{B_o}+\frac{r_v S_g}{B_g}\right]\right\} \qquad (A-31)$$

and for water

$$c_1\left(\frac{\rho_{wsc}}{M_w}\right)\nabla\cdot[\frac{[k]\lambda_{rw}}{B_w}(\nabla(p_o-p_{cow})+\rho_w g\nabla z)] = \left(\frac{\rho_{wsc}}{M_w}\right)\frac{\partial}{\partial t}\left[\phi\left(\frac{S_w}{B_w}\right)\right]. \qquad (A-32)$$

Finally, multiplying Eq. A-30 by (M_1/ρ_{gsc}), Eq. A-31 by (M_2/ρ_{osc}) and Eq. A-32 by (M_w/ρ_{wsc}) we obtain the primary equations of the conventional black oil formulation; i.e., for the light hydrocarbon component we obtain

$$c_1\nabla\cdot\left[\frac{[k]R_s\lambda_{ro}}{5.615B_o}(\nabla p_o+\rho_o g\nabla z)+\frac{[k]\lambda_{rg}}{B_g}(\nabla(p_o+p_{cog})+\rho_g g\nabla z)\right]$$

$$= \frac{\partial}{\partial t}\left\{\phi\left[\frac{(1-S_w-S_g)R_s}{5.615B_o}+\frac{S_g}{B_g}\right]\right\}, \qquad (A-33)$$

for the heavy hydrocarbon component we obtain

$$c_1\nabla\cdot[\frac{[k]\lambda_{ro}}{B_o}(\nabla p_o+\rho_o g\nabla z)+\frac{[k]r_v\lambda_{rg}}{B_g}(\nabla(p_o+p_{cog})+\rho_g g\nabla z)]$$

$$= \frac{\partial}{\partial t}\left\{\phi\left[\frac{(1-S_w-S_g)}{B_o}+\frac{r_v S_g}{B_g}\right]\right\} \qquad (A-34)$$

and for water we obtain

$$c_1\nabla\cdot[\frac{[k]\lambda_{rw}}{B_w}(\nabla(p_o-p_{cow})+\rho_w g\nabla z)] = \frac{\partial}{\partial t}\left[\phi\left(\frac{S_w}{B_w}\right)\right]. \qquad (A-35)$$

APPENDIX B

JACOBIAN COEFFICIENTS

In this appendix we present expressions for the Jacobian coefficients required for the implementation of Newton's method; i.e., all of the partial derivatives of our primary equations with respect to the primary variables. As noted in Chapter II, we employ single-point upstream weighting of the nonlinear terms, and, therefore, the functional relationship between those terms and the primary variables is dependent upon the flow direction of the fluids. Determination of the flow direction for each phase is based on the differential of the individual phase potentials across grid block boundaries and is discussed in Section 2.4.2.c of Chapter II. Recall that we do not place any restrictions on the direction of flow and so different phases can be flowing in different directions. As a matter of notational convenience, however, statements of flow direction in the following derivations are assumed to hold for all three phases. Here, we concern ourselves only with the calculation of the Jacobian coefficients based on a knowledge of the flow direction determine previously according to the methods discussed in Chapter II.

To simplify the nomenclature, position identifying subscripts (e.g., $i+1,k$) will be omitted whenever possible in the following derivations. As an example, when a subsection heading in this appendix specifies a partial derivative with respect to a particular pressure (e.g., *Derivative w.r.t.* $p_{o,i-1,k}$), then it will be understood that all partial derivatives with respect to pressure in that subsection actually represent the partial derivative with respect to the specific pressure listed

in the subsection heading (in this case, $p_{o,i-1,k}$). Additionally, let

$$\alpha_{i+\frac{1}{2},k} = c_1 a_{i+\frac{1}{2},k} k_{i+\frac{1}{2},k} \ , \qquad (B-0.1)$$

$$\alpha_{i-\frac{1}{2},k} = c_1 a_{i-\frac{1}{2},k} k_{i-\frac{1}{2},k} \ , \qquad (B-0.2)$$

$$\alpha_{i,k+\frac{1}{2}} = c_1 a_{i,k+\frac{1}{2}} k_{z,i,k+\frac{1}{2}} \ , \qquad (B-0.3)$$

$$\alpha_{i,k-\frac{1}{2}} = c_1 a_{i,k-\frac{1}{2}} k_{z,i,k-\frac{1}{2}} \ , \qquad (B-0.4)$$

where c_1 is a units conversion factor, a is given by Eqs. 2.4.37-2.4.39 and the absolute horizontal and vertical permeabilities, k and k_z, at the grid block boundaries are defined by Eqs. 2.4.42.

Due to the length of some of the derivations to be presented, we also employ the following definitions to help simplify the expressions to be presented: First, for the discrete phase potential difference we have

$$\begin{aligned}
\Phi_{ro\,,i+\frac{1}{2},k} &= (p_{o\,,i+1,k} - p_{o\,,i,k}) \ , \\
\Phi_{rg\,,i+\frac{1}{2},k} &= (p_{o\,,i+1,k} - p_{o\,,i,k} + p_{cog\,,i+1,k} - p_{cog\,,i,k}) \ , \\
\Phi_{rw\,,i+\frac{1}{2},k} &= (p_{o\,,i+1,k} - p_{o\,,i,k} + p_{cow\,,i,k} - p_{cow\,,i+1,k}) \ , \\
\Phi_{ro\,,i-\frac{1}{2},k} &= (p_{o\,,i,k} - p_{o\,,i-1,k}) \ , \\
\Phi_{rg\,,i-\frac{1}{2},k} &= (p_{o\,,i,k} - p_{o\,,i-1,k} + p_{cog\,,i,k} - p_{cog\,,i-1,k}) \ , \\
\Phi_{rw\,,i-\frac{1}{2},k} &= (p_{o\,,i,k} - p_{o\,,i-1,k} + p_{cow\,,i-1,k} - p_{cow\,,i,k}) \ , \\
\Phi_{zo\,,i,k+\frac{1}{2}} &= (p_{o\,,i,k+1} - p_{o\,,i,k} + \overline{\gamma}_{o\,,i,k+\frac{1}{2}} \Delta z_{k+\frac{1}{2}}) \ , \\
\Phi_{zg\,,i,k+\frac{1}{2}} &= (p_{o\,,i,k+1} - p_{o\,,i,k} + p_{cog\,,i,k+1} - p_{cog\,,i,k} + \overline{\gamma}_{g\,,i,k+\frac{1}{2}} \Delta z_{k+\frac{1}{2}}) \ , \\
\Phi_{zw\,,i,k+\frac{1}{2}} &= (p_{o\,,i,k+1} - p_{o\,,i,k} + p_{cow\,,i,k} - p_{cow\,,i,k+1} + \overline{\gamma}_{w\,,i,k+\frac{1}{2}} \Delta z_{k+\frac{1}{2}}) \ , \\
\Phi_{zo\,,i,k-\frac{1}{2}} &= (p_{o\,,i,k} - p_{o\,,i,k-1} + \overline{\gamma}_{o\,,i,k-\frac{1}{2}} \Delta z_{k-\frac{1}{2}}) \ , \\
\Phi_{zg\,,i,k-\frac{1}{2}} &= (p_{o\,,i,k} - p_{o\,,i,k-1} + p_{cog\,,i,k} - p_{cog\,,i,k-1} + \overline{\gamma}_{g\,,i,k-\frac{1}{2}} \Delta z_{k-\frac{1}{2}}) \\
\Phi_{zw\,,i,k-\frac{1}{2}} &= (p_{o\,,i,k} - p_{o\,,i,k-1} + p_{cow\,,i,k-1} - p_{cow\,,i,k} + \overline{\gamma}_{w\,,i,k-\frac{1}{2}} \Delta z_{k-\frac{1}{2}}) \ ;
\end{aligned} \qquad (B-0.5)$$

Second, let us define the following multipliers for each phase to account for the flow direction of each phase (recall, we are using single-point upstream weighting based on the discrete flow potential difference between grid blocks, i.e., Eq. B-0.5)

$$d_{hm\,,i+\frac{1}{2},k} = \begin{cases} 0 & \text{for } \Phi_{rm\,,i+\frac{1}{2},k} < 0 \\ 1 & \text{for } \Phi_{rm\,,i+\frac{1}{2},k} \geq 0 \end{cases} \;,\; m = o, w, g \;, \qquad (B-0.6)$$

and

$$d_{zm\,,i,k+\frac{1}{2}} = \begin{cases} 0 & \text{for } \Phi_{zm\,,i,k+\frac{1}{2}} < 0 \\ 1 & \text{for } \Phi_{rm\,,i,k+\frac{1}{2}} \geq 0 \end{cases} \;,\; m = o, w, g \;. \qquad (B-0.7)$$

Lastly, we mention the Jacobian coefficients derived here are for a general three-phase live-oil system. We do not present the specific coefficients for simpler systems (e.g., two-phase dry gas and water) since these are but simplifications of the Jacobian coefficients presented here. Additionally, the specific simplifications of the Jacobian coefficients arising due to no-flow boundary conditions are not discussed here.

B.1 Jacobian Coefficients of Component #1 Equation

Employing the definitions above in the flow equation for component #1 (i.e., Eq. 2.4.54) and further defining groups of terms, we obtain

$$\mathcal{A} = [x_1 \mathcal{T}_{ro}]_{i+\frac{1}{2},k} \Phi_{ro\,,i+\frac{1}{2},k} \;\;,$$
$$\mathcal{B} = [y_1 \mathcal{T}_{rg}]_{i+\frac{1}{2},k} \Phi_{rg\,,i+\frac{1}{2},k} \;\;,$$
$$\mathcal{C} = [x_1 \mathcal{T}_{ro}]_{i-\frac{1}{2},k} \Phi_{ro\,,i-\frac{1}{2},k} \;\;,$$
$$\mathcal{D} = [y_1 \mathcal{T}_{rg}]_{i-\frac{1}{2},k} \Phi_{rg\,,i-\frac{1}{2},k} \;\;,$$
$$\mathcal{E} = [x_1 \mathcal{T}_{zo}]_{i,k+\frac{1}{2}} \Phi_{zo\,,i,k+\frac{1}{2}} \;\;,$$
$$\mathcal{F} = [y_1 \mathcal{T}_{zg}]_{i,k+\frac{1}{2}} \Phi_{zg\,,i,k+\frac{1}{2}} \;\;,$$
$$\mathcal{G} = [x_1 \mathcal{T}_{zo}]_{i,k-\frac{1}{2}} \Phi_{zo\,,i,k-\frac{1}{2}} \;\;,$$

$$\mathcal{H} = [y_1 \mathcal{T}_{zg}]_{i,k-\frac{1}{2}} \Phi_{zg\,,i,k-\frac{1}{2}}$$

and

$$\mathcal{I} = \frac{V_{i,k}}{\Delta t}\{[\phi(x_1 \overline{\rho}_o S_o + y_1 \overline{\rho}_g S_g)]_{i,k}^{n+1} - [\phi(x_1 \overline{\rho}_o S_o + y_1 \overline{\rho}_g S_g)]_{i,k}^{n}\} \quad . \tag{$B-1.1a$}$$

Using the definitions (Eq. B-1.1), our fully-implicit finite-difference equation for component #1 can be written

$$F_{1\,,i,k} = \mathcal{A} + \mathcal{B} - \mathcal{C} - \mathcal{D} + \mathcal{E} + \mathcal{F} - \mathcal{G} - \mathcal{H} - \mathcal{I} = 0 \ . \tag{$B-1.2$}$$

B.1.1 Derivatives w.r.t. Pressure

Derivative w.r.t. $p_{o\,,i,k-1}$

Examining our flow equation, it is apparent that only the terms $\mathcal{G}$ and $\mathcal{H}$ are functions of $p_{o\,,i,k-1}$, and, therefore,

$$\frac{\partial F_{1\,,i,k}}{\partial p_{o\,,i,k-1}} = -\frac{\partial \mathcal{G}}{\partial p_{o\,,i,k-1}} - \frac{\partial \mathcal{H}}{\partial p_{o\,,i,k-1}} \ , \tag{$B-1.1.1a$}$$

where,

$$\frac{\partial \mathcal{G}}{\partial p_o} = d_{zo\,,i,k-\frac{1}{2}}\left[\alpha_{i,k-\frac{1}{2}} x_1 k_{ro}\left(\frac{1}{\mu_o}\frac{\partial \overline{\rho}_o}{\partial p_o} - \frac{\overline{\rho}_o}{{\mu_o}^2}\frac{\partial \mu_o}{\partial p_o}\right) + \mathcal{T}_{zo}\frac{\partial x_1}{\partial p_o}\right]\Phi_{zo\,,i,k-\frac{1}{2}}$$
$$+ [x_1 \mathcal{T}_{zo}]_{i,k-\frac{1}{2}}\left[-1 + \left(\frac{\partial \rho_o}{\partial p}\right)_{i,k-1}\left(\frac{\Delta z_{k-1}\Delta z_{k-\frac{1}{2}}}{144[\Delta z_{k-1} + \Delta z_k]}\right)\right] \tag{$B-1.1.1b$}$$

and

$$\frac{\partial \mathcal{H}}{\partial p_o} = d_{zg\,,i,k-\frac{1}{2}}\left[\alpha_{i,k-\frac{1}{2}} y_1 k_{rg}\left(\frac{1}{\mu_g}\frac{\partial \overline{\rho}_g}{\partial p_o} - \frac{\overline{\rho}_g}{{\mu_g}^2}\frac{\partial \mu_g}{\partial p_o}\right) + \mathcal{T}_{zg}\frac{\partial y_1}{\partial p_o}\right]\Phi_{zg\,,i,k-\frac{1}{2}}$$
$$+ [y_1 \mathcal{T}_{zg}]_{i,k-\frac{1}{2}}\left[-1 + \left(\frac{\partial \rho_g}{\partial p}\right)_{i,k-1}\left(\frac{\Delta z_{k-1}\Delta z_{k-\frac{1}{2}}}{144[\Delta z_{k-1} + \Delta z_k]}\right)\right] \ . \tag{$B-1.1.1c$}$$

Derivative w.r.t. $p_{o,i-1,k}$

Only the terms $\mathcal{C}$ and $\mathcal{D}$ are functions of $p_{o,i-1,k}$, and, therefore,

$$\frac{\partial F_{1,i,k}}{\partial p_{o,i-1,k}} = -\frac{\partial \mathcal{C}}{\partial p_{o,i-1,k}} - \frac{\partial \mathcal{D}}{\partial p_{o,i-1,k}} \ , \qquad (B-1.1.2a)$$

where,

$$\frac{\partial \mathcal{C}}{\partial p_o} = d_{ho,i-\frac{1}{2},k}\left[\alpha_{i-\frac{1}{2},k} x_1 k_{ro}\left(\frac{1}{\mu_o}\frac{\partial \overline{\rho}_o}{\partial p_o} - \frac{\overline{\rho}_o}{{\mu_o}^2}\frac{\partial \mu_o}{\partial p_o}\right) + \mathcal{T}_{ro}\frac{\partial x_1}{\partial p_o}\right]\Phi_{ro,i-\frac{1}{2},k}$$
$$- [x_1 \mathcal{T}_{ro}]_{i-\frac{1}{2},k} \qquad (B-1.1.2b)$$

and

$$\frac{\partial \mathcal{D}}{\partial p_o} = d_{hg,i-\frac{1}{2},k}\left[\alpha_{i-\frac{1}{2},k} y_1 k_{rg}\left(\frac{1}{\mu_g}\frac{\partial \overline{\rho}_g}{\partial p_o} - \frac{\overline{\rho}_g}{{\mu_g}^2}\frac{\partial \mu_g}{\partial p_o}\right) + \mathcal{T}_{rg}\frac{\partial y_1}{\partial p_o}\right]\Phi_{rg,i-\frac{1}{2},k}$$
$$- [y_1 \mathcal{T}_{rg}]_{i-\frac{1}{2},k} \ . \qquad (B-1.1.2c)$$

Derivative w.r.t. $p_{oi,k}$

An examination of Eqs. B-1.1 to B-1.3 indicates that it is possible for every term in Eq. B-1.3 to be a function of $p_{oi,k}$, and we therefore obtain

$$\frac{\partial F_{1,i,k}}{\partial p_{o,i,k}} = \frac{\partial \mathcal{A}}{\partial p_{o,i,k}} + \frac{\partial \mathcal{B}}{\partial p_{o,i,k}} - \frac{\partial \mathcal{C}}{\partial p_{o,i,k}} - \frac{\partial \mathcal{D}}{\partial p_{o,i,k}}$$
$$+ \frac{\partial \mathcal{E}}{\partial p_{o,i,k}} + \frac{\partial \mathcal{F}}{\partial p_{o,i,k}} - \frac{\partial \mathcal{G}}{\partial p_{o,i,k}} - \frac{\partial \mathcal{H}}{\partial p_{o,i,k}} - \frac{\partial \mathcal{I}}{\partial p_{o,i,k}} \ , (B-1.1.3a)$$

where:

$$\frac{\partial \mathcal{A}}{\partial p_o} = d_{ho,i+\frac{1}{2},k}\left[\alpha_{i+\frac{1}{2},k} x_1 k_{ro}\left(\frac{1}{\mu_o}\frac{\partial \overline{\rho}_o}{\partial p_o} - \frac{\overline{\rho}_o}{{\mu_o}^2}\frac{\partial \mu_o}{\partial p_o}\right) + \mathcal{T}_{ro}\frac{\partial x_1}{\partial p_o}\right]\Phi_{ro,i+\frac{1}{2},k}$$
$$- [x_1 \mathcal{T}_{ro}]_{i+\frac{1}{2},k} \ , \qquad (B-1.1.3b)$$

$$\frac{\partial \mathcal{B}}{\partial p_o} = d_{hg\,,i+\frac{1}{2},k}\left[\alpha_{i+\frac{1}{2},k} y_1 k_{rg}\left(\frac{1}{\mu_g}\frac{\partial \overline{\rho}_g}{\partial p_o} - \frac{\overline{\rho}_g}{{\mu_g}^2}\frac{\partial \mu_g}{\partial p_o}\right) + \mathcal{T}_{rg}\frac{\partial y_1}{\partial p_o}\right]\Phi_{rg\,,i-\frac{1}{2},k} - [y_1 \mathcal{T}_{rg}]_{i+\frac{1}{2},k}\ , \qquad (B-1.1.3c)$$

$$\frac{\partial \mathcal{C}}{\partial p_o} = (1-d_{ho\,,i-\frac{1}{2},k})\left[\alpha_{i-\frac{1}{2},k} x_1 k_{ro}\left(\frac{1}{\mu_o}\frac{\partial \overline{\rho}_o}{\partial p_o} - \frac{\overline{\rho}_o}{{\mu_o}^2}\frac{\partial \mu_o}{\partial p_o}\right) + \mathcal{T}_{ro}\frac{\partial x_1}{\partial p_o}\right]\Phi_{ro\,,i-\frac{1}{2},k} + [x_1 \mathcal{T}_{ro}]_{i-\frac{1}{2},k}\ , \qquad (B-1.1.3d)$$

$$\frac{\partial \mathcal{D}}{\partial p_o} = (1-d_{hg\,,i-\frac{1}{2},k})\left[\alpha_{i-\frac{1}{2},k} y_1 k_{rg}\left(\frac{1}{\mu_g}\frac{\partial \overline{\rho}_g}{\partial p_o} - \frac{\overline{\rho}_g}{{\mu_g}^2}\frac{\partial \mu_g}{\partial p_o}\right) + \mathcal{T}_{rg}\frac{\partial y_1}{\partial p_o}\right]\Phi_{rg\,,i-\frac{1}{2},k} + [y_1 \mathcal{T}_{rg}]_{i-\frac{1}{2},k}\ , \qquad (B-1.1.3e)$$

$$\frac{\partial \mathcal{E}}{\partial p_o} = d_{zo\,,i,k+\frac{1}{2}}\left[\alpha_{i,k+\frac{1}{2}} x_1 k_{ro}\left(\frac{1}{\mu_o}\frac{\partial \overline{\rho}_o}{\partial p_o} - \frac{\overline{\rho}_o}{{\mu_o}^2}\frac{\partial \mu_o}{\partial p_o}\right) + \mathcal{T}_{zo}\frac{\partial x_1}{\partial p_o}\right]\Phi_{zo\,,i,k+\frac{1}{2}} - [x_1 \mathcal{T}_{zo}]_{i,k+\frac{1}{2}}\left[1+\left(\frac{\partial \rho_o}{\partial p}\right)_{,i,k}\left(\frac{\Delta z_k \Delta z_{k+\frac{1}{2}}}{144[\Delta z_{k+1}+\Delta z_k]}\right)\right]\ , \qquad (B-1.1.3f)$$

$$\frac{\partial \mathcal{F}}{\partial p_o} = d_{zg\,,i,k+\frac{1}{2}}\left[\alpha_{i,k+\frac{1}{2}} y_1 k_{rg}\left(\frac{1}{\mu_g}\frac{\partial \overline{\rho}_g}{\partial p_o} - \frac{\overline{\rho}_g}{{\mu_g}^2}\frac{\partial \mu_g}{\partial p_o}\right) + \mathcal{T}_{zg}\frac{\partial y_1}{\partial p_o}\right]\Phi_{zg\,,i,k+\frac{1}{2}} - [y_1 \mathcal{T}_{zg}]_{i,k+\frac{1}{2}}\left[1+\left(\frac{\partial \rho_g}{\partial p}\right)_{,i,k}\left(\frac{\Delta z_k \Delta z_{k+\frac{1}{2}}}{144[\Delta z_{k+1}+\Delta z_k]}\right)\right]\ , \qquad (B-1.1.3g)$$

$$\frac{\partial \mathcal{G}}{\partial p_o} = (1-d_{zo\,,i,k-\frac{1}{2}})\left[\alpha_{i,k-\frac{1}{2}} x_1 k_{ro}\left(\frac{1}{\mu_o}\frac{\partial \overline{\rho}_o}{\partial p_o} - \frac{\overline{\rho}_o}{{\mu_o}^2}\frac{\partial \mu_o}{\partial p_o}\right) + \mathcal{T}_{zo}\frac{\partial x_1}{\partial p_o}\right]\Phi_{zo\,,i,k-\frac{1}{2}} + [x_1 \mathcal{T}_{zo}]_{i,k-\frac{1}{2}}\left[1+\left(\frac{\partial \rho_o}{\partial p}\right)_{i,k}\left(\frac{\Delta z_k \Delta z_{k-\frac{1}{2}}}{144[\Delta z_{k-1}+\Delta z_k]}\right)\right]\ , \qquad (B-1.1.3h)$$

$$\frac{\partial \mathcal{H}}{\partial p_o} = (1 - d_{zg\,,i,k-\frac{1}{2}}) \left[\alpha_{i,k-\frac{1}{2}} y_1 k_{rg} \left(\frac{1}{\mu_g} \frac{\partial \overline{\rho}_g}{\partial p_o} - \frac{\overline{\rho}_g}{{\mu_g}^2} \frac{\partial \mu_g}{\partial p_o} \right) + \mathcal{T}_{zg} \frac{\partial y_1}{\partial p_o} \right] \Phi_{zg\,,i,k-\frac{1}{2}}$$
$$+ [y_1 \mathcal{T}_{zg}]_{i,k-\frac{1}{2}} \left[1 + \left(\frac{\partial \rho_g}{\partial p} \right)_{i,k} \left(\frac{\Delta z_k \Delta z_{k-\frac{1}{2}}}{144[\Delta z_{k-1} + \Delta z_k]} \right) \right] \qquad (B - 1.1.3i)$$

and, finally,

$$\frac{\partial \mathcal{I}}{\partial {p_o}_{,i,k}} = \frac{V_{i,k}}{\Delta t} \Bigg\{ (x_1 \overline{\rho}_o S_o + y_1 \overline{\rho}_g S_g)_{,i,k} \left(\frac{\partial \phi}{\partial p_o} \right)$$
$$+ \phi_{i,k} \Bigg[S_o \left(x_1 \frac{\partial \overline{\rho}_o}{\partial p} + \overline{\rho}_o \frac{dx_1}{dp} \right)$$
$$+ S_g \left(y_1 \frac{\partial \overline{\rho}_g}{\partial p} + \overline{\rho}_g \frac{dy_1}{dp} \right) \Bigg]_{i,k} \Bigg\} \, . \qquad (B - 1.1.3j)$$

Derivative w.r.t. ${p_o}_{,i+1,k}$

Only the terms $\mathcal{A}$ and $\mathcal{B}$ are functions of ${p_o}_{,i+1,k}$, and, therefore,

$$\frac{\partial {F_1}_{,i,k}}{\partial {p_o}_{,i+1,k}} = \frac{\partial \mathcal{A}}{\partial {p_o}_{,i+1,k}} + \frac{\partial \mathcal{B}}{\partial {p_o}_{,i+1,k}} \, , \qquad (B - 1.1.4a)$$

where,

$$\frac{\partial \mathcal{A}}{\partial p_o} = (1 - d_{ho\,,i+\frac{1}{2},k}) \left[\alpha_{i+\frac{1}{2},k} x_1 k_{ro} \left(\frac{1}{\mu_o} \frac{\partial \overline{\rho}_o}{\partial p_o} - \frac{\overline{\rho}_o}{{\mu_o}^2} \frac{\partial \mu_o}{\partial p_o} \right) + \mathcal{T}_{ro} \frac{\partial x_1}{\partial p_o} \right] \Phi_{ro\,,i+\frac{1}{2},k}$$
$$+ [x_1 \mathcal{T}_{ro}]_{i+\frac{1}{2},k} \qquad (B - 1.1.4b)$$

and

$$\frac{\partial \mathcal{B}}{\partial p_o} = (1 - d_{hg\,,i+\frac{1}{2},k}) \left[\alpha_{i+\frac{1}{2},k} y_1 k_{rg} \left(\frac{1}{\mu_g} \frac{\partial \overline{\rho}_g}{\partial p_o} - \frac{\overline{\rho}_g}{{\mu_g}^2} \frac{\partial \mu_g}{\partial p_o} \right) + \mathcal{T}_{rg} \frac{\partial y_1}{\partial p_o} \right] \Phi_{rg\,,i-\frac{1}{2},k}$$
$$+ [y_1 \mathcal{T}_{rg}]_{i+\frac{1}{2},k} \, . \qquad (B - 1.1.4c)$$

Derivative w.r.t. $p_{o,i,k+1}$

Examining our flow equation, it is apparent that only the terms $\mathcal{E}$ and $\mathcal{F}$ are functions of $p_{,i,k+1}$, and, therefore,

$$\frac{\partial F_{1,i,k}}{\partial p_{o,i,k+1}} = \frac{\partial \mathcal{G}}{\partial p_{o,i,k+1}} + \frac{\partial \mathcal{H}}{\partial p_{o,i,k+1}} \ , \qquad (B-1.1.5a)$$

where,

$$\frac{\partial \mathcal{E}}{\partial p_o} = (1 - d_{zo\,,i,k+\frac{1}{2}}) \left[\alpha_{i,k+\frac{1}{2}} x_1 k_{ro} \left(\frac{1}{\mu_o} \frac{\partial \overline{\rho}_o}{\partial p_o} - \frac{\overline{\rho}_o}{{\mu_o}^2} \frac{\partial \mu_o}{\partial p_o} \right) + \mathcal{T}_{zo} \frac{\partial x_1}{\partial p_o} \right] \Phi_{zo\,,i,k+\frac{1}{2}}$$
$$+ [x_1 \mathcal{T}_{zo}]_{i,k+\frac{1}{2}} \left[1 + \left(\frac{\partial \rho_o}{\partial p} \right)_{i,k+1} \left(\frac{\Delta z_{k+1} \Delta z_{k+\frac{1}{2}}}{144[\Delta z_{k+1} + \Delta z_k]} \right) \right] \qquad (B-1.1.5b)$$

and

$$\frac{\partial \mathcal{F}}{\partial p_o} = (1 - d_{zg\,,i,k+\frac{1}{2}}) \left[\alpha_{i,k+\frac{1}{2}} y_1 k_{rg} \left(\frac{1}{\mu_g} \frac{\partial \overline{\rho}_g}{\partial p_o} - \frac{\overline{\rho}_g}{{\mu_g}^2} \frac{\partial \mu_g}{\partial p_o} \right) + \mathcal{T}_{zg} \frac{\partial y_1}{\partial p_o} \right] \Phi_{zg\,,i,k+\frac{1}{2}}$$
$$+ [y_1 \mathcal{T}_{zg}]_{i,k+\frac{1}{2}} \left[1 + \left(\frac{\partial \rho_g}{\partial p} \right)_{i,k+1} \left(\frac{\Delta z_{k+1} \Delta z_{k+\frac{1}{2}}}{144[\Delta z_{k+1} + \Delta z_k]} \right) \right] \ . \qquad (B-1.1.5c)$$

B.1.2 Derivatives w.r.t. Gas Saturation

Derivative w.r.t. $S_{g\,,i,k-1}$

Here, only $\mathcal{G}$ and $\mathcal{H}$ can be functions of $S_{g\,,i,k-1}$, and so we obtain

$$\frac{\partial F_{1,i,k}}{\partial S_{g\,,i,k-1}} = -\frac{\partial \mathcal{G}}{\partial S_{g\,,i,k-1}} - \frac{\partial \mathcal{H}}{\partial S_{g\,,i,k-1}} \ , \qquad (B-1.2.1a)$$

where

$$\frac{\partial \mathcal{G}}{\partial S_{g\,,i,k-1}} = d_{zo\,,i,k-\frac{1}{2}} \alpha_{i,k-\frac{1}{2}} \left[\frac{x_1 \overline{\rho}_o}{\mu_o} \left(\frac{\partial k_{ro}}{\partial S_g} \right) \right]_{i,k-1} \Phi_{zo\,,i,k-\frac{1}{2}} \qquad (B-1.2.1b)$$

and

$$\frac{\partial \mathcal{H}}{\partial S_{g\,,i,k-1}} = d_{zg\,,i,k-\frac{1}{2}} \alpha_{i,k-\frac{1}{2}} \left[\frac{y_1 \overline{\rho}_g}{\mu_g} \left(\frac{\partial k_{rg}}{\partial S_g} \right) \right]_{i,k-1} \Phi_{zg\,,i,k-\frac{1}{2}} - \left[y_1 \mathcal{T}_{zg} \right]_{i,k-\frac{1}{2}} \left(\frac{\partial p_{cog}}{\partial S_g} \right)_{i,k-1} . \qquad (B-1.2.1c)$$

Derivative w.r.t. $S_{g\,,i-1,k}$

The terms $\mathcal{C}$ and $\mathcal{D}$ are possible functions of $S_{g\,,i-1,k}$ and so we obtain

$$\frac{\partial F_{1\,,i,k}}{\partial S_{g\,,i-1,k}} = -\frac{\partial \mathcal{C}}{\partial S_{g\,,i-1,k}} - \frac{\partial \mathcal{D}}{\partial S_{g\,,i-1,k}} , \qquad (B-1.2.2a)$$

where

$$\frac{\partial \mathcal{C}}{\partial S_{g\,,i-1,k}} = d_{ho\,,i-\frac{1}{2},k} \alpha_{i-\frac{1}{2},k} \left[\frac{x_1 \overline{\rho}_o}{\mu_o} \left(\frac{\partial k_{ro}}{\partial S_g} \right) \right]_{i-1,k} \Phi_{ro\,,i-\frac{1}{2},k} \qquad (B-1.2.2b)$$

and

$$\frac{\partial \mathcal{D}}{\partial S_{g\,,i-1,k}} = d_{hg\,,i-\frac{1}{2},k} \alpha_{i-\frac{1}{2},k} \left[\frac{y_1 \overline{\rho}_g}{\mu_g} \left(\frac{\partial k_{rg}}{\partial S_g} \right) \right]_{i-1,k} \Phi_{rg\,,i-\frac{1}{2},k} - \left[y_1 \mathcal{T}_{rg} \right]_{i-\frac{1}{2},k} \left(\frac{\partial p_{cog}}{\partial S_g} \right)_{i-1,k} . \qquad (B-1.2.2c)$$

Derivative w.r.t. $S_{g_{i,k}}$

An examination of Eqs. B-1.1 to B-1.3 indicates that it is possible for every term in Eq. B-1.3 to be a function of $S_{g_{i,k}}$, and we therefore obtain

$$\frac{\partial F_{1\,,i,k}}{\partial S_{g\,,i,k}} = \frac{\partial \mathcal{A}}{\partial S_{g\,,i,k}} + \frac{\partial \mathcal{B}}{\partial S_{g\,,i,k}} - \frac{\partial \mathcal{C}}{\partial S_{g\,,i,k}} - \frac{\partial \mathcal{D}}{\partial S_{g\,,i,k}} + \frac{\partial \mathcal{E}}{\partial S_{g\,,i,k}} + \frac{\partial \mathcal{F}}{\partial S_{g\,,i,k}} - \frac{\partial \mathcal{G}}{\partial S_{g\,,i,k}} - \frac{\partial \mathcal{H}}{\partial S_{g\,,i,k}} - \frac{\partial \mathcal{I}}{\partial S_{g\,,i,k}} \qquad (B-1.2.3a)$$

where:

$$\frac{\partial \mathcal{A}}{\partial S_{g\,,i,k}} = d_{ho\,,i+\frac{1}{2},k}\alpha_{i+\frac{1}{2},k}\left[\frac{x_1\overline{\rho}_o}{\mu_o}\left(\frac{\partial k_{ro}}{\partial S_g}\right)\right]_{i,k}\Phi_{ro\,,i+\frac{1}{2},k}\ , \qquad (B-1.2.3b)$$

$$\frac{\partial \mathcal{B}}{\partial S_{g\,,i,k}} = d_{hg\,,i+\frac{1}{2},k}\alpha_{i+\frac{1}{2},k}\left[\frac{y_1\overline{\rho}_g}{\mu_g}\left(\frac{\partial k_{rg}}{\partial S_g}\right)\right]_{i,k}\Phi_{rg\,,i+\frac{1}{2},k} + [y_1\mathcal{T}_{rg}]_{i+\frac{1}{2},k}\left(\frac{\partial p_{cog}}{\partial S_g}\right)_{i,k}\ , \qquad (B-1.2.3c)$$

$$\frac{\partial \mathcal{C}}{\partial S_{g\,,i,k}} = (1-d_{ho\,,i-\frac{1}{2},k})\alpha_{i-\frac{1}{2},k}\left[\frac{x_1\overline{\rho}_o}{\mu_o}\left(\frac{\partial k_{ro}}{\partial S_g}\right)\right]_{i,k}\Phi_{ro\,,i-\frac{1}{2},k}\ , \qquad (B-1.2.3d)$$

$$\frac{\partial \mathcal{D}}{\partial S_{g\,,i,k}} = (1-d_{hg\,,i-\frac{1}{2},k})\alpha_{i-\frac{1}{2},k}\left[\frac{y_1\overline{\rho}_g}{\mu_g}\left(\frac{\partial k_{rg}}{\partial S_g}\right)\right]_{i,k}\Phi_{rg\,,i-\frac{1}{2},k} - [y_1\mathcal{T}_{rg}]_{i-\frac{1}{2},k}\left(\frac{\partial p_{cog}}{\partial S_g}\right)_{i,k}\ , \qquad (B-1.2.3e)$$

$$\frac{\partial \mathcal{E}}{\partial S_{g\,,i,k}} = d_{zo\,,i,k+\frac{1}{2}}\alpha_{i,k+\frac{1}{2}}\left[\frac{x_1\overline{\rho}_o}{\mu_o}\left(\frac{\partial k_{ro}}{\partial S_g}\right)\right]_{i,k}\Phi_{zo\,,i,k+\frac{1}{2}}\ , \qquad (B-1.2.3f)$$

$$\frac{\partial \mathcal{F}}{\partial S_{g\,,i,k}} = d_{zg\,,i,k+\frac{1}{2}}\alpha_{i,k+\frac{1}{2}}\left[\frac{y_1\overline{\rho}_g}{\mu_g}\left(\frac{\partial k_{rg}}{\partial S_g}\right)\right]_{i,k}\Phi_{zg\,,i,k+\frac{1}{2}} + [y_1\mathcal{T}_{zg}]_{i,k+\frac{1}{2}}\left(\frac{\partial p_{cog}}{\partial S_g}\right)_{i,k}\ , \qquad (B-1.2.3g)$$

$$\frac{\partial \mathcal{G}}{\partial S_{g\,,i,k}} = (1-d_{zo\,,i,k-\frac{1}{2}})\alpha_{i,k-\frac{1}{2}}\left[\frac{x_1\overline{\rho}_o}{\mu_o}\left(\frac{\partial k_{ro}}{\partial S_g}\right)\right]_{i,k}\Phi_{zo\,,i,k-\frac{1}{2}}\ , \qquad (B-1.2.3h)$$

$$\frac{\partial \mathcal{H}}{\partial S_{g\,,i,k}} = (1-d_{zg\,,i,k-\frac{1}{2}})\alpha_{i,k-\frac{1}{2}}\left[\frac{y_1\overline{\rho}_g}{\mu_g}\left(\frac{\partial k_{rg}}{\partial S_g}\right)\right]_{i,k}\Phi_{zg\,,i,k-\frac{1}{2}} - [y_1\mathcal{T}_{zg}]_{i,k-\frac{1}{2}}\left(\frac{\partial p_{cog}}{\partial S_g}\right)_{i,k} \qquad (B-1.2.3i)$$

and, finally,

$$\frac{\partial \mathcal{I}}{\partial S_{g\,,i,k}} = \frac{V_{,i,k}}{\Delta t}\{[\phi(y_1\overline{\rho}_g - x_1\overline{\rho}_o)]_{i,k}\}\ . \qquad (B-1.2.3j)$$

Derivative w.r.t. $S_{g\,,i+1,k}$

The terms $\mathcal{A}$ and $\mathcal{B}$ are the only possible functions of $S_{g\,,i+1,k}$ and so we obtain

$$\frac{\partial F_{1\,,i,k}}{\partial S_{g\,,i+1,k}} = \frac{\partial \mathcal{A}}{\partial S_{g\,,i+1,k}} - \frac{\partial \mathcal{B}}{\partial S_{g\,,i+1,k}} \ , \qquad (B-1.2.4a)$$

where

$$\frac{\partial \mathcal{A}}{\partial S_{g\,,i+1,k}} = (1 - d_{ho\,,i+\frac{1}{2},k})\alpha_{i+\frac{1}{2},k}\left[\frac{x_1\overline{\rho}_o}{\mu_o}\left(\frac{\partial k_{ro}}{\partial S_g}\right)\right]_{i+1,k}\Phi_{ro\,,i+\frac{1}{2},k} \qquad (B-1.2.4b)$$

and

$$\frac{\partial \mathcal{B}}{\partial S_{g\,,i+1,k}} = (1 - d_{hg\,,i+\frac{1}{2},k})\alpha_{i+\frac{1}{2},k}\left[\frac{y_1\overline{\rho}_g}{\mu_g}\left(\frac{\partial k_{rg}}{\partial S_g}\right)\right]_{i+1,k}\Phi_{rg\,,i+\frac{1}{2},k}$$
$$+ \left[y_1\mathcal{T}_{rg}\right]_{i+\frac{1}{2},k}\left(\frac{\partial p_{cog}}{\partial S_g}\right)_{i+1,k} . \qquad (B-1.2.4c)$$

Derivative w.r.t. $S_{g\,,i,k+1}$

Here, only $\mathcal{E}$ and $\mathcal{F}$ can be functions of $S_{g\,,i,k+1}$, and so we obtain

$$\frac{\partial F_{1\,,i,k}}{\partial S_{g\,,i,k+1}} = \frac{\partial \mathcal{E}}{\partial S_{g\,,i,k+1}} + \frac{\partial \mathcal{F}}{\partial S_{g\,,i,k+1}} \ , \qquad (B-1.2.5a)$$

where

$$\frac{\partial \mathcal{E}}{\partial S_{g\,,i,k+1}} = (1 - d_{zo\,,i,k+\frac{1}{2}})\alpha_{i,k+\frac{1}{2}}\left[\frac{x_1\overline{\rho}_o}{\mu_o}\left(\frac{\partial k_{ro}}{\partial S_g}\right)\right]_{i,k+1}\Phi_{zo\,,i,k+\frac{1}{2}} \qquad (B-1.2.5b)$$

and

$$\frac{\partial \mathcal{F}}{\partial S_{g\,,i,k+1}} = (1 - d_{zg\,,i,k+\frac{1}{2}})\alpha_{i,k+\frac{1}{2}}\left[\frac{y_1\overline{\rho}_g}{\mu_g}\left(\frac{\partial k_{rg}}{\partial S_g}\right)\right]_{i,k+1}\Phi_{zg\,,i,k+\frac{1}{2}}$$
$$+ \left[y_1\mathcal{T}_{zg}\right]_{i,k+\frac{1}{2}}\left(\frac{\partial p_{cog}}{\partial S_g}\right)_{i,k+1} . \qquad (B-1.2.5c)$$

B.1.3 Derivatives w.r.t. Bubble-Point Pressure

Here we note that only the oil phase PVT properties can be functions of the bubble-point pressure, and we, therefore, need only consider the terms $\mathcal{A}$, $\mathcal{C}$, $\mathcal{E}$, $\mathcal{G}$ and $\mathcal{I}$.

Derivative w.r.t. $p_{b,i,k-1}$

Of the five terms noted above, it is apparent that only the term $\mathcal{G}$ can be a function of $p_{b,i,k-1}$, and, therefore,

$$\frac{\partial F_{1,i,k}}{\partial p_{b,i,k-1}} = -\frac{\partial \mathcal{G}}{\partial p_{b,i,k-1}} \ , \qquad (B-1.3.1a)$$

where,

$$\frac{\partial \mathcal{G}}{\partial p_b} = d_{zo,i,k-\frac{1}{2}} \left[\alpha_{i,k-\frac{1}{2}} x_1 k_{ro} \left(\frac{1}{\mu_o} \frac{\partial \overline{\rho}_o}{\partial p_b} - \frac{\overline{\rho}_o}{{\mu_o}^2} \frac{\partial \mu_o}{\partial p_b} \right) + \mathcal{T}_{zo} \frac{\partial x_1}{\partial p_b} \right] \Phi_{zo,i,k-\frac{1}{2}}$$
$$+ \left[x_1 \mathcal{T}_{zo} \right]_{i,k-\frac{1}{2}} \left[\left(\frac{\partial \rho_o}{\partial p_b} \right)_{i,k-1} \left(\frac{\Delta z_{k-1} \Delta z_{k-\frac{1}{2}}}{144[\Delta z_{k-1} + \Delta z_k]} \right) \right] . \qquad (B-1.3.1b)$$

Derivative w.r.t. $p_{b,i-1,k}$

Only the term $\mathcal{C}$ is a function of $p_{b,i-1,k}$, and, therefore,

$$\frac{\partial F_{1,i,k}}{p_{b,i-1,k}} = -\frac{\partial \mathcal{C}}{\partial p_{b,i-1,k}} \ , \qquad (B-1.3.2a)$$

where,

$$\frac{\partial \mathcal{C}}{\partial p_b} = d_{ho,i-\frac{1}{2},k} \left[\alpha_{i-\frac{1}{2},k} x_1 k_{ro} \left(\frac{1}{\mu_o} \frac{\partial \overline{\rho}_o}{\partial p_b} - \frac{\overline{\rho}_o}{{\mu_o}^2} \frac{\partial \mu_o}{\partial p_b} \right) + \mathcal{T}_{ro} \frac{\partial x_1}{\partial p_b} \right] \Phi_{ro,i-\frac{1}{2},k} \ . \qquad (B-1.3.2b)$$

Derivative w.r.t. $p_{bi,k}$

Here, we note that all five of the terms mentioned above can be functions of $p_{bi,k}$, and we therefore have,

$$\frac{\partial F_{1,i,k}}{p_{b,i,k}} = \frac{\partial \mathcal{A}}{\partial p_b, i, k} - \frac{\partial \mathcal{C}}{\partial p_b, i, k} + \frac{\partial \mathcal{E}}{\partial p_b, i, k} - \frac{\partial \mathcal{G}}{\partial p_b, i, k} - \frac{\partial \mathcal{I}}{\partial p_b, i, k} \ , \qquad (B-1.3.3a)$$

where,

$$\frac{\partial \mathcal{A}}{\partial p_b} = d_{ho,i+\frac{1}{2},k}\left[\alpha_{i+\frac{1}{2},k} x_1 k_{ro}\left(\frac{1}{\mu_o}\frac{\partial \overline{\rho}_o}{\partial p_b} - \frac{\overline{\rho}_o}{{\mu_o}^2}\frac{\partial \mu_o}{\partial p_b}\right) + \mathcal{T}_{ro}\frac{\partial x_1}{\partial p_b}\right]\Phi_{ro,i+\frac{1}{2},k} \ , \qquad (B-1.3.3b)$$

$$\frac{\partial \mathcal{C}}{\partial p_b} = (1-d_{ho,i-\frac{1}{2},k})\left[\alpha_{i-\frac{1}{2},k} x_1 k_{ro}\left(\frac{1}{\mu_o}\frac{\partial \overline{\rho}_o}{\partial p_b} - \frac{\overline{\rho}_o}{{\mu_o}^2}\frac{\partial \mu_o}{\partial p_b}\right) + \mathcal{T}_{ro}\frac{\partial x_1}{\partial p_b}\right]\Phi_{ro,i-\frac{1}{2},k} \ , \qquad (B-1.3.3c)$$

$$\begin{aligned}\frac{\partial \mathcal{E}}{\partial p_b} = {} & d_{zo,i,k+\frac{1}{2}}\left[\alpha_{i,k+\frac{1}{2}} x_1 k_{ro}\left(\frac{1}{\mu_o}\frac{\partial \overline{\rho}_o}{\partial p_b} - \frac{\overline{\rho}_o}{{\mu_o}^2}\frac{\partial \mu_o}{\partial p_b}\right) + \mathcal{T}_{zo}\frac{\partial x_1}{\partial p_b}\right]\Phi_{zo,i,k+\frac{1}{2}} \\ & + [x_1 \mathcal{T}_{zo}]_{i,k+\frac{1}{2}}\left[\left(\frac{\partial \rho_o}{\partial p_b}\right)_{i,k}\left(\frac{\Delta z_k \Delta z_{k+\frac{1}{2}}}{144[\Delta z_{k+1} + \Delta z_k]}\right)\right] \ ,\end{aligned} \qquad (B-1.3.3d)$$

$$\begin{aligned}\frac{\partial \mathcal{G}}{\partial p_b} = {} & (1-d_{zo,i,k-\frac{1}{2}})\left[\alpha_{i,k-\frac{1}{2}} x_1 k_{ro}\left(\frac{1}{\mu_o}\frac{\partial \overline{\rho}_o}{\partial p_b} - \frac{\overline{\rho}_o}{{\mu_o}^2}\frac{\partial \mu_o}{\partial p_b}\right) + \mathcal{T}_{zo}\frac{\partial x_1}{\partial p_b}\right]\Phi_{zo,i,k-\frac{1}{2}} \\ & + [x_1 \mathcal{T}_{zo}]_{i,k-\frac{1}{2}}\left[\left(\frac{\partial \rho_o}{\partial p_b}\right)_{i,k}\left(\frac{\Delta z_k \Delta z_{k-\frac{1}{2}}}{144[\Delta z_{k-1} + \Delta z_k]}\right)\right]\end{aligned} \qquad (B-1.3.3e)$$

and, finally,

$$\frac{\partial \mathcal{I}}{\partial p_{b,i,k}} == \frac{V_{,i,k}}{\Delta t}\left\{\phi_{i,k}\left[S_o\left(x_1\frac{\partial \overline{\rho}_o}{\partial p_b} + \overline{\rho}_o\frac{dx_1}{dp_b}\right)\right]_{i,k}\right\} \ . \qquad (B-1.3.3f)$$

Derivative w.r.t. $p_{b,i+1,k}$

Only the term $\mathcal{A}$ is a function of $p_{b,i+1,k}$, and, therefore,

$$\frac{\partial F_{1,i,k}}{\partial p_{b,i+1,k}} = \frac{\partial \mathcal{A}}{\partial p_{b,i+1,k}} \ , \qquad (B-1.3.4a)$$

where,

$$\frac{\partial \mathcal{A}}{\partial p_b} = (1 - d_{ho,i+\frac{1}{2},k})\left[\alpha_{i+\frac{1}{2},k} x_1 k_{ro}\left(\frac{1}{\mu_o}\frac{\partial \overline{\rho}_o}{\partial p_b} - \frac{\overline{\rho}_o}{{\mu_o}^2}\frac{\partial \mu_o}{\partial p_b}\right) + \mathcal{T}_{ro}\frac{\partial x_1}{\partial p_b}\right]\Phi_{ro,i+\frac{1}{2},k} \ . \qquad (B-1.3.4b)$$

Derivative w.r.t. $p_{b,i,k+1}$

Here, only the term $\mathcal{E}$ can be a function of $p_{b,i,k+1}$, and, therefore,

$$\frac{\partial F_{1,i,k}}{\partial p_{b,i,k+1}} = -\frac{\partial \mathcal{E}}{\partial p_{b,i,k+1}} \ , \qquad (B-1.3.5a)$$

where,

$$\frac{\partial \mathcal{E}}{\partial p_b} = (1 - d_{zo,i,k+\frac{1}{2}})\left[\alpha_{i,k+\frac{1}{2}} x_1 k_{ro}\left(\frac{1}{\mu_o}\frac{\partial \overline{\rho}_o}{\partial p_b} - \frac{\overline{\rho}_o}{{\mu_o}^2}\frac{\partial \mu_o}{\partial p_b}\right) + \mathcal{T}_{zo}\frac{\partial x_1}{\partial p_b}\right]\Phi_{zo,i,k+\frac{1}{2}}$$
$$+ [x_1 \mathcal{T}_{zo}]_{i,k+\frac{1}{2}}\left[\left(\frac{\partial \rho_o}{\partial p_b}\right)_{i,k+1}\left(\frac{\Delta z_{k+1}\Delta z_{k+\frac{1}{2}}}{144[\Delta z_{k+1} + \Delta z_k]}\right)\right] \ . \qquad (B-1.3.5b)$$

B.1.4 Derivative w.r.t. Dew-Point Pressure

Note that only the gas phase PVT properties can be functions of the dew-point pressure, and we, therefore, need only consider the terms $\mathcal{B}$, $\mathcal{D}$, $\mathcal{F}$, $\mathcal{H}$ and $\mathcal{I}$.

Derivative w.r.t. $p_{d,i,k-1}$

Of the five terms noted above, it is apparent that only the term $\mathcal{H}$ can be a function of $p_{d,i,k-1}$, and, therefore,

$$\frac{\partial F_{1,i,k}}{\partial p_{d,i,k-1}} = -\frac{\partial \mathcal{H}}{\partial p_{d,i,k-1}} \ , \qquad (B-1.4.1a)$$

where,

$$\frac{\partial \mathcal{H}}{\partial p_d} = d_{zg\,,i,k-\frac{1}{2}} \left[\alpha_{i,k-\frac{1}{2}} y_1 k_{rg} \left(\frac{1}{\mu_g} \frac{\partial \overline{\rho}_g}{\partial p_d} - \frac{\overline{\rho}_g}{{\mu_g}^2} \frac{\partial \mu_g}{\partial p_d} \right) + \mathcal{T}_{zg} \frac{\partial y_1}{\partial p_d} \right] \Phi_{zo\,,i,k-\frac{1}{2}}$$
$$+ \left[y_1 \mathcal{T}_{zg} \right]_{i,k-\frac{1}{2}} \left[\left(\frac{\partial \rho_g}{\partial p_d} \right)_{i,k-1} \left(\frac{\Delta z_{k-1} \Delta z_{k-\frac{1}{2}}}{144[\Delta z_{k-1} + \Delta z_k]} \right) \right] \ . \qquad (B-1.4.1b)$$

Derivative w.r.t. $p_{d,i-1,k}$

Only the term $\mathcal{D}$ is a function of $p_{d,i-1,k}$, and, therefore,

$$\frac{\partial F_{1,i,k}}{\partial p_{d,i-1,k}} = -\frac{\partial \mathcal{D}}{\partial p_{d,i-1,k}} \ , \qquad (B-1.4.2a)$$

where,

$$\frac{\partial \mathcal{D}}{\partial p_d} = d_{hg\,,i-\frac{1}{2},k} \left[\alpha_{i-\frac{1}{2},k} y_1 k_{rg} \left(\frac{1}{\mu_g} \frac{\partial \overline{\rho}_g}{\partial p_d} - \frac{\overline{\rho}_g}{{\mu_g}^2} \frac{\partial \mu_g}{\partial p_d} \right) + \mathcal{T}_{rg} \frac{\partial y_1}{\partial p_d} \right] \Phi_{ro\,,i-\frac{1}{2},k} \ . \qquad (B-1.4.2b)$$

Derivative w.r.t. $p_{di,k}$

Here, we note that all five of the terms mentioned above can be functions of $p_{di,k}$, and we therefore have,

$$\frac{\partial F_{1,i,k}}{\partial p_{d,i,k}} = \frac{\partial \mathcal{B}}{\partial p_d, i, k} - \frac{\partial \mathcal{D}}{\partial p_d, i, k} + \frac{\partial \mathcal{F}}{\partial p_d, i, k} - \frac{\partial \mathcal{H}}{\partial p_d, i, k} - \frac{\partial \mathcal{I}}{\partial p_d, i, k} \ , \qquad (B-1.4.3a)$$

where,

$$\frac{\partial \mathcal{B}}{\partial p_d} = d_{hg\,,i+\frac{1}{2},k}\left[\alpha_{i+\frac{1}{2},k} y_1 k_{rg}\left(\frac{1}{\mu_g}\frac{\partial \overline{\rho}_g}{\partial p_d} - \frac{\overline{\rho}_g}{{\mu_g}^2}\frac{\partial \mu_g}{\partial p_d}\right) + \mathcal{T}_{rg}\frac{\partial y_1}{\partial p_d}\right]\Phi_{ro\,,i+\frac{1}{2},k} \ , \qquad (B-1.4.3b)$$

$$\frac{\partial \mathcal{D}}{\partial p_d} = (1-d_{hg\,,i-\frac{1}{2},k})\left[\alpha_{i-\frac{1}{2},k} y_1 k_{rg}\left(\frac{1}{\mu_g}\frac{\partial \overline{\rho}_g}{\partial p_d} - \frac{\overline{\rho}_g}{{\mu_g}^2}\frac{\partial \mu_g}{\partial p_d}\right) + \mathcal{T}_{rg}\frac{\partial y_1}{\partial p_d}\right]\Phi_{ro\,,i-\frac{1}{2},k} \ , \qquad (B-1.4.3c)$$

$$\begin{aligned}\frac{\partial \mathcal{F}}{\partial p_d} = {} & d_{zg\,,i,k+\frac{1}{2}}\left[\alpha_{i,k+\frac{1}{2}} y_1 k_{rg}\left(\frac{1}{\mu_g}\frac{\partial \overline{\rho}_g}{\partial p_d} - \frac{\overline{\rho}_g}{{\mu_g}^2}\frac{\partial \mu_g}{\partial p_d}\right) + \mathcal{T}_{zg}\frac{\partial y_1}{\partial p_d}\right]\Phi_{zo\,,i,k+\frac{1}{2}} \\ & + [y_1 \mathcal{T}_{zg}]_{i,k+\frac{1}{2}}\left[\left(\frac{\partial \rho_g}{\partial p_d}\right)_{i,k}\left(\frac{\Delta z_k \Delta z_{k+\frac{1}{2}}}{144[\Delta z_{k+1}+\Delta z_k]}\right)\right] \ ,\end{aligned} \qquad (B-1.4.3d)$$

$$\begin{aligned}\frac{\partial \mathcal{H}}{\partial p_d} = {} & (1-d_{zg\,,i,k-\frac{1}{2}})\left[\alpha_{i,k-\frac{1}{2}} y_1 k_{rg}\left(\frac{1}{\mu_g}\frac{\partial \overline{\rho}_g}{\partial p_d} - \frac{\overline{\rho}_g}{{\mu_g}^2}\frac{\partial \mu_g}{\partial p_d}\right) + \mathcal{T}_{zg}\frac{\partial y_1}{\partial p_d}\right]\Phi_{zo\,,i,k-\frac{1}{2}} \\ & + [y_1 \mathcal{T}_{zg}]_{i,k-\frac{1}{2}}\left[\left(\frac{\partial \rho_g}{\partial p_d}\right)_{i,k}\left(\frac{\Delta z_k \Delta z_{k-\frac{1}{2}}}{144[\Delta z_{k-1}+\Delta z_k]}\right)\right]\end{aligned} \qquad (B-1.4.3e)$$

and

$$\frac{\partial \mathcal{I}}{\partial p_{d,i,k}} == \frac{V_{,i,k}}{\Delta t}\left\{\phi_{i,k}\left[S_g\left(y_1\frac{\partial \overline{\rho}_g}{\partial p_d} + \overline{\rho}_g\frac{dy_1}{dp_d}\right)\right]_{i,k}\right\} \ . \qquad (B-1.4.3f)$$

Derivative w.r.t. $p_{d,i+1,k}$

Only the term $\mathcal{B}$ is a function of $p_{d,i+1,k}$, and, therefore,

$$\frac{\partial F_{1\,,i,k}}{\partial p_{d,i+1,k}} = \frac{\partial \mathcal{B}}{\partial p_{d,i+1,k}} \ , \qquad (B-1.4.4a)$$

where,

$$\frac{\partial \mathcal{B}}{\partial p_d} = (1-d_{hg\,,i+\frac{1}{2},k})\left[\alpha_{i+\frac{1}{2},k} y_1 k_{rg}\left(\frac{1}{\mu_g}\frac{\partial \overline{\rho}_g}{\partial p_d} - \frac{\overline{\rho}_g}{{\mu_g}^2}\frac{\partial \mu_g}{\partial p_d}\right) + \mathcal{T}_{rg}\frac{\partial y_1}{\partial p_d}\right]\Phi_{ro\,,i+\frac{1}{2},k} \ . \qquad (B-1.4.4b)$$

Derivative w.r.t. $p_{d,i,k+1}$

Here, only the term $\mathcal{F}$ can be a function of $p_{d,i,k+1}$, and, therefore,

$$\frac{\partial F_{1,i,k}}{\partial p_{d,i,k+1}} = -\frac{\partial \mathcal{F}}{\partial p_{d,i,k+1}} \ , \qquad (B-1.4.5a)$$

where,

$$\frac{\partial \mathcal{F}}{\partial p_d} = (1 - d_{zg,i,k+\frac{1}{2}}) \left[\alpha_{i,k+\frac{1}{2}} y_1 k_{rg} \left(\frac{1}{\mu_g} \frac{\partial \overline{\rho}_g}{\partial p_d} - \frac{\overline{\rho}_g}{{\mu_g}^2} \frac{\partial \mu_g}{\partial p_d} \right) + \mathcal{T}_{zg} \frac{\partial y_1}{\partial p_d} \right] \Phi_{zo,i,k+\frac{1}{2}}$$
$$+ [y_1 \mathcal{T}_{zg}]_{i,k+\frac{1}{2}} \left[\left(\frac{\partial \rho_g}{\partial p_d} \right)_{i,k+1} \left(\frac{\Delta z_{k+1} \Delta z_{k+\frac{1}{2}}}{144[\Delta z_{k+1} + \Delta z_k]} \right) \right] \ . \qquad (B-1.4.5b)$$

B.1.5 Derivative w.r.t. Water Saturation

Here, we breifly note that only terms containing the oil relative permeability and the oil saturation can be functions of the water saturation, i.e., $\mathcal{A}$, $\mathcal{C}$, $\mathcal{E}$, $\mathcal{G}$ and $\mathcal{I}$.

Derivative w.r.t. $S_{w,i,k-1}$

Only $\mathcal{G}$ is a functions of $S_{w,i,k-1}$, and so we obtain

$$\frac{\partial F_{1,i,k}}{\partial S_{w,i,k-1}} = -\frac{\partial \mathcal{G}}{\partial S_{w,i,k-1}} \ , \qquad (B-1.5.1a)$$

where

$$\frac{\partial \mathcal{G}}{\partial S_{w,i,k-1}} = d_{zo,i,k-\frac{1}{2}} \alpha_{i,k-\frac{1}{2}} \left[\frac{x_1 \overline{\rho}_o}{\mu_o} \left(\frac{\partial k_{ro}}{\partial S_w} \right) \right]_{i,k-1} \Phi_{zo,i,k-\frac{1}{2}} \ . \qquad (B-1.5.1b)$$

Derivative w.r.t. $S_{w,i-1,k}$

When the term $\mathcal{C}$ is a function of $S_{w,i-1,k}$ we obtain

$$\frac{\partial F_{1,i,k}}{\partial S_{w,i-1,k}} = -\frac{\partial \mathcal{C}}{\partial S_{w,i-1,k}} \ , \qquad (B-1.5.2a)$$

where

$$\frac{\partial \mathcal{C}}{\partial S_{w,i-1,k}} = d_{ho,i-\frac{1}{2},k}\alpha_{i-\frac{1}{2},k}\left[\frac{x_1\overline{\rho}_o}{\mu_o}\left(\frac{\partial k_{ro}}{\partial S_w}\right)\right]_{i-1,k}\Phi_{ro,i-\frac{1}{2},k} \ . \qquad (B-1.5.2b)$$

Derivative w.r.t. $S_{wi,k}$

Examination of Eqs. B-1.1 to B-1.3 indicate only terms involving the oil phase can be functions of $S_{wi,k}$, and we, therefore, obtain

$$\frac{\partial F_{1,i,k}}{\partial S_{w,i,k}} = \frac{\partial \mathcal{A}}{\partial S_{w,i,k}} - \frac{\partial \mathcal{C}}{\partial S_{w,i,k}} + \frac{\partial \mathcal{E}}{\partial S_{w,i,k}} - \frac{\partial \mathcal{G}}{\partial S_{w,i,k}} - \frac{\partial \mathcal{I}}{\partial S_{w,i,k}} \ , \qquad (B-1.5.3a)$$

where:

$$\frac{\partial \mathcal{A}}{\partial S_{w,i,k}} = d_{ho,i+\frac{1}{2},k}\alpha_{i+\frac{1}{2},k}\left[\frac{x_1\overline{\rho}_o}{\mu_o}\left(\frac{\partial k_{ro}}{\partial S_w}\right)\right]_{i,k}\Phi_{ro,i+\frac{1}{2},k} \ , \qquad (B-1.5.3b)$$

$$\frac{\partial \mathcal{C}}{\partial S_{w,i,k}} = (1-d_{ho,i-\frac{1}{2},k})\alpha_{i-\frac{1}{2},k}\left[\frac{x_1\overline{\rho}_o}{\mu_o}\left(\frac{\partial k_{ro}}{\partial S_w}\right)\right]_{i,k}\Phi_{ro,i-\frac{1}{2},k} \ , \qquad (B-1.5.3c)$$

$$\frac{\partial \mathcal{E}}{\partial S_{w,i,k}} = d_{zo,i,k+\frac{1}{2}}\alpha_{i,k+\frac{1}{2}}\left[\frac{x_1\overline{\rho}_o}{\mu_o}\left(\frac{\partial k_{ro}}{\partial S_w}\right)\right]_{i,k}\Phi_{zo,i,k+\frac{1}{2}} \ , \qquad (B-1.5.3d)$$

$$\frac{\partial \mathcal{G}}{\partial S_{w,i,k}} = (1-d_{zo,i,k-\frac{1}{2}})\alpha_{i,k-\frac{1}{2}}\left[\frac{x_1\overline{\rho}_o}{\mu_o}\left(\frac{\partial k_{ro}}{\partial S_w}\right)\right]_{i,k}\Phi_{zo,i,k-\frac{1}{2}} \qquad (B-1.5.3e)$$

and, finally,

$$\frac{\partial \mathcal{I}}{\partial S_{w,i,k}} = \frac{V_{,i,k}}{\Delta t}\{[\phi(-x_1\overline{\rho}_o)]_{i,k}\} \ . \qquad (B-1.5.3f)$$

Derivative w.r.t. $S_{w,i+1,k}$

The term $\mathcal{A}$ is the only possible function of $S_{w,i+1,k}$, giving us

$$\frac{\partial F_{1,i,k}}{\partial S_{w,i+1,k}} = \frac{\partial \mathcal{A}}{\partial S_{w,i+1,k}} \ , \qquad (B-1.5.4a)$$

where

$$\frac{\partial \mathcal{A}}{\partial S_{w,i+1,k}} = (1 - d_{ho,i+\frac{1}{2},k})\alpha_{i+\frac{1}{2},k}\left[\frac{x_1\overline{\rho}_o}{\mu_o}\left(\frac{\partial k_{ro}}{\partial S_w}\right)\right]_{i+1,k}\Phi_{ro,i+\frac{1}{2},k} \ . \qquad (B-1.5.4b)$$

Derivative w.r.t. $S_{w,i,k+1}$

Here, only $\mathcal{E}$ can be a function of $S_{w,i,k+1}$, and so we obtain

$$\frac{\partial F_{1,i,k}}{\partial S_{w,i,k+1}} = \frac{\partial \mathcal{E}}{\partial S_{w,i,k+1}} \ , \qquad (B-1.5.5a)$$

where

$$\frac{\partial \mathcal{E}}{\partial S_{w,i,k+1}} = (1 - d_{zo,i,k+\frac{1}{2}})\alpha_{i,k+\frac{1}{2}}\left[\frac{x_1\overline{\rho}_o}{\mu_o}\left(\frac{\partial k_{ro}}{\partial S_w}\right)\right]_{i,k+1}\Phi_{zo,i,k+\frac{1}{2}} \ . \qquad (B-1.5.5b)$$

B.1.6 Derivative w.r.t. Wellbore Pressure

Derivative w.r.t. p_{wb}

Because the well exists only at the inner boundary of our reservoir system, we need only consider equations written for grid blocks along the inner boundary, i.e., $F_{1,1,k}$ $1 \le k \le N_z$. Additionally, the only terms which can be functions of the wellbore pressure, p_{wb}, are $\mathcal{C}$ and $\mathcal{D}$, and then, only for those grid blocks for which the well is open to flow. Also, recall in Chapter II we had

$$p_{wf,k} = f(p_{wb}) \neq f(S_{w,k}, S_{g,k}, p_{o,1,k}) \ , \qquad (B-1.6.1a)$$

which based on Eq. 2.4.65 implies

$$\frac{\partial p_{wf,k}}{\partial p_{wb}} = 1 \qquad (B-1.6.1b)$$

or

$$\frac{\partial X}{\partial p_{wb}} = \frac{\partial X}{\partial p_{wf,k}} \ . \qquad (B-1.6.1c)$$

We can, therefore, write

$$\frac{\partial F_{1,1,k}}{\partial p_{wb}} = -\frac{\partial \mathcal{C}}{\partial p_{wf,k}} - \frac{\partial \mathcal{D}}{\partial p_{wf,k}} - \ , \qquad (B-1.6.1d)$$

where,

$$\frac{\partial \mathcal{C}}{\partial p_{wf,k}} = \left[\alpha_{i-\frac{1}{2},k} x_1 k_{ro} d_{ho,i+\frac{1}{2},k}\left(\frac{1}{\mu_o}\frac{\partial \overline{\rho}_o}{\partial p_{wf}} - \frac{\overline{\rho}_o}{{\mu_o}^2}\frac{\partial \mu_o}{\partial p_{wf}}\right) + \mathcal{T}_{ro}\frac{\partial x_1}{\partial p_{wf}}\right]\Phi_{ro,i-\frac{1}{2},k}$$
$$- \left[x_1 \mathcal{T}_{ro}\right]_{i-\frac{1}{2},k} \qquad (B-1.6.1e)$$

and

$$\frac{\partial \mathcal{D}}{\partial p_{wf,k}} = \left[\alpha_{i-\frac{1}{2},k} y_1 k_{rg} d_{hg,i+\frac{1}{2},k}\left(\frac{1}{\mu_g}\frac{\partial \overline{\rho}_g}{\partial p_{wf}} - \frac{\overline{\rho}_g}{{\mu_g}^2}\frac{\partial \mu_g}{\partial p_{wf}}\right) + \mathcal{T}_{rg}\frac{\partial y_1}{\partial p_{wf}}\right]\Phi_{rg,i-\frac{1}{2},k}$$
$$- \left[y_1 \mathcal{T}_{rg}\right]_{i-\frac{1}{2},k} \ . \qquad (B-1.6.1f)$$

B.2 Jacobian Coefficients of Component #2 Equation

Since the Jacobian coefficients for the component #2 equation are of exactly the same form as those presented above for the component #1 equation, they are not presented here. The Jacobian coefficients for the component #2 equation are simply attained by substituting the mole fraction of component #2 in both the oil and gas phase (i.e., both x_2 and y_2) into the equations presented in Section B.2 above.

B.3 Jacobian Coefficients of Water Equation

Using the definitions in Eq. B-1.1, we can express the water equation as

$$
\begin{aligned}
F_{3,i,k} = & \\
& [\mathcal{T}_{rw}]_{i+\frac{1}{2},k}\Phi_{rw,i+\frac{1}{2},k} - \\
& [\mathcal{T}_{rw}]_{i-\frac{1}{2},k}\Phi_{rw,i-\frac{1}{2},k} + \\
& [\mathcal{T}_{zw}]_{i,k+\frac{1}{2}}\Phi_{zw,i,k+\frac{1}{2}} - \\
& [\mathcal{T}_{zw}]_{i,k-\frac{1}{2}}\Phi_{zw,i,k-\frac{1}{2}} - \\
& \frac{V_{,i,k}}{\Delta t}\{[\phi\overline{\rho}_w S_w]^{n+1}_{i,k} - [\phi\overline{\rho}_w S_w]^{n}_{i,k}\} \\
= & \ 0 \qquad (B-3.1)
\end{aligned}
$$

Furthermore, defining groups of terms as

$$
\begin{aligned}
\mathcal{A} &= [\mathcal{T}_{rw}]_{i+\frac{1}{2},k}\Phi_{rw,i+\frac{1}{2},k} \ , \\
\mathcal{B} &= [\mathcal{T}_{rw}]_{i-\frac{1}{2},k}\Phi_{rw,i-\frac{1}{2},k} \ , \\
\mathcal{C} &= [\mathcal{T}_{zw}]_{i,k+\frac{1}{2}}\Phi_{zw,i,k+\frac{1}{2}} \ , \\
\mathcal{D} &= [\mathcal{T}_{zw}]_{i,k-\frac{1}{2}}\Phi_{zw,i,k-\frac{1}{2}}
\end{aligned}
$$

and

$$
\mathcal{E} = \frac{V_{,i,k}}{\Delta t}\{[\phi\overline{\rho}_w S_w]^{n+1}_{i,k} - [\phi\overline{\rho}_w S_w]^{n}_{i,k}\} \qquad (B-3.2)
$$

our difference equation can be expressed as

$$
F_{3,i,k} = \mathcal{A} - \mathcal{B} + \mathcal{C} - \mathcal{D} - \mathcal{E} \ . \qquad (B-3.3)
$$

Note that under the assumptions made in the model development, our water equation is only a function of the oil phase pressure, water saturation and the wellbore pressure.

B.3.1 Derivative w.r.t. Pressure

Derivative w.r.t. $p_{o,i,k-1}$

Examining our flow equation, it is apparent that only the term $\mathcal{D}$ can be a function of $p_{o,i,k-1}$, and, therefore,

$$\frac{\partial F_{3,i,k}}{\partial p_{o,i,k-1}} = -\frac{\partial \mathcal{D}}{\partial p_{o,i,k-1}} \ , \qquad (B-3.1.1a)$$

where,

$$\frac{\partial \mathcal{D}}{\partial p_o} = d_{zw\,,i,k-\frac{1}{2}} \left[\alpha_{i,k-\frac{1}{2}} k_{rw} \left(\frac{1}{\mu_w} \frac{\partial \overline{\rho}_w}{\partial p_o} - \frac{\overline{\rho}_w}{{\mu_w}^2} \frac{\partial \mu_w}{\partial p_o} \right) \right] \Phi_{zw\,,i,k-\frac{1}{2}}$$
$$+ \left[\mathcal{T}_{zw} \right]_{i,k-\frac{1}{2}} \left[-1 + \left(\frac{d\rho_w}{dp} \right)_{i,k-1} \left(\frac{\Delta z_{k-1} \Delta z_{k-\frac{1}{2}}}{144[\Delta z_{k-1} + \Delta z_k]} \right) \right] \ . \qquad (B-3.1.1b)$$

Derivative w.r.t. $p_{o,i-1,k}$

Here, only the term $\mathcal{B}$ can be a function of $p_{o,i-1,k}$ and so we obtain

$$\frac{\partial F_{3,i,k}}{\partial p_{o,i-1,k}} = -\frac{\partial \mathcal{B}}{\partial p_{o,i-1,k}} \ , \qquad (B-3.1.2a)$$

where,

$$\frac{\partial \mathcal{B}}{\partial p_o} = d_{hw\,,i-\frac{1}{2},k} \left[\alpha_{i-\frac{1}{2},k} k_{rw} \left(\frac{1}{\mu_w} \frac{\partial \overline{\rho}_w}{\partial p_o} - \frac{\overline{\rho}_w}{{\mu_w}^2} \frac{\partial \mu_w}{\partial p_o} \right) \right] \Phi_{rw\,,i-\frac{1}{2},k}$$
$$- \left[\mathcal{T}_{rw} \right]_{i-\frac{1}{2},k} \ . \qquad (B-3.1.2b)$$

Derivative w.r.t. $p_{o\,i,k}$

Examination of Eqs. B-1.1, B-3.1 and B-3.2 indicates that it is possible for every term in Eq. B-3.3 to be a function of $p_{o\,i,k}$, and we therefore obtain

$$\frac{\partial F_{3\,,i,k}}{\partial p_{o\,,i,k}} = \frac{\partial \mathcal{A}}{\partial p_{o\,,i,k}} - \frac{\partial \mathcal{B}}{\partial p_{o\,,i,k}} + \frac{\partial \mathcal{C}}{\partial p_{o\,,i,k}} - \frac{\partial \mathcal{D}}{\partial p_{o\,,i,k}} - \frac{\partial \mathcal{E}}{\partial p_{o\,,i,k}} \ , \qquad (B-3.1.3a)$$

where:

$$\frac{\partial \mathcal{A}}{\partial p_o} = d_{hw\,,i+\frac{1}{2},k}\left[\alpha_{i+\frac{1}{2},k} k_{rw}\left(\frac{1}{\mu_w}\frac{\partial \overline{\rho}_w}{\partial p_o} - \frac{\overline{\rho}_w}{{\mu_w}^2}\frac{\partial \mu_w}{\partial p_o}\right)\right]\Phi_{rw\,,i+\frac{1}{2},k} - [\mathcal{T}_{rw}]_{i+\frac{1}{2},k} \ , \qquad (B-3.1.3b)$$

$$\frac{\partial \mathcal{B}}{\partial p_o} = (1-d_{hw\,,i-\frac{1}{2},k})\left[\alpha_{i-\frac{1}{2},k} k_{rw}\left(\frac{1}{\mu_w}\frac{\partial \overline{\rho}_w}{\partial p_o} - \frac{\overline{\rho}_w}{{\mu_w}^2}\frac{\partial \mu_w}{\partial p_o}\right)\right]\Phi_{rw\,,i-\frac{1}{2},k} + [\mathcal{T}_{rw}]_{i-\frac{1}{2},k} \ , \qquad (B-3.1.3c)$$

$$\frac{\partial \mathcal{C}}{\partial p_o} = d_{zw\,,i,k+\frac{1}{2}}\left[\alpha_{i,k+\frac{1}{2}} k_{rw}\left(\frac{1}{\mu_w}\frac{\partial \overline{\rho}_w}{\partial p_o} - \frac{\overline{\rho}_w}{{\mu_w}^2}\frac{\partial \mu_w}{\partial p_o}\right)\right]\Phi_{zw\,,i,k+\frac{1}{2}} [\mathcal{T}_{zw}]_{i,k+\frac{1}{2}}\left[-1+\left(\frac{d\rho_w}{dp}\right)_{i,k+1}\left(\frac{\Delta z_{k+1}\Delta z_{k+\frac{1}{2}}}{144[\Delta z_{k+1}+\Delta z_k]}\right)\right] \ , \qquad (B-3.1.3d)$$

$$\frac{\partial \mathcal{D}}{\partial p_o} = (1-d_{zw\,,i,k-\frac{1}{2}})\left[\alpha_{i,k-\frac{1}{2}} k_{rw}\left(\frac{1}{\mu_w}\frac{\partial \overline{\rho}_w}{\partial p_o} - \frac{\overline{\rho}_w}{{\mu_w}^2}\frac{\partial \mu_w}{\partial p_o}\right)\right]\Phi_{zw\,,i,k-\frac{1}{2}} + [\mathcal{T}_{zw}]_{i,k-\frac{1}{2}}\left[1+\left(\frac{d\rho_w}{dp}\right)_{i,k-1}\left(\frac{\Delta z_{k-1}\Delta z_{k-\frac{1}{2}}}{144[\Delta z_{k-1}+\Delta z_k]}\right)\right] \qquad (B-3.1.3e)$$

and

$$\frac{\partial \mathcal{E}}{\partial p_{o\,,i,k}} = \frac{V_{i,k}}{\Delta t}\left\{(\overline{\rho}_w S_w\left(\frac{\partial \phi}{\partial p_o}\right) + \phi_{i,k}\left[S_w\left(\frac{d\overline{\rho}_w}{dp}\right)\right]_{i,k}\right\} \ . \qquad (B-1.1.3f)$$

Derivative w.r.t. $p_{o\,,i+1,k}$

Only the term $\mathcal{A}$ is a function of $p_{o\,,i+1,k}$, and, therefore,

$$\frac{\partial F_{3\,,i,k}}{\partial p_{o\,,i+1,k}} = \frac{\partial \mathcal{A}}{\partial p_{o\,,i+1,k}} \ , \qquad (B-3.1.4a)$$

where,

$$\frac{\partial \mathcal{A}}{\partial p_o} = (1 - d_{hw\,,i+\frac{1}{2},k}) \left[\alpha_{i+\frac{1}{2},k} k_{rw} \left(\frac{1}{\mu_w} \frac{\partial \overline{\rho}_w}{\partial p_o} - \frac{\overline{\rho}_w}{{\mu_w}^2} \frac{\partial \mu_w}{\partial p_o} \right) \right] \Phi_{rw\,,i+\frac{1}{2},k}$$
$$+ \left[\mathcal{T}_{rw} \right]_{i+\frac{1}{2},k} \ . \qquad (B-3.1.4b)$$

Derivative w.r.t. $p_{o\,,i,k+1}$

Here, only the term $\mathcal{C}$ is a function of $p_{o\,,i,k+1}$, and, therefore,

$$\frac{\partial F_{3\,,i,k}}{\partial p_{o\,,i,k+1}} = \frac{\partial \mathcal{C}}{\partial p_{o\,,i,k+1}} \ , \qquad (B-3.1.5a)$$

where,

$$\frac{\partial \mathcal{C}}{\partial p_o} = (1 - d_{zw\,,i,k+\frac{1}{2}} (\left[\alpha_{i,k+\frac{1}{2}} k_{rw} \left(\frac{1}{\mu_w} \frac{\partial \overline{\rho}_w}{\partial p_o} - \frac{\overline{\rho}_w}{{\mu_w}^2} \frac{\partial \mu_w}{\partial p_o} \right) \right] \Phi_{zw\,,i,k+\frac{1}{2}}$$
$$+ \left[\mathcal{T}_{zw} \right]_{i,k+\frac{1}{2}} \left[1 + \left(\frac{d\rho_w}{dp} \right)_{i,k+1} \left(\frac{\Delta z_{k+1} \Delta z_{k+\frac{1}{2}}}{144[\Delta z_{k+1} + \Delta z_k]} \right) \right] \ . \qquad (B-3.1.5b)$$

B.3.2 Derivative w.r.t. Water Saturation

Derivative w.r.t. $S_{w,i,k-1}$

Because only $\mathcal{D}$ is a function of $S_{w,i,k-1}$, we obtain

$$\frac{\partial F_{3,i,k}}{\partial S_{w,i,k-1}} = -\frac{\partial \mathcal{D}}{\partial S_{w,i,k+1}} \ , \qquad (B-3.2.1a)$$

where,

$$\frac{\partial \mathcal{D}}{\partial S_{w,i,k-1}} = d_{zw,i,k-\frac{1}{2}} \alpha_{i,k-\frac{1}{2}} \left[\frac{\overline{\rho}_w}{\mu_w} \left(\frac{\partial k_{rw}}{\partial S_w} \right) \right]_{i,k-1} \Phi_{zw,i,k-\frac{1}{2}} + [\mathcal{T}_{zw}]_{i,k-\frac{1}{2}} \left(\frac{\partial p_{cow}}{\partial S_w} \right)_{i,k-1} . \qquad (B-3.2.1b)$$

Derivative w.r.t. $S_{w,i-1,k}$

Only the term $\mathcal{B}$ is a function of $S_{w,i-1,k}$ and so we obtain

$$\frac{\partial F_{3,i,k}}{\partial S_{w,i-1,k}} = -\frac{\partial \mathcal{B}}{\partial S_{w,i-1,k}} \ , \qquad (B-3.2.2a)$$

where

$$\frac{\partial \mathcal{B}}{\partial S_{w,i-1,k}} = d_{hw,i-\frac{1}{2},k} \alpha_{i-\frac{1}{2},k} \left[\frac{\overline{\rho}_w}{\mu_w} \left(\frac{\partial k_{rw}}{\partial S_w} \right) \right]_{i-1,k} \Phi_{rw,i-\frac{1}{2},k} + [\mathcal{T}_{rw}]_{i-\frac{1}{2},k} \left(\frac{\partial p_{cow}}{\partial S_w} \right)_{i-1,k} . \qquad (B-3.2.2b)$$

Derivative w.r.t. $S_{wi,k}$

Examining our flow equation, we find that all of the terms are functions of $S_{wi,k}$, and, therefore, we obtain

$$\frac{\partial F_{3\,,i,k}}{\partial S_{w\,,i,k}} = \frac{\mathcal{A}}{\partial S_{w\,,i,k}} - \frac{\mathcal{B}}{\partial S_{w\,,i,k}} + \frac{\mathcal{C}}{\partial S_{w\,,i,k}} - \frac{\mathcal{D}}{\partial S_{w\,,i,k}} - \frac{\partial \mathcal{E}}{\partial S_{w\,,i,k}} \ , \qquad (B-3.2.3a)$$

where:

$$\frac{\partial \mathcal{A}}{\partial S_{w\,,i,k}} = d_{hw\,,i+\frac{1}{2},k}\alpha_{i+\frac{1}{2},k}\left[\frac{\overline{\rho}_w}{\mu_w}\left(\frac{\partial k_{rw}}{\partial S_w}\right)\right]_{i,k}\Phi_{rw\,,i+\frac{1}{2},k} - [\mathcal{T}_{rw}]_{i+\frac{1}{2},k}\left(\frac{\partial p_{cow}}{\partial S_w}\right)_{i,k} \ , \qquad (B-3.2.3b)$$

$$\frac{\partial \mathcal{B}}{\partial S_{w\,,i,k}} = (1-d_{hw\,,i-\frac{1}{2},k})\alpha_{i-\frac{1}{2},k}\left[\frac{\overline{\rho}_w}{\mu_w}\left(\frac{\partial k_{rw}}{\partial S_w}\right)\right]_{i,k}\Phi_{rw\,,i-\frac{1}{2},k} + [\mathcal{T}_{rw}]_{i-\frac{1}{2},k}\left(\frac{\partial p_{cow}}{\partial S_w}\right)_{i,k} \ , \qquad (B-3.2.3c)$$

$$\frac{\partial \mathcal{C}}{\partial S_{w\,,i,k}} = d_{zw\,,i,k+\frac{1}{2}}\alpha_{i,k+\frac{1}{2}}\left[\frac{\overline{\rho}_w}{\mu_w}\left(\frac{\partial k_{rw}}{\partial S_w}\right)\right]_{i,k}\Phi_{zw\,,i,k+\frac{1}{2}} - [\mathcal{T}_{zw}]_{i,k+\frac{1}{2}}\left(\frac{\partial p_{cow}}{\partial S_w}\right)_{i,k} \ , \qquad (B-3.2.3d)$$

$$\frac{\partial \mathcal{D}}{\partial S_{w\,,i,k}} = (1-d_{zw\,,i,k-\frac{1}{2}})\alpha_{i,k-\frac{1}{2}}\left[\frac{\overline{\rho}_w}{\mu_w}\left(\frac{\partial k_{rw}}{\partial S_w}\right)\right]_{i,k}\Phi_{zw\,,i,k-\frac{1}{2}} + [\mathcal{T}_{zw}]_{i,k-\frac{1}{2}}\left(\frac{\partial p_{cow}}{\partial S_w}\right)_{i,k} \qquad (B-3.2.3e)$$

and, finally,

$$\frac{\partial \mathcal{E}}{\partial S_{w\,,i,k}} = \frac{V_{,i,k}}{\Delta t}[\phi(\overline{\rho}_w)]_{i,k} \ . \qquad (B-3.2.3f)$$

Derivative w.r.t. $S_{w\,,i+1,k}$

The term $\mathcal{A}$ is the only possible function of $S_{w\,,i+1,k}$ and so we obtain

$$\frac{\partial F_{3\,,i,k}}{\partial S_{w\,,i+1,k}} = \frac{\partial \mathcal{A}}{\partial S_{w\,,i+1,k}} \ , \qquad (B-3.2.4a)$$

where

$$\frac{\partial \mathcal{A}}{\partial S_{w,i+1,k}} = (1 - d_{hw,i+\frac{1}{2},k})\alpha_{i+\frac{1}{2},k}\left[\frac{\overline{\rho}_w}{\mu_w}\left(\frac{\partial k_{rw}}{\partial S_w}\right)\right]_{i+1,k}\Phi_{rw,i+\frac{1}{2},k} - [\mathcal{T}_{rg}]_{i+\frac{1}{2},k}\left(\frac{\partial p_{cow}}{\partial S_w}\right)_{i+1,k}. \qquad (B-3.2.4b)$$

Derivative w.r.t. $S_{w,i,k+1}$

Here, only $\mathcal{C}$ is a function of $S_{w,i,k+1}$, and we obtain

$$\frac{\partial F_{3,i,k}}{\partial S_{w,i,k+1}} = \frac{\partial \mathcal{C}}{\partial S_{w,i,k+1}}, \qquad (B-3.2.5a)$$

where

$$\frac{\partial \mathcal{C}}{\partial S_{w,i,k+1}} = (1 - d_{zw,i,k+\frac{1}{2}})\alpha_{i,k+\frac{1}{2}}\left[\frac{\overline{\rho}_w}{\mu_w}\left(\frac{\partial k_{rw}}{\partial S_w}\right)\right]_{i,k+1}\Phi_{zw,i,k+\frac{1}{2}} - [\mathcal{T}_{zw}]_{i,k+\frac{1}{2}}\left(\frac{\partial p_{cow}}{\partial S_w}\right)_{i,k+1}. \qquad (B-3.2.5b)$$

B.3.3 Derivative w.r.t. Wellbore Pressure

Derivative w.r.t. p_{wb}

Because of the inner boundary condition considered in this study, we need only consider equations written for grid blocks along the inner boundary, i.e., $F_{3,1,k}$ $1 \leq k \leq N_z$. Here we find that the only term which is a function of the wellbore pressure, p_{wb}, is $\mathcal{B}$, and then, only for those grid blocks for which the well is open to flow. Recalling Eqs. B-1.6.1a to B-1.6.1c, we can, therefore, write

$$\frac{\partial F_{3,1,k}}{\partial p_{wb}} = -\frac{\partial \mathcal{B}}{\partial p_{wf,k}}, \qquad (B-3.3.1a)$$

where,

$$\frac{\partial \mathcal{B}}{\partial p_{wf\,,k}} = d_{hw\,,i-\frac{1}{2},k}\left[\alpha_{i-\frac{1}{2},k}\, k_{rw}\left(\frac{1}{\mu_w}\frac{\partial \overline{\rho}_w}{\partial p_{wf}} - \frac{\overline{\rho}_w}{{\mu_w}^2}\frac{\partial \mu_w}{\partial p_{wf}}\right)\right]\Phi_{rw\,,i-\frac{1}{2},k} - [\mathcal{T}_{rw}]_{i-\frac{1}{2},k}\ . \qquad (B-3.3.1b)$$

B.4 Jacobian Coefficients of Wellbore Constraint Equation

Recall from Chapter II that in addition to a constant wellbore pressure inner boundary condition, options for seven different constant rate production modes (constant surface oil rate, constant surface gas rate, constant surface water rate, constant surface total rate, constant reservoir total rate, as well as a constant total molar rate and constant total mass rate) are incorporated into our model. Because all of these rates are either simplifications of the total surface rate equation (Eq. 2.4.61), or simple multiples (e.g., by molecular weights) of the total surface rate equation, only it is considered here. From Eq. 2.4.61 we have

$$\begin{aligned} F_4 = {} & \frac{1}{\overline{\rho}_{osc}}\left\{\sum_{k=N_{zw_1}}^{N_{zw_2}} [x_{2\,,1/2,k}\mathcal{T}_{ro\,,1/2,k}(p_{o\,,1,k} - p_{wf\,,k}) + \right. \\ & \left. [y_{2\,,1/2,k}\mathcal{T}_{rg\,,1/2,k}(p_{o\,,1,k} + p_{cog\,,1,k} - p_{wf\,,k})]^{n+1}\right\} + \\ & \frac{1}{\overline{\rho}_{gsc}}\left\{\sum_{k=N_{zw_1}}^{N_{zw_2}} [x_{1\,,1/2,k}\mathcal{T}_{ro\,,1/2,k}(p_{o\,,1,k} - p_{wf\,,k}) + \right. \\ & \left. y_{1\,,1/2,k}\mathcal{T}_{rg\,,1/2,k}(p_{o\,,1,k} + p_{cog\,,1,k} - p_{wf\,,k})]^{n+1}\right\} + \\ & \frac{1}{\overline{\rho}_{wsc}}\left\{\sum_{k=N_{zw_1}}^{N_{zw_2}} [\mathcal{T}_{rw\,,1/2,k}(p_{o\,,1,k} - p_{cow\,,1,k} - p_{wf\,,k})]^{n+1}\right\} - q_{tsc} \\ = {} & 0\ . \end{aligned} \qquad (B-4.1)$$

Defining the following terms,

$$\mathcal{A}_k = \frac{1}{\overline{\rho}_{osc}}[x_2\,\mathcal{T}_{ro}]_{1/2,k}(p_{o\,,1,k} - p_{wf\,,k})\ ,$$

$$\mathcal{B}_k = \frac{1}{\overline{\rho}_{osc}}[y_2\mathcal{T}_{rg}]_{1/2,k}(p_{o,1,k} + p_{cog,1,k} - p_{wf,k}) \ ,$$

$$\mathcal{C}_k = \frac{1}{\overline{\rho}_{gsc}}[x_1\mathcal{T}_{ro}]_{1/2,k}(p_{o,1,k} - p_{wf,k}) \ ,$$

$$\mathcal{D}_k = \frac{1}{\overline{\rho}_{gsc}}[y_1\mathcal{T}_{rg}]_{1/2,k}(p_{o,1,k} + p_{cog,1,k} - p_{wf,k})$$

and

$$\mathcal{E}_k = \frac{1}{\overline{\rho}_{wsc}}[\mathcal{T}_{rw}]_{1/2,k}(p_{o,1,k} - p_{cow,1,k} - p_{wf,k}) \ , \qquad (B-4.2)$$

we can express our wellbore constraint equation as

$$F_4 = \sum_{k=N_{zw_1}}^{N_{zw_2}} \Big\{(\mathcal{A}_k + \mathcal{B}_k) + (\mathcal{C}_k + \mathcal{D}_k) + (\mathcal{E}_k)\Big\} - q_{tsc} \ . \qquad (B-4.3)$$

Note, that when we take the derivative of F_4, the summation disappears and we are left with the derivatives at the k^{th} level only.

B.4.1 Derivative w.r.t. Pressure

Derivative w.r.t. $p_{o,1,k}$

All of the terms defined in Eq. B-4.2 are functions of $p_{o,1,k}$ and we obtain

$$\frac{\partial F_4}{\partial p_{o,1,k}} = \frac{\partial \mathcal{A}_k}{\partial p_{o,1,k}} + \frac{\partial \mathcal{B}_k}{\partial p_{o,1,k}} + \frac{\partial \mathcal{C}_k}{\partial p_{o,1,k}} + \frac{\partial \mathcal{D}_k}{\partial p_{o,1,k}} + \frac{\partial \mathcal{E}_k}{\partial p_{o,1,k}} \ , \qquad (B-4.1.1a)$$

where

$$\frac{\partial \mathcal{A}_k}{\partial p_o} = \frac{1}{\overline{\rho}_{osc}}\left[\alpha_{i-\frac{1}{2},k}x_2 k_{ro}\left(\frac{1}{\mu_o}\frac{\partial \overline{\rho}_o}{\partial p_o} - \frac{\overline{\rho}_o}{{\mu_o}^2}\frac{\partial \mu_o}{\partial p_o}\right) + \mathcal{T}_{ro}\frac{\partial x_2}{\partial p_o}\right](p_{o,1,k} - p_{wf,k})$$
$$\times (1 - d_{ho,i-\frac{1}{2},k}) + \frac{1}{\overline{\rho}_{osc}}[x_2\mathcal{T}_{ro}]_{1/2,k} \ , \qquad (B-4.1.1b)$$

$$\frac{\partial \mathcal{B}_k}{\partial p_o} = \frac{1}{\overline{\rho}_{osc}}\left[\alpha_{i-\frac{1}{2},k}y_2 k_{rg}\left(\frac{1}{\mu_g}\frac{\partial \overline{\rho}_g}{\partial p_o} - \frac{\overline{\rho}_g}{{\mu_g}^2}\frac{\partial \mu_g}{\partial p_o}\right) + \mathcal{T}_{rg}\frac{\partial y_2}{\partial p_o}\right](p_{o,1,k} + p_{cog,1,k} - p_{wf,k})$$
$$\times (1 - d_{hg,i-\frac{1}{2},k}) + \frac{1}{\overline{\rho}_{osc}}[y_2\mathcal{T}_{rg}]_{1/2,k} \ , \qquad (B-4.1.1c)$$

$$\frac{\partial \mathcal{C}_k}{\partial p_o} = \frac{1}{\overline{\rho}_{gsc}}\left[\alpha_{i-\frac{1}{2},k} x_1 k_{ro}\left(\frac{1}{\mu_o}\frac{\partial \overline{\rho}_o}{\partial p_o} - \frac{\overline{\rho}_o}{{\mu_o}^2}\frac{\partial \mu_o}{\partial p_o}\right) + \mathcal{T}_{ro}\frac{\partial x_1}{\partial p_o}\right](p_{o,1,k} - p_{wf,k})$$
$$\times (1 - d_{ho,i-\frac{1}{2},k}) + \frac{1}{\overline{\rho}_{gsc}}[x_1 \mathcal{T}_{ro}]_{1/2,k} \ , \qquad (B-4.1.1d)$$

$$\frac{\partial \mathcal{D}_k}{\partial p_o} = \frac{1}{\overline{\rho}_{gsc}}\left[\alpha_{i-\frac{1}{2},k} y_1 k_{rg}\left(\frac{1}{\mu_g}\frac{\partial \overline{\rho}_g}{\partial p_o} - \frac{\overline{\rho}_g}{{\mu_g}^2}\frac{\partial \mu_g}{\partial p_o}\right) + \mathcal{T}_{rg}\frac{\partial y_1}{\partial p_o}\right](p_{o,1,k} + p_{cog,1,k} - p_{wf,k})$$
$$\times (1 - d_{hg,i-\frac{1}{2},k}) + \frac{1}{\overline{\rho}_{gsc}}[y_1 \mathcal{T}_{rg}]_{1/2,k} \ , \qquad (B-4.1.1e)$$

and

$$\frac{\partial \mathcal{E}_k}{\partial p_o} = \frac{1}{\overline{\rho}_{wsc}}\left[\alpha_{i-\frac{1}{2},k} k_{rw}\left(\frac{1}{\mu_w}\frac{\partial \overline{\rho}_w}{\partial p_o} - \frac{\overline{\rho}_w}{{\mu_w}^2}\frac{\partial \mu_w}{\partial p_o}\right)\right](p_{o,1,k} - p_{cow,1,k} - p_{wf,k})$$
$$\times (1 - d_{hw,i-\frac{1}{2},k}) + \frac{1}{\overline{\rho}_{wsc}}[\mathcal{T}_{rw}]_{1/2,k} \ . \qquad (B-4.1.1f)$$

B.4.2 Derivative w.r.t. Gas Saturation

Derivative w.r.t. $S_{g,1,k}$

Here, only the first four terms of our wellbore constraint equation are functions of $S_{g,1,k}$ and we have

$$\frac{\partial F_4}{\partial S_{g,1,k}} = \frac{\partial \mathcal{A}_k}{\partial S_{g,1,k}} + \frac{\partial \mathcal{B}_k}{\partial p_{o,1,k}} + \frac{\partial \mathcal{C}_k}{\partial S_{g,1,k}} + \frac{\partial \mathcal{D}_k}{\partial S_{g,1,k}} \ , \qquad (B-4.2.1a)$$

where

$$\frac{\partial \mathcal{A}_k}{\partial S_g} = \frac{1}{\overline{\rho}_{osc}}\left[\alpha_{i-\frac{1}{2},k}\frac{x_2 \overline{\rho}_o}{\mu_o}\frac{\partial k_{ro}}{\partial S_g}(p_{o,1,k} - p_{wf,k})\right](1 - d_{ho,i-\frac{1}{2},k}) \ , \qquad (B-4.2.1b)$$

$$\frac{\partial \mathcal{B}_k}{\partial S_g} = \frac{1}{\overline{\rho}_{osc}}\left[\alpha_{i-\frac{1}{2},k}\frac{y_2 \overline{\rho}_g}{\mu_g}\frac{\partial k_{rg}}{\partial S_g}(p_{o,1,k} + p_{cog,1,k} - p_{wf,k})\right](1 - d_{hg,i-\frac{1}{2},k})$$
$$+ \frac{1}{\overline{\rho}_{osc}}\left[y_2 \mathcal{T}_{rg}\right]_{1,k}\left(\frac{\partial p_{cog}}{\partial S_g}\right) \ , \qquad (B-4.2.1c)$$

$$\frac{\partial \mathcal{C}_k}{\partial S_g} = \frac{1}{\overline{\rho}_{gsc}}\left[\alpha_{i-\frac{1}{2},k}\frac{x_1\overline{\rho}_o}{\mu_o}\frac{\partial k_{ro}}{\partial S_g}(p_{o,1,k} - p_{wf,k})\right](1 - d_{ho,i-\frac{1}{2},k}) \ , \qquad (B-4.2.1d)$$

and

$$\begin{aligned}\frac{\partial \mathcal{D}_k}{\partial S_g} =& \frac{1}{\overline{\rho}_{gsc}}\left[\alpha_{i-\frac{1}{2},k}\frac{y_2\overline{\rho}_g}{\mu_g}\frac{\partial k_{rg}}{\partial S_g}(p_{o,1,k} + p_{cog,1,k} - p_{wf,k})\right](1 - d_{hg,i-\frac{1}{2},k}) \\ &+ \frac{1}{\overline{\rho}_{gsc}}\left[[y_2\mathcal{T}_{rg}]_{1,k}\left(\frac{\partial p_{cog}}{\partial S_g}\right)\right] \ . \qquad (B-4.2.1e)\end{aligned}$$

B.4.3 Derivative w.r.t. Bubble-Point Pressure

Derivative w.r.t. $p_{b,1,k}$

Since only the oil phase PVT properties can be functions of the bubble-point pressure, we need only consider $\mathcal{A}_k$ and $\mathcal{C}_k$ and, therefore, obtain

$$\frac{\partial F_4}{\partial p_{b,1,k}} = \frac{\partial \mathcal{A}_k}{\partial p_{b,1,k}} + \frac{\partial \mathcal{C}_k}{\partial p_{b,1,k}} \ , \qquad (B-4.3.1a)$$

where

$$\begin{aligned}\frac{\partial \mathcal{A}_k}{\partial p_b} =& \frac{1}{\overline{\rho}_{osc}}\left[\alpha_{i-\frac{1}{2},k}x_2 k_{ro}\left(\frac{1}{\mu_o}\frac{\partial \overline{\rho}_o}{\partial p_b} - \frac{\overline{\rho}_o}{{\mu_o}^2}\frac{\partial \mu_o}{\partial p_b}\right) + \mathcal{T}_{ro}\frac{\partial x_2}{\partial p_b}\right] \\ & (p_{o,1,k} - p_{wf,k})(1 - d_{ho,i-\frac{1}{2},k}) \qquad (B-4.3.1b)\end{aligned}$$

and

$$\begin{aligned}\frac{\partial \mathcal{C}_k}{\partial p_b} =& \frac{1}{\overline{\rho}_{gsc}}\left[\alpha_{i-\frac{1}{2},k}x_1 k_{ro}\left(\frac{1}{\mu_o}\frac{\partial \overline{\rho}_o}{\partial p_b} - \frac{\overline{\rho}_o}{{\mu_o}^2}\frac{\partial \mu_o}{\partial p_b}\right) + \mathcal{T}_{ro}\frac{\partial x_1}{\partial p_b}\right] \\ & (p_{o,1,k} - p_{wf,k})(1 - d_{ho,i-\frac{1}{2},k}) \ . \qquad (B-4.3.1c)\end{aligned}$$

B.4.4 Derivative w.r.t. Dew-Point Pressure

Derivative w.r.t. $p_{d,1,k}$

Similarly, Since only the gas phase PVT properties can be functions of the dew-point pressure, we need only consider $\mathcal{B}_k$ and $\mathcal{D}_k$ and, therefore, obtain

$$\frac{\partial F_4}{\partial p_{d,1,k}} = \frac{\partial \mathcal{B}_k}{\partial p_{d,1,k}} + \frac{\partial \mathcal{D}_k}{\partial p_{d,1,k}} \ , \qquad (B-4.4.1a)$$

where

$$\frac{\partial \mathcal{B}_k}{\partial p_d} = \frac{1}{\overline{\rho}_{osc}} \left[\alpha_{i-\frac{1}{2},k} y_2 k_{rg} \left(\frac{1}{\mu_g} \frac{\partial \overline{\rho}_g}{\partial p_d} - \frac{\overline{\rho}_g}{{\mu_g}^2} \frac{\partial \mu_g}{\partial p_d} \right) + \mathcal{T}_{rg} \frac{\partial y_2}{\partial p_d} \right] (p_{o,1,k} + p_{cog,1,k} p_{wf,k})(1 - d_{hg,i-\frac{1}{2},k}) \qquad (B-4.4.1b)$$

and

$$\frac{\partial \mathcal{D}_k}{\partial p_d} = \frac{1}{\overline{\rho}_{gsc}} \left[\alpha_{i-\frac{1}{2},k} y_1 k_{rg} \left(\frac{1}{\mu_g} \frac{\partial \overline{\rho}_g}{\partial p_d} - \frac{\overline{\rho}_g}{{\mu_g}^2} \frac{\partial \mu_g}{\partial p_d} \right) + \mathcal{T}_{rg} \frac{\partial y_1}{\partial p_d} \right] (p_{o,1,k} + p_{cog,1,k} - p_{wf,k})(1 - d_{hg,i-\frac{1}{2},k}) \ . \qquad (B-4.4.1c)$$

B.4.5 Derivative w.r.t. Water Saturation

Derivative w.r.t. $S_{w,1,k}$

Here, only $\mathcal{A}_k$, $\mathcal{C}_k$ and $\mathcal{E}_k$ are functions of $S_{w,1,k}$ and we have

$$\frac{\partial F_4}{\partial S_{w,1,k}} = \frac{\partial \mathcal{A}_k}{\partial S_{w,1,k}} + \frac{\partial \mathcal{C}_k}{\partial S_{w,1,k}} + \frac{\partial \mathcal{E}_k}{\partial S_{w,1,k}} \ , \qquad (B-4.5.1a)$$

where

$$\frac{\partial \mathcal{A}_k}{\partial S_w} = \frac{1}{\overline{\rho}_{osc}} \left[\alpha_{i-\frac{1}{2},k} \frac{x_2 \overline{\rho}_o}{\mu_o} \frac{\partial k_{ro}}{\partial S_w} (p_{o,1,k} - p_{wf,k}) \right] (1 - d_{ho,i-\frac{1}{2},k}) \ , \qquad (B-4.5.1b)$$

$$\frac{\partial \mathcal{C}_k}{\partial S_w} = \frac{1}{\overline{\rho}_{gsc}}\left[\alpha_{i-\frac{1}{2},k}\frac{x_1\overline{\rho}_o}{\mu_o}\frac{\partial k_{ro}}{\partial S_w}(p_{o,1,k} - p_{wf,k})\right](1 - d_{ho,i-\frac{1}{2},k}) \qquad (B-4.5.1c)$$

and

$$\frac{\partial \mathcal{E}_k}{\partial S_w} = \frac{1}{\overline{\rho}_{wsc}}\left[\alpha_{i-\frac{1}{2},k}\frac{\overline{\rho}_w}{\mu_w}\left(\frac{\partial k_{rw}}{\partial S_w}\right)(p_{o,1,k} - p_{cow,1,k} - p_{wf,k})\right.$$
$$\left.\times(1 - d_{hw,i-\frac{1}{2},k}) + [\mathcal{T}_{rw}]_{1/2,k}\left(\frac{\partial p_{cow}}{\partial S_w}\right)\right] . \qquad (B-4.5.1d)$$

B.4.6 Derivative w.r.t. Wellbore Pressure

Derivative w.r.t. p_{wb}

Lastly, we see that all five of the terms in our wellbore constraint equation are functions of the wellbore pressure and we, therefore, have

$$\frac{\partial F_4}{\partial p_{wb}} = \frac{\partial \mathcal{A}_k}{\partial p_{wf,k}} + \frac{\partial \mathcal{B}_{,k}}{\partial p_{wf,k}} + \frac{\partial \mathcal{C}_k}{\partial p_{wf,k}} + \frac{\partial \mathcal{D}_k}{\partial p_{wf,k}} + \frac{\partial \mathcal{E}_k}{\partial p_{wf,k}} , \qquad (B-4.6.1a)$$

where

$$\frac{\partial \mathcal{A}_k}{\partial p_{wf,k}} = \frac{1}{\overline{\rho}_{osc}}\left[\alpha_{i-\frac{1}{2},k}x_2 k_{ro}\left(\frac{1}{\mu_o}\frac{\partial \overline{\rho}_o}{\partial p_{wf,k}} - \frac{\overline{\rho}_o}{{\mu_o}^2}\frac{\partial \mu_o}{\partial p_{wf,k}}\right) + \mathcal{T}_{ro}\frac{\partial x_2}{\partial p_{wf,k}}\right]$$
$$\times(p_{o,1,k} - p_{wf,k})(1 - d_{ho,i-\frac{1}{2},k}) - \frac{1}{\overline{\rho}_{osc}}[x_2\mathcal{T}_{ro}]_{1/2,k} , \qquad (B-4.6.1b)$$

$$\frac{\partial \mathcal{B}_k}{\partial p_{wf,k}} = \frac{1}{\overline{\rho}_{osc}}\left[\alpha_{i-\frac{1}{2},k}y_2 k_{rg}\left(\frac{1}{\mu_g}\frac{\partial \overline{\rho}_g}{\partial p_{wf,k}} - \frac{\overline{\rho}_g}{{\mu_g}^2}\frac{\partial \mu_g}{\partial p_{wf,k}}\right) + \mathcal{T}_{rg}\frac{\partial y_2}{\partial p_{wf,k}}\right]$$
$$\times(p_{o,1,k} + p_{cog,1,k} - p_{wf,k})(1 - d_{hg,i-\frac{1}{2},k}) - \frac{1}{\overline{\rho}_{osc}}[y_2\mathcal{T}_{rg}]_{1/2,k} , \qquad (B-4.6.1c)$$

$$\frac{\partial \mathcal{C}_k}{\partial p_{wf,k}} = \frac{1}{\overline{\rho}_{gsc}}\left[\alpha_{i-\frac{1}{2},k}x_1 k_{ro}\left(\frac{1}{\mu_o}\frac{\partial \overline{\rho}_o}{\partial p_{wf,k}} - \frac{\overline{\rho}_o}{{\mu_o}^2}\frac{\partial \mu_o}{\partial p_{wf,k}}\right) + \mathcal{T}_{ro}\frac{\partial x_1}{\partial p_{wf,k}}\right]$$
$$\times(p_{o,1,k} - p_{wf,k})(1 - d_{ho,i-\frac{1}{2},k}) - \frac{1}{\overline{\rho}_{gsc}}[x_1\mathcal{T}_{ro}]_{1/2,k} , \qquad (B-4.6.1d)$$

$$\frac{\partial \mathcal{D}_k}{\partial p_{wf,k}} = \frac{1}{\overline{\rho}_{gsc}}\left[\alpha_{i-\frac{1}{2},k} y_1 k_{rg}\left(\frac{1}{\mu_g}\frac{\partial \overline{\rho}_g}{\partial p_{wf,k}} - \frac{\overline{\rho}_g}{{\mu_g}^2}\frac{\partial \mu_g}{\partial p_{wf,k}}\right) + \mathcal{T}_{rg}\frac{\partial y_1}{\partial p_{wf,k}}\right]$$
$$\times (p_{o,1,k} + p_{cog,1,k} - p_{wf,k})(1 - d_{hg,i-\frac{1}{2},k}) - \frac{1}{\overline{\rho}_{gsc}}[y_1 \mathcal{T}_{rg}]_{i-\frac{1}{2},k} \quad (B.4.6.1e)$$

and

$$\frac{\partial \mathcal{E}_k}{\partial p_{wf,k}} = \frac{1}{\overline{\rho}_{wsc}}\left[\alpha_{i-\frac{1}{2},k} k_{rw}\left(\frac{1}{\mu_w}\frac{\partial \overline{\rho}_w}{\partial p_{wf,k}} - \frac{\overline{\rho}_w}{{\mu_w}^2}\frac{\partial \mu_w}{\partial p_{wf,k}}\right)\right]$$
$$\times (p_{o,1,k} - p_{cow,1,k} - p_{wf,k})(1 - d_{hw,i-\frac{1}{2},k}) - \frac{1}{\overline{\rho}_{wsc}}[\mathcal{T}_{rw}]_{i-\frac{1}{2},k} \quad (B.4.6.1f)$$

APPENDIX C

ALGORITHMS FOR ITERATIVE SOLVERS

C.1 Algorithm GMRES(k)

BEGIN:

$x = 0$

$\varepsilon = \varepsilon_0 \|b\|_2$

FOR $j = 1, 2, \ldots$ **Until Convergence, DO:**

$r = Q^{-1}(b - Ax)$

$\rho = \|r\|_2$

$v^1 = r/\rho$

$s^1 = \rho e_1$; $e_1 = \{1, 0, 0, \ldots, 0\}^T$

For $i = 1, 2, \ldots, k$ **Do:**

$w = Q^{-1} A v^i$

for $l = 1, \ldots, i$ **do:**

$h_{l,i} = (w, v^l)$

$w = w - h_{l,i} v^l$

enddo l

$h_{i+1,i} = \|w\|_2$

$v^{i+1} = w/h_{i+1,i}$

If $i > 1$ **then**

for $l = 1, \ldots, i-1$ **do:**

$h_{l,i} = \hat{c}_l h_{l,i} - \hat{s}_l h_{l+1,i}$

$h_{l+1,i} = \hat{c}_l h_{l+1,i} + \hat{s}_l h_{l,i}$

enddo l

Endif

$\alpha = \sqrt{h_{i,i}^2 + h_{i+1,i}^2}$

$\hat{c}_i = h_{i,i}/\alpha$

$\hat{s}_i = -h_{i+1,i}/\alpha$

$h_{i,i} = \alpha$

$h_{i+1,i} = 0$

$s_i = \hat{c}_i s_i - \hat{s}_i s_{i+1}$

$s_{i+1} = \hat{c}_i s_{i+1} + \hat{s}_i s_i$

If $s_{i+1} \leq \varepsilon$ **then**

UPDATE

QUIT

Endif

Enddo i

UPDATE

ENDDO j

where **UPDATE** represents the code:

Solve $Hy = s$

for $l = 1, \ldots, \min(i, k)$ **do:**

$x = x + y_l v^l$

enddo l

C.2 Algorithm Orthomin(k)

BEGIN:

$x = 0$

$r = b$

For $n = 0, 1, 2, ...$**Do**

$l = \mathrm{mod}(n, k+1)$

$m = \min(n, k)$

$z = Q^{-1} r$

$u = Az$

$q^l = z$

$p^l = u$

for $i = 0, ..., m; i \neq l$ **do**

$a_i = \gamma_i(p^i, u)$

$q^l = q^l - a_i q^i$

$p^l = p^l - a_i p^i$

enddo i

$\gamma_l = 1/(p^l, p^l)$

$\omega = \gamma_l(r, p^l)$

$x = x + \omega q^l$

$r = r - \omega p^l$

if $\|r\|_2 < \varepsilon \|b\|_2$ **QUIT.**

Enddo n

C.3 Algorithm Bi-CGSTAB and Bi-CGSTAB-P

BEGIN:

$x_0 = 0$

$r_0 = b - Ax_0$

$\tilde{r}_0 = r_0$

$\rho_0 = \alpha = \omega_0 = 1$

$v_0 = p_0 = 0$

For $i = 1, 2, 3, ...$**do**

$\rho_i = (\tilde{r}_0, r_{i-1})$

$\beta = (\rho_i/\rho_{i-1})(\alpha/\omega_{i-1})$

$p_i = r_{i-1} + \beta(p_{i-1} - \omega_{i-1}v_{i-1})$

$\hat{p} = Q^{-1}p_i$

$v_i = A\hat{p}$

$\alpha = \rho_i/(\tilde{r}_0, v_i)$

$s = r_{i-1} - \alpha v_i$

$\hat{s} = Q^{-1}s$

$t = A\hat{s}$

If Bi-CGSTAB THEN

$\tilde{t} = Q^{-1}t$

$\omega_i = (\tilde{t}, \hat{s})/(\tilde{t}, \tilde{t})$

Else If Bi-CGSTAB-P THEN

$\omega_i = (t, s)/(t, t)$

Endif

$x_i = x_{i-1} + \alpha\hat{p} + \omega_i\hat{s}$

$r_i = s - \omega_i t$

if $\|r\|_2 < \varepsilon\|b\|_2$ **QUIT.**

Enddo i